

Journal of **Geophysics** Zeitschrift für **Geophysik**

Volume 62 1988

Managing Editors **W. Dieminger, G. Müller, P. Weidelt**

Editorial Board

K. M. Creer Edinburgh, Scotland
W. Dieminger Lindau, F.R.G.
C. Kisslinger Boulder, Colorado
Th. Krey Hannover, F.R.G.
G. Müller Frankfurt, F.R.G.
G. C. Reid Boulder, Colorado
U. Untiedt Münster, F.R.G.
S. Uyeda Tokyo, Japan
P. Weidelt Braunschweig, F.R.G.

Advisory Board

A. A. Ashour , Cairo	St. Müller , Zürich
H.-J. Burkhardt , Berlin	F. Neubauer , Köln
K. Fuchs , Karlsruhe	H. Neugebauer , Clausthal- Zellerfeld
N. Fukushima , Tokyo	F. Rummel , Bochum
H. Gebrande , München	S. Saxov , Aarhus
V. Haak , Berlin	U. Schmucker , Göttingen
W. Jacoby , Mainz	M. Siebert , Göttingen
T. Kirsten , Heidelberg	H. Soffel , München
I. P. Kosminskaja , Moskwa	H. Stiller , Potsdam
G. Kremser , Katlenburg-Lindau	J. Zschau , Kiel
W. Lowrie , Zürich	



Springer International

Journal of Geophysics – Zeitschrift für Geophysik

This journal was founded by the Deutsche Geophysikalische Gesellschaft on the initiative of L. Mintrop in 1924 as the Zeitschrift für Geophysik and edited by G. Angenheister from Vol. 1–18 (1944). It reappeared in 1954, edited by B. Brockamp from Vol. 19 to 26 (1960), by W. Dieminger from Vol. 27 to 33 (1961), by W. Dieminger and J. Untiedt from Vol. 34 to 44 (1968), by W. Dieminger, J. Untiedt and G. Müller from Vol. 45 to Vol. 60 (1986). After Vol. 40 (1970) the title was changed to Journal of Geophysics – Zeitschrift für Geophysik. As of Vol. 61, the journal has been edited by W. Dieminger, G. Müller and P. Weidelt.

Published: Vols. 19–39 by Physica-Verlag, Würzburg, from Vol. 40 by Springer Berlin, Heidelberg, New York, Tokyo.

Copyright

Submission of a manuscript implies that the work described has not been published before (except in the form of an abstract or as part of a published lecture, review or thesis), that it is not under consideration for publication elsewhere, that its publication has been approved by all the authors and by the responsible authorities – tacitly or explicitly – in the laboratories where the work was carried out and that, if accepted, it will not be published elsewhere in the same form, in either the same or another language, without the consent of the copyright holders. By submitting a manuscript, the authors agree that the copyright for their article is transferred to the publisher if and when the article is accepted for publication. The copyright covers the exclusive rights to reproduce and distribute the article, including reprints, photographic reproductions, microform, electronic data-base, video-disks, or any other reproductions of similar nature, and translations.

Photographic reproduction, microform, electronic data-base, video-disks, or any other reproduction of text, figures, or tables from this journal is prohibited without permission obtained from the publisher.

The use of general descriptive names, trade names, trade marks, etc., in this publication, even if the former are not specifically identified, is not to be interpreted as exempt from the relevant protective laws and regulations and may accordingly be used freely by anyone.

Special Regulations for the USA

The Article Fee Code on the first page of an article in this journal indicates the copyright owner's consent that in the USA copies may be made for personal or internal use, provided the stated fee for copying beyond that permitted by Section 107 or 108 of the United States Copyright Law is paid through the Copyright Clearance Center, Inc., 21 Congress Street, Salem, Mass. 01970, USA.

If a code does not appear, copies of the article may be made without charge, provided permission is obtained from the publisher.

The copyright owner's consent does not extend to copying for general distribution, for promotion, for creating new works, or for resale. Specific written permission must be obtained from the publisher for such copying.

Springer-Verlag Berlin Heidelberg New York Tokyo

Printed in Germany by Universitätsdruckerei H. Stürtz AG Würzburg

© Deutsche Geophysikalische Gesellschaft. München 1988

7 1988 4037

Author Index

- | | | | |
|--------------------|---------------------------|---------------------------|-------------------|
| Bahr, K. 119 | Hellweg, M. 158 | Meissner, R. 69 | Seidl, D. 158 |
| Bard, P.-Y. 38 | Herzog, M. 180 | Menges, D. 1 | Sieron, B. 69 |
| Bittner, R. 69 | Hron, F. 31 | Moczo, P. 38 | Söllner, W. 1, 69 |
| Böhnel, H. 50, 180 | Jäger, G. 50 | Negendank, J.F.W. 50, 180 | Stenger, R. 1 |
| Bopp, M. 69 | Janoth, W. 1 | Neurieder, P. 69 | Stiller, M. 1, 69 |
| Bortfeld, R.K. 69 | Junge, A. 193 | Oncescu, M.C. 62 | Tezkan, B. 109 |
| Dohr, G. 69 | Kadziaiko-Hofmohl, M. 102 | Peters, J. 128 | Thomas, R. 1, 69 |
| Dürbaum, H.-J. 69 | Kampfmann, W. 163 | Pšenčík, I. 38 | Vinnik, L.P. 138 |
| Eisbacher, G. 1 | Keller, F. 1, 69 | Reichert, C. 69 | Vollbrecht, A. 69 |
| Franke, W. 69 | Kind, R. 138 | Reismann, N. 50 | Weber, K. 69 |
| Fuchs, K. 1 | Kohnen, H. 180 | Rühl, Th. 1 | Wendt, J. 175 |
| Gebrande, H. 69 | Krohe, A. 1 | Sandmeier, K.-J. 1 | Wenzel, F. 1, 148 |
| Haverkamp, U. 50 | Kruczyk, J. 102 | Schmidt, T. 69 | Westphal, M. 102 |
| Heinrichs, T. 69 | Kümpel, H.-J. 128 | Schminke, H.-U. 50 | Wilhelm, H. 1 |
| | Lüschen, E. 1 | Schmoll, J. 69 | Zahradník, J. 31 |

Subject Index

Black Forest

Near-vertical and wide-angle seismic surveys in the Black Forest, SW Germany (Lüschen, E., et al.) 1

Electromagnetic sounding experiments in the Schwarzwald central gneiss massif (Tezkan, B.) 109

Book reviews

Book review 68

Continental crust

Near-vertical and wide-angle seismic surveys in the Black Forest, SW Germany (Lüschen, E., et al.) 1

Results of the DEKORP 4/KTB Oberpfalz deep seismic reflection investigations – DEKORP Research Group (Bortfeld, R.K., et al.) 69

A study of diffraction-like events on DEKORP 2-S by Kirchhoff theory (Kampfmann, W.) 163

Converted waves

The upper-mantle discontinuities underneath the GRF array from *P*-to-*S* converted phases (Kind, R., Vinnik, L.P.) 138

DEKORP

Results of the DEKORP 4/KTB Oberpfalz deep seismic reflection investigations – DEKORP Research Group (Bortfeld, R.K., et al.) 69

Earthquakes

On the stress tensor in Vrancea region (Oncescu, M.C.) 62

Eart tides

Investigation of non-linear tilt tides from the Charlevoix seismic zone in Quebec (Peters, J., Kümpel, H.-J.) 128

Eifel volcanism

Paleomagnetic investigation of Quaternary West Eifel volcanics (Germany): indication for increased volcanic activity during geomagnetic excursion/event? (Böhnel, H., et al.) 50

Variation of magnetic properties and oxidation state of titanomagnetites within selected alkali-basalt lava flows of the Eifel-Area, Germany (Herzog, M., et al.) 180

Electrical conductivity

Electromagnetic sounding experiments in the Schwarzwald central gneiss massif (Tezkan, B.) 109

Electromagnetic induction

Electromagnetic sounding experiments in the Schwarzwald central gneiss massif (Tezkan, B.) 109

Interpretation of the magnetotelluric impedance tensor: regional induction and local telluric distortion (Bahr, K.) 119

Analytical presentation of statistically estimated magnetotelluric transfer func-

tions by a set of polynomials (Junge, A.) 193

Explosion seismology

Near-vertical and wide-angle seismic surveys in the Black Forest, SW Germany (Lüschen, E., et al.) 1

Results of the DEKORP 4/KTB Oberpfalz deep seismic reflection investigations – DEKORP Research Group (Bortfeld, R.K., et al.) 69

Focal mechanism

On the stress tensor in Vrancea region (Oncescu, M.C.) 62

Geomagnetism

Numerical methods for *K*-scaling from digital data, applied to records from Wingst Observatory (Wendt, J.) 175

In memoriam

In memoriam 66

Kindex

Numerical methods for *K*-scaling from digital data, applied to records from Wingst Observatory (Wendt, J.) 175

Loading tides

Investigation of non-linear tilt tides from the Charlevoix seismic zone in Quebec (Peters, J., Kümpel, H.-J.) 128

Magnetotelluric transfer functions

Electromagnetic sounding experiments in the Schwarzwald central gneiss massif (Tezkan, B.) 109

Interpretation of the magnetotelluric impedance tensor: regional induction and local telluric distortion (Bahr, K.) 119
 Analytical presentation of statistically estimated magnetotelluric transfer functions by a set of polynomials (Junge, A.) 193

Migration

The relation between Born inversion and standard migration schemes (Wenzel, F.) 148

Paleomagnetism

Paleomagnetic investigation of Quaternary West Eifel volcanics (Germany): indication for increased volcanic activity during geomagnetic excursion/event? (Böhnel, H., et al.) 50

Paleomagnetism of Jurassic sediments from the western border of the Rheingraben, Alsace (France) (Kadziatko-Hofmohl, M., et al.) 102

Variation of magnetic properties and oxidation state of titanomagnetites within selected alkali-basalt lava flows of the Eifel-Area, Germany (Herzog, M., et al.) 180

Rock magnetism

Variation of magnetic properties and oxidation state of titanomagnetites within selected alkali-basalt lava flows of the Eifel-Area, Germany (Herzog, M., et al.) 180

Seismic absorption

Seismic response of two-dimensional absorbing structures by the ray method (Moczo, P., et al.) 38

Seismic ray theory

Seismic response of two-dimensional absorbing structures by the ray method (Moczo, P., et al.) 38

Seismic wave theory

The relation between Born inversion and standard migration schemes (Wenzel, F.) 148

A study of diffraction-like events on DEKORP 2-S by Kirchhoff theory (Kampfmann, W.) 163

Seismometry

Restoration of broad-band seismograms (Part II): Signal moment determination (Seidl, D., Hellweg, M.) 158

Strong ground motion

Seismic ground motion of sedimentary valleys – example La Molina, Lima, Peru (Zahradník J., Hron, F.) 31

Synthetic seismograms

Near-vertical and wide-angle seismic surveys in the Black Forest, SW Germany (Lüschen, E., et al.) 1

The upper-mantle discontinuities underneath the GRF array from *P*-to-*S* converted phases (Kind, R., Vinnik, L.P.) 138

A study of diffraction-like events on DEKORP 2-S by Kirchhoff theory (Kampfmann, W.) 163

Upper-mantle structure

The upper-mantle discontinuities underneath the GRF array from *P*-to-*S* converted phases (Kind, R., Vinnik, L.P.) 138

Journal of Geophysics Zeitschrift für Geophysik

Volume 62 Number 1 1987

Original investigations

**E. Lüschen, F. Wenzel, K.-J. Sandmeier,
D. Menges, Th. Rühl, M. Stiller, W. Janoth,
F. Keller, W. Söllner, R. Thomas, A. Krohe,
R. Stenger, K. Fuchs, H. Wilhelm, G. Eisbacher**
Near-vertical and wide-angle seismic surveys in the
Black Forest, SW Germany 1

J. Zahradník, F. Hron
Seismic ground motion of sedimentary valleys –
example La Molina, Lima, Peru 31

P. Moczo, P.-Y. Bard, I. Pšenčík
Seismic response of two-dimensional absorbing
structures by the ray method 38

**H. Böhnel, N. Reismann, G. Jäger, U. Haverkamp,
J.F.W. Negendank, H.-U. Schmincke**
Paleomagnetic investigation of Quaternary West
Eifel volcanics (Germany): indication for increased
volcanic activity during geomagnetic excursion/
event? 50

Short communication

M.C. Onescu
On the stress tensor in Vrancea region 62

In memoriam 66

Book review 68

Indexed in *Current Contents*

Evaluated and abstracted for *PHYS* on *STN*

8 Z Nat. 2148

Z 1988. 4137

09. Dez. 1987

1-3, T.1

X, 501

Niedersächsische Staats- u.
Universitätsbibliothek
Göttingen

G4



Springer International

Journal of Geophysics – Zeitschrift für Geophysik

Edited for the Deutsche Geophysikalische Gesellschaft by W. Dieminger, G. Müller, and P. Weidelt

The Journal accepts

- Review articles (invited by the editors)
- Original papers
- Short communications
- Letters to the editors
- Book reviews

in the field of Geophysics and Space Physics.

Manuscripts may be addressed to any of the Editors. For addresses see last cover page. Manuscripts should conform with the journal's accepted practice as described in the Instructions to Authors.

Copyright

Submission of a manuscript implies: that the work described has not been published before (except in the form of an abstract or as part of a published lecture, review, or thesis); that it is not under consideration for publication elsewhere; that its publication has been approved by all coauthors, if any, as well as by the responsible authorities at the institute where the work has been carried out; that, if and when the manuscript is accepted for publication, the authors agree to automatic transfer of the copyright to the society; and that the manuscript will not be published elsewhere in any language without the consent of the copyright holders. All articles published in this journal are protected by copyright, which covers the exclusive rights to reproduce and distribute the article (e.g., as offprints), as well as all translation rights. No material published in this journal may be reproduced photographically or stored on microfilm, in electronic data bases, video disks, etc., without first obtaining written permission from the publisher.

The use of general descriptive names, trade names, trademarks, etc., in this publication, even if not specifically identified, does not imply that these names are not protected by the relevant laws and regulations.

While the advice and information in this journal is believed to be true and accurate at the date of its going to press, neither the authors, the editors, nor the publisher can accept any legal responsibility for any errors or omissions that may be made. The publisher makes no warranty, express or implied, with respect to the material contained herein.

Special regulations for photocopies in the USA: Photocopies may be made for personal or in-house use beyond the limitations stipulated under Section 107 or 108 of U.S. Copyright Law, provided a fee is paid. This fee is US \$ 0.20 per page, or a minimum of US \$ 1.00 if an article contains fewer than five pages. All fees should be paid to the Copyright Clearance Center, Inc., 21 Congress Street, Salem, MA 01970, USA, stating the ISSN 0340-062X, the volume, and the first and last page numbers of each article copied. The copyright owner's consent does not include copying for general distribution, promotion, new works, or resale. In these cases, specific written permission must first be obtained from the publisher.

Subscription information

Volumes 61–62 (3 issues each) will appear in 1987.

Members. Members of the Deutsche Geophysikalische Gesellschaft are entitled to purchase the Journal for their own use at a privilege price of DM 110.00, plus carriage charges, payable with the Membership dues. Orders should be sent to the Society's office at the following address: Deutsche Geophysikalische Gesellschaft e.V., Dr. A. Bertold, Theresienstrasse 41/IV, D-8000 München 2, FRG.

North America. Annual subscription rate: Approx. US \$226.00 (single issue price: Approx. US \$ 45.00), including carriage charges. Subscriptions are entered with prepayment only. Orders should be addressed to: Springer-Verlag New York Inc. Service Center Secaucus 44 Hartz Way Secaucus, NJ 07094, USA Tel. (2 01) 3 48-40 33, Telex 0 23-125 994.

All other countries. Annual subscription rate: DM 432.00 plus carriage charges. Airmail delivery on request only. Volume price: DM 216.00, single issue price: DM 86.40, plus carriage charges. Carriage charges for SAL (Surface Airmail Lifted) to Japan, India, Australia and New Zealand are available on request. Orders can either be placed with your bookdealer or sent directly to: Springer-Verlag Heidelbergberger Platz 3 1000 Berlin 33 Tel. (0)30/82 07-1, Telex 1-83 319.

Changes of address: Allow six weeks for all changes to become effective. All communications should include both old and new addresses (with Postal Codes) and should be accompanied by a mailing label from a recent issue.

Back volumes: Prices are available on request.

Microform: Microform editions are available from: University Microfilms International 300 N. Zeeb Road Ann Arbor, MI 48106, USA

Production

Springer-Verlag
Journal Production Department II
Postfach 10 52 80
D-6900 Heidelberg 1
Federal Republic of Germany
Tel. (0)62 21/4 87-3 42, Telex 4-61 690.

Responsible for advertisements

Springer-Verlag
E. Lückermann
Heidelbergberger Platz 3
1000 Berlin 33
Tel. (0)30/8 20 71, Telex 1-85 411.

Printers

Universitätsdruckerei H. Stürtz AG Würzburg
© the Deutsche Geophysikalische Gesellschaft, München, 1987
Springer-Verlag GmbH & Co. KG
1000 Berlin 33
Printed in Germany



Springer International

*Original investigations***Near-vertical and wide-angle seismic surveys
in the Black Forest, SW Germany**E. Lüschen¹, F. Wenzel¹, K.-J. Sandmeier¹, D. Menges¹, Th. Rühl¹, M. Stiller², W. Janoth², F. Keller²,
W. Söllner², R. Thomas², A. Krohe³, R. Stenger⁴, K. Fuchs¹, H. Wilhelm¹, and G. Eisbacher³¹ Geophysikalisches Institut, Universität Karlsruhe, Hertzstrasse 16, D-7500 Karlsruhe 21, Federal Republic of Germany² Institut für Geophysik, Technische Universität Clausthal, Arnold-Sommerfeld-Strasse 1,
D-3392 Clausthal-Zellerfeld, Federal Republic of Germany³ Geologisches Institut, Universität Karlsruhe, Kaiserstrasse 12, D-7500 Karlsruhe, Federal Republic of Germany⁴ Mineralogisch-petrographisches Institut, Universität Freiburg, Albertstrasse 23b, D-7800 Freiburg,
Federal Republic of Germany

Abstract. A unified seismic exploration program, consisting of 345 km of deep reflection profiling, a 240-km refraction profile, an expanding-spread profile and near-surface high-resolution measurements, revealed a strongly differentiated crust beneath the Black Forest. The highly reflective lower crust contains numerous horizontal and dipping reflectors at depths of 13–14 km down to the crust-mantle boundary (Moho). The Moho appears as a flat and horizontal first-order discontinuity at a relatively shallow level of 25–27 km above a transparent upper mantle. In the seismic model based on near-vertical and wide-angle data, the lower crust consists of lamellae with an average thickness of about 100 m and velocity contrasts increasing with depth. The upper crust is characterized by a discontinuous pattern of mostly dipping reflectors which are related to Hercynian overthrusting and accretion and to late-Hercynian extensional faulting. A bright spot at 9.5 km depth is interpreted to be due to low-velocity material. The lower part of the upper crust appears as a relatively transparent zone which is also identified as a low-velocity zone situated directly above the laminated lower crust.

Key words: Reflection seismology – Deep-crustal reflection profiling – Refraction seismology – Hercynian crustal evolution

1 Introduction

Continental deep drilling is one of the key projects of the International Lithosphere Program (ILP) which is aimed at unravelling the dynamics and evolution of the lithosphere. The contribution of the Federal Republic of Germany consists of the continental deep-drilling program, KTB (Kontinentales Tiefbohrprogramm; Althaus et al., 1984), and the continental seismic reflection program, DEKORP (Deutsches Kontinentales Reflexionsseismik Programm; Bortfeld et al., 1985).

Deep drilling interest concentrated on two potential sites, both located within Hercynian crystalline basement complexes: the Oberpfalz (Upper Palatinate) in eastern Bavaria and the Schwarzwald (Black Forest) in southwestern

Germany. In both areas comprehensive efforts have been made to apply all kinds of geoscience investigations (Alfred-Wegener-Stiftung, 1985) for reconnaissance studies. Reflection measurements were organized within the framework of the DEKORP. In this paper we describe the contribution of seismic methods to the understanding of structural and physical properties of the Hercynian crust beneath the Black Forest in conjunction with other geophysical sounding methods. The seismic survey consisted of four types of investigations:

A) Deep reflection profiling (near-vertical incidence; Sect. 3).

B) Deep refraction profiling (long range profiles; Sect. 4, 4.1).

C) Expanding-spread profile (ESP; Sect. 4, 4.2).

D) High-resolution methods (near-surface, borehole measurements; Sect. 3.4.2).

This article deals with programs A, C and D and with a combined reflection-refraction interpretation, using other geophysical data as well. Details of the refraction experiment B can be found in Gajewski and Prodehl (1987).

The reflection network was planned to get regional structural control from a 170-km-long NS profile and spatial control of the central Black Forest region from three shorter intersecting profiles. The NS profile 8401 follows approximately the morphological axis of the Black Forest crossing the Central Schwarzwald Gneiss Complex (CSGC), which is bounded in the west by the Tertiary Rhinegraben, in the north by the southward-dipping Saxothuringian-Moldanubian suture zone, in the south by the NW-dipping “Badenweiler-Lenzkirch” crustal thrust zone and in the east by gently eastward-dipping Mesozoic sediments (Fig. 1). Two other profiles (8402, 8403) are focussed on the proposed drilling area. A fourth supplementary line (8514) was planned to study the tectonic significance and lateral extent of the “Badenweiler-Lenzkirch” zone. The profile net is connected with reflection profiles in the south (Finckh et al., 1986) and in the east (Bartelsen et al., 1982; Walther et al., 1986).

The field and processing parameters were chosen to provide good resolution throughout the entire crust. In order to link the crustal seismic sections to surface structures for their geologic-petrological interpretation, we performed

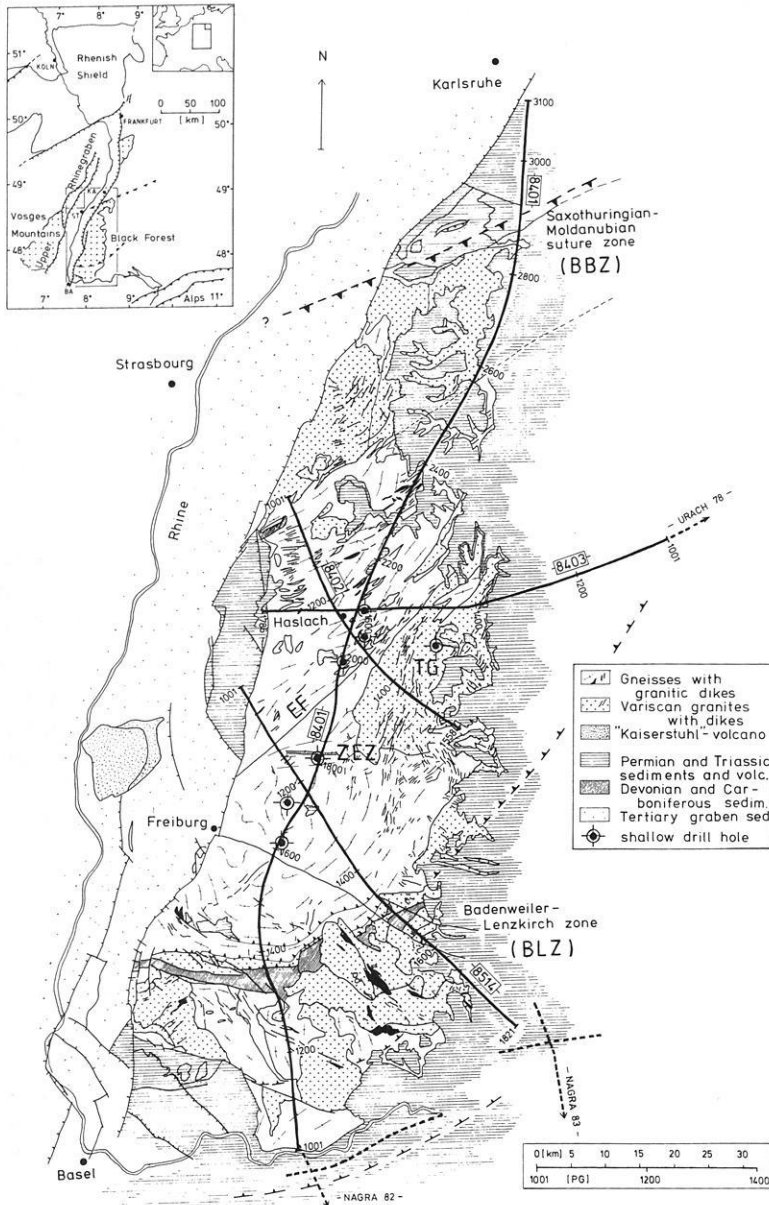


Fig. 1. Geological-tectonic map of seismic reflection profiles 8401, 8402, 8403 and 8514. The Central Schwarzwald Gneiss Complex is bounded by two Hercynian thrust zones: the Baden-Baden zone (*BBZ*) in the north (Saxothuringian-Moldanubian suture zone) and the Badenweiler-Lenzkirch zone (*BLZ*) in the south. *ZEZ* Zinken-Elme zone, *TG* Triberg Granite, *EF* Elztal Fault, *PG* geophone location

near-surface high-resolution measurements at selected sites and a systematic evaluation and tomographic inversion of first arrivals of the reflection recordings. From the interpretation of the refraction data, an outline of the two-dimensional velocity structure of the Black Forest emerged. Additional velocity information of the target area and further constraints on the physical nature of the crust were established by intensive one- and two-dimensional seismic modelling of reflection and refraction data and by an expanding-spread profile (ESP) focussed on the central Black Forest.

In the past, intensive geophysical studies in the region concentrated mainly on the Rhinegraben. Results of these studies, in particular of the seismic investigations, are documented in, e.g. Illies and Mueller (1970), Illies and Fuchs (1974), Edel et al. (1975), Prodehl et al. (1976), Illies (1981) and Zucca (1984). Fuchs et al. (1987) opened a new phase of discussion on the properties and evolution of the lower crust beneath the Rhinegraben system, relating seismic reflection results in the Rhinegraben proper (Dohr, 1970) with corresponding results described in this paper.

2 Geological and petrological environment

The Black Forest is the uplifted eastern shoulder of the Rhinegraben rift, where rocks of the Hercynian basement complex of Central Europe are exposed.

The structural zonation of the European Hercynian fold belt is described in Behr et al. (1984). It is subdivided into two external zones and one internal crystalline zone. The external Rhenohercynian and Saxothuringian zones consist of Paleozoic sedimentary rocks, volcanics and a minor proportion of crystalline blocks.

The Black Forest and Vosges are part of the internal Moldanubian zone which consists of Precambrian and Paleozoic terranes accreted during the Acadian/Hercynian orogenic cycle between the southern continent, Gondwana, and a northern continent, N. America-Europe. Thrust belts formed north and south of the internal crystalline zone. The northern belt (Saxothuringian zone, northern part of the Armorican Massif) is characterized by NW vergence of the major structures, whereas the southern belt (Mora-

vian zone, Southern Central Massif, Southern Armorican Massif) shows SE- and S-directed vergence.

During an early stage of the Acadian/Hercynian orogenic cycle, oceanic crust was subducted along both mobile belts. This event was followed by continent-continent collision in Carboniferous time (Lorenz and Nicholls, 1984; Matte, 1986). The later stage is characterized by complex wrench faulting and extensional tectonics of Basin-and-Range type.

The crystalline basement of the Black Forest consists of high-grade gneisses and migmatites intruded by Hercynian granitoids. The Paleozoic Badenweiler-Lenzkirch zone separates two crystalline blocks: the Central Schwarzwald Gneiss Complex (CSGC) and the Southern Schwarzwald Complex (SSC), which differ significantly both in their petrological and geophysical characteristics.

The CSGC consists of intensely deformed and transposed metapsammitic and metapelitic gneisses of Precambrian age.

The high-grade gneisses and migmatites of the basement complex (CSGC) display a polyphase metamorphic evolution. Numerous small bodies of eclogites (or eclogitic amphibolites), ultramafics (both spinel- and garnet-bearing serpentinites and pyroxenites) and granulitic gneisses indicate older high- and medium-pressure metamorphic events (Klein and Wimmenauer, 1984; Wimmenauer and Adam, 1985).

The Hercynian tectonic evolution of the CSGC can be documented along two NE- to ENE-trending belts of strongly deformed Paleozoic sediments and volcanics: the Baden-Baden zone in the north and the Badenweiler-Lenzkirch zone in the south. These zones represent thrust faults opposed to each other with northwestward and southeastward vergences. The Baden-Baden zone is regarded as the boundary between the Moldanubian and the Saxothuringian zone of the Hercynian fold belt. NW-directed tectonic transport is indicated by transposed foliations in weakly metamorphosed sediments which dip to the SE beneath higher-grade micaschists and gneisses. Overthrusting was followed by dextral strike-slip motions along this zone. The Badenweiler-Lenzkirch zone separates the Central Schwarzwald Gneiss Complex from the Southern Schwarzwald Complex. SE-directed tectonic transport is indicated by a 2- to 4-km-wide, strongly deformed WE-striking zone of Paleozoic sediments, metasediments, volcanics and mylonitic gneisses which dip to the NW beneath the CSGC. Sporadic fossils indicate that sedimentation occurred between around 370 and 335 Ma. In this time span the sedimentary environment changed from deep-water deposition to shallow marine and continental sedimentation (Sittig, 1969). This may be the result of considerable tectonic shortening in this time span. The mylonites and inverse metamorphic isograds demonstrate overthrusting of the hanging-wall CSGC over the sedimentary sequence to the SE. As in the Baden-Baden zone, thrust movements were followed by strike-slip motions. Within the CSGC, further convergent zones exist (e.g. Zinken-Elme zone).

Hercynian crustal evolution culminated with the emplacement of several suites of granitic plutons mostly of S-type character, the oldest of which show penetrative mylonitic/cataclastic deformation (370–335 Ma). The suite of the syn- to post-tectonic granites covers a time span of more than 70 Ma (370–290 Ma). Structural and geochemical investigations reveal the evolutionary trends both in time and space

of the various granite suites (Emmermann, 1977). Ignimbrites and rhyolites of Permian age mark the final stage of the Hercynian magmatic activity (Lippolt et al., 1983).

Late-Carboniferous to Permian intramontane troughs filled with clastic sedimentary rocks and extrusive magmatic activity indicate a change in tectonic style towards extension of the Hercynian basement during this time. Within the basement, the pattern of late-Hercynian extension is indicated by porphyric and lamprophyric dikes and by post-metamorphic cataclastic deformation within the CSGC, the SSC and within the granite plutons.

In Mesozoic time, subsidence of platform type is characterized by non-marine redbeds and shallow marine epicontinental deposits.

Due to the stress regime in the foreland of the Alpine collision zone, a system of grabens formed in the early Tertiary. Subsidence in the Rhinegraben started at 45–40 Ma. Uplift of the graben shoulders of more than 2000 m caused exposure of the Hercynian basement. Related to the rift event, the Moho rose to extremely shallow depths by updoming in the southern Rhinegraben, where a depth of 24 km is shown by intensive seismic refraction studies (Edel et al., 1975).

A specific goal of the seismic sounding was to clarify the role and extent of Hercynian thrust and extension tectonics for the entire Black Forest region and, in particular, for the central Black Forest area.

3 Seismic reflection profiling and structural image

For economic reasons and difficult terrain and permitting conditions we decided to use the Vibroseis technique, bearing in mind the convincing results of the COCORP (USA) and ECORS (France) programs for crustal reflection profiling. Explosive sources were used in additional wide-angle measurements with equipment of various research institutions, in order to get velocity control (Sect. 4).

The general goal of the geophysical reconnaissance program was to collect all kinds of data for a long N–S crustal section. Consequently, the N–S reflection profile was regarded as a key profile for studying the regional geological and tectonic setting of the Black Forest. Since COCORP started deep crustal reflection profiling in 1975, it has been demonstrated that profiles at least 100–200 km long are necessary to identify the structural-tectonic style of a crustal segment. Profile 8401, therefore, follows the morphological axis of the Black Forest along 170 km across the Central Gneiss Complex and the adjacent thrust zones: “Baden-Baden” in the north and “Badenweiler-Lenzkirch” in the south (Fig. 1). At the southern end the line joins the reflection network of northern Switzerland (Finckh et al., 1986). For three-dimensional structural control, the central target area was covered by two intersecting profiles generating a triangle of 3–4 km side length together with line 8401. Profile 8402 is about 45 km long and traverses the crystalline basement almost perpendicularly to the Hercynian strike. Profile 8403 is a prolongation of the Urach profile U 1 (Bartelsen et al., 1982) forming a 120-km E–W transect, roughly perpendicular to the Rhinegraben. It will be extended into France in 1988, crossing the Rhinegraben and the Vosges mountains, as a joint ECORS-DEKORP program.

These three profiles, 8401–8403, with a total length of 278 km were accomplished in a 3-month campaign in 1984.

Table 1. Acquisition parameters

Source	5 vibrators VVDA (14 t) on profiles 8401, 8402, 8403 and VVEA (19 t) on profile 8514		
	spacing between vibrators	20 m (8514: 10 m)	
	moveup between sweeps	6 m (8514: 2 m)	
	total source array length	146 m (8514: 48 m)	
	vibrator point (VP) spacing	80 m (8514: 40 m)	
	signal	upsweep 12–48 Hz, logarithmic, duration 20 s	
	no. of sweeps per VP	12 (8514: 5)	
	in-line offset	2 × 200 m	
	max. off-line offset	700 m	
	Receiver	no. of geophone groups	200
		group spacing	80 m
spread length		16.24 km	
spread		split spread (8514: asymmetric)	
no. of geophones (10 Hz) per group		24	
pattern		in-line, weighting uniform	
spacing between geophones		3.5 m	
Recording	total array length per group	80 m	
	equipment SERCEL 348 (8514: SERCEL 368), telemetric, automatic noise reduction		
	before correlation, correlator-stacker CS 2502		
	traces	200	
	correlation before vertical stack, sampling rate	4 ms	
	total recording time (uncorrelated)	32 s	
	correlated record length	12 s	
	vertical stacking of correlated records	12-fold (8514: 5)	
	preamplification	2 ⁷ = 42 dB	
	low-cut filter	12.5 Hz	
	high-cut filter	62.5 Hz	
Coverage	reflection	max. 100-fold	
	refraction	max. 200-fold (8514: 400-fold)	
	CDP spacing	40 m (8514: 20 m)	

A fourth profile, 65 km long (8514), was recorded in order to investigate prominent reflectors of profile 8401 in the upper crust in greater detail, particularly the northward-dipping Paleozoic “Badenweiler-Lenzkirch” thrust zone (BLZ) and its implications for the proposed drill site near Haslach (Fig. 1). This profile was recorded in November 1985.

3.1 Field survey

The field work was performed by a Vibroseis crew of the Prakla-Seismos AG company, Hannover. The routine oil-and-gas exploration crew was supplemented by additional vibrators, trucks and personnel recruited from the University of Karlsruhe who assisted in the weathering survey, in static corrections, geological mapping and in other crew operations. The total crew consisted of 57 persons and about 30 trucks, all operating within a range up to 40 km.

The field parameters (Table 1) were chosen to meet the following conditions: a multifold horizontal coverage of about 100 [as estimated from a comparative Vibroseis-explosion test on profile DEKORP 2-S; Bortfeld et al. (1985)], a CDP spacing of 40 m and a daily progress of 4–5 km; i.e. a 200-channel recording system along a 16-km spread with 80-m source and geophone group spacing had to be utilized. A symmetric split-spread with 200-m in-line offset was chosen to increase the shallow coverage and resolution. Upper-crustal resolution and velocity control by normal move-out require different spread configurations. We decided in favour of structure resolution (split-spread), while velocity control was achieved separately by an expanding-spread profile (Sect. 4.2) and by a refraction experiment also along the main N-S line [Gajewski and Prodehl (1987)

and Sect. 4.1]. A source pattern of five vibrators and 146 m length, with 10- to 12-fold vertical stacking, yielded reliable suppression of groundroll noise. A 12- to 48-Hz upsweep of 20 s length was chosen, based on a start-up test. The received signal was filtered and digitized at each geophone group consisting of an 80-m in-line array of 24 geophones and a remote box. The data were then multiplexed and telemetrically transmitted to the recording truck by a 16-km-long cable. Automatic noise rejection and full precision correlation were applied before 12-fold vertical stacking and storage on magnetic tapes.

In contrast to the explosion technique, the Vibroseis method allows choice of bandwidth of the emitted signal. In practice, however, vibrator-ground interaction may influence the spectral content of the seismic signal, depending on mechanical properties of the vibrator system and elastic properties of the ground. During the Vibroseis survey, daily similarity tests were performed under different geological and coupling conditions. The baseplate signal can be regarded as seismic source signal (Lerwill, 1981). The amplitude spectra of the similarity recordings were compared with the spectra of the field recordings acquired at the same vibrator locations. In Fig. 2 four examples are shown to demonstrate the ground-dependent differences between amplitude spectra of the pilot signal (12–48 Hz), baseplate signals of five vibrators, and five seismogram portions of 0.5 s length at different recording times.

The upper example shows an ideal broadband source spectrum, which is similar to the pilot signal showing the normal situation in the crystalline area of the Black Forest. In the other three examples of Fig. 2 resonant frequencies appear, which in most cases are low above thick Permian and Triassic sediments and high on paved roads. The stu-

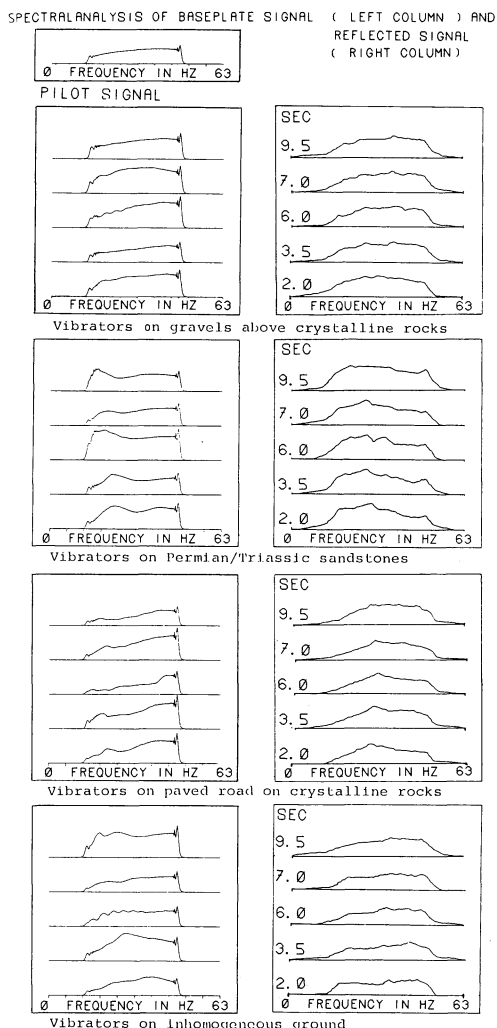


Fig. 2. Spectral analysis of baseplate signals of five vibrators from similarity tests (*left panels*) and of corresponding seismic records (*right panels*); sum spectra of high S/N ratio traces from five 1-s time sections starting at TWT indicated on left-hand side). Amplitudes are normalized, scales are linear. Pilot signal (upswep, 12–48 Hz, 20-s length) on top

udies of Vibroseis source characteristics showed that mainly broadband seismic signals resulting from favourable vibrator-ground interactions were emitted.

A detailed study of vibrator-ground interactions has been carried out by Schnell (1987), who considered the influence of the road and the near-surface geology.

3.2 Data processing

The data processing for Black Forest profiles was carried out at the DEKORP Processing Center, Institut für Geophysik, Technische Universität Clausthal. Details and problems of the processing sequence have been discussed by Bortfeld et al. (1985) regarding the DEKORP profile 2-South. True-amplitude and crooked-line processing were applied routinely and post-stack coherency-filtering optionally. The high signal/noise ratio, even in the common source gathers, is shown in Fig. 3.

Common midpoint (CMP) sorting took crooked-line geometry into account. A lateral deviation of vibrator points of up to 700 m due to terrain conditions and a slightly

bent receiver line required crooked-line processing, for which a processing line through the centre of the midpoint distribution was defined.

Stacking-velocity analysis was based on visual inspection of constant-velocity stacks of groups of 20–50 CMPs using 28 velocities in the range 4000–9760 m/s. Often, the picking of optimum velocities was hampered by the lack of continuous reflectors in the upper crust. There the quality of stacked sections could often be enhanced by unconventional, high stacking velocities (see also Sect. 6).

Figures 4–6 illustrate the different character of imaging by AGC (automatic gain control) stacking, TA (true amplitude) stacking and FD (finite difference) migration and their specific advantages, chosen from the central part of profile 8401.

For interpretational purposes, all processing modes were taken into account in order to exploit the special advantages of each section. The stacked sections reveal a better signal/noise ratio and often a better readability than the migrated sections. The AGC-stacked data, even the weaker elements whose amplitudes are below the ambient noise level, make reflections visible mostly by their coherence. The TA-stacked data allow a good estimate of the real amplitude differences and reflection coefficients. On the other hand, they show a rather heterogeneous quality within the first 2 s TWT due to varying coupling conditions at the surface.

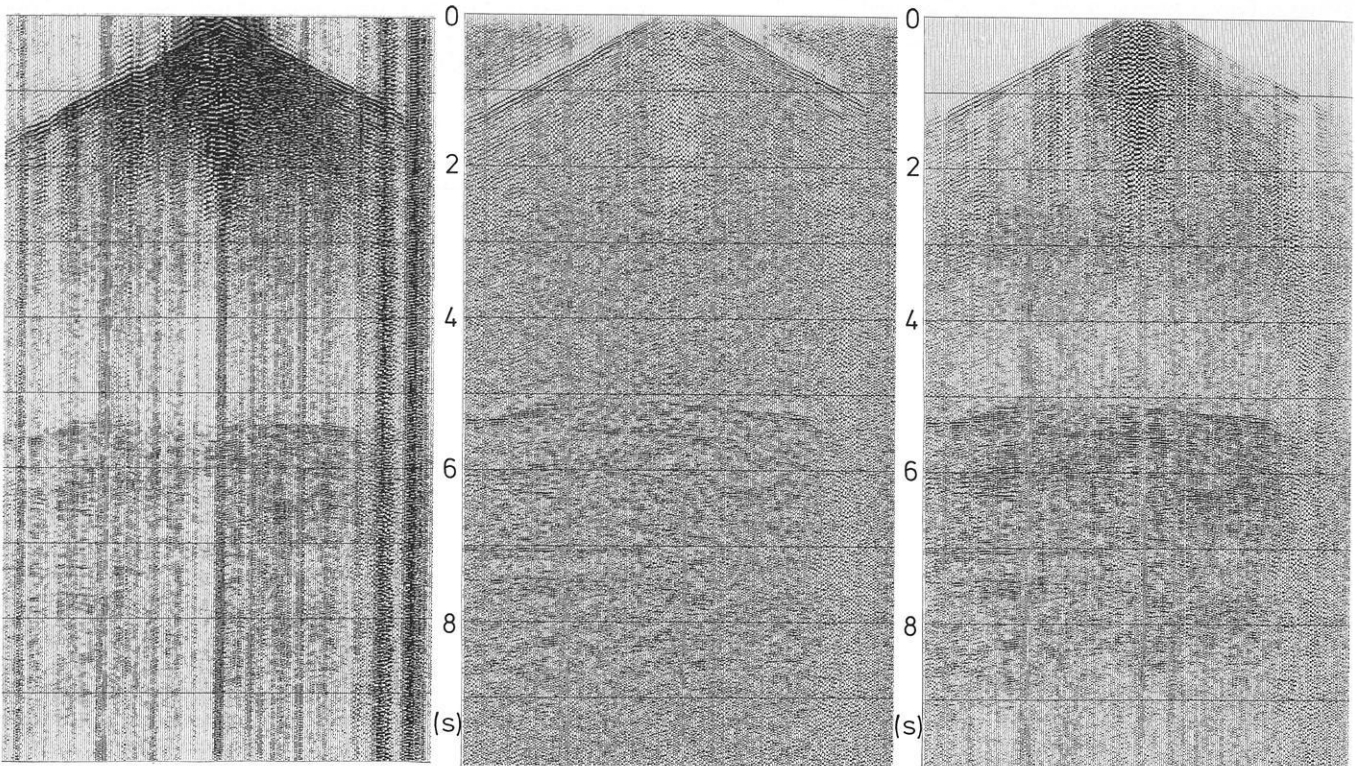
Migration corrects for structural distortions by focussing diffractions and moving dipping events to their real location. Migration often produces artificial effects known as “smiles”, especially in the deeper parts of the sections (Warner, 1987); therefore, three-dimensional control by the intersecting profiles is essential for reliable interpretation of the data.

Migration velocities were based on smoothed stack velocities. In addition to finite-difference migration, constant-velocity migrations were applied on selected portions. A high-amplitude event at a midcrustal level, which shows clear diffractions at each side, was used as a test object for migration efficiency. Based on imaging-time variation (De Vries and Berkhou, 1984), migrated sections for different migration velocities were generated in one single, recursive downward-continuation process (Fig. 7). The variation between 6220 and 5090 m/s shows that the migration process for these data is rather insensitive to velocity variations. Using the criterion of optimal focussing we determined 5700 m/s as the maximum velocity for this particular data set.

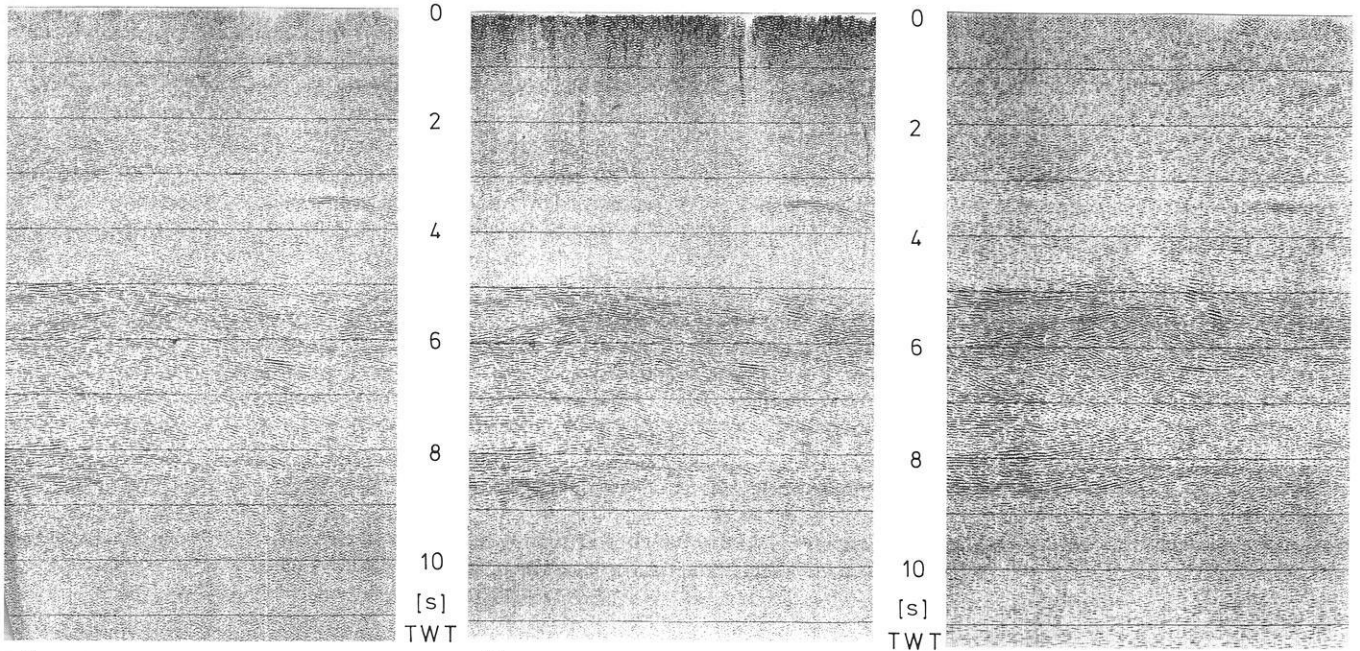
3.3 Presentation of data

Figure 8 shows a compilation of structural information obtained by the complete profile net, based on migrated sections presented as simplified line drawings.

Each line or reflection event does not necessarily represent a first-order discontinuity. Laminated zones, with a thickness below the seismic wavelength, increase the reflectivity by constructive interference of multiple internal reflections in certain frequency bands (Fuchs, 1969). The crustal structure image is dominated by a strong differentiation into a highly reflective lower crust of laminated character, between 5 and 9 s TWT, and an upper crust of lower reflection density. Figure 9 shows a selected seismogram close-up from the TA-stacked profile 8401 which demonstrates this



3



4

5

6

Fig. 3. Examples of common source gathers (profile 8401, VP 2178) in three different display and scaling modes. *Left*: original field recording without further processing; *middle*: AGC (automatic gain control)-scaled record after application of static corrections; *right*: TA (true amplitude) record. TA includes horizontal trace equalization and amplitudes are multiplied between 0 and 3 s TWT by kTe^{aT} (k constant, T travel time, a constant of absorption) to compensate for spherical divergence and absorption. The values have been assessed empirically in order to obtain a balanced seismogram. Note the strong reflections from the lower crust beginning at 5 s TWT (two-way travel time), even in single-fold seismograms. Length of spread = 16.24 km

Fig. 4. Example of a conventional AGC stack from the central part of line 8401. Note the balanced energy which is determined from a moving time window of 500 ms. Frequency filtering, bandpass characterized by lower stop – pass band frequency/upper pass – stop band frequency: 0.0–2.4 s TWT – 14–20/37–48 Hz; 2.4–4.4 s TWT – 11–18/37–48 Hz; 4.4–12.0 s TWT – 8–15/37–48 Hz. Length of section = 22.4 km

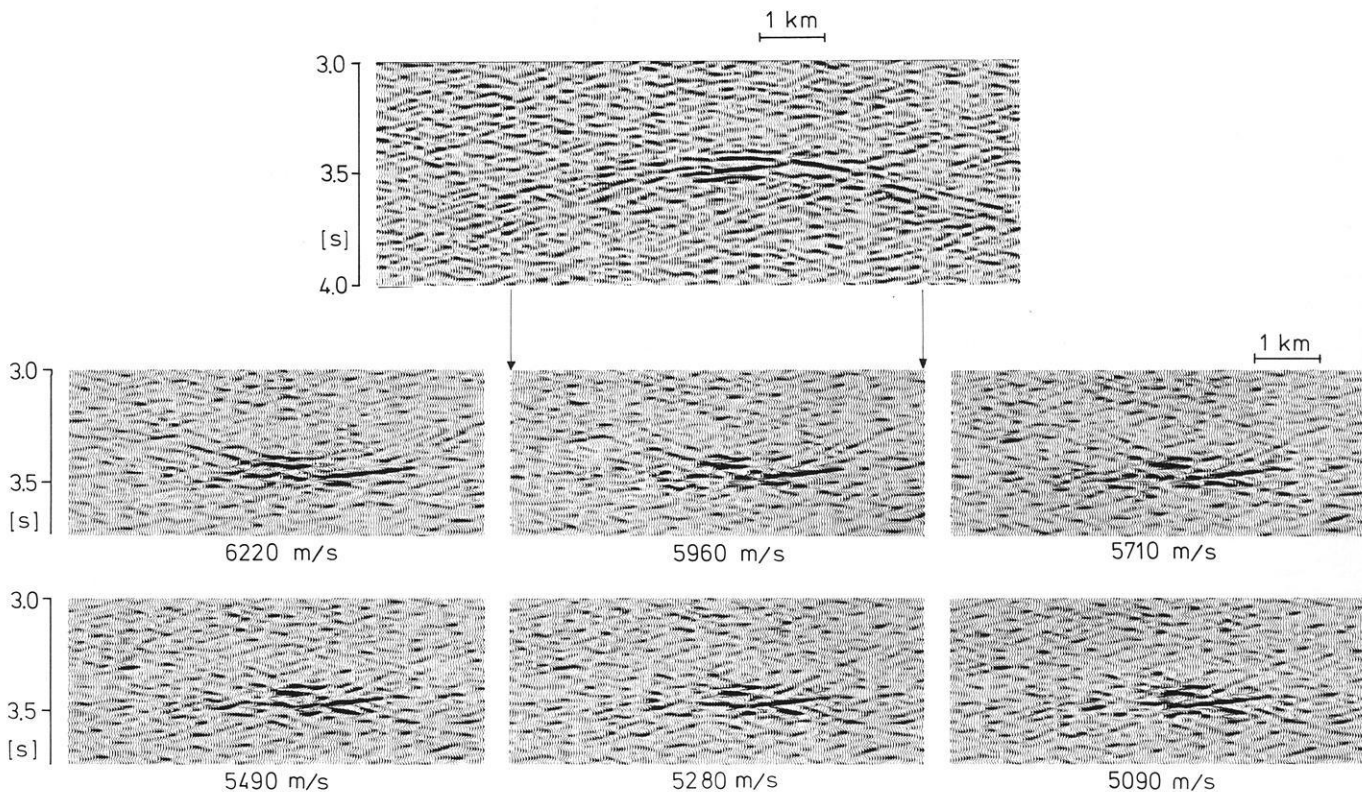


Fig. 7. Constant-velocity migrations of a high-amplitude event (bright spot) beneath Haslach (location 2070 of line 8401). Using the criterion of optimal focussing, the migration velocity of approximately 5700 m/s may be regarded as the maximum acceptable value

contrast. The lower part of the upper crust all over the profile net is characterized by a mostly transparent zone. The top of the laminated lower crust was found at an almost constant level of 5 s TWT, corresponding to a depth of 14 km with small undulations. The reflective character of the lower crust breaks down abruptly at about 8.5 s TWT, corresponding to a depth of 25.5 km with slight undulations and a relative updoming beneath the Kirchzarten basin (location 1600, 8401). This observation leads us to define the crust-mantle boundary by the deepest continuous reflectors, and which coincides with the conventional Moho defined by refraction seismics (cf. Sect. 4.1 and 7). The upper mantle is the most transparent part in the seismic sections. No significant reflection signals could be identified within the last 3 s of recording time; maximum time was 12 s, corresponding to a maximum depth of approximately 36–38 km. Figure 10 shows an example from profile 8514 which demonstrates the abrupt change of the reflectivity pattern at the Moho.

The lower crust is widely characterized by horizontally layered reflections, which are sometimes consistent over 10–20 km, with some discordant patterns of dipping elements. Smiles appear at some deeper locations: in the central part of profile 8401 (Fig. 6) and in the southeastern part of profile 8514 (Fig. 11). Locally, the lower crust also

contains transparent patterns above the Moho: for instance, in the southern part of profile 8401, at location 1500 of profile 8403 and in the northwestern part of profile 8514. Between locations 2300 and 2500 of profile 8401 (Fig. 8) the reflection energy fades out throughout the whole crust. This is probably caused by scattering of seismic energy due to an accumulation of vertically arranged fractures and dikes in the upper crust, rather than due to disturbances during data acquisition. The laminated lower crust was intensively modelled (Sect. 5) in order to derive physical constraints for petrological interpretations.

The upper crust contains mostly dipping, often cross-cutting and high-amplitude events of local character. At the northern end of profile 8401 the Rotliegend trough appears in the seismic section with some internal formations and vertical faults. In this sedimentary basin the frequency content of the seismic signals is reduced so that the laminated character of the lower crust cannot be resolved. Seismic stripping and long-term statics (cf. Sect. 3.4.1) can improve the data quality beneath the Permian sedimentary basin. In the middle and lower crust at the northern end of line 8401 a pattern of southward-dipping reflectors is clearly visible (Figs. 8 and 9); only a few reflectors penetrate the horizontally layered crust-mantle boundary. This may be a relic feature of a Hercynian thrust, possibly the Saxothur-

Fig. 5. TA stack corresponding to the section of Fig. 4. This section gives a better estimation of true reflection energy, but is of rather heterogeneous quality within the first 2 s TWT due to varying coupling conditions of detectors and sources and varying ambient noise. A horizontal scaling is included, normalizing the trace energy between 3.5 and 12.0 s TWT

Fig. 6. Finite-difference migration based on the AGC stack of Fig. 4. The curved reflector pattern in the deeper part of the section is partly due to sideswipe. The majority of these elements correspond to true dipping reflections controlled spatially by the intersecting lines 8402 and 8403

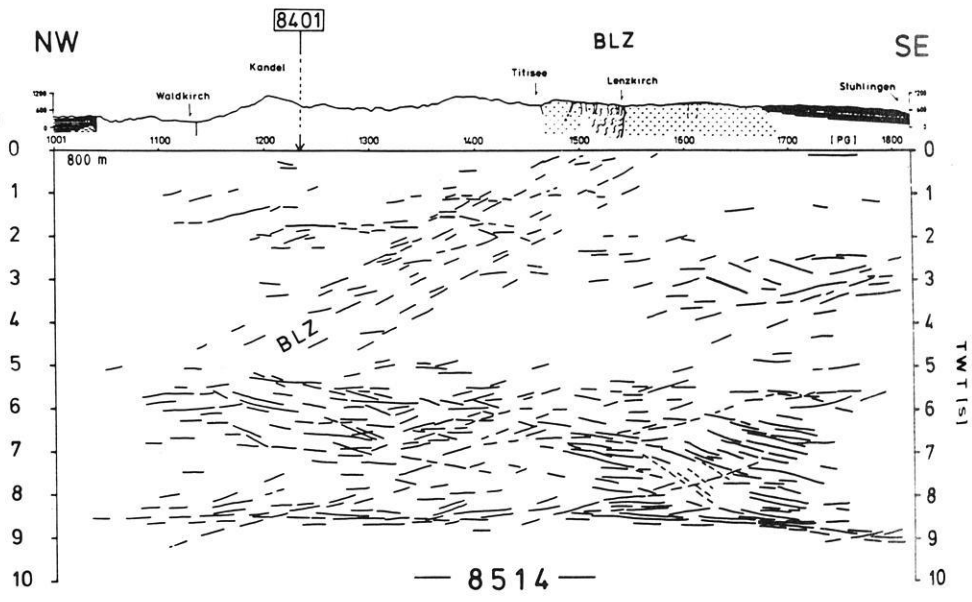
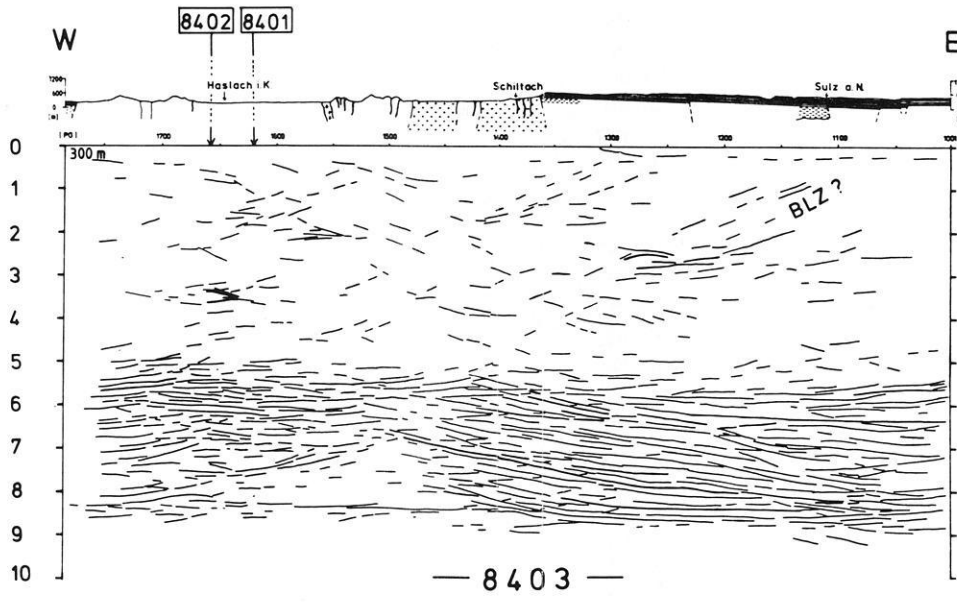
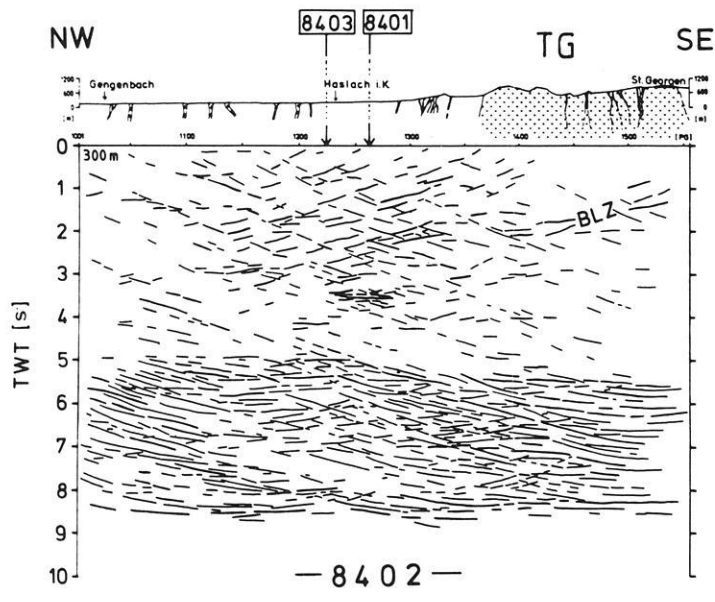
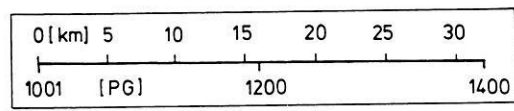
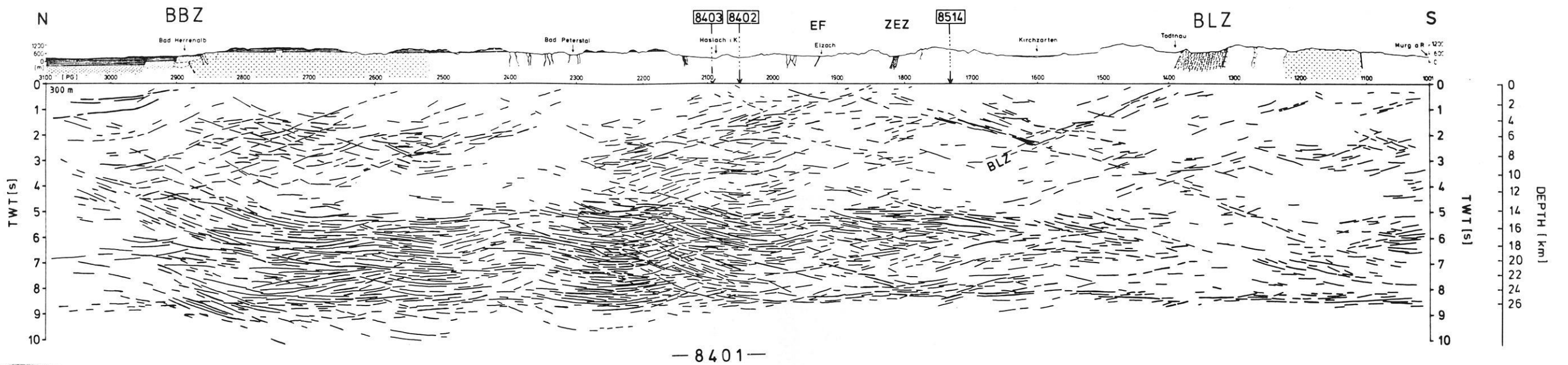


Fig. 8a. Line drawings for profiles 8401, 8402, 8403 and 8514, based on migrated sections. Lines correspond to coherent phases. The depth scale at the right-hand side of profile 8401 is derived from wide-angle data. *BBZ* Baden-Baden zone, *BLZ* Badenweiler-Lenzkirch zone, *EF* Elztal Fault, *TG* Triberg Granite, *ZEZ* Zinken-Elme zone, *PG* geophone location

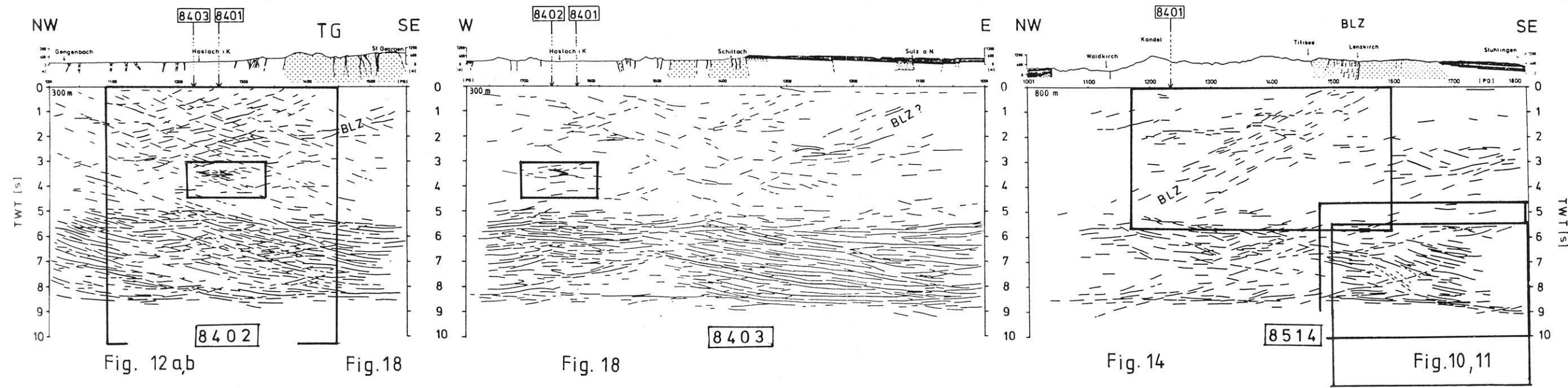
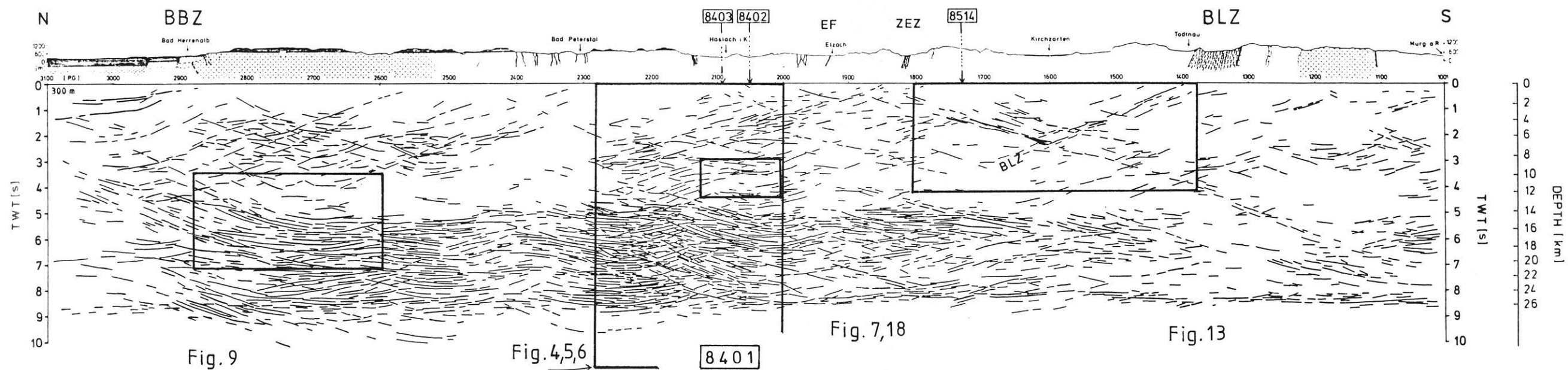


Fig. 8b. Same as Fig. 8a. Positions of seismogram sections presented in Figs. 4-7, 9-14 and 18 are marked

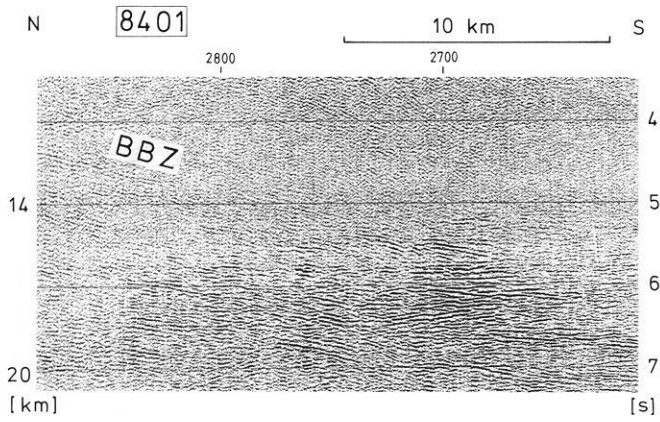


Fig. 9. Section of the TA stack from the northern part of line 8401 showing strong differentiation between the highly reflective lower crust, beginning at about 5 s TWT, and the transparent middle crust. The dipping element on the left (4–5 s TWT) may be related to the Baden-Baden thrust zone

ingian-Moldanubian suture zone of the Hercynian belt, also called the Baden-Baden zone (BBZ, Sect. 2). Further to the south, particularly in the Central Schwarzwald Gneiss Complex, a criss-cross pattern of low-angle reflectors prevails in the upper crust (compare seismogram close-ups in Figs. 4 and 5 for profile 8401 and Fig. 12a and b for profile 8402). In this area cataclastic shear zones dipping to the SE are found at the surface and which are identified as reflectors by high-resolution seismics (Sect. 3.4.2). These SE-dipping reflectors of the upper crust are interpreted as late-Hercynian extensional faults. On the other hand, north- and northwest-dipping reflectors of the criss-cross pattern can be correlated with mylonitic, ductile deformation zones associated with intraplate convergence and thrust zones of Hercynian age in the southern Black Forest (Zinken-Elme zone, ZEZ, and Badenweiler-Lenzkirch zone, BLZ).

The BLZ is a relic of a major Hercynian thrust and can be traced clearly on profiles 8401 and 8514. It dips N to NW, down to a depth of 10–12 km (Fig. 13 from

profile 8401, Fig. 14 from profile 8514), and intersects or is intersected by another reflector. This Glottertal reflector cannot be traced clearly to the surface. It shows the strongest reflection amplitudes observed in the upper crust of the Black Forest. From profiles 8401 and 8514, its strike is determined to be parallel to 8514 and its dip to be to the SSW. It is probably an extension fault related to corresponding shear zones of normal-fault character and Hercynian origin which were mapped at the surface. Recently collected seismicity data demonstrate that this reflector represents an active fault (Bonjer et al., 1986), indicating that the present stress field is released along ancient structures. Hence, brittle deformations may be responsible for the pronounced Glottertal reflections.

The criss-cross pattern of low-angle reflectors reveals that low-angle convergent and divergent structures contribute a much greater deal to the architecture of the crust than previously assumed. In accordance with geological findings (Sect. 2 and 7.2), we believe that thrusts penetrating the entire crust are overprinted by low-angle normal faults in the upper crust and by a strong horizontal ‘lamination’ in the lower crust, including the crust-mantle boundary. Alternatively, such an irregular pattern could be influenced by strong shallow velocity inhomogeneities which tend to smear out individual reflections into a complex pattern (Peddy et al., 1986). However, the persistence and continuity of lower-crustal reflectors indicate that a strong influence of distortions in the upper crust can be excluded.

3.4 Special investigations

3.4.1 Velocity structure from first arrivals. First arrivals and subsequent refracted arrivals, as well as surface waves, are systematically eliminated by the muting procedure in standard reflection data processing. This causes a lack of coverage and structural information in the topmost part of the seismic section, mainly within the first 0.5 s TWT corresponding to a depth of about 1 km. To compensate for this loss of information, the first arrivals were evaluated separately to determine in detail the lateral variation of

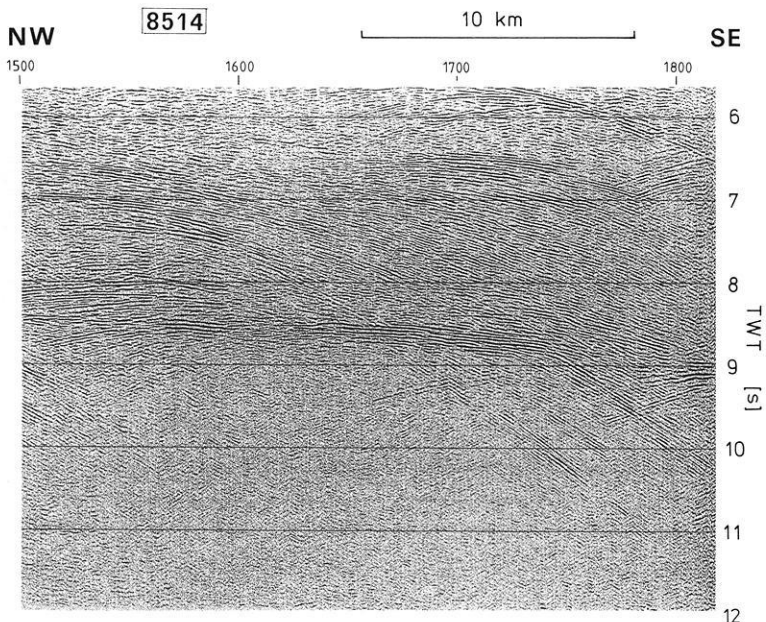


Fig. 10. Stack section from the southeastern part of line 8514. Note the strong reflections in the lower crust and, in particular, the strong continuous reflection from the crust-mantle boundary. This section is dominated by diffractions, even for more than 9 s TWT, having their apices in the lower crust. Diffractions originating at the crust-mantle boundary (e.g. on the right side) indicate vertical steps or small-scale undulations

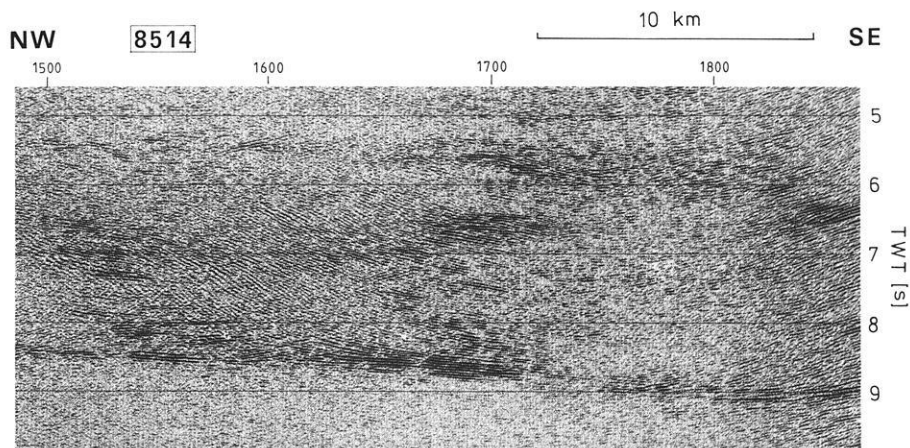


Fig. 11. Migration of stack section from Fig. 10. Note that deep diffractions are focussed mostly at their source structures. Also, migration produces artificial, curved elements (6–8 s TWT)

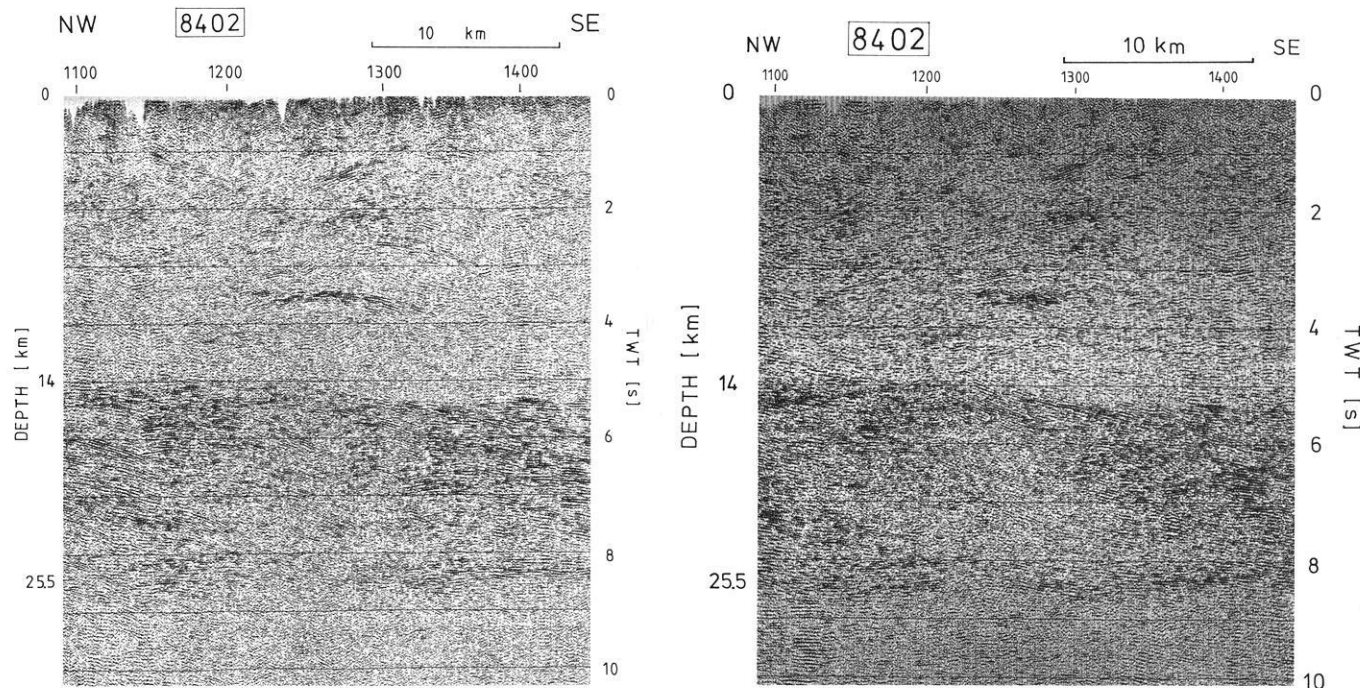


Fig. 12. Stacked section (a) and migrated section (b) of the central part of profile 8402 within the intersection area of profiles 8401–8403 near Haslach; bright spot at 3.5 s TWT

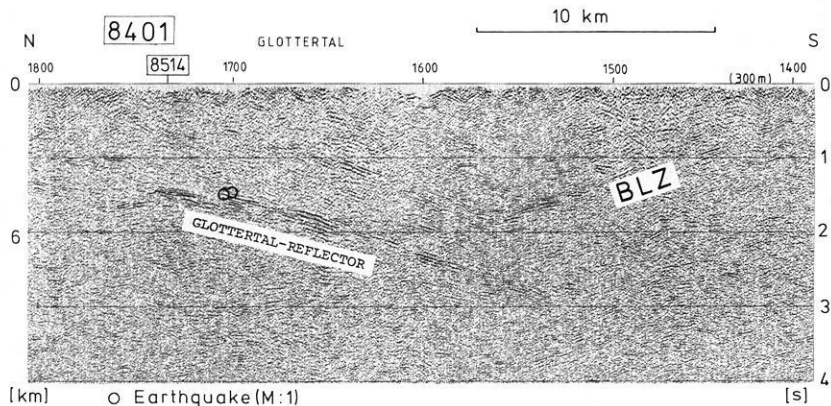
velocity structure for the upper 2 km. The refraction technique benefits from the extremely high data redundancy that reaches a maximum coverage of nearly 200 for each subsurface point.

The first arrivals of selected high-gain field records were picked manually and transferred to travel-time-distance plots. The “plus-minus” method of Hagedoorn (1959) was applied graphically to determine the laterally varying refractor velocity of the crystalline basement and its depth. Short refraction lines (weathering surveys) were carried out additionally at spacings of about 2 km to obtain information about the thickness and the velocity of the weathering zone and to control the intercept times and to calibrate the first arrivals of the Vibroseis data, since an in-line offset of 200 m of the Vibroseis split-spread geometry had to be bridged.

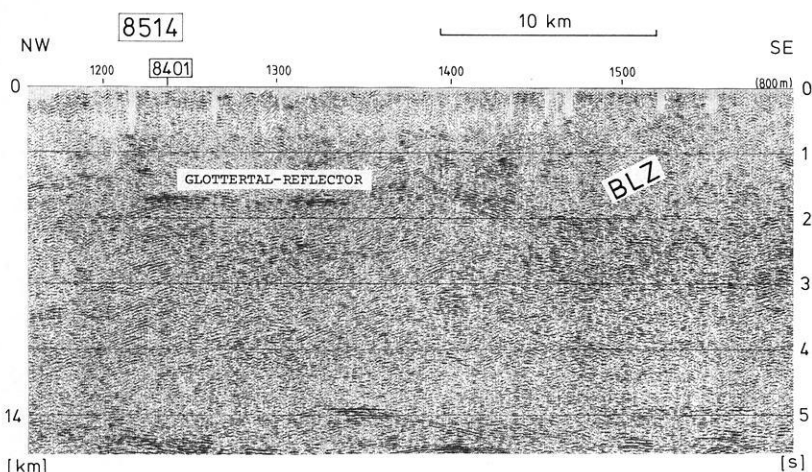
Basic static corrections were computed based on the results of the “plus-minus” method, topographic data and

the interpolated results of the weathering survey. Statistical improvement of these static corrections (Fromm, 1984) was obtained by automatic evaluation of first arrivals. Short-period perturbations on the travel-time curves were transformed into delay times of the weathering layer, which were added to the basic corrections. Static corrections included an offset correction and were computed for a reference level of 300 m above mean sea level (profile 8514: 800 m).

Although surface rocks are composed of crystalline basement, gneiss or granite with occasional cover of a few metres of Quaternary deposits, the evaluation of the refraction data clearly shows a considerable thickness of low-velocity material varying between 2000 and 3500 m/s and with thicknesses between 50 and 300 m (see upper parts of sections in Fig. 16). This is probably due to lateral variations of rock weathering. The refractor velocity of the “solid” basement varies between 5000 and 5700 m/s. In Fig. 15 these velocities are related to different petrological assem-



13



14

Fig. 13. Upper-crustal reflections from a southern part of the stacked line 8401. The northward-dipping elements on the right-hand side are connected with the Badenweiler-Lenzkirch thrust zone (*BLZ*). The southward-dipping prominent Glottertal reflector is interpreted as a low-angle normal fault. An earthquake sequence is located within this element (Bonjer et al., 1986). Precision of location is ± 100 m. Focal mechanism is of shallow thrust type. Three-dimensional control is provided by the intersecting line 8514 (cf. Fig. 14)

Fig. 14. Part of the stacked profile 8514. The Glottertal and Badenweiler-Lenzkirch elements are delineated in a NW-SE direction allowing a reconstruction of dip and strike with the aid of profile 8401. The Glottertal reflector dips to SSW and strikes NW-SE. The surface trace of the *BLZ* is curved (cf. location map, Fig. 1). Its dip of about 30° can be followed to a depth of about 12 km

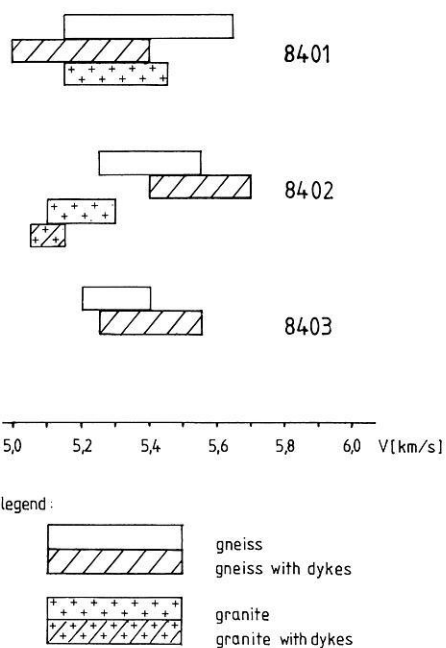


Fig. 15. Representative basement velocities for zone beneath weathering layer derived from first arrivals of Vibroseis field recordings. Length of bars corresponds to standard deviation of the mean values

blages which are documented by abundant exposures. Generally, granites tend to have lower velocities than gneisses. If associated with granitic dikes, both units show a relatively wide scattering of velocities. This might be explained by an azimuthal velocity dependence on the strike directions of the dikes with respect to the orientation of the profiles.

To investigate the velocity structure of the uppermost crust in greater detail, the complete set of first arrivals was picked by using the single channel algorithm (Ketelsen et al., 1983). This data set provides a maximum 200-fold coverage which is on average reduced to about 70- to 100-fold because of missing vibrator stations and missing picked values. The travel-time distance curves were inverted by different techniques (Giese, 1976; Slichter, 1932) yielding velocity-depth functions. As the most powerful and economical method, the maximum depth estimation method of Slichter (1932), making use of the triple data set comprising distance, travel time and apparent velocity, was used for preference.

Computations with synthetic, even laterally varying, models have demonstrated the reliability of this method. The high redundancy of velocity-depth data was used to smooth the velocity structure by averaging. Its reference level is the topography of the seismic basement (Fig. 16). A CMP-sorting technique (Gebrande, 1986) was applied but gave no further improvement. Another approach to control the velocity structure is the application of iterative

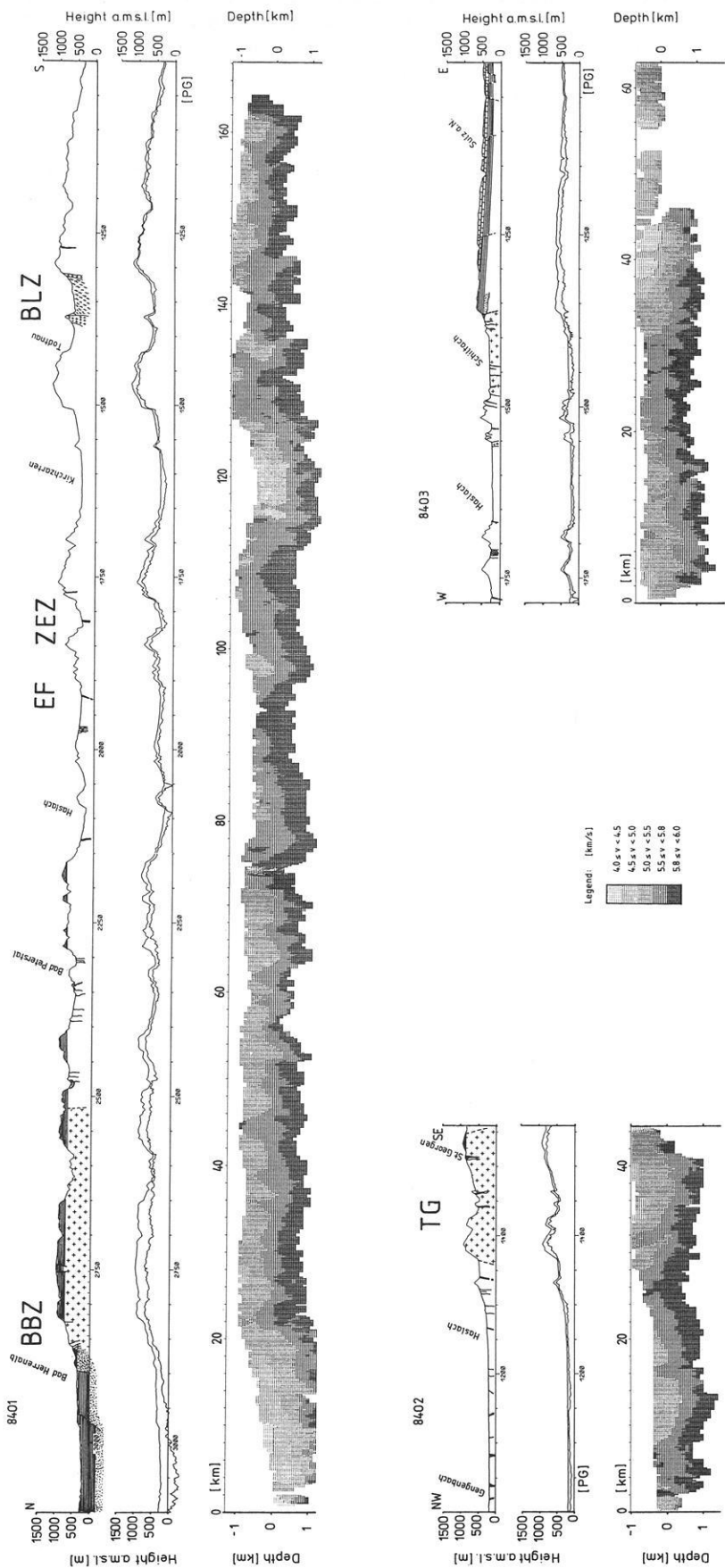


Fig. 16. Evaluation of the Vibroseis first arrivals for profiles 8401, 8402 and 8403. *Upper sections*: surface geology; *crosses*: granites; *white*: gneisses (with dikes); *other signatures*: Permian rocks and Paleozoic sediments of the Badenweiler-Lenzkirch zone. *Intermediate sections*: thickness of the weathering zone (heterogeneous, velocities of 2000–3500 m/s); *upper line* – topography, *lower line* – seismic basement. *Lower sections*: two-dimensional velocity structure of the basement. For velocities, see legend. Vertical exaggeration of topography is 4

tomographic methods (e.g. Gordon et al., 1970; Censor, 1983) which provide a velocity image directly from travel-time. The results correspond to those obtained by the Slichter-Method with only slight improvements (Rühl, 1987).

The velocity sections of Fig. 16 (lower parts) display considerable lateral variation of the velocity structure, ranging from 4000 to 6000 m/s. The lower velocities clearly correlate with a Permian and Triassic sedimentary cover in the northern part of profile 8401 and in the eastern part of profile 8403. Some conspicuous correlations between known petrological complexes are obvious. On profile 8401 higher-velocity material updomes in the core of the central complex of gneisses and anatexites. The section of profile 8402 reflects a significant velocity difference between the Triberg granite (5200 ± 100 m/s) and the gneisses (5400 ± 150 m/s, cf. Fig. 15) and a synclinal basin within the gneisses. High near-surface velocities at km 5 and 25 of profile 8402, km 25 of profile 8403, km 92 and 108 of profile 8401 correlate with belts of granulitic gneisses and mylonites (Hacker and Hirschmann, 1986).

In addition to geological interpretations, the assessment of long-term statics offers an important practical application. Based on the velocity model of Fig. 16, long-term effects of the order of 20–30 ms (comparable to a seismic period) were estimated within a CMP gather using a deeper reference level. These statics have not yet been applied to the data presented in this paper.

3.4.2 Seismic probing of near-surface crystalline rocks. One important but indirect approach to explain the nature of deep crustal reflectors is sophisticated modelling that estimates the physical parameters as described in Sect. 5.

As another approach, in-situ probing of seismic reflectors in crystalline rocks has been attained through geophysical logging tools and vertical seismic profiling (VSP) in a series of boreholes, and through their correlation with structures and lithologies of the cored rocks. The borehole studies were complemented by near-surface reflection and refraction profiles of high resolution in order to link deep seismic sections to known near-surface structures and lithology. Out of a great variety of seismic imaging tools and widespread resolution capabilities applied at different sites in the central Black Forest, two are presented in this paper.

For the investigations, a car-mounted high-pressure pneumatic hammer was used at 20-m intervals for generating compressional (P) waves and horizontally polarized shear waves (SH). Twenty-four receiver arrays of vertical geophones or, alternatively, horizontal geophones for SH recording, were deployed at 10-m intervals. Recording with a 24-channel digital signal-enhancement unit deployed in off-end geometry yielded a 6-fold coverage with CMP spacing of 5 m. The daily progress was 600–800 m.

First arrivals and refraction lines yield P velocities of 600 m/s (SH : 340 m/s) in the upper few metres and basement velocities increasing from 2800 to 4200 m/s (SH : 1700–2000 m/s) in the upper 50 m. In P - and SH -reflection sections near Haslach an interrupted reflection can be traced over the complete sections, dipping 30° – 40° to the east. This reflection can be traced upward into a cataclastic zone related to a low-angle normal fault. This fault could thus be followed from the outcrop to a depth of about 700 m by this shallow reflection survey. Comparison with the deep reflection section 8402 (Sect. 3.3, Fig. 12) shows

a continuation of this fault reflector to a system of reflectors which, dipping to the SE, penetrate the entire upper crust. We therefore interpret these and similar reflectors as indicators of late-Hercynian extension (cf. Sect. 7.2). However, in general, the shallow seismic sections show weak amplitudes and little consistency of reflectors, especially when using SH waves. This may be a consequence of complicated ductile folding and metamorphic transposition on a scale less than the seismic wavelength (P : 40–100 m, SH : 40–130 m), which might also account for the relative transparency and complexity of the entire upper crust.

Figure 17 shows an example for a data compilation for the “Hechtsberg” well (300-m depth) near Haslach. The original VSP record section displays the downgoing direct wave and the tube wave. The averaged P -wave velocity decreases from top to bottom from 5400 to 4400 m/s, which is confirmed by the sonic log. This corresponds to a petrographic change (decrease of mafic constituents, decrease of degree of foliation) from orthogneisses to paragneisses. The upgoing wavefield delineates a sequence of reflections which can be correlated with sudden velocity breaks in the sonic log and with structural and petrographic variations revealed by the core evaluation. At 290 m depth, a strong reflection corresponds to a cataclastic shear zone which is interpreted as a late-Hercynian extensional fault zone. It is probably connected to a similar zone outcropping about 500 m north of the borehole.

3.4.3 Haslach “bright spot”. An isolated reflection event beneath Haslach at about 9.5 km depth, which looks like a bright spot (Sheriff and Geldart, 1983), is located beneath the crossing area of three profiles near Haslach (cf. Fig. 12). Therefore, good three-dimensional control exists for stacked and migrated sections. They are presented in Fig. 18, together with a position map indicating the lateral extent of 3–5 km. The reflection amplitudes observed in true-amplitude sections are comparable to those of prominent reflections from the lower crust.

In view of the strong reflections from the bright spot, even in single-fold seismograms (source-point gathers), we tried to determine the polarity of the reflection coefficient. Single-fold uncorrected seismograms from source-point gathers were plotted in wiggle-area mode in two ways. Positive and negative values, respectively, above a certain threshold value were blackened and then compared to each other (Fig. 19). In traces with a high signal/noise ratio we may visually identify a symmetrical form of a Klauder wavelet consisting of a main lobe and two side lobes. This waveform represents a negative polarity of the reflection. The inspection of a variety of source-point gathers shows that wherever a Klauder wavelet can be recognized, its polarity is negative. This observation indicates that if the reflection is from a single interface, then it is caused by material of lower impedance than the surrounding medium. A velocity of 5.4–5.5 km/s of the surrounding medium is obtained from wide-angle experiments (see Sect. 4.1). Therefore, a velocity clearly below 5.4 km/s must be associated with material causing high-amplitude reflections with negative polarity. A possible explanation might be a concentration of trapped fluid. Its origin could be related to dehydration of Hercynian-age overthrusting of “wet” sediments. A similar bright spot appears on section 8514 (location 1350, 5 s TWT, cf. Fig. 14). The strong reflection amplitudes could result from contact between impervious rocks

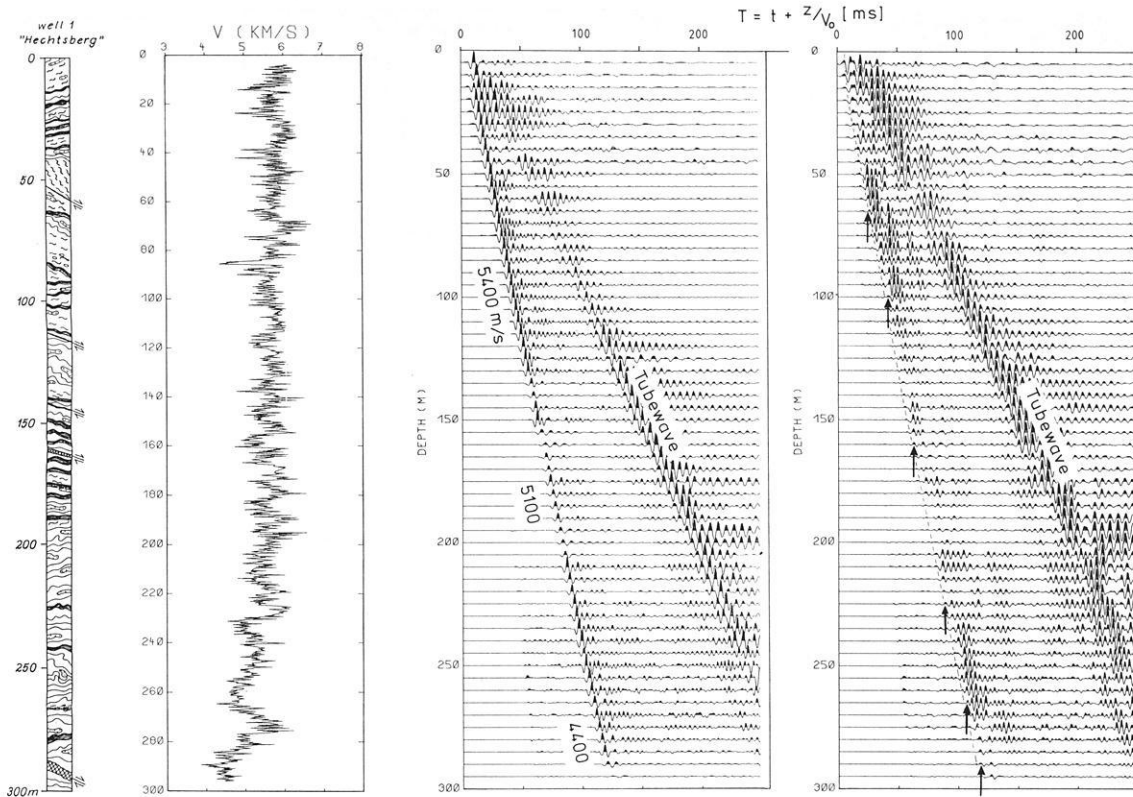


Fig. 17. Borehole data of “Hechtsberg” site. From left to right: – Structures and lithology derived from cores (simplified). Different gneisses and shear zones indicated. – Sonic log (digitized from analog data of Vogelsang, 1986). – Vertical seismic profiling (original data, vertical component). Clearly recognizable is the direct wave (labelled by corresponding velocities) and the tube wave. Note modified time scale. – Upgoing wavefield after application of a f - k filter. Note strong reflections, particularly from a cataclastic shear zone (depth 280 m). Arrows indicate reflections

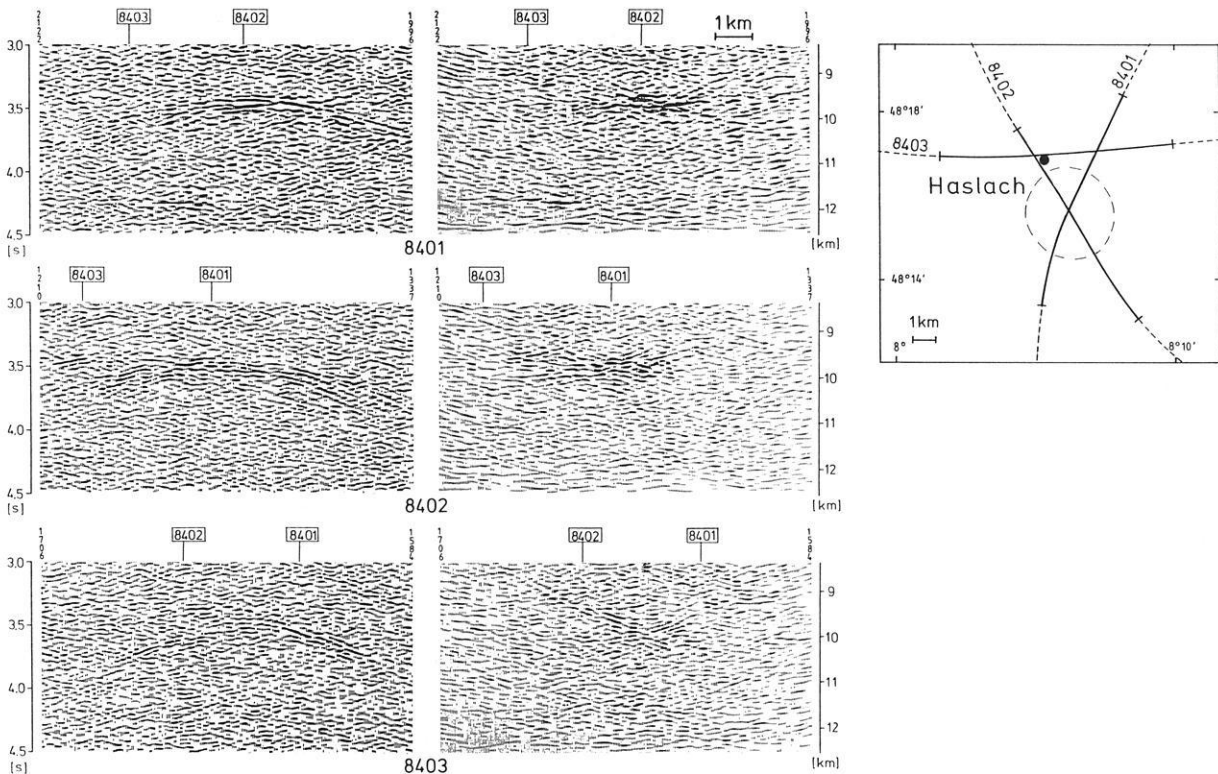


Fig. 18. Haslach “bright spot” represented by stacked (left) and migrated sections (right) of profiles 8401, 8402, 8403. Migration velocity 5700 m/s. Position sketch shows location and extent of the high-amplitude event (dashed oval). Point marks Haslach village

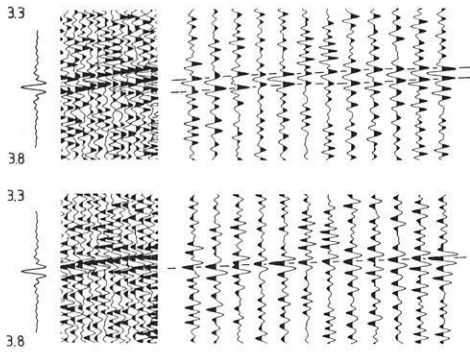


Fig. 19. Single-fold seismicograms (line 8402) of the Haslach "bright spot" between 3.3 and 3.8 s TWT. Twelve traces are plotted with different spacings. In the *upper part*, the positive values are blackened; in the *lower part*, the negative ones. The theoretical Klauder wavelet with negative polarity is shown on the *left-hand side*. Positive values correspond to compression at the surface. The signals exhibit negative polarity because maximum correlation appears to the left

and rocks with fluid-filled porosity. Lower crust or mantle-derived gases (CO_2 , H_2O) may be trapped in addition to, or alternatively to, fluids from underthrust sediments.

Similar bright spots were found in recent COCORP surveys (Brown et al., 1986). They are typically at midcrustal levels and can be of variable origin. Morton and Sleep (1985) inferred a magma chamber beneath an actively spreading back-arc basin from similar phenomena.

4 Velocity control by refraction and wide-angle reflection measurements

Whereas near-vertical reflection profiling provides detailed images of crustal structure, the reliability of the resulting velocity information is usually poor. For instance, the analysis of stacking velocities alone gives no hint of a low-velocity zone in the middle crust. Therefore, additional wide-angle measurements are required to determine the velocity needed for time-depth conversion and petrological interpretations. A gross two-dimensional velocity distribution was derived from refraction profiles. Expanding-spread soundings, focussed on the potential drilling site, were performed to deliver a high-precision velocity-depth distribution. In addition, a wide-angle Vibroseis experiment under-shooting the Rhinegraben yielded velocity control for the adjacent graben proper and served to prepare a feasibility study for the Rhinegraben experiment in 1988 (Damotte et al., 1987).

4.1 Refraction profile

In August 1984 the Black Forest was studied by a seismic refraction survey along a 240-km NS profile from its northern end to the Swiss Molasse Basin (Gajewski and Prodehl, 1987; Fig. 20). Five shots, offset by 30–40 km, were recorded with stations spaced between 1.5 and 2 km apart. The geometry was designed to resolve a two-dimensional velocity distribution. The velocity model, displayed in Fig. 32, is essentially based on the correlation of the P_G wave diving through the uppermost crust, reflections P_L from the top of the lower crust and P_M from the crust-mantle boundary. The model was successively improved

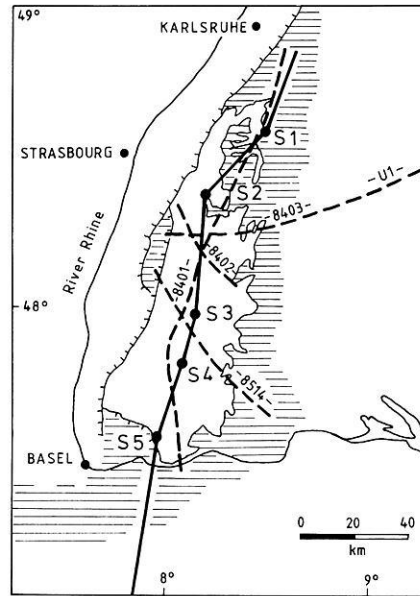


Fig. 20. Location map showing reflection profiles and the NS refraction profile. *Black circles* are shotpoints observed to both sides with receiver spacings of 1.5–2.0 km (from Gajewski and Prodehl, 1987)

by synthetic seismicograms based on two-dimensional asymptotic ray theory (Gajewski and Prodehl, 1987).

The main finding is a low-velocity zone (5.4–5.5 km/s) which is pronounced in the northern and central Black Forest and which fades out to the south. It is located directly on top of the lower crust which has an average velocity of 6.6 km/s. The top of the lower crust is at a depth of 14–15 km beneath the central Black Forest. In this model the crust-mantle boundary appears as a first-order discontinuity and does not show any major depth variations north of the Swiss Molasse Basin.

The refraction line and the NS reflection profile 8401 practically coincide. Structural features observed in near-vertical reflection sections and velocity information inferred from wide-angle measurements were jointly evaluated.

4.2 Expanding-spread profile

From the results of the refraction and reflection profiles, the region around Haslach appeared as typical normal Moldanubian crust right in the centre between two large thrust zones (Baden-Baden zone in the north and Badenweiler-Lenzkirch zone in the south). It was therefore decided to explore this crustal section and its velocity structure by an expanding-spread profile (ESP). The principal goals of this experiment were:

- 1) To investigate the nature of the bright spot at about 9.5 km depth (see Sect. 3.4.3).
- 2) To determine the average velocities in the upper crust and the entire crust for precise time-depth conversions.
- 3) To investigate the wide-angle characteristics of the lamellar lower-crustal reflections.

Our intention was to get high-resolution observations in the wide-angle range, comparable to the resolution of the near-vertical recordings. Small explosive charges of 10–50 kg were used as sources, distributed in patterns of 30–50 shallow drillholes (depth 2–3 m) in crystalline rock.

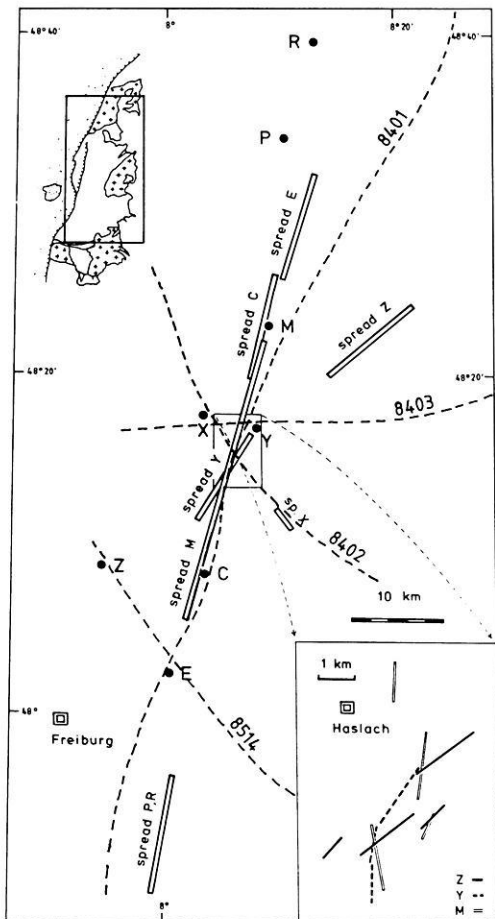


Fig. 21. Schematic map of the "expanding-spread" profile with shotpoints and corresponding geophone layouts consisting of four independent digital recording units. The inset shows the blown-up central region with true midpoint configurations for shots *M*, *Y* and *Z* covering the lateral extent of the Haslach "bright spot". The map also shows the location of reflection profiles

This arrangement produced a broadband signal with dominant frequencies between 20 and 30 Hz. Shot *R* in the north (Fig. 21) was fired in a similar arrangement and with 60-kg charge in a small pond. The recording spread consisted of 144 channels spaced 80 m apart, enabling exact phase correlation; whereas in the refraction experiment (Sect. 4.1), a spacing of 1.5–2.0 km was used.

The field experiment was performed in October 1985. The locations and corresponding geophone spreads, together with common midpoint ranges of some selected recordings (shots *M*, *Y* and *Z*), are given in Fig. 21. In total, eight different shotpoints were chosen for data evaluation. The recordings from shotpoints *Y* and *Z* are shown in Figs. 22 and 23. In both seismogram sections a clear P_G phase from the first arrivals can be identified. Phases reflected from the bright spot at about 9.5 km depth (phase P_B) can only be correlated in the record section of shot *Y* in the near-vertical range. It is followed by a band of strong reflections from the laminated lower crust, beginning with phase P_L caused by the same laminated structure seen in near-vertical sections. With the small geophone spacing of 80 m, it is possible to correlate individual phases over 400–1500 m. Consequently, the lateral extent of single lamellae is of the order of 200–800 m (see also Sect. 5.2).

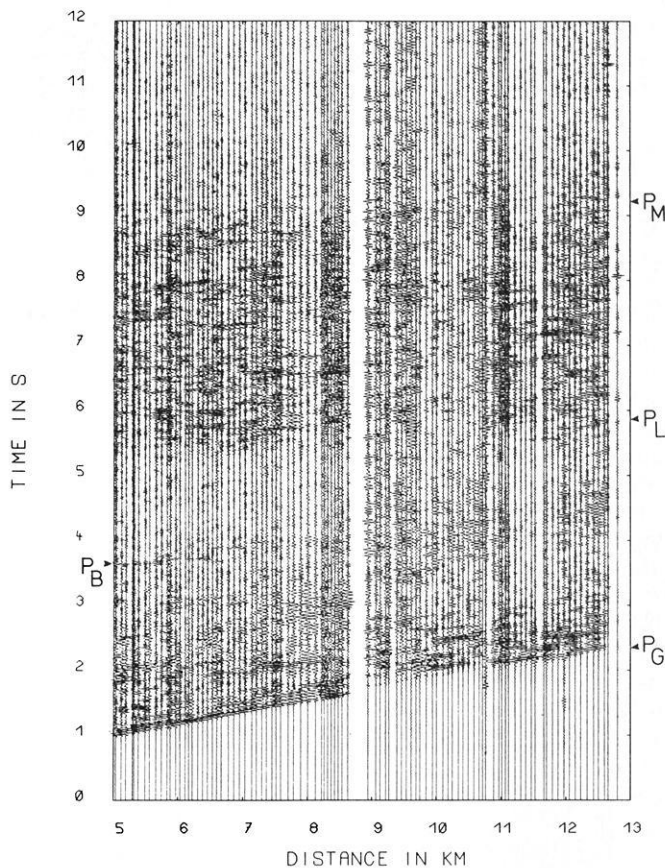


Fig. 22. Section of shotpoint *Y* observed by three multichannel digital recording units in the offset range 5–13 km. Time scale is unreduced. P_G – first arrivals from crystalline diving wave, followed by upper-crustal reflections of local character. P_B – bright spot phase. These signals are missing at greater offsets (cf. Fig. 23). P_L – first of lower-crustal reflections. P_M – latest reflections which correlate with the Moho phase from refraction survey and from modelling. Amplitudes are normalized for each trace

By contrast, in the refraction profile with a geophone spacing of 1.5–2.0 km, these small-scale reflecting structures cannot be resolved. Therefore, a correlation in widely spaced refraction measurements is subject to spatial aliasing simulating large-scale structures.

From the geometric configuration of the expanding-spread profile, the average velocity down to the first lamellae of the lower crust is determined using the T^2-X^2 diagram for the combined sections of shots *M*, *Y* and *Z* (Fig. 24). The slope of the solid straight line fitting the beginning of lower-crustal reflections yields an average velocity of 5.62 km/s. The error bounds are not more than $\pm 2\%$, taking vertical two-way travel times and travel times of reflections at individual common midpoints from the original data set into account. The sensitivity of this procedure is demonstrated by the dashed lines in Fig. 24, corresponding to a velocity increase of 0.1 and 0.2 km/s. This approach is only valid for a homogeneous medium. In a stratified medium this is an approximate procedure, and velocity and depth do not necessarily coincide with the true RMS values. For the upper crust we studied the possible variations by comparing the true and the apparent RMS velocities for a variety of realistic models. We never found deviations larger than 0.02 km/s. The average velocity of 5.62 km/s \pm

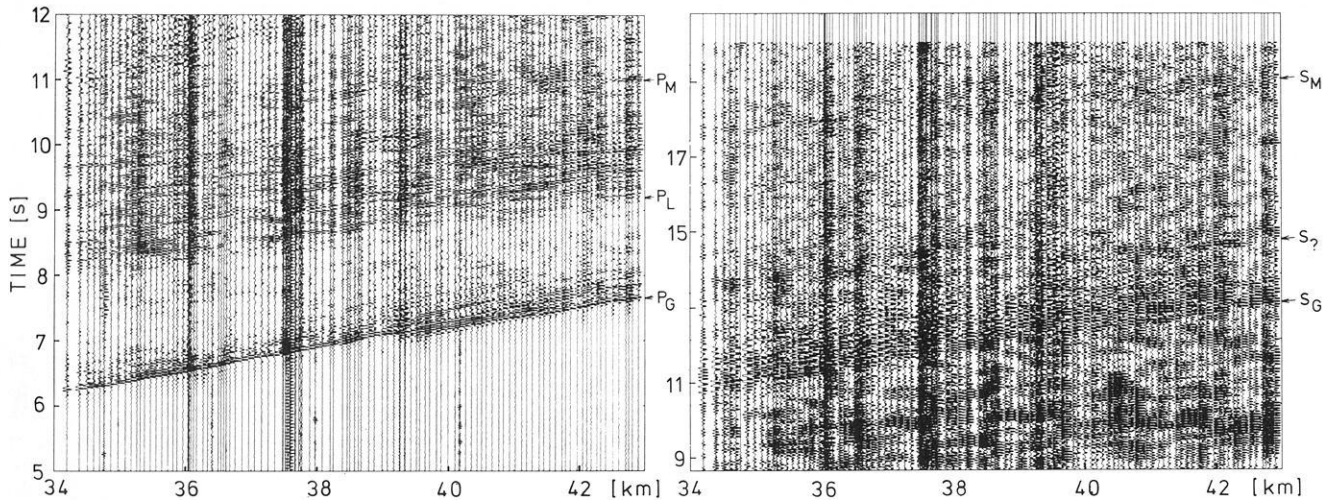


Fig. 23. Section from shotpoint Z with offset range 34–43 km. The *left part* shows compressional-wave arrivals P_G , P_L , P_M (cf. Fig. 22). The *right part* is from the same recording with a time scale multiplied by $\sqrt{3}$. Coherent phases can be compared with corresponding P phases. S_G and S_M are clearly identified as shear waves. The S_7 phase can be alternatively interpreted as S_L or as a converted phase (S_MP) from the crust-mantle boundary

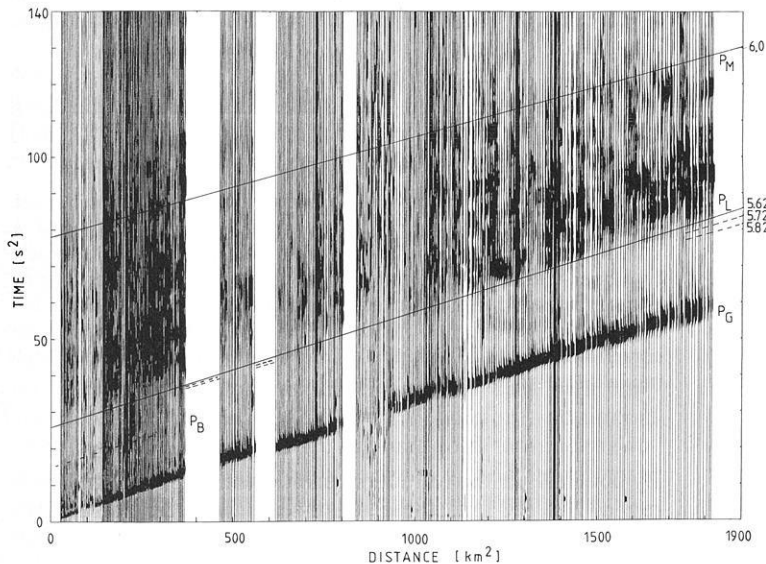


Fig. 24. T^2 - X^2 presentation of expanding-spread data for shots M , Y , Z and corresponding spreads arranged according to distance from shotpoints within 0–43 km offset range. The seismograms are displayed as energy traces. *Solid straight lines* yield RMS velocities (values in km/s at the *right-hand side*) for the upper crust and for the whole crust, respectively. They are determined by the vertical TWT, i.e. t_0 , fixed by the near-vertical reflection profiles within ± 0.2 s for the whole Haslach region and by the first and last reflected energy from the lower crust in this diagram. The sensitivity of this procedure is indicated by *dashed lines* with greater values and fixed time t_0 .

2% for the upper crust confirms the results of modelling the refraction data (Sect. 5.1), especially the reality of the low-velocity zone between 7 and 14 km depth.

The average velocity down to the crust-mantle boundary defined by the last reflected energy corresponding to phase P_M is estimated to be $6.0 \text{ km/s} \pm 4\%$, giving an interval velocity of about 6.5 km/s for the lower crust in agreement with the refraction modelling (Sect. 5).

In the ESP sections, shear-wave phases from the upper crust and the crust-mantle boundary can be correlated and compared with the corresponding P phases in the undercritical as well as in the supercritical range. Two seismogram sections for different distance ranges have been subdivided into a P - and a S -wave section in Figs. 23 and 25. The time-scale of the S -wave section is amplified by $\sqrt{3}$, corresponding to a Poisson's ratio of 0.25. In Fig. 23 the P -wave section shows the characteristic response of the crust in the upper (P_G phase) and lower part (phase P_L and P_M characterizing top and bottom of the laminated lower

crust). In the S wave section, the diving wave from the upper crust (S_G) has the same velocity in the amplified time scale as the corresponding P phase. Therefore, Poisson's ratio is normal in the penetrated part of the upper crust. A distinct onset from the Moho (S_M) can also be correlated, yielding the same Poisson's ratio for the whole crust; whereas the lower crustal S -wave reflections cannot be identified unequivocally. The phase S_7 can be interpreted in two ways:

A) It represents the converted P - S phase from the Moho.

B) It characterizes the S -wave reflection from the top of the lower crust, which would imply a strong reduction of Poisson's ratio in the low-velocity zone in order to explain the time-shift with respect to the P -wave reflection.

A similar comparison at supercritical offsets shows the same results in this range (Fig. 25). In contrast to the situation in the undercritical range, the travel time differences between converted P - S phases from the Moho and the shear-wave reflections from the top of the lower crust are

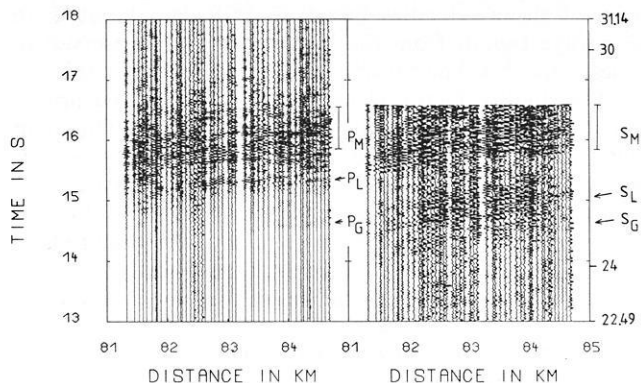


Fig. 25. Section from shotpoint *R* with a selected offset range of 81–85 km. *P* waves on the left, *S* waves on the right. The right-hand part is from the same recording with a time scale multiplied by $1/3$. Coherent phases can be compared with corresponding *P* phases. S_L arrivals are faster than P_L with respect to a ratio of 1.73. This indicates that the mean value of the V_p/V_s ratio (or Poisson's ratio) for the upper crust is less than 1.73

large enough to allow for the unequivocal identification of the S_L phase. P_L and S_L exhibit a significant time difference with an average V_p/V_s ratio of only 1.67 down to the top of the lower crust. With respect to this low mean value, the velocity ratio in the *P*-wave low-velocity zone must be further reduced regarding the value 1.73 in the first 6–7 km depth obtained from shotpoint *Z*. For the whole crust, a V_p/V_s ratio of 1.73 as a mean value is inferred from P_M and S_M phases. In order to compensate for the reduction within the *P*-wave low-velocity zone, an increase of the V_p/V_s ratio in the lower crust must be assumed. These observations are based on shotpoints *Z* (Fig. 23), *P* and *R* (Fig. 25). The other shotpoints did not generate

enough shear-wave energy to provide reliable correlations on vertical-component recordings. These qualitative results need further justification by a controlled shear-wave experiment scheduled for 1987.

During the KTB reflection campaign, a wide-angle Vibroseis experiment was carried out as a joint ECORS/DEK-ORP operation as a feasibility study concerning a future seismic reflection survey of the Rhinegraben rift. Details concerning data acquisition, communication, data processing and influence of near-surface geology are given in Damotte et al. (1987). In Fig. 26 the data of this Rhinegraben undershooting test are compared with expanding-spread records of the Black Forest in the offset range 70–85 km. The *P* arrivals of the lower crust beneath the Rhinegraben are about 0.3 s later than from beneath the Black Forest, both phases being propagated on a purely crystalline path. The duration of the lower-crustal reverberations amounts to about 1 s in the Rhinegraben compared to 2 s in the Black Forest, indicating a thickness ratio of about 1:2 in the lower crust. These observations agree very well with the reflection-seismic findings of Dohr (1970). In his section obtained in the central graben near Rastatt, south of Karlsruhe, the difference in TWT between the top of the lamellae at about 7 s and the bottom of the sedimentary fill near 2 s is just 5 s; as is the TWT through the crystalline basement from the surface to the top of the lamellae in this KTB reflection data in the Black Forest. One possible interpretation is that the entire brittle upper crust of the graben subsided without appreciable change in thickness during Tertiary graben formation. A comprehensive discussion of consequences of this hypothesis for crustal development can be found in Fuchs et al. (1987).

Probably the most outstanding feature is the different energy distribution in Fig. 26. In the Black Forest the greatest amplitudes come from lamellae near the crust-mantle

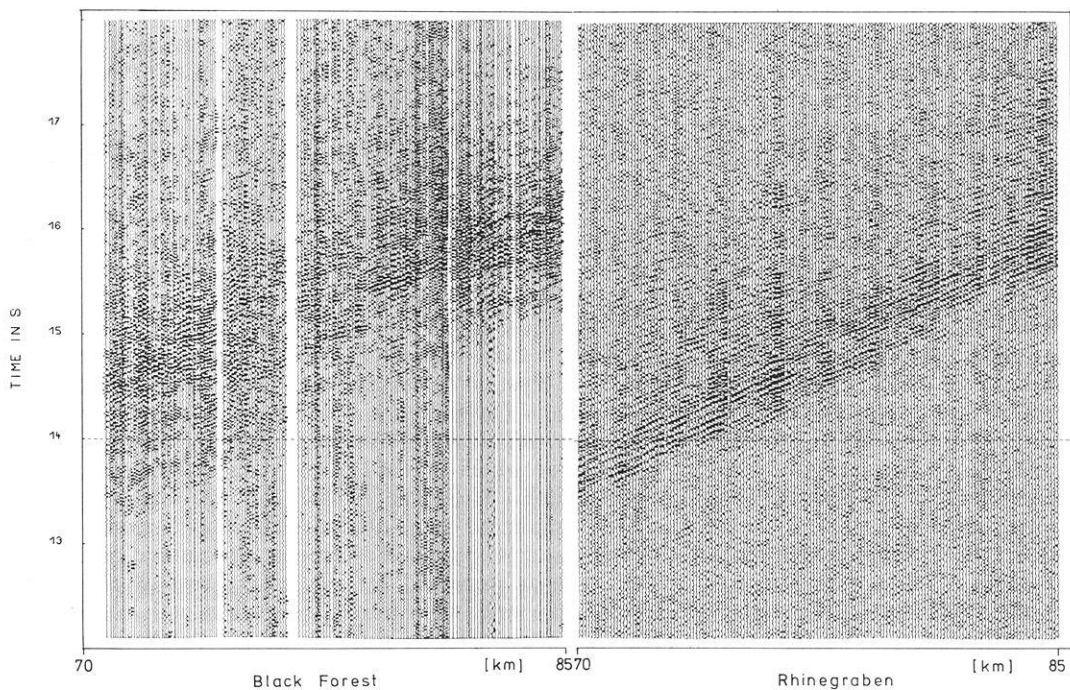


Fig. 26. Comparison of wide-angle seismograms from the expanding-spread profile in the Black Forest (left panel; shots *R*, *P* and corresponding spreads) and the Rhinegraben undershooting (right panel; vibrators in the Black Forest, recording spread in the Vosges Mountains of WE profile at 48°15' latitude). Time scales not reduced

boundary, whereas in the Rhinegraben most of the energy is concentrated in the earlier reflections from the lower crust. This indicates stronger velocity contrasts of the upper part of the lower crust in the Rhinegraben than beneath the Black Forest.

5 Seismic modelling

Important constraints on the physical properties of the earth's crust are provided by determining compressional and shear wave velocities from refraction seismic data. Gajewski and Prodehl (1987) derived a two-dimensional model by ray-tracing methods and asymptotic ray theory (see Sect. 4.1). Here we focus on the central Black Forest, modelling the record section of shotpoint S3 (Figs. 20 and 27) by the reflectivity method (RM) of Fuchs and Mueller (1971). Several circumstances are favourable in this respect. The shot was detonated in crystalline basement rocks and generated a broadband source signal with frequencies up to 25 Hz. In the two-dimensional velocity model of Gajewski and Prodehl (1987) and in the structural image of the Vibroseis survey, the crustal region north of S3 appears to be sufficiently laterally homogeneous that the RM can be applied. The computations are performed on a CDC CYBER 205 so extremely fast that we do not face any practical limits concerning vertical complexity, frequency content and number of models (Sandmeier and Wenzel, 1986). Since reflection profile 8401 almost coincides with the refraction line, we can compare results of two-dimensional modelling of source-point gathers with those of the RM.

The interpretation of refraction and reflection data sets of the same region with different sophisticated modelling techniques yields a detailed image of the crustal velocity structure of the central Black Forest.

5.1 Modelling of wide-angle seismograms

As the modelling procedure has been described in detail in Sandmeier and Wenzel (1986), the results are only summarized here. An attempt was made to match not only particular phases such as those from the upper and lower crust (P_G , P_L), the Moho reflection (P_M), and shear-wave onsets, but the entire wavefield in the observational parameter space of offset and travel time. We do not consider the data set to be composed of several distinct phases and some kind of noise; but, rather, we realize that the long reverberations are mainly caused by the lamination of the lower crust and that their amplitude and frequency behaviour reflects properties of the lamination. This point of view turns out to be significant because the classic idea of phase correlation inherently contains a high-frequency approximation and breaks down if it is applied to a structure layered on a scale less than a dominant wavelength. However, this is the case in the lower crust of the central Black Forest. We elaborate this point further in Sect. 6. In order to find error bounds for our model, the parameter space consisting of compressional and shear velocity and attenuation as functions of depth was systematically sampled. About 60 different models were calculated for this purpose.

Figure 27 shows the data of shotpoint S3, the best model we found and the corresponding synthetic seismogram section. The ratio of compressional to shear velocities is assumed to be $\sqrt{3}$. This value does not contradict the interpre-

tation of shear velocities based on ESP data because no shear-wave signals from the lower crust were observed in the section of S3. The density is given by $\rho = 0.252 + 0.3788 \cdot V_p$. The quality factor Q amounts to 400 in the upper, 1000 in the middle and 2000 in the lower crust. The main results can be summarized as follows. There is a pronounced low-velocity channel in the upper crust with a reduction in seismic velocity from 6.0 to 5.5 km/s. It is located directly above the laminated lower crust. The thickness of the lamellae is randomly varied with an average value of 120 ± 30 m. The average local velocity in the lower crust increases from 6.0 to 6.8 km/s. The magnitude of the reflection coefficients increases from top to bottom. The crust-mantle boundary is modelled as a step-like transition zone consisting of first-order discontinuities. The mean V_p/V_s ratio has been proved to be normal.

In Fig. 28 [panels (b)–(f)] synthetic seismograms for 5 out of about 60 models are presented in order to give an impression of the sensitivity of the synthetics in reaction to model variations. Panel (a) displays the data at offsets between 50 and 80 km reduced with 8 km/s. The main phases labelled P_G , P_L , P_M in Fig. 27 are clearly recognizable in this range. In (b) the synthetic seismograms of the best solution are displayed. In (c) the average thickness of the lamellae is increased to 200 m instead of 120 m. The reverberations from the lower crust change significantly. They are small at small offsets and become larger beyond 75 km, and the amplitudes around 70 km grow compared to those of the Moho reflection. A similar obvious misfit with the data appears if the average thickness is decreased to 50 m [panel (d)]. The amplitudes of the P_L wavetrain become much smaller relative to P_G and they almost disappear between 65 and 75 km. In the model of Fig. 27, the lamellae ride on a gradient structure of 0.21 s^{-1} between 15 and 18.5 km and 0.07 s^{-1} between 18.5 and 23.5 km depth. The variation of the gradient is not arbitrary. If it is replaced by a constant gradient, the P_L reverberations get only gradually weaker between 60 and 75 km as panel (e) demonstrates; whereas the double gradient results in a sharper drop in amplitude at 65 km, in agreement with the observation [cf. panel (a)]. An evidently unsatisfactory synthetic record section arises if the gradient is assumed to be zero, so that the lamellae are simply superimposed on a constant velocity of 6.7 km/s [panel (f)].

In order to test the significance of the frequency content for modelling a complex structure, we have applied a 15-cps low-pass filter (Fig. 29) to the particular seismogram sections of Fig. 28. In this case it is not possible to draw the same conclusions from modelling the data as in the high-frequency case. Apart from panel (f), the response from the lower crust is remarkably diminished and from the real data of panel (a) we would not expect a laminated structure with high reflectivity above the crust-mantle boundary. It is not clear which model fits the data best, although the characteristics described above for the high-frequency source remain the same qualitatively. This example shows that physical properties of a complex structure (e.g. a laminated zone as proposed for the lower crust of the Black Forest) can only be inferred from data with sufficiently high frequencies. As in most of the earlier refraction profiles, low frequencies around 10 Hz are dominant; their interpretation generally cannot reveal the complexity of the crust, but represents only an average over the prevailing wavelength.

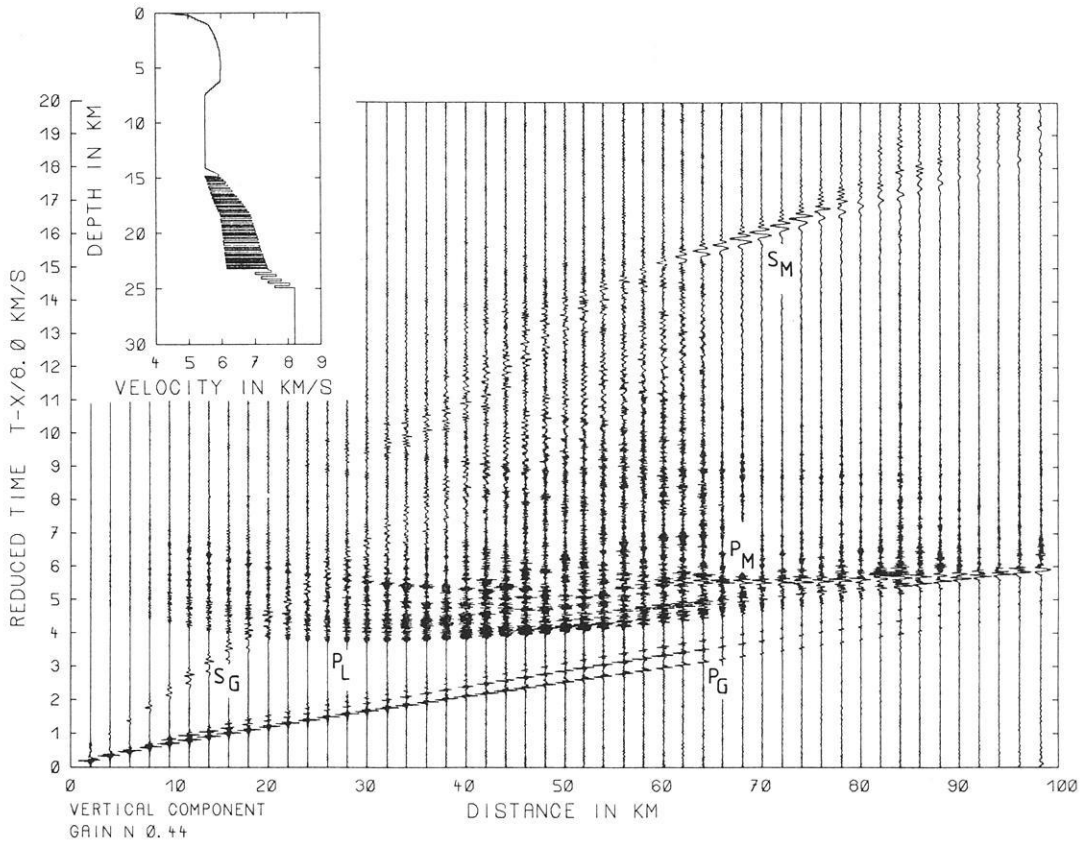
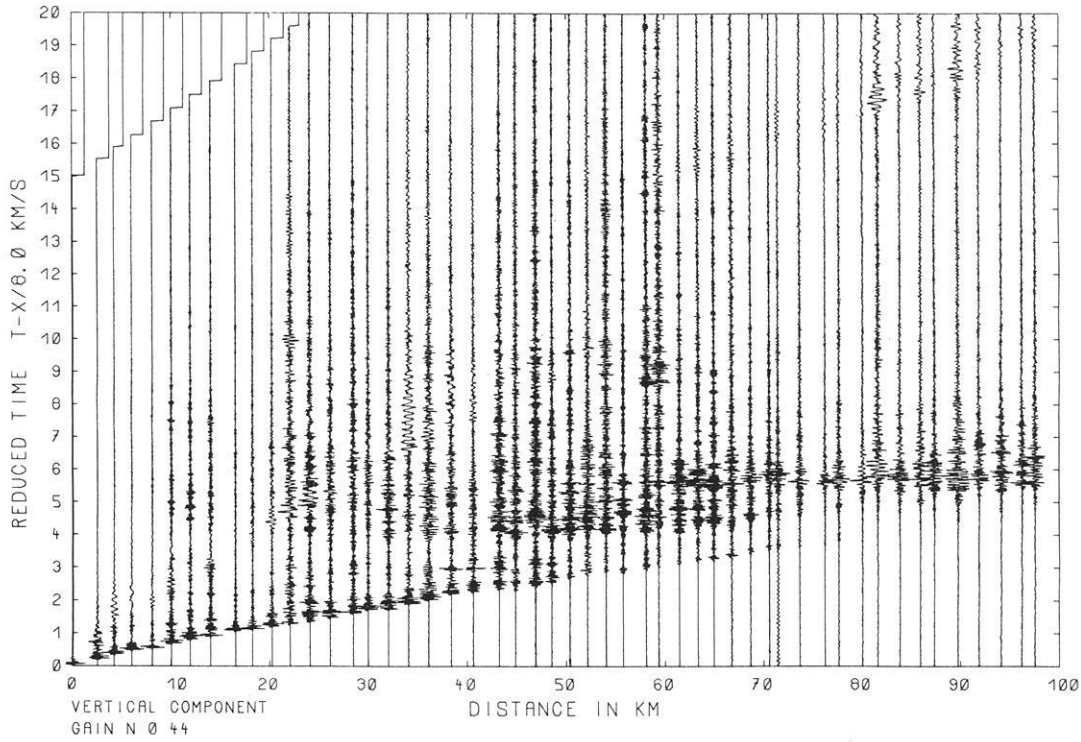


Fig. 27. Reflectivity-modelling of the refraction profile S3-North. Observed data in the *upper part*, synthetic seismograms in the *lower part* (time scale reduced with 8 km/s). *Inset* shows corresponding velocity-depth function. The splitting of P_G phases is due to surface multiples

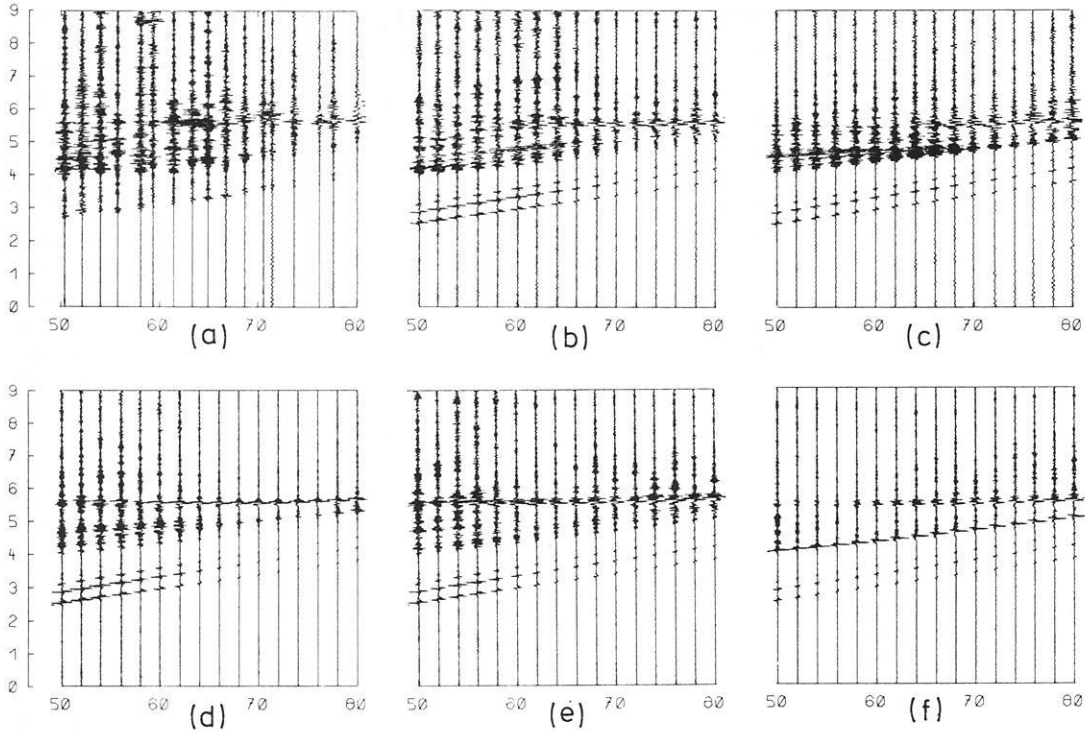


Fig. 28. Synthetic seismogram sections for offset range 50–80 km: (a) observed data (same as in Fig. 27 upper part); (b) synthetic data of final model (same as in Fig. 27 lower part), average lamellae thickness 120 m; (c) synthetic data corresponding to modified model with lamellae of average thickness of 200 m; (d) thickness of lamellae = 50 m; (e) single lower-crustal velocity gradient instead of two gradients; (f) no gradient superimposed on lamellae. Average crustal velocities are the same in (b)–(f)

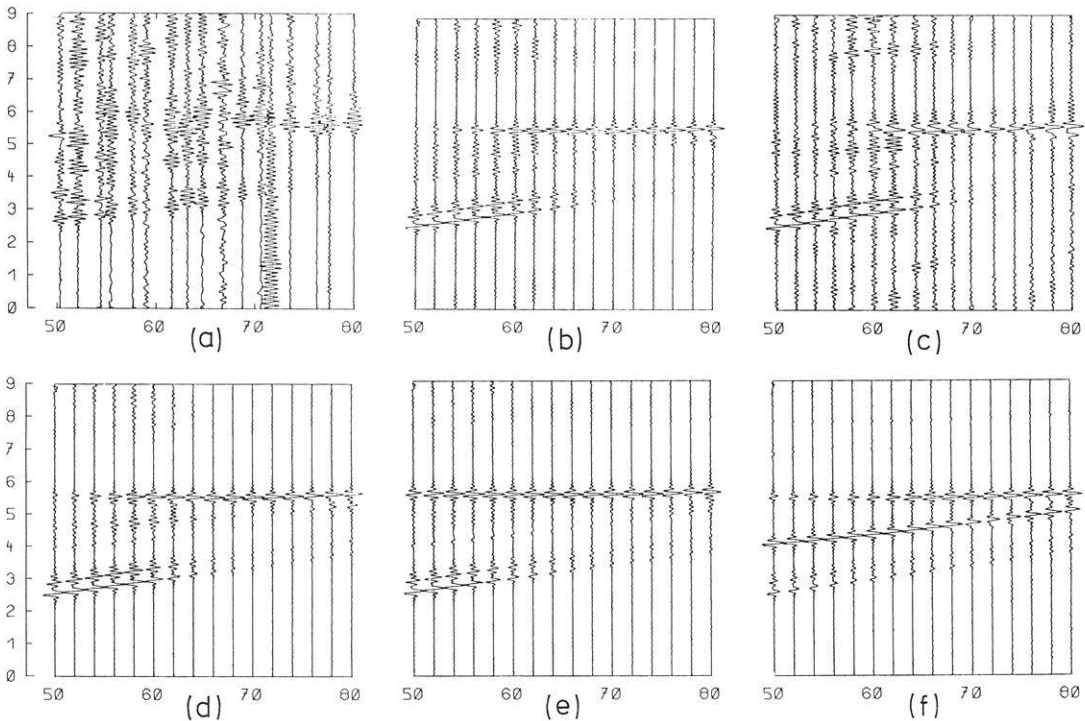


Fig. 29. Observed and synthetic seismograms corresponding to the same models as in Fig. 28, but low-pass filtered with 15 Hz cut-off. Note that lower-crustal reverberations are not clearly recognizable

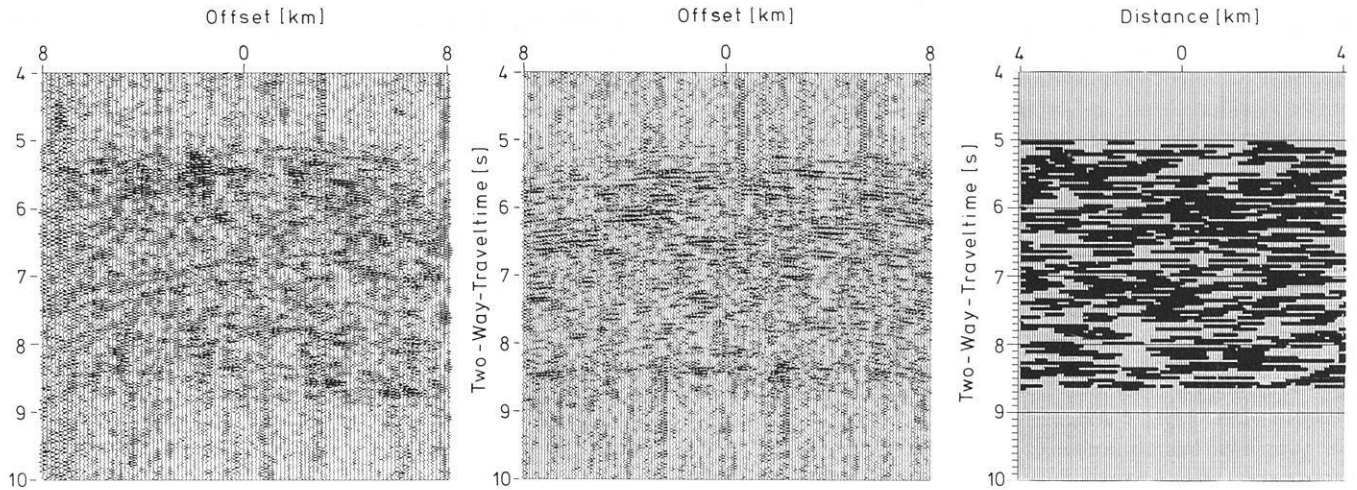


Fig. 30. Two-dimensional modelling of a common vibrator-point gather. Observed data are shown in the *left-hand panel* from 4 to 10 s TWT. Synthetic seismograms are displayed in the *central panel*; the corresponding model in the *right-hand panel*. Dark areas represent high-velocity lamellae imbedded in a lower back-ground velocity. Special emphasis was placed on the lamellar structure of the lower crust. The lamella distribution with depth is varied laterally. Lamellae have randomly distributed horizontal extents of 1–2 km. See text for further explanations

5.2 Modelling of near-vertical seismograms

A shortcoming of the RM is that the medium has to be laterally homogeneous. Despite the fact that velocities in the central Black Forest are only slowly varying laterally, we know from reflection sections that the lower crust contains numerous reflecting elements with apparent lengths in the kilometre range and that it is therefore laterally variable on this scale. We focussed our interest on two problems: (1) What kind of two-dimensional structure has to be assumed to provide reflection seismograms as observed in the central Black Forest? (2) How do those models compare with the one-dimensional model derived with the RM? For this purpose we employed a program that solves the two-dimensional acoustic wave equation numerically (Wenzel et al., 1987). It follows the approach of Gazdag (1981) and Kosloff and Baysal (1982) who calculate the spatial derivatives in the wave equation with Fourier transform methods. With this algorithm, which is implemented on the CDC CYBER 205, the seismic response of a crustal block of $30 \times 30 \text{ km}^2$, a size large enough to synthesize source-point gathers, can be calculated. Steep travel paths of lower-crustal reflections are assumed in order to prevent conversion so that the equations of elasticity degenerate into acoustic equations. On the other hand, full wave solutions are required because the fact that the lower crust apparently contains many features in the range of a wavelength or less prohibits high-frequency approximations.

The utilisation of the two-dimensional acoustic wave equation does not allow a quantitative comparison of synthetic seismograms and data because a line source is assumed instead of a point source, and only velocity variations (i.e. compressibility variations) are considered while density remains constant. However, a qualitative comparison based on the abundance of reflection events, their lateral extent and consistence is possible.

The lower crust is modelled with randomly distributed lamellae of variable length, thickness and concentration. A single lamella is generated by imbedding a high-velocity

rectangle within a lower background velocity. Figure 30 shows an observed source-point gather and a synthetic one containing only lower-crustal reflections. Here we used lamellae with a thickness of 120 m and lengths between 1 and 2 km. The number of high-velocity lamellae is such that the total area filled with lower-velocity material equals the area with higher values. If we deviate significantly from this selection of parameters, the overall appearance of the synthetics loses its similarity with the data in the sense that reflections become laterally too consistent or too numerous. The wavelet is a sweep autocorrelation function with frequencies between 10 and 35 Hz. The data have been filtered with the same frequency window to allow comparison. Details of the numerical method and of the results are given in Wenzel et al., (1987). Here we only present one example of the results: a structure containing randomly distributed lamellae shows a reflection response with characteristics similar to the data if the parameters mentioned before are used. Along vertical cross-sections through the two-dimensional model we get sequences of alternating high- and low-velocity layers with an average thickness of 120 m. This is in agreement with the result derived by modelling of refraction data with the RM.

6 Compilation of velocity information

Following our concept of unified interpretation of all accessible data, we analyse observed and modelled velocities in terms of their compatibility. Figure 31 shows the available velocity information derived for the central Black Forest near Haslach. Physical velocities are displayed as local and root-mean-square values (RMS), respectively. Solid lines represent these compressional-wave velocities inferred from modelling of refraction seismograms with the reflectivity method (RM). Dashed lines correspond to refraction interpretations of the same record section based on asymptotic ray theory (ART). For details, see Sects. 4.1 and 5. Dotted lines represent stacking velocities used for processing the data of reflection profiles 8401, 8402, 8403 near Haslach.

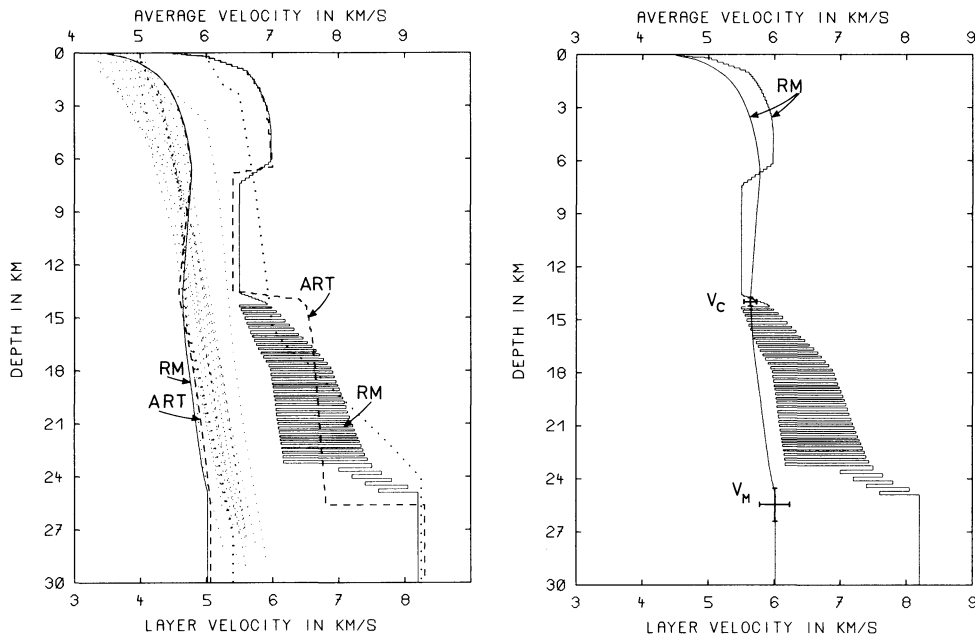


Fig. 31. Velocity compilation for the central Black Forest (near Haslach). *Left panel:* local velocities from ray-tracing (ART) and reflectivity (RM) modelling (dashed and solid lines, respectively; scale at the bottom). Corresponding RMS velocities are displaced by one unit to the left (scale on top; dashed and solid lines) together with stacking velocities of the reflection survey (dotted lines). Thick dots represent interval velocities derived from a typical stacking velocity function. *Right panel:* comparison of RMS velocities of the final RM model and ESP-derived values of $V_c = 5.62 \text{ km/s} \pm 2\%$ for the upper crust and of $V_M = 6 \text{ km/s} \pm 4\%$ for the entire crust (cf. Fig. 24). Corresponding depth uncertainties are $\pm 2\%$ and $\pm 4\%$, respectively. For completeness, the interval velocities of the RM model are shown at the same scale

Physical velocities. Two velocity-depth functions were independently derived from the 1984 refraction experiment using RM and ART for interpretation. Both models coincide in the upper 7 km and in the thickness of the low-velocity channel, where the velocities differ only slightly. Consequently, the position of the top of the lower crust is in agreement. A striking difference appears in the lower crust. For its upper part, a relatively high velocity (6.5 km/s) is derived by Gajewski and Prodehl (1987) from a phase correlated at the outermost parts of the profile and interpreted as a diving wave. This phase cannot be clearly recognized in the profile of shotpoint S3 displayed in Fig. 27 because of its restricted offset range. Better evidence is attained in the sections of adjacent shotpoints S2 and S4 which have a larger offset. The details of the lower-crustal RM model are essentially constrained by the data in the offset range between 40 and 90 km. Our RM model does not reproduce the diving wave from the lower crust. It could only be generated in the synthetic seismograms by increasing the velocities between 14 and 18 km depth to 6.5 km/s. However, in this case a much poorer fit of the data, in terms of amplitude and frequency characteristics in the offset range up to 90 km, would result. Consequently, we conclude that an interpretation of the record sections in the frame of a one-dimensional model is incomplete. The remaining discrepancies must be attributed to lateral variations of depth and magnitude of velocity contrasts.

Both interpretations of the data agree in the RMS velocities throughout the whole crust and in the depth of the crust-mantle boundary at about 25 km as a first-order discontinuity. The major features of the velocity-depth profile presented here are qualitatively in good agreement with previously derived models; see Mueller et al. (1969), Mueller (1977) and Deichmann and Ansorge (1983).

Stacking velocities. Representative stacking velocities for the central Black Forest are displayed as dotted lines in the left panel of Fig. 31. They show considerable variation within a range of 1 km/s at all depths. In order to examine their compatibility with refraction velocities, one has to be aware of their meaning and accuracy. Stacking velocities are formal velocities used to produce a stacked section with optimum contrasting structures; consequently, they must be considered processing velocities. In our case 20–50 CDPs were first stacked with trial velocities, then displayed and, finally, the best section was chosen by individual judgement. Under certain circumstances stacking velocities are closely related to physical velocities. If a horizontal reflector is overlain by a laterally homogeneous medium and if the recording offsets are within the hyperbolic range, the best stack should arise if the stacking velocity is the physical RMS velocity (Dix, 1955). The accuracy of its determination is limited however (Hajnal and Sereda, 1981). Dipping reflectors and point diffractors have optimum stacking velocities larger than the physical ones (Dinstel, 1971). As both events and diffractors are observed in the lower crust of the central Black Forest, we attribute the systematic deviation of the stacking velocity from the physical RMS value to these features. Similar observations are reported from the DEKORP 2-South reflection profile (Bortfeld et al., 1985). Further discrepancies are introduced if lateral velocity inhomogeneities along a CDP are present. These effects have been studied, e.g. by Miller (1974) and Blackburn (1980), with respect to sedimentary regions. However, in the crystalline environment of the Black Forest the physical velocities do not change dramatically. Another point is that CDPs very often do not show consistent reflectors in the crystalline basement. Therefore, an interpretation of stacking velocities of the type familiar from exploration

experience in sedimentary regions must be regarded with caution. If, however, the stacking process is focussed on a consistent reflection, e.g. from the Moho using a recording spread of more than 20 km, a reliable interpretation of stacking velocities in terms of physical velocities is possible. This has been demonstrated on the 1978 Urach reflection profile (Bartelsen et al., 1982).

The stacking velocities are biased towards low values in the upper crust and towards high values in the lower crust (left panel of Fig. 31). We cannot yet present a straightforward explanation of this fact.

Comparing stacking and refraction velocities we have to consider that the stacking velocity involves vertical ray paths and the refraction velocity mostly horizontal ray paths. Discrepancies could then be caused by seismic anisotropy (Winterstein, 1986).

7 Compilation of geophysical data and geological-petrological interpretation

7.1 Data

The deployment of a variety of geophysical sounding tools on a regional scale gives a synchronous view of crustal properties through different imaging techniques. Physical anomalies and gradients may be tested for their compatibility and consistency. In Fig. 32 structural information from the Vibroseis reflection profile 8401 (from Fig. 8), the refraction seismic model from Gajewski and Prodehl (1987), the Bouguer gravity anomaly along the seismic profile 8401 (Götze et al., 1986), the heat-flow distribution derived from borehole measurements (Stiefel et al., 1985) and the seismicity distribution (Bonjer and Apopei, personal communication) are displayed. Additional information obtained on electrical conductivity from magnetotelluric and electromagnetic sounding methods has been presented by Berkthold et al. (1985) and by the LOTEM Working Group (1986).

One of the most exciting questions concerns the compatibility of crustal discontinuities defined by refraction and reflection methods, i.e. the compatibility of wide-angle and near-vertical measurements. Wide-angle refraction ray paths are sensitive to large-scale vertical and horizontal velocity gradients. Near-vertical incidence of elastic waves more accurately images the vertical sequences of fine structures, in terms of their reflectivity, at a resolution within the scale of the seismic wavelength. Gajewski and Prodehl (1987) transformed their refraction velocity-depth model to a velocity-vertical-travel-time (TWT) model and compared it to the near-vertical (TWT) reflection section 8401. They found coincidence of the Moho (velocity step from 6.8 to 8.2 km/s) with the deepest accumulation of consistent near-vertical reflections, and coincidence of the Conrad discontinuity (midcrustal velocity step from 5.4–6.0 to 6.5 km/s) with the upper level of the highly reflective lower crust. An equivalent approach is a depth conversion of the reflection section using the refraction velocity model. Both presume identical horizontal and vertical velocities and are not conclusive in the case of seismic anisotropy. We have preserved the vertical travel-time scale on the reflection sections because of its objective measured character.

A more reliable test for compatibility of reflecting structures in the near-vertical, with first- or second-order velocity discontinuities in the wide-angle range beneath a fixed surface location, is an expanding-spread experiment. In our

case the most important crustal discontinuities, the boundary between upper and lower crust and the crust-mantle boundary, are documented continuously from the near-vertical to the wide-angle range in the Haslach region (Sect. 4.2). High-frequency signals and a detector spacing of 80 m enabled a continuous phase correlation and showed coincidence of these discontinuities. This is confirmed by near-vertical and wide-angle modelling presented in Sect. 5.

Another very striking coincidence is observed between the upper-crustal low-velocity zone and a zone of relative transparency in the reflection sections. The base of the low-velocity zone also coincides with the first reflections from the lower crust. Gajewski et al. (1987) determined that the regional extent of the low-velocity zone agrees with the exposed crystalline area of the Black Forest. To the south the low-velocity zone fades out, accompanied by a progressively weaker reflectivity of the lower crust. The coincidence of the low-velocity zone and relatively transparent zone appears to be considered as a special local phenomenon. Otherwise, if correlated with the transparent zone in the EW profile 8403, the low-velocity zone would extend further to the east, as far as the region of the Urach geothermal anomaly (Bartelsen et al., 1982).

The top of the low-velocity zone is neither clearly marked by the reflectivity distribution nor by wide-angle reflections in the expanding-spread profile. It may be of transitional character as well as of undulatory form, following the reflection pattern in the upper crust. Its depth and its interval velocity of 5.4–5.5 km/s are constrained first by the velocity-depth function inferred from the first arrivals, P_G , which show an increase of velocity up to 6 km/s at 6–7 km depth, and second by the average velocity of 5.62 km/s between the surface and the lower crust as inferred from the ESP and the bulk of wide-angle and refraction data.

Strong lateral gravity gradients in the north and south may be related to the “Baden-Baden” and “Badenweiler-Lenzkirch” thrust belts. The gravity minimum in the south coincides with a decrease of reflectivity in the lower crust and the fading out of the low-velocity zone in the upper crust.

Two- and three-dimensional gravity modelling has been performed by Götze et al. (1986). The velocity model of Fig. 32 was transformed to a 2D density model using an empirical velocity-density relationship and inversion techniques. The computed gravity (Fig. 33) fits the observed curve satisfactorily. In the central Black Forest a slight misfit might suggest an additional influence of low-density material in the upper or middle crust. The fading out of the low-velocity/density zone in the south and the subsidence of the lower-crustal isolines is fairly well matched by the computed gravity and the observed data.

In contrast to the velocity-density model, a structure-density model was tested for an accretion hypothesis of underthrust Paleozoic metasediments, which is supported by structural imaging by the reflection seismics. By optimizing structures and densities, a complete fit could be forced. Gravity modelling may constrain structural models if the results are inconsistent with the data, but consistence is not a general proof of the models. Severe uncertainties may arise from three-dimensional effects of the Rhinegraben which strikes nearly parallel to the gravity survey.

A special phenomenon of interest is the strong Bouguer maximum near the “Baden-Baden” zone in the north,

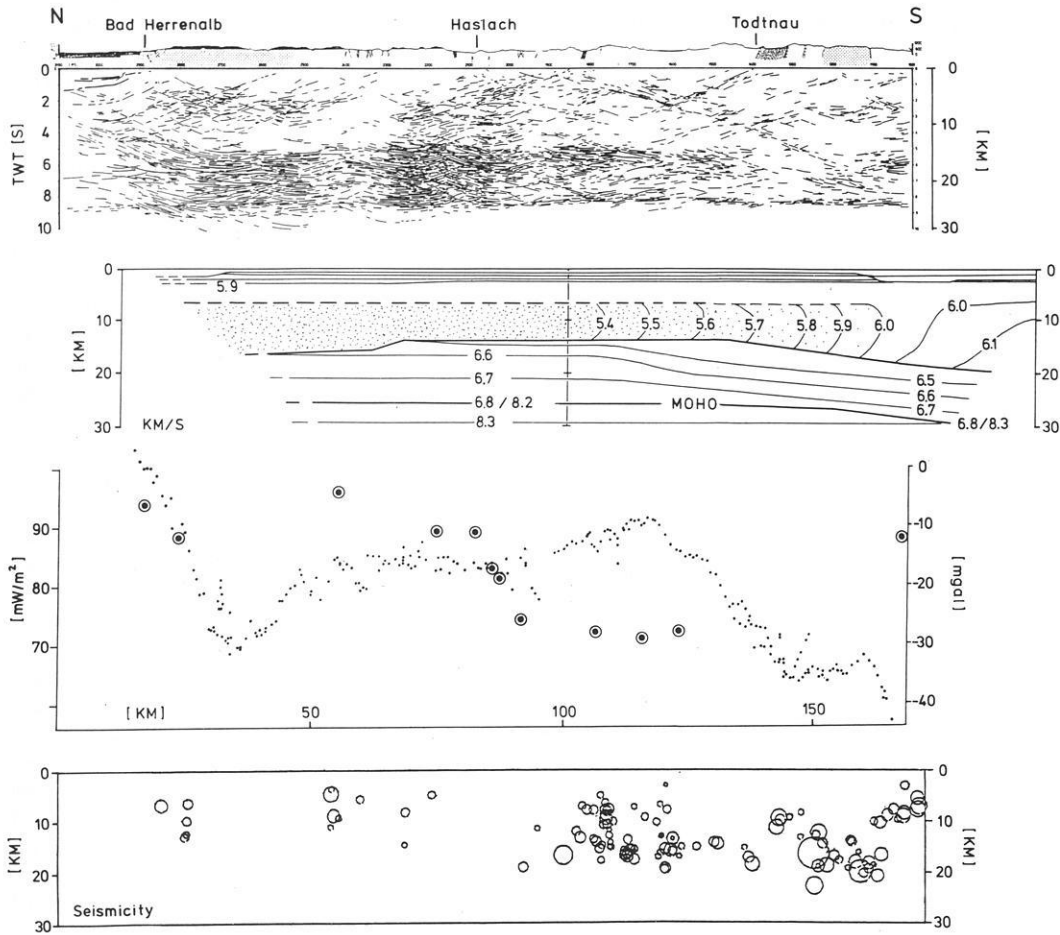


Fig. 32. Compilation of geophysical data for the N-S profile. *From top to bottom:* structural data from the Vibroseis reflection survey (line drawing of migrated line 8401); velocity model from the refraction survey; Bouguer gravity anomaly (*small dots*) and heat flow (*big dots*); seismicity distribution (magnitudes between 1 and 5; projected within a strip of ± 10 km width). For references, see text

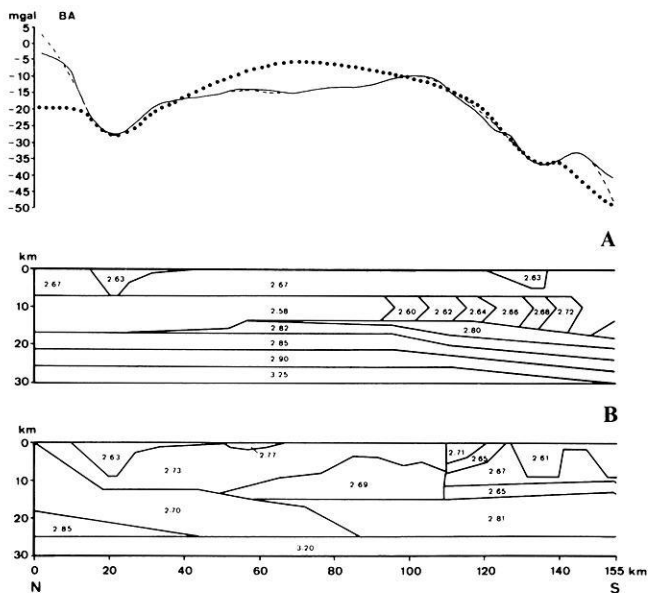


Fig. 33. Gravity modelling. *Upper part:* observed (---) and computed (.... model A, — model B) Bouguer anomaly. *Lower part:* A – velocity model converted to a density model using an empirical relationship. Lower-crustal densities were obtained by an inversion technique. Granite massifs are added for completeness. B – structure model based on a hypothetical geological-tectonic model. *Numbers* are densities in g/cm^3 (from Götze et al., 1986)

known as the “Kraichgau” anomaly (Fig. 33, left side). The gravity high could be related to a shallow body of mafic-ultramafic material within the Saxothuringian-Moldanubian suture zone. The suture zone is delineated clearly by a strong lateral gravity gradient [cf. gravity map by Gerke (1957)]. Fountain and Salisbury (1981) reported similar gravity anomalies in other continental suture zones. Just north of the Baden-Baden suture zone the reflective character of the lower crust seems to continue into the “Kraichgau” area, revealed by reflections at 5.2 s, 7 s and 9 s (Demnati and Dohr, 1965). This indicates that it originated after the Hercynian suturing, provided that the “lamination” represents the same geological phenomenon both north and south of the Baden-Baden zone. The widespread appearance of the lamination in large areas in Europe suggests non-local geological and physical processes.

Gravity and geomagnetic mapping in the central Black Forest reveal relatively small anomalies with SW-NE trends coincident with the strike of the Hercynian tectonic fabric. Granite bodies such as the “Triberg” granite are clearly displayed by local gravity minima. The maximum depths of the granite bodies are estimated to be about 4-8 km, calculated for granite densities of 2.62 g/cm^3 and gneiss densities of 2.73 g/cm^3 determined by weighing core samples (Plaumann et al., 1986). This density decrease of 4% corresponds to a velocity decrease of the same amount (cf. Sect. 3.4.1). Reflections from the expected base of the gran-

ite bodies are widely scattered so that corresponding correlations are ambiguous (cf. northern part of profile 8401, locations 2500–2900, Fig. 8). The basal contact between granites and gneisses must be of discontinuous or scattered geometry compared to a seismic wavelength, or it does not represent a contrast of impedance at that depth.

The surface heat flow (Stiefel et al., 1985) is relatively high (70–95 mW/m²) and shows strong lateral variations. This may be due to increased basal heat flow from the upper mantle, as a consequence of the Rhinegraben rift formation with increased convective and conductive heat transport still active today.

From the rheological point of view, the crust may be subdivided into an upper brittle and a lower ductile part (Chen and Molnar, 1983; Meissner and Strehlau, 1982). The brittle-ductile transition is expected to be represented by the deepest earthquake foci. In the northern part of the cross-section (Fig. 32, lower section), the seismicity is low and maximum hypocentral depth correlates with the reflection-refraction-defined boundary between the upper and lower crust. In the southern part, the seismic activity increases and the foci reach depths of about 20 km. The deepest earthquakes are located within the laminated lower crust.

Magnetotelluric studies revealed a high-conductivity layer (650 S) at midcrustal depths, which cannot, however, be correlated to either the low-velocity zone or to the laminated lower crust, and a pronounced conductivity anisotropy (factor of anisotropy ≥ 5) with maximum conductivity in Hercynian (NE–SW) direction (Berkthold et al., 1985; Schmucker and Tezkan, 1987). Recently performed transient electromagnetic soundings in the central Black Forest near Haslach yielded another high-conductivity layer of about 5 Ohm·m dipping to the NW between 9 and 6 km depth (LOTEM Working Group, 1986), correlating with the top of the low-velocity layer.

7.2 Discussion and conclusions

Jones and Nur (1984) and Smithson et al. (1986) have shown by specific field studies, laboratory data of physical properties and seismic modelling that cataclastic fault zones and ductile mylonite zones can be regarded as candidates for upper-crustal reflectors. The seismic structural image of the upper crust in this view is considered as a marker of tectonic events. Figure 34 reflects the basic tectonic interpretation of the seismic sections in the Black Forest. The upper crust is characterized by a rather heterogeneous seismic image. Reflectors are much less continuous than in the lower crust and reveal an increased complexity of structures on a scale of the seismic wavelength (150–300 m). Dominant dipping reflectors seem to die out at a depth of about 8–10 km. In the Black Forest this might be related to a change of the reflective character of a fault zone due to a change of deformation style from a brittle regime with non-cohesive gouge, breccias and random-fabric cataclastics to mylonites. Alternatively, an overprint by recent fluid activity could be taken into account, resulting in a homogenization of seismic structures caused by alterations in mineralogy and petrology. Prominent reflectors in the upper crust in the Black Forest are interpreted in terms of Hercynian tectonic processes. The convergent zones of the Baden-Baden suture zone (BBZ) in the north and the Badenweiler-Lenzkirch zone (BLZ) in the south are visible

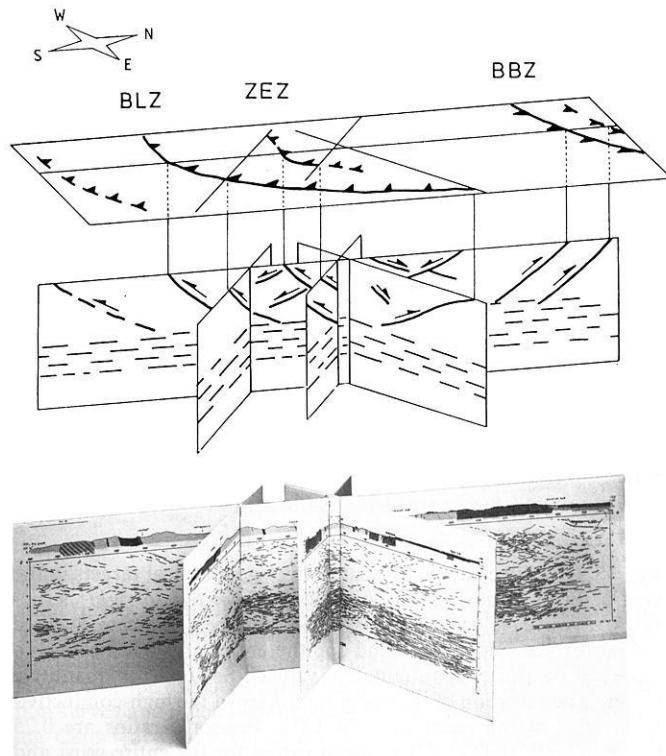


Fig. 34. Lower part: Three-dimensional structure diagram provided by line drawings of the net of four reflection profiles. View is from ESE. Upper part: Interpretational fence diagram showing Hercynian thrust and late-Hercynian extension tectonics. BLZ “Badenweiler-Lenzkirch” zone, ZEZ “Zinken-Elme” zone, BBZ “Baden-Baden” zone

in the seismic reflection profiles as bands of inclined reflectors. The reflecting band related to the Baden-Baden zone dips 40° to the south and reaches into the deeper crust. On profiles 8401 and 8514, the Badenweiler-Lenzkirch zone can be traced from the surface to a depth of more than 12 km as a number of strongly reflecting elements dipping NW. NW-dipping structures in the eastern section of profiles 8402 and 8403 indicate the continuation of the Badenweiler-Lenzkirch structure beneath the Mesozoic sedimentary cover to the NE. Other NW-dipping reflectors south of the Elztal fault reach a depth of at least 5 km and are interpreted as belonging to another intraplate convergent zone similar to the Badenweiler-Lenzkirch area (“Zinken-Elme” zone, ZEZ). These zones, BBZ, BLZ and ZEZ, constitute thrust faults opposed to each other with north-westward and southeastward vergences (cf. Sect. 2).

Low-angle normal faults characterized by cataclastic deformation in the central Black Forest are identified as reflectors by near-surface high-resolution measurements (Sect. 3.4.2) and are correlated with several SE- and NW-dipping reflectors in this area (see profile 8402). These reflectors, often cross-cutting the reflector pattern, described above, are related to extensional tectonic processes during the late Hercynian and are regarded as markers of the change from compressional to extensional character of the tectonic style.

The lower part of the upper crust (e.g. 7–14 km) is seismically characterized by a *P*-wave low-velocity zone, a reduced V_p/V_s ratio (but no shear-wave velocity inversion) and a zone of relative transparency. This coincides with

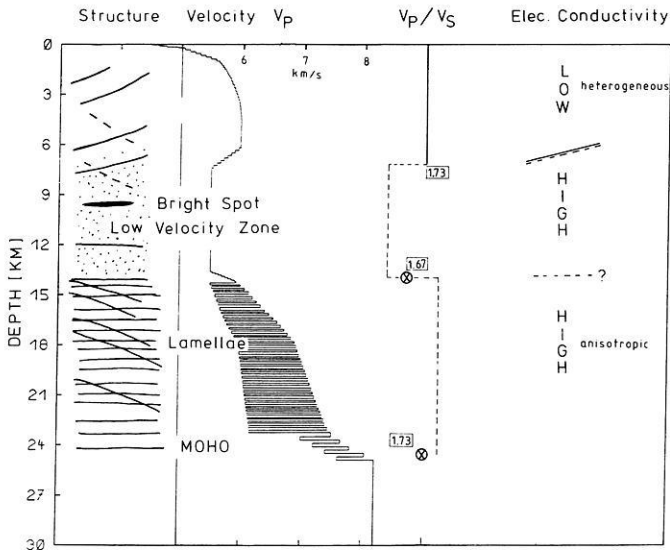


Fig. 35. One-dimensional presentation of geophysical targets in the central Black Forest (Haslach region). From left to right: structures, P -wave velocities, V_p/V_s ratio (numbers indicate average values for the upper crust and for the entire crust, respectively), electrical conductivity (qualitative values). See text for quantitative values. The precision of the upper boundary of the high-conductivity layer is of the order of 10%–15%. Poisson's ratios are 0.25 ($V_p/V_s=1.73$), 0.22 (1.67) as mean values for the entire crust and for the upper crust, respectively. The dashed line is approximate distribution of local values

a zone of high electrical conductivity (Fig. 35). Model interpretations of the nature of low-velocity zones in re-activated continental crust may include granitic layers (Mueller, 1977), underthrusting of sedimentary rocks and fluid overpressure related to metamorphic or tectonic processes (e.g. Fyfe and Kerrich, 1985). Dehydration reactions during metamorphic processes can reduce the effective pressure at a given crustal level, leading to the formation of new microcracks and thereby lowering the P -wave velocity [but increasing the S -wave velocity; Kern (1982)]. Velocity inversions can also be triggered by phase transitions in the solid state (quartz) in regions of high heat flow (Kern, 1982).

A bright spot situated in the low-velocity channel is probably caused by a body of lower impedance, which might be taken as evidence for fluid accumulation (Sect. 3.4.3). These completely different observations favour a major role of fluids in a porous or fractured medium, determining physical properties and triggering petrological processes in addition to temperature and pressure. In the Kola deep borehole a low-velocity zone between 4.5 and 9 km depth is characterized by the presence of mineralizing fluids in connection with hydrofracturing, increase in porosity and strong textural variations of the Precambrian rocks (Kremenetsky and Ovchinnikov, 1987). Fuchs et al. (1987) propose a similar mechanism involving dehydration of parts of the lower crust by decompression. The generation of microcracks by fluid overpressure may explain the combined effects of both low-velocity and high electrical conductivity. Also, a layer of decreased velocity and increased conductivity has been found in crystalline rocks of the Urach 3 borehole (Swabian Alb), displaying high microcrack density and strong hydrothermal alteration (Stenger, 1982). The same relationships have been found in the NAGRA borehole, "Böttstein" (NAGRA, 1985).

The lower crust is characterized by a strong and laterally consistent lamination with alternating high and low P velocities differing by about 10% and a vertical layering on a scale of 100 m. The horizontal extent of single reflecting elements is in the range of a few hundred metres. The average V_p/V_s ratio in the lower crust is slightly above the crustal mean value of $\sqrt{3}$ (cf. Sect. 4.2). Seismic lamination of the lower crust is a common feature in Hercynian and Caledonian consolidated continental crust (Meissner et al., 1983; Bois et al., 1986; Bortfeld et al., 1985; Matthews and Cheadle, 1986). Lithological interpretations involve compositional or metamorphic layering, underplating, magmatic differentiation, partial melting, fluid enrichment, penetrative ductile deformation (mylonitic banding) or anisotropy.

A great amount of experimental data on velocities of presumed lower-crustal rocks has been published in recent years (Christensen, 1979; Christensen and Fountain, 1975; Fountain, 1976; Kern 1982; Kern and Schenk, 1985; and others). Information on the composition of the lower crust is obtained from outcropping rock series or by analysis of xenoliths in volcanic host rocks. Exposures representing complete lower-crustal sections in Europe (Ivrea zone/western Alps; Calabria/southern Italy) reveal granulite facies rocks, of alternating mafic to acidic composition, as major constituents (Fountain and Salisbury, 1981; Schenk, 1984). Measurements of compressional- and shear-wave velocities in these rocks at lower-crustal PT conditions (Fountain, 1976; Kern and Schenk, 1985) have demonstrated the following relations:

- Both V_p and V_s increase with increasing amount of pyroxene, amphibole, garnet and sillimanite.
- Poisson's ratio is high with high feldspar content and low with high quartz content.
- Strong anisotropy of seismic velocity is caused by preferred lattice orientation of minerals and by metamorphic/compositional layering.
- Metapelitic granulite-facies rocks of intermediate silica and high alumina content have velocities equivalent to mafic granulites ($V_p=6.8$ – 7.5 km/s).

Using geophysical and geological data from the Ivrea zone, Hale and Thompson (1982) generated synthetic seismograms with interfering reflections from a stack of thin layers similar to those observed in our reflection data. Blundell and Raynaud (1986) suggested, alternatively, a contribution by sideswipes from a single undulatory surface. Although these lateral effects cannot be completely excluded, a major influence is ruled out by spatial control provided by the intersecting lines.

Anisotropy may be an important factor with respect to the strongly reflecting character of the lower crust. Experimental data on the elastic properties of mylonitic rocks (with anisotropy up to 20%) demonstrate that deep crustal reflections can be explained by extensive ductile deformation of rocks, provided the mylonitic zone is thick enough relative to the seismic wavelength (Jones and Nur, 1984). Late-Hercynian extension of the crust in the Black Forest, which produced cataclastic fault zones in the upper crust, could be accompanied by ductile deformation in the lower crust, thus producing the laminated seismic structure.

Comparative near-vertical and wide-angle observations provide additional hints on the Rhinegraben rift evolution. Fuchs et al. (1987) stressed the identical thickness of about 14 km of the crystalline upper crust beneath both graben

and shoulders, based on near-vertical reflections from the lower crust. They concluded that the upper crust could have subsided about 4 km, without considerable deformation, into the lower crust. Wide-angle observations (Sect. 4.2) indicate a reduced thickness and stronger impedance contrasts of the lamellar structure in the graben proper. These observations favour an origin of the lamellae prior to the beginning of Rhinegraben subsidence and uplift in the Eocene which have modified the pre-existing lamellae. In reflection profiles 8402 and 8514 (see Figs. 10 and 12a), the image of lower-crustal lamination is characterized by more widespread diffraction legs and shorter reflection elements than in profiles 8401 and 8403. This may be due to the presence of line diffractors or elongated lamellae with Hercynian strike perpendicular to profiles 8402 and 8514. This observation is consistent with profiles U1 and U2 of the Urach geothermal project (Bartelsen et al., 1982) and DEKORP 2-South (Bortfeld et al., 1985) and may be regarded as indication of lamellae origin during late Hercynian or Mesozoic extension. Another relationship probably exists to the conductivity anisotropy with preferred Hercynian strike (Berkthold et al., 1985). The lower-crustal lamination found by various authors from the BIRPS, ECORS and DEKORP groups, cited above as typical for Hercynian Central and Western Europe, may have its counterpart in the Mesozoic rift margin of the eastern North American coastal plain (Cook et al., 1983).

The crust-mantle boundary has a highly variable appearance in reflection profiles, particularly in those of the COCORP, due to different tectonic regimes, thus reflecting different origins (Oliver, 1982). Its formation might be triggered by thermal events and could represent the final stage of an advanced differentiation process (Meissner and Wever, 1986). Strongly reflecting crust-mantle boundaries often seem to be associated with rifted areas. Klemperer et al. (1986) studied pronounced, mostly horizontally layered Moho reflections in the Basin and Range and found indications favouring an origin by magmatism and extension.

The Moho beneath the Black Forest is developed throughout the entire study area as the deepest horizontally layered and laterally consistent accumulation of high-amplitude reflectors at a relatively shallow depth of 25–27 km. Increasing amplitudes at greater source-receiver offsets indicate that sharp discontinuities or lamellae are superimposed on a velocity-gradient zone of the type determined by Deichmann and Ansorge (1983) for the eastern border of the Black Forest by a refraction survey (Fig. 30). Continuity and truncation relationships with dipping reflectors suggest an age younger than Hercynian. The Moho and horizontal lamellae in the lower crust seem to have overprinted dipping crustal reflectors which delineate thrust zones of Hercynian age (BB zone and BL zone).

The age of the Moho is constrained on one hand by these truncations and by its continuity across suture zones and, on the other hand, by small vertical offsets which are clearly recognized by overlapping diffractions with apices within the Moho, especially in the southeastern part of line 8514 (Fig. 10). If these offsets are markers of tectonic events disrupting a generally rather smooth Moho, they are related to the Alpine orogeny; this favours a Moho age of late-Hercynian to Mesozoic time.

Figure 35 summarizes the relevant geophysical information for the Haslach region. From the structural image of

the near-vertical reflection survey, several relics of thrusting and normal faulting can be expected in the upper crust above a very pronounced low-velocity zone coinciding with a relatively transparent zone at 7–8 km depth. A local object of special interest is a bright spot at about 9.5 km depth.

A series of coincident geophysical observations raises crucial geologic-petrological questions concerning recent metamorphic processes and hydrothermal mineralization. The upper-crustal low-velocity zone coincides with a transparent zone where dipping reflectors die out, with a zone of decreased Poisson's ratio (meaning that the *S*-wave velocity is not decreased as much as the *P*-wave velocity) and with a level of high electrical conductivity. These crustal properties seem to be related to recent fluid activity in a porous or fractured medium, to increased basal heat flow and to the brittle-ductile transition. The origin of the geophysical anomalies and gradients is strongly associated with crustal structure, composition and processes.

Acknowledgements. The funding of the KTB reconnaissance program (project RG 8314 6) by the Federal Ministry of Science and Technology, Bonn, is gratefully acknowledged. We thank, especially, H. Schwanitz and his crew from Prakla-Seismos AG, Hannover, for excellent performance during the Vibroseis reflection survey and much helpful cooperation. The DEKORP-Processing Center at Clausthal, directed by R.K. Bortfeld, using hard- and software from Mobil Oil AG, Celle, and Seismograph Service Ltd, London, performed the standard processing. The Geological Survey of Lower Saxony and the DEKORP management, Hannover, A. Hahn, H.-J. Dürbaum, Ch. Reichert and J. Schmöll provided administrative and consultative service. The Thor Geophysikalische Prospektion GmbH, Kiel, provided their pneumatic hammer device and specialists; and the University of Kiel, R. Meissner and H. Stümpel, the recording equipment for the high-resolution surveys. We thank the university teams from the Geophysical Institutes of Zürich, Hamburg, Kiel, Clausthal and Karlsruhe for their enthusiastic participation in the ESP and other experiments. R. Vees (Clausthal) organized pond shot R of the ESP. We are indebted to the entire interdisciplinary Black Forest Working Group for many fruitful and encouraging discussions. In particular, we appreciate the contributions of W. Wimmenauer, K. Schädel, J. Jenkner, B. Jenkner, H. Klein (Freiburg), G. Kleinschmidt, Th. Flöttmann, B. Gallus (Frankfurt), H.-J. Behr (Göttingen), K.-M. Strack (Köln), H.-J. Götze, J. Schmalfeldt (Clausthal), A. Stiefel, K.-P. Bonjer, I. Apopei, J. Ebel, D. Gajewski, St. Holbrook, H.-P. Schnell, W. Wälde, P. Blümling, J. Mechie, C. Prodehl (Karlsruhe). A. Stiefel provided the heat-flow data, and K.-P. Bonjer and I. Apopei the seismicity data of Fig. 32. Special thanks are given to D. Gajewski and C. Prodehl for continuous discussions and for their seismic refraction data and results and to K.-M. Strack for the LOTEM contribution.

We appreciate very much the continuous support by the local authorities and individuals, forestry offices, the Baden-Württemberg Mines Office and Geological Survey (Freiburg) and the public media. They all created an animating environment for geoscientific research in the Black Forest. The mayor and the municipal offices of Haslach provided buildings, which served as headquarters for our activities for two years.

We owe our thanks to S.L. Klemperer (BIRPS) for careful and critical reading of the manuscript and for many helpful and stimulating suggestions concerning its content and presentation. We wish to thank G. Müller for his support in editing and publishing this paper.

We thank Mrs. S. Stuhler for typing the manuscript.

Contribution No. 339 of the Geophysical Institute, Karlsruhe.
Contribution No. 207 of Special Research Program SFB 108 "Stress and Stress Release in the Lithosphere" of Karlsruhe University.

References

- Alfred-Wegener-Stiftung: 2nd International Symposium on Observation of the Continental Crust through Drilling (Abstracts) Seeheim, Federal Republic of Germany, Oct. 4–6, 1985, Bonn, 1985
- Althaus, E., Behr, H.J., Eder, F.W., Goerlich, F., Maronde, D., Ziegler, W.: Kontinentales Tiefbohrprogramm ("KTB") (Continental Deep Drilling Program) of the Federal Republic of Germany – Advances and status 1984. *Terra Cognita* **4**, 389–397, 1984
- Bartelsen, H., Lüschen, E., Krey, Th., Meissner, R., Schmoll, J., Walther, Ch.: The combined seismic reflection-refraction investigation of the Urach Geothermal anomaly. In: The Urach geothermal project, R. Haenel, ed.: pp. 247–262. Schweizerbart'sche Verlagsbuchhandlung, Stuttgart 1982
- Behr, H.-J., Engel, W., Franke, W., Giese, P., Weber, K.: The Variscan belt in Central Europe: main structures, geodynamic implications, open questions. In: H.J. Zwart, H.-J. Behr and J. Oliver (eds.), *Appalachian and Hercynian Fold Belts. Tectonophysics* **109**, 15–40, 1984
- Berkold, A., Musmann, G., Tezkan, B., Wohlenberg, J.: Electrical conductivity studies, Schwarzwald Working Group. Abstract, 2nd International Symposium on Observation of the Continental Crust through Drilling, Alfred-Wegener-Stiftung, Bonn, October 4–6, 1985, p. 70, 1985
- Blackburn, G.: Errors in stacking velocity – true velocity conversion over complex geologic situations. *Geophysics* **45**, 1465–1488, 1980
- Blundell, D.J., Raynaud, B.: Modeling lower crust reflections observed on BIRPS profiles. In: *Reflection seismology: a global perspective*, M. Barazangi, L. Brown, eds.: pp. 287–295. *Geodynamics Series Volume 13*, American Geophysical Union, Washington, D.C. 1986
- Bois, C., Cazes, M., Damotte, B., Galdéano, A., Hirn, A., Mascle, A., Matte, P., Raoult, J.F., Torrelles, G.: Deep seismic profiling of the crust in northern France: the ECORS project. In: *Reflection seismology: a global perspective*, M. Barazangi, L. Brown, eds.: pp. 21–29. *Geodynamics Series Volume 13*, American Geophysical Union, Washington, D.C. 1986
- Bonjer, K.-P., Apopei, I., Lüschen, E., Fuchs, K., Sandmeier, K.-J.: The Glottertal – 1986 micro-earthquake sequence – evidence of brittle deformation in the upper crustal reflector. Abstract of Poster Program, 2. KTB Kolloquium 19.9–21.9.1986 Seeheim, p. 54, 1986
- Bortfeld, R.K., Gowin, J., Stiller, M., Baier, B., Behr, H.J., Heinrichs, T., Dürbaum, H.J., Hahn, A., Reichert, C., Schmoll, J., Dohr, G., Meissner, R., Bittner, R., Milkereit, B., Gebrande, H.: First results and preliminary interpretation of deep-reflection seismic recordings along profile DEKORP 2-South. *J. Geophys.* **57**, 137–163, 1985
- Brown, L., Barazangi, M., Kaufman, S., Oliver, J.: The first decade of COCORP: 1974–1984. In: *Reflection seismology: a global perspective*, M. Barazangi, L. Brown, eds.: pp. 107–120. *Geodynamics Series Volume 13*, American Geophysical Union, Washington, D.C. 1986
- Censor, Y.: Finite series-expansion reconstruction methods. *Proc. IEEE* **71**, 409–419, 1983
- Chen, W.-P., Molnar, P.: Focal depths of intercontinental and intraplate earthquakes and their implications for the thermal and mechanical properties of the lithosphere. *J. Geophys. Res.* **88**, 4183–4214, 1983
- Christensen, N.I.: Compressional wave velocities in rocks at high temperatures and pressures. Critical thermal gradients, and crustal low-velocity zones. *J. Geophys. Res.* **84**, 6849–6857, 1979
- Christensen, N.I., Fountain, D.M.: Constitution of the lower crust based on experimental studies of seismic velocities in granulite. *Geol. Soc. Amer. Bull.* **86**, 227–236, 1975
- Cook, F.A., Brown, L.D., Kaufman, S., Oliver, J.E.: The COCORP seismic reflection traverse across the southern Appalachians. *American Association of Petroleum Geologists Studies in Geology* **14**, 61 p., 1983
- Damotte, B., Fuchs, K., Lüschen, E., Wenzel, F., Schlich, R., Torrelles, G.: Wide angle Vibroseis test across the Rhinegraben. *Geophys. J.R. Astron. Soc.* **89**, 313–318, 1987
- Deichmann, N., Ansorge, J.: Evidence for lamination in the lower continental crust beneath the Black Forest (southwestern Germany). *J. Geophys.* **52**, 109–118, 1983
- Demnati, A., Dohr, G.: Reflexionsseismische Tiefensondierungen im Bereich des Oberrheingrabens und des Kraichgaues. *Z. Geophys.* **31**, 229–245, 1965
- De Vries, D., Berkhout, A.J.: Influence of velocity errors on the focusing aspects of migration. *Geophys. Prospecting* **32**, 629–648, 1984
- Dinstel, W.L.: Velocity spectra and diffraction patterns. *Geophysics* **36**, 415–417, 1971
- Dix, C.H.: Seismic velocities from surface measurements. *Geophysics* **20**, 68–86, 1955
- Dohr, G.: Reflexionsseismische Messungen im Oberrheingraben mit digitaler Aufzeichnungstechnik und Bearbeitung. In: *Graben problems*, J.H. Illies, S. Mueller, eds.: pp. 207–218. Schweizerbart'sche Verlagsbuchhandlung, Stuttgart 1970
- Edel, J.B., Fuchs, K., Gelbke, C., Prodehl, C.: Deep structure of the southern Rhinegraben area from seismic refraction investigations. *J. Geophys.* **41**, 333–356, 1975
- Emmermann, R.: A petrogenetic model for the origin and evolution of the Hercynian granite series of the Schwarzwald. *Neues Jahrb. Mineral. Abh.* **128**, 219–253, 1977
- Finckh, P., Frei, W., Fuller, B., Johnson, R., Mueller, St., Smithson, S., Sprecher, Chr.: Detailed crustal structure from a seismic reflection survey in northern Switzerland. In: *Reflection seismology: a global perspective*, M. Barazangi, L. Brown, eds.: pp. 43–54. *Geodynamics Series Volume 13*, American Geophysical Union, Washington, D.C. 1986
- Fountain, D.M.: The Ivrea-Verbano and Strona-Ceneri zones, northern Italy: a cross-section of the continental crust – New evidence from seismic velocities of rock samples. *Tectonophysics* **33**, 145–165, 1976
- Fountain, D.M., Salisbury, M.H.: Exposed cross-sections through the continental crust: implications for crustal structure, petrology, and evolution. *Earth Planet. Sci. Letts.* **56**, 263–277, 1981
- Fromm, G.: Ermittlung statischer Grundkorrekturen. In: *Erfassung seismischer Daten*, 4. Mintrop-Seminar 1984, L. Dresen, J. Fertig, H. Rüter, W. Budach, eds.: pp. 253–313, 1984
- Fuchs, K.: On the properties of deep crustal reflectors. *Z. Geophys.* **35**, 133–149, 1969
- Fuchs, K., Mueller, G.: Computation of synthetic seismograms with the reflectivity method and comparison with observations. *Geophys. J.R. Astron. Soc.* **23**, 417–423, 1971
- Fuchs, K., Bonjer, K.-P., Gajewski, D., Lüschen, E., Prodehl, C., Sandmeier, K.-J., Wenzel, F., Wilhelm, H.: Crustal evolution of the Rhinegraben area. I. Exploring the lower crust in the Rhinegraben rift by unified geophysical experiments. *Tectonophysics*, in press, 1987
- Fyfe, W.S., Kerrich, R.: Fluids and thrusting. *Chem. Geol.* **49**, 353–362, 1985
- Gajewski, D., Prodehl, C.: Seismic refraction investigation of the Black Forest. *Tectonophysics*, in press, 1987
- Gajewski, D., Holbrook, W.S., Prodehl, C.: Three-dimensional crustal structure of southwest Germany, derived from seismic-refraction data. *Tectonophysics*, in press, 1987
- Gazdag, J.: Modeling of the acoustic wave equation with transform methods. *Geophysics* **46**, 854–859, 1981
- Gebrande, H.: CMP-Refraktionsseismik. In: *Seismik auf neuen Wegen*, 6. Mintrop-Seminar 1986, L. Dresen, J. Fertig, H. Rüter, W. Budach, eds.: pp. 191–205, 1986
- Gerke, K.: Die Karte der Bouguer-Isanomalien 1:1.000.000 von Westdeutschland. Frankfurt/Main: Institut für Angewandte Geodäsie 1957
- Giese, P.: Depth calculation. In: *Explosion seismology in Central Europe*, P. Giese, C. Prodehl, A. Stein, eds.: pp. 146–161, 1976

- Gordon, R., Bender, R., Herman, G.T.: Algebraic reconstruction techniques (ART) for three-dimensional electron microscopy and x-Ray photography. *J. Theor. Biol.* **29**, 471–481, 1970
- Götze, H.-J., Schmalfeldt, J., Wagener, M.: Gravimetrische und magnetische Vorerkundung im Schwarzwald. Internal KTB communication, reported in: Kontinentales Tiefbohrprogramm der Bundesrepublik Deutschland KTB, Ergebnisse der Vorerkundungsarbeiten Lokation Schwarzwald, v. Gehlen et al., eds.: pp. 29–30. 2. KTB-Kolloquium Seeheim/Odenwald, 19.9.–21.9.1986, 1986
- Hacker, W., Hirschmann, G.: Ältere und jüngere Thrust-Tektonik im Zentralschwarzwälder Gneiskomplex. Internal KTB communication, reported in: Kontinentales Tiefbohrprogramm der Bundesrepublik Deutschland KTB, Ergebnisse der Vorerkundungsarbeiten Lokation Schwarzwald, v. Gehlen et al., eds.: p. 76ff. 2. KTB-Kolloquium Seeheim/Odenwald, 19.9.–21.9.1986, 1986
- Hagedoorn, J.G.: The plus-minus method of interpreting seismic refraction sections. *Geophys. Prospecting* **7**, 158–182, 1959
- Hajnal, Z., Sereda, I.T.: Maximum uncertainty of interval velocity estimates. *Geophysics* **46**, 1543–1547, 1981
- Hale, L.D., Thompson, G.A.: The seismic reflection character of the continental Mohorovicic discontinuity. *J. Geophys. Res.* **87**, 4625–4635, 1982
- Illies, J.H.: Mechanism of graben formation. *Tectonophysics* **73**, 249–266, 1981
- Illies, J.H., Fuchs, K. (eds.): Approaches to taphrogenesis. Stuttgart: Schweizerbart'sche Verlagsbuchhandlung 1974
- Illies, J.H., Mueller, S. (eds.): Graben problems. Stuttgart: Schweizerbart'sche Verlagsbuchhandlung 1970
- Jones, T.D., Nur, A.: The nature of seismic reflections from deep crustal fault zones. *J. Geophys. Res.* **89**, 3153–3171, 1984
- Kern, H.: P- and S-wave velocities in crustal and mantle rocks under the simultaneous action of high confining pressure and high temperature and the effect of the rock microstructure. In: High-pressure researches in geoscience, W. Schreyer, ed.: pp. 15–45. Schweizerbart'sche Verlagsbuchhandlung, Stuttgart 1982
- Kern, H., Schenk, V.: Elastic wave velocities in rocks from a lower crustal section in southern Calabria (Italy). *Phys. Earth Planet. Inter.* **40**, 147–160, 1985
- Ketelsen, K., Marschall, R., Fromm, G.: Automatic picking of first arrivals with two-sided signals (Vibroseis). 45th E.A.E.G. Meeting, Oslo, Norway 1983
- Klein, H., Wimmenauer, W.: Eclogites and their retrograde transformation in the Schwarzwald. *Neues Jahrb. Mineral. Monatsh.* 25–38, 1984
- Klemperer, S.L., Hauge, T.A., Hauser, E.C., Oliver, J.E., Potter, C.J.: The Moho in the northern Basin and Range province, Nevada, along the COCORP 40° N seismic-reflection transect. *Geol. Soc. Amer. Bull.* **97**, 603–618, 1986
- Kosloff, D.D., Baysal, E.: Forward modeling by a Fourier method. *Geophysics* **47**, 1402–1412, 1982
- Kremenetsky, A.A., Ovchinnikov, L.N.: The Precambrian continental crust: its structure, composition and evolution as revealed by deep drilling in the U.S.S.R. *Precambrian Res.* **33**, 11–43, 1987
- Lerwill, W.E.: The amplitude and phase response of a seismic vibrator. *Geophys. Prospecting* **29**, 503–528, 1981
- Lippolt, H.J., Schleicher, H., Raczek, I.: Rb–Sr systematics of Permian volcanics in the Schwarzwald (SW Germany). *Contrib. Mineral. Petrol.* **84**, 272–280, 1983
- Lorenz, V., Nicholls, I.A.: Plate and intraplate processes of Hercynian Europe during the Late Paleozoic. *Tectonophysics* **107**, 25–56, 1984
- LOTEM Working Group: Schwarzwald, LOTEM-Tiefensondierung. Abstract of Poster Program, 2. KTB-Kolloquium, 19.9.–21.9.1986, Seeheim, p. 48, 1986
- Matte, Ph.: Tectonics and plate tectonics model for the Variscan belt of Europe. *Tectonophysics* **126**, 329–374, 1986
- Matthews, D.H., Cheadle, M.J.: Deep reflections from the Caldonides and Variscides west of Britain and comparison with the Himalayas. In: Reflection seismology: a global perspective, M. Barazangi, L. Brown, eds.: pp. 5–19. Geodynamics Series Volume 13, American Geophysical Union, Washington, D.C. 1986
- Meissner, R., Strehlau, J.: Limits of stresses in continental crusts and their relation to the depth-frequency distribution of shallow earthquakes. *Tectonics* **1**, 73–89, 1982
- Meissner, R., Wever, Th.: Nature and development of the crust according to deep reflection data from the German Variscides. In: Reflection seismology: a global perspective, M. Barazangi, L. Brown, eds.: pp. 31–42. Geodynamics Series Volume 13, American Geophysical Union, Washington, D.C. 1986
- Meissner, R., Lüschen, E., Flüh, E.R.: Studies of the continental crust by near-vertical reflection methods: a review. *Phys. Earth Planet. Inter.* **31**, 363–376, 1983
- Miller, M.K.: Stacking of reflections from complex structures. *Geophysics* **39**, 427–440, 1974
- Morton, J.L., Sleep, N.H.: Seismic reflections from a Lau Basin magma chamber. In: Geology and offshore resources of Pacific island arcs – Tonga region, D.W. Scholl, T.L. Vallier, eds.: pp. 441–453. Circum-Pacific Council for Energy and Mineral Resources Earth Science Series, vol. 2, Houston, 1985
- Mueller, St.: A new model of the continental crust. In: The Earth's crust, J.G. Heacock, ed.: pp. 289–317. *Geophys. Monogr. Series* **20**, American Geophysical Union, Washington, D.C. 1977
- Mueller, St., Peterschmitt, E., Fuchs, K., Ansorge, J.: Crustal structure beneath the Rhinegraben from seismic refraction and reflection measurements. *Tectonophysics* **8**, 529–542, 1969
- NAGRA: Technischer Bericht 85-01, Textband und Beilagenbände A und B. Nationale Genossenschaft für die Lagerung radioaktiver Abfälle, Baden, 1985
- Oliver, J.E.: Changes at the crust-mantle boundary. *Nature* **299**, 398–399, 1982
- Peddy, C., Brown, L.D., Klemperer, S.L.: Interpreting the deep structure of rifts with synthetic seismic sections. In: Reflection seismology: a global perspective, M. Barazangi, L. Brown, eds.: pp. 301–311. Geodynamics Series Volume 13, American Geophysical Union, Washington, D.C. 1986
- Plaumann, S., Groschopf, R., Schädel, K.: Kompilation einer Schwerekarte und einer geologischen Karte für den mittleren und nördlichen Schwarzwald mit einer Interpretation gravimetrischer Detailvermessungen. *Geol. Jahrb.* **E 33**, 15–30, 1986
- Prodehl, C., Ansorge, J., Edel, J.B., Emter, D., Fuchs, K., Mueller, S., Peterschmitt, E.: Explosion seismology research in the central and southern Rhine Graben – a case history. In: Explosion seismology in Central Europe. P. Giese, C. Prodehl, A. Stein, eds.: pp. 313–328. Berlin: Springer Verlag 1976
- Rühl, Th.: Tauchwellen-Tomographie für Stripping-Korrekturen und geologische Interpretationen bei den reflexionsseismischen KTB-Profilen im Schwarzwald. Diploma Thesis, Geophysical Institute of the University of Karlsruhe, 1987
- Sandmeier, K.-J., Wenzel, F.: Synthetic seismograms for a complex crustal model. *Geophys. Res. Lett.* **13**, 22–25, 1986
- Schenk, V.: Petrology of felsic granulites, metapelites, metabasics, ultramafics, and metacarbonates from Southern Calabria (Italy): prograde metamorphism, uplift and cooling of a former lower crust. *J. Petrol.* **25**, 255–298, 1984
- Schmucker, U., Tezkan, B.: Zur Deutung regional einheitlicher Richtungsabhängigkeiten tellurischer Variationen. 47th Ann. Meeting of Dtsch. Geophys. Gesell., Clausthal-Zellerfeld, 31.3.–4.4.1987
- Schnell, H.P.: Untersuchung des Einflusses oberflächennaher Schichten auf seismische Signale und Beiträge zur Optimierung des Vibroseis-Verfahrens. Diploma Thesis, Geophysical Institute of the University of Karlsruhe, 1987
- Sheriff, R.E., Geldart, L.P.: Exploration seismology, Volume 2. Data-processing and interpretation. Cambridge: Cambridge University Press, 1983
- Sittig, E.: Zur geologischen Charakterisierung des Moldanubikums

- am Oberrhein (Schwarzwald). *Oberrh. Geol. Abh.* **18**, 119–161, 1969
- Slichter, L.B.: The theory of the interpretation of seismic travel time curves in horizontal structures. *Physics* **3**, 273–295, 1932
- Smithson, S.B., Johnson, R.A., Hurich, C.A.: Crustal reflections and crustal structure. In: *Reflection seismology: the continental crust*, M. Barazangi, L. Brown, eds.: pp. 21–32. *Geodynamics Series Volume 14*, American Geophysical Union, Washington, D.C. 1986
- Stenger, R.: Petrology and geochemistry of the basement rocks of the Research Drilling Project Urach 3. In: *The Urach Geothermal Project*, R. Haenel, ed.: pp. 41–47. Schweizerbart'sche Verlagsbuchhandlung, Stuttgart 1982
- Stiefel, A., Wilhelm, H., Finkbeiner, K., Haack, U.: Geothermal studies, Schwarzwald. Abstract of poster, 2nd International Symposium on Observation of the Continental Crust through Drilling, Alfred-Wegener-Stiftung, October 4–6, 1985, Seeheim, p. 72, 1985
- Vogelsang, D.: Geothermische und geologische Vorerkundung der Tiefbohrlokation Oberpfalz und Schwarzwald. Teilgebiet Bohrlochgeophysik Schwarzwald. Bericht NLFb Hannover, Archiv-Nr. 99126, 1986
- Warner, M.: Migration – why doesn't it work for deep continental data? *Geophys. J.R. Astron. Soc.* **89**, 21–26, 1987
- Walther, Ch., Trappe, H., Meissner, R.: The detailed velocity structure of the Urach geothermal anomaly. *J. Geophys.* **59**, 1–10, 1986
- Wenzel, F., Sandmeier, K.-J., Wälde, W.: Properties of the lower crust from modeling refraction and reflection data. *J. Geophys. Res.*, in press, 1987
- Wimmenauer, W., Adam, A.: High-pressure phenomena in acid rocks accompanying eclogites in the Schwarzwald (SW Germany). *Terra Cognita* **5**, 426, 1985
- Winterstein, D.F.: Anisotropy effects in P-wave and SH-wave stacking velocities contain information on lithology. *Geophysics* **51**, 661–672, 1986
- Zucca, J.J.: The crustal structure of the southern Rhinegraben from re-interpretation of seismic refraction data. *J. Geophys.* **55**, 13–22, 1984

Received January 27, 1987; revised June 16, 1987

Accepted June 17, 1987

Seismic ground motion of sedimentary valleys – example La Molina, Lima, Peru

J. Zahradník¹ and F. Hron²

¹ Institute of Geophysics, Charles University, Ke Karlovu 3, 121 16 Praha 2, Czechoslovakia

² Institute of Earth and Planetary Physics, University of Alberta, Edmonton, Alberta T6G 2J1, Canada

Abstract. Strong motion accelerograms recorded at two sites in Lima, Peru, during the earthquake of November 9, 1974, exhibit serious dissimilarities although the sites have nearly the same epicentral distance. The two sites are the Instituto Geofísico del Perú in central Lima and the La Molina sediment-filled valley on the periphery of the city. The anomalously strong and prolonged ground motion at the La Molina site seems to be explained by a *combined* effect of the *complex topography of the bedrock* and the presence of *low-velocity subsurface sediments*. In contrast to an intuitive feeling, a strong velocity contrast along the whole sediment-bedrock interface is not necessary. Because severe earthquake effects in La Molina are of site origin, they should be expected to repeat in the future. As indicated by synthetic accelerograms, the anomaly refers to large areas of the La Molina valley and not only to the immediate vicinity of the recording point. For purposes of seismic microzoning and land-use planning, two microzones in the studied part of the valley will probably be appropriate.

Key words: Strong ground motion – Seismic microzoning – Local site effects – Sedimentary basins – Finite-difference method

Introduction

On November 9, 1974, at 12 h 59 m 49.8 s UT, an earthquake of magnitude $M_S=7.2$ occurred in the Pacific, $12^\circ30' S$, $77^\circ47' W$ (see Giesecke et al., 1980), at a distance of about 100 km from Lima. At two sites in the city (Fig. 1) the earthquake was recorded by standard strong motion accelerographs (Brady and Perez, 1977). While the first site, Instituto Geofísico del Perú (IGP) in central Lima, belongs to an area only weakly shaken by this earthquake as well as by previous earthquakes, the La Molina (MOL) site on the periphery is well known to be one of a few areas in Lima with extremely severe earthquake effects (Deza et al., 1976; Espinosa et al., 1977; J. Alva Hurtado, J. Kuroiwa, L. Ocola – personal communications). Correspondingly, the accelerograms from the IGP and MOL sites differ considerably.

In this paper we deal with low-passed (0–12.5 Hz) horizontal components (Fig. 2). The difference between the IGP and MOL components refers not only to peak acceleration

values a_{max} , but to the whole wave pattern. The MOL record is of longer duration and exhibits sharp later onsets. In the next section, the explanation of these differences will be given in terms of local site conditions. For more details, see Zahradník and Hron (1986). Practical implications for earthquake engineering and land-use planning will then be given in the following section. The paper was stimulated by the fact that the campus of Universidad Nacional Agraria, located at the La Molina site, was much more heavily damaged than similar buildings in central Lima in 1970 and 1974. This fact calls for detailed investigations and decisive antiseismic measures.

Explaining the La Molina anomaly

In contrast to the weakly horizontally varying IGP subsurface structure, the MOL site is a complex (three-dimensional) sediment-filled valley. The bedrock is probably rep-

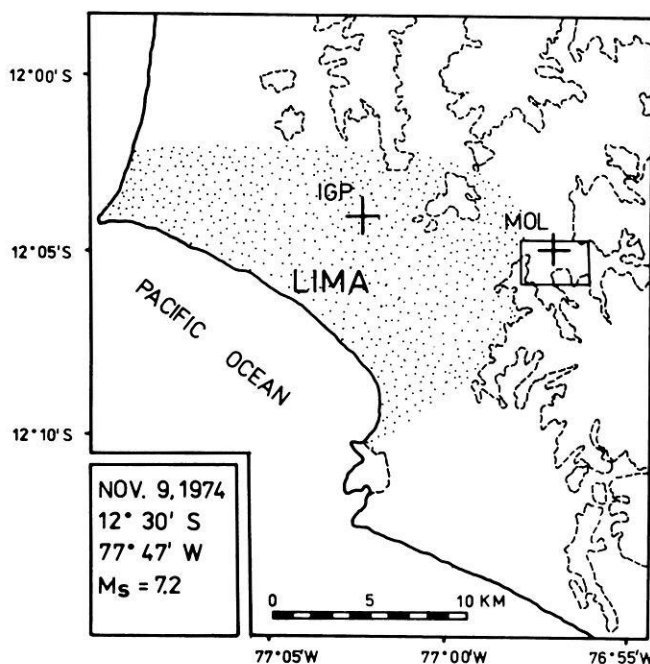


Fig. 1. Location of the IGP and MOL sites. The Lima territory is shown schematically as a *dotted area*. Surrounding hills are denoted by *dashed lines*. Parameters of the studied earthquake are given at the *left-hand corner*. A detailed map of the La Molina site (MOL) is given in Fig. 3

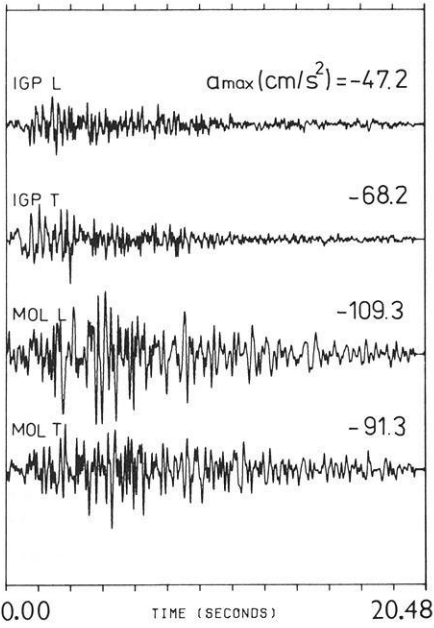


Fig. 2. Comparison of the low-pass filtered (0–12.5 Hz) accelerograms at the IGP and MOL sites of Lima, November 9, 1974; data from Brady and Perez (1977)

resented by hard crystalline rocks, as exposed on surrounding hills. Topography of the bedrock is approximately known from electrical resistivity measurements, as shown by the isolines in Fig. 3. Based on this map, we constructed eight cross-sections along linear profiles intersecting at the point where the La Molina strong motion accelerogram of November 9, 1974, was taken (Fig. 4). The intersection point is denoted by an arrow in each cross-section. Note that along some of the profiles the bedrock forms a local elevation, reaching the ground surface on profile 5 (see the small hill inside the valley in Fig. 3). This obstacle will be shown to play an important role in forming the seismic response of the whole site.

Sediments filling the La Molina valley are of Quaternary age. Their velocity-depth variation is not well known. We

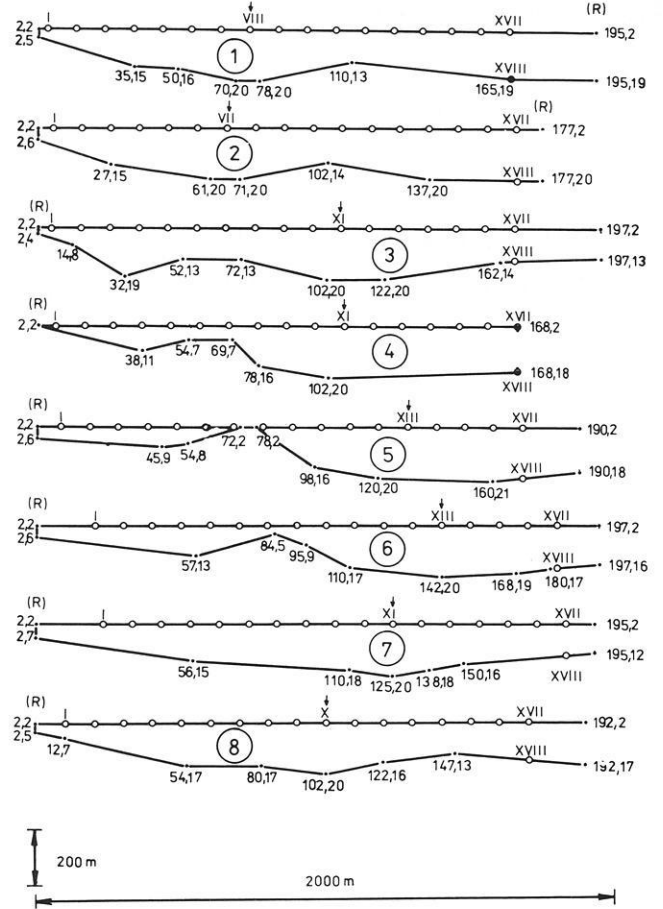


Fig. 4. Cross-sections of the La Molina basin along the individual profiles of Fig. 3 (their orientation shown by *R*). For the finite-difference method, the cross-sections are represented by polygons. Each corner is denoted by two integers, NX and NZ . The horizontal and vertical coordinates x and z of the corners (in metres) are given by $x = (NX - 2) \cdot 10$ and $z = (NZ - 2) \cdot 10$, respectively. The bottom line of each cross-section is the sediment-bedrock interface. The open circles indicate the locations ("receivers"), numbered I–XVIII, for which the synthetics were computed. The arrow on each profile marks the point of intersection of all eight profiles

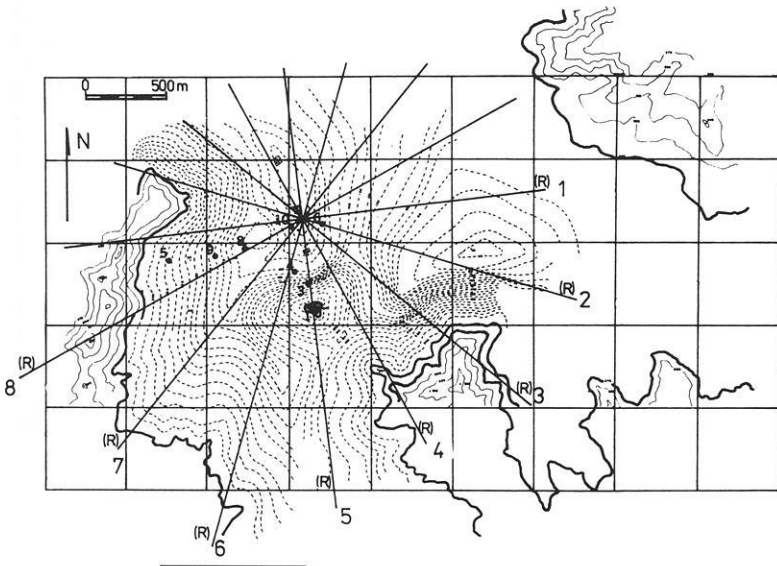


Fig. 3. The La Molina (MOL) site of Lima and eight radial profiles intersecting at the point of the strong motion recording station of November 9, 1974. The right-hand sides (*R*) of the profiles are shown, to which we refer in Fig. 4. The background map (after R. Benites, personal communication) illustrates the topography of the basin bottom by dashed lines; for a quantitative description see Fig. 4. The hills surrounding the sediment-filled basin are represented by full lines. Numbered dots denote the recording points of Tucker and Benites, mentioned in the text

only definitely know that the uppermost layer, about 10 m thick, is much less consolidated as compared to central Lima. It is likely that the same applies up to depths of about 50 m, as indicated by a few bore-hole data.

We attempt to explain the La Molina anomaly by computing synthetic accelerograms. The incompleteness of the subsurface data is believed to be at least partly compensated by extensive numerical experiments (more than 20 two-dimensional models and more than 500 synthetic accelerograms). Successful models, in which synthetics reasonably fit the specific features of the MOL record, serve for analysing physical factors influencing the ground motion. At the same time, they serve for extrapolating the ground motion from the recording point to the whole surface of the valley (points denoted by circles in Fig. 4).

The procedure is very simple. We start with the IGP record of November 9, 1974. Using a horizontally layered model of the IGP site and the simplest assumption of vertically propagating plane shear body waves, we deconvolve the surface record to obtain the acceleration time history of the *incident wave*. A possible IGP structure is shown by curve 3 of Fig. 5. This is a velocity-depth section for shear waves averaged from two extremes, labelled 1 and 2 in Fig. 5, proposed by P. Orihuela of IGP (personal communication). Figure 5 also displays the modulus of the IGP transfer function computed for model 3 by the matrix method. As the predominant frequencies of the November 9, 1974, accelerogram at IGP are 2.5–4.0 Hz (not shown here) and, since the transfer function varies slowly in that range, the incident waveform is very similar to that of the surface record. The whole difference can be well described by a factor 4 amplitude reduction. For this reason we do not present the incident wave graphically here.

Next, we assume the MOL site to be excited by the same incident wave, but now the wavefield is *numerically propagated upwards* and the individual two-dimensional La Molina cross-sections are analysed. The velocity-depth variation of the valley sediments is (optionally) taken into account. Only *SH* waves, vertical incidence, and non-absorbing media are considered for simplicity. The computational method based on finite differences is used (Zahradnik, 1982, 1985; Zahradnik and Urban, 1984). It consists of two steps. In the first one we compute an approximation to the impulse response of the basin using a simple delta-like impulse of short duration $T (= 0.06$ or 0.08 s). In the second step we convolve this response with the incident wave. The space and time grid steps are $\Delta x = 10$ m and $\Delta t = 0.0027$ s, respectively. The method is of acceptable accuracy up to frequencies $f_{ac} = \beta_{min}/12 \Delta x$, where β_{min} denotes the minimum shear velocity. With $\beta_{min} = 500$ m/s in the models used, $f_{ac} \doteq 4$ Hz. Although relatively small, this value is sufficient for explaining the main features of the MOL record whose predominant frequencies are 1–4 Hz (MOL spectra are not shown here). This fact, together with the predominance of frequencies $f = 2$ –4 Hz in the incident wave mentioned above, makes it possible to retain formally in our synthetic accelerograms even frequencies $f > 4$ Hz with low accuracy. In other words, the incident wave together with the structure act as a filter to suppress the numerical error connected with higher frequencies.

Obviously, this approach works well only when the numerical error has no character of spurious resonances (i.e. a strongly band-limited ringing). The resonance does occur in a vicinity of the highest frequency transmitted by the

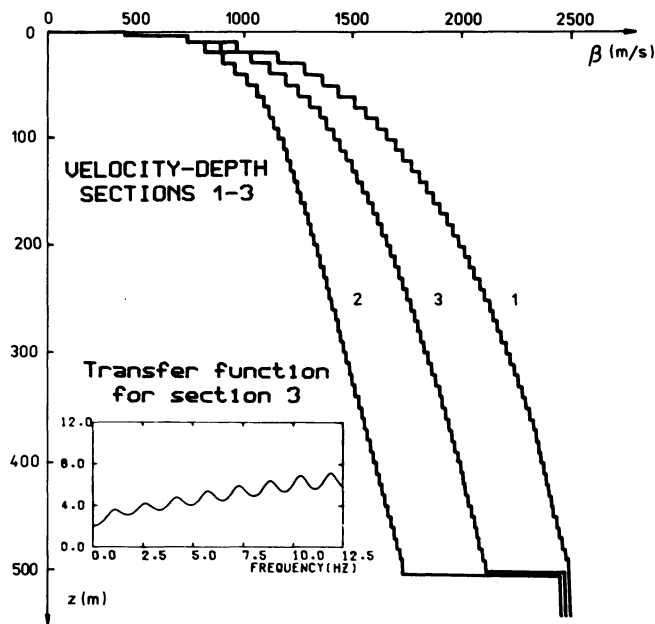


Fig. 5. Shear-wave velocity-depth sections. Curves 1 and 2 represent two extremes (curve 3 is their average) assumed for the IGP site. The inset shows the modulus of the transfer function corresponding to curve 3

grid, $f_{cut-off} = \beta_{min}/2 \Delta x = 25$ Hz, if the impulse spectrum does not fall to zero for $f < f_{cut-off}$. Our impulse spectrum falls to zero at $f \doteq 3/T (= 50$ or 37.5 Hz). To avoid the influence of the resonance close to 25 Hz we restrict ourselves to $f = 0$ –12.5 Hz only, i.e. frequencies beyond 12.5 Hz are filtered out from the impulse response, synthetic accelerograms, and also (for comparison) from the observed records.

As a consequence at $4 < f < 12.5$ Hz we have no accurate computations, but the error has no resonant character and, moreover, its influence is limited by the incident wave and the structure as explained above. Retaining $4 < f < 12.5$ Hz is advantageous because it makes a qualitative interpretation of the computed wavefield easier as compared to the case of filtering out all inaccurate frequencies; e.g., see, Figs. 9 and 10.

Three different classes of La Molina computational models were considered: (i) homogeneous basins with low-velocity sediments, (ii) two-layered basins with a relatively strong interface between the upper low-velocity and the lower high-velocity sediments and (iii) multilayered basins with a quasi-smooth velocity-depth increase (weak interfaces between the individual layers 10 m thick) and relatively high velocities in deep sediments. In *each class*, some successful models have been found, thus illustrating the non-uniqueness of the interpretation. However, *all together* they provide a strong indication of the primary role of the bedrock topography at the La Molina site. This will be shown here by three examples.

The first example, model 403, corresponds to a relatively low (500 m/s) *constant* shear-wave velocity in the sediments and cross-section 4; the bedrock velocity is supposed to be 2500 m/s. In Fig. 6 the synthetic accelerogram of this model is compared to the original IGP and MOL records. The synthetic is just for the point of intersection of the profiles (point XI of cross-section 4). We emphasize, of

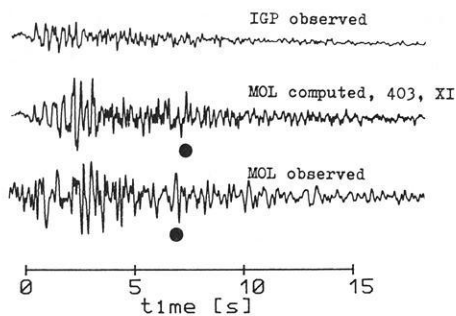


Fig. 6. Comparison of the observed IGP (*top*) and MOL (*bottom*) accelerograms with the synthetic MOL accelerogram computed for the receiver location XI of profile 4 (cf. Fig. 4) in model 403 (*middle*). Model 403 is the basin with *constant* sediment velocity. The dots indicate one of the later arrivals. We emphasize that the *middle* trace was obtained in the course of computation from the top one, without any knowledge of the bottom trace

course, that what are plotted are the mutually shifted records (so as to give the best fit) because we do not know the actual time shift between the IGP and MOL original records. As seen from Fig. 6, the synthetic accelerogram fits not only peak acceleration well, but also the bell-shaped envelope and one of the sharp later onsets (see the dots). It can be shown, by a figure analogous to Fig. 9 presented below, that the success of model 403 is due to strong interference waves propagating horizontally from the valley edge, and also from the local bedrock elevation inside the valley. Such waves, interpreted as local surface waves by Bard and Bouchon (1980), result from overcritical reflections at the strongly inclined bottom. A necessary condition for a good fit with a homogeneous basin is the relatively low sediment velocity; otherwise the local surface waves are too weak.

To complete the presentation of model 403, synthetic accelerograms (left) and their normalized Fourier amplitude spectra (right) are given for the whole profile 4 in Fig. 7. The curves denoted 1, 2, 3, ... correspond to *odd* receivers I, III, V, ... of Fig. 4. Their discussion will be given in the next section.

The second example corresponds to the *two-layered*

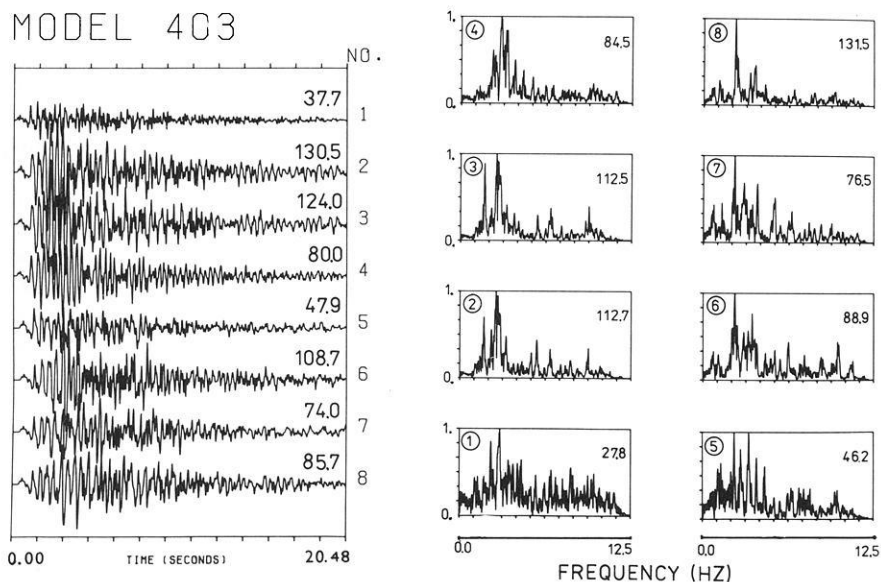


Fig. 7. Synthetic accelerograms (*left*) and their normalized Fourier amplitude spectra (*right*) of the La Molina basin model 403. The peak accelerations a_{\max} in cm/s^2 and the actual maxima of the spectra, in cm/s , are given on the individual curves. Curves 1, 2, ... 8 correspond to the *odd* receiver locations I, III, ... XV on cross-section 4 of Fig. 4

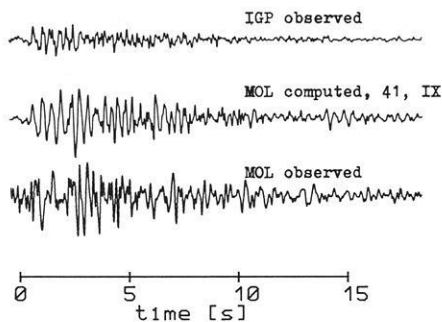


Fig. 8. The same as Fig. 6, but for receiver IX of profile 4 and model 41. Model 41 is the *two-layered* basin. Again, the *middle* trace was obtained from the top one, without any knowledge of the bottom "target" trace. For other examples with different models and profiles, see Zahradník and Hron (1986)

model 41, Fig. 8. It again refers to profile 4. The upper layer (50 m thick) now has a shear-wave velocity of 500 m/s and the velocity in the lower layer is 1500 m/s. The bedrock velocity is again 2500 m/s. Here a slightly better fit to the real MOL record was found with the synthetic accelerogram No. 5 (point IX) than with No. 6 (strictly equivalent to the recording point XI). In model 41 the local surface wave is even better developed than in model 403, and it dominates the wavefield. Because of the internal discontinuity in the sediments, this wave (L) is now *trapped* by the low-velocity subsurface layer acting as a *waveguide*. This can best be seen from the low-pass filtered impulse response (Fig. 9).

The response was computed with $T=0.06$ s. Although for further computation the response was filtered by means of a simple cosine taper between 10.7 and 12.5 Hz, for purposes of its qualitative interpretation we present another filtering in Fig. 9. In this case the filtering is realized through convolving the computed response with the impulse $g(t) = \sin(2\pi t/\tilde{T}) - 0.5 \sin(4\pi t/\tilde{T})$, $\tilde{T}=0.24$ s. Such presentation is advantageous for two reasons: (i) $g(t)$ is not very long, thus the individual waves can be identified and (ii) using $g(t)$, the predominant frequency of which is near to 4 Hz, the frequencies $4 < f < 12.5$ Hz are sup-

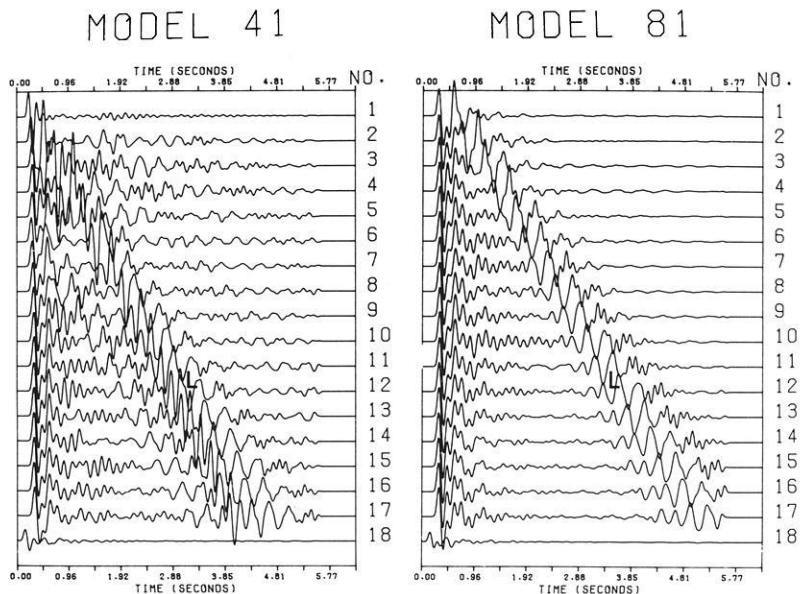


Fig. 9. The low-pass filtered (0–12.5 Hz) impulse responses computed for profiles 4 and 8 with *two-layered* models 41 and 81, respectively. For filter details see the text. *The curves labelled 1–18* correspond to locations I–XVIII of Fig. 4. *L* is the local surface wave generated at the edge of each cross-section (and, to a lesser degree, also at the local bedrock elevation of cross-section 4). The *L* wave dominates the wavefield because of the guiding effect of the upper low-velocity sedimentary layer of the models used. Note the long duration of the impulse response, caused by the *L* wave, explaining the observed long duration of the MOL accelerogram (cf. Fig. 8)

pressed in a similar way to the low-pass incident wave used for computing accelerograms. The fundamental, as well as the first higher waveguide mode, is evident from Fig. 9. Nevertheless, the sloping bedrock still represents the primary factor needed for developing the waveguide phenomenon. The same applies in general for all profiles, although each of them has its specific features corresponding to the bedrock geometry. See, for example, profile 8 (i.e. model 81, fully analogous to 41), included in Fig. 9 for comparison. The response of profile 4 is more complex due to its very shallow edge part and due to the local bedrock elevation.

The third example (Fig. 10) is to confirm the guided local surface waves even for *multilayered models* 432 and 832 with a *quasi-smooth* velocity-depth increase. Figure 10 refers again to profiles 4 and 8, but (in contrast to Fig. 9) the velocity-depth section of the valley sediments is now given by curve 2 of Fig. 5 and $T=0.08$ s is used. The cosine tapering between 10.7 and 12.5 Hz is used instead of convolving with $g(t)$ here. Thus the inaccurately computed frequencies $f > 4$ Hz are less suppressed, but the individual waves are qualitatively better seen. The model also exhibits an interesting *focusing* of the reflected wave *R*, caused by the local bedrock depression below the points denoted by the arrow, e.g. at point *X* of profile 8, but *the role of this focusing is smaller than that of the wave L*. Note again the more complex response of profile 4 with respect to profile 8 (and also with respect to other profiles not presented here).

In other words, neither a very strong velocity contrast across the deep valley bottom nor a strong internal discontinuity inside the sediments is necessary for generating strong local surface waves. Instead, shallow low-velocity subsurface sediments overlying the steeply sloping bedrock at the edges of the valley (or in the vicinity of the local bedrock outcrop inside the valley) are sufficient. This is an important and generally valid finding of the present paper, a feature of sedimentary basins to which no sufficient attention has yet been paid by other investigators. Although the available geophysical data on the La Molina site are very sparse, it is quite definitely known that both conditions

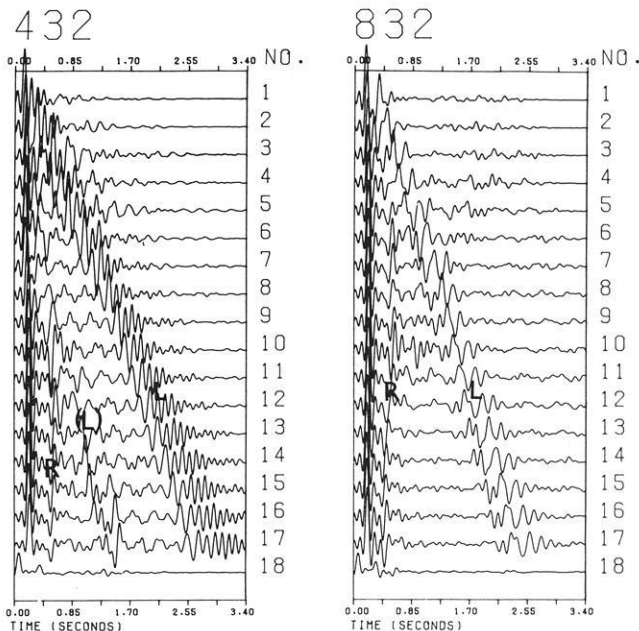


Fig. 10. Analogous to Fig. 9 but for *multilayered models* 432 and 832, respectively. For filter details, different from those of Fig. 9, see the text. *L* is the local surface wave, *R* is the wave reflected from the bedrock. Although the *R* wave exhibits a strong focusing effect, e.g. at point *X* of profile 8, the *L* wave still dominates the whole response. *The bracketed L, (L)*, denotes the local surface wave generated on profile 4 at the local bedrock elevation

(i.e. very soft subsurface sediments and the steeply sloping bedrock beneath them) are fulfilled there. Consequently, it is very likely that strong local surface waves guided mainly in the uppermost sediments do play an important role at that site. It is just these waves of very small apparent velocities (like *L* in Fig. 9) that yield a significant *lengthening* of the impulse response and, as a result, the prolongation of the accelerograms.

Another important fact is that the steeply sloping bedrock bounds the La Molina valley on several sides. Thus not only one, but several local surface waves originate

which (besides other effects) contribute to producing sharp late onsets. This applies probably to profiles 1 and 8 most strongly.

Before concluding this section, more attention should be devoted to the potential effect of *absorption*. Our computational method makes it possible to consider causal or non-causal absorption models, when neither β nor the phase velocity and the absorption coefficient depend on spatial coordinates. For basins with a spatially variable velocity, the non-causal (constant phase velocity) model with a spatially independent quality factor Q is easily applicable. The same approach as originally proposed for basins with absolutely rigid bottom may be used, as given by Eqs. (3)–(12) of Zahradník (1982). For more exact, but also more expensive, incorporation of absorption, see Emmerich and Korn (1987). We assumed that the effect of absorption is very large in the valley sediments, and thus we analysed several profiles taking absorption into account. However, in none of these models were we able to fit the observed MOL record; the synthetics were of smaller amplitudes and shorter durations than necessary, even though our Q was relatively large ($Q=40$). For this reason we do not present the synthetics with absorption here at all. Of course, this result is purely *formal* and by no means implies extremely high Q at the La Molina site. Rather, it means that the assumed velocities are wrong, or that neglecting the 3-D character of the valley in our 2-D computations makes the synthetics too weak. The latter explanation seems to be supported theoretically: the so-called transverse spreading of certain 3-D structures may have a strongly amplifying effect (Eq. 10.26, p. 102 of Červený, 1985), as lateral effects may lead to a contraction of ray tubes of the waves under consideration. We do not want to go into more detailed speculations here, but rather to analyse the effect of Q at another sedimentary basin where better data on shear velocities are available.

In summary, what probably makes the La Molina ground shaking so strong and long is the position of the site inside the valley of a complex bedrock topography (steeply sloping bedrock on several sides, and the inner bedrock elevation), together with the presence of surficial unconsolidated sedimentary layers. The layers themselves (i.e. without the sloping bedrock) would amplify the ground motion at selected frequencies, but they would probably never be able to prolong the ground motion as much as the La Molina site does.

Practical implications

Being of site origin, the severe earthquake effects should be expected to occur in La Molina repeatedly. Thus seismologists are forced to specify not only the expected differences of the La Molina ground motion with respect to central Lima, but to *microzone* the La Molina valley in detail. This is not the aim of this paper; thus we only intend to illustrate the efficiency of the computational approach to this problem. In fact, once we find a model for which the synthetics fit the La Molina record at most of the studied profiles, we can assume that the synthetics corresponding to other receiver positions in the same model also give a reasonable approximation to the actual La Molina ground motion. For example, in our case we have more than 100 synthetics (8 profiles) for the whole studied part of the valley, a number large enough to delineate areas of similar

expected ground motions. Such an *extrapolation* seems to represent a very interesting feature of the computational approach to seismic microzoning problems, not widely used till now. Without going into details, we only emphasize that the microzoning map of the La Molina valley near the campus will probably be extremely *simple*, perhaps with *two microzones* only. We base this assumption on our present knowledge of several profiles, e.g. profile 4 in Fig. 7 where all synthetics (and their spectra) group into two classes only; type A – Nos. 2, 3, 4 and Nos. 6, 7, 8; and type B – No. 1, and No. 5. The synthetics of type A are strongly amplified and have a much narrower spectral band with respect to those of type B. Type A seems to be very common (on profile 4 as well as on the other profiles), thus indicating that the anomalous ground motion recorded on November 9, 1974, at one point in the valley was *not* a very local phenomenon of this point and its immediate vicinity, but rather that large areas of the valley behaved similarly. Of course, there is variability within type A too (see Fig. 7), but it is probably insignificant from the viewpoint of our knowledge of the subsurface geology and simplifying assumptions. Moreover, a more detailed microzoning would be impractical from the viewpoint of earthquake engineering. On the other hand, the difference between type A and type B is very large, and the transition between them quite abrupt (a factor 3 difference between accelerations No. 1 and No. 2 over a distance of only 200 m, as well as the broad-band and the narrow-band spectrum, respectively, Fig. 7), to justify their discrimination for practical purposes.

Our computational result of a very common occurrence of qualitatively the same (type A) seismic response in large areas of the La Molina site is consistent with the instrumental results of B. Tucker and R. Benites (personal communication). Based on simultaneous recordings of weak earthquakes at selected points of the La Molina valley (numbered points of Fig. 3), these authors derived ratios of spectra at the individual points with respect to point 1 at the rock outcrop on the small hill inside the valley. These ratios did not significantly differ from one point to another inside the valley.

In this respect the La Molina valley seems to behave similarly to the Chusal Valley, Garm (Tadjik SSR), but differently from the other valleys of the Garm region; see Tucker and King (1984).

We also mention that instrumentally determined spectral ratios were found to be practically independent of the earthquake azimuth (in Garm as well as in La Molina). Investigating azimuths different from those of the profiles, i.e. solving 3-D problems, represents serious difficulties for computational methods. In this respect, the instrumental methods are very useful. On the other hand, where applicable, the computational methods give better physical understanding of site anomalies.

Conclusion

The importance of local surface waves generated in sedimentary basins by earthquakes has been theoretically well established over the past years. This paper confirms their existence at a specific site, but also (and what is methodically more important) shows how relatively shallow low-velocity sediments strongly contribute to the generation and guiding of these waves. Our results also indicate that, in contrast to an intuitive feeling, a strong velocity contrast

along the *whole* sediment-bedrock interface is *not* necessary for making local surface waves intensive. Obviously, conditions for local surface waves being strong are probably fulfilled at many sites, including sediment-filled valleys with relatively high velocity gradients, since the presence of very soft surficial sediments above steeply sloping rocks at the edges of sedimentary basins is common enough.

A second point to emphasize is the efficiency of computational methods for extrapolating strong ground motions recorded at one or a few points of a sedimentary structure to the whole surface of the structure; a procedure valuable for seismic microzoning and land-use planning purposes.

Acknowledgements. The first-named author expresses his deepest gratitude to the Instituto Geofísico del Perú, Lima, and the Institute of Earth and Planetary Physics, Edmonton, for support and hospitality during his study visits to these institutions. The authors also thank two anonymous reviewers and G. Müller for their valuable comments which substantially helped them to improve the text.

References

- Bard, P.Y., Bouchon, M.: The seismic response of sediment-filled valleys. Part 1. The case of incident SH waves. *Bull. Seismol. Soc. Am.* **70**, 1263–1286, 1980
- Brady, A.G., Perez, V.: Strong-motion earthquake accelerograms, digitization and analysis; records from Lima, Peru: 1951 to 1974. Open-file report No. 77-587, U.S. Geological Survey, Menlo Park, 1977
- Červený, V.: The application of ray tracing to the numerical modeling of seismic wavefields in complex structures. In: *Seismic shear waves*, G.P. Dohr, ed.: pp. 1–124, London: Geoph. Press 1985
- Deza, E., Berrocal, J., Silgado, E., Rodriguez, A., Carbonel, C.: Intensidades observadas en Lima por el terremoto del 3 de Octubre de 1974 (informe). Instituto Geofísico del Perú, Lima, 1976
- Emmerich, H., Korn, M.: Incorporation of attenuation into time-domain computations of seismic wavefields. *Geophysics* **52**, 1987 (in press)
- Espinosa, A.F., Husid, R., Algermissen, S.T., De las Casas, J.: The Lima earthquake of October 3, 1974: intensity distribution. *Bull. Seismol. Soc. Am.* **67**, 1429–1439, 1977
- Giesecke, A., Ocola, L., Silgado, E., Herrera, J., Giuliani, H.: El terremoto de Lima del 3 de Octubre de 1974 (informe). Lima: CERESIS/UNESCO 1980
- Tucker, B.E., King, J.L.: Dependence of sediment-filled valley response on input amplitude and valley properties. *Bull. Seismol. Soc. Am.* **74**, 153–165, 1984
- Zahradník, J.: Seismic response analysis of two-dimensional absorbing structures. *Studia Geophys. at Geodaet.* **26**, 24–41, 1982
- Zahradník, J.: Programs for computing and analysing SH wavefields in two-dimensional absorbing block structures. In: *Programs for interpreting seismic observations 3* (in Russian), N.N. Matveeva, ed.: pp. 124–186, Leningrad: Nauka 1985
- Zahradník, J., Hron, F.: Earthquake ground motion at the La Molina sedimentary basin, Lima, Peru. Res. Report to CERESIS, Lima (60 pp., 18 figs., available on request) 1986
- Zahradník, J., Urban, L.: Effect of a simple mountain range on underground seismic motion. *Geophys. J.R. Astron. Soc.* **79**, 167–183, 1984

Received December 1, 1986; revised version May 25, 1987

Accepted May 29, 1987

Seismic response of two-dimensional absorbing structures by the ray method

P. Moczo¹, P.-Y. Bard², and I. Pšenčík³

¹ Geophysical Institute, Centre of Geoscience Research, Slovak Academy of Sciences, Dúbravská cesta, 84228 Bratislava, Czechoslovakia

² Université Scientifique et Médicale de Grenoble, Laboratoire de Géophysique Interne et Tectonophysique, I.R.I.G.M., BP 68, F-38402 St. Martin d'Hères, Cedex, France

³ Geophysical Institute, Czechoslovak Academy of Sciences, Boční II, 141 31 Praha 4, Czechoslovakia

Abstract. A method of seismic response analysis of 2–*D* inhomogeneous structures, based on the ray method and on the application of the Debye procedure to include slight absorption, is presented. Program package RESPO, designed for such an analysis of the seismic response on the free surface of a general 2–*D* laterally varying, geological near-surface structure assuming *P*, *SV* or *SH* plane-wave incidence from below, is briefly described. The package is tested on the classical model of a sedimentary basin. The study differs from previous applications of the ray method to the basin model in the following aspects. The frequency-domain approach is used. A comparison of the ray method results with the results of the discrete wavenumber method for long periods is made. More attention is paid to the analysis of the formation of the wave field. This analysis reveals two main types of wave propagation inside the basin: the dominant horizontally propagating local interference waves and less expressive vertically propagating waves in the central part of the basin. Effects of slight absorption (Futterman's causal absorption) are considered. The absorption causes a decrease in amplitudes and time delays at later times. The decrease in the amplitudes is not so expressive because of large periods and relatively short travel times of the waves investigated.

Key words: Seismic response – Ray method – Frequency-domain approach – Slight causal absorption – Classical basin problem

Introduction

Surface and subsurface topography and/or the presence of sediments on a rock basement can cause local anomalies of ground motion or of a macroseismic field. These local effects have been studied by observing macroseismic effects, instrumentally and also theoretically. The instrumental and theoretical (e.g., numerical) methods enable the transfer properties of local geological structures to be studied. An advantage of the instrumental methods is that they simplify neither the local structure nor the incident wave field. The principal advantage of the numerical methods is that they enable us to predict a time history of vibrations and make possible detailed parametric studies and a physical understanding of the wave phenomena. A detailed insight into the wave field in the local structures has not only a theoretic-

cal meaning. The understanding of the basic wave phenomena allows us to make the first qualitative judgement of the seismic mobility of a site assuming certain knowledge of the geological structure; this helps, e.g., in better organization of experiments at the site. Finally, understanding the basic wave phenomena obtained for a certain group of exciting signals enables us to generalize conclusions on the seismic mobility of a site due to other exciting signals.

Various methods have been used to compute the seismic response of local geological structures. Let us mention the matrix method (Johnson and Silva, 1981), the finite-difference method (Zahradník and Hron, 1986), the discrete wavenumber method (Bard and Gariel, 1986), the boundary integral method (Dravinski, 1983; Sanchez-Sesma et al., 1985) and analytical methods (Yerokhin, 1985). The ray method has been used by Hong and Helmberger (1978), Langston and Lee (1983), Lee and Langston (1983a, b) and Moczo et al. (1986). The Gaussian beam method has also been used for this purpose by Nowack and Aki (1984). Only some recent papers have been mentioned here, in which a number of other references can be found.

Hong and Helmberger (1978), Langston and Lee (1983) and Lee and Langston (1983a, b) successfully used simple variants of the ray method to study seismic responses of simple models of sedimentary basins. Their success and the availability of program package SEIS83 (Červený and Pšenčík, 1984) that makes ray computations possible in more general 2–*D* laterally varying, possibly absorbing media have led us to a modification of SEIS83 to program package RESPO (Moczo et al., 1985). RESPO is designed for the computation of the seismic response on the free surface of 2–*D* laterally inhomogeneous geological near-surface structures, assuming incidence of a *P*, *SV* or *SH* plane wave from below. To test RESPO, the classical model of the sedimentary basin (Boore et al., 1971) was used. The presented study differs from the study of Hong and Helmberger (1978) and Lee and Langston (1983a) in several aspects. The frequency-domain approach is used here. More attention is paid to the analysis of the formation of the wave field. A comparison with the discrete wavenumber computations for long periods is made. The effects of slight absorption are considered.

The terminology used in the seismic response analysis is introduced in the next section. Then, advantages and limitations of the application of the ray method to seismic response analysis are discussed. The frequency-domain approach to the computation of the seismic response for slight-

ly absorbing media is then described. In principle, any available model of causal absorption, e.g. Futterman (1962), Kjartansson (1979), Mueller (1983), can be considered. Here, Futterman's causal model is adopted. An algorithm of the seismic response computations is described and results of computations are presented. *SH*-wave ray synthetic seismograms are evaluated on the free surface of the sedimentary basin assuming a vertical plane wave incident from below. The synthetics are compared with the results of other methods (discrete wavenumber method, glorified optics, finite-element and finite-difference methods). Various features of the computed wave field are explained in detail with the use of the decomposition of the wave field into elementary seismograms of individual multiples and by inspecting their rays. The limits of applicability of the ray method in low-frequency response computations are partially studied by comparing ray synthetics with discrete wavenumber synthetics. Finally, the effect of slight Futterman's causal absorption on ray synthetics for different degrees of absorption is shown.

Let us note that some preliminary results have been published in Moczo et al. (1986).

Seismic response of local structures

Seismic response analysis (or analysis of seismic mobility) of a certain local structure should involve an analysis of the transfer properties of the structure itself and an analysis of responses to a set of signals that are supposed to represent possible excitations of the structure during an earthquake. From this point of view, the seismic response of the local structure may be defined as a set of four characteristics of seismic ground motion: namely, an impulse response, a frequency response, a time history of a response and a Fourier spectrum of the time history of the response. If the structure is excited by Dirac δ -impulse, the generated vibration of the structure is the impulse response. The Fourier spectrum of the impulse response is the frequency response (spectral characteristics, transfer function). Often, the modulus of the frequency response is used as the frequency response. Both the impulse response and the frequency response only depend upon the properties of the structure (for a given type of wave, angle of incidence, azimuth), i.e., they only characterize the transfer properties of the structure. In practical computations, it is of no use to consider higher frequencies that are not important from the point of view of engineering seismology. Removing the high frequencies, we obtain a pseudo-impulse response. If the structure is excited by an arbitrary signal having a finite effective width of the spectrum, the generated vibration of the structure is the time history of the response. Instead of the complex Fourier spectrum of the time history, the amplitude Fourier spectrum is more often used.

Application of the ray method in seismic response analysis – advantages and limitations

Let us mention the most important aspects of the application of the ray method in seismic response analysis. The ray method is relatively fast and inexpensive. It is applicable to laterally inhomogeneous, possibly absorbing media with a complex surface and subsurface topography, layered and block structure, and an arbitrary distribution of velocities and density inside layers. The wave field may be generated

by an incoming wave with an arbitrary curved wavefront, incident from an arbitrary direction on the bottom of the investigated structure. Any high-frequency source-time function can be used.

In the ray method, the wave field is decomposed into elementary waves. Thus, individual waves forming the seismic response may be identified, no matter whether the waves form an interference group or not. This enables the computed wave field to be decomposed and its physical nature to be better understood. It is possible to estimate the importance of individual elementary waves such as refracted, reflected, multiply reflected, converted waves. The ray method enables us to investigate the physical nature of wave groups with large amplitudes which may be caused, for example, by constructive interference or focusing effects. Since for each wave, rays are traced through the structure, it is easy to detect the interfaces or regions which are responsible for generating local effects. From the point of view of a possible decomposition of the computed wave field, the ray method is very useful even if the seismic response is computed by other methods such as finite-difference or finite-element methods that only yield the complete wave field. The interpretation of the complete wave field computed by these methods can be complicated even in relatively simple structures.

The ray method is a high-frequency method. It is applicable if the prevailing wavelength of considered signals is substantially smaller than any characteristic quantity of the length dimension (e.g., radius of curvature of boundaries including the free surface, measure of spatial changes of velocity, density, impedance, etc.), see Červený et al. (1977). As is shown later, the ray method can give reasonable results even if the above conditions are not strictly satisfied. In the high-frequency range, the ray method can complement the computations by other methods which are more effective for models whose dimensions are of the order of several wavelengths (finite differences) or, in principle, low-frequency methods (discrete wavenumber method). The ray method is especially important at those sites where only the study of high-frequency propagation has a practical meaning.

Since the number of elementary waves in the decomposition of the wave field may be infinite, only a finite number of the most important waves is considered in the ray method. Thus, the ray method does not generally give the complete wave field. Moreover, the computed wave field does not contain some types of waves, e.g. diffracted waves or so-called non-ray waves. For this reason, the ray method does not provide good results in such structures in which intense diffracted or non-ray waves are generated. For example, for diffracted waves caused by topographical anomalies see Zahradník and Urban (1984). Certain types of diffracted waves can be included in the computations if generalizations of the ray method, such as the edge wave method (Klem-Musatov and Aizenberg, 1984) or Gaussian beam method (Červený, 1985a), are used.

The ray method may be less effective if a large number of rays is required, especially rays which are reflected many times inside the structure. Such a situation may arise, for example, in the computation of the seismic response of a sedimentary basin with a very large impedance contrast between sediments and the underlying rocks.

The ray method does not work properly or even fails in singular regions, such as a caustic region, critical region

or transition from shadow to illuminated region. The ray amplitudes are infinite at caustics, and they are not accurate enough in the vicinity of caustics. This problem could be removed, for example, by applying the Gaussian beam method. The caustic may, however, be simply detected in the computed ray field and taken into account in the interpretation of the computed results. In applications, the problems connected with the existence of caustics can be avoided simply by slightly shifting the receiver from the caustic location on the surface, as suggested by Hong and Helmberger (1978) and used, for example, by Lee and Langston (1983b).

Computation of the seismic response of slightly absorbing structures

The so-called Debye procedure (see Kravtsov and Orlov, 1980; Červený, 1985a), and Futterman's model of causal absorption (see Futterman, 1962) are used to describe the behaviour of high-frequency seismic waves in laterally inhomogeneous slightly absorbing media. In absorbing media, Lamé's parameters λ and μ are complex-valued quantities:

$$\lambda = \lambda_R - i\lambda_I, \quad \mu = \mu_R - i\mu_I. \quad (1)$$

In slightly absorbing media, λ_I and μ_I are small quantities. They are formally considered to be of order ω^{-1} for $\omega \rightarrow \infty$. Let us insert the parameters (1) into the elastodynamic equation and seek its approximate solution in the form

$$\mathbf{u} = \mathbf{U} \exp[-i\omega(t - \tau)]. \quad (2)$$

Here \mathbf{U} is a complex-valued vectorial amplitude, τ is the phase function (eikonal), and ω and t are frequency and time. We do not repeat the whole procedure of determining \mathbf{U} and τ since it is very similar to that used for perfectly elastic media (see Červený and Ravindra, 1971; Červený and Hron, 1980; Kravtsov and Orlov, 1980). We pay attention only to those steps in the procedure in which it differs from the procedure for perfectly elastic media.

Inserting Eq. (2) into the elastodynamic equation yields the basic system of equations of the ray method (Červený, 1985a, Section 2.3). Since λ_I and μ_I are of order ω^{-1} , they do not appear in the first equation from which the eikonal equations are obtained:

$$(\nabla \tau)^2 = \rho/(\lambda_R + 2\mu_R) \quad (3a)$$

for P waves, and

$$(\nabla \tau)^2 = \rho/\mu_R \quad (3b)$$

for S waves. In Eq. (3), ρ denotes density.

Because of the complexity of Lamé's parameters, we also have complex-valued velocities $\alpha = \alpha_R - i\alpha_I$ and $\beta = \beta_R - i\beta_I$ of P and S waves propagating in a slightly absorbing medium. As for perfectly elastic media, we use the notation

$$\alpha^2 = (\lambda + 2\mu)/\rho, \quad \beta^2 = \mu/\rho, \quad (4)$$

from which we get

$$(\lambda_R + 2\mu_R)/\rho = \alpha_R^2 - \alpha_I^2, \quad \mu_R/\rho = \beta_R^2 - \beta_I^2, \quad (5a)$$

$$(\lambda_I + 2\mu_I)/\rho = 2\alpha_R\alpha_I, \quad \mu_I/\rho = 2\beta_R\beta_I. \quad (5b)$$

It follows from Eq. (5b) that α_I and β_I are of order ω^{-1} , like λ_I , μ_I . Neglecting terms of second order in ω^{-1} , we

may therefore write the eikonal equation, Eq. (3), in the form

$$(\nabla \tau)^2 = v_R^{-2}, \quad (6)$$

where v_R stands for either α_R or β_R . Thus, the rays in slightly absorbing media are real and may be constructed in the very same way as in perfectly elastic media (see Červený et al., 1977) with local velocities of P and S waves, α_R and β_R .

Let us now investigate the second basic equation of the ray method, which yields the transport equation. The second basic equation for slightly absorbing media has the form

$$\mathbf{M}(\mathbf{U}; \lambda_R, \mu_R) + \omega[(\lambda_I + \mu_I) \nabla \tau (\mathbf{U} \nabla \tau) + \mathbf{U} \mu_I (\nabla \tau)^2].$$

For the term $\mathbf{M}(\mathbf{U}; \lambda_R, \mu_R)$, see Červený (1985a) Eq. (2.11), in which λ, μ should be substituted by λ_R, μ_R . Thus, the second basic equation of the ray method for slightly absorbing media differs from the equation for perfectly elastic media by the term

$$\omega[(\lambda_I + \mu_I) \nabla \tau (\mathbf{U} \nabla \tau) + \mathbf{U} \mu_I (\nabla \tau)^2] \sim 2\rho \omega \mathbf{U} v_R^{-1} v_I.$$

The transport equation then has the form

$$2\rho v_R dU_i/ds + \rho v_R U_i d[\ln(J \rho v_R)]/ds + 2\rho \omega U_i v_R^{-1} v_I = 0. \quad (7)$$

Here, the components of the vectorial amplitude, U_i , are taken in the ray-centred coordinate system. The ray-centred coordinate system is an orthogonal system, two basis vectors of which are mutually perpendicular in the plane perpendicular to the ray. The third vector is tangent to the ray. The quantity J is the Jacobian of the transformation from the ray to the Cartesian coordinates. For details and methods of the determination of the ray-centred coordinate system and J , see Červený (1985a). The quantities v_R and v_I stand for α_R, α_I or β_R, β_I , s is an arclength along the ray.

The solution of Eq. (7) gives

$$\mathbf{U} = \Psi (J v_R \rho)^{-1/2} \exp\left(-\omega \int_{s_0}^s v_R^{-2} v_I ds\right), \quad (8)$$

the exponential term describing the decay of the amplitude due to a slight absorption along the ray path from s_0 to s . Ψ is a vector constant along the ray. Inserting Eq. (8) into Eq. (2), we get

$$\mathbf{u} = \Psi (J v_R \rho)^{-1/2} \cdot \exp\left[-i\omega t + i\omega \int_{s_0}^s v_R^{-1} (1 + i v_I v_R^{-1}) ds\right]. \quad (9)$$

The integrand of Eq. (9) in our approximation (i.e. neglecting terms of higher order in ω^{-1}) is equal to the reciprocal value of the complex velocity,

$$v^{-1} = v_R^{-1} (1 + i v_I v_R^{-1}). \quad (10)$$

We now assume the frequency dependence of v , and thus v_R and v_I , to be expressed by Futterman's relations

$$v^{-1}(\omega) = v_R^{-1}(\omega) [1 + i/(2Q(\omega))], \quad (11)$$

$$v_R^{-1}(\omega) = v_R^{-1}(\omega_r) \{1 - [1/(\pi Q(\omega_r))] \ln(\omega/\omega_r)\}, \quad (12a)$$

$$Q(\omega) = Q(\omega_r) \{1 - [1/(\pi Q(\omega_r))] \ln(\omega/\omega_r)\}, \quad (12b)$$

where ω_r is a reference frequency.

Comparing Eq. (10) with Eq. (11), we get

$$Q^{-1}(\omega) = 2v_I(\omega)/v_R(\omega), \quad (13)$$

i.e. the reciprocal value of the quality factor Q is a quantity of the order ω^{-1} . From Eq. (12) immediately follows

$$v_R(\omega) Q(\omega) = v_R(\omega_r) Q(\omega_r), \quad (14)$$

i.e. the product $v_R Q$ is independent of the frequency. Let us assume that we know the velocity and Q distribution for the reference frequency ω_r . Then the integrand of Eq. (9) may be rewritten, by using Eqs. (12)–(14), in the form

$$\begin{aligned} v_R^{-1}(\omega) + \frac{i}{2} Q^{-1}(\omega) v_R^{-1}(\omega) \\ = v_R^{-1}(\omega_r) [1 - \pi^{-1} Q^{-1}(\omega_r) \ln(\omega/\omega_r)] \\ + \frac{i}{2} Q^{-1}(\omega_r) v_R^{-1}(\omega_r). \end{aligned} \quad (15)$$

For the term $v_R(\omega)$ under the square root in Eq. (9) we may write

$$v_R(\omega) \sim v_R(\omega_r), \quad (16)$$

since the second term in Eq. (12a) would produce an additional amplitude term of the order ω^{-1} . In the following, we consider only one component of \mathbf{u} in an arbitrary orthogonal coordinate system. For simplicity, we denote this component u . Similarly, Ψ is the corresponding component of $\mathbf{\Psi}$. Since the term $\Psi(J v_R \rho)^{-1/2}$ is generally complex valued, we can rewrite it as follows:

$$\Psi(J v_R \rho)^{-1/2} = A \exp(i\chi). \quad (17)$$

Inserting Eqs. (15)–(17) into Eq. (9), we get

$$u = A \exp \left\{ -\frac{1}{2} \omega t^* - i\omega \left[t - \tau + \frac{t^*}{\pi} \ln(\omega/\omega_r) \right] + i\chi \right\}, \quad (18)$$

where $\tau = \int_{s_0}^s v_R^{-1}(\omega) ds$ and $t^* = \int_{s_0}^s [v_R(\omega_r) Q(\omega_r)]^{-1} ds$ are the travel time and the global absorption factor. Let us note that for $\omega < \omega_r$, $t^* \pi^{-1} \ln(\omega/\omega_r) < 0$, i.e. the travel time is greater for a lower frequency, and vice versa, which is in agreement with the causality principle.

Expression (18) represents a contribution of one elementary wave. In the ray method, the resulting wave field u^T is a superposition of all elementary waves arriving at a receiver: $u^T = \sum_k u^k$, where u^k is the contribution (18) of the

k -th elementary wave. From u^T we immediately get the frequency response of the structure

$$\begin{aligned} U^T(\omega) = \sum_k A_k \exp(-\frac{1}{2} \omega t_k^*) \\ \cdot \exp \left\{ i \left[\chi_k - \frac{\omega}{\pi} t_k^* \ln(\omega/\omega_r) + \omega \tau_k \right] \right\}. \end{aligned}$$

In the case of a perfectly elastic medium, $t^* = 0$ and

$$U^T(\omega) = \sum_k A_k \exp[i(\chi_k + \omega \tau_k)].$$

In both cases, the fast frequency response algorithm (see Červený, 1985b) can be used for an effective evaluation of the frequency response.

The impulse response is the inverse Fourier transform of the frequency response. Undesired high frequencies greater than $\omega = \omega_{\max}$, can be removed by a smoothing filter $W(\omega)$: $W(\omega) = 0$ for $|\omega| > |\omega_{\max}|$, $U^W(\omega) = U^T(\omega) W(\omega)$. Applying the inverse Fourier transform to $U^W(\omega)$, we obtain the pseudo-impulse response. A response $R(\omega)$ of the structure to a signal $s(t)$ with the spectrum $S(\omega)$ is $R(\omega) = S(\omega) U^W(\omega)$ in the frequency domain. Applying the inverse Fourier transform to $R(\omega)$, we obtain the time history of the response corresponding to $s(t)$.

The above approach to the computation of the seismic response, in which the frequency response is computed from travel times, amplitude moduli, phase shifts and global absorption factors, represents the frequency-domain approach.

An alternative to this approach is the time-domain approach. In this case we obtain from (18)

$$\begin{aligned} u = A \exp(i\chi) \frac{1}{\pi} \int_0^\infty S(\omega) \exp \left[-\frac{1}{2} \omega t^* - i \frac{\omega}{\pi} t^* \ln(\omega/\omega_r) \right. \\ \left. - i\omega(t - \tau) \right] d\omega, \end{aligned} \quad (19)$$

where $S(\omega)$ is the spectrum of the source-time function $s(t)$. Let us denote

$$\begin{aligned} F(\omega) = S(\omega) \exp \left[-\frac{1}{2} \omega t^* - i \frac{\omega}{\pi} t^* \ln(\omega/\omega_r) \right], \\ \frac{1}{\pi} \int_0^\infty F(\omega) \exp(-i\omega \vartheta) d\omega = \hat{\mathbf{f}}(\vartheta) + i \hat{\mathbf{g}}(\vartheta), \end{aligned} \quad (20)$$

where $\vartheta = t - \tau$. Then, for the real part of Eq. (19) we can write

$$\text{Re } u = A [\hat{\mathbf{f}}(\vartheta) \cos \chi - \hat{\mathbf{g}}(\vartheta) \sin \chi]. \quad (21)$$

Here, as can be seen from Eq. (20), $\hat{\mathbf{g}}(\vartheta)$ is the Hilbert transform of $\hat{\mathbf{f}}(\vartheta)$. Equation (21) corresponds to one elementary wave and it is the well-known formula for an elementary seismogram in the zero-order approximation of the ray method. However, $\hat{\mathbf{f}}(\vartheta)$ in Eq. (21) is not the source-time function since $\hat{\mathbf{f}}(\vartheta)$ includes the effect of absorption. The resulting wave field $\text{Re } u^T$ will be a superposition of all elementary waves: $\text{Re } u^T = \sum_k \text{Re } u^k$, where

$$\text{Re } u^k = A_k [\hat{\mathbf{f}}_k(\vartheta_k) \cos \chi_k - \hat{\mathbf{g}}_k(\vartheta_k) \sin \chi_k]. \quad (22)$$

$\text{Re } u^T$ represents the time history of the response of the structure to the signal $s(t)$.

Thus, it is possible to choose between the two approaches. In the time-domain approach it is necessary to evaluate the inverse Fourier transform in the computation of each elementary wave, see Eqs. (20)–(22). In the frequency-domain approach it is sufficient to evaluate the inverse Fourier transform only once. Moreover, once the fre-

quency response has been evaluated, it is easy to compute time histories for different source-time functions. The frequency-domain approach is therefore more convenient (faster) than the time-domain approach. The time-domain approach could be convenient in the case of the computation of time histories of the responses to special analytical signals, like Gabor signal, for which simple approximate formulae for their Hilbert transform and for elementary seismograms are derived, see Červený (1976) and Červený and Frangié (1980, 1982).

A short description of program package RESPO

Program package RESPO (Moczo et al., 1985) is designed for the computation of the seismic response on the free surface of 2-D laterally inhomogeneous geologic structures assuming P , SV or SH plane-wave incidence from below. The basic part of package RESPO is a modified version of the main program of package SEIS83 (Červený and Pšenčík, 1984). The algorithm of the computation of the wave field is based on the zero-order approximation of the ray method. The computation is performed in two steps. In the first step, rays, travel times, complex-valued ray amplitudes and global absorption factors of individual elementary waves (e.g. direct, multiply reflected/refracted waves) are computed by program SEIM and stored. In the second step, four characteristics of the seismic response (mentioned earlier) may be computed in program FSYNT from the quantities stored in SEIM. The frequency-domain approach is used. Let us mention that such a "two-step approach" to the computation of the seismic response, which includes the computation of the impulse response in the first step, has been suggested for finite-difference computations by Zahradník and Urban (1984).

Two-dimensional, laterally inhomogeneous, possibly absorbing layered structures with curved interfaces and a free surface, including block structures, vanishing layers and isolated bodies, can be considered. The interfaces may be specified by a system of points and then approximated by cubic splines or approximated by analytic formulae. Within a layer, the velocity distribution is specified at grid points of a rectangular network and then approximated by bicubic spline interpolation. It is possible to specify several Q -factor distributions for one velocity model and to compute corresponding global absorption factors along each ray. Non-causal absorption, as well as various models of causal absorption (Futterman, 1962; Kjartansson, 1979; Mueller, 1983), may be considered.

The angle of incidence of the incident plane wave may be arbitrary. P , SV , SH and converted waves may be computed. The rays arriving at specified receivers are computed by boundary-value ray tracing based on shooting. The same procedure as in Červený and Pšenčík (1984) is used for this purpose. The amplitudes are evaluated by standard ray formulae. In the case of an S wave, the SV and SH ray amplitude components are evaluated simultaneously.

Once rays, travel times, complex-valued amplitudes and global absorption factors are evaluated, an arbitrary number of responses for various types of exciting signals can be computed. As the exciting signal, an analytic impulse or an arbitrary digitized seismic record may be used, no matter whether it corresponds to a seismic displacement, velocity or acceleration. Selections of receivers and elemen-

tary waves are possible. A more detailed description of package RESPO can be found in Moczo et al. (1985).

Numerical examples

Comparison of ray computations with other computations for a perfectly elastic medium

SH ray synthetic seismograms at the free surface of a sedimentary basin excited by a vertically incident plane SH wave were computed. The model of the basin (see Fig. 1) had been studied by Boore et al. (1971) and subsequently by many authors using various methods. The seismograms presented here were computed by program package RESPO.

Figure 2 shows a comparison of synthetic seismograms evaluated by five different methods: (1) ray method calculations by RESPO, (2) discrete wavenumber method by Bard and Bouchon (1980), (3) glorified optics method by Hong and HelMBERGER (1978), (4) finite-element method by Hong and Kosloff, see Hong and HelMBERGER (1978), (5) finite-difference method by Boore et al. (1971). Seismograms 2-5 are taken from Bard and Bouchon (1980).

Since 1980 several other authors have computed seismograms for the basin model. Let us mention Virieux (1984), who computed seismograms up to 180 s with velocity-stress finite-difference method, and Kohketsu (1987), who used the 2-D reflectivity method for the same model. The agreement of the ray method results with the results of the last two mentioned authors seems to be quite good, at least for shorter times.

Besides the direct wave, our computation includes the waves multiply reflected inside the basin. The multiples are classified by the number of reflections from the basin bottom. Multiples with up to a maximum of ten reflections from the bottom are considered.

The basin was successively illuminated by the direct wave, once-reflected wave, etc., up to the 10-times-reflected

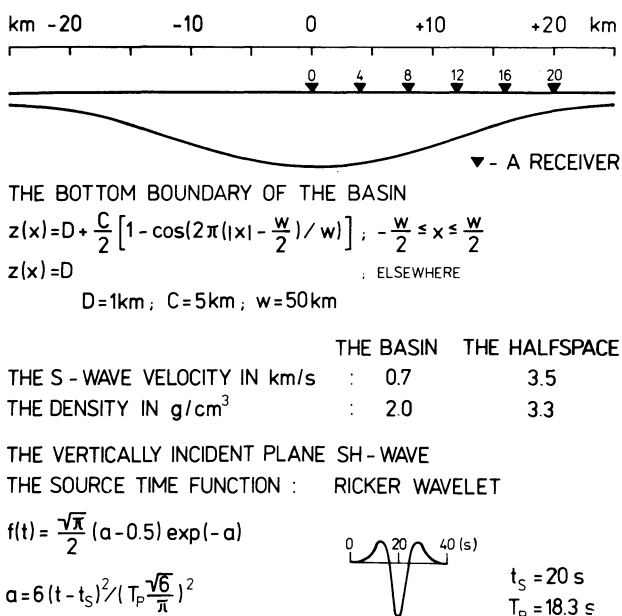


Fig. 1. Description of the basin model and the exciting wave. The maximum depth of the basin is 6 km

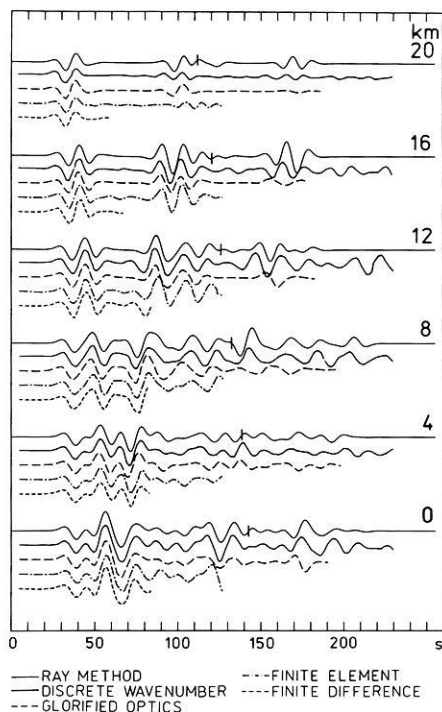


Fig. 2. Comparison of *SH* synthetic seismograms computed by ray (program package RESPO), discrete wavenumber (Bard and Bouchon, 1980), glorified optics (Hong and Helmberger, 1978), finite-element (Hong and Kosloff) and finite-difference (Boore et al., 1971) methods for the basin model shown in Fig. 1

wave. The higher the multiple, the greater the number of rays forming the multiple. Because of the symmetry of the basin, it was sufficient to illuminate only one-half of the basin. The results of the boundary-value ray tracing were carefully checked in order to obtain all rays arriving at the receivers.

Due to the missing multiples of higher order than 10, the later parts of the seismograms can be distorted. Time intervals that should not be distorted by missing higher multiples are marked by vertical bars (confidence bars) in Fig. 2. The determination of confidence bars can be demonstrated on the frame for the receiver at 20 km in Fig. 3a. We can see that the seismograms of individual multiples form three nearly vertical branches. We do not expect the first branch to become stronger for higher multiples than those shown. Therefore, we define the confidence bar by the arrival time of the fastest ray of the 10-times-reflected multiple contributing to the second branch. In this way, for the receiver at 20 km we get a confidence bar at about 112 s. Confidence bars are frequency independent in perfectly elastic media. They shift to larger arrival times when absorption is considered, see Fig. 3b.

We have to take confidence bars into consideration when comparing the seismograms in Fig. 2. At shorter times, the agreement of all five computations is very good. At later times, some differences occur. Let us point out the especially good agreement of ray results with the discrete wavenumber results. Somewhat surprisingly, there are certain differences between the glorified optics and our results. A partial explanation is that the glorified optics method does not involve 10-times-reflected waves. However, the absence of these waves cannot fully account for the differences. This may be seen, for example by comparing the interval

160–180 s on seismograms for the basin centre in Fig. 2 and seismograms of multiples presented in Fig. 3a. In this time interval the strongest contributor is the 8-times-reflected wave. Possible explanation of discrepancies in later arrivals are incorrect phase shifts caused by caustics in the glorified optics method.

There is disagreement in amplitudes between the ray and discrete wavenumber synthetics at their ends for receivers at 16 and 20 km, see Fig. 2, which is probably caused by missing higher multiples in the ray computations. The corresponding wave groups are due to interference of a large number (several tens) of contributors with comparable amplitudes. Only two of all contributors in the 9-times-reflected wave at the receiver at 20 km are stronger due to geometrical focusing.

Decomposition of the wave field into contributors along rays

In order to understand the formation of the wave field, let us investigate the seismograms of multiples and their rays separately.

Individual lines in Fig. 3a show, starting from the top, the seismograms of the direct wave (*D*), the once-reflected wave (1), etc. for receivers at 0, 4, 8, 12, 16 and 20 km. The seismograms at the bottom are superpositions of all the above elementary seismograms. Short vertical lines again denote confidence bars. In Fig. 3a, a perfectly elastic medium is considered. The seismograms in Fig. 3b correspond to an absorbing medium and are discussed later.

Three nearly vertical branches may be clearly seen on seismograms of multiples at receiver positions 12, 16 and 20 km in Fig. 3a. These branches correspond to three clearly separated wave groups in synthetics.

An inspection of the rays arriving at the receiver at 12 km shows the following. The first branch (20–65 s) corresponds to rays entering the basin on the right of the receiver, travelling between the basin bottom and the free surface and arriving at the receiver from the right after the respective number of reflections. An example of rays of this type is the 8-times-reflected ray shown in Fig. 4a. The second branch (65–140 s) corresponds to rays (see Fig. 4b) entering on the opposite (left) side of the basin, travelling across the basin and arriving at the receiver from the left (ray 2 in Fig. 4b). Some rays travel to the right of the receiver, where they are reflected to the opposite direction and finally arrive at the receiver from the right (ray 3 in Fig. 4b). The third branch (140–200 s) corresponds to rays (see Fig. 4c) entering on the right side of the basin, travelling across the basin, reflected on the left side of the basin, again travelling across the basin and arriving at the receiver. As in the second branch, some rays arrive at the receiver from the left (ray 4 in Fig. 4c), other rays travel to the right of the receiver, where they are reflected to the opposite direction and finally arrive at the receiver from the right (ray 5 in Fig. 4c).

Practically the same holds for the receiver position at 20 km. The branches are, however, better separated in time and the rays similar to ray 5 in Fig. 4c are not present. They would probably appear in higher multiples. The examples of the rays of the 8-times-reflected wave arriving at the receiver at 20 km are shown in Fig. 5.

The form of the seismograms at receiver positions 0, 4 and 8 km is more complicated. At 0 km, there are four branches in seismograms. They are marked by lines 1–4

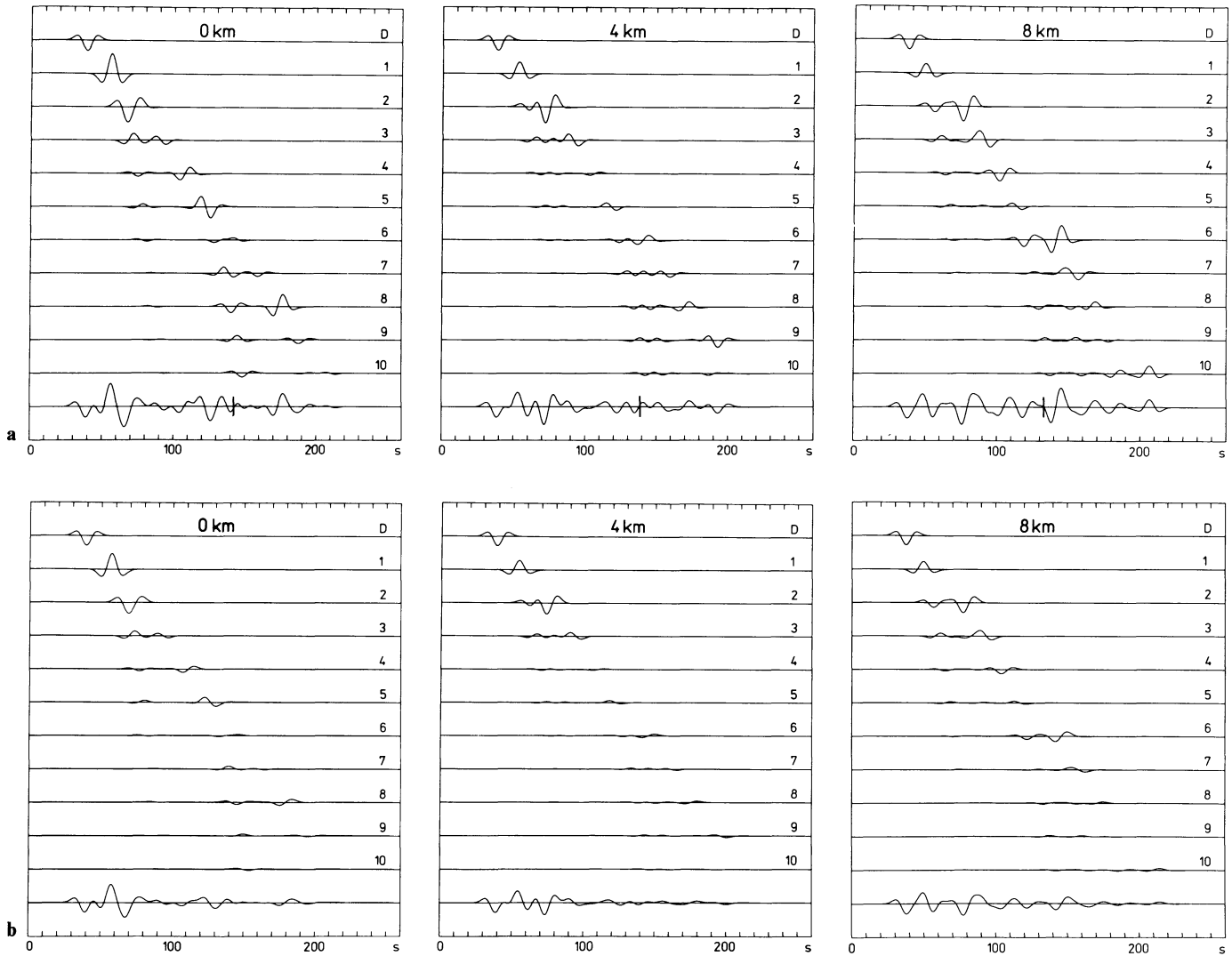


Fig. 3a, b. Elementary seismograms of multiples: **a** without absorption; **b** with Futterman's causal absorption, $Q=20$ at 1 Hz. D denotes the direct wave, 1 – the wave reflected once from the bottom of the basin, 2 – the wave reflected twice from the bottom of the basin, etc. The synthetic seismograms (shown also in Fig. 2) at the bottom of each frame are superpositions of all the above elementary seismograms

in Fig. 6a. Since the receiver is situated at the symmetry axis of the basin, there are, with the exception of the rays normally incident at the receiver, always two rays which arrive symmetrically at the receiver. In Fig. 6c–e, only one of these rays is fully depicted (denoted by R); of the other one (denoted by L), only the incident part is shown. Line 1 in Fig. 6a corresponds to rays propagating along the vertical axis of symmetry of the basin, see Fig. 6b. Line 2 corresponds to rays entering on one side of the basin, travelling between the basin bottom and the free surface and arriving after the respective number of reflections at the receiver. Figure 6c gives such an example for a ray corresponding to the 8-times-reflected wave. Line 3 corresponds to rays entering on one side of the basin, travelling to the opposite side, reflecting there and arriving at the receiver, see Fig. 6d. Line 4 corresponds to rays that travel only in that part of the basin where the depth is greater than roughly half the maximum depth. (It corresponds approximately to the range interval from -14 to $+14$ km.) These rays do not reach the margins of the basin and they are reflected on both slopes of the basin. Some of them propagate almost

vertically in the narrower central part of the basin. An example is shown in Fig. 6e.

There is a slightly different situation at the receiver at 4 km, see Fig. 3a. Since the receiver is not at the symmetry axis of the basin, branches 2 and 3 from the previous case (see Fig. 6a) are split into two sub-branches. One sub-branch corresponds to rays entering on the left side of the basin, the other to rays entering on the right side. There are no rays propagating strictly along the vertical axis, as in the case of the receiver at 0 km. Thus, the maximum travel times in each multiple correspond to the rays propagating almost vertically in the narrow central part of the basin and, in the case of higher multiples, also to the rays that travel inside that part of the basin corresponding approximately to the range interval from -15 to $+15$ km and are reflected on both slopes of the basin.

Let us mention several general features of rays and contributions connected with them. The higher the multiple, the greater the number of rays forming this multiple at a receiver. The rays with almost vertical elements often become weak contributors after several reflections (small re-

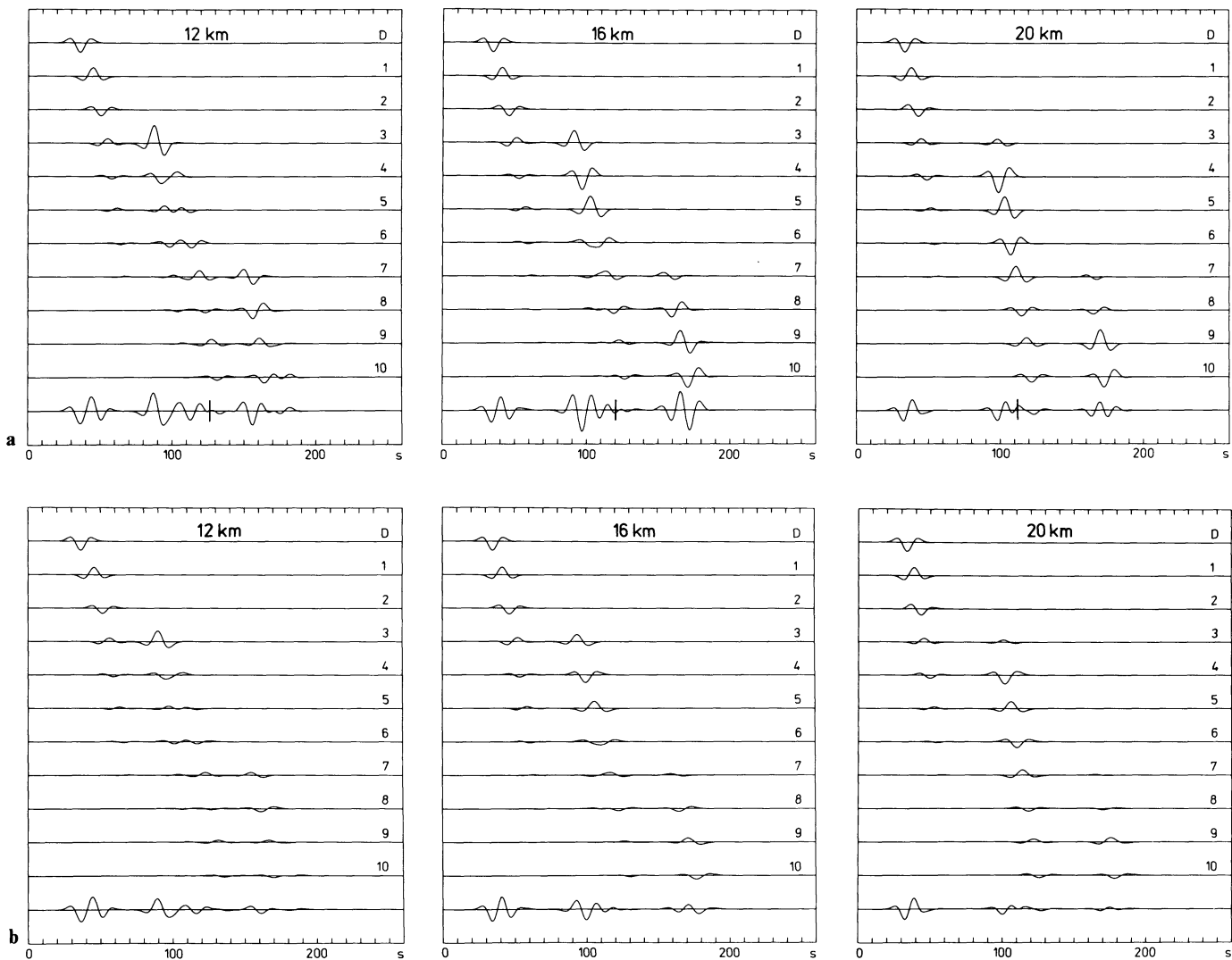


Fig. 3 (cont.)

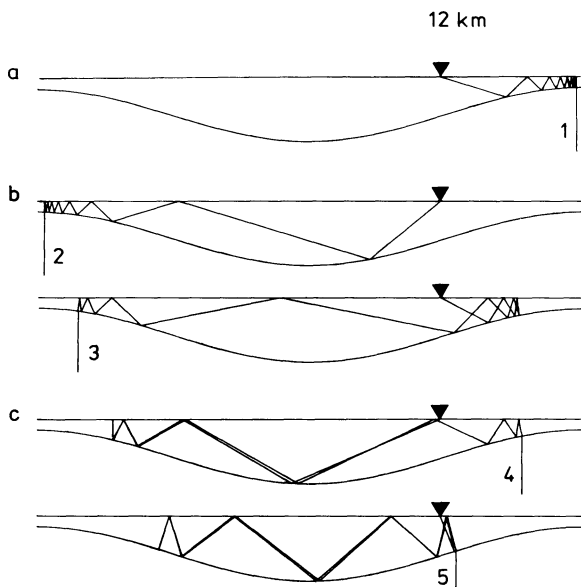


Fig. 4a-c. Examples of various types of rays, 8-times reflected from the basin bottom and arriving at the receiver position at 12 km

flexion coefficients). This is different for the vertically propagating rays at the centre of the basin. They are relatively strongly focused and thus the amplitude decrease due to reflections is partially compensated for by the focusing. The number of rays with nearly horizontal elements between the left and right margins of the basin is higher than those with nearly vertical elements. Most of these rays are over-critically reflected. Thus, the decrease in their amplitudes due to reflections is negligible. The amplitudes connected with these rays, however, are often decreased by a large geometrical spreading.

An inspection of the rays corresponding to the seismograms in Fig. 3a (all shown in Fig. 7) suggests the following explanation of the resultant synthetics. The waves corresponding to the rays entering the basin on the right margin and travelling (with a respective number of reflections) to the opposite side of the basin mutually interfere and form a local interference wave propagating from the right to the left margin of the basin (sometimes called local Love wave). Rays 1, 6 and 11 R shown in Figs. 4, 5 and 6, respectively, are examples of the rays of the waves forming this interference wave. This wave is denoted by line 1 in Fig. 7. Due to the symmetry of the problem, a similar interference wave

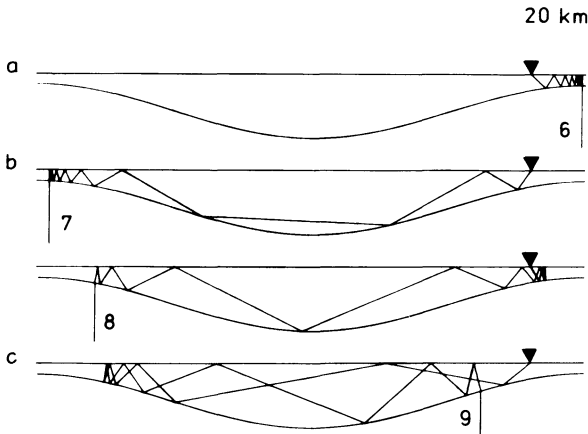


Fig. 5a-c. The same as in Fig. 4, but for the receiver position at 20 km

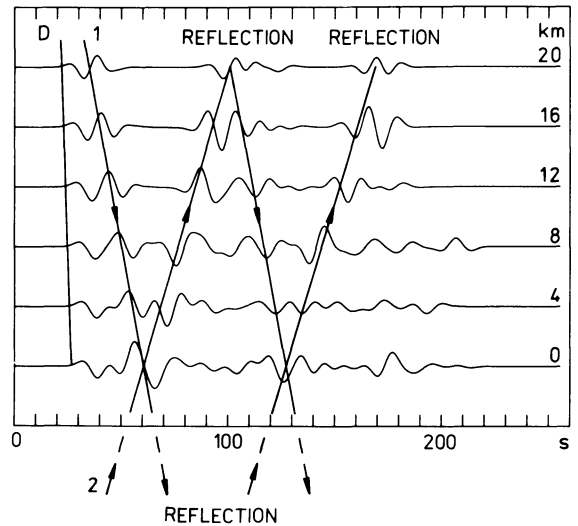


Fig. 7. Synthetic section with marked direct wave denoted by D and local interference waves propagating horizontally from the right (left) margin of the basin to the left (right) denoted by 1 (2). After reaching the opposite side of the basin, waves 1 and 2 are reflected back

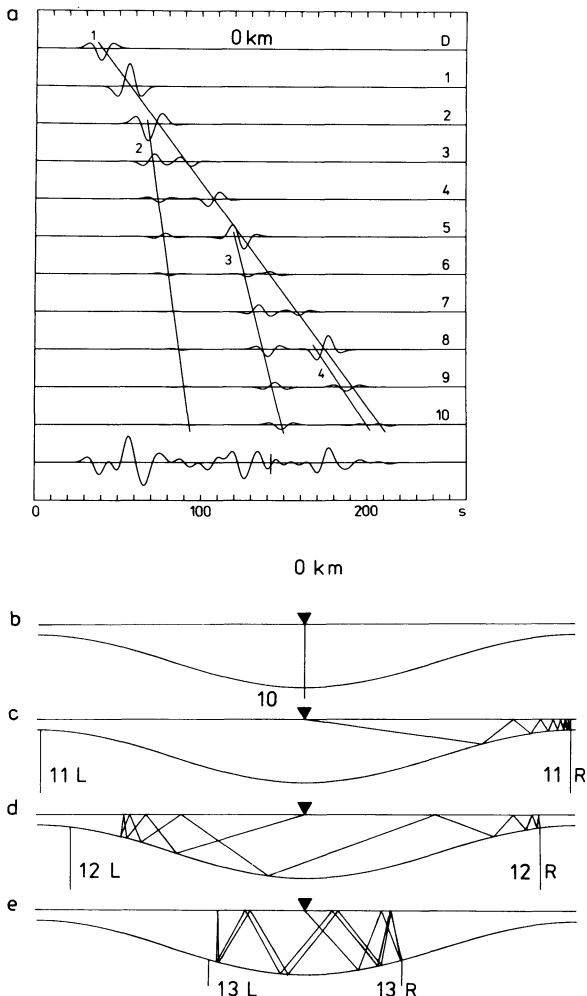


Fig. 6. a Formation of the wave field at the receiver at 0 km. Four branches formed by various waves propagating along various types of rays are denoted by numbers 1-4. b-e Examples of 8-times-reflected rays; the rays incident on the left margin of the basin and denoted by L would have trajectories symmetrical to the rays incident on the right margin of the basin. The rays of type b contribute to line 1 in a; of type c to 2; d to 3 and e to 4

propagates from the left to the right margin (line 2). Examples of the corresponding rays are rays 2, 7 and 11 L in Figs. 4, 5 and 6, respectively. The interference waves meet at the centre of the basin. At the margins, the waves are reflected and propagate back to the side of their origin (rays 4, 9 and 12 R and rays 3, 8 and 12 L). There they are again reflected (ray 5 in Fig. 4 is an example).

A certain part of the elastic energy is focused in the central part of the basin and oscillates vertically between the bottom boundary and the free surface. Rays 10, 13 R and 13 L in Fig. 6 are examples.

Thus, we have two main types of wave propagation inside the basin: (1) the horizontally propagating local interference waves (local Love waves) that are observable at all receivers, see Fig. 7; (2) the vertically propagating wave that can be seen clearly in the seismograms of multiples for the receivers in the central part of the basin (0, 4 and 8 km), see Fig. 6a. It is evident from Fig. 7 that the horizontal wave propagation is dominant.

Comparison of ray and discrete wavenumber synthetics for long periods (low frequencies)

The agreement of the ray and discrete wavenumber synthetics in Fig. 2 may be surprising because of the simplicity and high-frequency character of the ray method. In the situation shown in Fig. 2, the prevailing wavelength λ_p of the incident wave is approximately twice as large as the maximum basin depth ($\lambda_p = 13$ km, and the depth at the centre of the basin is 6 km). The radii of curvature of the basin boundary are approximately 25, 93, 67 and 33 km at 0, 10, 16 and 20 km from the centre of the basin, respectively, i.e. larger than the prevailing wavelength of the incident wave. It is of interest to find out how accurate the ray synthetics are for wavelengths comparable with and larger than the radii of curvature. In the following, we present the results for prevailing wavelengths of about 28, 42 and 56 km (corresponding to prevailing periods of 40, 60 and

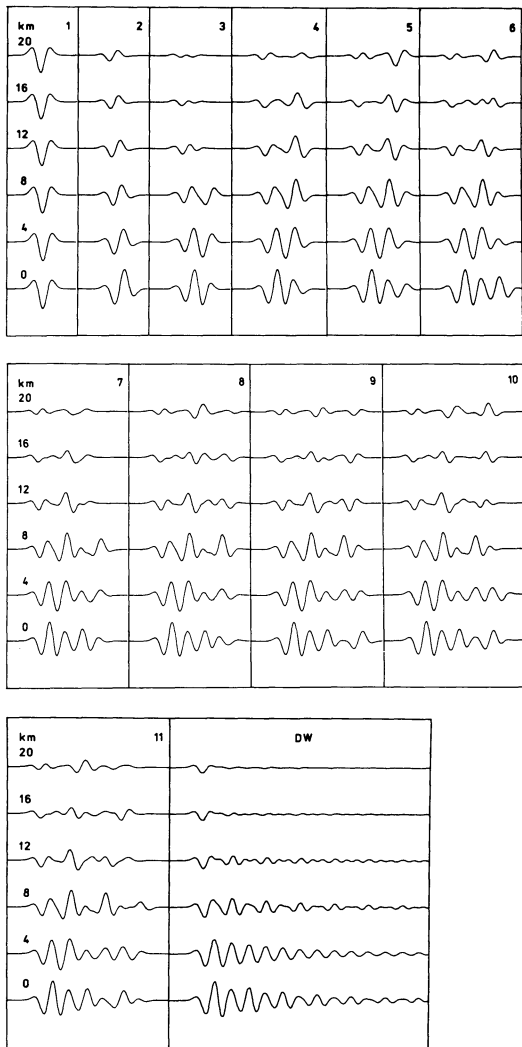


Fig. 8. Comparison of ray and discrete wavenumber synthetics for a prevailing wavelength of approximately 28 km ($T_p=40$ s). The results of the discrete wavenumber method are denoted by DW. The synthetics with numbers are ray synthetics which include successively increasing numbers of multiples: 1 direct wave only, 2 superposition of the direct wave and once-reflected wave etc.

80 s). Since the discrete wavenumber method is a low-frequency method, the accuracy of its results is expected to be higher for these large wavelengths.

Eleven synthetics for $\lambda_p=28$ km ($T_p=40$ s) for each receiver are presented in Fig. 8. The synthetics with numbers are ray synthetics which include a successively increasing number of multiples: 1 corresponds to the direct wave only, 2 to the superposition of the direct and once-reflected waves etc., up to 11, which corresponds to the superposition of the direct wave and all the multiples up to the 10-times-reflected wave. DW denotes the discrete wavenumber results. The horizontal and vertical scales are the same for all seismograms in Figs. 8–10. Although the conditions of applicability of the ray method are not strictly satisfied, the ray results for the maximum number of multiples included (i.e. synthetics 11) resemble the results of the DW method, especially in the central part of the basin and for shorter times. In the central part of the basin, even the amplitudes of oscillations in both results differ only slightly.

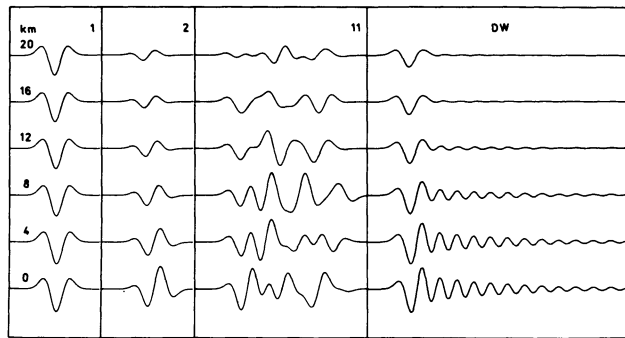


Fig. 9. The same as in Fig. 8, but for a prevailing wavelength of approximately 42 km ($T_p=60$ s)

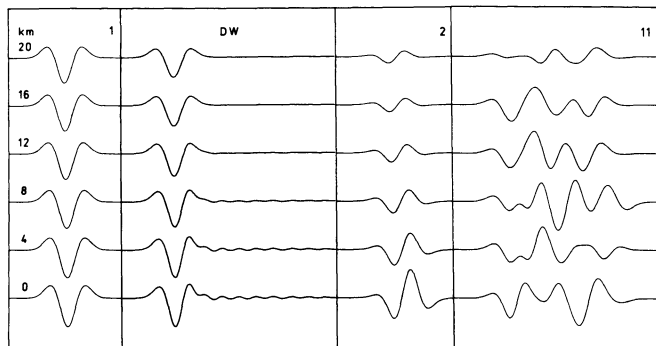


Fig. 10. The same as in Fig. 8, but for a prevailing wavelength of approximately 56 km ($T_p=80$ s)

Figure 9 shows the ray synthetics 1, 2 and 11, and DW synthetics, for the prevailing wavelength 42 km ($T_p=60$ s), i.e. nearly twice the minimum radius of curvature of the basin boundary. As expected, the discrepancies between the ray and DW synthetics are considerably greater than in the previous case.

Finally, Fig. 10 shows the synthetics for the prevailing wavelength 56 km ($T_p=80$ s). In this case, the ray synthetics including only the direct wave are comparable with DW synthetics. Addition of any number of higher multiples would yield worse results.

We can see that the concept of approximating the wave field by a superposition of multiply reflected waves propagating along the geometrical ray paths fails for wavelengths larger than the minimum radius of curvature of the basin boundary. For wavelengths comparable with the minimum radius of curvature and considerably larger than the depth of the basin, the concept already yields reasonably good results in the central part of the basin for shorter times. The relatively good fit between the direct wave and DW synthetics for the prevailing wavelength 56 km is probably a consequence of the lower sensitivity of such a long incident wave to the basin structure.

The above tests illustrate that the ray method can give good results even in those frequency ranges where it is not expected. The ray synthetics are, however, more accurate and more effective for higher frequencies, with which we deal in many applications. In Fig. 11, ray synthetics are shown for four different frequencies which correspond to prevailing wavelengths of 1.5, 3, 6 and 12 km (i.e. lower than and comparable with those in Fig. 2). The longest wavelength is approximately half the radius of curvature of

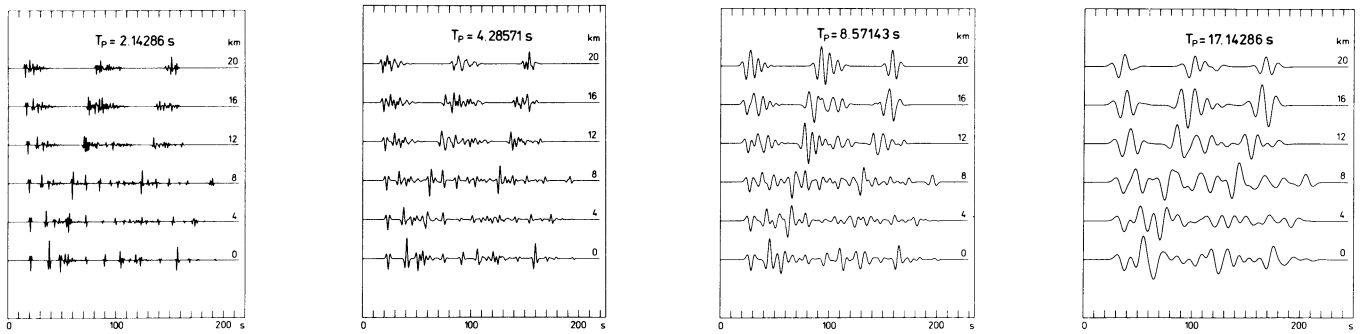


Fig. 11. The dependence of the ray synthetics on the prevailing period T_p . The corresponding prevailing wavelengths are 1.5, 3, 6 and 12 km

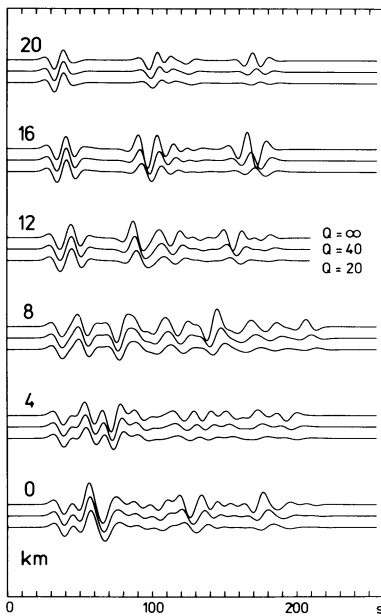


Fig. 12. The effect of Futterman's causal absorption. Comparison of the ray synthetics for three values of the quality factor Q : ∞ (perfect elasticity), 40, 20. The Q values are specified for 1 Hz

the basin boundary in its central part. It is interesting to see how the synthetics vary due to interference of contributors of various wavelengths.

Absorbing effects on the ray method synthetics

Figure 3b and Fig. 12 show the effect of the Futterman causal absorption on the ray synthetics. Only the absorption effects along a ray path are considered, the effects due to reflection/transmission (e.g. see Krebes, 1983) are omitted. The quality factor Q and velocity are specified for the frequency of 1 Hz. Figure 3b shows the seismograms of individual multiples and complete seismograms for $Q=20$. In Fig. 12, ray synthetics for $Q=\infty$ (perfectly elastic medium), $Q=40$ and 20 are shown. The prevailing wavelength is approximately 13 km in all cases. The decrease in amplitudes and the time delay are clearly seen at later times. Although the quality factor is relatively low, the decrease in the amplitudes due to absorption is not so expressive. This is due to the relatively large periods of the waves and relatively short travel times. Note that a similar result has been obtained by Zahradnik and Urban (1984).

In the previous comparisons of the ray method with the discrete wavenumber method we have seen that the discrepancies between both methods were partially caused by not considering enough multiples. In models with absorption, the situation simplifies in this respect since the higher multiples are more attenuated (due to their longer travel paths) than the first onsets. Thus, it seems that the ray method is not only well suited for the computation in slightly absorbing media, but it may be even more adequate there.

Conclusion

A method of seismic response analysis of 2-D absorbing structures, based on the ray method, is presented. The frequency-domain approach to computing the seismic response has been chosen since it is more effective than the construction of ray synthetic seismograms by the summation of elementary seismograms (i.e. time-domain approach). Moreover, the frequency-domain approach allows simple recomputation of time histories for different source-time functions once the frequency response is known.

The computation of the seismic response is performed in two steps. In the first step, rays, travel times, complex-valued ray amplitudes and global absorption factors of individual elementary waves are computed. In the second step, four characteristics of the seismic response (the frequency response, impulse response, time history of the response, spectrum of the time history) are computed from travel times, complex-valued amplitudes and, if required, also from global absorption factors. Once we know these quantities, we can compute seismic responses for practically any high-frequency exciting signal.

SH ray synthetic seismograms have been computed on the free surface of the classical sedimentary basin assuming vertical SH plane-wave incidence. The synthetics were compared with synthetics computed by the discrete wavenumber, glorified optics, finite-element and finite-difference methods. Within the bars of confidence, especially good agreement has been found between the discrete wavenumber and ray method results.

A detailed inspection of individual elementary waves forming the seismograms and their rays revealed two main types of propagation inside the basin: the horizontally propagating local interference waves observable at all receivers, and the vertically propagating wave in the central part of the basin.

The comparison of ray synthetics with discrete wavenumber synthetics for wavelengths comparable with and

larger than the minimum radius of curvature of the basin boundary has shown the following. The concept of approximating the wave field by a superposition of multiply reflected waves with geometrical ray paths fails for wavelengths larger than the minimum radius of curvature of the basin boundary. For wavelengths comparable with the minimum radius of curvature and considerably larger than the depth of the basin, the concept yields reasonably good results in the central part of the basin for shorter times.

The effect of Futterman's causal absorption on the ray synthetics has also been demonstrated. It produces a decrease in amplitudes and time delays at later times.

Without doubt, the ray method is a useful tool in seismic response analysis. It can be applied to rather complicated, even slightly absorbing media and enables a detailed insight into the computed wave field. It is relatively fast and gives sufficiently accurate results, especially for higher frequencies. If waves reflected many times are to be computed (as they were in our study in the case of a perfectly elastic medium), it is advisable to use some new concepts like paraxial ray approximation to make the procedure more efficient. It would not be difficult to consider, instead of plane-wave incidence, incidence of a wave generated by a point source or even by an extended earthquake source and to study combined effects of the structure and the source.

Acknowledgements. The authors are greatly indebted to Prof. V. Červený and Dr. J. Zahradník for critical reading of the manuscript. We thank two anonymous reviewers for their helpful comments.

References

- Bard, P.-Y., Bouchon, M.: The seismic response of sediment-filled valleys. Part 1. The case of incident *SH* waves. *Bull. Seismol. Soc. Am.* **70**, 1263–1286, 1980
- Bard, P.-Y., Gariel, J.Ch.: The seismic response of 2–*D* sedimentary deposits with large vertical velocity gradients. *Bull. Seismol. Soc. Am.* **76**, 343–366, 1986
- Boore, D.M., Lerner, K.L., Aki, K.: Comparison of two independent methods for the solution of wave scattering problems: response of a sedimentary basin to vertically incident *SH* waves. *J. Geophys. Res.* **76**, 558–569, 1971
- Červený, V.: Approximate expressions for the Hilbert transform of a certain class of functions and their application to the ray theory of seismic waves. *Stud. Geophys. Geod.* **20**, 125–132, 1976
- Červený, V.: The application of ray tracing to the numerical modeling of seismic wavefields in complex structures. In: *Handbook of Geophysical Exploration*. Section I: Seismic exploration, K. Helbig and S. Treitel, eds., volume on Seismic shear waves, G. Dohr, ed.: pp. 1–124. London: Geophysical Press 1985a
- Červený, V.: Ray synthetic seismograms for complex two-dimensional and three-dimensional structures. *J. Geophys.* **58**, 2–26, 1985b
- Červený, V., Frangié, A.B.: Elementary seismograms of seismic body waves in dissipative media. *Stud. Geophys. Geod.* **24**, 365–372, 1980
- Červený, V., Frangié, A.B.: Effects of causal absorption on seismic body waves. *Stud. Geophys. Geod.* **26**, 238–253, 1982
- Červený, V., Hron, F.: The ray series method and dynamic ray tracing systems for 3–*D* inhomogeneous media. *Bull. Seismol. Soc. Am.* **70**, 47–77, 1980
- Červený, V., Pšenčík, I.: SEIS83 – Numerical modeling of seismic wave fields in 2–*D* laterally varying layered structures by the ray method. In: *Documentation of earthquake algorithms*, Report SE-35, E.R. Engdahl, ed.: pp. 36–40. Boulder: World Data Center (A) for Solid Earth Geophysics 1984

- Červený, V., Ravindra, R.: *Theory of seismic head waves*. Toronto: University of Toronto Press 1971
- Červený, V., Molotkov, I.A., Pšenčík, I.: *Ray method in seismology*. Praha: Karlova Universita 1977
- Dravinski, M.: Scattering of plane harmonic *SH* wave by dipping layers of arbitrary shape. *Bull. Seismol. Soc. Am.* **73**, 1303–1319, 1983
- Futterman, W.I.: Dispersive body waves. *J. Geophys. Res.* **67**, 5279–5291, 1962
- Hong, T.L., Helmberger, D.V.: Glorified optics and wave propagation in nonplanar structure. *Bull. Seismol. Soc. Am.* **68**, 1313–1330, 1978
- Johnson, L.R., Silva, W.: The effects of unconsolidated sediments upon the ground motion during local earthquakes. *Bull. Seismol. Soc. Am.* **71**, 127–142, 1981
- Kjartansson, E.: Constant *Q* wave propagation and attenuation. *J. Geophys. Res.* **84**, 4737–4748, 1979
- Klem-Musatov, K.D., Aizenberg, A.M.: The ray method and the theory of edge waves. *Geophys. J.R. Astron. Soc.* **79**, 35–50, 1984
- Kohketsu, K.: 2-*D* reflectivity method and synthetic seismograms for irregularly layered structures – I. *SH*-wave generation. *Geophys. J.R. Astron. Soc.* **89**, 821–838, 1987
- Kravtsov, Yu.A., Orlov, Yu.I.: *Geometrical optics of inhomogeneous media* (in Russian). Moscow: Nauka 1980
- Krebes, E.S.: The viscoelastic reflection/transmission problem: two special cases. *Bull. Seismol. Soc. Am.* **73**, 1673–1683, 1983
- Langston, Ch.A., Lee, J.J.: Effect of structure geometry on strong ground motions: the Duwamish river valley, Seattle, Washington. *Bull. Seismol. Soc. Am.* **73**, 1851–1863, 1983
- Lee, J.J., Langston, Ch.A.: Three-dimensional ray tracing and the method of principal curvature for geometric spreading. *Bull. Seismol. Soc. Am.* **73**, 765–780, 1983a
- Lee, J.J., Langston, Ch.A.: Wave propagation in a three-dimensional circular basin. *Bull. Seismol. Soc. Am.* **73**, 1637–1653, 1983b
- Moczo, P., Červený, V., Pšenčík, I.: Documentation of earthquake algorithm – RESPO (program package). In: *Short description of computer programs for studying seismic response of near-surface geological structures*, J. Zahradník, ed.: pp. 14–17. Prague: Inst. Geophysics, Charles University 1985
- Moczo, P., Červený, V., Pšenčík, I.: Application of ray method in seismic response analysis. In: *Proc. of the 3rd Inter. Symp. on the Analysis of Seismicity and on Seismic Risk*, V. Schenk, Z. Schenková, eds., vol. II, pp. 455–463. Prague: Geophys. Inst. Czechosl. Acad. Sci. 1986
- Mueller, G.: Rheological properties and velocity dispersion of a medium with power-law dependence of *Q* on frequency. *J. Geophys.* **54**, 20–29, 1983
- Nowack, R., Aki, K.: The two-dimensional Gaussian beam synthetic method: testing and application. *J. Geophys. Res.* **89**, 7797–7819, 1984
- Sanchez-Sesma, F.J., Bravo, M.A., Herrera, I.: Surface motion of topographical irregularities for incident *P*, *SV* and Rayleigh waves. *Bull. Seismol. Soc. Am.* **75**, 263–269, 1985
- Virieux, J.: *SH*-wave propagation in heterogeneous media: velocity-stress finite-difference method. *Geophysics* **49**, 1933–1957, 1984
- Yerokhin, L.Yu.: The seismic propagation in a valley with semi-elliptical boundary (in Russian). *Izv. Akad. Nauk SSSR, Fizika Zemli*, No. 8, 60–73, 1985
- Zahradník, J., Hron, F.: Seismic ground motion of sedimentary valley La Molina, Lima, Peru. In: *Proc. of the 3rd Inter. Symp. on the Analysis of Seismicity and on Seismic Risk*, V. Schenk, Z. Schenková, eds., vol. II, pp. 340–346. Prague: Geophys. Inst. Czechosl. Acad. Sci. 1986
- Zahradník, J., Urban, L.: Effect of a simple mountain range on underground seismic motion. *Geophys. J.R. Astron. Soc.* **79**, 167–183, 1984

Paleomagnetic investigation of Quaternary West Eifel volcanics (Germany): indication for increased volcanic activity during geomagnetic excursion/event?

H. Böhnelt^{1*}, N. Reismann^{1**}, G. Jäger^{1***}, U. Haverkamp^{1****}, J.F.W. Negendank², and H.-U. Schmincke³

¹ Institut für Geophysik, Universität Münster, Corrensstraße 24, D-4400 Münster, Federal Republic of Germany

² Abteilung Geologie, Universität Trier, Postfach 3825, D-5500 Trier, Federal Republic of Germany

³ Institut für Mineralogie, Ruhr-Universität Bochum, Postfach 102148, D-4630 Bochum, Federal Republic of Germany

Abstract. Eighty-five sites of West Eifel volcanoes were investigated paleomagnetically, giving 64 independent virtual geomagnetic poles (VGP). The VGP distribution is strongly asymmetric: about 30% of the VGPs have latitudes below 60° N and are confined to the longitude sector between 30° E and 120° E. This leads to a mean VGP situated at 74.0° N/63.9° E, deviating significantly from the north geographical pole. The VGP distribution is non-Fisherian, but the radial component is rather similar to that observed for Tertiary to Quaternary Icelandic lavas. Tectonic, petrographic, rock magnetic properties and secular variation do not seem to be responsible for the anomalous VGP positions. We propose that the volcanoes with anomalous VGPs erupted in a short period during an excursion or event of the earth's magnetic field.

Key words: Paleomagnetism – Virtual geomagnetic poles – Geomagnetic excursion/event – Volcanics – Ore petrography – Quaternary – West Eifel (Germany)

Introduction

Secular variation of the Quaternary magnetic field of East Eifel volcanics was studied by Kohlen and Westkämper (1978). The distribution of the VGPs obtained was largely Fisherian (Fisher, 1953), and their dispersion around the north geographic pole was in agreement with several models for the secular variation. Some lava flows were correlated to certain volcanic eruption centres based on paleomagnetic data (Böhnelt et al., 1982). The results encouraged us to carry out similar studies in the nearby Quaternary volcanic field of the West Eifel. The main problems to be studied were: (1) to assign lava flows to one of the nearby eruption centres, (2) to obtain an approximate but independent control on radiometric age determinations of volcanics by po-

Present addresses:

* H. Böhnelt, Instituto de Geofísica, Universidad Nacional Autónoma de México, Del. Coyoacán, 04510 México, D.F., México

** N. Reismann, Mannesmann Kienzle, Waldstraße, D-7730 Villingen, Federal Republic of Germany

*** G. Jäger: BEB Erdgas und Erdöl GmbH, Riethorst 12, D-3000 Hannover, Federal Republic of Germany

**** U. Haverkamp: Radiologische Klinik, Roxeler Straße, D-4400 Münster, Federal Republic of Germany

Offprint requests to: H. Böhnelt

larity of magnetization and (3) to compare the secular variation of this region with that determined in the eastern part of the Eifel.

The West Eifel volcanic field

The Quaternary West Eifel volcanic field (covering about 600 km²) extends for 50 km NW-SE and comprises about 240 eruptive centres (Büchel and Mertes, 1982; Schmincke, 1982; Mertes, 1983; Schmincke et al., 1983) (Fig. 1). The basement consists of Devonian clastic sedimentary rocks and local Middle- to Upper-Devonian limestone, locally overlain by Triassic sandstones.

West Eifel volcanism started during the Pleistocene, the main activity about 0.7 M.a. ago, with the eruption of foiditic lavas, slightly post-dating the onset of the Pleistocene phase of uplift in the Rhenish massif (Illies et al., 1979; Lippolt and Fuhrmann, 1981; Mertes and Schmincke, 1983) and lasted to about 0.01 M.a. B.P. (Büchel and Lorenz, 1982). Rising magmas used dominantly NW-SE- and rarely N-S-oriented fractures as eruptive fissures (Mertes, 1983). The eruptive centres consist mainly of scoria cones (66%, about half of them with lava flows), 30% maars and tuff rings, about 2% scoria rings and 2% pyroclastic vents.

The Quaternary West Eifel lavas are dominantly leucites and nephelinites (42% of the 174 eruptive centres studied), melilite-bearing foidites (32%), olivine-free foidites (ol < 1 vol.-%) (6%), olivine nephelinites (ol > 10 vol.-%) (5%), melilite-free sodalite-bearing foidites (4%), basanites (8%), tephrites (1%), phonolites (2%) (Mertes and Schmincke, 1985).

Mineralogically, the foidite suite is dominated by clinopyroxene (Ti-augite), accompanied by olivine and minor phlogopite phenocrysts. Phenocrystal olivine exceeds clinopyroxene in the younger (< 0.1 M.a.; Mertes and Schmincke, 1985) olivine-nephelinite and basanite suite which occurs mainly in the southeastern part of the field. Rare differentiated rocks – tephrites and phonolites – are restricted to the centre of the field and are characterized by leucite, sodalite, plagioclase and sanidine. A detailed petrographic description of West Eifel lavas is given by Mertes (1983).

About two-thirds of the volcanoes contain nodules, both of mantle-derived peridotites up to several decimetres in diameter and cumulates of low- to intermediate-pressure

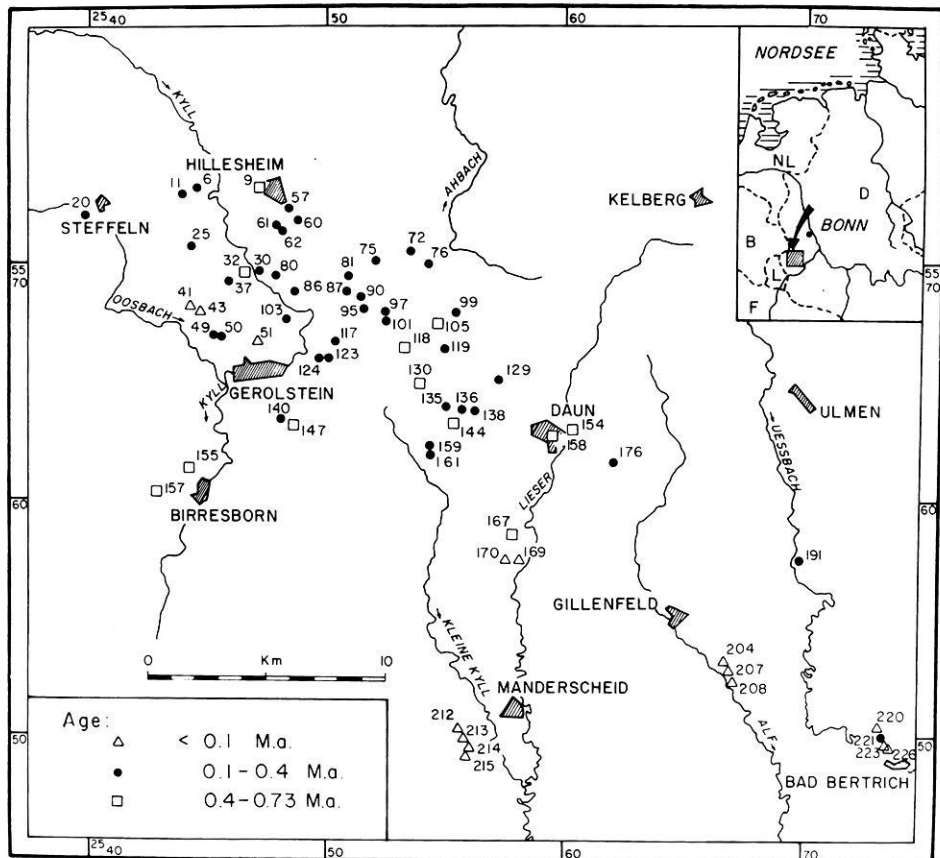


Fig. 1. Locations of sites sampled for paleomagnetic measurements. Three age ranges (according to Mertes and Schmincke, 1983) are indicated with different symbols. Numbers refer to Table 1 and to the eruption centre catalogue (Büchel and Mertes, 1982) for the West Eifel

Table 1. EC: eruption centre according to Büchel and Mertes (1982), different sites from one and the same eruption centre being distinguished by affixed letters and an uncertain correlation to this or a neighbouring eruption centre being indicated by the symbol #; topographic map and coordinates; name of site; chemical composition (*Bs*: basanite, *Lc*: leucitite, *Mel*: melilite nephelinite, *Ne*: nephelinite, *Ol*: olivine nephelinite; *Mel-b.Ne*: melilite-bearing nephelinite, *Ol-fr.Lc*: olivine-free leucitite, etc.); type of exposure (*plug*: volcanic plug, *tuff*: palagonite-tuff, *scor*: scoria, *sill*: sill-like flows within cinder cones); age estimates (geological evidence) and K/Ar ages ($^{40}\text{Ar}/^{39}\text{Ar}$ indicated by star symbol) for West Eifel volcanics sampled for paleomagnetic measurements according to Lippolt and Fuhrmann (1981) and Mertes and Schmincke (1983)

EC	Map	r-25	h-55	Name	Rock	Exp.	Age-Est.	Radiometric age
6a	5705	4470	7315	Ruderbüsch I	Lc-Ne	flow	0.1-0.4	1.37 ± 0.04
6b	5705	4495	7315	Ruderbüsch II	Lc-Ne	dike	0.1-0.4	
9	5705	4715	7305	Steinrausch	Ne-Lc	scor	0.4-0.73	
11	5705	4410	7260	Basberg	Lc-Ne	flow	0.4-0.73	
14	5705	5270	6900	Mühlenberg	Mel-Ne	flow		
20	5705	3920	7205	Steffelner Kopf	Lc-Ne	flow	0.1-0.4	
25	5705	4490	7135	Rossbüsch	Mel-Ne	flow	0.1-0.4	
30	5705	4715	6965	Dohm	Lc-Ne	flow	0.1-0.4	
32	5705	4655	6900	Beilstein	Lc-Ne	flow	0.1-0.4	
37	5705	4580	6925	Wolfsbeuel	Lc-Ne	dike	0.1-0.4	
41	5705	4420	6820	Rother Kopf II	Mel-b.Ne	flow	0.1-0.4	
43	5705	4440	6800	Rother Kopf I	Mel-b.Ne	sill	0.1-0.4	
49	5705	4500	6650	Rother Hecke I	Mel-Ne	flow	0.1-0.4	
50	5705	4545	6695	Rother Hecke II	Ne-Lc	dike	0.1-0.4	
51	5705	4670	6540	Sarresdorf	Bs	flow	0.1-0.4	
57	5706	4800	7210	Am Lier	Mel-Ne	flow	0.1-0.4	
60	5706	4910	7180	Kyller Höhe	Mel-Ne	flow	0.1-0.4	
61	5706	4775	7195	Graulei I	Lc?	flow	0.1-0.4	
62	5706	4820	7080	Graulei III	Mel-Ne	flow	0.1-0.4	
72a	5706	5345	7075	Kahlenberg Süd	Ne-Lc	flow	0.1-0.4	
72b	5706	5385	7065	Kahlenberg	Ne-Lc	dike	0.1-0.4	
75	5706	5190	6995	Gonnenstall	Ne	flow	0.1-0.4	
76	5706	5440	6995	Döhmberg	Lc	scor	0.1-0.4	
80a	5706	4750	6925	Giesenheld I	Lc-Ne	flow	0.1-0.4	
80b	5706	4755	6960	Giesenheld II	Lc-Ne	flow	0.1-0.4	

Table 1 (continued)

EC	Map	r-25	h-55	Name	Rock	Exp.	Age-Est.	Radiometric age
81	5706	5085	6980	Am Köpfchen	Lc-Ne	flow	0.1–0.4	
86	5706	4840	6840	Rockeskyller Kopf	Lc-Ne	flow	0.1–0.4	0.63 ± 0.03, 0.36 ± 0.04, 0.44 ± 0.04
87	5706	5080	6870	Gypenberg	Mel-Ne	sill	0.1–0.4	
90	5706	5140	6850	Bickenberg	Mel-b.Ne	dike	0.1–0.4	
94	5706	5215	6810	Feuerberg	Mel-b.Ne	plug	0.1–0.4	
95a	5706	5150	6800	Alter Voß I	Ne-Lc	scor	0.1–0.4	
95b	5706	5150	6800	Alter Voß II	n.d.	dike	0.1–0.4	
95c	5706	5100	6750	Alter Voß III	Ne-Lc	flow	0.1–0.4	
97a	5706	5260	6820	Feuerberg	Mel-b.Ne	dike	0.1–0.4	
97b	5706	5250	6760	Feuerberg	Mel-b.Ne	flow	0.1–0.4	
97c	5706	5190	6750	Feuerberg	Mel-b.Ne	flow	0.1–0.4	
99	5706	5540	6845	Dockweiler	Ne-Lc	flow	0.1–0.4	
99	5706	5625	6945	Steinlei	n.d.	flow	0.1–0.4	
101	5706	5230	6760	Auf Winkel	Ne	flow	0.1–0.4	
105	5706	5450	6750	Hangelberg	Lc	dike	0.1–0.4	
103 #	5706	4800	6770	Hahn	Mel-Ne	flow	0.1–0.4	
117	5706	5020	6640	Sellbüsch	Mel-b.Ne	flow	0.1–0.4	
118	5706	5335	6650	Beuel/Kirchweiler	Mel-b.Ne	plug	0.4–0.73	2.09 ± 0.10
119	5706	5520	6620	Ernstberg	Ol-fr.Ne-Lc	flow	0.1–0.4	
123a #	5706	4980	6600	Baarley II	Ol-fr.Lc	dike	0.1–0.4	
123b #	5706	4980	6600	Baarley I	Ol-fr.Lc	sill	0.1–0.4	
129	5706	5705	6540	Asseberg	Ne	flow	0.1–0.4	
130	5706	5385	6490	Scharteberg	Ol-fr.Hau-Ne	scor	0.4–0.73	0.51 ± 0.2
135	5706	5505	6395	Goosberg	Mel-b.Ne	scor	0.1–0.4	
136	5706	5505	6450	Hippersbach		tuff	0.1–0.4	
138	5706	5595	6380	Held		tuff	0.1–0.4	
140	5706	4785	6335	Krekelsberg	Mel-b.Ne	flow	0.1–0.4	
144	5706	5535	6320	Riemerich	Mel-b.Ne	flow	0.4–0.73	2.34 ± 0.05
147	5706	4840	6320	Dietzenley	Mel-b.Ne	plug	0.4–0.73	0.73 ± 0.15, 0.62 ± 0.11, 0.62 ± 0.15*
154	5707	5990	6300	Firmerich	Ne-Lc	flow	0.4–0.73	0.75 ± 0.04, 0.95 ± 0.18, 0.60 ± 0.14*
155a	5705	4510	6205	Kalem	Mel-Ne	flow	0.4–0.73	0.82 ± 0.03,
155b	5705	4510	6205	Kalem	Mel-Ne	flow	0.4–0.73	0.66 ± 0.16, 0.54 ± 0.18*
157a	5805	4280	6040	Fischbachtal West	Lc-Ne	flow	0.4–0.73	
157b	5805	4360	6025	Fischbachtal Ost	Ne	flow	0.4–0.73	
158	5806	5885	6290	Burgberg	Mel-b.Ne	plug	0.4–0.73	
159	5806	5435	6230	Neroth Kopf	Lc-Ne	flow	0.1–0.4	
161	5806	5432	6200	Kahlenberg/Neroth	Lc-Ne	dike	0.1–0.4	
167	5806	5815	5815	Üdersdorf (Liley)	Mel-Ne	flow	0.4–0.73	0.74 ± 0.09
169	5806	5800	5750	Mühlenkaul I	Ol-Ne	flow	<0.1	
170a	5806	5740	5740	Emmelberg	Ol-Ne	sill	<0.1	
170b	5806	5785	5735	Emmelberg II	Ol-Ne	scor	<0.1	
176	5807	6200	6150	Auf der Haardt	Ne-Lc	scor	0.1–0.4	
191	5807	6980	5730	Roter Berg	Ne-Lc	scor	0.1–0.4	
204	5807	6685	5320	Wartgesberg Nord	Bs	scor	<0.1	
207a	5807	6680	5285	Wartgesberg	Bs	scor	<0.1	0.23 ± 0.10
207b	5807	6675	5285	Wartgesberg Ost	Bs	dike	<0.1	0.23 ± 0.10
208a #	5807	6655	5285	Strohner Mühlen	Bs	scor	<0.1	
208b #	5807	6680	5265	Strohner Mühlen	Bs	scor	<0.1	
208c #	5807	6670	5235	Alftal	Bs	flow	<0.1	
212	5906	5555	5040	Windsborn	Ol-Ne	scor	<0.1	
213 #	5906	5555	4970	Mosenberg	Ol-Ne	dike	<0.1	
215a #	5906	5585	4985	Mosenberg	Ol-Ne	scor	<0.1	
215b #	5906	5560	4960	Mosenberg	Ol-Ne	sill	<0.1	
215c #	5906	5580	4925	Mosenberg	Ol-Ne	sill	<0.1	
215d #	5906	5740	4905	Horngraben	Ol-Ne	flow	<0.1	
220	5908	7285	4985	Falkenley	Bs	flow	<0.1	
221a	5908	7320	4915	Bad Bertrich	Bs	flow	<0.1	1.16 ± 0.04,
221b	5908	7280	4950	Bad Bertrich	Bs	flow	<0.1	0.06 ± 0.03
223	5908	7360	4950	Dachslöcher	Bs	flow	<0.1	
224	5908	7330	4960	Facher Höhe	Bs	flow	<0.1	

origin (Sachtleben and Seck, 1981; Stosch and Seck, 1980; Mertes, 1983; Duda and Schmincke, 1985).

Sampling

Eighty-five sites were sampled, based on the detailed field-work of Büchel and Mertes (1982) and in coordination with H. Mertes. These sites represent 73, and thus one-third, of all known eruption centres in the West Eifel. Further paleomagnetic sampling is not possible because suitable exposures of the remaining maars and cinder cones are lacking.

Table 1 lists the sites with their coordinates, rock type, type of exposures and estimated ages (geological evidence) or radiometric ages. Most sites are in lava flows, others are from dikes and sill-like small flows within scoria cones, plugs and two palagonite tuffs.

To avoid systematic errors due to local tectonic movements, 8–12 cores distributed over an entire site were taken with a portable gasoline-powered corer. The cores were oriented with an inclinometer and a magnetic and/or a sun compass (Collinson, 1983).

Laboratory procedures

The cores were subdivided into 21-mm-long specimens. Generally, the specimens were demagnetized with alternating-field static or tumbling demagnetizers. Only a few selected samples were thermally demagnetized. Intensity and direction of magnetization were determined with a Digico-Spinner magnetometer (Molyneaux, 1971), magnetic susceptibility with a Bison bridge 3101 A and in part with a Minisep bridge (Molspin Ltd.), which was also used for measurements of anisotropy of magnetic susceptibility (AMS). IRM-acquisition curves and reversed-field demagnetization curves were obtained using a pulse magnetizer producing up to 1200 kA/m. H_c and M_s were determined with a hysteresis curve tracer similar to the instrument described by Likhite et al. (1963), in fields up to 160 kA/m. Polished sections were studied in reflected light and scanning electron microscope (SEM) (Cambridge S 250 Mk II with Link semiquantitative microanalyser for the determination of elements with atomic weight >20).

For each site, three or more pilot specimens were demagnetized in at least seven steps, depending on the directional behaviour of magnetization. The characteristic remanent magnetization (CARM) was then determined using Zijdeveld diagrams (Zijdeveld, 1967), stability indices (Symons and Stupavsky, 1974) and analysis of demagnetization paths (Kirshvink, 1980) and difference-vector variations (Hoffman and Day, 1978). Whenever all pilot specimens from one site exhibited simple and similar variations of magnetization direction, the remaining specimens were all demagnetized in 3–5 selected steps of coinciding field strengths. Otherwise, every specimen was demagnetized individually in seven or more steps.

Experimental results

Only results from standard treatment of specimens from all sites, i.e. demagnetization and ore petrography, are regarded. Further measurements made on selected specimens are discussed later.

Ore petrography

One or more polished sections were prepared for most sites and studied by reflected light microscopy and SEM. Table 2 contains results separated for the most common oxides and minor important oxides. Most oxides are titanomagnetites in the range 3 μm (pigment) to about 60 μm , phenocrysts often exceeding 100 μm . Anhedral grains dominate, but euhedral grains were also observed, most of which are smaller than 10 μm .

Titanomagnetites (TM) commonly contain impurities (<3%) of Al, Mn, Mg and Cr. The TiO_2 content ranges between 3% and about 26%. Most TM belong either to the oxidation class 1 or 5 and 6 (Ade-Hall et al., 1968; Wilson and Haggerty, 1966). The less oxidized grains are largely maghemitized and/or granulated, presumably resulting from hydrothermal alteration.

Subordinate TM were observed belonging to another oxidation class, e.g. they are less oxidized or more oxidized than the dominating ore phase. Some samples contained chromite, ilmenite, ilmenite-hematite, hematite, ferritespinels and pyrite. In 11 samples, secondary hematite formed from olivine and augite.

Figure 2 shows typical examples of SEM: TM of HT-oxidation class 1, partly euhedral, with grain diameters of about 20 μm are typical for many rocks (Fig. 2a). Many TM suffered maghemitization at a different degree. Figure 2b shows the typical maghemitization shrinking cracks (Wilson and Haggerty, 1966). An example for strongly oxidized TM is given in Fig. 2c. The grains are dissolved, partly persisting only as a hematite skeleton. Some hematite skeletons resulted from alteration of olivine (Fig. 2d).

Magnetic properties

Table 3 (columns 2–6) lists site mean values for the NRM intensity M_0 , the intensity M_8 after af demagnetization with 8 kA/m, susceptibility χ , Königsberger factor Q and the medium destructive field MDF. One representative sample per site was subjected to magnetic hysteresis measurements at field strengths up to 160 kA/m. Saturation magnetization M_s , coercive force H_c and the corresponding values of the remanent hysteresis curve, M_{rs} and H_{cr} , are given in the last four columns.

All magnetic properties range widely. NRM intensity ranges between 0.6 and 60 A/m and susceptibility between 0.003 and 0.1 m^3/m^3 (Fig. 3). In correspondence with petrographic observations, low values are due to strong high-temperature oxidation and/or hydrothermal alteration, with partial transformation of strongly magnetic TM to weakly or non-magnetic oxidation products. The Q factor generally has values greater than about 1, indicating the presence of (pseudo-) single-domain particles (Day, 1977).

There is no obvious correlation of magnetic parameters with rock composition. Only melilite-nephelinites have higher susceptibilities at quite normal NRM intensities, which results in comparatively small Q factors between 1 and 3. The high-temperature oxidation number M_{ox} is generally 1 for these rocks, whereas the other rock types are more oxidized ($M_{ox}=4 \dots 6$) and have higher Q factors between 3 and 30. This is most likely due to the reduction of grain size by exsolution lamellae. This interpretation is further supported by the fact that rocks with high M_{ox} values also exhibit high MDF values.

Scoria shows greater magnetic stability than lava, be-

Table 2. Petrographic results from reflected light microscopy and SEM. Left part represents dominating titanomagnetites, right subordinate oxides. EC: eruption centre; grain diameter d ; grain form: *eu*: euhedral, *sub*: subhedral, *an*: anhedral; high-temperature oxidation number M_{ox} ; TiO_2 content and contamination of titanomagnetite by Al, Mn, Mg, Cr; granulation, dissolution and maghemitization of grains; *TM*: titanomagnetites with low-temperature oxidation number M_{ox} ; other oxides: *Cr*: chromite, *Hem*: hematite, *Mag*: magnetite, *Il*: ilmenite, *Sec. Hem*: secondary hematite

EC	Dominant ore phase											Subordinate ore phases		
	d (μm)	Grain form	M_{ox}	TiO_2 wt.-%	Al	Mn	Mg	Cr	Gran	Diss	Magh	TM M_{ox}	Other	Sec. Hem
6	<40	sub	1	20		×					×	–	Cr	
25	5–50	eu-an	1	19		×					×	–		
57	5–50	eu-an	1	18–19		×	×				×	–	Cr	
72b	4–60	eu-an	3–5	22	×	×	×		×			1–2		
72a	2–30	an	5	11					×	×		1–2		
86	6–60	eu-an	3–4									5	Cr	
94	4–60	eu-an	6	10–12		×	×			×		–	Ferrit	
97a	2–30	an	6							×		–	Hem, Ferrit	×
97b	4–40	eu-an	6	16			×	×				1		
99	2–60	eu-an	3–5						×			1–2	Pyrit	
117	4–30	eu-an	1	20		×					×	–		
118	5–50	eu-an	1	19							×	–		
119	4–60	an	1–2	16		×					×	–		
129	<30	eu-sub	1	20		×					×	–		
130	2–80	an	6	10						×		1		×
135	10–100	an	6									3	Mag	
140	10–20	eu-an	1	18		×	×				×	–		
144	5–100	an	6	16								3–4	Mag	
147	5–50	eu-an	1	22		×					×	–	Hem	
154	2–40	eu-an	1	18		×					×	1–2		
155a	6–60	eu-sub	1	17	×		×					–		
155b	3–60	eu-an	1	19–24		×					×	–		
157	4–30	eu-an	6	4						×		4–5		×
158	10–20	eu-an	1	18–21	×	×	×	×			×	–		
204	<4	eu-an	6	23								–	Cr, Il	×
207a	<10	an	1	22			×				×	–		×
207b	<5	eu-an	3		×							–	Cr	×
208b	10	eu-an	6									–	Hem	
208c	4–40	eu-an	1	26				×			×	–		
212	4–20	eu-an	1	16			×					1–2		
213	5–60	eu-an	4–6	26					×	×		3	Cr, Il-Hem	×
215a	<50	eu-an	Chromite									1		×
215b	3–80	eu-an	3–6	4					×	×		1–2	Cr, Hem	
215b	3–50	eu-an	1		×		×				×	–	Il-Hem	
215c	4–40	an	6							×		5	Cr	
221	<10	eu	1	26			×		×			1–2	Cr	
223	<30	an	5									3–4	Cr, Mag	

cause faster cooling resulted in smaller TM grain sizes and, therefore, more (pseudo-) single-domain particles.

Hysteresis values of selected samples (Table 3) are subjected to a domain-structure diagnosis (Day et al., 1977; Dunlop, 1981). Figure 4 suggests the occurrence of predominantly pseudo-single-domain particles which are believed to have high stability of remanence.

Paleodirections and VGP distribution

Table 4 lists the paleomagnetic results. If different sites were suspected of belonging to the same eruption centre, their data were subjected to the F-test. The lower part of Table 4 lists those sites from one and the same eruption centre or from several coeval eruption centres within one volcanic complex, together with their mean direction and statistical parameters.

Figure 5a shows the remaining 64 independent direc-

tions and VGPs in equal-area plots. Error circles α_{95} are not given, as this would totally obscure the distribution of directions and poles. The directions/VGPs are of normal polarity. These rocks studied probably erupted during the Brunhes epoch and are thus younger than 0.73 M.a. These data have been one of the constraints in postulating that apparent K/Ar ages older than 0.73 M.a. are probably in error due to excess argon (Mertes and Schmincke, 1983).

Many directions clearly diverge from the dipolar direction of the earth's magnetic field. This also holds for the mean direction. The VGP distribution is strongly asymmetric: a considerable part has latitudes $<60^\circ$ and is concentrated in the longitude sector between 30° E and 120° E. Consequently, the mean VGP lies at 63.9° E/ 74.0° N and the error circle α_{95} indicates a significant departure from the north geographical pole (NGP).

The VGP density distribution (Fig. 5b) shows two clearly separated maxima: one near the NGP with the cor-

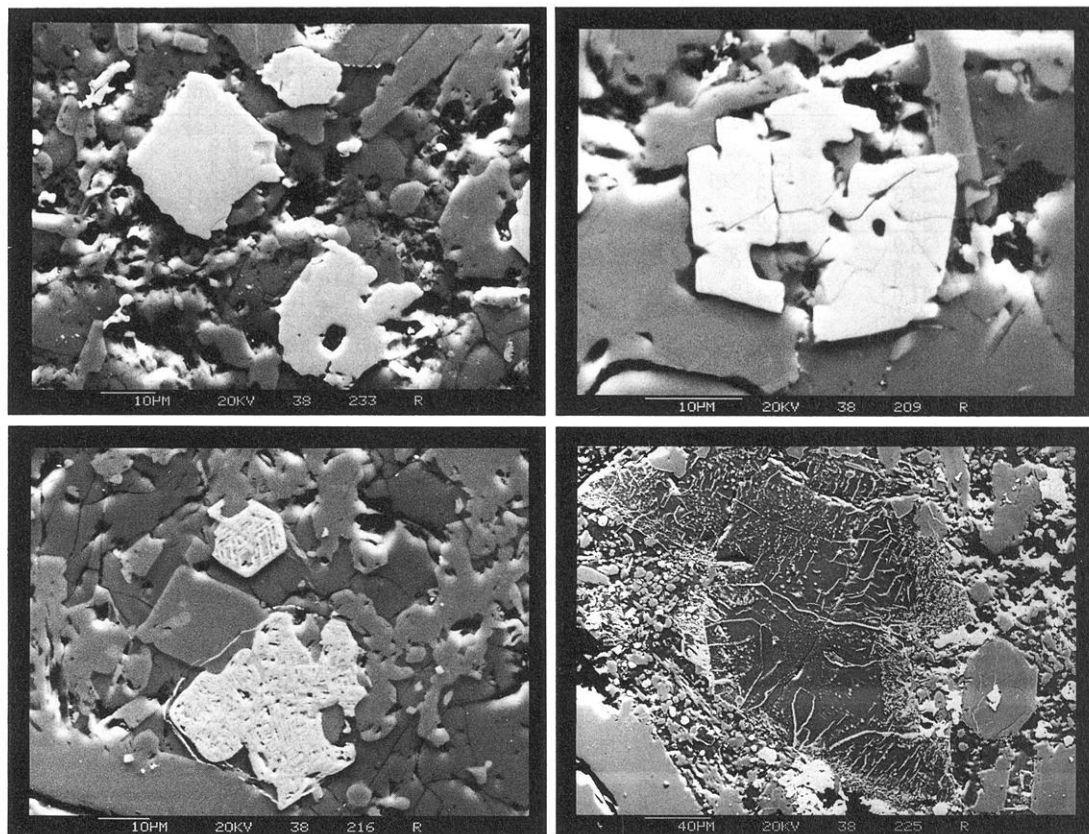


Fig. 2a–d. Examples for SEM studies on polished sections. **a** partly anhedral titanomagnetites, typical for many specimens; **b** maghemitized titanomagnetite; **c** strongly oxidized titanomagnetite; **d** hematite skeleton as alteration product of olivine

Table 3. Rock magnetic properties. Eruption centre; mean NRM intensity M_0 , mean intensity M_8 after af demagnetization with 8 kA/m; susceptibility χ and Q factor; medium destructive field MDF; saturation magnetization M_s ; remanent saturation magnetization M_{rs} ; coercive force H_c ; remanent coercive force H_{cr} ; n.d. not determined

EC	M_0 (A/m)	M_8 (A/m)	χ (10^{-3})	Q	MDF (kA/m)	M_s (kA/m)	M_{rs} (kA/m)	H_c (kA/m)	H_{cr} (kA/m)
6a	2.9	1.6	32.0	3.0	15	n.d.	n.d.	n.d.	n.d.
6b	4.6	2.4	35.3	3.4	10	n.d.	n.d.	n.d.	n.d.
9	2.4	2.9	46.1	2.4	10	n.d.	n.d.	n.d.	n.d.
11	2.9	1.7	91.3	0.8	10	9.0	0.5	4.0	14.4
14	2.7	n.d.	44.1	3.4	12	n.d.	n.d.	n.d.	n.d.
20	9.2	5.5	20.7	11.6	16	0.55	0.55	10.4	16.9
25	4.3	1.8	51.6	2.2	13	n.d.	n.d.	n.d.	n.d.
30	4.0	2.5	46.3	2.2	10	3.9	0.66	6.4	14.4
32	8.7	5.3	51.3	4.4	8	5.0	1.34	10.8	23.4
37	4.2	3.8	25.2	4.3	31	0.35	0.08	12.4	15.2
41	4.8	2.2	18.1	6.9	11	3.8	1.13	12.8	37.8
43	11.7	2.8	33.3	9.2	13	1.35	0.20	3.2	9.6
49	19.8	n.d.	71.1	7.3	4	n.d.	n.d.	n.d.	n.d.
50	3.5	1.9	23.4	3.9	9	2.6	0.69	9.6	16.8
51	5.1	3.9	18.1	7.3	12	n.d.	n.d.	n.d.	n.d.
57	2.7	0.6	57.4	1.2	n.d.	n.d.	n.d.	n.d.	n.d.
60	1.3	0.5	67.0	0.5	15	3.99	1.09	12.8	40.0
61	1.0	0.6	54.8	0.4	11	8.25	0.38	5.6	24.0
62	1.4	0.4	116.8	0.3	5	7.25	1.04	5.6	21.8
72a	4.1	2.1	50.3	2.2	12	n.d.	n.d.	n.d.	n.d.
72b	16.9	1.5	14.0	31.4	15	n.d.	n.d.	n.d.	n.d.
75	5.9	2.4	87.6	1.7	10	9.0	1.50	9.6	27.2
76	3.5	4.4	2.8	32.5	70	n.d.	n.d.	n.d.	n.d.
80a	7.6	2.7	13.8	14.4	25	1.9	0.49	10.4	29.0
80b	58.6	17.8	80.9	19.0	6	4.75	0.70	6.4	13.8
81	4.6	2.6	43.1	2.8	19	4.1	0.72	16.3	27.3
86	2.4	0.9	39.8	1.8	21	n.d.	n.d.	n.d.	n.d.

Table 3 (continued)

EC	M_0 (A/m)	M_8 (A/m)	χ (10^{-3})	Q	MDF (kA/m)	M_s (kA/m)	M_{rs} (kA/m)	H_c (kA/m)	H_{cr} (kA/m)
87	7.7	4.8	43.1	2.8	19	4.4	1.10	9.6	37.6
90	34.9	12.2	75.2	12.2	4	8.5	1.21	6.4	19.2
94	3.2	1.2	24.3	5.0	60	n.d.	n.d.	n.d.	n.d.
95a	42.7	5.1	80.1	14.0	2	1.4	0.15	3.2	12.8
95b	30.3	25.2	23.9	33.3	16	0.51	0.12	8.1	32.4
95c	3.8	2.3	8.8	11.3	25	0.85	0.32	23.6	32.4
97a	4.6	2.0	21.0	8.4	24	n.d.	n.d.	n.d.	n.d.
97b	9.0	5.5	45.8	5.4	4	n.d.	n.d.	n.d.	n.d.
97c	1.9	0.9	7.1	7.7	37	n.d.	n.d.	n.d.	n.d.
99a	1.8	n.d.	38.3	8.0	6	n.d.	n.d.	n.d.	n.d.
99b	3.4	3.0	38.9	2.3	30	5.0	0.61	4.0	13.8
101	6.4	3.4	36.2	5.4	7	n.d.	n.d.	n.d.	n.d.
103 #	16.6	6.7	25.3	17.2	8	1.2	0.71	10.4	25.6
105	10.0	3.5	6.7	39.2	53	0.95	0.21	66.1	117.3
117	15.3	n.d.	75.0	5.3	2	n.d.	n.d.	n.d.	n.d.
118	17.8	2.5	97.1	4.8	5	n.d.	n.d.	n.d.	n.d.
119	10.0	3.2	31.2	8.3	6	n.d.	n.d.	n.d.	n.d.
123a #	7.9	0.6	68.0	3.0	5	10.0	1.78	9.6	25.6
123b #	0.7	2.5	7.4	2.4	29	0.3	0.12	48.0	57.2
129	2.4	0.7	61.4	1.2	9	n.d.	n.d.	n.d.	n.d.
130	6.3	1.8	11.9	13.8	10	n.d.	n.d.	n.d.	n.d.
135	3.7	n.d.	8.1	12.1	4	n.d.	n.d.	n.d.	n.d.
136	0.5	0.2	12.2	1.2	5	n.d.	n.d.	n.d.	n.d.
138	0.4	0.2	8.9	1.2	12	n.d.	n.d.	n.d.	n.d.
140	3.8	1.7	53.9	1.8	9	n.d.	n.d.	n.d.	n.d.
144	3.4	1.2	3.1	30.6	24	n.d.	n.d.	n.d.	n.d.
147	32.0	2.6	36.5	22.8	6	n.d.	n.d.	n.d.	n.d.
154	4.0	2.9	33.3	3.1	22	n.d.	n.d.	n.d.	n.d.
155a	4.4	2.7	71.7	2.5	8	n.d.	n.d.	n.d.	n.d.
155b	3.9	n.d.	58.6	2.6	n.d.	n.d.	n.d.	n.d.	n.d.
157a	1.9	n.d.	12.0	4.1	20	n.d.	n.d.	n.d.	n.d.
157b	3.6	1.7	61.1	2.7	20	n.d.	n.d.	n.d.	n.d.
158	4.0	0.7	70.7	1.5	2	n.d.	n.d.	n.d.	n.d.
159	4.3	3.8	19.8	8.6	22	n.d.	n.d.	n.d.	n.d.
161	4.3	3.5	42.2	2.6	22	7.12	2.0	14.4	33.3
167	3.7	2.2	88.5	1.2	11	n.d.	n.d.	n.d.	n.d.
169	89.1	6.2	8.8	19.7	32	0.52	0.21	12.1	22.3
170a	4.1	3.4	7.2	14.9	24	0.4	0.14	9.6	24.8
170b	7.3	5.9	5.8	33.1	42	0.4	0.06	54.4	79.5
176	1.1	1.0	3.8	7.6	44	0.4	0.06	52.8	60.0
191	5.7	4.6	5.2	28.8	38	0.9	0.16	67.2	78.5
204	7.8	2.9	10.0	20.7	39	n.d.	n.d.	n.d.	n.d.
207a	11.2	7.9	11.2	26.0	63	n.d.	n.d.	n.d.	n.d.
207b	8.9	13.1	15.0	15.4	27	n.d.	n.d.	n.d.	n.d.
208a #	7.8	9.8	8.1	25.1	29	n.d.	n.d.	n.d.	n.d.
208b #	12.8	9.9	21.5	15.5	25	n.d.	n.d.	n.d.	n.d.
208c #	4.3	2.5	29.4	3.8	14	n.d.	n.d.	n.d.	n.d.
212	14.9	10.6	11.9	32.5	46	n.d.	n.d.	n.d.	n.d.
213 #	7.7	2.8	9.8	20.5	15	n.d.	n.d.	n.d.	n.d.
215a #	13.4	n.d.	10.5	33.2	15	n.d.	n.d.	n.d.	n.d.
215b #	26.0	n.d.	33.1	20.5	20	n.d.	n.d.	n.d.	n.d.
215c #	8.8	3.5	8.8	26.0	28	n.d.	n.d.	n.d.	n.d.
220	3.8	2.7	20.8	5.1	29	n.d.	n.d.	n.d.	n.d.
221a	6.6	4.6	22.1	7.9	9	n.d.	n.d.	n.d.	n.d.
221b	10.4	2.8	18.2	14.0	8	n.d.	n.d.	n.d.	n.d.
223	4.8	4.3	18.7	7.9	24	n.d.	n.d.	n.d.	n.d.
224	7.5	3.2	23.2	13.5	19	n.d.	n.d.	n.d.	n.d.

responding VGP distribution resembling that of other Quaternary distributions, e.g. from the East Eifel (Kohnen and Westkämper, 1978). The other maximum at about 60° N/45° E leads to the mean pole diverging from the NGP. This is in strong contrast to results from the East Eifel. Here

the mean VGP coincided with the NGP and the distribution of the VGPs followed a Fisherian distribution.

The observed azimuthal and radial distributions around the mean VGP and the NGP, respectively, are compared with the corresponding theoretical curves according to Fish-

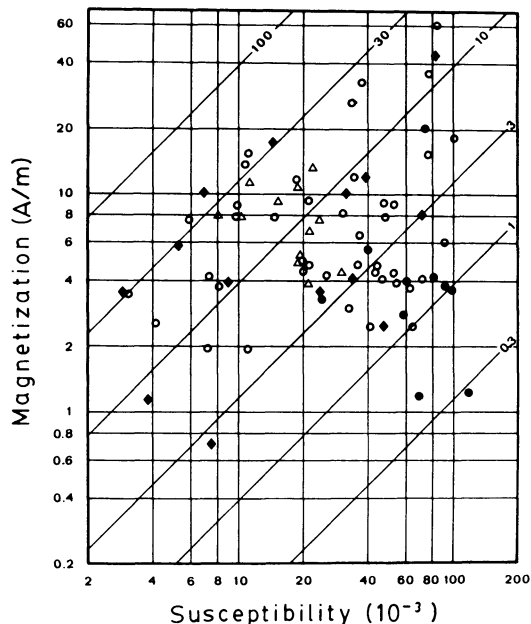


Fig. 3. Site mean values for NRM intensity (in A/m) plotted against site mean susceptibility. *Diagonals* indicate lines of constant Q factor. Chemical composition of rocks is given by different symbols. *Circles*: Melitite-nephelinites; *open circles*: nephelinites; *rhomboids*: leucitites; *open triangles*: basanites

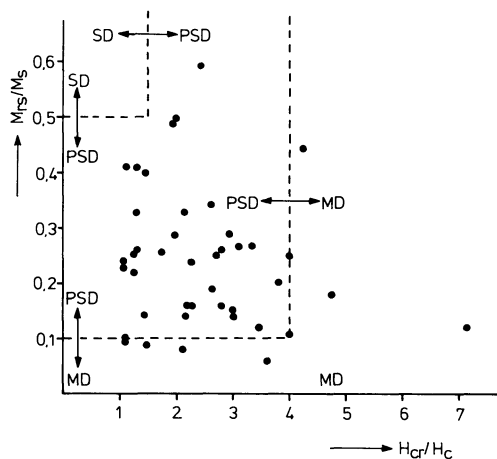


Fig. 4. H_{cr}/H_c plotted against M_{rs}/M_s for selected samples. Different domain configurations for magnetite (Dunlop, 1981) are marked: SD = single-domain, PSD = pseudo-single-domain, MD = multi-domain

er (1953) (Fig. 6). Radial and/or azimuthal observed and theoretical curves clearly diverge. Mathematically, this can be demonstrated using the χ^2 -test (Table 5). The radial or azimuthal, or both theoretical and observed distributions, diverge significantly. The VGPs do not, therefore, follow a Fisherian distribution.

Kristjansson and McDougall (1982), in the most comprehensive compilation of data from Tertiary and Quaternary Icelandic volcanics, also observed a higher than expected percentage of low-latitude VGPs. They combined a Fisherian distribution with $k=8.5$ and a 10% portion of statistically distributed VGPs as a satisfactory approximation of the observed VGP distribution. According to Fig. 6, this radial distribution (dashed line) fits the data

Table 4. Paleomagnetic results. Eruption centre; number n_s/n of samples studied/used for site mean calculation; precision parameters k and α_{95} ; site mean declination/inclination Dec/Inc; VGP latitude/longitude Lat/Long. The lower part of the table comprises mean values calculated for two or more sites

EC	n_s/n	k	α_{95} (°)	Dec (°E)	Inc (°)	Lat (°N)	Long (°E)	
6a	9/ 7	1126	1.7	65.2	73.2	52.8	57.6	
6b	11/11	63	5.8	60.5	73.6	55.3	57.3	
9	10/ 9	170	3.9	58.5	75.9	56.7	51.0	
11	14/14	249	2.5	102.7	73.8	36.4	44.2	
14	22/17	273	2.2	24.4	57.0	68.6	123.1	
20	11/10	196	3.5	47.1	75.3	62.0	53.2	
25	12/12	49	6.2	13.6	78.8	70.6	21.7	
30	13/11	67	5.6	347.8	64.5	80.9	255.9	
32	10/10	72	5.8	19.2	66.6	77.5	95.9	
37	8/ 7	112	5.7	8.7	66.6	84.3	104.8	
41	13/13	500	1.9	94.3	70.7	37.1	52.4	
43	15/14	148	3.3	88.9	71.7	40.4	53.0	
49	11/10	13	14.1	350.9	24.6	51.9	201.1	
50	8/ 7	72	7.1	16.7	61.7	76.4	122.9	
51	11/ 9	200	3.6	5.0	66.1	86.3	122.9	
57	12/12	No stable remanence was determined						
60	13/ 6	84	7.4	101.7	80.2	43.2	33.7	
61	12/12	133	3.8	57.6	73.3	56.7	59.0	
62	13/13	78	4.7	55.7	75.9	58.1	51.3	
72a	11/10	77	5.5	96.4	68.0	33.6	55.2	
72b	11/ 9	133	4.4	96.8	78.0	42.7	38.6	
75	13/11	103	4.5	21.5	66.5	76.1	93.8	
76	11/10	758	1.7	90.1	76.7	43.6	43.1	
80a	11/ 9	61	6.6	347.6	58.7	76.0	230.2	
80b	11/ 7	51	8.5	354.4	58.1	77.8	207.8	
81	13/13	204	2.9	49.6	77.6	60.6	45.3	
86	10/ 9	310	2.9	35.7	54.1	59.8	114.0	
87	12/12	203	3.1	72.1	77.5	51.5	45.0	
90	8/ 6	48	9.8	337.3	67.6	75.5	286.2	
94	9/ 9	473	2.3	51.6	72.0	59.4	63.7	
95a	5/ 5	470	3.5	350.8	86.7	56.8	4.8	
95b	6/ 5	No stable remanence was determined						
95c	8/ 8	256	3.4	42.5	46.3	64.3	56.5	
97a	10/10	367	2.5	58.2	78.8	56.9	41.7	
97b	10/ 9	39	8.3	33.0	63.7	67.4	96.3	
97c	9/ 9	167	3.9	9.3	75.1	77.1	26.6	
99a	15/ 8	76	6.3	45.1	65.2	60.5	84.7	
99b	14/12	102	4.3	18.0	65.3	77.8	103.2	
101	10/10	94	4.3	26.0	76.0	70.7	43.1	
103#	14/11	128	4.1	24.5	62.8	72.4	107.4	
105	16/13	23	8.8	358.1	64.2	85.5	203.8	
117	11/10	35	8.2	79.8	31.0	19.5	93.8	
118	12/12	71	5.1	352.0	88.3	53.5	5.9	
119	12/ 8	28	10.5	24.4	53.5	65.9	129.4	
123a#	12/ 8	23	11.7	38.9	42.4	50.6	122.7	
123b#	11/11	78	5.2	58.4	33.8	34.2	109.2	
129	8/ 8	93	5.7	322.4	56.0	59.8	264.4	
130	10/ 9	222	3.4	244.3	77.4	36.1	339.7	
135	11/11	127	4.0	13.2	63.2	79.5	123.3	
136	12/11	47	6.7	21.7	74.9	73.4	44.8	
138	11/10	52	6.7	12.3	67.2	82.1	93.9	
140	11/10	149	3.9	9.6	71.9	81.2	43.7	
144	11/10	173	3.6	38.1	57.2	60.3	106.7	
147	13/ 7	63	7.6	6.8	64.4	84.0	134.5	
154	13/12	229	2.8	64.4	72.3	53.0	57.4	
155a	32/29	60	3.4	15.9	69.2	79.8	76.0	
155b	10	45	7.1	21.7	62.0	73.6	113.4	
157a	8/ 8	97	5.6	53.9	54.4	48.4	96.9	
157b	9/ 7	96	6.1	60.3	49.7	41.5	96.8	
158	10/10	93	5.0	348.3	51.5	70.1	216.9	
159	9/ 8	265	3.4	109.5	72.4	40.1	32.4	
161	12/11	504	2.0	110.4	80.5	41.1	30.0	

Table 4 (continued)

EC	n_s/n	k	α_{95} (°)	Dec (°E)	Inc (°)	Lat (°N)	Long (°E)
167	11/ 9	151	4.2	340.3	66.8	77.3	280.3
169	28/20	168	2.5	7.9	64.6	83.6	129.1
191	13/13	101	4.1	12.2	69.0	82.0	74.9
170a	13/12	164	3.3	353.1	70.2	84.1	323.6
170b	10/ 9	344	2.7	13.9	66.3	80.8	100.3
176	13/13	305	2.3	105.5	77.1	38.8	37.8
204	12/12	201	3.0	3.4	63.1	84.0	163.0
207a	10/10	719	1.8	357.0	63.0	84.3	209.1
207b	14/12	268	2.6	355.7	55.6	86.3	239.0
208a#	10/10	421	2.3	5.8	66.1	85.8	118.3
208b#	11/ 9	45	7.7	359.9	53.3	73.7	187.2
208c#	14/13	40	6.6	351.5	59.7	78.7	222.2
212	12/12	251	2.7	329.0	69.7	70.6	298.9
213#	10/ 8	146	4.6	338.2	65.0	68.8	280.6
215a#	11/11	432	2.2	333.7	66.2	72.9	281.8
215b#	10/ 9	30	9.4	335.4	59.0	69.8	255.3
215c#	10/ 9	386	2.6	326.0	68.3	68.6	293.7
215d#	Only NRM-measurements available						
220	8/ 7	462	2.8	4.5	63.1	83.6	156.3
221a	9/ 9	398	2.5	13.3	64.2	80.2	116.8
221b	9/ 9	115	4.8	19.5	69.3	77.5	76.3
223	10/ 8	300	3.2	357.4	67.8	88.2	300.3
224	No stable remanence was determined						
6a, b	18	102	3.7	62.4	73.5	54.3	57.5
30, 80a, b	27	59	3.6	349.6	61.0	79.1	231.7
32, 37	17	84	3.9	14.9	66.5	80.3	98.7
41, 43	27	224	1.9	91.6	71.2	38.8	52.8
61, 62	25	98	2.9	56.7	74.7	57.5	55.0
72a, 76	19	241	2.1	93.1	77.3	43.3	44.1
97, 101	18	116	3.2	17.4	75.7	74.2	36.7
99a, b	20	65	3.9	28.7	65.8	71.2	92.5
157a, b	15	90	3.8	57.1	52.2	45.1	97.1
159, 161	19	375	1.6	109.9	80.0	40.7	31.1
169, 170a, b	41	135	1.9	5.6	66.8	86.3	107.2
204, 207a, b,							
208c#	47	98	2.6	356.6	63.7	84.6	213.2
212, 215c#	21	298	1.8	327.7	69.1	69.9	269.3
213#, 215b, c#	28	71	3.3	335.6	63.6	72.9	269.2

of the West Eifel much better and the χ^2 -test shows no significant difference (Table 5), although the azimuthal distribution remains non-Fisherian.

Discussion of low-latitude VGPs

Different processes may have resulted in the anomalous low-latitude pole positions: measuring errors, tectonic rotation and tilting, alteration of oxides, anisotropy of magnetization.

Systematic measuring and/or evaluation errors can be excluded. Sampling, measuring and evaluation were done by different workers (Haverkamp, 1980; Jäger, 1982; Reismann, 1985), giving identical results for different sites of the same eruption centre. Special attention was paid to sites showing low-latitude VGPs using different af-demagnetization techniques: static demagnetization as well as different 2- and 3-axes tumblers. Stepwise thermal demagnetization results of selected specimens fully agree with results from af demagnetization.

Tectonic rotation or tilting of sites is improbable but can not be excluded for individual cases. Nevertheless, for the sites in question this was checked in the field at least twice and no evidence for such tectonic effects was found. Moreover, it is unlikely that all sites could have been displaced accidentally in the same manner, as would be implied by the restriction of their VGPs to a well-defined longitude sector. On the other hand, a common movement of all sites with low-latitude VGPs by regional tectonic processes can be excluded, because these sites are distributed throughout the main part of the volcanic field (cf. Fig. 1 and Table 4), only being absent from the SE part of the field.

We have found no correlation between the oxidation state or occurrence of secondary magnetic minerals, nor the magnetic properties, and the low-latitude of VGPs. Oxidation, maghemitization and/or hydrothermal alteration are thus not responsible for the anomalous pole positions. Likewise, there is no correlation of the rock types sampled (scoria, dikes, etc.) with the VGP latitude. On the other

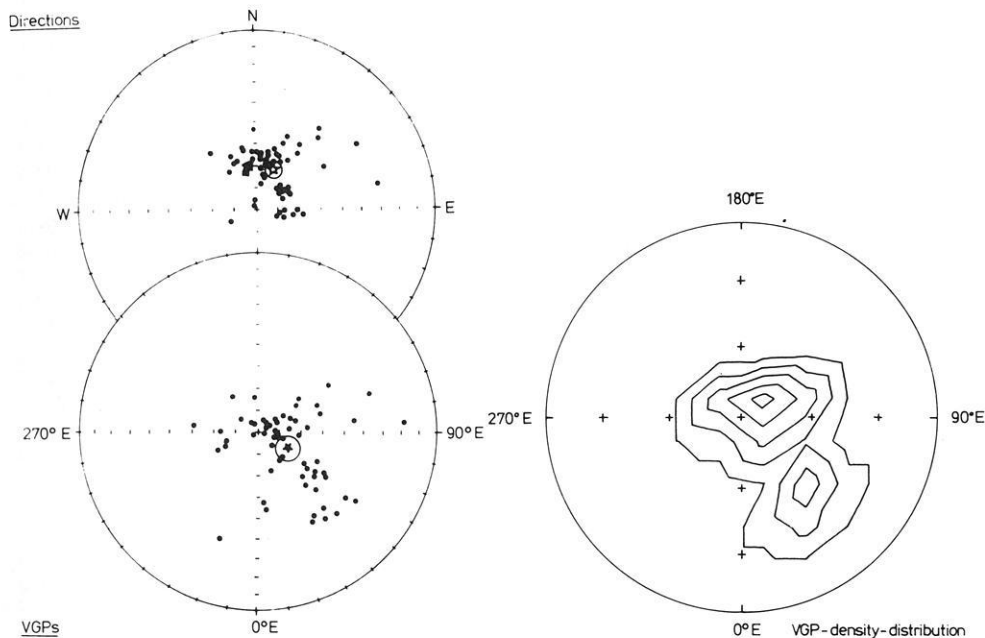


Fig. 5. Site mean directions and VGPs of 64 independent volcanoes. (a) Points directions or VGPs, star mean direction or VGP, with 95% error limit, respectively; arrow dipole field direction. (b) VGP density distribution, lines represent constant number of VGPs per unit area

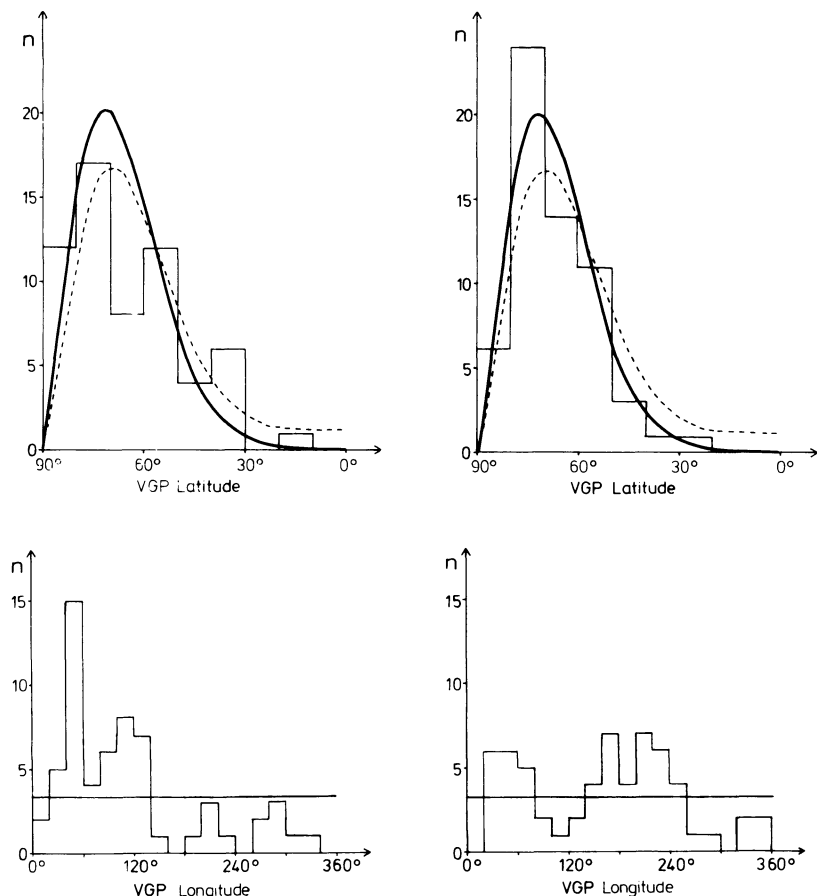


Fig. 6. Theoretical Fisherian distribution (*solid line*) and observed distribution for the West Eifel (*step function*) and the distribution obtained from 2462 Tertiary to Quaternary Icelandic lavas (Kristjansson and McDougall, 1982), relative to the north geographic pole (*left*) and the mean VGP (*right*), respectively. *n*: number of VGPs per latitude increment or longitude segment (this study)

Table 5. Comparison of VGP distributions around the north geographic pole (NGP) and the mean VGP with a Fisherian distribution by means of the χ^2 -test

	Azimuthal distribution		Radial distribution	
	$\chi^2_{\text{obs.}}$	$\chi^2_{95\%}$	$\chi^2_{\text{obs.}}$	$\chi^2_{95\%}$
Mean VGP	45.63	27.59	4.32	14.07
NGP	74.52	27.59	30.85	14.07

hand, there are no volcanoes of the ONB (olivine nephelinite and basanite) group among the anomalous samples. These are restricted to the SE part of the field and are younger than 0.1 M.a. Any magnetic property determined (magnetization intensity, susceptibility, Königsberger factor, medium destructive field, hysteresis parameters) as well as within-site dispersion parameters k and α_{95} show no relation with VGP latitude.

Anisotropy of magnetic susceptibility (AMS) was measured for samples of selected sites exhibiting anomalous pole positions (Table 6). The low values of the precision parameters k and α_{95} indicate that no preferred anisotropy direction (defined by the principal axes of AMS) exists in any of the sites, and therefore no correlation with the respective paleodirections.

We conclude that the observed low-latitude VGPs are not the result of any extraordinary process having changed the original magnetization, nor of anisotropy of magnetism, nor of tectonic processes. Obviously the paleodirections are

Table 6. Anisotropy of magnetic susceptibility. Eruption centre; number of samples measured; site mean direction of principle anisotropy axes; site mean direction and corresponding VGP

No.	Mean principle anisotropy axis					Paleo-direction		Paleo-pole	
	<i>n</i>	<i>k</i>	α_{95} (°)	Dec (°E)	Inc (°)	Dec (°E)	Inc (°)	Lat (°N)	Long (°E)
20	9	2.7	39.3	7.1	50.2	102.7	73.8	36.4	44.2
6	9	3.1	34.8	20.0	19.2	94.3	70.7	31.1	52.4
28	8	1.2	43.5	324.9	39.0	88.9	71.7	40.4	53.0
38	8	5.9	24.8	49.4	36.6	55.7	75.9	58.1	51.3
8	9	2.7	39.5	138.5	5.5	110.4	80.5	41.1	30.0
40	10	1.7	54.5	221.2	-5.6	105.5	77.1	38.8	37.8
46	10	2.6	40.7	258.4	34.8	58.4	33.8	34.2	109.2
67	9	2.9	36.9	138.5	5.5	110.4	80.5	41.1	30.0

reliable and represent real variations of the earth's magnetic field. Finally, a very strong argument for this interpretation is the coincidence of paleodirections from different sites with anomalous pole positions, included in the lower part of Table 4. Many sites are separated by several hundreds of metres and sometimes the rock type differed (scoria, lava flow, dike etc.; cf. Table 1 and Table 4).

The low latitude of many VGPs obtained, together with the restriction of a well-defined longitude sector, rules out the possibility that this could be due to secular variation. More probably, these VGPs represent the earth's magnetic field during excursions or polarity transitions. Kristjansson

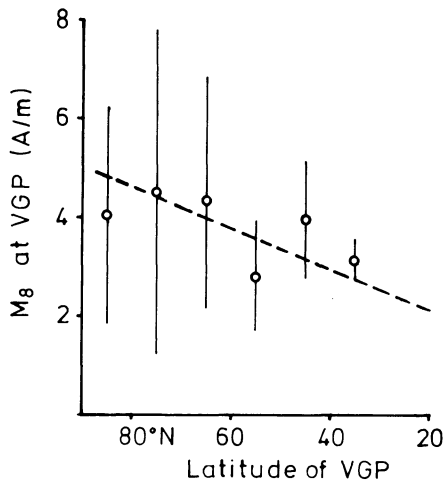


Fig. 7. Arithmetic mean of remanence intensities M_8 (af demagnetized with 8 kA/m) after transformation to virtual geomagnetic pole by 10° increments in VGP latitude. Dashed line represents trend observed for Tertiary to Quaternary Icelandic lavas (Kristjansson and McDougall, 1982)

and McDougall (1982) ascribe the low-latitude VGPs of Icelandic lavas to excursions and polarity transitions. This is supported by the positive correlation of remanence intensity M_8 [magnetization intensity after af demagnetization with 8 kA/m and thus more or less representing the thermoremanence TRM, which linearly depends on the field intensity; see, e.g. Day (1977)] with VGP latitude. Such a correlation is to be expected because of the reduction of the field intensity during polarity transitions or excursions as aborted polarity transitions (Jacobs, 1984).

Arithmetic means of remanence intensities M_8 after af demagnetization with 8 kA/m are given in 10°-latitude increments and compared with the line fitting the data from Iceland (Kristjansson and McDougall, 1982) (Fig. 7). The standard deviation is large for the West Eifel data, which is a result of the comparatively small number of data and the heterogeneity of rock magnetic properties. Nevertheless, a similar trend is recognizable. The low-latitude VGPs observed in the West Eifel probably represent the magnetic field during one of the excursions or events in the Brunhes epoch. According to the age range of the corresponding volcanoes of 0.1–0.4 M.a., four events have to be considered: Blake, Biwa I and II and the Emperor event (Jacobs, 1984). The duration of these events was less than about 0.03 M.a., but the restriction of the VGPs to a small longitude sector seems to imply a much smaller period of volcanic activity. Consequently, if a magnetic excursion is the reason for the anomalous VGPs, this would confine the age of a considerable part of all West Eifel volcanoes to a very small period compared to the total period of volcanic activity. All samples are from volcanoes within the main field, i.e. the F-suite magmas (Schmincke, 1982; Mertes and Schmincke, 1985), none from the SE subfield (i.e. ONB-suite magmas). We thus conclude that eruption of F-type magmas in the main part of the West Eifel field occurred in at least two different phases, one of which is correlated with a period of anomalous low latitudes of magnetic poles. This interpretation raises the question of eruption frequency during the evolution of the entire volcanic field. Recent high-precision dating of basanite volcanoes in the East Eifel has shown that most erupted during a relatively short time

span, ca. 0.2–0.25 M.a. (Bogaard et al., 1986). It would be interesting to study the radiometric ages of the volcanoes with low VGP in detail in order to define the evolution of volcanic periodicity more precisely.

Acknowledgements. This investigation was financially supported by the Deutsche Forschungsgemeinschaft (funds UN 29/24, 29/29-2, 29/29-3). Prof. Dr. H.U. Schmincke would like to thank the Ministerium für Wissenschaft und Forschung, NRW, for general financial support of the Eifel project. It is appreciated that Dr. N. Nun made most of the SEM studies.

References

- Ade-Hall, J.M., Khan, M.A., Dagley, P., Wilson, R.L.: A detailed opaque petrological and magnetic investigation of a single Tertiary lava from Skye, Scotland. Part I and II. *Geophys. J. R. Astron. Soc.* **16**, 374–399, 1968
- Böhhnel, H., Kohnen, H., Negendank, J., Schmincke, H.-U.: Paleomagnetism of Quaternary volcanics of the East-Eifel, Germany. *J. Geophys.* **51**, 29–37, 1982
- Bogaard, P. van den, Hall, C.M., York, D., Schmincke, H.-U.: High precision single grain 40 Ar/39 Ar laser ages from Pleistocene tephra deposits, East Eifel volcanic field, FRG. *Eos* **67**(44), 1248, 1986
- Büchel, G., Lorenz, V.: Zum Alter des Maarvulkanismus der Westeifel. *Neues Jb. Geol. Paläont. Abh.* **163**, 1–22, 1982
- Büchel, G., Mertes, H.: Die Eruptionen des Westeifeler Vulkanfeldes. *Z. Dt. geol. Ges.* **133**, 409–429, 1982
- Collinson, D.W.: *Methods in rock magnetism and palaeomagnetism*. London-New York: Chapman & Hall 1983
- Day, R.: TRM and its variation with grain size. *J. Geomagn. Geoelectr.* **29**, 233–265, 1977
- Day, R., Fuller, M., Schmidt, V.A.: Hysteresis properties of titanomagnetites. Grain-size and compositional dependence. *Phys. Earth Planet. Inter.* **13**, 260–267, 1977
- Duda, A., Schmincke, H.-U.: Polybaric evolution of alkali basalts from the West Eifel: evidence from green-core clinopyroxenes. *Contr. Mineral. Petrol.* **91**, 340–353, 1985
- Dunlop, D.J.: The rock magnetism of fine particles. *Phys. Earth Planet. Inter.* **26**, 1–26, 1981
- Fisher, R.A.: Dispersion on a sphere. *Proc. R. Soc. London A*-**127**, 295–305, 1953
- Haverkamp, U.: Paläomagnetische Untersuchungen an quartären Vulkaniten der Westeifel. Diploma thesis, Inst. Geophys. Münster, 1980
- Hoffman, K.A., Day, R.: Separation of multi-component NRM: a general method. *Earth Planet. Sci. Lett.* **40**, 433–438, 1978
- Illies, H.J., Prohdehl, C., Schmincke, H.-U.: The Quaternary uplift of the Rhenish Shield in Germany. *Tectonophysics* **61**, 197–225, 1979
- Jacobs, J.A.: *Reversals of the earth's magnetic field*. Bristol: Adam Hilger Ltd. 1984
- Jäger, G.: Paläomagnetische Untersuchungen im quartären Vulkanfeld der Westeifel. Diploma thesis, Inst. Geophys. Münster, 1982
- Kirshvink, J.L.: The least-squares line and plane and the analysis of palaeomagnetic data. *Geophys. J.R. Astron. Soc.* **62**, 699–718, 1980
- Kohnen, H., Westkämper, H.: Palaeosecular variation studies of the Brunhes epoch in the volcanic province of the East-Eifel, Germany. *J. Geophys.* **44**, 545–555, 1978
- Kristjansson, J., McDougall, I.: Some aspects of the late Tertiary geomagnetic field in Iceland. *Geophys. J.R. Astron. Soc.* **68**, 273–294, 1982
- Likhite, S.D., Radhakrishnamurty, C., Sasharabudhe, P.W.: Alternating current electromagnetic type hysteresis loop tracer for minerals and rocks. *Rev. Sci. Instr.* **36**, 1558–1560, 1963
- Lippolt, H.J., Fuhrmann, U.: Isotopische Altersbestimmungen an tertiären und quartären Vulkaniten des Rheinischen Schildes.

- DFG Protokoll 5. Kolloquium Schwerpunkt Vertikalbewegungen, Neustadt 1980, 171–176, 1981
- Mertes, H.: Aufbau und Genese des Westeifeler Vulkanfeldes. Bochumer geol. and geotechn. Arb. **9**, Bochum, 1983
- Mertes, H., Schmincke, H.-U.: Age distribution of volcanoes in the West Eifel. *N. Jb. Geol. Paläont. Abh.* **166**, 260–293, 1983
- Mertes, H., Schmincke, H.U.: Mafic potassic lavas of the Quaternary West Eifel volcanic field. I. Major and trace elements. *Contrib. Mineral. Petrol.* **89**, 330–345, 1985
- Molyneux, L.: A complete result magnetometer for measuring the remanent magnetization of rocks. *Geophys. J. R. Astron. Soc.* **24**, 429–433, 1971
- Reismann, N.: Abschließende paläomagnetische Untersuchungen der Verteilung der virtuellen geomagnetischen Pole für das quartäre Vulkanfeld der Westeifel. Diploma thesis, Inst. Geophys. Münster, 1985
- Sachtleben, T., Seck, H.A.: Chemical control on Al-solubility in orthopyroxene and its implications on pyroxene geothermometry. *Contrib. Mineral. Petrol.* **78**, 157–165, 1981
- Schmincke, H.-U.: Vulkane und ihre Wurzeln. Rhein. Westf. Akad. Wiss., Westd. Verl. Opladen, Vortrag N 315, 35–78, 1982
- Schmincke, H.-U., Lorenz, V., Seck, H.A.: The Quaternary Eifel volcanic fields. In: Mode and mechanics of the uplift of the Rhenisch Shield: a case history, K. Fuchs et al., eds.: pp. 139–151. Heidelberg – New York – Tokyo: Springer Verlag 1983
- Stosch, H.G., Seck, H.A.: Geochemistry and mineralogy of two spinel peridotite suites from Dreiser Weiher, West Germany. *Geochim. Cosmochim. Acta* **44**, 457–470, 1980
- Symons, D.T.A., Stupavsky, M.: A rational palaeomagnetic stability index. *J. Geophys. Res.* **79**, 1718–1720, 1974
- Wilson, R., Haggerty, S.E.: Reversals of the earth's magnetic field. *Endeavour* **25**, 103–109, 1966
- Zijderveld, J.D.A.: A.c. demagnetization of rocks: analysis of results. In: *Methods in palaeomagnetism*, D.W. Collinson, K.M. Creer and S.K. Runcorn, eds. Amsterdam: Elsevier 1967

Received March 17, 1987; revised version June 25, 1987

Accepted June 26, 1987

*Short communication***On the stress tensor in Vrancea region****M.C. Oncescu**

Centre of Earth Physics and Seismology, P.O. Box MG-2, Bucharest-Magurele, Romania

Key words: Stress tensor – Vrancea region**Introduction**

Vrancea region (Romania) is a complex tectonic zone characterized by a clustered but intense intermediate-depth seismic activity and by a 'continent-continent-like' collision between three tectonic units (East-European Platform, Moesian Sub-plate and Inter-Alpine Sub-plate) which leads also to moderate-size crustal earthquakes. Both crustal and sub-crustal events present some diversity in focal mechanisms that made early seismotectonic interpretation difficult (Roman, 1970; Ritsema, 1974).

As was shown by McKenzie (1969), if there are pre-existing zones of weakness on which slip can occur, the directions of the principal stresses σ_1 , σ_2 , σ_3 may not be close to the P , B and T axes from focal mechanisms. In such cases, only the direction and sense of resolved shear stress on the fault plane, as indicated by the slip vector, can be used to constrain the stresses. Assuming that the variety of focal mechanisms are consistent with a single regional stress tensor, Gephart and Forsyth (1984) developed a new inverse technique to seek a uniform stress field that predicts directions and senses of slip in agreement with the observations.

The aim of this short note is (1) to present a new application of this attractive method, (2) to point out that in Vrancea region the compression axis acts in a NE–SW direction and not in a SE–NW direction, as is commonly thought from focal mechanism results, and (3) to give additional evidence that the stresses in the crust are decoupled from those in the subducted slab.

Method and data

Gephart and Forsyth (1984) chose to describe the deviatoric part of the model stress tensor by four independent parameters, the directions of the principal stress axes $\sigma_1 < \sigma_2 < \sigma_3$ and the ratio $R = (\sigma_2 - \sigma_1) / (\sigma_3 - \sigma_1)$, thus dealing only with shear-stress directions on the fault planes and neglecting shear-stress magnitudes and hydrostatic stress. This parameterization is particularly useful for data sets for which P and T axes from focal mechanism (principal strain axes) are not well clustered. The ratio R specifies the magnitude of σ_2 relative to σ_1 and σ_3 , and is defined between 0 and 1, both situations describing a bi-axial stress state.

The inversion is performed by a grid search over the three stress directions (characterized by three independent angles) and R , looking for the minimization of the sum of absolute values of the rotation angles about any axis needed to bring the observed and predicted slip direction and senses into coincidence. When the fault plane is not known 'a priori', there are two rotation angles for the two nodal planes. Thus, in performing the inversion, one selects the plane that is more consistent with the stress model. The inversion is performed in two steps: first, the whole stress model space is searched, on a 10° – 15° grid for angles and 0.1 units for R , using an approximate method (the rotation axes were pre-specified to be the poles of the two nodal planes and the null vector); second, the exact method (with the much more time-consuming determination of the minimum rotation axes) was applied in the vicinity of the isolated minima.

The data set consists of two sub-sets: one is formed by 27 intermediate-depth earthquakes (see Table 1) which occurred between 1934 and 1986 with magnitudes in the range $5.0 \leq M \leq 7.4$ (with one exception, and M 4.0 event on May 16, 1982 at about 200 km depth); the other sub-set is formed by 12 crustal events (see Table 2) which occurred between 1959 and 1986 with $4.0 \leq M \leq 5.4$ (with one exception, an M 3.0 event on April 27, 1986 in Vrancea foredeep). The first sub-set consists of fault-plane solutions obtained with a minimum of 20 and an average of 65 P -wave first motion signs (Fig. 1); the solutions of the second sub-set were obtained with a minimum of 15 and an average of 39 signs (Fig. 2). The fault-plane solutions were determined with short-period P -wave first motion signs with good azimuthal coverage using a grid search of all possible orientations of the two nodal planes and finally inspecting the first ten top-score solutions that best separate dilatational from compressional quadrants. The input data were taken from national, international or station bulletins, except for the March 4, 1977 main event whose solution was not re-determined and corresponds to shock E_1 from Räkera and Müller (1982).

Results*Intermediate-depth earthquakes*

After searching the stress model space in two steps, we found the best-fitting model presented in Fig. 3, with relative values of principal stresses $\sigma_1 = -0.67 \sigma_3$ and $\sigma_2 = -$

Table 1. Intermediate-depth earthquakes used in this study. γ is the smallest misfit angle for the two nodal planes, and φ_s and δ are their strike and dip angles, respectively

No.	Date	Origin time	Lat.N (°)	Lon.E (°)	h (km)	M	Nodal planes					Source ^a	No. of P signs	Score (%)
							φ_s (°)	δ (°)	φ_s (°)	δ (°)	$ \gamma $ (°)			
1	340329	20:06	45.8	26.5	90	6.2	200	66	317	45	4	RO'80	33	97
2	400624	09:17	45.9	26.6	115	5.5	220	58	32	32	1	RO'80	27	100
3	401022	06:37	45.8	26.4	122	6.5	223	61	49	30	3	RO'80	57	97
4	401110	01:39	45.8	26.7	133	7.4	224	62	73	31	8	RO'80	58	93
5	450907	15:48	45.9	26.5	75	6.5	224	60	39	30	0	RO'80	30	93
6	451209	06:08	45.7	26.8	80	6.0	134	63	359	36	24	RO'80	24	96
7	480529	04:48	45.8	26.5	140	5.7	196	48	25	42	1	RO'80	33	91
8	550501	21:22	45.5	26.3	135	5.4	103	51	347	61	22	RO'80	28	86
9	600126	20:27	45.8	26.8	140	5.0	155	32	332	58	2	RO'80	53	83
10	601013	02:21	45.7	26.4	160	5.5	163	40	343	50	5	RO'80	47	89
11	630114	18:33	45.7	26.6	133	5.4	146	36	326	54	2	RO'80	54	80
12	650110	02:52	45.8	26.6	120	5.4	348	50	156	41	9	RO'80	54	83
13	661015	06:59	45.6	26.4	140	5.1	134	84	286	7	3	RO'80	39	80
14	730820	15:18	45.7	26.5	73	5.5	262	23	27	80	11	RO'80	49	82
15	731023	10:50	45.7	26.5	170	5.1	117	56	331	39	5	RO'80	34	82
16	740717	05:09	45.8	26.5	145	5.4	216	26	82	72	21	RO'80	55	84
17	761001	17:50	45.7	26.5	146	5.5	169	43	333	48	2	RO'80	85	85
18	770304	19:21	45.8	26.8	93	5.0	275	78	78	12	8	RO'80	61	87
19	770304	19:26	45.8	26.8	93	7.2	238	76	8	21	10	RM'82	78	99
20	781002	20:28	45.7	26.7	140	5.3	131	34	316	56	5	RO'80	108	85
21	790531	07:28	45.6	26.4	120	5.4	233	80	124	27	5	RO'80	89	83
22	790911	15:36	45.6	26.5	158	5.4	210	13	12	77	2	RO'80	100	87
23	810718	00:03	45.7	26.4	146	5.3	184	46	92	88	15	RCO'81	106	78
24	820516	04:03	45.4	26.4	201	4.0	206	81	298	75	15	RO'82	20	82
25	830125	07:34	45.7	26.7	156	5.3	84	50	323	58	18	This paper	72	86
26	850801	14:35	45.8	26.5	107	5.3	200	76	298	61	0	OA'85	86	86
27	860830	21:28	45.5	26.5	134	6.8	235	65	73	24	5	RO'87	232	87

^a *RO'80* Radu and Oncescu (1980); *RM'82* Räckers and Müller (1982); *RCO'81* Radu et al. (1981); *RO'82* Radu and Oncescu (1982); *OA'85* Oncescu and Apolozan (1985); *RO'87* Radu and Oncescu (1987)

Table 2. Crustal earthquakes used in this study. γ is the smallest misfit angle for the two nodal planes, and φ_s and δ are their strike and dip angles, respectively

No.	Date	Origin time	Lat.N (°)	Lon.E (°)	h (km)	M	Nodal planes					Source ^a	No. of P signs	Score (%)
							φ_s (°)	δ (°)	φ_s (°)	δ (°)	$ \gamma $ (°)			
1	590531	12:15	45.7	27.2	35	5.2	40	17	149	84	24	RO'80	41	88
2	600104	12:21	44.6	27.0	41	5.4	138	40	271	60	18	RO'80	35	74
3	690418	20:38	45.3	25.1	10	5.2	137	83	231	60	14	RO'80	38	79
4	750208	08:21	45.1	26.0	23	4.7	144	74	48	70	12	RO'80	20	80
5	750307	04:13	45.9	26.6	21	5.1	237	83	143	60	3	RO'80	39	77
6	770305	00:00	45.3	27.1	10	4.3	106	86	13	53	2	RO'80	20	88
7	800911	23:24	45.4	28.2	15	4.7	282	89	12	90	8	RO'80	45	76
8	801208	19:51	44.4	27.2	15	4.0	331	89	240	45	1	RCO'81	23	96
9	811113	09:07	45.2	29.0	10	5.2	314	57	171	39	4	RCO'81	81	73
10	830221	18:03	45.3	27.1	19	4.5	234	63	18	32	2	OA'84	20	95
11	860427	00:04	45.5	27.1	26	5.0	226	44	30	47	2	OT'87	95	90
12	860427	00:47	45.5	27.1	19	3.0	294	62	159	37	10	OT'87	15	93

^a *RO'80* Radu and Oncescu (1980); *RCO'81* Radu et al. (1981); *OA'84* Oncescu and Apolozan (1984); *OT'87* Oncescu and Trifu (1987a)

$0.33 \sigma_3$ ($\sigma_2 = 0.5 \sigma_1$). This model has an average misfit (absolute value of rotation angle about any axis) of 7.7° with a 95% confidence limit of 11.6° . If the three events that do not fit the model (with misfits greater than 20° and marked with a rectangle in Fig. 1) are removed, the average misfit is reduced to 5.3° . Of the other 24 events, 5 have misfits between 10° and 20° and the remaining 19 fit the stress model within a few degrees. Errors of only several

degrees are less than the uncertainty of the focal mechanism determinations, which in this case are estimated to be of the order of 10° .

Crustal events

Again, after searching the stress model space in two steps, we found the best-fitting model presented in Fig. 4, with

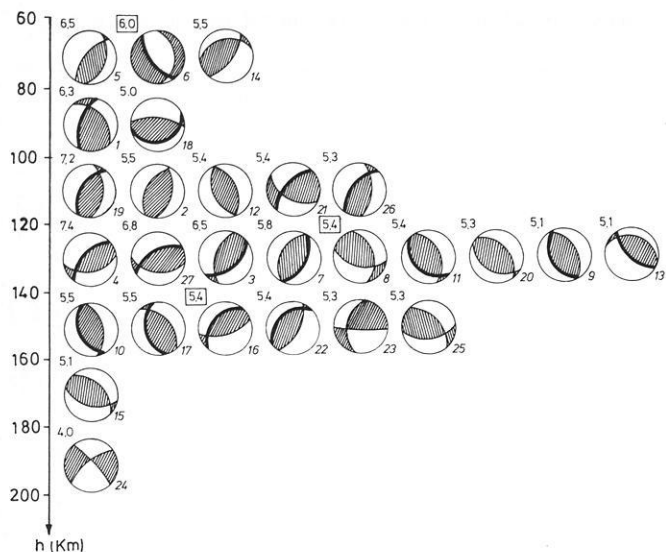


Fig. 1. Stereographic projections of the lower hemisphere of fault-plane solutions for 27 intermediate-depth earthquakes. Magnitudes are indicated near each solution, as well as the corresponding sequence numbers from Table 1. Within each depth interval the earthquakes are ordered with decreasing magnitude; the *first column* may be regarded as a variation of maximum magnitude with depth. *Thick curves* denote identified fault planes (see text)

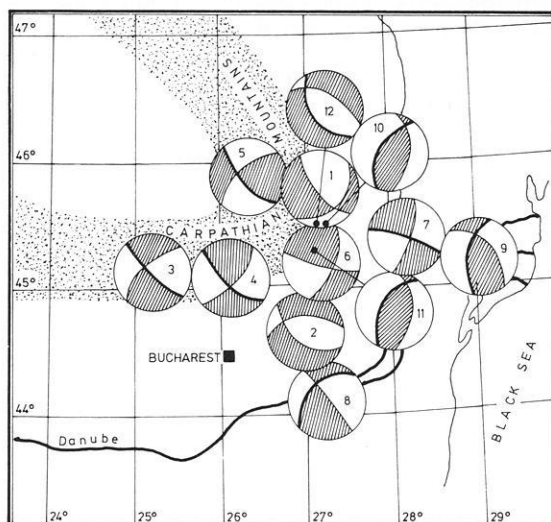


Fig. 2. Stereographic projections of the lower hemisphere of fault-plane solutions for 12 crustal earthquakes. The projections are centred on the epicentres, except where otherwise indicated. *Thick curves* denote identified fault planes (see text). *Numbers* correspond to those from Table 2

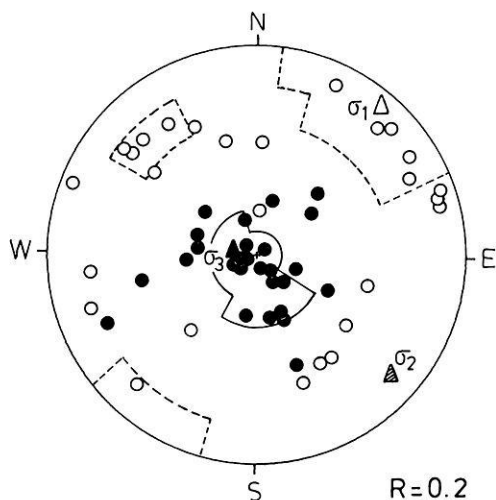


Fig. 3. Principal stress axes (*triangles*), individual *P* axes (*open circles*) and *T* axes (*full circles*) for Vrancea intermediate-depth region. Stereographic projections of the lower hemisphere are used. *Contours* indicate 95% confidence regions for σ_1 (*dotted line*) and σ_3 (*solid line*) axes

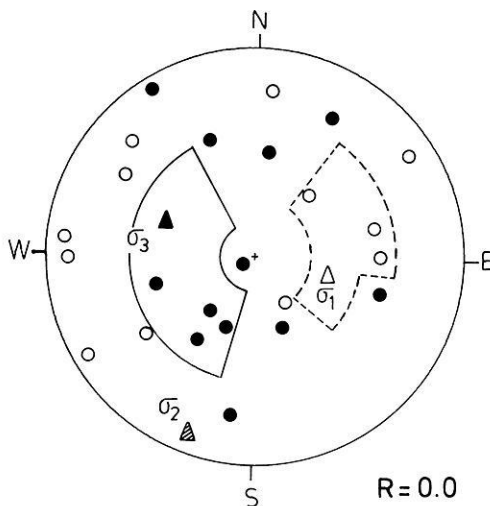


Fig. 4. Same as Fig. 3, but for crustal earthquakes

relative values of principal stresses $\sigma_1 = \sigma_2 = -0.5 \sigma_3$. This model has an average misfit of 8.4° with a 95% confidence limit of 17.9° . One event has a misfit greater than 20° ; if this one is removed, the average misfit is reduced to 6.3° . Of the remaining 11 events, three have misfits between 10° and 20° . The uncertainty of focal mechanism determinations for these crustal events is estimated to be about 15° – 20° , so that the fit seems reasonably good.

Discussion

On the basis of this analysis we arrive at the following interpretation concerning the intermediate-depth seismic re-

gion. (1) the minimum compression axis (σ_3) acts vertically, as was observed by all previous investigators. (2) The maximum compression axis (σ_1) acts in a NE–SW direction, the direction of the paleo-subduction in Eastern Carpathians, as was pointed out by Bleahu et al. (1973) from volcanological data and by Oncescu et al. (1984) from seismological data. (3) The intermediate stress axis (σ_2) has also a negative sign and acts in a SE–NW direction, the direction of *P* axes of all strong and most moderate earthquakes; it follows that there are pre-existing planes of weakness on which at least strong and moderate events occur, as suggested by Constantinescu and Enescu (1984). On the other hand, small events with the same orientation of the principal strain axes tend to have high values of fracture energy per unit area of the fault (Oncescu, 1986), a feature generally associated with fresh fracture of rocks. The pattern is not very far from a bi-axial state of stress, as was

first observed by Oncescu and Trifu (1987b) from a statistical analysis of principal strain axes of 120 small earthquakes. A cause of compression along the σ_2 axis (SE–NW) could be the advancement of the Black Sea or Moesian platelet. (4) There is no strong requirement that the stresses are heterogeneous; the few events that do not fit the model are of moderate magnitudes and scattered in space. Following Gephart (1985), we tried to discriminate between the two nodal planes exploiting the fact that the null (B) axes from focal mechanisms are generally not parallel to the σ_2 axis. The choice was made only when the differences in misfits were greater than 10° . For two events, the identified fault planes are coincident with those independently determined by Müller et al. (1978) for the March 4, 1977 $M7.2$ earthquake and by Trifu and Oncescu (1987) for the August 30, 1986 $M6.8$ earthquake. These two cases give significance to the other fault-plane identifications, so that one can conclude that (5) when the nodal planes strike NE–SW the rupture plane is that one dipping toward NW, and when the nodal planes strike NW–SE the rupture planes plane is that one dipping toward SW (with two exceptions, the $M6.5$ and $M5.8$ events between 120 and 140 km depth).

As to the crustal earthquakes, we obtained that: (1) the most vertical principal stress is the maximum compression (σ_1) axis. (2) The intermediate stress axis (σ_2) equals the σ_1 axis in magnitude (a pure bi-axial stress state), so that their orientation is difficult to determine. Moreover, it is in this situation that the greatest diversity in nodal plane orientations is observed (Harmsen and Rogers, 1986), a feature that can be noticed from Fig. 2. (3) The stress tensor within the crust appears to be quite homogeneous. (4) The clear difference between the stress tensor within the crust and the stress tensor in the intermediate-depth region supports the hypothesis of the existence of a gravitationally sinking slab now decoupled from the crust. Again, following Gephart (1985) and observing that B axes from focal mechanisms are generally not coplanar with the equal principal stress axes, we tried to identify the rupture plane in cases where the differences in misfits were greater than 10° . In all five cases where the fault plane was known independently (although not introduced specifically in the stress inversion), the agreement was perfect.

In conclusion, although this method does not take into consideration stress magnitudes, many interesting new results were obtained (and old results confirmed or proved) about the stress tensor in Vrancea region, which on the basis of P , B , T axes alone could not be inferred, at least not so elegantly and straightforwardly.

Acknowledgements. I thank J.W. Gephart for permitting the use of his stress inversion programs. I thank G. Müller for carefully reading the manuscript and for valuable remarks which helped to improve this paper.

References

- Bleahu, M.D., Boccaletti, M., Manetti, P., Peltz, S.: Neogene Carpathian Arc: a continental arc displaying the features of an 'Island Arc'. *J. Geophys. Res.* **78**, 5025–5032, 1973
- Constantinescu, L., Enescu, D.: A tentative approach to possibly explaining the occurrence of the Vrancea earthquakes. *Rev. Roum. Géol. Géophys. Géogr. Géophys.* **28**, 19–32, 1984
- Gephart, J.W.: Principal stress directions and the ambiguity in fault plane identification from focal mechanisms. *Bull. Seismol. Soc. Am.* **75**, 621–625, 1985
- Gephart, J.W., Forsyth, D.W.: An improved method for determining the regional stress tensor using earthquake focal mechanism data: application to the San Fernando earthquake sequence. *J. Geophys. Res.* **89**, 9305–9320, 1984
- Harmsen, S.C., Rogers, A.M.: Inferences about the local stress field from focal mechanisms: application to earthquakes in the Southern Great Basin of Nevada. *Bull. Seismol. Soc. Am.* **76**, 1560–1572, 1986
- McKenzie, D.P.: The relation between fault plane solutions for earthquakes and the directions of principal stresses. *Bull. Seismol. Soc. Am.* **59**, 591–601, 1969
- Müller, G., Bonjer, K.P., Stöckl, H., Enescu, D.: The Romanian earthquake of March 4, 1977. I Rupture process inferred from fault plane solution and multiple-event analysis. *J. Geophys.* **44**, 203–218, 1978
- Oncescu, M.C.: Relative seismic moment tensor determination for Vrancea intermediate depth earthquakes. *Pure Appl. Geophys.* **124**, 931–940, 1986
- Oncescu, M.C., Apolozan, L.: The earthquake sequence of Rîmnicu Sărat, Romania, of 21–22 February 1983. *Acta Geophys Pol* **32**, 231–238, 1984
- Oncescu, M.C., Apolozan, L.: The seismic doublet from Vrancea region of August 1, 1985 (in Romanian). *Stud. Cerc. Geol. Geofiz. Geogr. Geofiz.* **24**, 12–16, 1985
- Oncescu, M.C., Trifu, C.I.: A large seismic sequence on April 27–29, 1986 in Vrancea foredeep. *Rev. Roum. Géol. Géophys. Géogr. Géophys.* **31**, 1987a (in press)
- Oncescu, M.C., Trifu, C.I.: Depth variation of moment tensor principal axes in Vrancea (Romania) seismic region. *Ann. Géophys.* **5B**, 149–154, 1987b
- Oncescu, M.C., Burlacu, V., Anghel, M., Smalberger, V.: Three-dimensional P-wave velocity image under the Carpathian Arc. *Tectonophysics* **106**, 305–319, 1984
- Radu, C., Oncescu, M.C.: Focal mechanism of Romanian earthquakes and their correlation with tectonics. I. Catalogue of fault plane solutions (in Romanian). Report CFPS/CSEN 30.78.1, 1980
- Radu, C., Oncescu, M.C.: A note on the deep Vrancea earthquake of May 16, 1982 (in Romanian). Report CFPS/CSEN 30.81.8, 1982
- Radu, C., Oncescu, M.C.: Focal process of August 30, 1986 Vrancea earthquake (in Romanian). Report CFPS/CSEN 30.86.3, 1987
- Radu, C., Crişan, E., Oncescu, M.C.: Fault plane solutions of Romanian earthquakes occurred in 1981 (in Romanian). Report CFPS/CSEN 30.81.8, 1981
- Räkers, E., Müller, G.: The Romanian earthquake of March 4, 1977. III. Improved focal model and moment determination. *J. Geophys.* **50**, 143–150, 1982
- Ritsema, A.R.: The earthquake mechanisms of the Balkan region. UNDP Project REM/70/172, UNESCO, 1974
- Roman, C.: Seismicity in Romania – evidence for the sinking lithosphere. *Nature* **228**, 1176–1178, 1970
- Trifu, C.I., Oncescu, M.C.: Fault geometry of August 30, 1986 Vrancea earthquake. *Ann. Géophys.* **6B**, 1987 (in press)

Received April 6, 1987; revised version July 8, 1987

Accepted August 3, 1987

*In memoriam***Erich Mundry (1933–1986)**

Am 20. Oktober 1986 verstarb nach schwerer Krankheit Dr. Erich Mundry, Direktor und Professor beim Niedersächsischen Landesamt für Bodenforschung, im Alter von 52 Jahren. Mit ihm ist ein angesehener Wissenschaftler von uns gegangen, dessen Name verbunden bleibt mit bedeutenden Beiträgen zur Theorie der Geoelektrik und Geothermik. Das Haus BGR/NLFB verdankt ihm wichtige Impulse für die Nutzung der automatischen Datenverarbeitung zur Lösung spezifisch geologischer Aufgaben. Auch um den Aufbau des Rechenzentrums von den Anfängen an hat er sich sehr verdient gemacht.

Erich Mundry wurde am 26. Dezember 1933 als Sohn des Landarbeiters Otto Mundry in Gut Detzel bei Haldensleben geboren. Von 1940 bis 1948 besuchte er die Grundschule Satuelle, anschließend die Oberschule Haldensleben, wo er 1952 die Reifeprüfung ablegte. Im gleichen Jahr begann er das Mathematikstudium an der Humboldt-Universität zu Berlin und legte dort 1957 die Diplomprüfung ab; das Thema der Diplomarbeit lautete: „Charakteristikenverfahren bei eindimensionalen, instationären Gasströmungen“.

Im Oktober 1957 nahm er die Tätigkeit als Mathematiker im VEB Entwicklungsbau Pirna auf. Hier arbeitete er an der Berechnung thermodynamischer Vorgänge in Düsenaggregaten für Verkehrsflugzeuge, an Regelungsaufgaben und an der Programmierung für einen Digitalrechner (ZRA 1). Er nutzte jede Gelegenheit, um sich in der Kenntnis von Analog- und Digitalrechnern weiterzubilden.

Seit dem Spätherbst 1960 ist sein weiterer beruflicher Werdegang mit dem Haus BGR/NLFB verknüpft. Bald wurde seine hohe wissenschaftliche Qualifikation deutlich. Die Computertechnik, damals in den Anfängen, gab ihm das Hilfsmittel, in kurzer Zeit wichtige anstehende mathematische Probleme zunächst in der Geothermik, dann auf fast allen Gebieten der Geophysik erfolgreich zu lösen. Die Dissertation an der Bergakademie Clausthal mit dem Thema „Zur Berechnung der Gebirgstemperatur bei der Grubenbewetterung mit Anwendung zur Vorausbestimmung von Bohrlochtemperaturen“ entstand dabei sozusagen als Nebenprodukt.

Er übernahm das neue, noch bescheiden eingerichtete Rechenzentrum von BGR/NLFB und wurde 1964 Leiter des Referates Theorie und Mathematik. Unter seinen Händen wurde das Rechenzentrum zu einem freundlichen Servicebetrieb, in dem Hilfesuchende bis spät in die Nacht oder am Wochenende Rat fanden. Schon bald hat er in enger Zusammenarbeit mit den Kollegen der geologischen Kartierung ein Programmsystem zur Dokumentation und Abfrage von Schichtenverzeichnissen konzipiert und realisiert. Diese Zusammenarbeit und ihre Ergebnisse bildeten sozusagen den Nucleus für den heute sehr ausgedehnten Einsatz der automatischen Datenverarbeitung in praktisch allen Bereichen der Geologie im NLFB und in der BGR.

In jenen Anfangsjahren war so etwas keineswegs selbstverständlich. Der Geologe alten Schlages konnte sich nicht vorstellen, daß Computer in seinem Fach nützlich sein könnten. Hier haben Erich Mundrys nüchterne Freundlichkeit und schnelle Auffassungsgabe das Vertrauen geschaffen, das für diese Arbeit unerlässlich war. Einen ersten Niederschlag seiner Aktivität in der Beratung von Geowissenschaftlern außerhalb der Geophysik stellt der Artikel „Mathematische Verfahren in der Geologie, Einsatz von Rechenautomaten“ (In: Lehrbuch der Angew. Geologie, II/2: 1884–1944, von A. Bentz, 1969) dar.

Schon früh hat er sich der Geoelektrik zugewandt. Hier hat er u.a. für das Gleichstromverfahren das Problem der von der Parallelschichtung abweichenden Konfiguration im Untergrund aufgegriffen und eine wichtige Gruppe von

Spezialfällen gelöst. Desgleichen hat er sich mit der Theorie der Wechselstrommethoden befaßt. Für beide Problemkreise, die bisher wegen der großen mathematischen Schwierigkeiten nur sehr unzureichend behandelt worden waren, stellten seine Lösungen deutliche Fortschritte dar.

1977 wurde ihm die Aufgabe übertragen, das personell starke Referat Geoelektrik in den Geowissenschaftlichen Gemeinschaftsaufgaben beim NLFb zu leiten. Schon in den ersten Jahren gelangen ihm hier wesentliche Fortschritte: Er trug entscheidend zur Lösung des Umkehr-Problems der Gleichstromsondierungen bei, d.h. zur Möglichkeit, aus geoelektrischen Meßdaten direkt die Schichtung im Untergrund zu bestimmen. Ihm verdanken wir die von vielen Wissenschaftlern gewünschte Neuerstellung eines umfangreichen Kurvenatlasses für die Widerstandsmethode.

Sein Interesse galt dann der Interpretation von Gleichstrommessungen über komplizierterem Untergrund. Er gab außerordentlich wichtige Impulse sowohl zur theoretischen Behandlung von zwei- und dreidimensionalen Problemen als auch zur praktischen Verbesserung der Meßwerterfassung. Der Einsatz von digitalen Meßgeräten und Kleinrechnern im Gelände wurde bald zur Routine.

In den letzten Jahren griff er die frequenzelektromagnetische Methode auf. Schon nach kurzer Zeit standen die grundlegenden Lösungswege als Rechenprogrammssystem zur Verfügung und konnten am Ergebnis von Geländemessungen erprobt werden. In konsequenter Weiterentwicklung bemühte er sich, trotz seiner Krankheit, die ihn immer stärker belastete, um die simultane Interpretation von Gleichstrom- und Wechselstrommessungen. Auch dabei

zeichneten sich bereits entscheidende Erfolge ab, als die Krankheit ihn zwang, die Arbeit abzubrechen.

Er hinterließ eine umfangreiche Programmbibliothek und 40 Veröffentlichungen, darunter mehrere Beiträge zu Lehrbüchern. Seine Texte und theoretischen Entwicklungen hatten die Eleganz der Klarheit und der geistigen Disziplin. Außer dem oben schon genannten Beitrag gibt es vier größere Darstellungen, die er z.T. mit Koautoren verfaßte: „Gleichstromverfahren“ und „Mathematische Verfahren in den Geowissenschaften“ (im Lehrbuch „Angewandte Geowissenschaften, II, von F. Bender 1985) und „Elektromagnetische Verfahren“ und „Das Umkehrproblem der Geoelektrik“ (im Lehrbuch „Die Wassererschließung“ von H. Schneider 1987). Die gesamten Titel seiner Veröffentlichungen sind im Geologischen Jahrbuch (Mitt. 7) publiziert.

Den Menschen Mundry hat jedoch kaum einer gekannt. Am 29. März 1958 heiratete er Hanneliese Erbuschewski. Er schloß seine Privatsphäre vor jedermann ab, verstand seine Gefühle zu verbergen, seine Probleme für sich zu behalten und sein Leiden allein zu tragen. Wenn er im Frühstadium seiner schweren Krankheit von dieser gewußt haben sollte, hat er doch niemanden damit belastet. Er lebte bescheiden und unterstützte seine Freunde im Osten, denen er weiterhin verbunden war. Selbst im Kreise seiner Kollegen blieb er solange zurückhaltend, bis es sachliche Dinge zu analysieren oder für die Gerechtigkeit zu plädieren galt. Auch verstand er es, sich mit Zähigkeit für eine Sache einzusetzen. Seine Leistungen erbrachte er schlicht, bescheiden und selbstverständlich.

J. Homilius

Book Review

Yang Zunyi, Cheng Yugi and Wang Hongzhen: The Geology of China. – Oxford Monographs on Geology and Geophysics, 303 p, 1986

China is a large country, therefore a book with this title and only 303 pages raises certain expectations. The first glance at this volume reveals the intention of the authors: the detailed and complete geological description is not the goal; after the publication of 'The Geology of China' by the late Professor Li Siguang in the year 1939, the authors now want to provide the second attempt at introducing this subject to foreign readers.

Thus, the text is arranged into four parts:

I Background

The development of Chinese geology and mining is reviewed.

II Stratigraphy

After the introduction of the stratigraphic provinces of China and their classification and terminology there follows a brief summary of the stratigraphic development during the geological eras. Thereafter, the main part of the text covers the description of all geological periods with regard to the different regions of China.

III Magmatic and metamorphic rocks in China

Here, the distribution of magmatic rocks and magmatism is given, as well as of metamorphic series and metamorphic belts.

IV Geotectonic development of China

The tectonic framework and the geotectonic units are described as well as their development. Principal tectonic domains and correlations are discussed.

The volume is completed by a comprehensive appendix: abbreviations of isotopic dating institutions including 19 plates with selected samples of prehistoric tools, proterozoic stromatolites, microplants and algae, as well as fossils from all geological periods, and microscopic views of thin sections of rock samples are given. Then selected references are added, and a stratigraphic index written in English and Chinese. Names are spelt throughout the volume according to the Pinyin system.

The text and the carefully drawn pictures and tables, as well as the photographs, are printed very well. Thus, the book provides not only an overview on the geology of China but also much detailed information. Especially in our time, when more and more western geoscientists use the chances to visit this exciting country, this book must be recommended as a handy guide to Chinese geology.

G. Jentzsch

Results of the DEKORP 4/KTB Oberpfalz deep seismic reflection investigations

DEKORP Research Group

Contributors: R.K. Bortfeld, F. Keller, B. Sieron, W. Söllner, M. Stiller, R. Thomas (DEKORP Processing Center, Institut für Geophysik, Arnold-Sommerfeld-Str. 1, 3392 Clausthal-Zellerfeld); W. Franke (Institut für Geowissenschaften, Senckenbergstr. 3, 6300 Gießen); K. Weber, A. Vollbrecht, T. Heinrichs (Institut für Geologie und Dynamik der Lithosphäre, Goldschmidtstr. 3, 3400 Göttingen); H.-J. Dürbaum, C. Reichert, J. Schmoll (Bundesanstalt für Geowissenschaften und Rohstoffe/Niedersächsisches Landesamt für Bodenforschung, Stilleweg 2, 3000 Hannover 51); G. Dohr (Preussag AG, Arndtstr. 1, 3000 Hannover 1); R. Meissner, R. Bittner (Institut für Geophysik, Olshausenstr. 40–60, 2300 Kiel 1); H. Gebrande, M. Bopp, P. Neurieder, T. Schmidt (Institut für Allgemeine und Angewandte Geophysik, Theresienstr. 41/IV, 8000 München 2)

Abstract. In the Oberpfalz-Oberfranken area (NE Bavaria) deep seismic reflection investigations were jointly carried out in 1985 for two important geo-scientific programmes: DEKORP and KTB. The network of lines consists of one long DEKORP profile, DEKORP 4/4-Q, and six shorter KTB profiles arranged parallel and perpendicular to the main tectonic lineaments, focussing on the suture between the Saxothuringian and Moldanubian units of the Mid-European Variscides. The Vibroseis method was used throughout the whole reflection survey. In addition, wide-angle observations and two expanding spreads were observed by using explosives. The processing was carried out by the DEKORP Processing Center (DPC) at the Technische Universität Clausthal and, additionally, by various contractors. Standard software was used, and with painstaking diligence yielded remarkable quality results despite the complicated structure of the subsurface. The handling of special problems met within the processing is explained, e.g. offset-restricted velocity analysis, offset-dependent stacking etc.. The results show a very heterogeneous crust with strong reflections distributed over almost the entire crust from surface to Moho level at about 30 km depth. Reflections dipping SE prevail in the middle and lower crust; a thin layer of remarkably high velocity is observed in the central part of DEKORP 4. The complex structure is preliminarily interpreted by a relatively simple model, essentially based on underthrusting of Saxothuringian units under Moldanubian units in the area of Erbdorf. The compressional tectonics has generated wedge-type structures of which the so-called Erbdorf body is of special interest. Moreover, the seismic results clearly show the

nappe character of the Münchberger Gneismasse and of the zone of Erbdorf-Vohenstrauß.

Key words: Deep seismic reflection profiling – KTB – Wide-angle reflection profiling – Crustal structure – Wedging – Mid-European Variscides – Moldanubian – Saxothuringian – Erbdorf body

1 Geological aims, planning, field investigations

1.1 Purpose of the investigations; geological situation

The seismic lines discussed in this paper explore a central part of the Variscan Belt of Europe. This belt is more than 1000 km wide and can be subdivided – in the Central European segment – into several zones, which were first recognized by Kossmat (1927). The validity of this zonal scheme has been confirmed by all modern investigations. The zonal boundaries are now regarded as sutures which originated from the closure of several Palaeozoic basins. The opening of most of these basins is essentially related to the break-up of Gondwana during an important rifting episode in Cambrian and Ordovician time. The resulting microcontinental blocks bear witness to a pan-African/Cadomian orogenic event. These microplates (or terranes) were then caught up, during the Devonian and Carboniferous, in the collision between Gondwana and Baltica, which has produced the Variscan Foldbelt. Summaries of this development are available in Weber and Behr (1983), Behr et al. (1984), Franke (1986), Matte (1986a, b), Weber (1986) and Ziegler (1984).

DEKORP lines 4 and 4-Q, as well as the closely related KTB lines 8501–8506, were intended to scan the border zone between the Moldanubian Zone and the northward adjacent Saxothuringian Zone (Fig. 1). The Saxothuringian (ST) represents the infill of a Cambro-Ordovician basin which opened beyond the rift stage at least into a narrow ocean, and the Moldanubian (MN) contains blocks of pre-Variscan crust (and their Palaeozoic cover) which were re-activated by the Variscan orogeny and thrust toward the NW over the Saxothuringian foreland. Tectonic deformation and co-related metamorphism are polyphase and have produced a highly complex crustal structure.

Offprint requests to: C. Reichert

Abbreviations: DEKORP Deutsches Kontinentales Reflexionsseismisches Programm; DPC DEKORP Processing Center; KTB Kontinentales Tiefbohrprogramm der Bundesrepublik Deutschland; EB Erbdorf body; FL Franconian Line; LL Luhe Line; MM Münchberg Massif; MN Moldanubian; ST Saxothuringian; ZEV zone of Erbdorf-Vohenstrauß; ZTM zone of Tirschenreuth-Mähring; ZTT zone of Tepla-Taus; A antiformal; S synform; LP low pressure; MP medium pressure; DMO dip move-out; NMO normal move-out; CSP common-shotpoint gather; CMP common-midpoint gather; TWT two-way travel time; COF common-offset gather; LVZ low-velocity zone

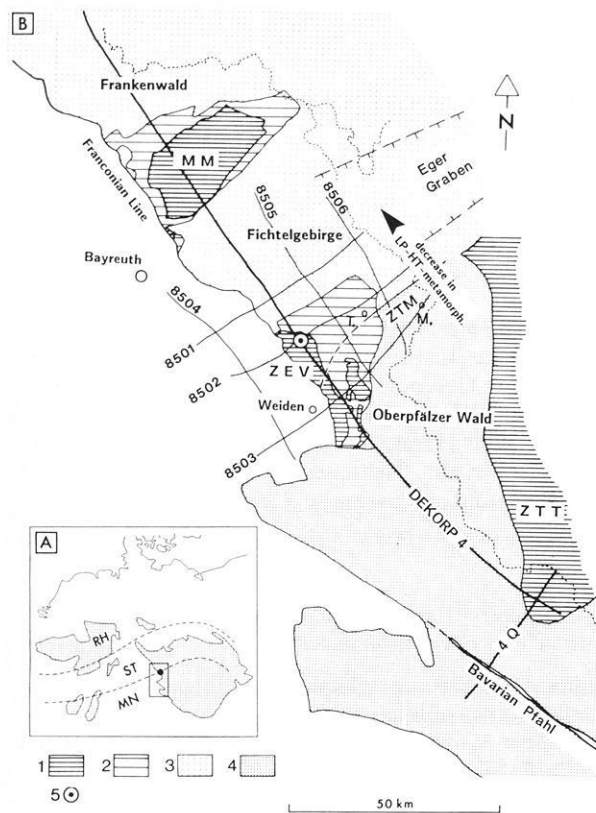


Fig. 1. Geological sketch map of NE Bavaria with the DEKORP-KTB seismic network indicated. **A.** Variscan basement outcrops in Middle Europe with zones after Kossmat (1927). *RH* = Rhenohercynian; *ST* = Saxothuringian; *MN* = Moldanubian. *Inset*: study area with deep drilling site (KTB). **B.** Geological map with main tectonometamorphic units and deep reflection seismic network. 1 = MP metamorphic nappes; 2 = lower nappes; 3 = Saxothuringian; 4 = Moldanubian; 5 = KTB deep drilling site. Late- to post-Variscan granites are not shown. Reflection seismic network: *heavy lines* = DEKORP; *thin lines* = KTB; *T.* = Tirschenreuth; *M.* = Mähring; *MM*, *ZEV*, *ZTM*, *ZTT* – see list of abbreviations

Saxothuringian (*ST*) zone

Most of the *ST* is made up of Precambrian(?) through Lower-Carboniferous sedimentary and volcanic rocks in a conspicuous “Thuringian” facies. Neritic clastics of the Cambrian and Ordovician were probably derived from sources to the NW and, during the Carboniferous, from a tectonic uplift to the SE. A further source area was active, in Givetian and Frasnian time, within the Thuringian basin. Coarse conglomerates are arranged along strike along a line that links areas to the NW of the Münchberg Klippe with the basement uplift of the Saxonian Granulitgebirge, approx. 100 km farther to the NE. This setting suggests an intra-basinal tectonic high along the Granulitgebirge axis.

The key to the tectonic structure of the *ST* and *MN* zones lies in a number of medium- to high-grade terranes, set within a major synform (Vogtländische Mulde), where they are in strange contrast with the surrounding sedimentary rocks. These are the metamorphic “Zwischengebirge” of Münchberg, Wildenfels and Frankenberg (the latter two on GDR territory). The metamorphic blocks have alternatively been interpreted as diapir-like uplifts of basement rocks, or as tectonic klippen derived from the *MN* zone. Recent structural, sedimentological and geophysical studies

in the Münchberg area have shown that the metamorphic blocks are truly allochthonous (Behr et al., 1982; Franke, 1984a, b; Haak and Blümecke, 1985).

The Münchberg Massif (*MM*) comprises the widest lithological spectrum of the “Zwischengebirge” named above. It represents a tectonic pile, in which both the metamorphic grades and the stratigraphic sequence appear in an inverted order (listed here from top to bottom):

1. Gneisses and amphibolites (medium-pressure metamorphism, with kyanite), and some lenses of high-pressure eclogite

2. Epidote-amphibolite

3. Greenschist-grade phyllites and basaltic volcanics

4. Very low-grade sedimentary and volcanic rocks of a conspicuous “Bavarian” facies (the Bavarian sequence, with respect to the Thuringian development, exhibits more deeper-water sediments and a more proximal Carboniferous flysch) subdivided as follows:

- Ordovician sediments with a bimodal suite of intra-plate volcanics
- Silurian and Devonian radiolarian cherts
- Lower Carboniferous flysch

The metamorphic rocks exhibit medium-pressure facies with kyanite. The peak of metamorphism was attained in the early Devonian (at about 390 Ma). Nappe thrusting and very low-grade metamorphism were not terminated before the Lower Carboniferous.

The Münchberg pile of nappes probably originated from an accretionary wedge, which overrode the parautochthonous Thuringian realm from the SE. Since the Saxothuringian rocks of the Fichtelgebirge, to the SE of the Münchberg Massif, are also composed of Thuringian facies rocks, the root zone of the Bavarian facies and the metamorphic units must be sought still further to the SE, i.e. within or at the northwestern border of the *MN* zone.

“Un-stacking” of the Münchberg pile of nappes and restoring it to a position to the SE of the Fichtelgebirge implies a minimum distance of tectonic transport of the order of 200 km, which testifies to the alpine-type character of tectonic deformation and crustal structure in the target area, and justifies plate-tectonic interpretations (see below).

NW-directed tectonic transport is also documented, at outcrop scale, by NW-verging folds and by numerous thrusts (brittle as well as ductile). All these features represent the first of the six deformation phases D_1, \dots, D_6 of the Variscan orogeny (see KTB, 1986, p. 19).

A second phase has produced more open, SE-verging folds and thrusts. A third phase, which is clearly detectable only in the Fichtelgebirge, led to the formation of still more open, upright folds with a steep crenulation cleavage (Stein, 1987).

At map scale, the structural pattern is dominated by a number of major synforms (*S.*) and antiforms (*A.*) which originated during the later stages of tectonic deformation. These are, in order from NW to SE: Schwarzburg *A.*, Teuschnitz *S.*, Berga *A.*, Vogtland *S.* (which contains the “Zwischengebirge” klippen), Fichtelgebirge *A.* and Hatzenreuth *S.* (Figs. 1 and 2).

With the exception of the Münchberg Klippe, most of the Saxothuringian rocks are of low to very low metamorphic grade. Greenschist facies rocks occur only in a transverse zone with enhanced heat flow to the NE of the *MM* (Franke, 1984a, b) and in the core regions of the Fichtelge-

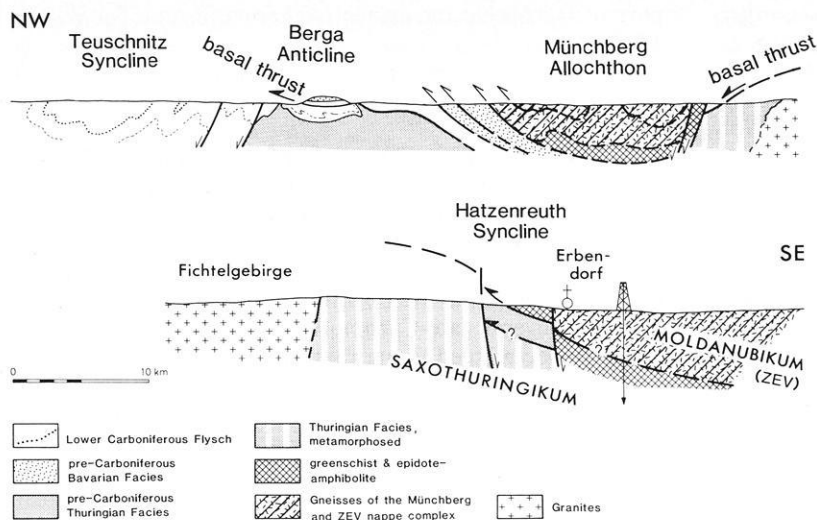


Fig. 2. Geological cross-section through the Oberpfalz area (NW-SE)

birge A. (staurolite-andalusite, Mielke et al., 1979). For reviews of the metamorphic development in the target area, see Blümel (1985), KTB (1986, p. 14), and Schüssler et al. (1986).

Saxothuringian/Moldanubian boundary region

The structure of the ST/MN boundary region is difficult to assess because it is intruded by important volumes of post-tectonic granite and because NW/SE block-faulting has brought to the surface very different levels of the tectonic structure. Individual segments of the boundary (the so-called "Erbendorf Line") probably differ in their origin.

North of Erbendorf, near the western margin of the basement outcrop, Thuringian facies rocks at the SE flank of the Fichtelgebirge A. are bounded by a SE-dipping thrust fault. Very low-grade Devonian sediments are overthrust by greenschist facies volcanics and lenses of serpentinite which closely resemble the Münchberg greenschists. This is especially true of their petrological affinities (calcic in both areas, see KTB, 1986, p. 27). The greenschists, in turn, are overlain by gneisses and amphibolites of the Erbendorf-Vohenstrauß Zone (ZEV). The ZEV rocks exhibit the same metamorphic facies (medium-pressure with kyanite) and the same metamorphic ages as the Münchberg gneisses (KTB, 1986, p. 14; Schüssler et al., 1986). Hence, the greenschists and gneisses at Erbendorf must be regarded as equivalents of the respective units at Münchberg, preserved in a position closer to the root zone. The Bavarian facies Palaeozoic rocks appear to pinch out toward the SE, since they are reduced in thickness at the SE margin of the Münchberg Klippe, and are no longer detectable at Erbendorf.

East of the Steinwald granite, in the Tirschenreuth-Mähring area, the ST/MN boundary is less evident. As already recognized by Schreyer (1966), and reaffirmed in much more detail by Wagener-Lohse and Blümel (1986), Stein (1987) and de Wall (1987), there is a continuous metamorphic transition from the chlorite-bearing schists of the Hatzenreuth S. towards the SE through the cordierite/K-feldspar gneisses of the Moldanubian proper. As in the Fichtelgebirge, the metamorphic facies is of the low-pressure type. Though the northern part of the MN is affected by a broad subvertical zone with high-temperature mylon-

ites (KTB, 1986, p. 21), the sequence of southward-increasing metamorphic grades is complete.

Hence, the ST/MN is difficult to define, and, from merely lithological aspects, the Moldanubian gneisses might just represent Saxothuringian Palaeozoic rocks of higher metamorphic grade. However, geochronological studies (KTB, 1986, p. 32; Teufel, 1987) have revealed traces of an older metamorphic event in the Moldanubian gneisses. Besides, there are relics of a medium-pressure metamorphic event which pre-dates the low-pressure metamorphism of the Moldanubian proper.

Hence, the Moldanubian rocks east of the Steinwald granite must be regarded as part of a separate tectonic entity, with an older and more complex tectono-metamorphic history, which was brought into tectonic contact with the ST rocks of the Fichtelgebirge and then was welded together with these during the subsequent low-pressure metamorphic event. The latter is dated at about 330 Ma, i.e. at about the Lower/Upper Carboniferous boundary (Teufel, 1987).

In summary, it is obvious that the ST/MN boundary in the Tirschenreuth-Mähring area is of great structural importance, though its exact position and significance are still being debated (see Section 5). It can be stated, however, that the Tirschenreuth-Mähring area represents a deeper structural level than that exposed at Erbendorf.

Moldanubian (MN) zone

Most of the MN region in Bavaria, Czechoslovakia and Austria is made up of metapsammitic and metapelitic gneisses with some intercalations of graphitic schist and marble. This association (the MN proper) has been further subdivided into lithological units and compared with Precambrian sequences elsewhere; at least part of the metamorphic alteration has been attributed to a Cadomian event (Stettner, 1981). However, recent isotopic studies (KTB, 1986, p. 32) have yielded Palaeozoic metamorphic events, and new palaeontological evidence has revealed the presence of Cambrian and Silurian sediments among the MN metamorphic sequences (KTB, 1986, p. 15). The history of the MN zone will have to be re-assessed with modern methods of investigation.

The MN proper has been affected by the same low-pressure metamorphism as the ST rocks of the Fichtelge-

birge to the north, but exhibits higher grades up to cordierite/K-feldspar. Accordingly, radiometric dating has revealed the same age as in the north (approx. 330 Ma; KTB, 1986, p. 32). Some relic minerals give evidence of an earlier medium- and high-pressure metamorphic event (probably around 390 Ma). Further to the SE, in the Bavarian Forest, there are indications of a still older anatexis event dated at about 460 Ma (Grauert et al., 1974).

The MN proper is structurally overlain by a sequence of gneisses with numerous inserts of amphibolite, which outcrops along the western margin of the Bohemian basement block and has been termed the "Zone of Erbenhof-Vohenstrauß" (ZEV) after two towns at its northern and southern margins. A direct equivalent of the ZEV rocks, in terms of lithology as well as of metamorphic character, is exposed to the east of the MN proper: the gneisses of the "Tepla-Taus Zone" (ZTT) in Czechoslovakia, which forms the western part of the extensive Tepla-Barrandean block, the core of the Bohemian crystalline massif.

ZEV and ZTT both exhibit medium-pressure metamorphic facies, without clear indication of a younger low-pressure event. Hence, it could be concluded that they occupied a higher and therefore cooler structural level during the time of low-pressure metamorphism. Alternatively, they might have been emplaced after the low-pressure metamorphic event. In most of the area, the contact between the overlying units is obscured by granites or younger block-faulting. It is at the SE border of the ZEV only, that a ductile mylonite zone can be observed.

Anyhow, the ZEV rocks must be regarded as an equivalent of the MM gneisses since they exhibit similar lithologies (with frequent mafic intercalations), the same medium-pressure metamorphism and also the same metamorphic age (approx. 390 Ma; KTB, 1986, p. 32), thus providing further evidence of the allochthonous nature of the MM.

The MN proper exhibits the same sequence of deformational events as does the Saxothuringian to the immediate north (KTB, 1986, p. 19). The peak of low-pressure metamorphism, in the MN rocks, occurred in an early stage of the D_3 deformation. The metamorphic isogrades were still folded around the ENE-trending D_3 fold axes, and, later, around a NS-oriented set of D_4 structures. A major D_4 antiform is responsible for the outcrop of the MN proper between the cover sequences of the ZEV (to the west) and the ZTT (to the east).

The ZEV rocks were not perceptibly heated during the low-pressure event and do not show, therefore, the synmetamorphic fabrics and structures acquired by the MN rocks. They exhibit, instead, a complex set of structures related to the earlier medium-pressure event (which, in turn, is not detectable in the low-pressure MN rocks proper).

Variscan granites

The central and southern parts of the target area are intruded by an important volume of post-tectonic granites. Their intrusion ages range from approx. 320 to 280 Ma (Besang et al., 1976; Köhler and Müller-Sohnius, 1976; Lenz, 1986; Richter and Stettner, 1979). One larger group of granites occupies the core of the Fichtelgebirge A. (D_3). Other granite bodies appear to follow NW/SE-oriented fracture zones. In the Flossenbürg and Bürgerwald granites (both within the MN zone), the spatial array of trace-element zoning suggests plate-like bodies which are probably

part of laccolithic intrusions (Ackermann and Tavakkoli, 1986).

Post-Variscan structures

The NW/SE alignment of some of the granites reflects a system of block-faults which was formed in Upper Carboniferous-Permian time and reactivated repeatedly until recently. One of these faults is the "Franconian Line" (FL) (Fig. 1), along which the Mesozoic and Tertiary rocks of the western foreland are downfaulted locally for more than 1000 m. Several late-Carboniferous/Permian depocenters appear to be aligned along that fault (e.g. Emmert, 1981), and it is possible that these basins represent pull-apart features associated with dextral strike-slip movements like those proposed by Arthaud and Matte (1977).

The main movement along the NW/SE faults, at least during Mesozoic and later times, is a more or less vertical downthrow to the SW. This is also evident from another important fault zone which runs from Bad Berneck (in the NW) to Pleystein (in the SE) at an acute angle with the FL, both including a narrow segment of basement rocks between them at the western margin of the Bohemian Massif. The site of the German continental drilling (KTB) lies within that segment. The Kulmbach Fault, which parallels the FL within the Mesozoic foreland is another example of the same kind of fault.

The FL, as well as the Bad Berneck-Pleystein fault, dips steeply (70° – 80°) to the NE, as is observable in surface outcrops. This might be due to gravitational spreading, at near-surface level, of the uplifted basement rocks and their encroachment upon soft Mesozoic foreland rocks, or else reflect a compressive tectonic regime.

Another important NW/SE element is the Bavarian "Pfahl" (Fig. 1), a dextral shear zone with cataclastic as well as ductile deformation and extensive quartz mineralization, which was still active in Triassic time (Horn et al., 1983). A similar quartz vein, the Bohemian "Pfahl", occurs close to the east of and parallel with the western margin of the ZTT (in Czechoslovakia).

One of the youngest tectonic elements is the Eger Graben (Fig. 1), which roughly follows the ST/MN boundary along approx. 200 km. It is characterized, in the target area, by local cover of Miocene sediments and by a number of basaltic pipes and lava flows of the same age, which can be traced across the FL into the Mesozoic foreland.

Purpose of survey and objectives of the seismic lines

The objective of the survey was the investigation of the crustal structure of the ST and MN zones, with special emphasis on the boundary region which was under consideration and has since been selected as the well site of the Continental Deep Drilling Project (KTB). The long profile, DEKORP 4, was intended as a general cross-section from the Teuschnitz S. in the north to the MN rocks in the south. The KTB lines 8501–8506 were arranged in the form of a grid to explore the ST/MN boundary region near Erbenhof (i.e. around the KTB drilling site). This array of lines (Fig. 1) represents a first step in obtaining a 3-D view of the target area.

The DEKORP 4-Q line is positioned at a right angle with respect to the DEKORP 4 line near its southern end. Line 4-Q runs across the regional tectonic trend of the Ba-

Table 1. Important data of the Oberpfalz survey 1985

Profile	Length	Source parameters for accompanying investigations
DEKORP 4	186.88 km	Number of shots: 96
DEKORP 4-Q	36.64 km	Drilling rigs: 6
KTB 8501	47.44 km	Drilling depth: 30 m
KTB 8502	50.48 km	Boreholes per shot: 3
KTB 8503	56.80 km	Charge per shot: 90 kg
KTB 8504	50.72 km	
KTB 8505	54.80 km	
KTB 8506	42.60 km	
Total	526.36 km	

varian Forest (NW/SE) and was intended to explore important tectonic structures such as the Bavarian "Pfahl" and the western margin of the Tepla-Taus Zone (ZTT), which is marked, in this area, by an important volume of mafic metamorphic rocks (Hoher Bogen).

Lines KTB 8505 and 8506 were arranged to explore the Tirschenreuth/Mähring segment of the ST/MN boundary region. The Erbdorf segment is crossed by the main DEKORP 4 line. KTB 8504 is situated in the Mesozoic foreland, in an area which is probably underlain by a westward continuation of the Erbdorf-Vohenstrauß Zone (ZEV).

While the above lines yield cross-sections with respect to the main tectonic trend (SW-NE) in the area, lines KTB 8501–8503 are arranged parallel to strike, but cut across the NW/SE-directed system of block-faults at the SW margin of the Bohemian Massif. These faults were expected to produce important steps in the reflection surfaces, even at greater depths.

1.2 Field technique

In order to accomplish a highly effective seismic reflection investigation, the survey of lines DEKORP 4 and 4-Q was carried out together with that of the six KTB lines in a joint field survey. Thus, uniform field parameters were chosen to allow a good comparison. Another important measure was the integration of wide-angle observations and expanding spread arrangements in the survey. This work was only partly carried out by the contractor, Prakla-Seismos AG: a great deal was taken over by crews from the universities and geological surveys with their own equipment. For this reason, explosives had to be used to provide a suitable energy source. Important data of the Oberpfalz survey 1985 are listed in Table 1.

In contrast to the DEKORP 2-South survey (DEKORP Research Group, 1985) where Mesozoic and Cenozoic sediments represent the prevailing outcrops, in the Oberpfalz pre-Permian metamorphic and crystalline rocks are present at the surface. This had an important influence on the decision of whether explosion seismics (as on DEKORP 2-South) or Vibroseis should be used; due to the difficulty in estimating the drilling progress, the Vibroseis method was chosen. This decision was also justified by the very good experience in surveying the Schwarzwald area in 1984 (Lüschen et al., 1987).

Hence, the field parameters were derived from experience of the former surveys. Regarding the geometry, two

Table 2. Field parameters for the near-vertical seismic reflection survey in the Oberpfalz 1985

Method	Vibroseis
Equipment	SERCEL SN 368, telemetric, 200 channels
Sampling rate	4 ms
Sweep	12–48 Hz upsweep
Sweep length	20 s
Listening time	12 s
Record length	20 s + 12 s = 32 s
Filters	12 Hz, 18 dB/oct; 89 Hz, 72 dB/oct
Number of geophone groups	200
Geophone group interval	80 m
Geophone pattern	24-fold, in-line
Pattern length	80 m
In-line offset	200 m
Geometry	asymmetric split-spread 4.12 km – 0.2 km – VP – 0.2 km – 12.12 km
Number + type of vibrators	5 VVEA, 16 tons peak force
Vibrator pattern length	145 m/49 m
Vibrator point interval	80 m
Vertical stacking	10-fold
Coverage (ideal)	100-fold
Mean coverage (actual)	75-fold

facts were decisive: a sufficiently high degree of coverage in the shallow subsurface should be reached and an adequate long offset should provide enough normal move-out for safe calculation of velocities. These considerations resulted in a compromise: an asymmetric split-spread with 4-km and 12-km spreads. A list of the parameters used is given in Table 2.

2 Data processing

2.1 Processing by the DEKORP Processing Center (DPC)

The processing was carried out by the DPC at Clausthal with the Raytheon RDS 500 and VAX 11/750 computers and standard software of Seismograph Service Ltd. In DEKORP Research Group (1985) the single processing steps were described in detail. The aim of this section is to emphasize the peculiarities of the processing of the Oberpfalz data.

CMP processing and stacking

The demultiplexed common-shotpoint gathers (CSP) were rearranged into common-midpoint gathers (CMP). Due to unavoidable lateral offsets (up to 1 km) and crooked-line field configurations, there was a strong scattering of the source-receiver midpoints. Thus, a processing line with CMP intervals of exactly 40 m was calculated and the corresponding traces were related to these points.

The following steps were optimized by special analyses. First, the strong energy decrease within the first seconds was compensated by an analytic gain function. Then, basic static and dynamic corrections, muting and scaling by AGC were applied. Subsequently, a brute stack was performed in order to facilitate a quick overview over all profiles. This stack was obtained by use of only a few velocity analyses and one single muting curve. Finally, the data were bandpass filtered. In order to obtain the final stack a large

number of specialized analyses regarding the respective processing parameters were performed, resulting in an improved resolution.

Special emphasis within the CMP processing was given to the assessment of NMO velocities derived from constant-velocity stacks. At 7–10 points per 50 km profile, test stacks were performed with about 30 constant velocities within groups of 20 CMPs. The evaluation of these velocity scans resulted only rarely in unambiguous velocity – TWT functions, i.e. coherent stacking at a particular reflection time is possible over a broad velocity range (DEKORP Research Group, 1985). This might be due to complicated geological structures on the one hand (e.g. different dips at the same travel time necessitating different NMO velocities) and, on the other hand, due to effects of seismic imaging at greater travel times (e.g. increasing spatial influence of diffractions with increasing travel times).

In order to identify the influence of lateral velocity variations, offset-restricted test stackings (30 constant velocities, five offset ranges) were performed in the centre area of profiles DEKORP 4 and KTB 8502. The stacking results were quantitatively equivalent for all offset- and time-domains within a broad velocity range, thus excluding a detailed analysis of lateral velocity variations. Therefore, only one velocity-time function was applied for ten different offset-domains of the respective central line parts mentioned before.

The results (Fig. 3) show that the different offset ranges contribute partial information to a complete image of the subsurface. The stack of small offsets (up to 4 km) evidences good reflections at 3–4 s TWT in the marginal domains of this part of the section: the central domain is more or less void of reflections. On the other hand, the stacks of the greater offsets (4.0–8.0 km and 8.0–12.0 km) give good reflections in the central part, the quality of reflections becoming poor in the marginal domains.

Three conclusions can be drawn from these results:

1. All offset domains produce different, but equally important, contributions to the final result.
2. The differences can be explained – at least partly – by the inhomogeneous overburden.
3. Generally, the signal/noise ratio is not as much improved with increasing coverage as expected.

In order to support better interpretation, the complete DEKORP 4 profile was stacked additionally with drastically increased velocities emphasizing strongly dipping reflections. Furthermore, the complete KTB 8502 profile was stacked using only offsets up to 4 km.

Automatic residual static corrections and coherency filtering

An essential improvement in processing the Oberpfalz data was obtained by calculation and application of residual static corrections before stack and by coherency filtering after stack. This procedure improved, in broad areas, the content of information and the resolution of the sections. For this reason a short description of these two time-consuming processing steps is given in the following.

Experience shows that static corrections calculated from short refraction lines and/or first arrivals of the reflection records are not sufficiently precise in most cases. Therefore, residual statics had to be assessed. This was done by the DPC using two independent algorithms.

The first method calculates surface-consistent residual

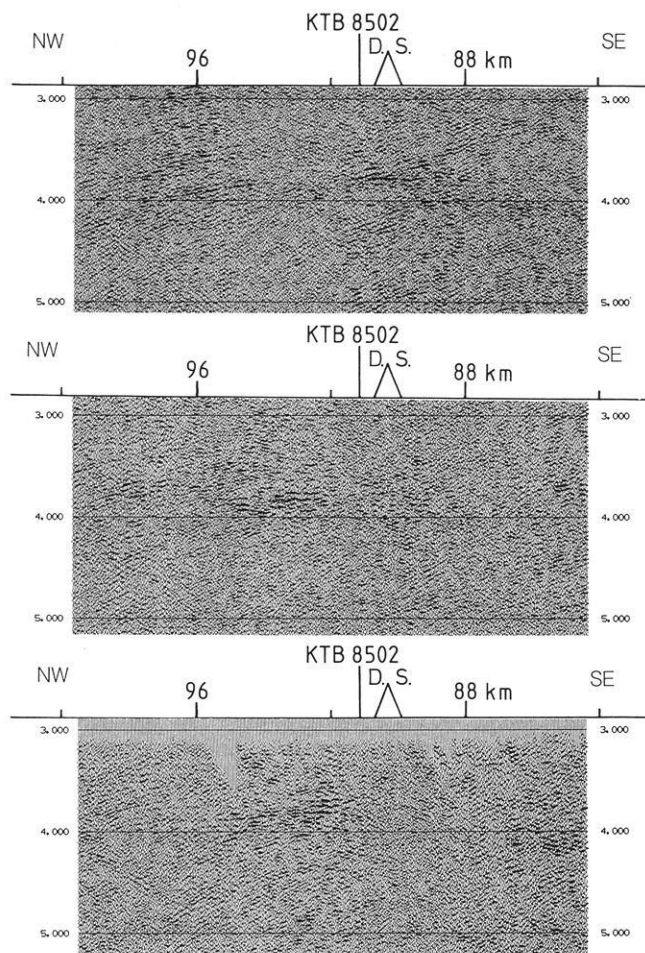


Fig. 3. Profile DEKORP 4: stacks of the offset domain up to 4 km (*top*), 4–8 km (*centre*) and 8–12 km (*bottom*) from the part including the Erbendorf body. *D.S.* = drilling site

static corrections for particular source and receiver positions under the assumption that near-surface influences (e.g. variations in altitude, thickness of the weathering layer and velocity) generate pure time shifts (neglecting the other parts of the ray paths). That is, a given surface position correlates with a constant time shift. The residual statics are calculated in two phases:

1. Estimation of relative time shifts by cross-correlation of dynamically corrected CMP traces with model traces
2. Calculation of source and receiver statics by the Gauss-Seidel iteration method (Taner et al., 1974)

The second method calculates subsurface-consistent residual static corrections for each CMP trace. The relative time shift of the respective trace is calculated by cross-correlation with a pilot trace obtained by weighted stacking of several adjacent CMPs. Up to two maxima of the correlation function are considered, provided that the second maximum exceeds a selected relative threshold value. Three cases have to be distinguished:

1. Only one maximum is found – its delay is taken as residual static value.
2. Two maxima fulfil the conditions – the correct value will be found by trial-and-error application and comparison with the pilot trace.
3. No unambiguous maximum is found – the residual static value is set equal to zero.

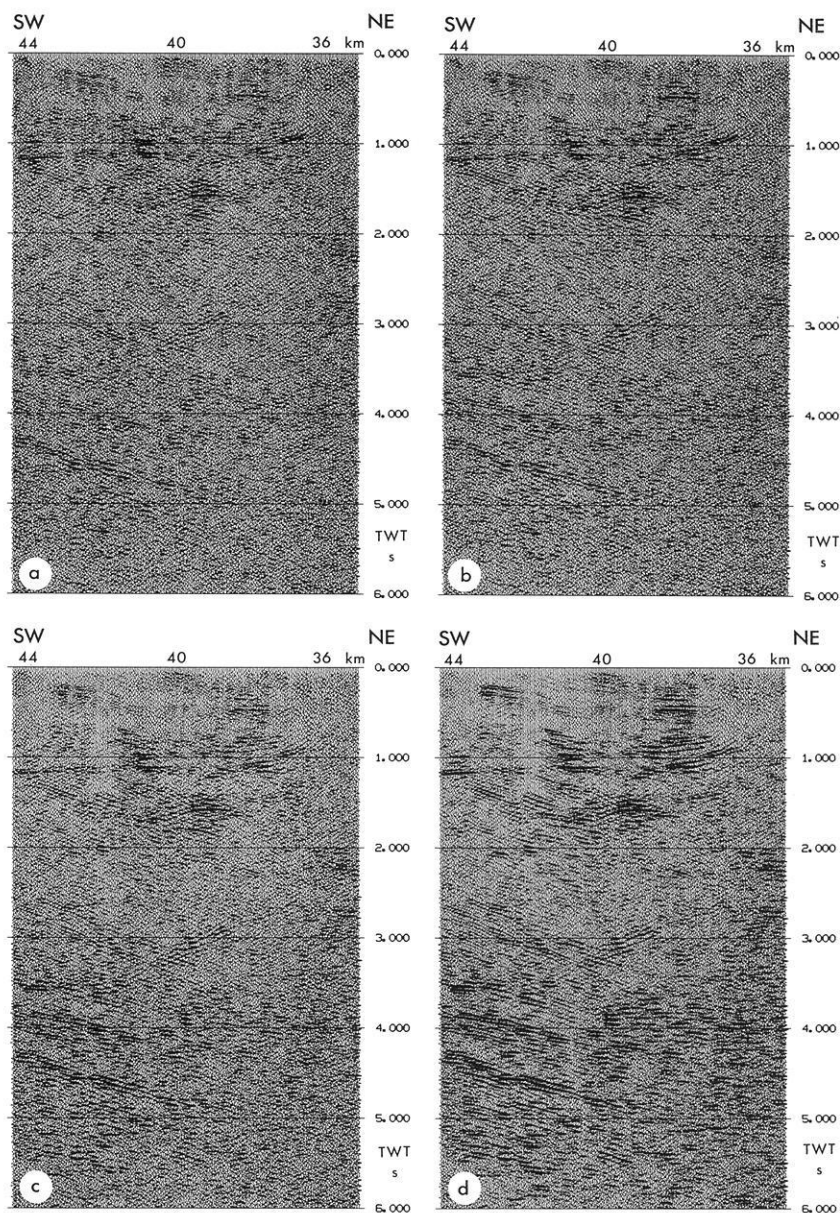


Fig. 4 a-d. Example for the improvement of results by applying automatic residual static corrections and coherency filtering:
a original section;
b with surface-consistent corrections;
c with surface- and subsurface-consistent corrections;
d with the same corrections as in c and subsequent coherency filtering

In both methods, surface- and subsurface-consistent residual statics, a certain maximum shift must not be exceeded (typically 20 ms). The efficiency of both methods is demonstrated in Fig. 4a-c and it is obvious that, with successive application, each of them produces an equivalent improvement.

Coherency filtering represents, especially in deep seismic profiling, a useful procedure for improving the clarity of the sections. This procedure was applied to stacked sections in order to suppress incoherent noise and to increase the amplitude of reflections extending over a number of traces. The procedure works as follows: trial stacks of a number of adjacent traces over a given window and along straight lines with a variety of different slopes result in summed trace windows. That one with maximum energy is chosen as part of a coherency trace. This part is added with a weighting factor to the centre trace of the original input, resulting in a coherency-filtered trace for the selected time window. Repeating this procedure for all time windows and for all traces yields the coherency-filtered section. Figure 4d

shows an example. It has to be mentioned that only particular linear alignments will be emphasized due to the prevailing dip within the respective window. By suitable choice of window lengths, number of traces and weighting factors, this disadvantage can be avoided.

Coherency filtering improves the display of the sections, emphasizing general trends and structures provided that the parameters are chosen carefully. If not, reflections may even be weakened. Nevertheless, a careful comparison with the unfiltered data is necessary. Under such precautions coherency filtering provides a useful tool for increasing the readability of deep seismic data.

Migration

Usually, the finite-difference (FD) migration is applied because velocity variations in all directions are permitted and an optimum signal/noise ratio is obtained. In order to diminish the processing time, the data were resampled at 8 ms sampling interval under the condition that fatal deviations

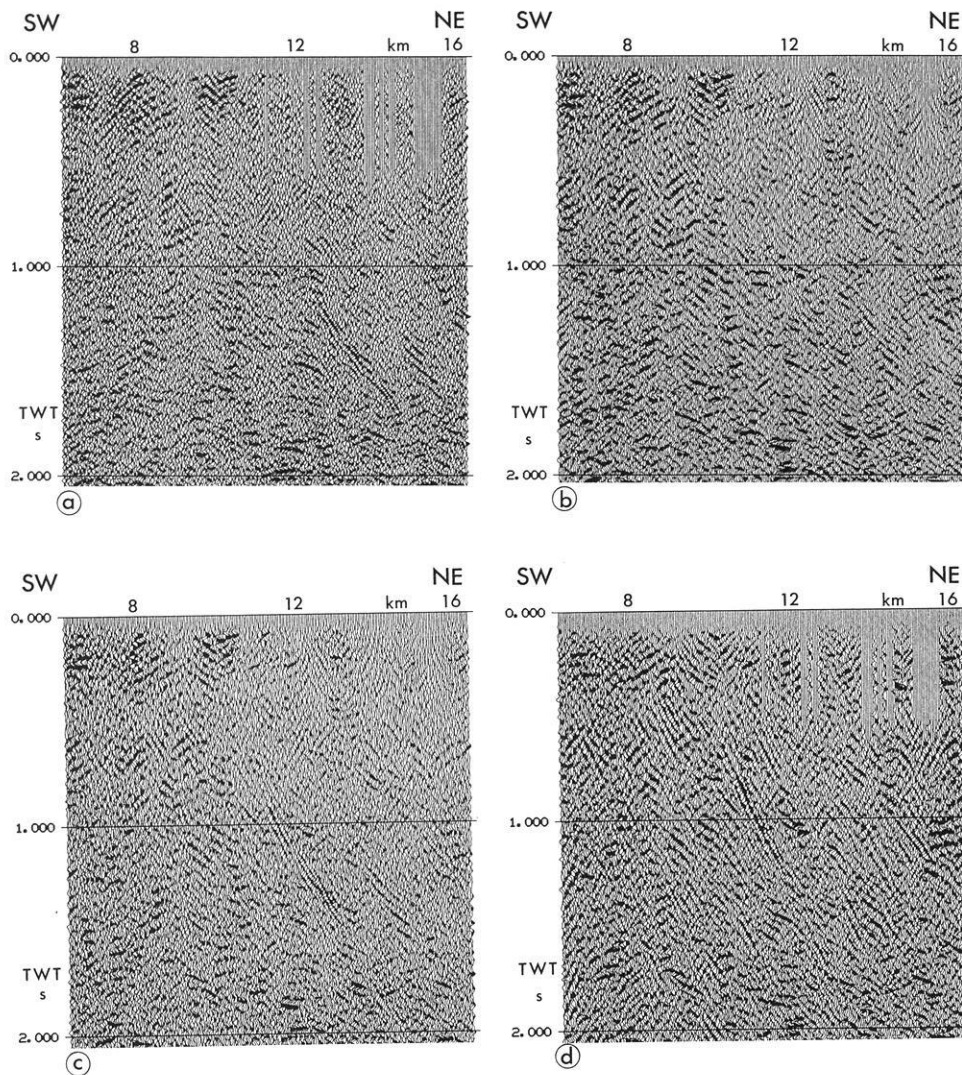


Fig. 5a-d. Stack of a part of profile DEKORP 4-Q
a unmigrated, **b** FD migrated, **c** FK migrated and **d** Kirchhoff migrated. The migration velocity at 1 s TWT was 3825 m/s

due to frequency dispersion can be excluded. Figure 5a shows a part of the DEKORP 4-Q profile and Fig. 5b the corresponding FD migration. From inspection of the steeply dipping structure of the Bavarian “Pfahl”, it is obvious that the migration is strongly affected by dispersion. In order to reduce this effect the following procedures can be applied:

1. Resampling input data at smaller sampling intervals
2. Using smaller downward continuation steps
3. Decreasing the spatial sampling interval by interpolation

All these steps have the disadvantage of a strong increase in processing time. Therefore, other migration methods could be suitable. The frequency-wavenumber (FK) migration and the Kirchhoff migration were at hand.

The fast FK migration does not lead to dispersion effects (Fig. 5c): the data can be migrated over a wide range of dips (this was also tested by the use of synthetic data). It is well known that this method is not suitable for providing final sections with complicated structures because it works only very unprecisely in the presence of velocity variations. However, due to its speed, this method is well suited to estimating migration velocities (focussing of diffractions). For this purpose trial migrations are performed with different velocities, finally choosing that migration velocity

which makes the diffractions contract to an area of minimum width.

The Kirchhoff migration works well in the presence of steep dips and variable velocities. In principle, this method migrates all dips correctly without remarkably increased processing time. But the result was often not clear, due to a bad signal/noise ratio (Fig. 5d).

Therefore, all final migrations were obtained with the FD method, using decreased, smoothed stacking velocities and additional velocity information from refraction seismics.

All migrations, especially of short profiles, are strongly affected by boundary effects. The amplitude energy of the marginal traces will be smeared along half-circles, the radii of which are the two-way travel times of these traces. This effect can be reduced by horizontal tapering of these traces. Best results have so far been obtained using synthetic data. This method has also been tested on real data, but additional efforts are necessary for further improvement.

Remarks

During the work we have tried to answer the question of whether deconvolution can contribute to a contraction of events in Vibroseis data. For this purpose, zero-phase wave-

lets were transformed into minimum-phase wavelets and a standard deconvolution was applied. These tests succeeded in several areas and the results encourage further efforts.

In order to obtain additional information about the subsurface lithology, instantaneous frequencies were calculated by Hilbert transforms in the centre parts of profiles DEKORP 4 and KTB 8502. But this method, which is often successful in exploration seismics, failed in this case. This might be due to the frequency limitation of the applied Vibroseis signals.

Finally, it should be mentioned that the processing of the DPC so far has been performed nearly exclusively with a standard software package. The demand for better adaptation of some subprograms to the problems of deep seismic profiling or for replacing them entirely became more and more evident.

2.2 Processing by companies

Five of the six KTB lines were given to four contractors with the intention of getting final processing of these lines within the limited time to prepare the decision on the location of the KTB and to test the results of different kinds of modern processing simultaneously: Compagnie Générale de Géophysique, Massy, France; Prakla-Seismos AG, Hannover, Germany; Preussag AG, Hannover, Germany; Seismograph Service Ltd., Keston, Great Britain. The companies were provided by DPC with already preprocessed data and with brute stacks of their respective profiles in order to try further improvements.

The results of the different processing sequences can be compared only with care because the procedures were applied to different profiles. Together with the brute stacks of all profiles from DPC, some conclusions may be drawn.

The most important distinctions resulted from different procedures to obtain residual statics, from offset restrictions and DMO processing (dip move-out). Residual statics provided a remarkable improvement, regarding the resolution and strength of reflections. However, special care should be taken in choosing methods and parameters. Strong improvement and a smoothing effect is obtained for long continuous Palaeozoic reflectors within sedimentary portions. On the other hand, short and weak events above and beneath these reflectors are not improved, but rather destroyed. Moreover, it is not proved that the reflectors are as smooth as they appear after application of these methods. A combination of surface-consistent and CMP-consistent residual statics seems to provide a more balanced result.

Offset restriction is an ambiguous method. A certain clarification of reflection patterns in very complicated domains was obtained, but it has to be kept in mind that in such cases some information is neglected. This became obvious when stacking tests with different offset domains were performed at the DPC (cf. Section 2.1).

DMO or partial pre-stack migration is a useful method in regions with complex geology. The data are dip-dependently corrected by DMO so that subsequent dynamic corrections can be applied using a unique velocity field. This method provides a better fit to the actual subsurface parameters (i.e. velocities and dip angles). Although the resulting section does not look much different from that without DMO, the velocities obtained from this method are more

consistent and better suited to discussing geology than those determined by routine velocity analyses which sometimes lead to unrealistically high values. Velocity-depth functions derived from this method along profile KTB 8506 are presented in Fig. 26.

It can be concluded, that special processing has advantages and disadvantages and the results have to be regarded carefully. Even the brute stacks of all profiles, as provided by the DPC, show that a cautious and experienced way of choosing the processing parameters yields sections which are qualitatively comparable to the final stacks provided by the companies.

3 Results of the near-vertical seismic reflection survey

All along DEKORP 4 a great number of reflections were recorded in the upper as well as in the lower crust. This long profile, which runs perpendicular to the general Variscan strike, represents a key to the structural character of the area under investigation. The description of this profile will serve as an introduction to the network of the other lines.

3.1 DEKORP lines 4 and 4-Q

A line-drawing showing the whole migrated DEKORP 4 profile is presented in Fig. 6. Parts of the migrated section are reproduced in Figs. 7–11 and 13–16. The description starts in the Saxothuringian (ST) part (NW) continuing to the Moldanubian (MN) domain (SE).

Figure 7 shows strong horizontal reflectors at approximately 1 s TWT to be correlated possibly with Upper Devonian spilites of Frankenswald. Underneath, several sub-horizontal bands of reflections appear down to about 6 s TWT. The lower crust shows only poor reflections (Figs. 6 and 51). But at its base the Moho is relatively strongly reflecting at 10.0–10.5 s TWT. This result is typical for the entire northern part of the profile. This image is in contrast to the southern part of the profile where strong reflections are observed both in the upper and in the lower crust. The results obtained along the entire DEKORP 4 profile represent a pronounced contrast to the so-called “typical continental crust”, i.e. poorly reflecting upper crust and highly reflecting “laminated” lower crust (e.g. Meissner et al., 1982; Lüschen et al., 1987; Matthews and Cheadle, 1986; Matthews et al., 1987; McGeary, 1987).

Just below the base of the Carboniferous in the SE a wide antiformal structure is visible between 1.5 and 2.0 s TWT (Figs. 7 and 8). It can be correlated with surface structures, the Berga A. and the Hirschberg A.. Other strong reflections can be observed down to 5 s TWT.

Following in the SE, a bowl-type structure appears in the uppermost crust with its deepest point at about 1.3 s TWT (Fig. 9). It represents the base of the Münchberg Massif (MM) between 130 and 155 km. This finding is an additional piece of evidence that this unit is to be interpreted as a nappe. Further to the SE another antiformal structure is observed at a level of less than 2 s TWT at about 120 km (Fig. 10). It is located below the Fichtelgebirge A.. Parallel reflections are seen down to 4.5 s TWT.

In the centre of the DEKORP 4 profile (Fig. 11) there is a zone of prominent reflections in the upper crust at about 3–4 s TWT. This zone has been observed along all NW/SE-running profiles and its basal zone coincides, along

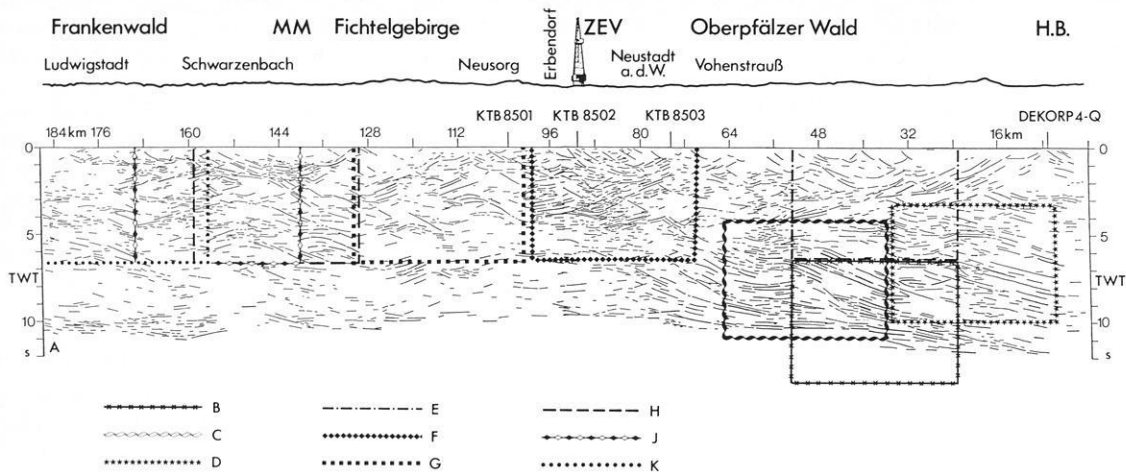


Fig. 6. Profile DEKORP 4: line-drawing of the migrated section. *Frames* indicate that part of the section which is given in more detail by a following figure, denoted by the corresponding letter

DEKORP 4, with a wide-angle reflector of abnormally high P -wave velocity material (Section 4.2). It has a wedge-type imbrication structure and overrides a SE-dipping band of reflectors which combines 50 km further to the SE with the Moho discontinuity. This imbricate structure will be called “Erbdorf body” (EB) in the following. The internal structure of the EB shows NW-dipping reflectors reaching, in many cases, up to the SE part of the base of the ZEV.

The strength of the reflections decreases remarkably below the EB. This might be due to a certain shielding effect of the EB. The wide-angle observations show clear and continuous Moho reflections below the EB and some subhorizontal reflections in the lower crust (Section 4.2).

Above the EB a bowl-type structure is seen (Figs. 6 and 11) which should be related to the base of the nappe complex of the ZEV at about 2 s TWT, corresponding to 5–6 km depth.

At the NW rim of the ZEV and at the adjacent green-schist zone, various fault systems with more or less E–W strike are observed at the surface. They might be an explanation for a particular phenomenon which became evident from stacking with different offset ranges (Section 2.1, Fig. 3). These near-surface inhomogeneities seem to dissipate seismic energy for certain domains at greater depth (Fig. 12). Analysing the results in more detail, a dependence on ray directions seems to play a role: rays travelling more or less parallel to these fault systems are disturbed more strongly than those rays travelling only a short distance perpendicularly through that zone. Presumably, these effects are not restricted to the afore-mentioned area and additional efforts should be made in order to investigate this problem more precisely.

Between the base of the ZEV and the top of the EB a complicated pattern of reflections is seen with different directions of apparent dip. Figure 13 presents the SE continuation of the above-mentioned strong band of reflections which might be a master décollement. It is best seen from about 6.5 s TWT at the NW edge of the figure to about 9.3 s TWT at the SE edge, forming a ramp-like structure in its middle part. A broad band of parallel reflections of about 1.5 s width is situated above this ramp-like structure

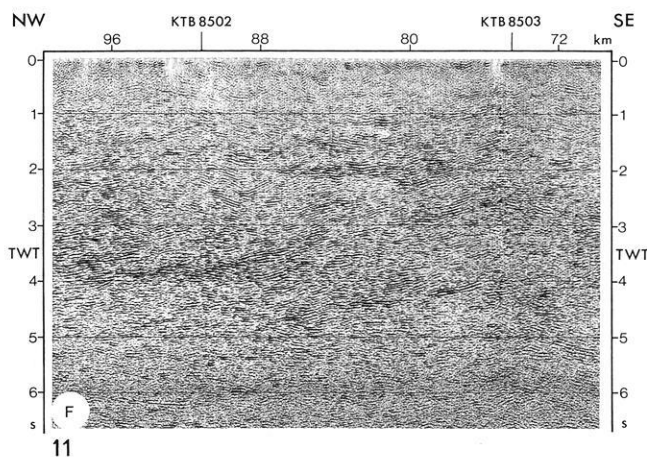
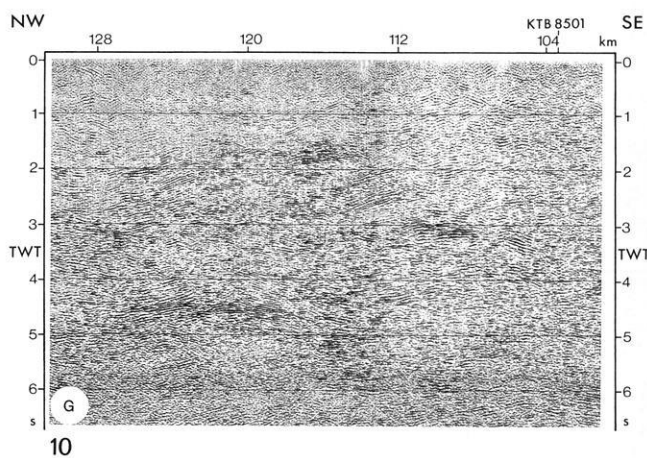
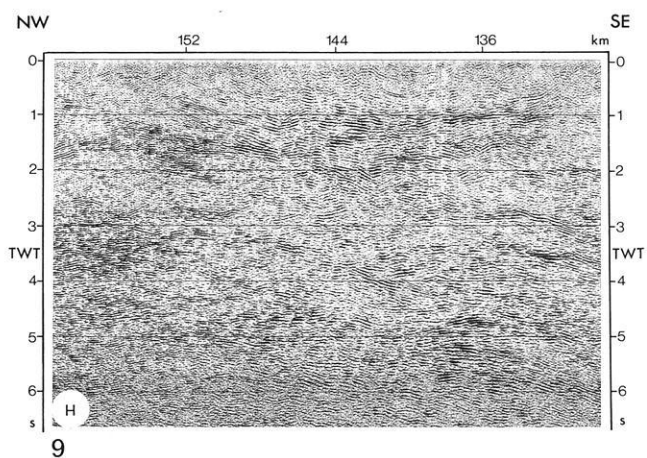
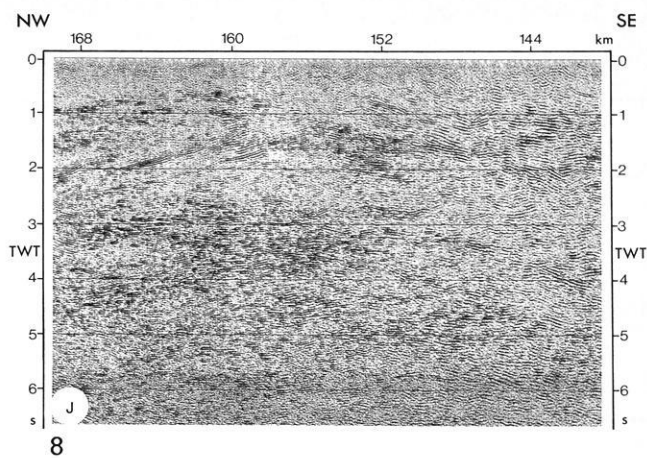
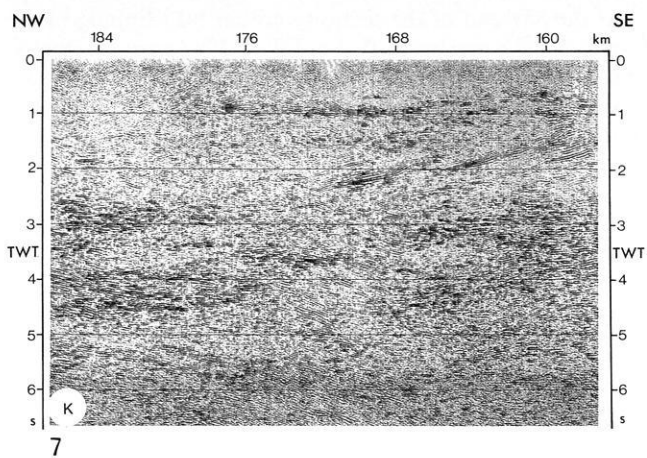
with its top culminating at about 5.5 s TWT. Above the culmination point there seems to be a structural discontinuity at approximately 4.8 s TWT, indicated by subhorizontal reflections extending from about 48 km to the SE end of Fig. 13. Below the ramp-like structure at 8.0 s TWT, a lens of strong reflections is visible from 54 to 60 km. At greater depths the reflections appear dipping weakly to the SE. The Moho is shown by clear subhorizontal reflections at about 10.2 s TWT.

Also in the upper crust good reflections appear as shown in Fig. 14. It shows subhorizontal reflections in its SE part between 2.6 and 5.0 s TWT. The subhorizontal reflections at 4.8 s TWT represent the afore-mentioned structural discontinuity. They are cut off by a strong band of NW-dipping reflections from 2 s in the SE to 4 s TWT in the NW. Their possible origin will be discussed in Section 5.

Further to the SE, Fig. 15 shows the continuation of the structural discontinuity. At about 20 km it bends down from 4.8 s to about 6.0 s at the SE end of the figure. Below the bending point another culmination of reflections appears at about 24 km and 6.5 s TWT; it is similar to that observed at 56 km. These findings reveal significant characteristics of the tectonic structures along DEKORP 4. It seems that SE-dipping elements and ramp structures are typical properties of the crust in this region.

Figure 16 shows remarkable features of the Moho level in the southern part of DEKORP 4. In the left and centre parts of the figure the Moho shows very strong subhorizontal reflections at about 10.0–10.5 s TWT. Distinct phases are observed correlating over long distances. At 36 km, however, the Moho bends down and dips SE down to about 11.5 s TWT where it cannot be followed further due to the restricted record length of 12.0 s. This corresponds to 34.5 km depth assuming a mean crustal velocity of 6.0 km/s.

Profile DEKORP 4-Q is situated at the SE end of DEKORP 4 and runs perpendicular to the NW–SE strike of the gneisses at the SW margin of the Bohemian Massif (“Bavaricum”). For its line-drawing see Fig. 17. At its NE end it crosses the Hoher Bogen – an amphibolitic nappe – belonging to the allochthonous Tepla-Taus complex (ZTT). In its SW part it intersects an important mylonite zone with the embedded “Bavarian Pfahl”.



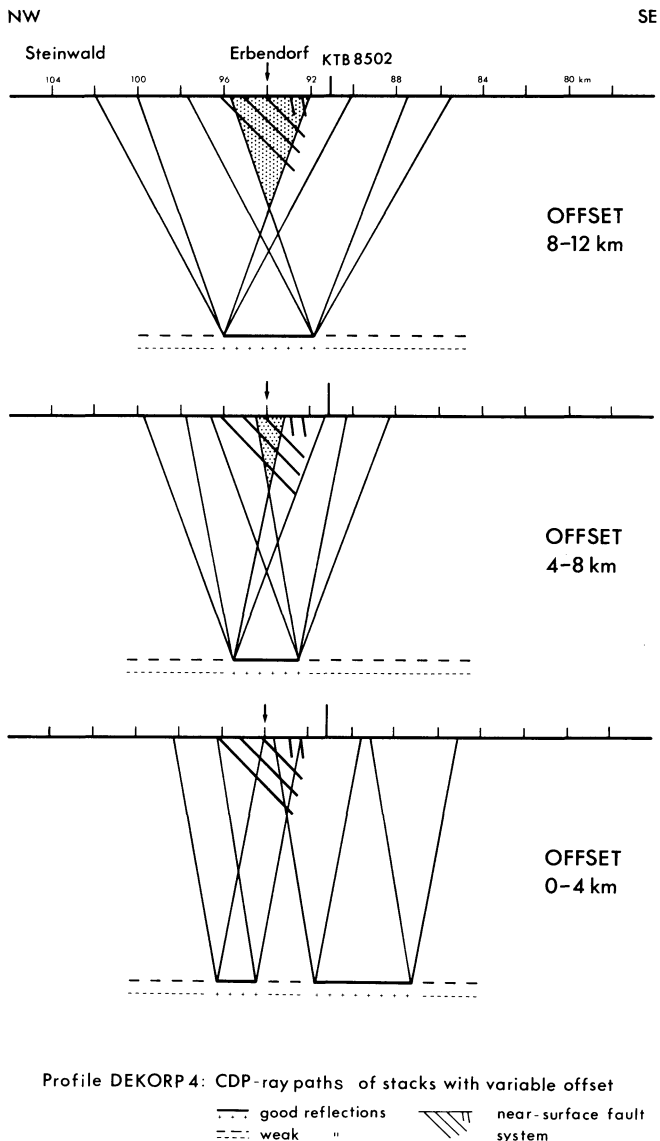
Figs. 7–11. Profiles DEKORP 4; parts of migrated section (see Fig. 6)

The seismic section shows only a few strong events. One of the most prominent results on this profile is a steeply NE-dipping reflection band (true dip angle, about 43°) to be observed over more than 10 km from 0.5–2.5 s TWT, which is to be correlated somehow to the “Pfahl” and its associated mylonites (Fig. 5) outcropping at the surface just at the linear extrapolation of the reflecting band. The event cannot be interpreted as a reflected refraction because the observed, corresponding refractor velocity would be 8.0 km/s and, therefore, is much too high. Moreover, no corresponding refractor is observed in this area and the possibility of side reflections can be excluded by the information from DEKORP 4. Perhaps the NE-dipping reflections with the same steep angle at 5.5–6.0 s TWT further

to the NE may be connected to this reflection band, revealing a very great depth range of the “Pfahl”.

The horizontal band of reflections at the NE end of 4 Q at 3 s TWT corresponds to likewise horizontal reflections on DEKORP 4 at the intersection of 4 and 4 Q. The corresponding horizon, therefore, has no essential dip and may be related to a deeper thrust plane. At about 7.5–8.0 s TWT a band of strong reflections forming a slight antiformal structure is recorded in the centre of the profile. This band corresponds to the SE-dipping reflectors observed along the SE part of DEKORP 4.

Reflections from the Moho cannot be found on this line. The Moho is probably too deep compared with the recorded reflection time of 12 s.



Profile DEKORP 4: CDP ray paths of stacks with variable offset
 — good reflections / near-surface fault system
 - - - weak " \

Fig. 12. Profile DEKORP 4: CDP ray paths for stacks with restricted offsets corresponding to Fig. 3

3.2 Lines KTB 8501–8506

KTB 8501

Profile KTB 8501 is the northernmost of the three lines running NE/SW, parallel to the Variscan strike 10–12 km north of the KTB borehole. Some of the features can be followed through all these lines. The line-drawing of KTB 8501 is given in Fig. 18.

At the SW end subhorizontal reflections occur, near the surface, corresponding to sedimentary structures west of the Franconian Line (FL). At this important tectonic lineament the reflections are cut off abruptly. The base of the Permo-Carboniferous is situated at about 0.5 s TWT, corresponding to approximately 1 km depth.

Steeply NE-dipping reflections appear on the NE side of the FL which should derive from a fault plane; they approach a band of strong subhorizontal reflections at about 3 s TWT. This band is related to the reflections originating from the base of the EB as observed in lines KTB 8505 and 8506.

At the SW end of the section another NE-dipping band of reflections appears at 3–5 s TWT. It cannot be interpreted as reflected refractions, but must be real reflections.

The Moho is represented by weak, but continuous, reflections at about 10.5 s TWT.

KTB 8502

Figure 19 shows the migrated section and Fig. 20 the line-drawing of KTB 8502. The sedimentary structures west of the FL are well depicted; they are dragged upwards and cut off abruptly by the crystalline rocks east of the FL. The base of the sediments is situated at 1.2 s TWT, corresponding to about 2.1 km depth.

Below the sediments, strong reflections come from within the crystalline basement showing a pronounced synformal structure. This feature is paralleled by an extended group of exceptionally strong reflections covering the range from 2–5 s TWT at the SW end of the profile with NE dip (Fig. 21). At their NE end one might see a narrow zone void of reflections, which could be interpreted as the subvertical continuation of the FL to depth.

Northeast of the FL, subhorizontal reflections at a level between about 2 and 4 s TWT are observed belonging to the top and base of the EB. They are intersected by several NE-dipping thrust faults along which the EB has been upthrown stepwise to the NE. An attempt to correlate the strong reflectors of the upper crust results almost necessarily in the construction of various steep-angle faults NE of the FL.

At the NE end of KTB 8502 the whole crust is highly reflective from about 2.5 s TWT down to the Moho range at about 11.0 s TWT. The Moho rises toward the SW to about 10.0 s TWT, exhibiting a slight antiform in the centre of the profile.

KTB 8503

Also on this line (see line-drawing in Fig. 22) the sediments west of the FL are represented by strong reflections reaching down to about 1.5 s TWT (approx. 2.9 km depth).

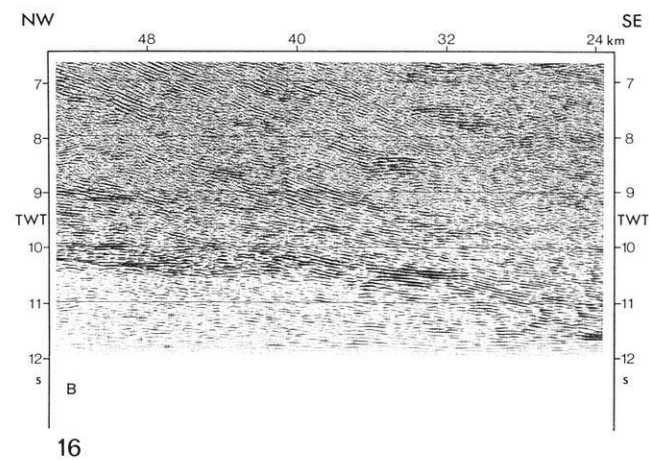
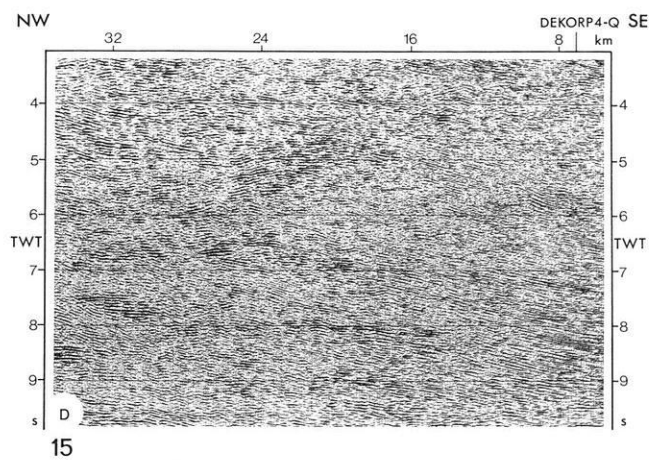
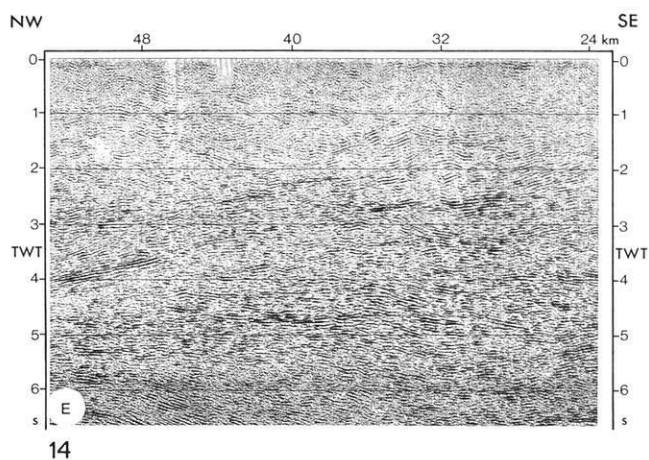
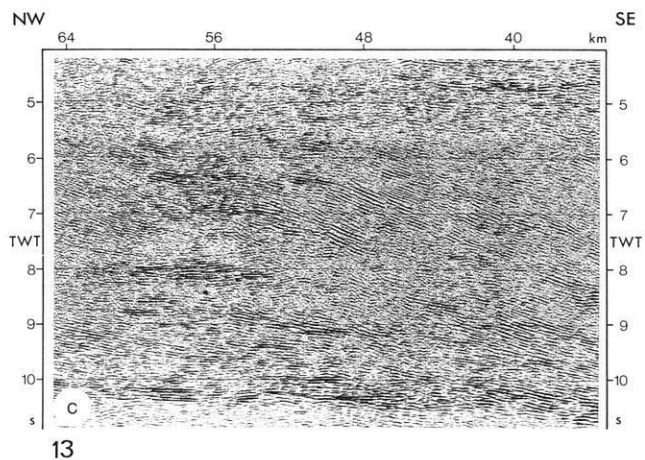
As on line KTB 8502 NE of the FL, NE-dipping reflections cross a broad band of subhorizontal reflections between 2.5 and 4.0 s TWT. These subhorizontal reflections are related to the EB. At the SW end of the section, again, strong synformal reflections appear at 2.5–4.0 s TWT. Their structure parallels the base of the Permo-Carboniferous, but they are certainly not multiples.

The Moho is represented by an antiformal band of reflections between 9.5 and 11.0 s TWT indicating an anticline in the centre of the profile, similar to that on profile KTB 8502.

KTB 8504

On line KTB 8504 (Fig. 23) the strongly structured morphology of the sedimentary trough west of the FL is apparent. Its basement is related to the base of the Permo-Carboniferous and shows two pronounced highs in the northern half of the profile and a remarkable depression in the SE at about 1.8 s TWT, corresponding to approximately 3 km depth.

At the NW end of the section strong reflectors appear at 2.0–2.5 s TWT, dipping SE. Their structure has no rela-



Figs. 13–16. Profile DEKORP 4; part of migrated section (see Fig. 6)

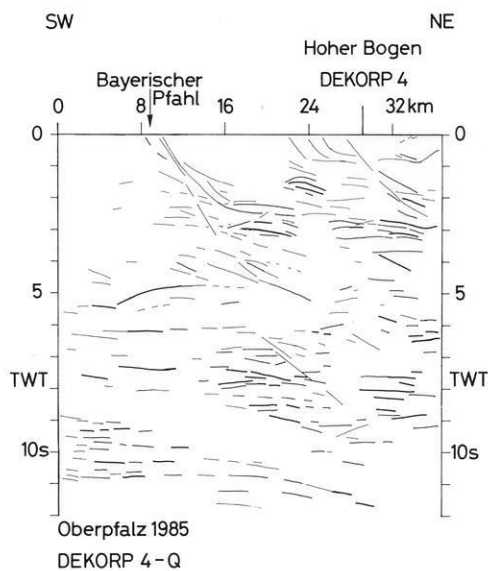


Fig. 17. Profile DEKORP 4-Q; line-drawing of the migrated section

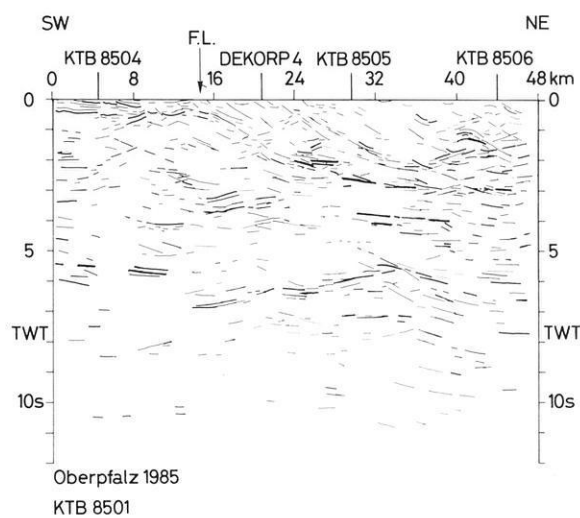


Fig. 18. Profile KTB 8501; line-drawing of the migrated section

tion to the base of the sediments. In the SE half of the profile below the sedimentary basement, another sharply pronounced synformal structure is observed approaching the basement at the intersection with line KTB 8502 and reaching its maximum depth at about 3.5 s TWT. A broad band of reflections follows from 3.5–5.0 s TWT, extending

from the SE end of the profile to about its centre. It might correspond to the SW extension of the EB, but this is mere speculation at this stage of the investigation. The range below is nearly void of reflections except for a small part at the utmost SE end between 9 and 10 s TWT, corresponding to the Moho level.

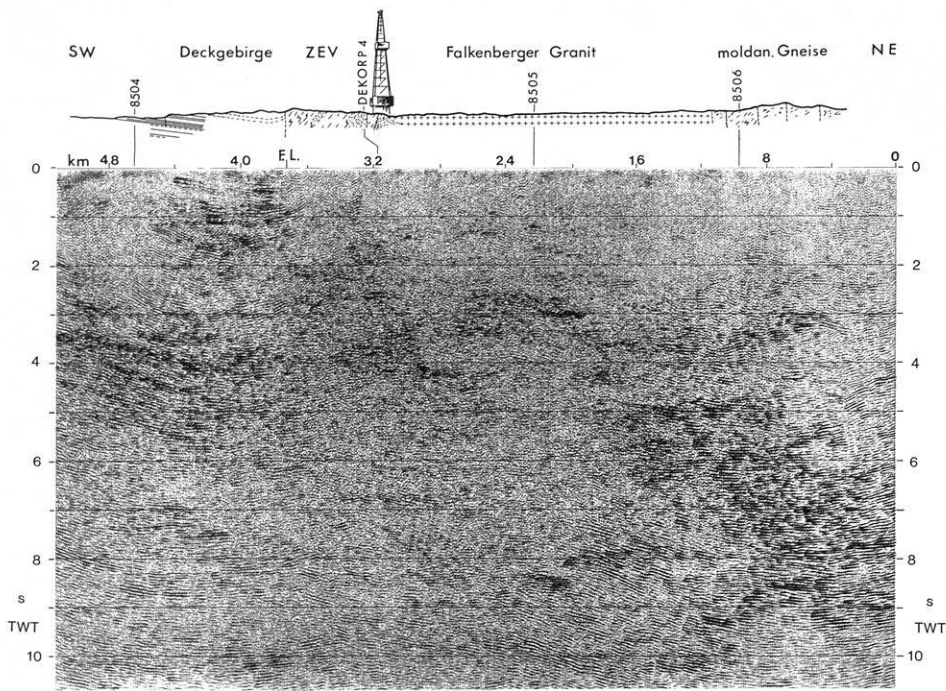


Fig. 19. Profile KTB 8502; migrated section

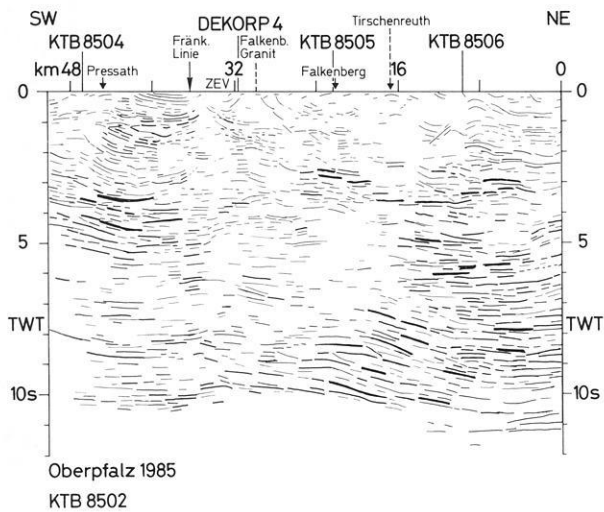


Fig. 20. Profile KTB 8502; line-drawing of the migrated section

KTB 8505

Profile KTB 8505 (see line-drawing in Fig. 24) is characterized by SE-dipping events crossing the entire crust. In the SE part a pronounced rhombic structure with an internal imbrication (“Schuppenkörper”) is observed at 2.5–4.0 s TWT, passing over into a subhorizontal strong reflector (Fig. 25). This pattern is related to the EB observed on line DEKORP 4 at a somewhat deeper level but with a similarly remarkable shape.

Beneath the EB – contrary to the observation on DEKORP 4 – a great number of SE-dipping and subhorizontal reflections show up over the range from 4.0 to 10.5 s TWT.

The Moho is represented by a flat band of reflections between 9.5 and 10.5 s TWT.

Generally, the seismic pattern is in close accordance with the structures found on line DEKORP 4, exhibiting

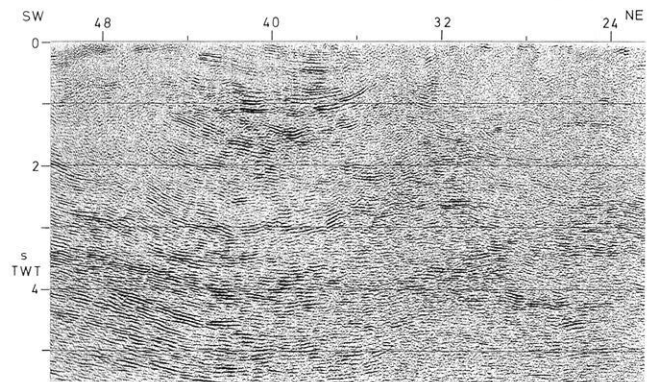


Fig. 21. Part of profile KTB 8502; migrated section

the steeply SE-dipping structures and the wedge-like shape of the EB as well.

KTB 8506

This line (line-drawing Fig. 26) differs from the other cross-strike profiles in showing a pronounced and nearly continuous SE dip all along the line.

Many SE-dipping reflections of great strength can be observed coherently over a long distance, crossing the crust from the uppermost to the lowermost parts. In the near-surface range, SE-bending events correspond to listric fault planes (Fig. 27).

Again, in the SE part of the profile a strong imbricated structure appears between 2.5 and 4.5 s TWT, overriding the SE-dipping band of reflections (Fig. 28). The reflection seismic correlation of these features along the network of seismic lines implies that this “Schuppenkörper” is also part of the EB. Thus, a lateral extension of this body in the Variscan direction, of at least 32 km, can be derived.

In contrast to the other two parallel lines, the Moho is only poorly recognizable. It is suspected at about 10.5–11.0 s TWT, corresponding to 31.5–33.0 km depth.

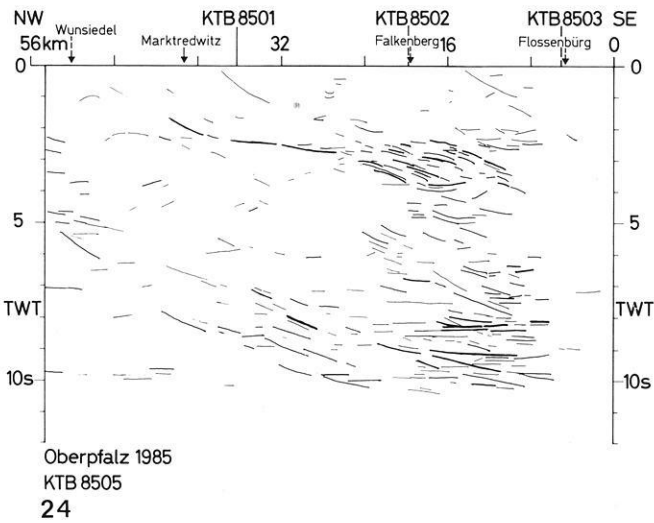
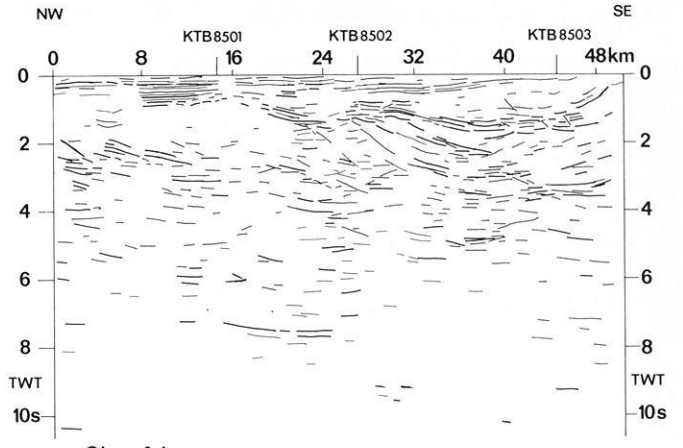
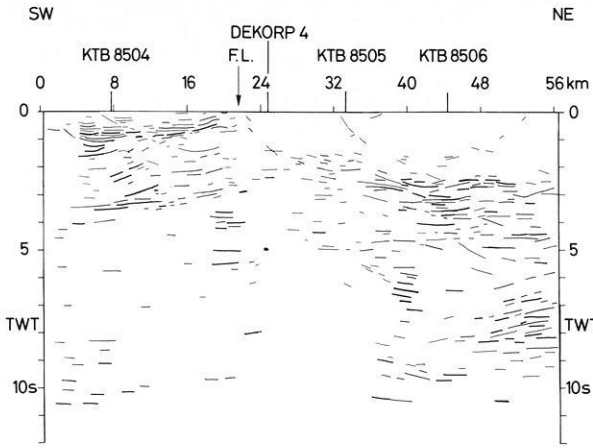


Fig. 22. Profile KTB 8503; line-drawing of the migrated section

Fig. 23. Profile KTB 8504; line-drawing of the migrated section

Fig. 24. Profile KTB 8505; line-drawing of the migrated section

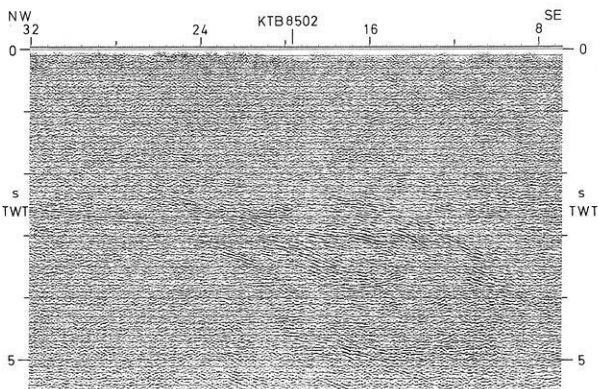


Fig. 25. Profile KTB 8505; part of migrated section with the Erben-dorf body

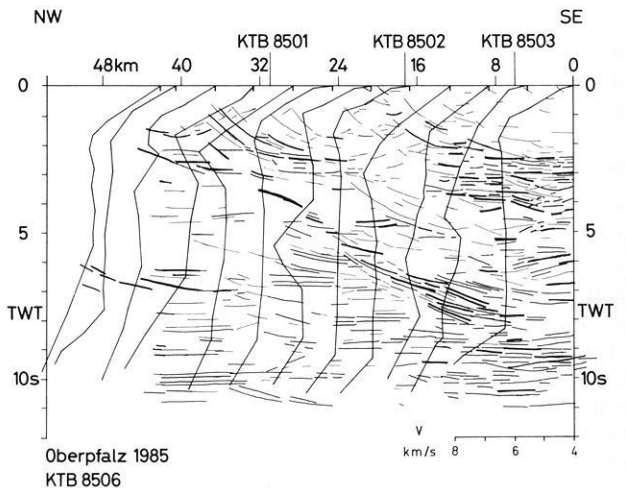


Fig. 26. Profile KTB 8506; line-drawing of the migrated section with interval velocities from DMO-processed stacking velocities

The line-drawing of Fig. 26 simultaneously presents the velocity-depth functions for profile KTB 8506 which have been derived from the DMO processing and which can be regarded as more reliable than velocity information derived from other routine processing techniques applied to deep reflection seismic data (cf. Section 2.2). The resulting veloci-

ty distribution is essentially similar to that obtained by wide-angle data along the parallel DEKORP 4 profile (Section 4).

Figure 29 shows an arrangement of line-drawings with the most important reflection elements of the parallel lines DEKORP 4, KTB 8505 and KTB 8506. The EB is indicated

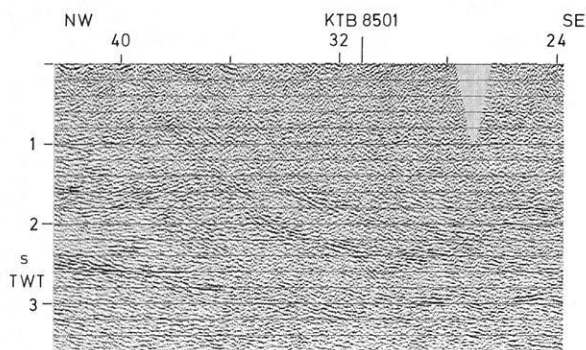


Fig. 27. Profile KTB 8506; part of migrated section with listric shear planes

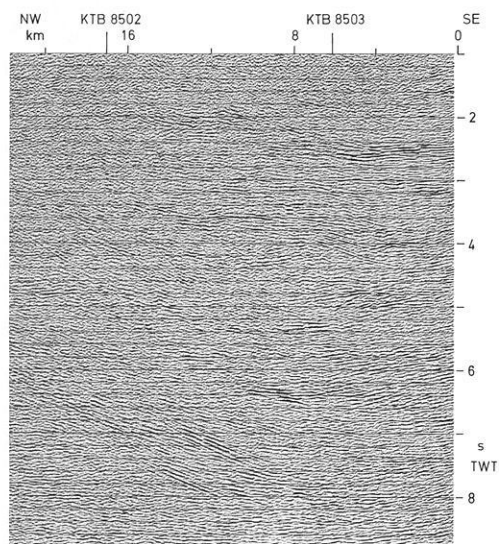


Fig. 28. Profile KTB 8506; part of migrated section with Erbdorf body and dipping reflections in the upper and lower crust

by the shaded area. Its size and extension on the three cross-strike lines and the dominance of the SE-dipping elements is clearly defined.

Results from first arrivals and shot-hole logging

Geological shot-hole logs served to complement general geological information when setting up the geological section along the centre part of profile DEKORP 4. Refractor velocities derived from first arrivals agree qualitatively with major lithologies as found in shot holes. The ZEV may serve as an example (Fig. 30). Here, refractor velocities above 6000 m/s confirm the massive occurrence of amphibolite in the northern half of the ZEV, whereas velocities in the diaphthoritic shear zone at its southern margin drop sharply to less than 4500 m/s. Within the Hoher Bogen complex at the southern end of DEKORP 4, refractor velocities may even reflect different amphibolite varieties. The rise of a refractor with 6300 m/s to less than 50 m below the surface seems to confirm a narrow zone of suspected eclogites and/or ultramafics within the "Gabbroic Amphibolite" (Fig. 31). Schistose fine-grained amphibolites (GAm) of presumably lower bulk density and larger V_p anisotropy (Christensen, 1965) show consistently lower refractor velocities than the coarse-grained amphibolites (Gb).

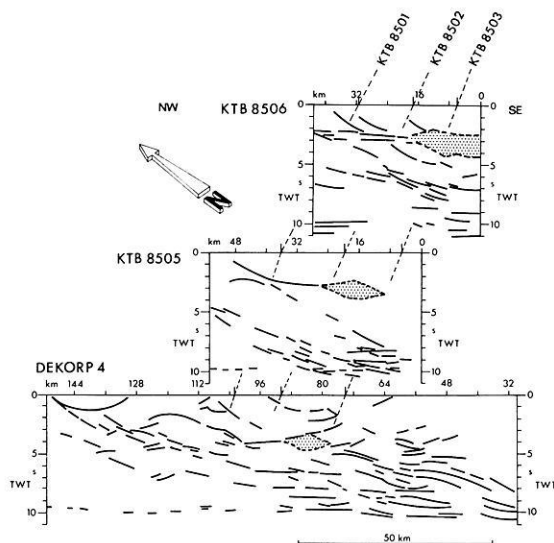


Fig. 29. Arrangement of line-drawings with the prominent elements of lines DEKORP 4, KTB 8505 and 8506. Hatched – Erbdorf body

One-dimensional velocity models from first arrivals on profiles KTB 8501–8504 were used to infer depths to the pre-Permian basement in the foreland basin SW of the FL. The modelling was hampered by the seismic spread being too short relative to the depth of the pre-Permian unconformity in the southern half of KTB 8504. This problem was partially overcome by additional observations of first arrivals from vibrator points at larger offsets. Reflection times calculated from the refraction data fit the reflection pattern fairly well so that the computed depth of the basement is believed to be correct within 10%. At the SW end of profile KTB 8503 the results are in agreement with a depth contour map of the basement derived from a number of wells (Helmkamp et al., 1982).

The results are shown in a block diagram (Fig. 32). They indicate high relief of the floor of the Permian basin, with troughs and highs probably extending parallel to the older Variscan trends. Permo-Carboniferous basin fill may reach 2.5 km in the Weiden area. These findings are in general agreement with earlier gravimetric models (Fuchs and Soffel, 1981). The relief was buried at the end of the Permian so that Triassic and probably Jurassic strata blanketed all earlier structures SW of the FL (Leitz and Schroeder, 1985). Post-Jurassic sedimentation and inversion produced shallow synclines and anticlines trending roughly NW/SE. They show up clearly in the reflector pattern: a brachyanticline on profile KTB 8501; a syncline with remnants of Upper Cretaceous on KTB 8502 and a part of the Kaltenbrunn antiform (Leitz and Schroeder, 1985) on KTB 8504 close to the intersection with KTB 8503. Only on profiles KTB 8501 and 8503 does the post-Cretaceous inversion seem to have appreciably overprinted the older basement topography by high-angle faults, apparently supporting contraction subperpendicular to the foreland basin axis.

3.3 Depth contour maps

Figure 33 shows the map of the base of the EB using the previously indicated correlation. For depth inversion, a mean crustal velocity of 6.0 km/s was assumed (see Section 4.2). Northwest of the dashed line, indicating the boundary

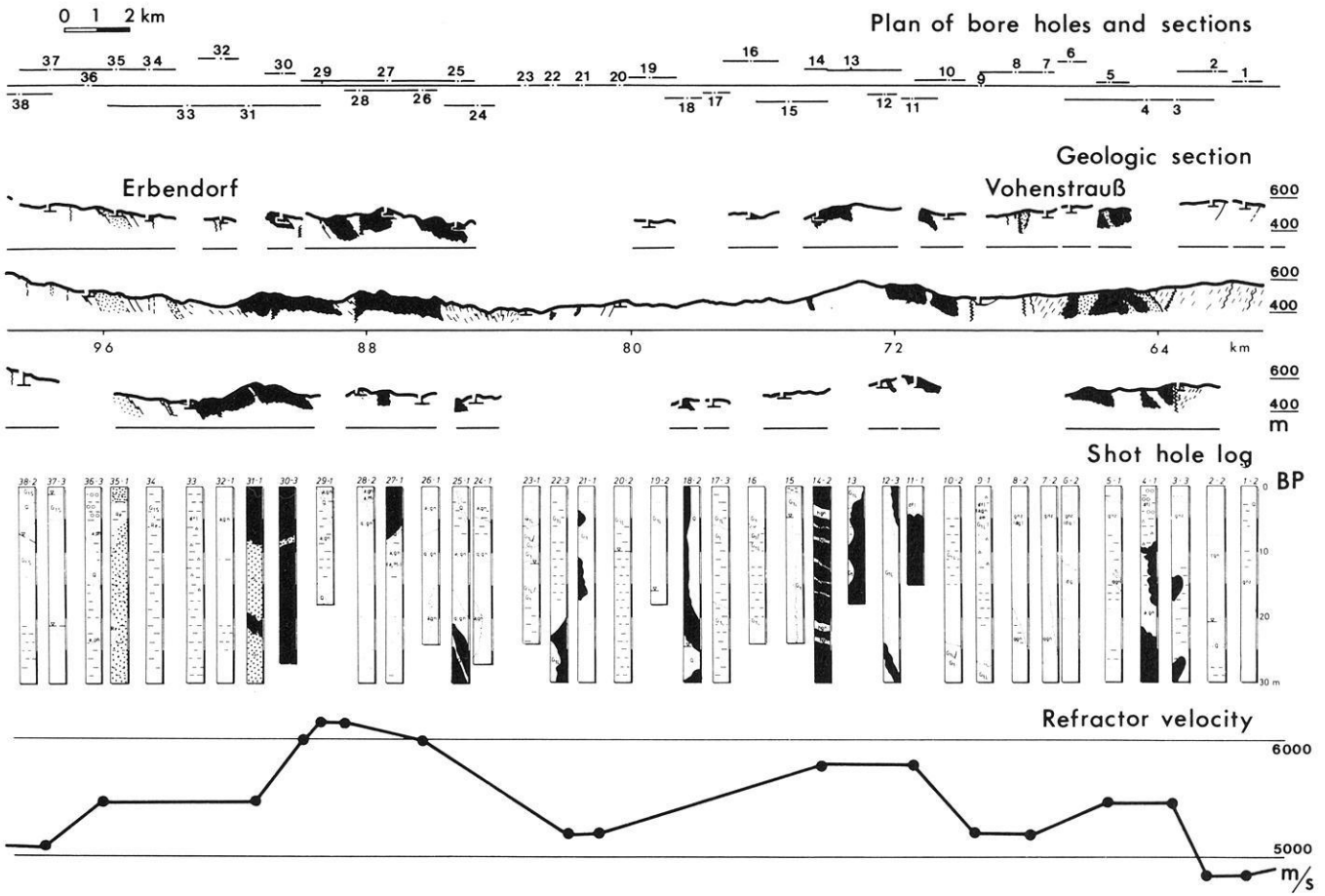


Fig. 30. Correlation of lithology and refractor velocity in the ZEV segment of DEKORP 4; *black* = amphibolite, *dots* = serpentinite, *dashes* = gneiss, *blank* = granite

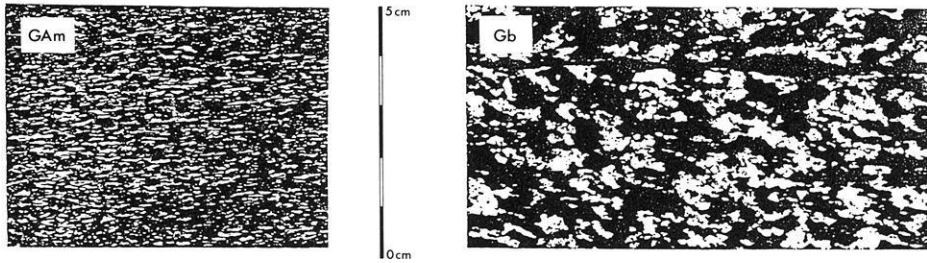
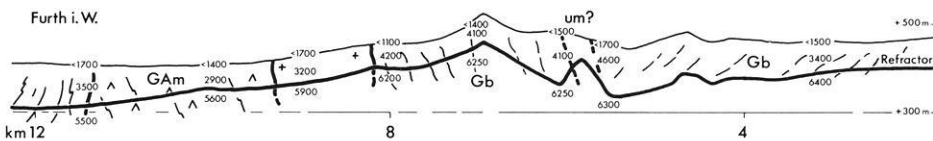


Fig. 31. DEKORP 4, southern end (Hoher Bogen amphibolite complex). *Top*: characteristic textures of amphibolites; *bottom*: geological section and velocities from first arrivals. Note: refractor velocities near 5600 m/s correspond to schistose amphibolite (GAm) of Hoher Bogen complex, velocities around 6200 m/s reflect gabbroic amphibolite (Gb); *um* = suspected ultramafics



of the EB, the mapped horizon represents the possible “master décollement”. The character of the reflections in the corresponding parts of the profiles is due to uncertainties: in the NW part of KTB 8506 two different décollement planes seem to be present, differing in depth by about 2.5 km. The depth of the shallower plane is indicated by numbers in square brackets.

In this interpretation the mapped horizon is intersected by several NW- to SE-striking reverse faults. Generally,

the horizon dips from NW to SE; on line DEKORP 4 its highest position is north of the intersection with KTB 8501 and another maximum occurs between KTB 8501 and 8502 near the drilling location.

The question of whether the EB continues west of the FL cannot be answered with the present data. However, at the appropriate depth range, good reflecting horizons occur. Their structural position is indicated by the symbols for a synform axis. This axis runs between KTB 8501 and

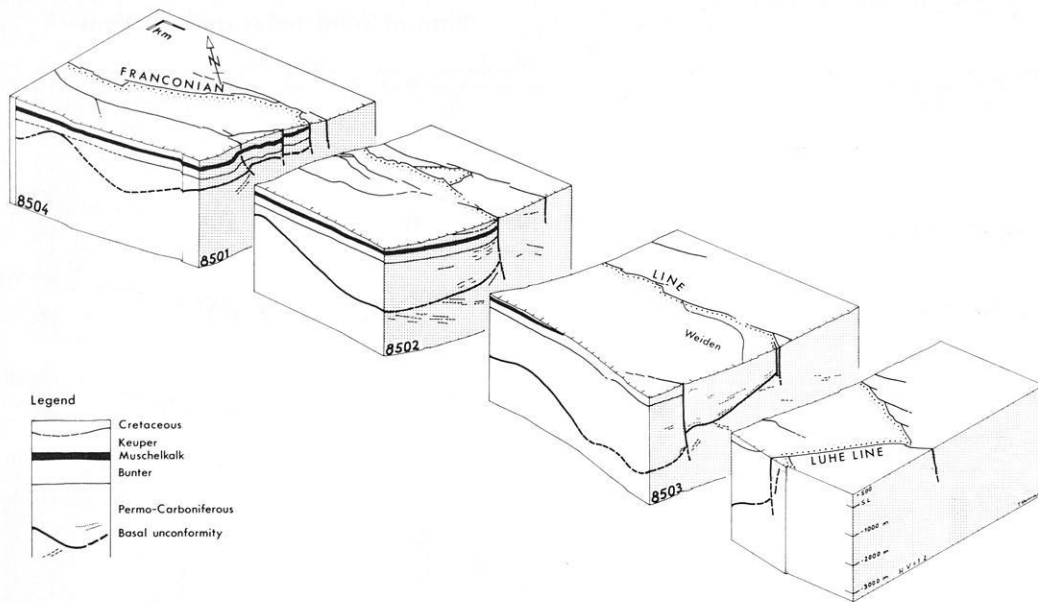
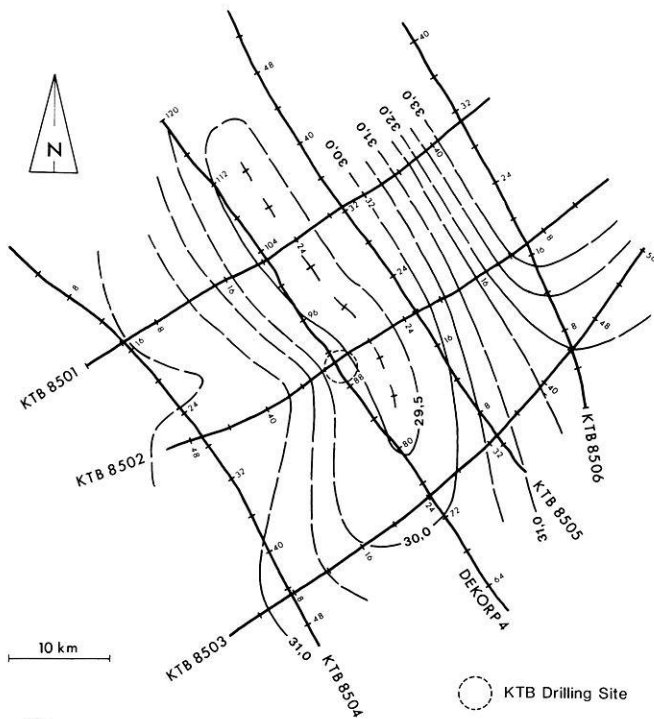
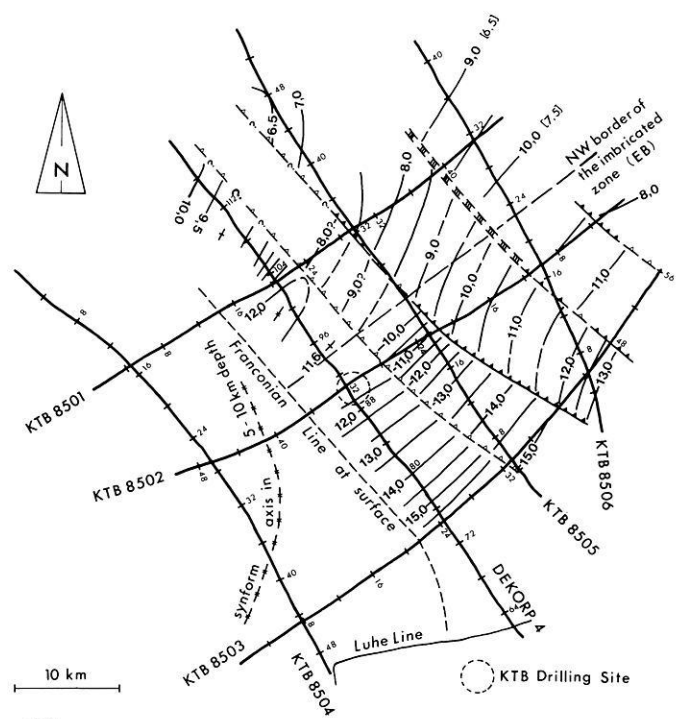


Fig. 32. Block diagram of Permo-Mesozoic foreland basin SW of Franconian Line. Mesozoic structure constrained by depth contour maps and boreholes Wollau and Parkstein (Haunschild and Schröder, 1960; Schröder and Siegling, 1966; Gudden and Schmid, 1985; Emmert, 1981)



33

Fig. 33. Depth contour map of the Erbdorf body base and the corresponding décollement plane (depth in km, $V_{\text{average}} = 6$ km/s)



34

Fig. 34. Depth contour map of the Moho (depth in km, $V_{\text{average}} = 6$ km/s)

8502 in a NW/SE direction, changing, however, north of KTB 8503 (NW of the Luhe Line) into a SW direction.

Figure 34 shows an attempt at a depth contour map of the Moho, again using a mean crustal velocity of 6.0 km/s. The dominating NW- to SE-striking anticlinal axis is based essentially on KTB 8502. Along the remaining profiles, speculative supplements were partly necessary. In the area of the drilling location the Moho presents a high with its axis striking NW/SE and changing north of the Luhe

Line into a S-to-SW (?) direction similar to the syncline axis of Fig. 33.

At the intersection of profiles DEKORP 4 and KTB 8502, i.e. close to the location of the KTB borehole, the true position in space and the true dip have been computed for such reflecting elements whose components of dip could be determined along both profiles (Fig. 35). There are two main azimuths of tectonic directions; NW/SE and SW/NE. The elements dipping NE probably derive from several

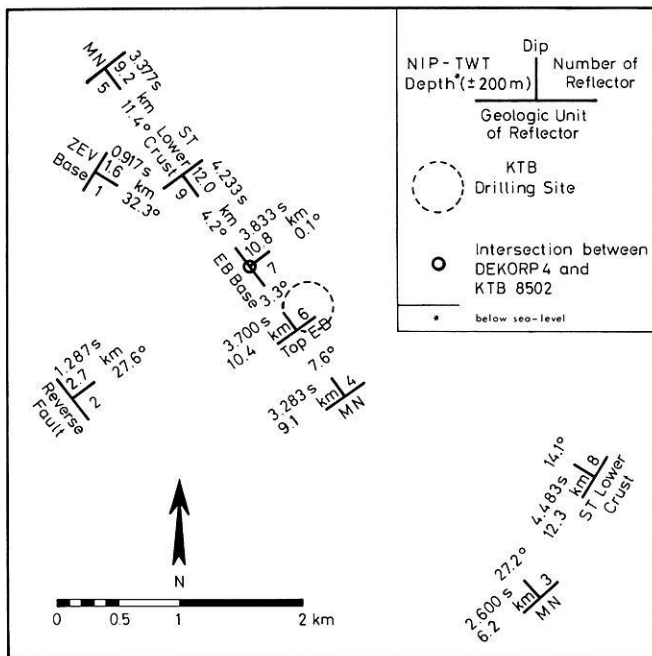


Fig. 35. True incidence and true position of the common reflection points of the intersecting lines DEKORP 4 and KTB 8502

faults, and not from lithological boundaries. A detailed discussion on these elements is given in Section 5.

4 Accompanying seismic surveys and their first results

4.1 Field techniques

In addition to the Vibroseis near-vertical reflection survey, a series of 96 borehole shots with charges of 90 kg and

1-km spacing was fired in the north-western part of the DEKORP 4 line. These shots were used for three different supplementary programs:

1. For mapping wide-angle reflections from the upper crust by means of the contractor's 200-channel reflection spread operated at 42–58 km offset
2. For mapping lower-crustal and Moho wide-angle reflections with a mobile array of 24 3-channel MARS stations at 60–90 km offset
3. For two expanding spread experiments with mid-points in the Moldanubian and Saxothuringian zones

The observational scheme is shown in Fig. 36. Shots moved 4 km/day from shotpoint 1 near Vohenstrauß towards the northwest, while the contractor's spread and the MARS array (operated by university teams from Berlin, Clausthal, Frankfurt and München) followed at constant mean shot-to-receiver offset. The expanding spread equipment with a total of 120 channels from the universities of Clausthal, Hamburg and Kiel, and from BGR/NLFB Hannover, moved with the same velocity in the opposite direction to keep common midpoints stationary.

The shots were fired in the late afternoons, after the daily Vibroseis work. With some exceptions, especially in dry and hard rocks, their seismic efficiency was sufficient and the noise level at the recording sites was low enough to yield good seismograms up to maximum distances of 100 km.

4.2 Results of the wide-angle reflection survey

Figure 37 shows a detailed location map of the shotpoints and the MARS stations. The shot-to-receiver midpoints are plotted in Fig. 38. They cover 100 km of the DEKORP 4 line and cross the tectonometamorphic boundary between the Saxothuringian and the Moldanubian units of the Var-

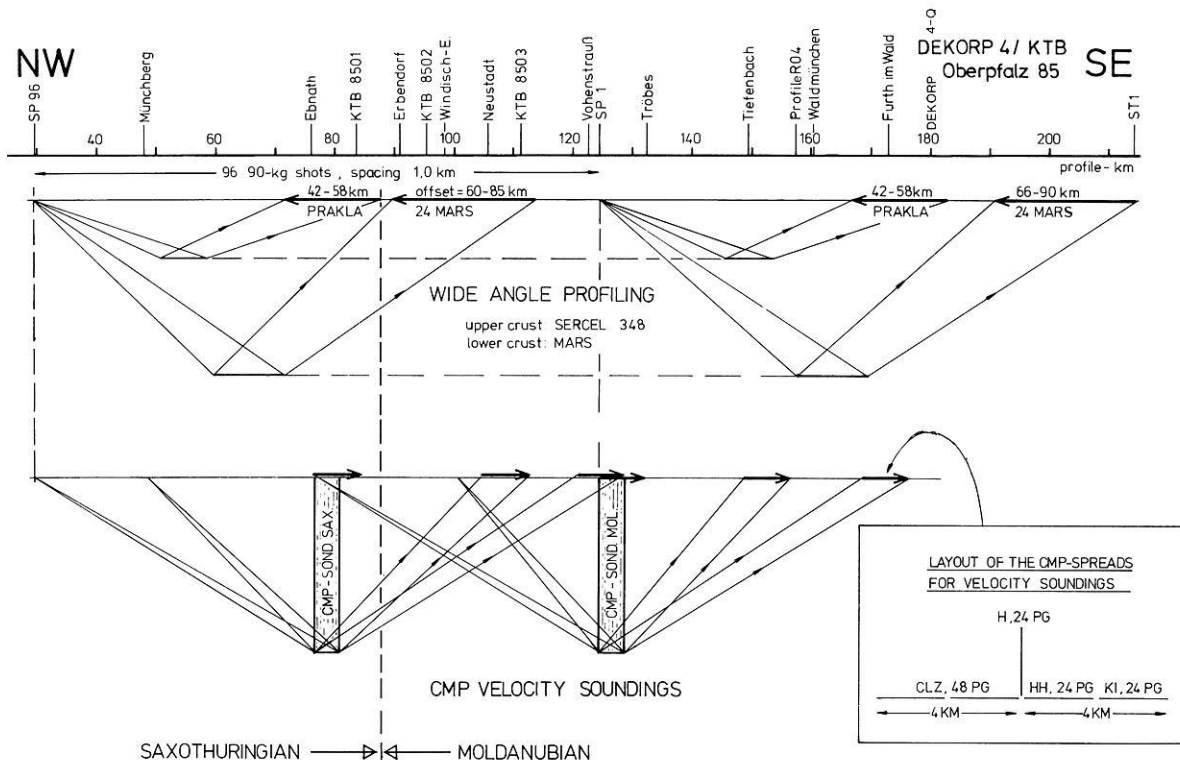
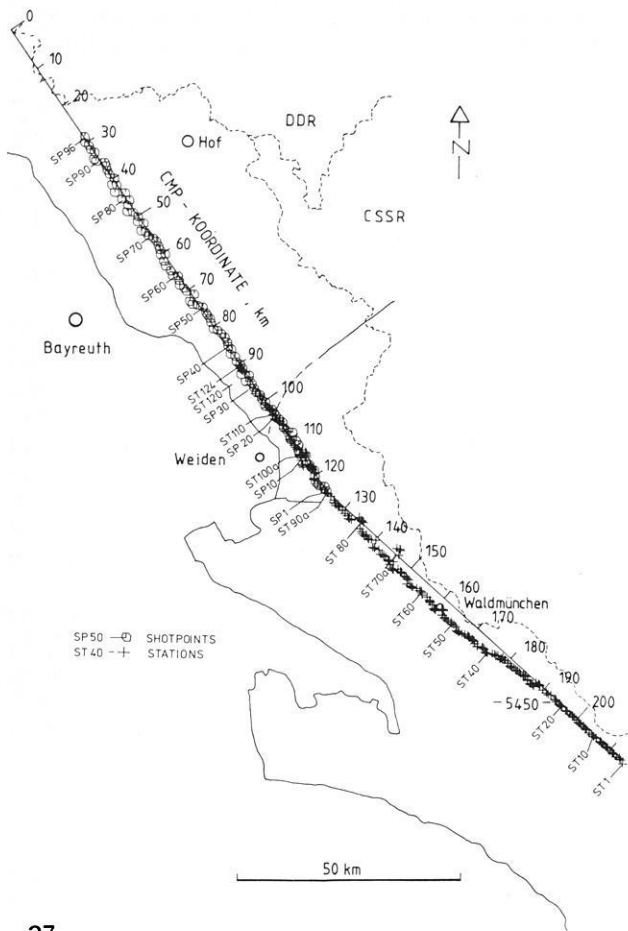
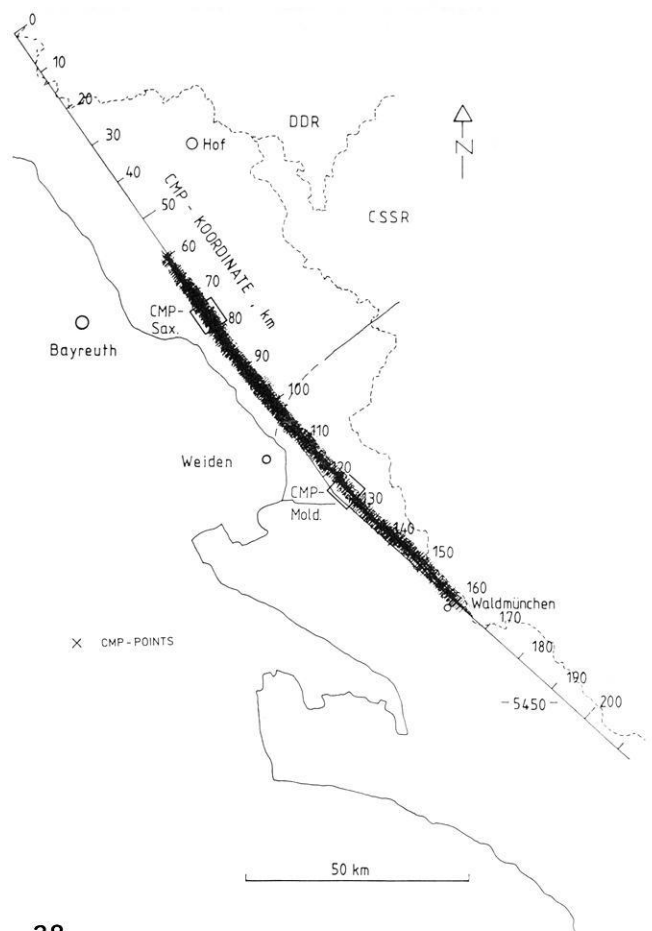


Fig. 36. Observational scheme of the wide-angle seismics, Oberpfalz 1985



37

Fig. 37. Location map of the shotpoints and MARS stations for the wide-angle mapping along DEKORP 4



38

Fig. 38. Location map of the shot-to-receiver midpoints (CMP) for the MARS wide-angle mapping. The CMP points for the velocity soundings (Section 4.3) are situated in the rectangular areas with centres at profile km 76 and 126

iscides. The CMPs of the expanding spread observations are indicated by open squares in Fig. 38. CMP locations are characterized in this section by a linear southeasterly increasing CMP coordinate, the origin of which is the northwestern end of the DEKORP 4 reflection line.

Due to the multiple coverage, the wide-angle reflections can be processed and presented in different ways. In the following, particular use is made of the common-midpoint (CMP) and common-offset (COF) sorting possibilities. CMP sorting suppresses the influence of dip and is therefore particularly suitable for velocity analysis, whereas COF sorting is particularly suitable for structural imaging.

Indications showing an unusual distribution of seismic wave velocities in the investigated area had already been obtained from regional refraction seismic surveys (KTB, 1986, p. 113). Wide-angle mapping combined with DEKORP 4 should serve to investigate this phenomenon, both in detail and in the regional context. A small part of the comprehensive observation material is given in Figs. 39 and 41–43 for the constant-shotpoint (CSP) and COF configurations.

Figure 39 shows three single shot observations in the 42–58 km distance range with predominant wave propagation in the ST, in the ST/MN boundary domain and in the MN. Structural changes become obvious along the

DEKORP 4 line, which with examination of the CMP sections in Fig. 41 a and b becomes even clearer. Immediately after the P_g first arrivals, which were clearly observed over about 60 km both in the ST and the MN with apparent velocities of about 6 km/s, complicated wave groups follow which cannot be individually resolved using the wide-angle seismics method but which must be interpreted as indications of a small-scale heterogeneous structure of the upper crust. The boundary domain between profile km 80 and 110 (Neusorg-Weiden) deviates from this by two important features:

1. The first arrivals terminate at a distance of 40–50 km, which implies a relatively shallow position of a low-velocity zone (LVZ) in the upper crust.

2. In the distance range of 40–70 km with reduced travel times of 1.5–0.5 s, an unusually intensive and well-correlatable wide-angle reflection appears (in Fig. 39, centre, indicated by P_gP), with apparent velocities up to 8 km/s.

This prominent wide-angle reflection, that had already been found during regional surveys by means of quarry blasts, is caused by a crustal domain at a depth of 8–13 km, the Erbendorf body (EB), that is also characterized in near-vertical angle seismics by an unusually high reflectivity (Figs. 6 and 11). Its NW/SE extension is best recognized in the CMP sections (Fig. 41 a and b) and the COF sections

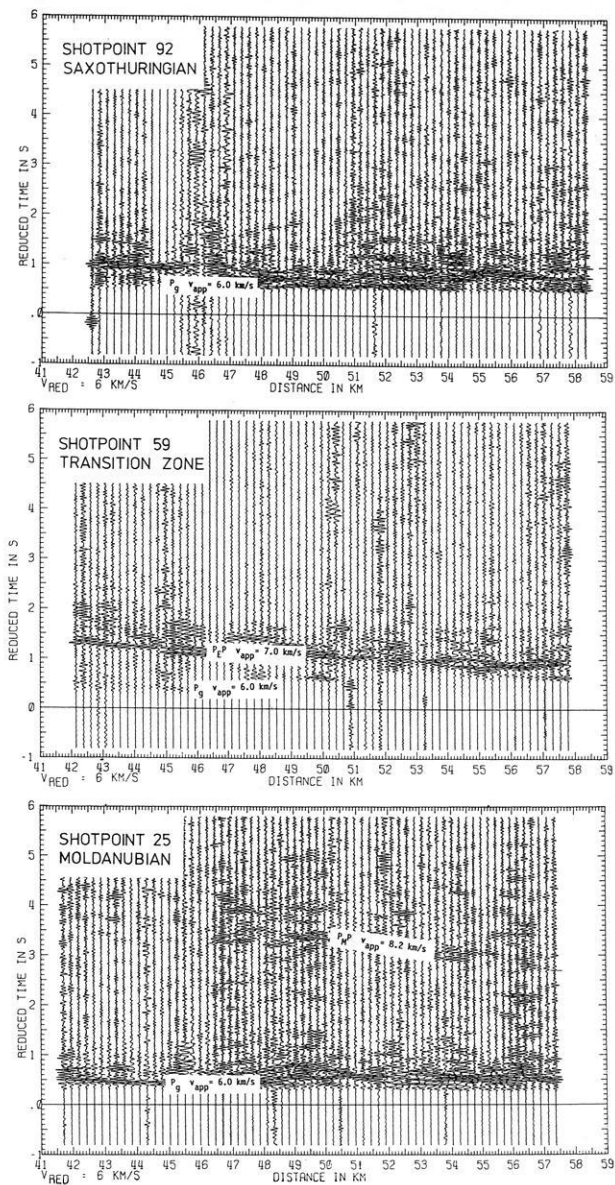


Fig. 39. Single-shot playbacks for the ST (SP 92, *top*), the MN (SP 25, *bottom*) and the boundary domain between them (SP 59, *centre*), reduced by 6 km/s. In the ST and in the MN, clear P_g first arrivals with apparent velocities of approx. 6.0 km/s can be observed in the distance range shown, followed by complicated, non-resolvable wave groups. In the boundary domain, the P_g first arrivals terminate at about 46 km and, with a clear gap in time, are followed by a pronounced wide-angle reflection $P_E P$ with apparent velocities of about 7.0 km/s

(Fig. 42a and b). Figure 41a and b gives a selection of 6 sections from a total of 46 CMP sections, in which that part of the profile between 60 and 150 km is covered at 2 km intervals (Fig. 37). The wide-angle image of the EB appears most clearly at CMP points 86–96; Fig. 41a, bottom, shows a typical example. CMP 84 (Fig. 41a, centre) and CMP 98 (Fig. 41b, top) indicate the margins beyond which the EB cannot be traced by wide-angle seismics.

Clear $P_i P$ reflections originate from the deeper crust at km 92 as separate phase groups (in Fig. 41b, centre, with reduced travel times between 2 and 3 s) and approaching the MN, Moho reflections ($P_M P$) occur more frequently. Between 102 and 106 km, the latter are characterized by

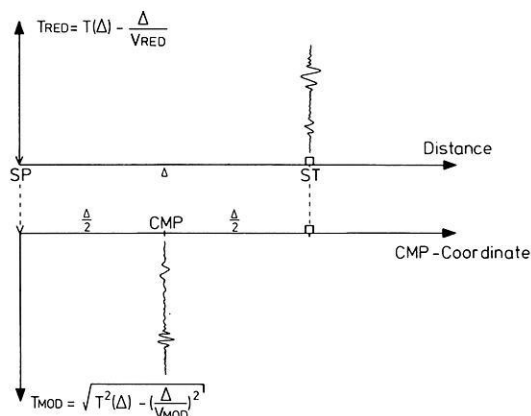


Fig. 40. Comments on the principle of presenting CMP and COF wide-angle sections: With common-shotpoint or common-receiver point sections the seismograms are usually plotted against the observation distance (offset) with reduced time T_{red} in the upward direction. CMP sections are represented in the same way, except that these are seismograms for shotpoints and receiver points with a common midpoint (CMP). On the other hand, in COF sections seismograms for source-receiver pairs with equal offset (constant offset) are plotted against the centre-point coordinates with modified time T_{mod} in the downward direction

apparent velocities up to 10 km/s even in the dip-insensitive CMP sections, from which (in connection with reversed observations) a SE dip of the Moho up to 10° must be concluded. In the MN proper, the CMP sections show a heterogeneous, but not clearly structured, upper crust, now and then good $P_i P$ reflections from the middle crust (top of the lower crust?) and usually clear Moho reflections (e.g. CMP 130 in Fig. 41b).

Crustal structuring becomes more clearly recognizable in the COF sections (Figs. 42a–c, 43). The construction principle of these constant-offset sections is explained in Fig. 40. Basically, zero-offset sections have been simulated by dynamic correction of COF wide-angle seismograms, corresponding to the dynamic correction of normal seismic reflection data. The near-surface domains cannot be resolved because of the minimum observation distance of 40 km; hence, the time scale for the “modified time” T_{mod} , that corresponds to the two-way travel time in the near-vertical sections begins at 2 s.

Figure 42a shows COF sections for 47 and 53 km offset. In both presentations, which are based on completely independent sets of data, the EB can be recognized as the dominant structure in the upper crust (between profile km 83 and 98 and between 3.5 and 5.0 s modified time). The wide-angle reflections outline an antiformal structure that continues in the NW and SE to deeper crustal levels. Figure 42b shows the EB focussed from other observation distances. The images are not completely identical and also deviate in some detail from the near-vertical reflection seismic image. The reasons are the dependence of reflectivity on the angle of incidence and the unknown detailed velocity structure. The general coincidence underlines the significance of the EB phenomenon.

The middle and lower crust are only inadequately resolved by the small offsets of 47 and 53 km. However, by enlargement of the aperture (COF 72 and 82 km, Fig. 42c), structures at greater depths can also be imaged. It appears that there is a further reflector below the EB with $T_{mod} =$

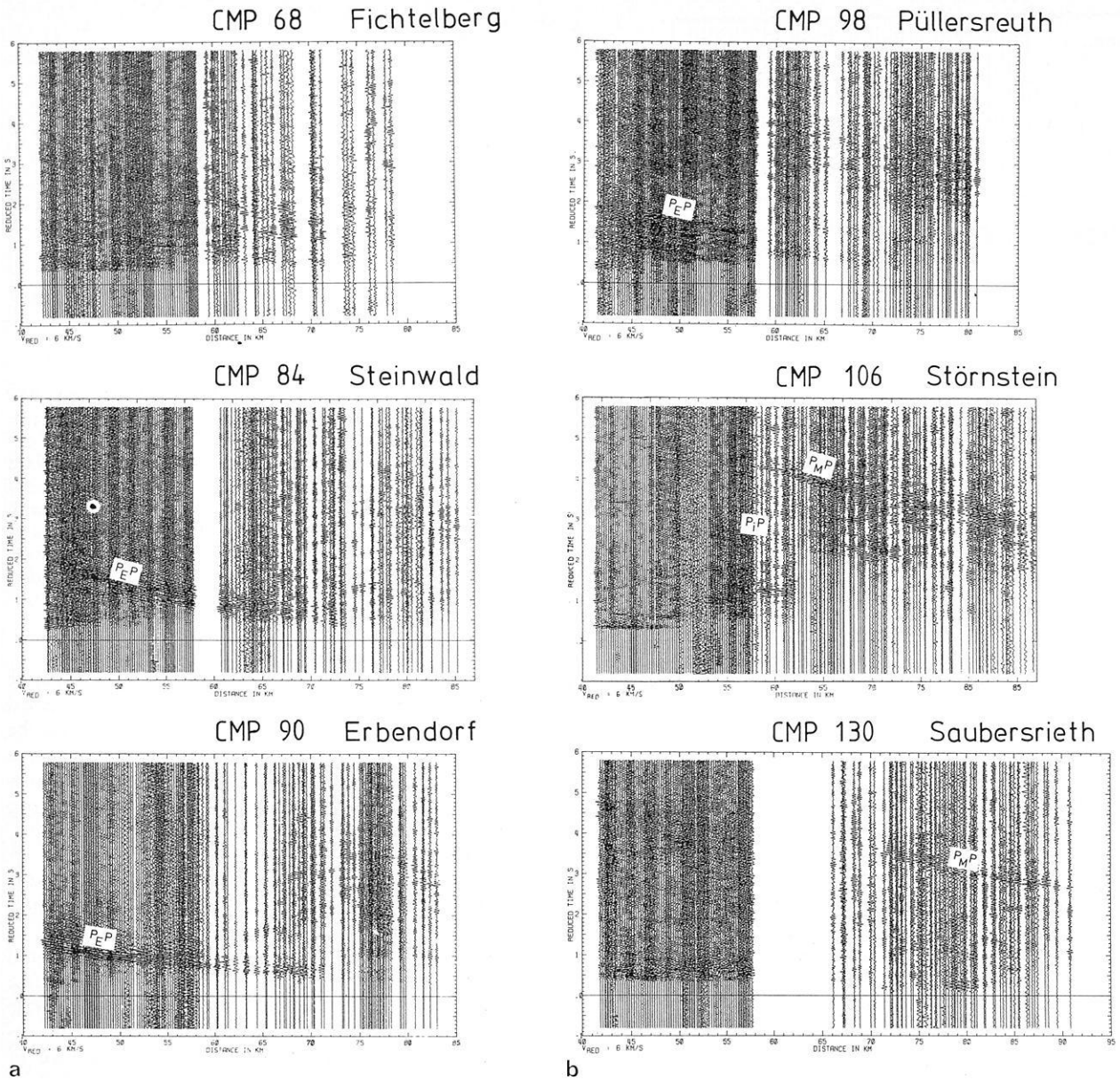


Fig. 41 a and b. Sequence of 6, from a total of 46, CMP sections between the Fichtelgebirge and Oberpfälzer Wald. The CMP gathers shown are derived in each case from an interval of ± 1 km around the given nominal value. CMP 68, Fichtelberg: heterogeneous crustal structure difficult to resolve by wide-angle observations; CMP 84, Steinwald: the EB starts to appear; CMP 90, Erbdorf: clear wide-angle reflection of the EB, high apparent velocities (up to 8.0 km/s) and large amplitudes in the 42–70 km distance range; CMP 98, Püllersreuth: splitting of the EB wide-angle reflection into three diffuse bands; after about 3 s reduced travel time, the typical wide-angle image of the heterogeneous lower crust; CMP 106, Störnstein: LVZ indicated by termination of the P_g branch; relatively clear P_iP reflections from the lower crust; Moho reflection with CMP apparent velocity of 10 km/s indicates Moho dipping to the SE; CMP 130, Saubersrieth: P_g onsets up to 80 km, no clearly structured crust but good Moho reflections

7.0–7.5 s (a depth of approximately 23 km) that presumably marks the top of the lower crust. Accordingly, the EB cannot represent an updoming of the lower crust. If the EB consists of lower-crustal material – both its characteristic reflection behaviour and its velocity advocate this – it must have been brought into its present position by overthrust tectonics (see Section 5).

In Fig. 42c, particularly at COF 82, the Moho is clearly recognized. It rises from the SE towards the NW. However, the rise is not continuous but consists, rather, of small-scale undulations and possible imbrications in the lower crust. Similar structures are imaged by near-vertical seismics (see Fig. 6). A high of the Moho is indicated below the ST/MN

boundary domain, but simultaneously the character of the Moho is also more diffuse.

A similar processing of the S waves (Bopp, 1986) likewise shows the rise of the Moho from SE to NW and – surprisingly – the Moho high in the ST/MN boundary domain even more clearly than the P waves (Fig. 43). On the other hand, it is worth noting that the lower crust, which is clearly imaged by the P waves (Fig. 42c), is hardly recognizable in the S waves. Sandmeier and Wenzel (1986) have reported similar observations in the Black Forest. This supports the assumption that this could be a general phenomenon of the lower crust.

A first two-dimensional velocity model was established

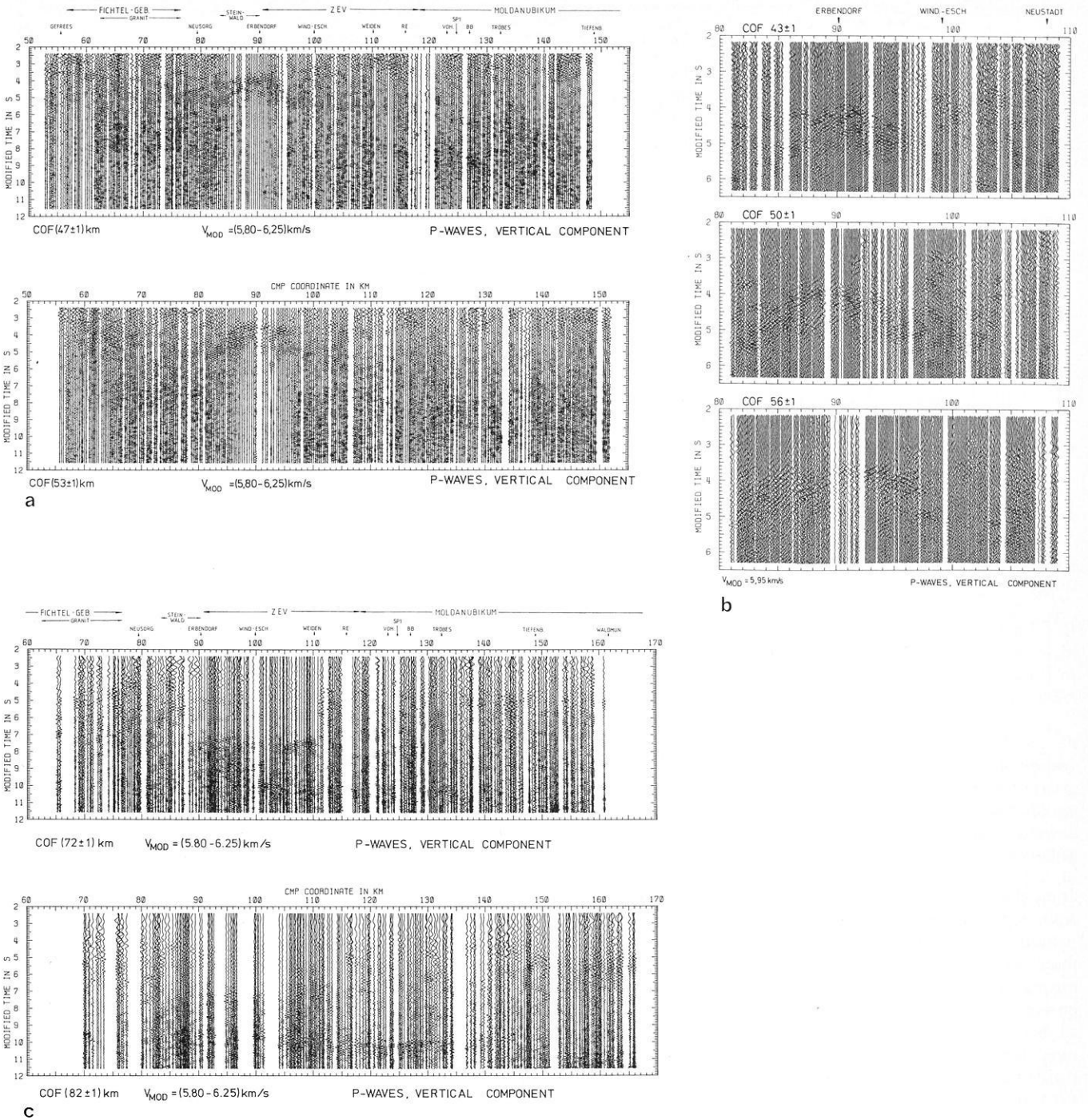


Fig. 42. **a** Dynamically corrected COF sections obtained from observations with the contractor equipment at (47 ± 1) km, *top*, and at (53 ± 1) km, *bottom*. The EB can be recognized as the dominant structure in the form of an updoming with its centre at profile km 90. The *transparent area* below the EB is an artefact of the seismogram normalization with regard to uniform maximum amplitude; in fact the amplitudes of the reflections from below the EB are not unusually small, but rather the EB reflects unusually strongly. Structures in the lower crust cannot be resolved by the selected offsets (in contrast, see Fig. 42c). A linear relationship from 5.8 km/s at $T_{mod} = 2$ s to 6.25 km/s at $T_{mod} = 12$ s is assumed for the correction velocity V_{mod} ; **b** The vicinity of the EB imaged by three different wide-angle COF sections; in this case a constant value of 5.95 km/s was applied as the correction velocity. The influence of the offsets and the different angle of incidence, respectively, cause different results; **c** Dynamically corrected COF sections, obtained from MARS observations at distance intervals (72 ± 1) km, *top*, and (82 ± 1) km, *bottom*. Through these offsets, the lower crust (at about 7 s) and the Moho (at 10–11 s) can be imaged, whereas the upper crust can no longer be resolved. Below the EB, the lower crust appears at a depth of about 23 km

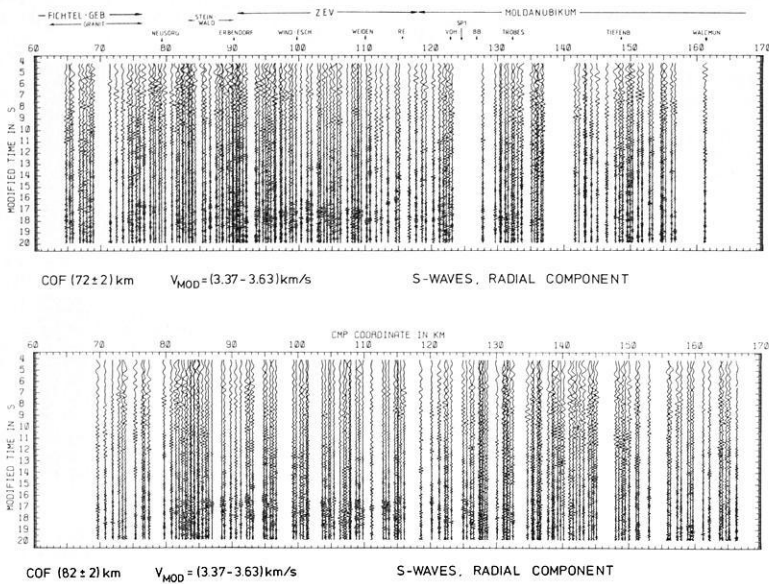


Fig. 43. Dynamically corrected *S*-wave COF sections for offset ranges 72 ± 2 and 82 ± 2 km. The time scale and the correction velocity V_{mod} have been chosen so that the same image should result as in Fig. 42c if the V_p/V_s relation in the whole crust were 1.72. However, the lower crust is, surprisingly, not imaged by the *S* waves, whereas the Moho in the ST/MN boundary domain becomes more clearly recognizable as an updoming than through the *P* waves

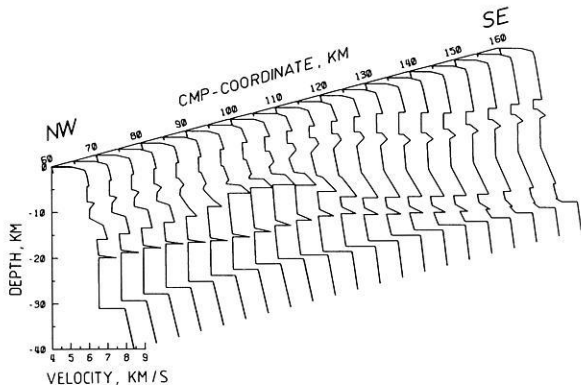


Fig. 44. Two-dimensional velocity model for the DEKORP 4 profile between profile km 60 (Gefrees) and 160 (Waldmünchen). Velocity-depth functions at intervals of 5 km

along the DEKORP 4 line on the basis of the previously explained qualitative findings and a large number of velocity analyses from CMP wide-angle sections and reversed observations, as well as results of earlier work (Stroessenreuther, 1982). The model was improved iteratively by extensive ray-tracing computations; the interpretation has not yet been completed. Nevertheless, the travel times of the most important wave groups in the essential parts of the profile have already been satisfactorily explained, i.e. within ± 0.1 – 0.2 s. Thus, the velocity model of Fig. 44 can, in essence, be regarded as well founded. The velocity modelling to obtain this two-dimensional velocity distribution has been performed with a new technique (Gebrande and Bopp, in preparation).

Superposing the velocity-depth functions, converted to two-way travel times, over the line-drawing of the near-vertical seismics is very informative; the result (Fig. 45) shows a remarkable coherence between the structural elements and the seismic velocities.

In view of the decision to sink the KTB borehole in the immediate vicinity of Erbdorf, particular importance is attached to the EB. To explain the high apparent velocities of the wide-angle reflections that were observed in CMP and CSP sections, as well as in sections with common receiver points, the EB was modelled as a high-velocity body

with *P*-wave velocities between 7.0 and 7.5 km/s, with its top at a depth of about 12 km (Fig. 44). Through the computation of synthetic seismograms, Sandmeier and Wenzel (personal communication) have shown that the chosen velocity distribution also explains the high amplitudes of the wide-angle reflections observed. However, this does not mean that a proof has been furnished therewith for the existence of a high-velocity body. Sandmeier and Wenzel (personal communication) have also shown that, theoretically, a stack of dipping lamellae with alternating velocities of 5 and 6 km/s can also produce the observed high apparent velocities and amplitudes. In fact, a lamination, as otherwise typical for the lower crust, is quite probable from the near-vertical reflection seismic image of the EB, especially on profile KTB 8505 (Fig. 25). However, the dips necessary for such lamellae models cannot be confirmed by the wide-angle image.

In detail, the velocity analyses of wide-angle seismics for the area around Erbdorf (CMP 90) show stronger heterogeneity (Fig. 46) than the relatively smooth velocity model of Fig. 44. Different results for slightly deviating travel-time correlations and various methods of inversion (Fig. 46) show that such details cannot be reliably resolved from wide-angle travel times. Nevertheless, it is worth noting that interval velocities above 7 km/s at depths of 12.5–13.5 km (the thick curve in Fig. 46) also result from investigations by Gebrande and Bopp (in preparation). The existence of high rock velocities, which are observed elsewhere in the lower crust only, thus becomes highly probable for the basal part of the EB. Whether tectonically displaced lower-crustal material is actually involved can certainly not be decided solely through observations at the surface.

The velocity model presented in Figs. 44 and 46 contains the entire inventory of crustal seismic structural elements in the upper 15 km: high- and low-velocity zones, discontinuities and gradient zones; that lamellae zones exist is highly probable. The significance of the observation data leads one to expect that the essential structural elements are particularly clearly developed in the location area. These are favourable prerequisites for obtaining extensive new knowledge about the true nature of seismic inhomogeneities and reflectors in the crystalline basement through the KTB.

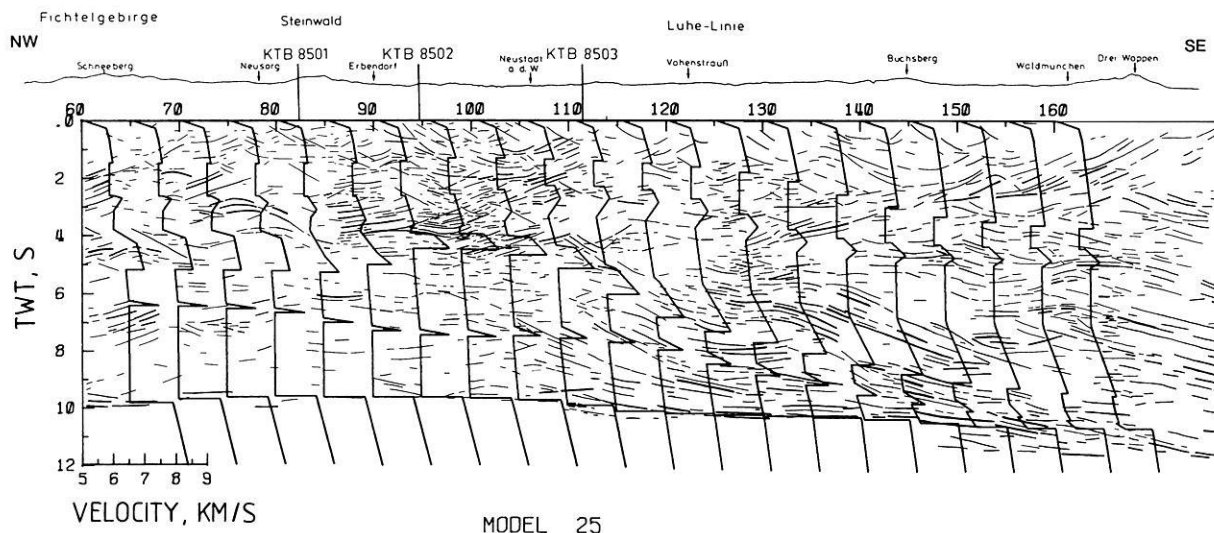


Fig. 45. Superposition of the velocity-depth functions of Fig. 44, converted to two-way travel time on the line-drawing of near-vertical seismics from Fig. 6

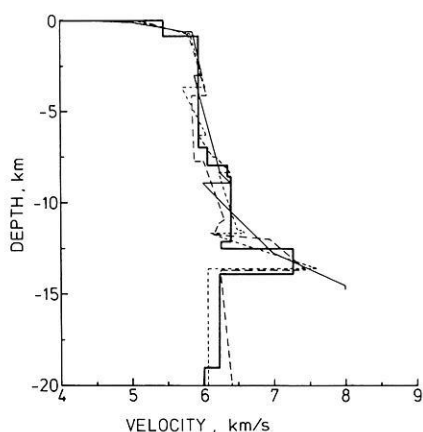


Fig. 46. Velocity-depth functions that were obtained for CMP 90 according to different interpretation techniques and for slightly differing travel-time correlations. The bandwidth of the solutions gives an idea of the resolving power of wide-angle seismics in the upper crust. All solutions have velocities larger than 7 km/s in the lower part of the EB at depths of 12–13 km

4.3 Results of the expanding spread experiment

The data of these experiments (see Section 4.1; Fig. 36) were sampled at 4 ms over the record length of 40 s. A bandpass filter of 5–32 Hz was used, the dominant signal frequency being around 20 Hz. For the interpretation of P waves, the record length was reduced to 20 s. Problems for data processing and interpretation were low signal/noise ratios, insufficient statics information, varying frequencies and wave forms (due to different equipment and coupling effects) and the very heterogeneous crust in the vicinity of the boundary between MN and ST. Thus, the chance of destroying signals by stacking of adjacent traces was quite high. Therefore, a special technique was applied using the “energy” characteristics of traces: squared amplitudes were normalized with regard to the maximum energy per trace. Subsequent mixing and smoothing by use of two moving windows over five traces and 80 ms resulted in the energy sections shown in Fig. 47. First arrivals can be ob-

served very clearly up to a distance of about 60 km in the southern part (MN). After some near-vertical reflection bands (P_c) from the lower crust in the offset range 20–55 km, the Moho reflection (P_mP) appears really strong in the near-vertical and wide-angle range.

In the northern part (ST) clear first arrivals can be observed up to a distance of 65 km. Here, only one strong reflection band (P_c) appears in the lower crust. In addition, there are weak indications for upper-crustal reflections and the P_mP .

Using squared amplitudes and moving windows, the picking of exact arrival times becomes difficult. Therefore, an “energy controlled gain” (ECG) was applied to the original traces (Bittner, in preparation). Due to this procedure, phases and arrival times are not distorted. Figure 48 shows the effect of this processing to selected parts of the seismogram sections from the ST domain (top) and the MN domain (bottom). A clear improvement is obvious: now several reflections can be followed after the first arrivals.

Figure 49 gives the results of a 1-dimensional interpretation consisting of a direct inversion of first arrivals combined with RMS velocities derived from x^2/t^2 values using the reflections of the entire sections shown in Fig. 47. In order to gain 2-dimensional velocity information, common-shot gathers (CSG) were constructed from single shots along the profile and 2-dimensional ray tracing was used. This investigation is not finished, yet, but first estimations were included in the 1-dimensional velocity-depth structure. Figure 50 shows the interval velocities derived from 1-D and 2-D inversions for the two ESPs.

For both ESPs a low-velocity zone appears in the depth range 5–10 km, but which is more pronounced in the MN. Comparing these two velocity-depth functions, there are no “typical” structures for the Moldanubian and Saxothuringian. A separation into upper and lower crust is not obvious. The mean velocities of the whole crust are identical: 6.25 km/s. The two ESP velocity-depth functions are similar, but not identical, to the 2-dimensional model of Fig. 44 at the appropriate locations. The high-velocity body has about the same depth and thickness in both interpretations; it is to be correlated with the observations of the EB at the KTB drilling site between the two ESPs.

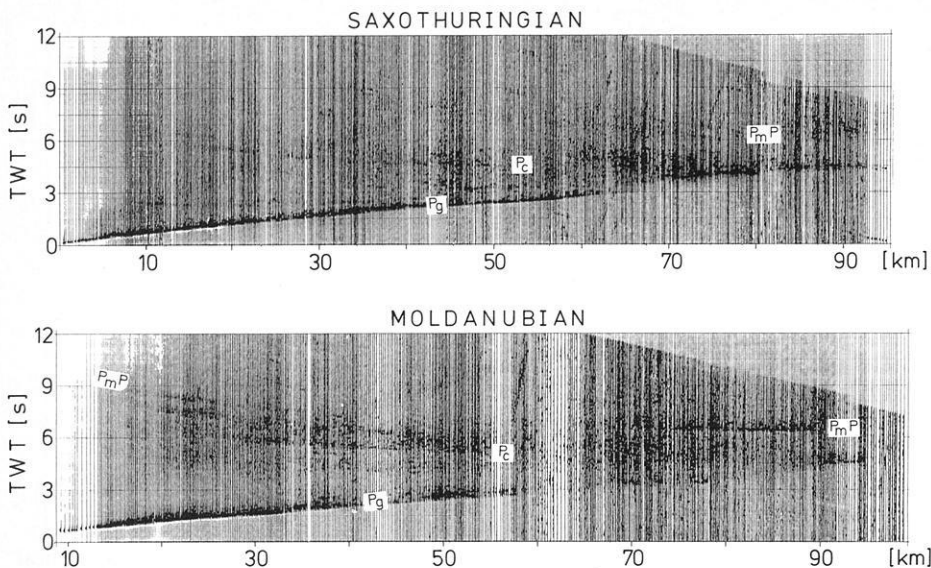


Fig. 47. Energy sections for the Saxothuringian (*top*) and the Moldanubian (*bottom*); time coordinate reduced by 8 km/s. For these sections, squared amplitudes and a moving window over five traces and 80 ms was used

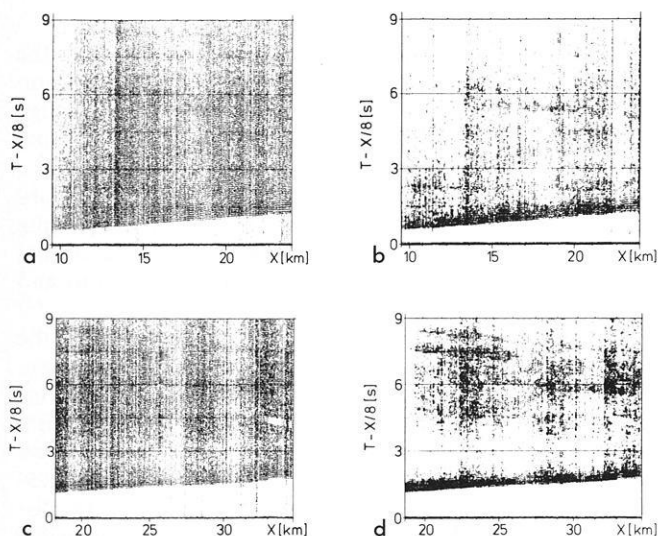


Fig. 48a-d. Original traces (**a, c**) for the ESP of the Saxothuringian (*top*) and the Moldanubian (*bottom*). Corresponding “ECG” traces (**b, d**) of the two corresponding ESPs. An energy controlled gain was applied by multiplication of the original traces (**a, c**) with the energy traces. Phases and arrival times are not distorted

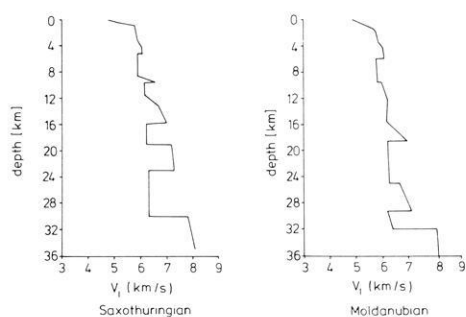


Fig. 50. Computed interval velocities for the two CMPs (*left*: Saxothuringian; *right*: Moldanubian). 1- and 2-dimensional inversion methods were used

5 Attempt at tectonic interpretation

5.1 General introduction; the northern part of DEKORP 4

SE-dipping reflectors are present in all NW/SE reflection seismic profiles (DEKORP 4, KTB 8504–8506). These reflectors confirm the extensive overthrusting of Moldanubian crust onto Saxothuringian crust interpreted from the geology at the surface: the ST/MN boundary is a tectonic suture zone (Fig. 51).

There are also NW-dipping reflectors, particularly on the DEKORP 4 profile. These reflectors, together with sub-horizontal reflectors occurring in various sections of the seismic profile, can be interpreted in several ways.

At first glance, the following structural units can be recognized on the DEKORP 4 profile (see Fig. 51). The MM and ZEV nappes clearly form bowl-shaped structures. The base of the synformal MM is more distinct than that of the ZEV. This can be explained by the fact that the gneisses of the MM are underlain by anchimetamorphic sediments; whereas the ZEV rocks, at least in their southern part, rest upon Moldanubian gneisses of similarly high metamorphic grade. In the anchimetamorphic sediments of the Frankenwald northwest of the MM there is a reflection horizon at about 1 s TWT which passes southeastward under the MM and can be correlated with the boundary between Upper-Devonian (Frasnian) spilites and the overlying late-Devonian and Lower-Carboniferous sediments.

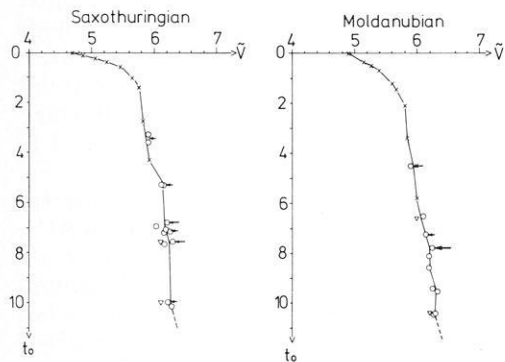


Fig. 49. RMS velocities derived from x^2/t^2 values using the reflections observed on the energy and ECG sections. *Crosses*: direct inversion of first arrivals (1-D); *circles*: RMS velocities from x^2/t^2 values; *triangles*: optimum stacking velocities from stack tests; *arrows*: dip corrections, computed from the migrated section of DEKORP 4 (RMS velocities divided by the cosine of the dip angle)

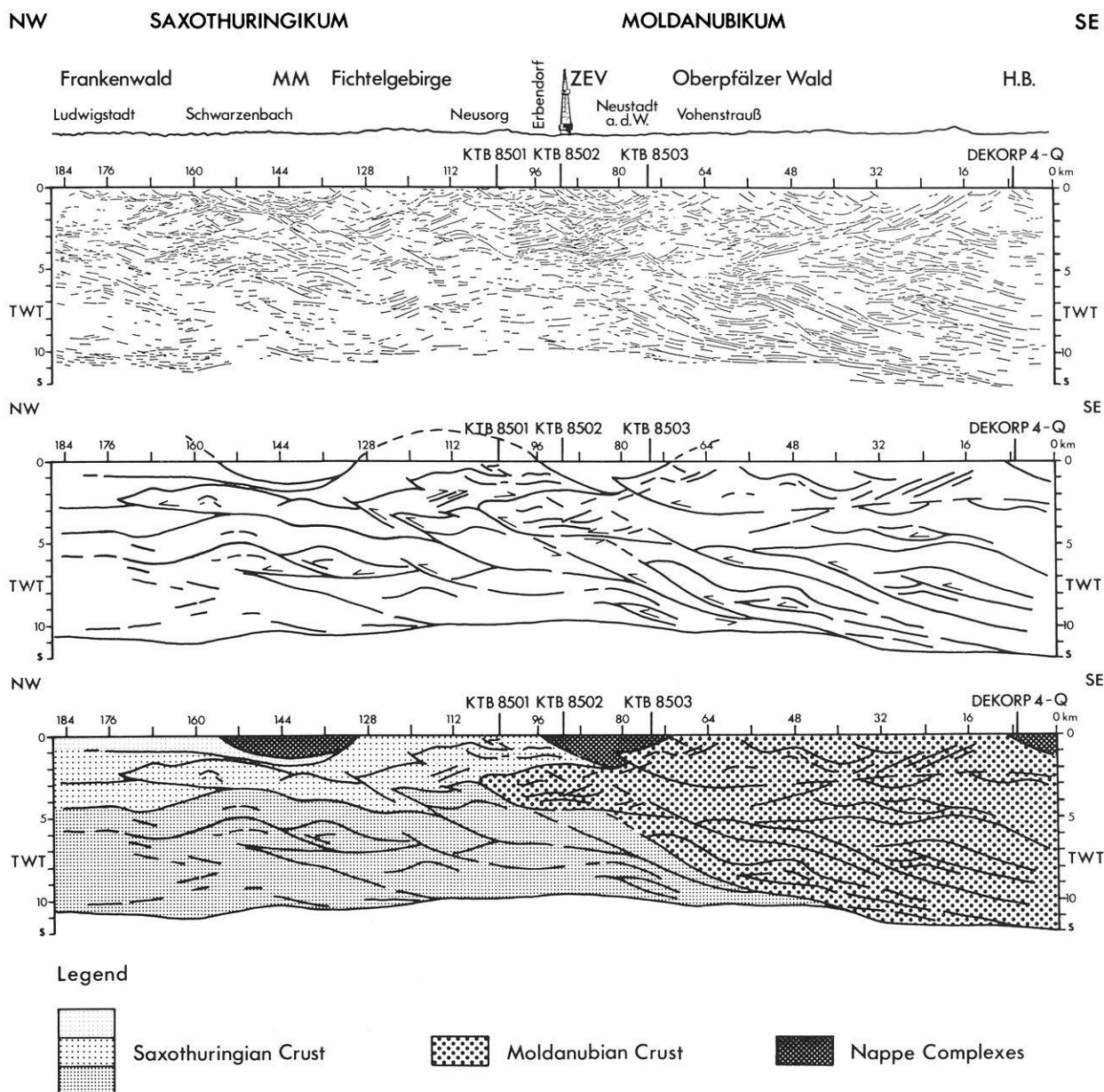


Fig. 51. Line-drawing of profile DEKORP 4, derived from the migrated and coherency-filtered section (top). Centre and bottom: preliminary structural model based on the line-drawing. MM – Münchberg Massif; ZEV – Zone of Erbendorf-Vohenstrauß; HB – Hoher Bogen

The ST region at middle- and upper-crustal levels is characterized by extensive, slightly asymmetric pre-deformed structures with a dominance of SE-dipping reflectors. Under the MN region this dominance of SE-dipping reflectors increases very clearly. On the other hand, in the upper-crustal levels a structural discontinuity can be recognized, starting at the base of the EB and continuing to the southeastern end of the section. Above this discontinuity NW-dipping reflectors and extensive previously deformed structures dominate, especially in the south.

There are several possibilities for interpreting these structures. In the line-drawings in Fig. 51 not only can the MM, ZEV and HB nappes be recognized, but MN and ST crust can be differentiated as well.

A subdivision of the ST crust into three different layers is attempted. The uppermost layer at the northwestern end

of the section represents the anchimetamorphic sediments of the Frankenwald above the prominent reflector at about 1 s TWT, i.e. above the presumed Frasnian spilites. The second layer is formed by the supposed equivalents to the Early-Palaeozoic to Upper-Proterozoic (?) metasediments of the Fichtelgebirge below the spilites. At the NW end of the profile, the third relatively homogeneous crustal level with predominantly SE-dipping reflectors is indicated below 4 s TWT. Possibly a pre-Variscan basement is reached here, whose Variscan overprinting by NW-vergent folding and thrusting increases clearly to the SE.

The anticlinal structure under the northwestern part of the Münchberg nappe complex (at about km 150) is presumably a more or less autochthonous structure. This is supported by a correlation with the SW-plunging Hirschberg-Gefell Anticline at the surface. Support is also offered

by the fact that this anticlinal structure, whose NE-striking extension can be traced to the Saxonian Granulite Mountains, is the source area for the Upper-Devonian conglomerates of the Frankenwald (Franke, 1984a). This interpretation is also advocated by the northwestward and southeastward increase in thickness of the metasediments away from the core of the anticlinal structure.

The SE-vergent D_2 folding of the Frankenwald and the Fichtelgebirge is not expressed in the seismic structure of any of the NW/SE profiles. Only in the ST portion of the DEKORP 4 profile down to about 3 s TWT can NW-dipping reflectors, which may be interpreted as SE-vergent structural elements, be recognized.

In the NW section of the DEKORP 4 profile around km 168 these SE-vergent structures can be assigned to the NW flank of the large anticlinal structure under the northwestern MM. Thereby the SE-vergent D_2 folds of the Frankenwald can be interpreted as adventive folds on the NW flank of a very large anticlinal structure, which would then be a D_2 structure. That this structure is, as a whole, NW vergent, is shown by the configuration of the reflectors in the northwesternmost upper part of the structure which can be interpreted as a subhorizontal NW-vergent overthrust (Fig. 51, bottom). This overthrust has displaced the upper part (widely dotted) of the anticlinal core to the northwest relative to the lower part (closely dotted). The asymmetry of the possible duplex structure below 5 s TWT indicates the same direction.

The Vogtland syncline, in which the MM is preserved, is a post-nappe (possibly D_2) structure, whereas the Fichtelgebirge anticline clearly represents a D_3 structure (Stein, 1987). The core of the Fichtelgebirge anticline with the stratigraphically oldest, exposed rocks (Stettner, 1972) coincides with the core of this structure on the DEKORP 4 profile (Fig. 51) at about 110 km. The main elevation of the Fichtelgebirge composed of granites is situated on the NW flank of the Fichtelgebirge anticline. The great extent of granites is indicated, on the DEKORP 4 profile, by a relatively transparent domain between 112 and 128 km and down to 2 s TWT.

5.2 The structure of the Erbdorf area

From the central Fichtelgebirge to the SE, the SE-vergent D_2 deformation gains importance. A possible explanation for this SE-vergent D_2 structure, which is time-equivalent with the peak of metamorphism in the southern Fichtelgebirge, is given by the interpretation of the EB.

If the EB is interpreted as part of the MN crust based on its seismic structures, it extends into the ST zone and must be underlain and overlain by ST rocks (Fig. 51). Thereby the picture of a MN crustal wedge which has penetrated ST crust has developed. This type of wedge tectonics, or flake tectonics in the sense of Oxburgh (1972), is also known from other orogenic belts (Price, 1986; Brown et al., 1986) and explains both the seismic crustal structure and the pronounced SE vergence of the D_2 deformation in the central and southern Fichtelgebirge, as well as the lack of this pronounced SE vergence on the NW flank of the Fichtelgebirge. The MN crustal wedge presumably penetrated into the middle ST crust along a structural or lithological discontinuity between a metasedimentary cover and a pre-Hercynian basement during D_2 deformation.

The relative southeastward movement at the top of this

wedge led to the SE-vergent D_2 folding in the Fichtelgebirge. This movement picture is similar to that of a passive-roof duplex, as described by Banks and Warburton (1986) for Pakistan. At the bottom of the wedge, northwestward overthrusting and southeastward underplating continued during the wedging.

Due to its velocity structure, the basal part of the EB could be composed of lower-crustal material, e.g. of mafic to ultramafic magmatites, or garnet-sillimanite-rich metapelites which can have compressional velocities of over 7 km/s according to Kern and Schenk (1985).

The internal structure of the EB shows SE- and NW-dipping reflections in addition to the predominantly horizontal ones (Fig. 11). A distinct NW boundary cannot be recognized. In Fig. 51 the NW end lies in a relatively transparent zone which conforms to a SE-dipping, ramp-shaped seismic structure. The seismic transparency is possibly the result of a particularly intense internal deformation of this frontal portion of the EB.

Individual tectonic structures can be reconstructed at upper- and middle-crustal levels of the ST part of the profile, using the position and orientation of the reflectors. In the lower crust, however, a relatively homogeneous, SE-dipping structural pattern dominates. Correlation with structures at the surface is not possible. The slightly SE-dipping reflectors which then become horizontal near the Moho are indicative of a flow regime which sustained constant, relative movements between the crust and mantle. This is also true for the lowest MN crust.

The boundary between the ST and MN below the EB is not yet clearly recognizable despite the general differences in their seismic structures. This boundary presumably lies where the relatively transparent crustal zone with mainly low-angle SE-dipping reflectors borders the strongly reflecting crustal zones marked by imbricate fold and ramp structures. The style of deformation of the lower MN crust presumably passed over into the lower ST during the collision process. At the boundary zone, where MN overrode ST rocks, strong imbrication may be assumed.

In the MN there is a structural discontinuity at about 4–5 s TWT, below which SE-dipping reflectors predominate. In the hanging wall, strong NW-dipping reflectors, such as those observed near the EB below the ZEV, occur in addition to subhorizontal, slightly sinuous reflectors (e.g. between km 32 and 56).

These NW-dipping reflectors could be SE-vergent overthrusts genetically related to the SE-vergent D_2 structure of the Fichtelgebirge. Although the SE-vergent D_2 structures at the surface of the Fichtelgebirge are the dominant features, they are hardly expressed in the seismic pictures of DEKORP 4 and KTB 8504–8506. It would be all the more surprising if there were SE-vergent overthrusts in the MN which could neither be observed in the field nor deduced from a geological map in the area of DEKORP 4.

However, SE-vergent structures are widely distributed in the MN and ST of the Variscan orogeny. Thus, it can be imagined, alternatively, that the clearly N-dipping reflectors, which rise from the EB southward to the southern margin of the ZEV, represent S-vergent overthrusts. Southward-directed folding and thrusting has also been proposed for the southern margin of the Tepla-Barrandean in Czechoslovakia (Tollmann, 1982), which can be regarded as an eastward equivalent of the ZEV.

It has been confirmed in the ST and northern MN that the SE vergence belongs to the deformational phase D_2 . In the central and northern ST, the age of the collective D_1 and D_2 deformation is stratigraphically limited to the uppermost Lower Carboniferous (about 320–330 Ma; Franke, 1984a). In the Fichtelgebirge, the syn- D_2 metamorphism has been dated at ± 320 Ma (Teufel, 1987). The shearing which occurred during the emplacement of the Bohemian granulite nappe was dated at ± 341 Ma by van Breemen et al. (1982).

All S-vergent elements appear to be of the same age (within geochronological error bounds) and it is therefore possible that they belong to the same event which is younger than the D_1 deformation in the ST. Since D_1 is doubtlessly N vergent, this would imply a reversal of the direction of overthrusting, as known from other orogenies. During the subsequent deformation, a NW-vergent sense of shear has been resumed (D_3), although with much shorter transport distances. During the indentation stage of collision (D_4), a SW-vergent sense of overthrusting developed (Weber, 1986).

For the geotectonic interpretation of the EB, this would mean that its roof and base were not active at the same time, but that the roof experienced younger backthrusting. This would not be wedge tectonics in the true sense, but would mean that the wedge form was a product of two successive acts of deformations.

From this point of view, the metabasite of the Erbindorf greenschist zone could be interpreted to represent the original, near-surface extension of the EB. The mafic and ultramafic rocks near Erbindorf and their equivalents in the Münchberg units (serpentinites, amphibolites) fit well into this hypothesis. In this sense, the Erbindorf line would be the root zone of the MM displaced southeastward through backthrusting.

However, at least a part of the N-dipping reflectors can be interpreted with concepts other than backthrusting. Comparison with the ZEV (Fig. 52) shows the trend of the metamorphic s-planes in the Moldanubian part of DEKORP 4. The ZEV is bowl-shaped in the seismic profile. In contrast to the MM, the ZEV is not a NE- to SW-striking but a generally NW- to SE-striking D_4 syncline. Correspondingly, in the DEKORP 4 profile the synclinal shape results from SE-dipping reflectors in the northwest, horizontal reflectors in the middle and NW-dipping reflectors in the southeast.

In the area of the Naabgebirge block (NGS in Fig. 52), there is an analogous situation between the Luhe Line and Hoher Bogen. Here, the NW- to SE-striking, SW-vergent structure (D_4 in the MN of the Oberpfalz) gains increasingly in intensity southeastward toward the Bavarian zone. The DEKORP 4-Q profile (Fig. 17) shows that the SW-vergent structure of the Bavarian zone can be correlated with NE-dipping listric reflectors which join at about 3 s TWT into a bundle of prominent, horizontal reflectors. Around the Naabgebirge the arc-shaped strike of the s-planes, which generally dip northeastward, indicates an anticlinal structure in the north, a synclinal structure in the central portion and an anticlinal structure in the south just before Hoher Bogen, a part of the ZTT nappe. This can be regarded as the result of a large-scale undulation of the axis of the generally NW- to SE-striking large-scale fold structure. The large-scale folds seen in the DEKORP 4 profile are clearly recognizable between km 32 and 56.

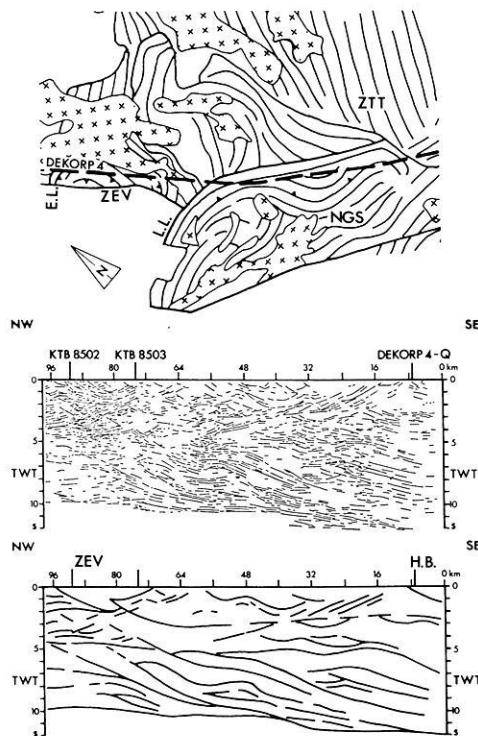


Fig. 52. Correlation between changes in dip and strike of tectono-metamorphic s-planes in the MN part of DEKORP 4 (*top*) and dipping reflectors above 4–5 s TWT (*centre*: line-drawing). Additionally, the structural model of the corresponding part of DEKORP 4 is shown in the *lowest* part of the figure

The ascent of the reflectors toward the southeast and northwest thus results from the DEKORP 4 profile running obliquely through the SW-vergent (NE-dipping) structures.

SW-vergent overthrusts, like those in profiles KTB 8501–8503 and DEKORP 4-Q (see Section 3), presumably belong to these reflectors as well. A sinistral deviation in their strike from the path of DEKORP 4 always leads to lines ascending southeastward, whereby the acute angle between the strike and DEKORP 4 causes the more frequent occurrence of side reflections.

The above interpretation is supported by the observation that NE-dipping reflectors and SW-vergent overthrusts in KTB 8501–8503 only occur more frequently above about 4–5 s TWT and join horizontal reflectors at 3–5 s TWT. This level corresponds approximately to the base of the EB between km 80 and 96 and a structural discontinuity with SE-dipping reflectors in the lower part and horizontal to NW-dipping reflectors in the upper part between km 56 and 80.

Southeast of km 56, there is a bundle of NW-dipping reflectors which are interpreted as NE-dipping structures cut at an oblique angle, as in the interpretation above. In the DEKORP 4-Q profile, which is perpendicular to the NW/SE strike of the “Pfahl” mylonites, the NE-dipping reflectors at about 2.5–3.0 s TWT pass into a prominent horizontal bundle of reflectors, which corresponds to the structural discontinuity at the SE end of DEKORP 4 at this depth (Fig. 51).

In the ST north of the Fichtelgebirge, the nappe transport has been dated as late Lower Carboniferous (320–330 Ma, Franke, 1984a). It is older than the oldest post-tectonic granites which are dated at 320 Ma.

The lithologies, metamorphic development and radiometric ages have proved that the MM and ZEV had the same evolution and origin. Behr et al. (1982) and Franke (1984a) regard the Erbdorf line at the NW margin of the ZEV as the tectonic suture marking the root zone of the MM. The existence of a nappe complex (ZEV) originating from and south of this root zone might be explained by D_2 backthrusting. Nappe transport must have occurred before the low-pressure (LP) metamorphism of the Fichtelgebirge and of the MN of the Oberpfalz since the nappes were not affected by this metamorphism. The base of the ZEV may have undergone a LP metamorphic overprinting, as indicated by the younger hornblende ages at the southern margin of the ZEV. However, a possible cause for these younger ages may also have been contact metamorphism produced by the adjacent Oberpfalz granite (Schüssler et al., 1986).

Zoubek (1979), Stettner (1979) and Blümel (1985) have pointed out the lithofacies and metamorphic relationship of the medium-pressure (MP) metamorphic ZEV and MM to the likewise MP metamorphic ZTT (Fig. 52) and inferred a formerly coherent MP metamorphic nappe complex which overlies the MN of the Oberpfalz and the Fichtelgebirge. Yet, the position of its root zone is, at present, uncertain.

The results of DEKORP 4 and the KTB seismic profiles may be taken to indicate that the ZEV overlies the ST/MN boundary in the form of a NW- to SE-striking syncline. In this sense, the "Erbdorf Line" would correspond to the boundary between the ZEV nappe and the ST rocks of the Fichtelgebirge, and not to a tectonic suture as previously assumed.

Orogenic shortening began with NW-vergent folding and thrusting. During continued collision, the style of deformation along the ST/MN boundary zone is increasingly controlled by crustal wedging, resulting in backfolding above the EB and continuous underplating or subfluence of ST under MN crust. This homo-axial structuring of the first and second phase of deformation is continued by the large upright, NE- to SW-striking folds of the third phase of deformation. During the fourth phase of deformation in the ST and MN zones, N/S- to NW/SE-striking, low-sinuuous folding took place, which decreases in intensity to the NW.

5.3 Discussion on effects of possible indentation processes

NW- to SE-striking structures occur more often south of the Luhe line. In the southwestern, marginal part of the Bohemian Massif (Bavarium), NW- to SE-striking structures in the form of pronounced mylonitization near the Bavarian "Pfahl" dominate. These NW- to SE-striking structures are SW vergent and have overprinted older NE- to SW-striking structures. In profile DEKORP 4-Q (Fig. 17) these SW-vergent structures are very clearly depicted by NE-dipping reflectors. One NE-dipping reflector can be correlated with the "Pfahl" mylonites at the surface and can be connected to the northeast to a listric overthrust with a subhorizontal reflection horizon at about 3 s TWT.

In sections KTB 8501–8503, E-dipping reflectors are recognized, particularly east of the Franconian line (Figs. 18–22). Prominent reflectors below 2 s occur, especially in section KTB 8502. These reflectors are intersected by steep,

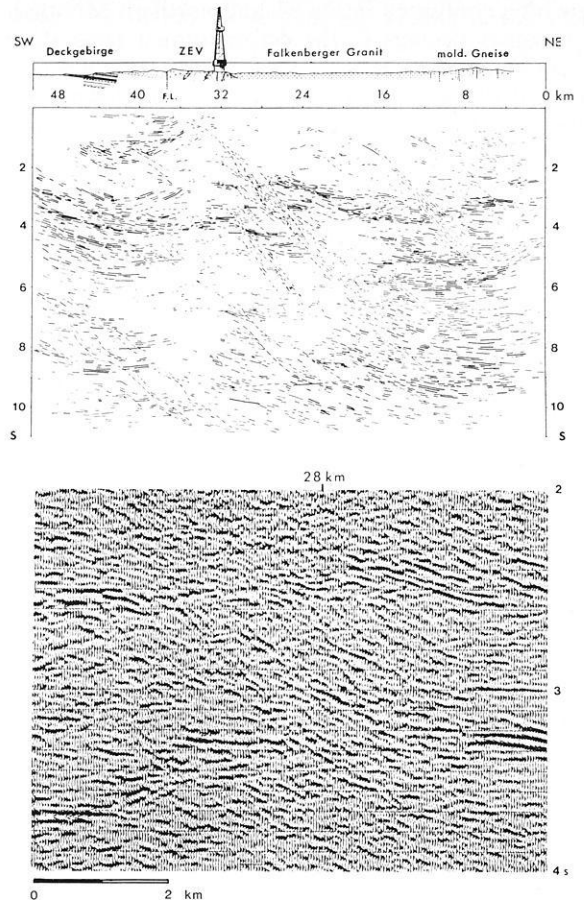


Fig. 53. Line-drawing of profile KTB 8502 (migrated section) and (bottom) detail of the section between 2 and 4 s below km 28 showing NE-dipping reflections which cut through strong, more or less horizontal reflectors. The internal structure of this fault zone is similar to that of the Pfahl mylonites in DEKORP 4-Q. It is interpreted as a ductile shear zone

E-dipping, relatively transparent zones which are composed of numerous E-dipping reflectors.

These transparent zones give the impression of zones of faulting in which the prominent subhorizontal reflectors are obliterated (Fig. 53). These relatively young, NW/SE- to N/S-striking structures are assumed to be equivalent to the NW- to SE-striking structures appearing at the surface. Thus, they could be assigned to the D_4 structures of the ST and MN boundary zone of the Oberpfalz (Stein, 1987) as well as the dominant NW/SE structures south of the Luhe line (DEKORP 4-Q). They are presumably zones of ductile shear, like those observed in the mylonite zone along the Bavarian "Pfahl".

Whereas SW vergence is observed on the SW margin of the Bohemian massif, SE-directed tectonic transport occurs in the region of the southern Black Forest, particularly in the area of the Zinken-Elme and the Badenweiler-Lenzkirch shear zone (Eisbacher and Krohe, 1986). The gravimetric and magnetic anomalies of the pre-Mesozoic basement between the Black Forest and the SW margin of the Bohemian massif reveal contours to the north, outlining the structural grain of the pre-Mesozoic basement (Edel, 1982). This arc structure is also seen in the form of the Permo-Carboniferous troughs in the region of the Southern German Massif (Fig. 54).

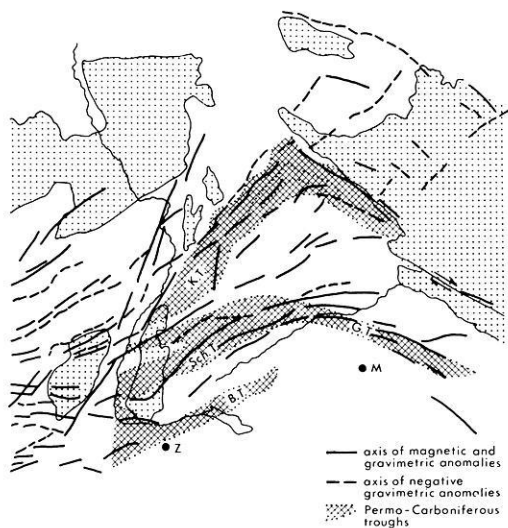


Fig. 54. Axes of magnetic and gravimetric anomalies and corresponding arc structure of Permo-Carboniferous troughs between Bohemian Massif and Black Forest. *B.T.* – Bodensee Trough; *Sch.T.* – Schramberg Trough; *G.T.* – Gifftal Trough; *K.T.* – Kraichgau Trough

As in the case of the Himalayas or the Ibero-Armorican arc (Taponnier and Molnar, 1976; Matte, 1986a), this structure can be interpreted after Weber (1986) as an indentation structure. Collectively, the arc shape of the suture zones around the various terranes of the European Variscan Belt is controlled by this later indentation process, presumably extending into the Upper Carboniferous. The indentation structures generally developed from a rather cylindrical configuration of the entire orogeny. This can explain the overprinting of older NE- to SW-trending structures by younger NW/SE structures along the southwestern margin of the Bohemian Massif by which the tectonic transport changes from SE/NW to NE/SW on the SW margin of the Bohemian Massif, and from SE/NW to NW/SE in the Black Forest. The NW-dipping reflectors in the Oberpfalz represent these thrusts formed during the indentation stage of the Vindelician Massif, which may be traced into the Hercynian basement of the Eastern Alps.

Further manifestations of the indentation process are the large dextral and sinistral shear zones. The dominance of dextral shear zones in the eastern part of central Europe, as also shown by Arthaud and Matte (1977), resulted from the movements of the terranes relative to the East-European platform. In detail, the dextral movements on the Bavarian mylonites and the sinistral movements between the Black Forest and Vosges can be assigned to the indentation process of the Vindelician Massif. During the indentation process, sutures can be transformed into wrench faults and orthogonal collision can be transformed into oblique collision.

A further argument for such an indentation structure is the rotation of the magnetic declination which is observed on both sides, but in opposite directions. In the southern Vosges Edel et al. (1984) have shown that the mean direction ($D=323^\circ$) deviates about 60° counterclockwise from the theoretical direction calculated with the Early-Carboniferous European pole position. This deviation is interpreted as resulting from a counterclockwise rotation of the southern Vosges between the late Viséan and Westphalian. The

same sense of rotation was also determined by Royer (1982) in the northern Vosges and by Bosum et al. (1973) in the crystalline Spessart.

In contrast, the rotations of the magnetic declination in the region of the Bohemian Massif amounted to 20° – 35° in a clockwise rotation during the Carboniferous and the Permian as shown by the studies of Krs (1978) and Kim and Soffel (1982). The sense of shear and rotation of magnetic declination does agree very well with the presumed indentation process. The rotation of magnetic declination is very analogous to that in northern Spain where it indicates the virgation of the Iberian arc (Ries et al., 1980; Perroud, 1982).

5.4 Conclusions

From the interpretation given here it can be seen that there are still many open questions regarding the geotectonic evolution of this region. Nevertheless, there is currently a good consensus on the basic elements of the crustal structure which is summarized in the following.

The crust is marked by northwestward overthrusting, whereby Moldanubian crust has overridden Saxothuringian crust. Tectonic deformation and the accompanying metamorphism are multi-phase. During the D_2 deformation there were also southward movements, at least in places. This has affected the northward penetration of a wedge of probably Moldanubian crust with partly higher seismic velocities into the Saxothuringian in the region of the EB.

The dominant, open, large-scale folds seen on the geological map and in the seismic profiles are the product of younger deformations (D_3 , D_4) whereby, at lower-crustal levels, folding has been compensated to some extent by overthrusting, also seen in the seismic sections. The large-scale nappes are older than the D_4 deformation. This interpretation seems to be well justified by the excellent correlation between the surface geology and seismic data.

Acknowledgements. The continued funding of the DEKORP project by the Bundesministerium für Forschung und Technologie, Bonn, is gratefully acknowledged. Administrative services were provided by the Niedersächsisches Landesamt für Bodenforschung, Hannover. The excellent performance of the Prakla-Seismos AG field crew under H. Schwanitz was remarkable, and there was smooth cooperation between the various groups in the field. The Raytheon RDS 500 is a donation of Mobil Oil AG Celle to the DEKORP Processing Center at Clausthal. The software was provided by Seismograph Service Ltd., London. BEB Erdgas und Erdöl GmbH, Hannover, supported the work by special processing. The close cooperation with Preussag AG was very helpful. Special thanks are due to the large number of students participating in the field work and all members of the DPC.

References

- Ackermann, H., Tavakkoli, P.: Granite – Form und räumliche Lage im metamorphen Grundgebirge. Abstracts, 76. Jahrestg. Geol. Vereinig., Giessen 1986, 1, 1986
- Arthaud, F., Matte, Ph.: Late Paleozoic strike slip faulting in Southern Europe and Northern Africa: result of a right lateral shear zone between the Appalachians and the Urals. Geol. Soc. Amer. Bull. **88**, 1305–1320, 1977
- Banks, C.J., Warburton, J.: “Passive-roof” duplex geometry in the frontal structures of the Kirthar and Sulaiman mountain belts, Pakistan. J. Struct. Geol. **8**, 229–237, 1986
- Behr, H.J., Engel, W., Franke, W.: Variscan Wildflysch and nappe

- tectonics in the Saxothuringian zone (Northeast Bavaria, West Germany). *Amer. J. Sci.* **282**, 1438–1470, 1982
- Behr, H.-J., Engel, W., Franke, W., Giese, P., Weber, K.: The Variscan Belt in Central Europe: main structures, geodynamic implications, open questions. *Tectonophysics* **109**, 15–40, 1984
- Besang, C., Harre, W., Kreuzer, H., Lenz, H., Müller, P., Wendt, I.: Radiometrische Datierung, geochemische und petrographische Untersuchungen der Fichtelgebirgsgranite. *Geol. Jb. E* **8**, 3–71, 1976
- Blümel, P.: Metamorphic history. In: Excursion guide Oberpfalz, Weber, K.: 2nd Inter. Symposium on observation of the continental crust through drilling. Seeheim/Odenwald, 7–9 October, 1985, 23–30, 1985
- Bopp, M.: Analyse und Interpretation von S-Wellenregistrierungen im Rahmen des Deutschen Reflexionsseismischen Programms DEKORP. Dipl.-Arbeit, Ludwig-Maximilians Universität, München, 1986
- Bosum, W., Geipel, H., Weinelt, W.: Magnetische Untersuchungen im kristallinen Spessart und ihre geophysikalisch-geologische Deutung. *Geol. Bavarica* **67**, 11–34, 1973
- Breemen, van O., Aftalion, M., Bowes, D.R., Dudek, A., Misat, Z., Povondra, P., Vrána, S.: Geochronological studies of the Bohemian massif, Czechoslovakia, and their significance in the evolution of Central Europe. *Trans. R. Soc. Edin.: Earth Sciences* **73**, 89–108, 1982
- Brown, R.L., Journeay, J.M., Lane, L.S., Murphy, D.C., Rees, C.J.: Obduction, backfolding and piggyback thrusting in the metamorphic hinterland of the southeastern Canadian Cordillera. *J. Struct. Geol.* **8**, 255–268, 1986
- Christensen, N.I.: Compressional wave velocities in metamorphic rocks at pressures to 10 kbars. *J. Geophys. Res.* **70**, 6147–6164, 1965
- DEKORP Research Group: First results and preliminary interpretation of deep-reflection seismic recordings along profile DEKORP 2-South. *J. Geophys.* **57**, 137–163, 1985
- Edel, J.B.: Le socle Varisque de l'Europe moyenne apports du magnétisme et de la gravimétrie. *Sci. Geol. Bull.* **35**, 207–224, 1982
- Edel, J.B., Coulon, M., Hernot, M.-P.: Mise en évidence par le paléomagnétisme d'une importante rotation antihoraire des Vosges méridionales entre le Viséen terminal et le Westphalien supérieur. *Tectonophysics* **106**, 239–257, 1984
- Eisbacher, G., Krohe, A.: Kontinentales Tiefbohrprogramm der Bundesrepublik Deutschland. Ergebnisse der Vorerkundungsarbeiten Lokation Schwarzwald. 2. KTB Kolloquium, Seeheim/Odenwald 19–21 September, 1986, 1986
- Emmert, U.: Perm nördlich der Alpen. In: Erläuterungen zur Geologischen Karte von Bayern 1:500000, 3. Auflage, Haunschild, H., Jerz, H., eds.: pp. 5–29, München, 1981
- Franke, W.: Variszischer Deckenbau im Raume der Münchberger Gneismasse – abgeleitet aus der Fazies, Deformation und Metamorphose im umgebenden Paläozoikum. *Geotekt. Forsch.* **68**, 1–153, 1984a
- Franke, W.: Late events in the tectonic history of the Saxothuringian zone. In: Variscan tectonics of the North Atlantic region: Hutton, D.W.H., Sanderson, D.J., eds.: pp. 33–45. Blackwell Scientific Publications, 1984b
- Franke, W.: Development of the Central European Variscides – a review. In: Proceedings 3rd Workshop on the European Geotraverse (EGT) Project, Freeman, R., Müller, St., Giese, P., eds.: pp. 65–72. European Science Foundation 1986
- Fuchs, H.K., Soffel, H.: Untersuchungen am Westabbruch der Böhmisches Einheit im oberfränkisch-oberpfälzischen Bruchschollenland mit Hilfe der Gravimetrie. *N. Jb. Geol. Paläont. Mh.* **1981**, 193–210, 1981
- Grauert, B., Wänny, R., Soptrajanova, G.: Geochronology of a polymetamorphic and anatexitic gneiss region: the Moldanubicum of the Area Lam – Deggendorf, Eastern Bavaria, Germany. *Contr. Mineral. Petrol.* **45**, 37–63, 1974
- Gudden, H., Schmid, W.: Die Forschungsbohrung Obernsees. *Geol. Bavarica* **88**, 5–21, München, 1985
- Haak, V., Blümecke, T.: In: Excursion guide Oberpfalz, Weber, K.: 2nd Int. Symposium on observation of the continental crust through drilling. Seeheim/Odenwald 7–9 October, 1985, 1985
- Haunschild, W., Schröder, B.: Geologische Karte von Bayern 1:25000, Blatt 6237, Grafenwöhr mit Erläuterungen. Bayer. Geol. Landesamt, München, 1960
- Helmkamp, K.E., Kuhlmann, J., Kaiser, D.: Das Rotliegende im Randbereich der Weidener Bucht. *Geol. Bavarica* **83**, 167–186, München, 1982
- Horn, P., Köhler, H., Müller-Sohnius, D.: A Rb/Sr WR-isochron (“fluid inclusion”) age of the Bayerischer Pfahl, eastern Bavaria. *Terra Cognita* **3**, 199, 1983
- Kern, H., Schenk, V.: Elastic wave velocities in rocks from the lower crustal section in southern Calabria (Italy). *Phys. Earth Planet. Inter.* **40**, 147–160, 1985
- Kim, I.-S., Soffel, H.C.: Palaeomagnetic results of Lower Palaeozoic diabases and pillow lavas from the Frankenwald area (northwestern edge of the Bohemian Massif). *J. Geophys.* **51**, 24–28, 1982
- Köhler, H., Müller-Sohnius, D.: Ergänzende Rb-Sr Altersbestimmung an Mineral- und Gesamtgesteinsproben des Leuchtenberger und des Flossenbürger Granits (NE Bayern). *N. Jb. Miner., Mh.* **1976**, **8**, 354–365, 1976
- Kossmat, F.: Gliederung des variszischen Gebirgsbaues. *Abh. sächs. Geol. Landesamt* **1**, 39 p., 1927
- Krs, M.: Palaeomagnetic evidence of tectonic deformation of blocks in the Bohemian Massif. *Geology* **31**, 141–150, 1978
- KTB 1986: Kontinentales Tiefbohrprogramm der Bundesrepublik Deutschland, KTB, Ergebnisse der Vorerkundungsarbeiten Lokation Oberpfalz, Weber, K. and Vollbrecht, A., eds.: 2. KTB-Kolloquium Seeheim/Odenwald, 19–21 September 1986, 1986
- Leitz, F., Schröder, B.: Die Randfazies der Trias und das Bruchschollenland südöstlich Bayreuth (Exkursion C). *Jber. Mitt. Oberrhein. Geol. Ver., N.F.* **67**, 51–63, Stuttgart, 1985
- Lenz, H.: Rb/Sr Gesamtgestein-Altersbestimmung am Weißenstadt-Marktleuthener Porphyrgnit des Fichtelgebirges. *Geol. Jb. E34*, 67–76, 1986
- Lüschen, E. et al.: Near-vertical and wide-angle seismic surveys in the Black Forest, SW Germany. *J. Geophys.* **62**, 1–30, 1987
- Matte, P.: La chaîne Varisque parmi les chaînes paléozoïques périalantiques, modèle d'évolution et position des grands blocs continentaux au Permo-Carbonifère. *Bull. Soc. Géol. France* **8**, (II), 9–24, 1986a
- Matte, P.: Tectonics and plate tectonics model for the Variscan Belt of Europe. *Tectonophysics* **126**, 329–374, 1986b
- Matthews, D.H., Cheadle, M.J.: Deep reflection from the Caledonides and Variscides west of Britain. In: Reflection seismology: a global perspective, Barazangi, M., Brown, L., eds.: pp. 5–19. *Geodynamics Series* **13**, 1986
- Matthews, D.H. and the BIRPS group: Some unsolved BIRPS problems. *Geophys. J.R. Astron. Soc.* **89**, 209–216, 1987
- McGeary, S.: Nontypical BIRPS on the margin of the North Sea: The SHET Survey. *Geophys. J.R. Astron. Soc.* **89**, 231–238, 1987
- Meissner, R., Bartelsen, H., Krey, Th., Schmoll, J.: Detecting velocity anomalies in the region of the Urach geothermal anomaly by means of new seismic field arrangements. In: Geothermics and geothermal energy, Cermak, V., Haenel, R., eds.: pp. 285–292, Stuttgart: E. Schweizerbart'sche Verlagsbuchhandlung, 1982
- Mielke, H. et al.: Regional low-pressure metamorphism of low and medium grade in metapelites and -psammites of the Fichtelgebirge area, NE Bavaria. *N. Jb. Miner. Abh.* **137**, 83–112, 1979
- Oxburgh, E.R.: Flake tectonics and continental collision. *Nature* **239**, 202–204, 1972
- Perroud, H.: Contribution a l'étude paléomagnétique de l'arc ibéro-armoricain. *Bull. Soc. Géol. Minéral. Bretagne* **15**, 1–114, 1982
- Price, R.A.: The southeastern Canadian Cordillera: thrust faulting, tectonic wedging, and delamination of the lithosphere. *J. Struct. Geol.* **8**, 239–254, 1986

- Richter, P., Stettner, G.: Geochemische und petrographische Untersuchungen der Fichtelgebirgsgranite. *Geol. Bavarica* **78**, 144 p., 1979
- Ries, A.C., Richardson, A., Shakleton, R.P.: Rotation of the Iberian arc; paleomagnetic results from North Spain. *Earth Planet. Sci. Lett.* **50**, 301–310, 1980
- Royer, J.Y.: Etude paléomagnétique et géochronologique de Vosges cristallines du Nord. *Mem. DEA, Institut Physique du Globe, Strasbourg I*, 1982
- Sandmeier, K.-J., Wenzel, F.: Synthetic seismograms for a complex crustal model. *Geophys. Res. Lett.* **13**, 22–25, 1986
- Schreyer, W.: Metamorpher Übergang Moldanubikum/Saxothuringikum östlich Tirschenreuth/Opf., nachgewiesen durch phasenpetrologische Analyse. *Geol. Rdsch.* **55**, 491–509, 1966
- Schröder, B., Siegling, M.: Geologische Karte von Bayern 1:25000, Blatt 6137, Kemnath mit Erläuterungen. Bayer. Geol. Landesamt, München, 1966
- Schüssler, U., Oppermann, U., Kreuzer, H., Seidel, E., Okrusch, M., Lenz, K.-L., Raschka, H.: Zur Altersstellung des ostbayerischen Kristallins. Ergebnisse neuer K-Ar-Datierungen. *Geol. Bavarica* **89**, 21–47, 1986
- Stein, E.: Die strukturgeologische Entwicklung im Übergangsbereich Saxothuringikum/Moldanubikum in NE-Bayern. *Diss. Universität Göttingen*, 125 p., 1987
- Stettner, G.: Zur geotektonischen Entwicklung im Westteil der Böhmisches Masse bei Berücksichtigung des Deformationsstils im orogenen Bewegungssystem. *Z.Dt. Geol. Ges.* **123**, 291–326, 1972
- Stettner, G.: Der Grenzbereich Saxothuringikum-Moldanubische Region im Raum Tirschenreuth-Mähring (Oberpfalz) und die Situation des Uran-führenden Präkambriums. *Z.Dt. Geol. Ges.* **130**, 561–574, 1979
- Stettner, G.: Grundgebirge. In: Erläuterungen zur Geologischen Karte von Bayern 1:500000, 3. Auflage, Haunschild, H., Jerz, H., eds.: pp. 5–29, München, 1981
- Strössenreuther, U.: Die Struktur der Erdkruste am Südwestrand der Böhmisches Masse, abgeleitet aus refraktions-seismischen Messungen der Jahre 1970 und 1978/79. *Diss. Ludwig-Maximilians Universität, München*, 1982
- Taner, M.T., Koehler, F., Alhilali, K.A.: Estimation and correction of near-surface time anomalies (CDP static correction). *Geophysics* **39**, 441–463, 1974
- Tapponier, P., Molnar, P.: Slip-line field theory and large-scale continental tectonics. *Nature* **264**, 319–324, 1976
- Teufel, S.: Vergleichende U-Pb- und Rb-Sr-Altersbestimmungen an Gesteinen des Übergangsbereiches Saxothuringikum/Moldanubikum, NE-Bayern. *Diss. Universität Göttingen*, 110 p., 1987
- Tollmann, A.: Großräumiger variszischer Deckenbau im Moldanubikum und neue Gedanken zum Variszikum Europas. *Geotekt. Forsch.* **64**. Stuttgart: Schweizerbart'sche Verlagsbuchhandlung, 1982
- Wagener-Lohse, C., Blümel, P.: Prograde Niederdruckmetamorphose und ältere Mitteldruckmetamorphose im Nordostbayerischen Abschnitt der Grenzzone Saxothuringikum/Moldanubikum (Abstract): Jahrestagg. *Geol. Ver., Gießen* 1986, p. 84, 1986
- de Wall, H.: Mikrostrukturelle Untersuchungen und strukturgeologische Kartierung der Gesteine aus dem Übergangsbereich Moldanubikum/Saxothuringikum westl. Mähring, Oberpfalz. *Dipl.-Arb., Universität Göttingen*, 1987
- Weber, K.: The Mid-European Variscides in terms of allochthonous terranes. In: *Proceedings of the 3rd EGT workshop, Bad Honnef, Freeman, R., Mueller, St., Giese, P., eds.: pp. 73–81. European Science Foundation* 1986
- Weber, K., Behr, H.J.: Geodynamic interpretation of the mid-European Variscides. In: *Intracontinental fold belts – case studies in the Variscan Belt of Europe and the Damara Belt in Namibia, Martin, H., Eder, W., eds.: pp. 427–469. Springer Verlag*, 1983
- Ziegler, P.A.: Caledonian and Hercynian crustal consolidation of Western and Central Europe – a working hypothesis. *Geol. en Mijnbouw* **63**, 93–108, 1984
- Zoubek, V.: Korrelation des präkambrischen Sockels der Mittel- und Westeuropäischen Varisziden. *Z. Geol. Wiss.* **7**, 1057–1064, 1979

Received August 6, 1987; revised version October 19, 1987

Accepted October 21, 1987

Paleomagnetism of Jurassic sediments from the western border of the Rheingraben, Alsace (France)*

M. Kądziałko-Hofmokl¹, J. Kruczyk¹, and M. Westphal²

¹ Institute of Geophysics, Polish Academy of Sciences, P.O. Box 155, 00-973 Warsaw, Poland

² Laboratoire de Paléomagnétisme, Institut de Physique du Globe, F-67000 Strasbourg, France

Abstract. Upper Bajocian oolitic limestones and Pliensbachian marls and marly ovoids from 9 sites distributed over 4 exposures at the western border of the Rheingraben (mean coordinates 47.8° N, 7.5° E) were sampled by 92 samples. The carriers of the natural remanent magnetization in the limestones are goethite and magnetite, and in the marls and ovoids the carrier is magnetite. After tectonic correction, the characteristic component of NRM isolated in the cleaning processes was mostly of normal polarity. The mean direction is $D = 30.1^\circ$, $I = 53.2^\circ$ ($N = 7$, $k = 92$, $\alpha_{95} = 6.3^\circ$) and the pole position is 63.1° N, 120.1° E. It is close to the Jurassic reference data for the stable European plate.

Key words: Paleomagnetism – Jurassic – Bajocian – France – Sediments

Introduction

Paleomagnetic data for the European Jurassic are scarce. This is mostly due to the fact that during the Jurassic mainly sediments poor in magnetic minerals, and therefore difficult for measurements, were formed. Nevertheless, in recent years several reliable publications appeared, concerning the stable European plate and mobile Europe. The data for stable Europe come from southern Germany (Heller, 1977, 1978), England (Hijab and Tarling, 1982), French-Swiss Jura (Johnson et al., 1984), Russian Platform (Khravov et al., 1984), Balkan in Bulgaria (Kruczyk et al., 1986) and Poland (Kądziałko-Hofmokl and Kruczyk, 1987). The available data helped Westphal et al. (1986) to calculate the reference pole positions. The rocks from mobile Europe were studied by: Mauritsch and Frisch (1978) – Austrian Alps; Soffel (1981) – Italy; Marton et al. (1980) and Marton and Marton (1981) – Hungary; Lowrie and Channel (1983) – Italy; Steiner et al. (1985) – Iberia; Kruczyk et al. (1985) – Tatra Mountains in Poland. All those papers speak about possible rotations of investigated regions relative to stable Europe and, together with paleomagnetic data obtained for the stable plate, help us to understand the Mesozoic history of Eurasia.

The purpose of the present note is to contribute to the paleomagnetic research by adding new data obtained from the region close to one of the most important geotectonic structures in Europe – the Rheingraben.

Geology and sampling

The sampling area lies in Alsace at the western border of the Rheingraben (Fig. 1). This region formed a post-Variscan peneplain that was covered by the sea during the Lower and Middle Jurassic, as was the rest of western Europe. The sediments studied were deposited during this transgression in the warm and shallow water. The regression began at the end of the Bajocian and this area rested above sea level during the Upper Jurassic and Cretaceous. Deformations due to Alpine orogenesis resulted in creation of synclines and anticlines of the basement, oriented WSW-ESE. This surface, which appeared to be horizontal, was later fossilized by Tertiary sediments. The formation of the Rheingraben began in the mid-Eocene. The uplift of border massifs, Vosges and Black Forest, took place mainly in the Oligocene. The Pliocene and Quaternary movements induced an erosional activity that brought these massifs to their present altitude. Some normal faulting in the horst and graben occurred due to graben tectonics, but there is no sign of relative rotations (von Eller, 1976).

The sampled sediments comprised the Pliensbachian and Upper Bajocian deposits. The Pliensbachian rocks consisted of horizontally deposited grey marls, forming one lithostratigraphical unit, and grey-yellowish ovoidal marly nodules (called ovoids) from Schaeffer quarry (Sf in Fig. 1), site 8 and 9, respectively. The ovoids appear as a horizontal bed in the marls; they are the size and shape of a double fist with a horizontal long axis.

The Upper Bajocian white-yellowish oolitic limestones belong to the so-called Great Oolite facies, characteristic of this period for eastern France. They were sampled in three quarries: Bouxwiller (Bo in Fig. 1) – site 7, one stratigraphic level dipping 12° to the SSE direction; Imbsheim (Im in Fig. 1) – sites 1 and 2, situated 2 km distant from Bo on the opposite site of the Bastberg syncline. At site 1, samples were taken from three layers situated one under the other. Site 2 lies 50 m from and 2 m below site 1, and samples collected here represent one layer. The Im sites are inclined 15° to the WWS. The third quarry sampled was Scharrachberg (Sb in Fig. 1) – sites 3, 4, 5 and 6, situated about 20 km south of the former ones. Sites 3, 4, and

* This research was supported by the Geodynamics of Poland Project – grant MR.I. 16.3.1.

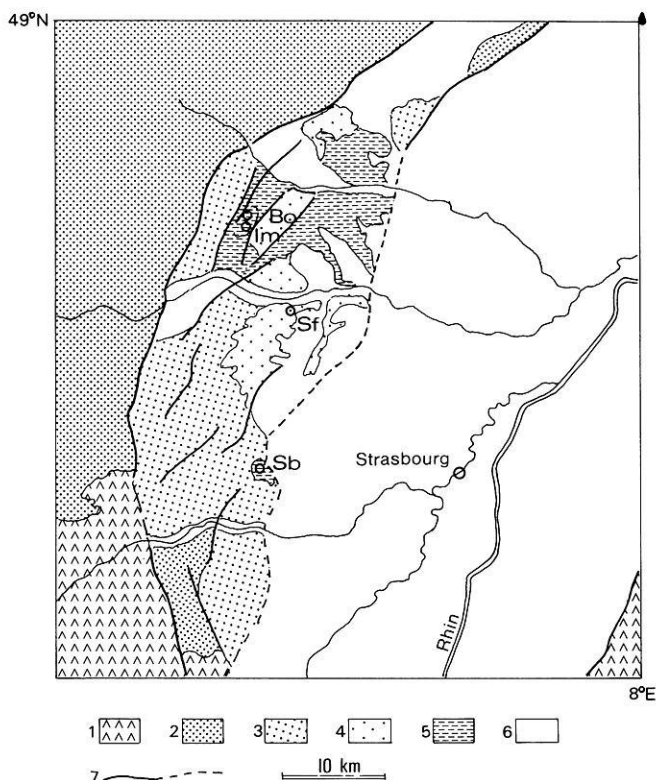


Fig. 1. Sampling area showing location of sites. 1, Pre-Triassic basement; 2, Buntsandstein; 3, Keuper and Muschelkalk; 4, Lias; 5, Middle Jurassic; 6, Post-Jurassic cover; 7, Main faults (hidden); Bo, Bouxwiller; Im, Imbsheim; Sb, Scharrachberg; Sf, Schaeffer quarry

5 lie on the north wall; sites 3 and 4 represent the same horizontal level and site 5 is situated higher. Site 6 lies on the south wall of the quarry and it represents one level whose relation to the other sites is unknown. The rocks here are inclined by 25° to EEN.

In each quarry, 15–25 oriented cores were drilled. At Sf, apart from the marl cores, seven separately oriented ovoids were also collected.

Laboratory methods and data analysis

Identification of magnetic minerals

Microscopic analysis of polished sections was applied to the oolitic limestones by means of a Min-4 ore microscope (resolution power 500). Limestones were also subjected to measurements of low-field magnetic susceptibility K before heating and after consecutive heating steps. The instrument used was a KLY-2 susceptibility bridge (noise level 4×10^{-8} SI). The K vs temperature T plots indicate mineralogical changes induced in specimens by heating in air. The continuous thermal demagnetization in field-free space of the isothermal remanence I_{rs} acquired in 1.8 T served as the main method of identification of magnetic minerals in all rock types studies. The I_{rs} vs T curves recorded during the first heating of a specimen to 600° C give the blocking temperatures T_b of magnetic minerals in rock in its natural state. The curves recorded during the second heating show the influence of the thermal treatment on the rock, resulting

in changes in I_{rs} and the T_b spectrum (Kądziałko-Hofmokl and Kruczyk, 1976). Supplementary evidence was obtained from thermal and alternating-field (af) demagnetization curves of the intensity I_n of natural remanent magnetization NRM. They give spectra of T_b and coercivity characteristics of the minerals – carriers of NRM.

NRM studies

NRMs were measured in Strasbourg with a Digico spinner magnetometer (noise level 3×10^{-5} Am $^{-1}$) and in Warsaw with a Jelinek's IR-4 spinner magnetometer (noise level 5×10^{-6} Am $^{-1}$). Thermal demagnetization experiments were performed by heating the specimens step-wise to progressively higher temperatures in a nonmagnetic furnace installed in three pairs of Helmholtz coils (Strasbourg) or in a five-fold permalloy screen (Warsaw). During af treatment, specimens were subjected to progressively higher field intensities in three orthogonal directions at the same peak intensities (Strasbourg) or in apparatus provided with a two-axis tumbler (Warsaw), in a field-free space in both laboratories.

Analysis of the experimental results for each specimen was performed using orthogonal and stereographic projections of the vector end points remaining after each demagnetizing step and, for limestones, by the least-squares method of Kirshvink (1980).

Rock-magnetic and paleomagnetic results

Upper Bajocian oolitic limestones

Microscopic analysis applied to samples from Bo, Im and Sb quarries revealed only the presence of iron hydroxides – goethite and, in some cases, small amounts of lepidocrosite. In Bo and Sb, goethite resides in the cores of oolites either forming aggregates of small (1–10 μ) xenomorphic grains or occurring as one xenomorphic grain of several hundred microns with inclusions of other rock-forming minerals (goethite A). In the Im samples, apart from this form, goethite also appears as an irregular net of thin veins filling interstices between oolites – goethite B. Such a situation allows us to surmise that goethite A was formed earlier (deposited?) and goethite B later than oolites. Rarely appearing xenomorphic grains of lepidocrosite form intergrowths with goethite.

The magnetic low-field susceptibility before heating for most samples is positive and low – it does not exceed 1×10^{-5} SI. In some samples from site 6, negative K values of -2×10^{-6} SI were observed, indicating the presence of some diamagnetic minerals. The K vs T plots (Fig. 2) show a decrease of susceptibility in the temperature range 200° – 300° C, due to dehydration of goethite. After heating to 300° C, K begins to rise and rises up to 10 times after the 400° heating step, indicating the appearance of new strongly magnetic minerals formed due to the heating. This result is consistent with the behaviour of magnetic susceptibility of goethite-containing marine limestones studied by Lowrie and Heller (1982).

The I_{rs} vs T curves typical of the limestones studied are shown in Fig. 3a and b. The low blocking temperatures (T_b about 80° – 100° C) are characteristic of goethite. The highest blocking temperatures (500 – 550° C) indicate the presence of magnetite (see plot for site 3), sometimes in

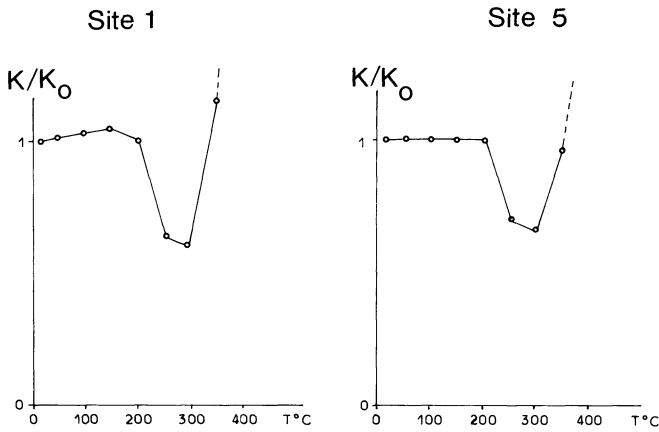


Fig. 2. Susceptibility as a function of temperature for two limestone samples

very small amounts. I_{rs} acquired by specimens after the first heating is several times greater than before the heat treatment. The second I_{rs} vs T curves show the presence of only one mineral with T_b characteristic of magnetite or maghemite.

The demagnetization curves of I_n are shown in Fig. 4a and b. A temperature of 50° C removes 20%–95% of NRM. This component is carried by low- T_b minerals (goethite) and its intensity depends on the low- T_b to high- T_b mineral ratio. The remaining component decreases during heating to 300°–400° C, and then its intensity begins to rise. The af treatment is not effective for specimens with goethite as the prevailing mineral, due to its high coercivity – site 5 in Fig. 4b. The I_n vs H plots for specimens also containing (apart from goethite) a considerable amount of high- T_b minerals indicate the existence of the two components of NRM with different coercivities – site 1 in Fig. 4b.

In view of the results presented, we argue that the NRM of the oolitic limestones is carried by goethite and magnetite. Magnetite is probably present in the form of very fine (superparamagnetic) grains and therefore invisible under the microscope Min-4. In Im, two forms of goethite are present.

The NRM intensities were found to be variable (see Table 1), but their response to demagnetization treatment was similar. Some of them could not be satisfactorily cleaned – the intensity of remanence quickly dropped below the noise level of the magnetometer.

Thirty-eight specimens from Im, 24 from Sb and 31 from Bo were demagnetized. The Bo results will not be discussed – the NRM intensities are very low and interpretation of demagnetization results is often impossible (see Table 1). Figure 5a and b presents the orthogonal and stereographic demagnetization plots characteristic of Im and Sb rocks. A temperature of 50° C removes the first, soft (against heating) component of NRM carried by goethite. Its direction is close to the present geomagnetic field direction ($D=358^\circ$, $I=64^\circ$), suggesting remagnetization of its carriers (goethite) in the present field. At higher temperatures, the orthogonal and stereographic plots become erratic due to the low intensity of the remaining component of NRM and it is often difficult to find linear parts of the cleaning diagrams going to the origin of the plot. After

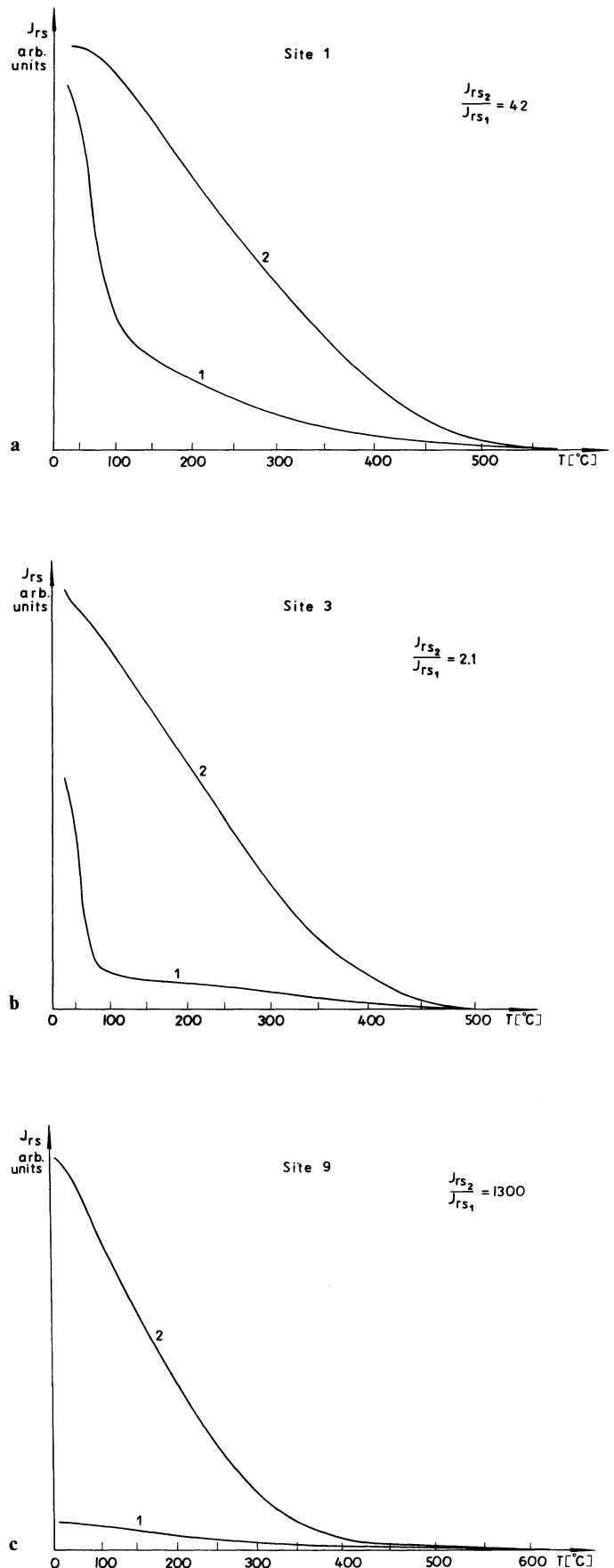


Fig. 3a–c. Thermomagnetic curves for a, b limestones and c ovoids. 1 – First heating curve; 2 – second heating curve

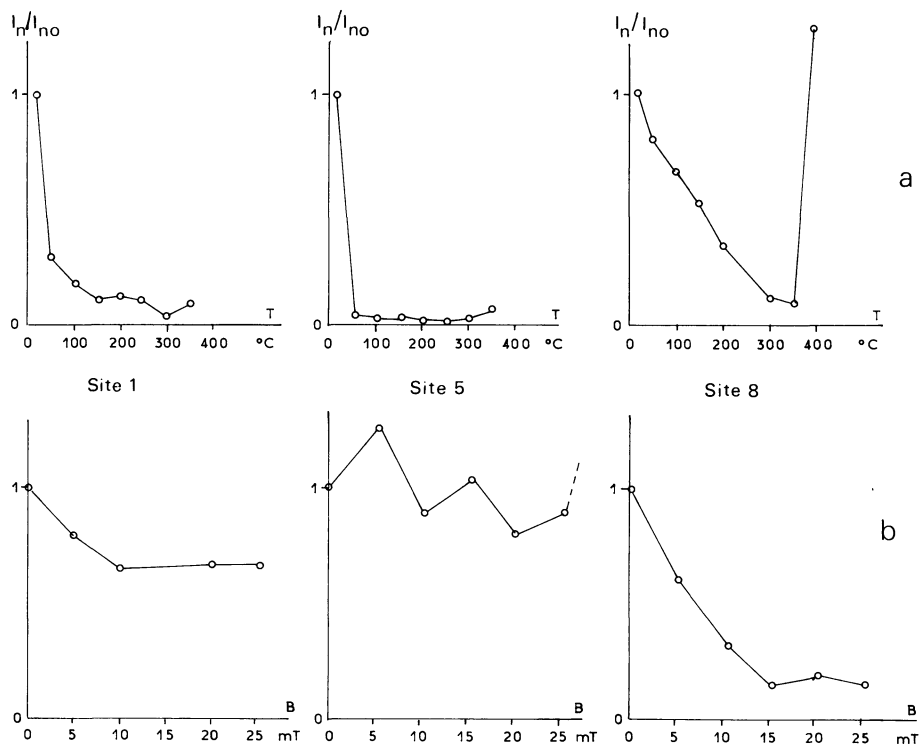


Fig. 4a and b. Decay of I_n **a** during thermal cleaning and **b** during af cleaning. Site 1 and 5 – limestones; site 8 – marls

Table 1. Site mean directions after bedding correction. n_1/n_2 – the number of sample directions used in the calculation to the number of samples demagnetized. D , I – declination, inclination. α_{95} , k – statistical parameters. NRM – intensity of the natural remanence. D , I and α_{95} in degrees

Exposure	Age	Site and polarity	n_1/n_2	D	I	α_{95}	k	NRM $\times 10^{-6} \text{ Am}^{-1}$
Imbsheim (Im) $\varphi = 48^\circ 47' \text{N}$ $\lambda = 7^\circ 28' \text{E}$	U. Bajocian	1N	6/18	16.6	58.9	9.5	50	20–500
		1R	6/10	212.9	–50.7	13.0	26	20–500
		2N	10/12	18.3	41.1	10.0	23	20–500
Scharrachberg (Sb) $\varphi = 48^\circ 36' \text{N}$ $\lambda = 7^\circ 30' \text{E}$	U. Bajocian	3N	8/9	34.6	50.4	14.0	18	100–650
		4N	6/6	36.9	60.1	7.7	76	60–370
		5N	4/4	35.7	55.8	7.0	155	150–600
		6N	7/7	38.2	52.7	4.5	169	50–170
		3R, 5R, 6R	5/7	223.1	–24.5	12.5	38	120–600
Bouxwiller (Bo) $\lambda = 48^\circ 49' \text{N}$ $\lambda = 7^\circ 28' \text{E}$	U. Bajocian	7N	5/31	56.0	61.5	20.0	15	10
Schaeffer (Sf) $\varphi = 48^\circ 45' \text{N}$ $\lambda = 7^\circ 35' \text{E}$	Pliensbachian	8N	13/20	329.0	57.3	6.7	39	200–550
		9N	22/25	0.4	55.4	4.8	43	250–550
Im + Sb								
Before bedding correction	U. Bajocian	1–6	7 ^a /8	16.6	59.7	12.3	25	
After bedding correction				30.1	53.2	6.3	92	

^a 3R, 5R, 6R excluded

heating to 350° C, the intensity of remanence increases following the mineralogical changes (see previous section).

In order to isolate the characteristic component of natural remanence CARM, the demagnetization results were analysed following the least-squares method. For the directions of CARM, we most often took either the Hoffman-Day directions or the directions of the longest lines fitted to the vectors subtracted in the temperature range preceding

the rise in I_n . Usually these temperature ranges began higher than 50° C. In some cases the direction of the component subtracted between two consecutive heating steps, or the component remaining after heating to at least 50° C, was assumed to be the CARM direction. Figure 6a shows CARM directions isolated for Im and Sb after tectonic correction.

The CARM isolated in Im and Sb resides mostly in

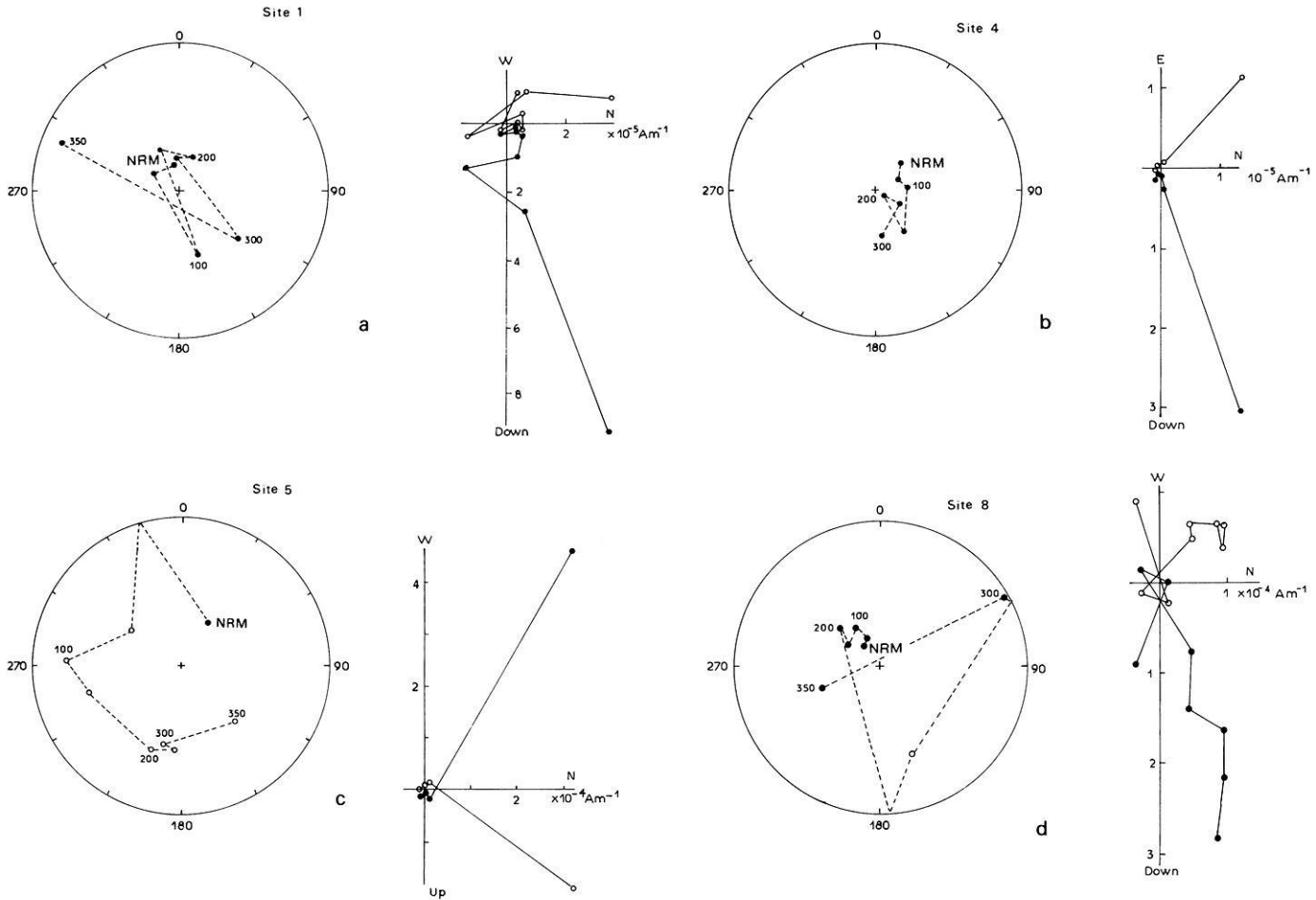


Fig. 5a–d. Orthogonal and stereographic demagnetization diagrams after bedding correction for **a**, **b** and **c** limestones and **d** marls. Full circles – horizontal plane. Open circles – vertical plane

magnetite. Only in some cases was CARM observed in the temperature range including room temperature (ex 20° – 300° C), suggesting that this component is carried not only by magnetite but also by goethite not remagnetized in the present field. Most of the CARMs are of normal polarity. The sites means after tectonic corrections, together with the corresponding parameters of Fisherian statistics, are included in Table 1.

The group of CARMs of reversed direction is less numerous. In both quarries they appear only after removing the component of the present field direction, which shows that reversed CARMs are carried exclusively by magnetite.

The reversed CARMs were isolated in some specimens from sites 1, 3, 5 and 6. The demagnetization results also suggest the presence of a reversed component of NRM in site 4. It is probably of very low intensity and therefore masked by the component of normal polarity. There is no trace of a reversed component in site 2. Figure 5c shows the orthogonal and stereographic plots obtained for one site-5 specimen where two components, normal and reversed, were isolated. The normal one was identified as the line in the temperature range 20° – 300° C, and the reversed one as the Hoffman-Day direction persisting from 100° C to the origin of the plot. The reversed directions

are more scattered than the normal ones (see Fig. 6a). The reversed site mean directions for Im and Sb, together with corresponding Fisherian parameters, are included in Table 1.

The mean reversed direction obtained for Im (1R in Table 1) is exactly opposite to the normal mean directions for sites 1 and 2. The result obtained for Sb (3R, 5R, 6R in Table 1) differs considerably and is excluded from further calculations.

The difference in tectonic parameters of Im and Sb (3R, 5R and 6R excluded), however slight, allowed us to apply the fold test to all Upper Bajocian sites. The between-site means calculated before and after tectonic correction are shown at the bottom of Table 1. The parameters of Fisherian statistics show better grouping after correction, suggesting pre-tectonic origin of the isolated CARM.

Pliensbachian

Only one magnetic mineral appears in the Pliensbachian marls and ovoids – magnetite. The I_{rs} vs T curves shown in Fig. 3c reveal the blocking temperatures of about 570° C characteristic of this mineral. Heating in air to 600° C results in an enormous increase of I_{rs} that follows the appear-

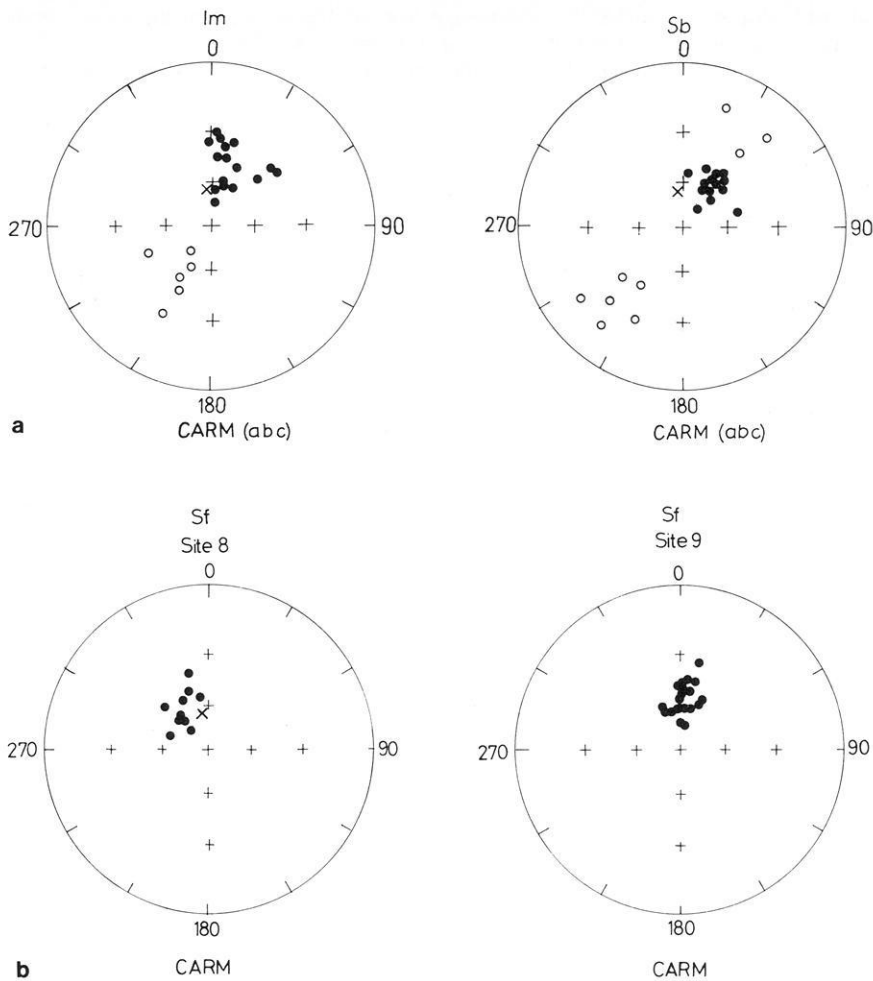


Fig. 6 a and b. Directions of CARM after bedding correction for **a** limestones from Im and Sb and **b** marls and ovoids from Sf

Table 2. Paleomagnetic pole positions. N – number of data entered. Latitude, longitude and α_{95} in degrees

Sampling area	Age	N	Lat. N	Long. E	α_{95}	k	Polarity
Alsace (Im + Sb)	U. Baj.	7	63.1	120.1	6.3	92	M
S. Germany, Heller (1978)	U. J.	79	68.0	130.0	5.0		N
England, Hijab and Tarling (1982)	L.J.	185	76.9	134.7	2.5	19	N
Swiss – French Jura, Johnson et al. (1984)	U.J.	24	77.7	148.4	5.9	26	N
ibid.	U.Baj.	3	61.1	123.3	22.2	32	N
Poland (stable), Kądziałko-Hofmokl and Kruczyk (1987)	M.-U.J.	8	72.3	150.4	7.3	58	M
Bulgaria (stable), Kruczyk et al. (1986)	L.-M.J.	12	72.3	120.2	5.4	66	N
Stable Eurasia, Westphal et al. (1986)	M.-U.J.	4	70.0	128.0	7.0	187	

ance of a great amount of magnetite from nonmagnetic (clay?) minerals present in the rock. The results of demagnetization of I_n support this evidence. The NRM intensities of both rock types are of the same order (see Table 1). Twenty-five specimens of ovoids and 20 of marls were de-

magnetized, some thermally up to 400° C and some by af with a peak field of 30–40 mT. The I_n vs T curves show smooth decay to 350° C; and after heating to higher temperatures, I_n increases sharply due to newly formed magnetite (see site 8 in Fig. 4).

The directions of NRM, as orthogonal and stereographic plots in Fig. 5d show, already become scattered after heating to 200°–500° C. An intensity of 30–40 mT lowers measured remanences to the noise level of the magnetometer.

In order to isolate the characteristic remanence residing in marls and ovoids, we have adopted the criterion of minimum dispersion of directions of remanence remaining after different cleaning steps. The best grouping was obtained after 100°–250° C or, in the case of af cleaning, after 25–30 mT. The intensity of the component isolated ranged from 10% to 50% of I_n before cleaning. We assume it to be the CARM preserved in the marls and ovoids. In both cases, its direction is of normal polarity. Figure 6b presents the stereographic projections of the CARM directions for sites 8 and 9. The site mean directions, together with parameters of Fisherian statistics, are included in Table 1.

Discussion and conclusions

The magnetic carriers in the oolitic limestones were stated to be goethite and magnetite. We suppose that goethite A, which forms cores of oolites, is synsedimentary. Part of this mineral is remagnetized in the present field, but part of it (especially with higher T_b) could conserve the remanence acquired at the time of deposition (some Sb samples).

Magnetite, stated mainly as a result of the thermomagnetic method, is probably very fine grained. According to the discussion of mineralogy of marine limestones by Lowrie and Heller (1982), we assume that the magnetite observed here is depositional. In view of the above arguments, we argue that the isolated CARM carried by magnetite and, in some cases, by goethite is Upper Bajocian. This conclusion is supported by results of the fold test applied to site mean directions of Im and Sb. The between-site mean after bedding correction has much better Fisherian confidence parameters than before correction – see Table 1 – indicating that CARM is pre-tectonic. Hence, we argue that the results obtained – mean paleomagnetic field direction $D=30.1^\circ$, $I=53.2^\circ$ and paleopole position latitude = 63.1° , longitude = 120.1° – represent the Upper Bajocian geomagnetic field.

The appearance of normal and reversed directions suggests varying field polarity in the Upper Bajocian.

The NRM of the Pliensbachian deposits is carried by magnetite. The directions of isolated remanence components differ from the reference data, suggesting post-Jurassic magnetization of marls and ovoids.

Acknowledgements. The authors wish to thank Dr. M. Jeleńska and Dr. J.B. Edel for assistance in the field work and helpful discussions.

References

von Eller, J.P.: Vosges-Alsace, collection guides géologiques régionaux. Masson 1976

- Heller, F.: Paleomagnetism of Upper Jurassic limestones from southern Germany. *J. Geophys.* **42**, 475–488, 1977
- Heller, F.: Rock magnetic studies of Upper Jurassic limestones from southern Germany. *J. Geophys.* **44**, 525–543, 1978
- Hijab, B.R., Tarling, D.H.: Lower Jurassic paleomagnetic results from Yorkshire, England, and their implications. *Earth Planet. Sci. Lett.* **60** (1), 147–154, 1982
- Johnson, R.J.E., Van der Voo, R., Lowrie, W.: Paleomagnetism and late diagenesis of Jurassic carbonates from the Jura Mountains, Switzerland and France. *Geol. Soc. Am. Bull.* **95**, 478–488, 1984
- Kądziaiko-Hofmokl, M., Kruczyk, J.: Complete and partial self-reversal of natural remanent magnetization in basaltic rocks from Lower Silesia. *Pageoph.* **114**, 207–213, 1976
- Kądziaiko-Hofmokl, M., Kruczyk, J.: Paleomagnetism of middle-late Jurassic from Poland and implications for the polarity of the geomagnetic field. *Tectonophysics* **139**, 53–66, 1987
- Khramov, A.N. (ed): Materials of the World Data Center B. Paleomagnetic directions and pole positions. Summary catalogue 1. Moskva Nauka: 1984
- Kirshvink, J.L.: The least-squares line and plane and the analysis of paleomagnetic data *Geophys. J. R. Astron. Soc.* **62**, 699–718, 1980
- Kruczyk, J., Kądziaiko-Hofmokl, M., Lefeld, J.: Results of paleomagnetic investigations and the tectonic position of Jurassic radiolarites and limestones of the Lower Sub-Tatric Nappe in the Tatra Mts. *Publ. Inst. Geophys. Pol. Acad. Sci.*, **A-16**(1975) 177–130, 1985
- Kruczyk, J., Kądziaiko-Hofmokl, M., Nozharov, P., Petkov., N., Nachev, I.: Paleomagnetism of Jurassic rocks from the Balkan (Bulgaria) *Bulg. Geophys. J.* **12**, 4, 1986
- Lowrie, W., Channel, J.E.T.: Magnetostatigraphy of the Jurassic-Cretaceous boundary in the Maiolica limestone (Umbria – Italy). *Geology* **12**, 44–47, 1983
- Lowrie, W., Heller, F.: Magnetic properties of marine limestones. *Rev. Geophys. Space Phys.* **20** (2), 171–172, 1982
- Marton, E., Marton, P.: Mesozoic paleomagnetism of the Transdanubian Central Mountains and its tectonic implications. *Tectonophysics* **72**, 129–140, 1981
- Marton, E., Marton, P., Heller, F.: Remanent magnetization of a Pliensbachian limestone sequence at Bakonycsernye (Hungary). *Earth Planet. Sci. Lett.* **48**, 218–226, 1980
- Mauritsch, H.J., Frisch, W.: Palaeomagnetic data from the central part of the northern Calcareous Alps, Austria. *J. Geophys.* **44**, 623–637, 1978
- Soffel, H.: Palaeomagnetism of a Jurassic ophiolite series in east Elba (Italy). *J. Geophys.* **49**, 1–10, 1981
- Steiner M.B., Ogg, J.G., Melendez, G., Sequeiros, L.: Jurassic magnetostratigraphy, 2. Middle-Late Oxfordian of Abuilon, Iberian Cordillera, northern Spain. *Earth Planet. Sci. Lett.* **76**, 151–166, 1985/86
- Westphal, M., Bazhenov, M.L., Lauer, J.P., Pechersky, D.M., Sibuet, J.C.: Paleomagnetic implications on the evolution of the Tethys Belt from the Atlantic Ocean to the Pamirs since the Triassic. *Tectonophysics* **123**, 37–82, 1986

Received December 11, 1986; revised version August 10, 1987 and October 9, 1987

Accepted October 12, 1987

Electromagnetic sounding experiments in the Schwarzwald central gneiss massif

B. Tezkan

Institut für Geophysik, Universität Göttingen, Herzberger Landstrasse 180, D-3400 Göttingen,
Federal Republic of Germany

Abstract. Geomagnetic and telluric pulsations were observed at nine stations, partially at the same time, and at two sites with additional recordings of variations. They occupied a $20 \times 30 \text{ km}^2$ area of high-grade metamorphism. There is a nearly perfect spatial uniformity of the magnetic variation field except for a small local anomaly attributable to the Rheingraben. The telluric field is highly polarized in a $N47 \pm 7W$ direction but with local differences in amplitude. In contrast, telluric phases are spatially uniform and, as a function of period, distinctly different for the $N47W$ orientation of the telluric field (=“*B*-polarisation”) and the $N43E$ orientation (=“*E*-polarisation”). Telluric and magnetic observations are not explainable by one-dimensional (1-D) models for the Schwarzwald alone. Therefore a 2-D model is derived, comprising Schwarzwald and Rheingraben, which can account for the graben *Z* anomaly and the phase curves in both polarisations. An unscaled 1-D model is obtained from the telluric phases in *E*-polarisation and then a 2-D model for Schwarzwald and Rheingraben in *E*- and *B*-polarisation. This latter model allows the scaling of the 1-D Schwarzwald model and shows a thin conductive layer under the gneiss massif at a depth of 12 km with a conductance of 650 S.

Key words: Geomagnetic and telluric time variations – Magnetotellurics – Geomagnetic deep sounding – Electric conductivity structure – Rheingraben – Schwarzwald

Introduction

The Schwarzwald (“Black Forest”) is one of the largest crystalline complexes of central Europe. It is 30 km wide and 100 km long, situated between the Rheingraben to the west and the Swabian Alps to the east. Two major crystalline rock types are exposed (Fig. 1): high-metamorphic and anatectic gneiss of probably Precambrian age and granitic rocks from Paleozoic plutonism during the Variscian orogenesis.

The electromagnetic sounding survey concentrated on the gneiss area which forms the central part of the Schwarzwald, known as „Hochschwarzwald“. These are the survey stations: HTZ (Hinterzarten), BRE (Breitnau), NEU (Neukirch), STM (St. Märgen), LAN (Landeck), FRE (Freiamt), ELZ (Elzach), SNH (Schonach), TRI (Triberg), TIE (Tiefenbach), ENZ (Enzklösterle), GUE (Gütenbach). To study the influence of foliation of metamorphic rocks

on the telluric field, to be expected in the gneiss area, two stations were placed on granitic rocks where foliation is absent: SNH and TRI, both on the so-called “Triberg Granite”. Two stations (ENZ and LAN) were set up outside the exposed crystalline complex on Mesozoic Buntsandstein. But in either case the crystalline basement rocks are expected at shallow depth. Station LAN was the nearest one to the Rheingraben. This rift system is filled with unconsolidated young Mesozoic and Cenozoic sediments. Their resistivity is as low as $1 \Omega\text{m}$. To the west of the Rheingraben, which is at least 40 km wide, there is a second crystalline complex: the Vogesen (“Vosges”).

At the east the Schwarzwald borders on Mesozoic sediments with resistivity not below $20 \Omega\text{m}$. Thus, along the eastern edge a less severe resistivity distribution was expected. The crystalline complex has been uplifted since late Cretaceous and early Tertiary, and afterwards deeply eroded. It shows strong signatures from the Variscian mountain building in the younger Paleozoics. The Variscian strike direction $N45E$ is preserved in lineaments crossing the gneiss complex and also visible in gravimetric and static magnetic anomalies trending in about the same direction. The Rheingraben belongs to a continental-wide rift system with a mean strike of $N15E$ in the portion which borders on the survey area. Subsidence began in the Tertiary and the sedimentary fill varies between 2500 m in the north and 1000 m in the south.

The purpose of the survey can be summarized as follows. From general experience it was to be expected that the telluric field on the exposed crystalline rock formation would be highly distorted, locally varying greatly in direction and amplitude over short distances. In the Bayerischer Wald („Bavarian Forest”) for example, changes in amplitude by orders of magnitude were observed at stations 2.5 km apart, here under the influence of graphite-bearing schists close to the surface (Tezkan, 1984). Results of earlier MT soundings in the Schwarzwald at stations ENZ, TIE and HTZ have been presented by Richards et al. (1981). A new analysis of their data, now involving a rotation of coordinates, revealed surprisingly uniform telluric directions with a strong dominance of the field in a northwest direction. The general validity of this remarkable result was to be tested with a denser network of stations. Also available were MT results from the Rheingraben (Winter, 1973; Reitmayr, 1974) which allowed estimation of the graben sediment conductance (1000–1600 S) and of the resistivity of crust and mantle below. This information was essential

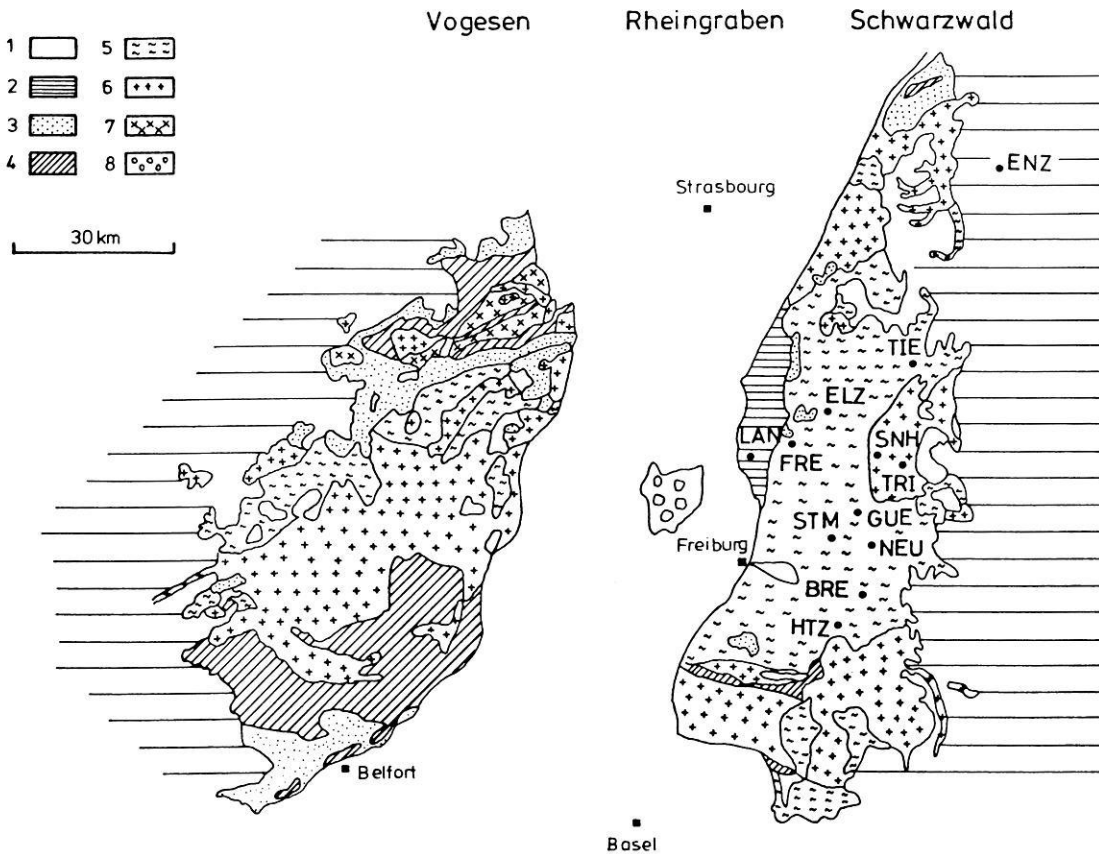


Fig. 1. Simplified geological map of Schwarzwald, Vogesen and the Rheingraben rift, showing the position of the survey stations. 1, Cenozoic and Mesozoic graben sediments; 2, Mesozoic sediments outside the graben; 3, Permian sediments; 4, Pre-Permian sediments; 5, gneiss and migmatites; 6, granite; 7, granodiorites; 8, Tertiary volcanics (Kaiserstuhl)

to estimate the induction effect of the Rheingraben sediments on the telluric and magnetic field in the survey area.

Teufel (1986) carried out a similar survey in the northern part of the Schwarzwald at about the same time, but with the inclusion of high frequencies. His results are in good agreement with the conclusion which can be drawn from the observations now to be presented.

Field survey and data analysis

The field survey was carried out with nine stations, recording simultaneously at four stations. They were equipped with induction coil magnetometers and *E*-field recording systems for the observation of pulsations. At one site a recording time of 2 or 3 weeks was needed to get responses of sufficient accuracy. At one station (GUE) it was impossible to record *E*-field pulsations because of industrial noise. Otherwise, for an industrial environment, low noise levels were observed. Variations were recorded for 8 weeks at two selected stations (TRI and NEU) equipped with flux-gate magnetometers. Altogether, a total of 20–30 h of about 100 time sections with strong activity for pulsations and 260–270 h of 70 time sections for variations were selected from the available records for spectral analysis.

The preliminary treatment of data in the time domain and the following analysis in the frequency domain were carried out with standard methods (Schmucker, 1978). Some of the essential results can be verified by visual inspection

of the traces in Fig. 2. These time series of 9 min contain irregular oscillations in the period range between 10 and 100 s. The displayed records are not corrected for instrumental responses, but since response curves are similar for all sites direct comparison is possible.

Differences barely exist between the *H*- and *D*-pulsations of the magnetic field at different sites (*H*: north component, *D*: east component). The subsequent analysis confirmed this impression, i.e. the respective transfer functions for *H* and *D* show no significant anomalies. However, small differences in the *Z* component (vertical) can be recognized. Maximum *Z* amplitudes are observed at the most western stations, particularly at LAN (not shown in Fig. 2). The spectral analysis shows that the magnetic transfer functions for *Z* have a characteristic dependence on period attributable to the sediments of the Rheingraben. They produce a pronounced local *Z* anomaly near to the border of the Rheingraben, whereas the associated smooth anomaly of the horizontal component normal to the Rheingraben is too small to be recognizable in the Schwarzwald.

From the telluric pulsations in north (*EN*) and east (*EO*) directions, local differences in amplitudes are noticeable but not as severe as expected from experiences in the Bavarian Forest (Tezkan, 1984). The analysis shows that they can be very well correlated from station to station. Not visible in this figure is a pronounced telluric polarisation in a northwest direction. But this does not apply for station SNH on Triberg Granite. The *EN* and *EO* pulsations for

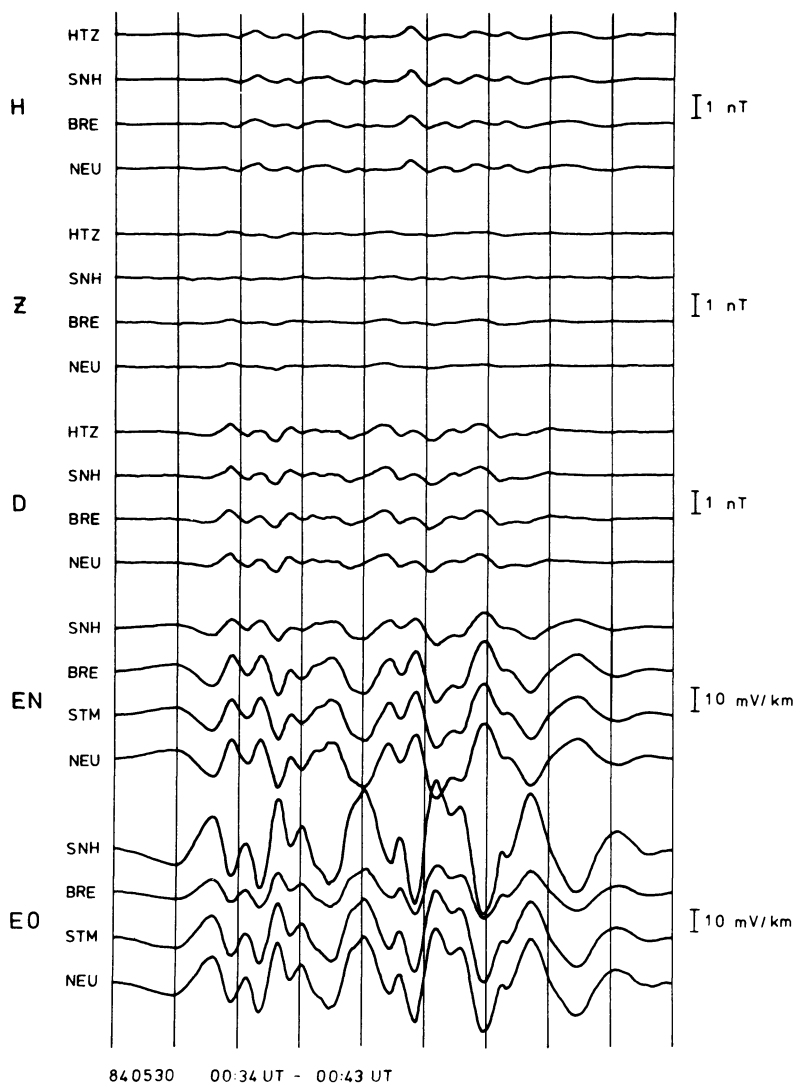


Fig. 2. Record sections of 9 min from four Schwarzwald stations. Nearly identical magnetic H , D , Z pulsations at all sites and similar telluric EN (north) and EO (east) pulsations at the gneiss stations BRE, NEU, STM. Station SNH on granite has different telluric amplitudes, reflecting different preferred coordinates

this station clearly differ from those at the other stations and the dominant telluric polarisation is different here, i.e. east-west.

For a fixed frequency and site, the complex Fourier coefficients of Z , EN and EO are connected with local H and D by the following set of transfer functions:

$$\begin{aligned} Z &= z_H H + z_D D + \delta Z \\ EN &= Z_{xx} H + Z_{xy} D + \delta EN \\ EO &= Z_{yx} H + Z_{yy} D + \delta EO \end{aligned} \quad (1)$$

where δZ , δEN and δEO express the uncorrelated part in Z , EN and EO . The best-fitting transfer functions z_H , z_D ... will be considered those which produce minimum $\langle |\delta Z|^2 \rangle$. Averaging $\langle \dots \rangle$ is not only over neighbouring frequencies with spectral filters (Parzen filter), but also over assemblages of time sections. (Schmucker and Weidelt, 1975; Schmucker, 1978).

The coherence, in conjunction with the degree of freedom of the averaging procedure, establishes confidence limits for the transfer functions. They refer to an error probability of 32%. A squared coherency threshold was used in the analysis: 0.64 for magnetic transfer functions and 0.81 for electric transfer functions.

The spectral analysis was carried out in four overlapping frequency ranges for pulsations and in three overlapping frequency ranges for variations, with

$\Delta f = 0.1$ cpm	and the central frequencies	0.1–0.8 cpm
0.2 cpm		0.2–3.0 cpm
0.5 cpm		0.5–3.0 cpm
1.0 cpm		1.0–8.0 cpm
$\Delta f = 0.1$ cph		0.2–0.8 cph
0.2 cph		0.6–2.0 cph
0.5 cph		1.0–5.0 cph.

The frequency unit is cpm = cycles per minute and cph = cycles per hour.

Electric and magnetic transfer functions for the Schwarzwald are presented and discussed in the following paragraphs. The derived linear relations in Eq. (1) can be explained as a function of frequency in such a way that the magnetic transfer functions z_H , z_D express the effect of lateral inhomogeneities of conductivity, i.e. the Rhein-graben anomaly; whereas in the magnetotelluric impedance, the depth distribution of conductivity becomes visible only after considering its extreme directional dependence.

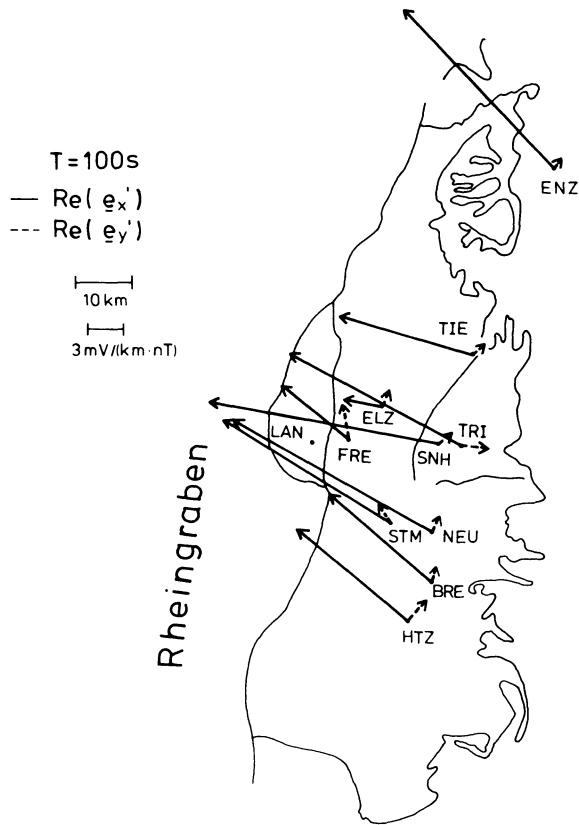


Fig. 3. Real part of the telluric vectors ($\mathbf{e}_{x'}$, $\mathbf{e}_{y'}$) in rotated preferred coordinates for all Schwarzwald stations except LAN (not included). It should be noted, however, that for stations SNH and TRI on the Triberg Granite, the chosen angle of rotation (43°) is not the optimum angle for the Swift criterion. A large but uniform directional dependence of the telluric field can be inferred: large-scale induced currents in a northwest direction, are 5–10 times stronger than those flowing in a northeast direction, isotropic conductivity assumed

Discussion of transfer functions

Magnetotellurics

For visual display, the tensor impedance Z for each site and frequency is represented by telluric vectors defined by:

$$\begin{aligned} \mathbf{e}_x &= Z_{xx}\hat{\mathbf{x}} + Z_{yx}\hat{\mathbf{y}} \\ \mathbf{e}_y &= Z_{xy}\hat{\mathbf{x}} + Z_{yy}\hat{\mathbf{y}} \end{aligned} \quad (2)$$

where $\hat{\mathbf{x}}$ and $\hat{\mathbf{y}}$ are unit vectors toward north and east. Assuming an isotropic conductivity distribution they indicate amplitude, phase and direction of the electric currents flowing in the subsurface for linearly polarized magnetic fields in the x and y direction. Swift's criterion (Swift, 1967) for optimal coordinates is used, in which $|Z_{xx} - Z_{yy}|$ is at a minimum. Tensor impedances are transferred to these new preferred coordinates (x' , y'), rotated clockwise by angle α . Such transformations will emphasize existing symmetries in the conductivity structure and are useful if the rotation angle turns out to be fairly independent of frequency and location.

With the exception of the stations on the Triberger Granite (TRI, SNH) and the Rheingraben border station (LAN), rotation angles are about the same for all Schwarzwald

stations and frequencies. Their rotation angle is 43° , averaged over all frequencies and stations, with a standard deviation of 7° . The impedances cited in the following refer exclusively to this rotated coordinate system.

Figure 3 shows the real part of the telluric vectors $\mathbf{e}_{x'}$ and $\mathbf{e}_{y'}$ for all Schwarzwald stations for a period of 100 s. They indicate a strong but uniform directional dependence of the telluric field. The regionally induced currents flow with maximum strength (for isotropic conductivity) through the Schwarzwald in a northwesterly direction and they are 5–10 times weaker in the perpendicular direction. Minor differences exist in strength and direction, but a rather uniform anisotropy parameter $A = |Z_{y'x'}|/|Z_{x'y'}|$ exists, large compared to unity.

Figure 4 shows telluric vectors over the entire period range for two selected Schwarzwald stations: a typical gneiss station, BRE, and the Rheingraben border station, LAN. Note that a different rotation angle $\alpha = 69^\circ$ was used for LAN. All vectors are normalized to period $T_0 = 100$ s, using the scaling factor $\sqrt{T/T_0}$ for a uniform half-space. This implies that all normalized vectors would have the same length and direction (normal to the magnetic field) if the subsurface structure were uniform.

As seen on the left, $\mathbf{e}_{x'}$ vectors point correctly in the y' direction, which is roughly northwest. The changing apparent resistivity and phase as a function of period is evident (see also Figs. 5 and 6). They are associated later with the B -polarisation of a 2-D structure where the phase begins and ends at 45° with a minimum phase of 35° at intermediate periods. The telluric $\mathbf{e}_{y'}$ vectors to the right are comparatively small and irregular. As shown later, the $Z_{x'y'}$ or x' -component of this vector, to be associated with the E -polarisation, contains the whole information about the conductivity-depth distribution. Also evident from Fig. 4 is the persistent large anisotropy with no indication of approaching unity at short periods.

Certain local differences in $Z_{y'x'}$, assigned to B -polarisation, cannot be overlooked. This is clear by comparing the neighbouring stations FRE and ELZ in Fig. 3. But in view of the anisotropy, an explanation of the $Z_{y'x'}$ variability with models will not be attempted. Instead, a general conclusion can be drawn from Fig. 3 and 4: the Schwarzwald crystalline complex is surprisingly homogeneous in its conductivity structure, but with a strongly directional-dependent impedance yielding an anisotropy of about ten.

Because of this dependence it is difficult to derive conceptions for the conductivity-depth distribution. This difficulty is demonstrated in Fig. 5 by displaying the apparent resistivity $\rho_{aij} (= \mu_0/\omega |Z_{ij}|^2)$ of the three stations TRI, BRE, LAN; a granite station, a gneiss and a border station. The ρ_a curves for both polarisations are orders of magnitude apart. Hence, a simple connection to the true deep resistivity is not evident. However, the ρ_a -curves of the three stations have remarkably similar dependences on period for the two polarisations. The 45° descent of ρ_a for $Z_{x'y'}$ (E -polarisation) between 10 and 50 s can be interpreted by a good conductor at an undetermined absolute depth. But, as demonstrated later, the Rheingraben Z -anomaly will provide an absolute scaling of this depth.

The phases ϕ of impedances $Z_{x'y'}$ and $Z_{y'x'}$ confirm the results obtained from the period dependence of ρ_a . They are presented in Fig. 6 and show clear differences for the two polarisations. The following discussion will be based on phases rather than the period dependence of ρ_a . There

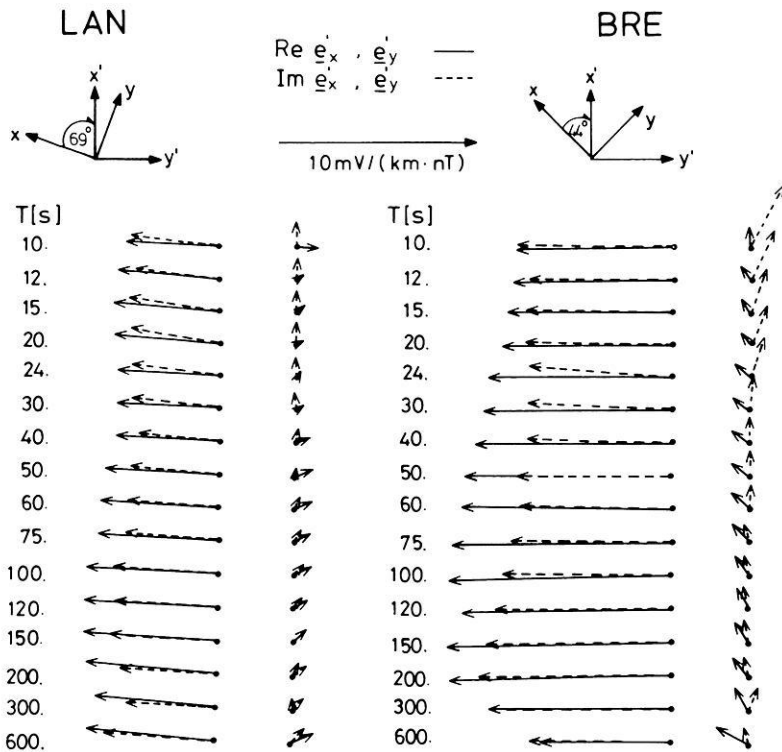


Fig. 4. Telluric vectors for two Schwarzwald stations in the period range 10–600 s, normalized to the period $T_o=100$ s, with scaling factor $\sqrt{T/T_o}$ for a uniform half-space. Most conspicuous is the different lengths for the two polarisations. Small telluric e_y vectors are associated with E -polarisation for a magnetic y' -polarisation and assumed to be close to the 1-D response of the Schwarzwald substratum. Their variable lengths with period reflect the changing conductivity with depth. Large and well-determined e_x vectors indicate phases close to 45° with no direct bearing on the conductivity-depth distribution

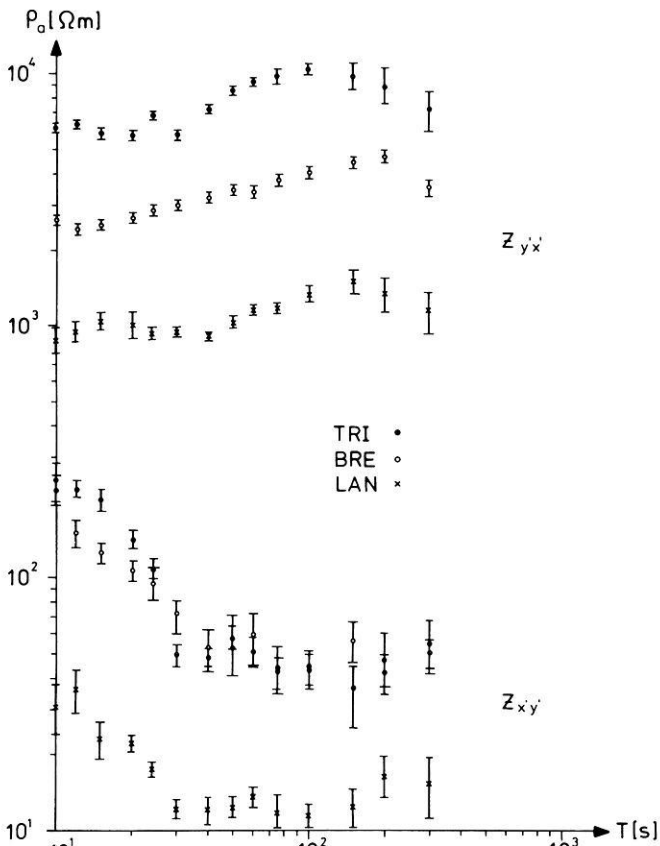


Fig. 5. Apparent resistivity curves for three typical Schwarzwald stations: upper curves for magnetic x' -polarisation (B) and lower curves for magnetic y' -polarisation (E) in rotated coordinates. The two sets of curves differ by one order of magnitude with systematically different period dependences. From the downward slope in the lower curves there is evidence for a good conductor beneath the Schwarzwald

Table 1. Apparent resistivities ρ_a (Ωm), phases ϕ ($^\circ$) and anisotropy values A for $T=60$ s

Station	A	E -polarisation ($Z_{x'y'}$)		B -polarisation ($Z_{y'x'}$)	
		ρ_a	ϕ	ρ_a	ϕ
BRE	0.96	60 ± 14	59.6 ± 6.8	3480 ± 120	35.7 ± 1.0
NEU	1.56	69 ± 15	60.8 ± 6.1	9360 ± 210	36.3 ± 0.6
STM ^a	1.36	16 ± 4	76.4 ± 8.0	7630 ± 340	35.1 ± 1.2
SNH ^c	4.54	89 ± 16	67.9 ± 5.0	8340 ± 210	35.6 ± 0.7
LAN ^b	0.272	79 ± 7	50.2 ± 2.4	1000 ± 40	37.4 ± 1.2
FRE ^b	0.735	165 ± 16	56.0 ± 2.7	1650 ± 90	39.7 ± 1.5
TRI ^c	2.12	100 ± 14	56.0 ± 3.9	880 ± 220	36.2 ± 0.7

^a Only telluric observations, reference magnetic field is BRE

^b Border stations

^c Granite stations

is an ascent of the phase for E -polarisation from 70° to 80° between 10 and 15 s and then a drop to 45° which implies that a good conductor forms the lower boundary of the Schwarzwald crystalline complex as mentioned in the discussion of ρ_a curves. In contrast, the phases for B -polarisation stay close to 45° with a drop to 35° between 10 and 100 s. These characteristic phases are observed at all Schwarzwald stations and the difference in the two polarisations can be understood as an influence of the Rhein-graben. Phases and apparent resistivities are tabulated in Table 1 for a period of 60 s. This table summarizes results from magnetotellurics as follows (Schmucker and Tezkan, 1985):

A) Amplitudes of E fields vary from station to station. The ρ_a curves of both polarisations lie far apart; for the E -polarisation below $100 \Omega\text{m}$ and for the B -polarisation above $1000 \Omega\text{m}$.

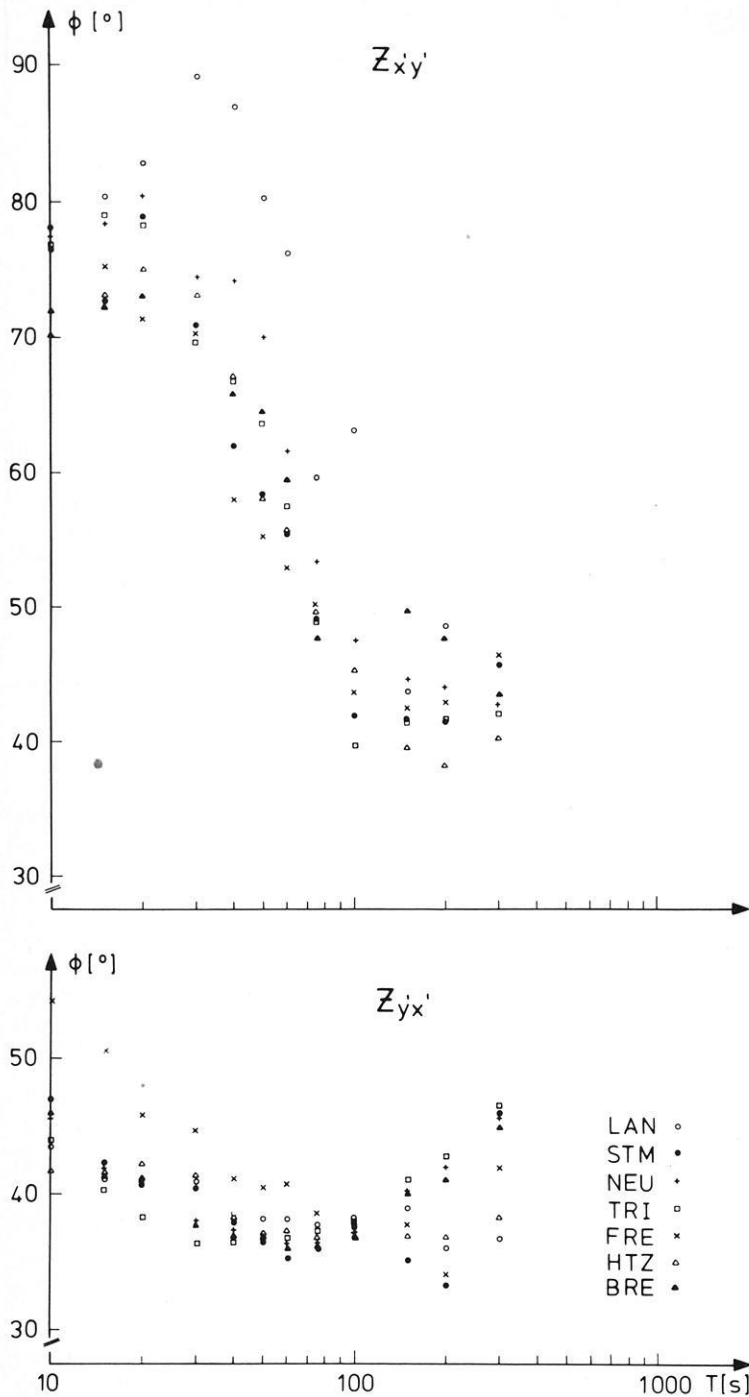


Fig. 6. Phase curves for all Schwarzwald stations in rotated coordinates. For easier visibility, no confidence limits are shown. Note their consistency for one polarisation and their systematic difference between E -($Z_{x'y'}$)- and B -($Z_{y'x'}$)-polarisation. The discrepancy in phase between the two polarisations can be understood as the 2-D effect of the Rheingraben sediments

B) Stable but different phases for the two polarisations; approximately 60° for the E -polarisation and 35° for the B -polarisation.

In addition, the impedance estimates are shown in Fig. 7, as a function of period, in the form of $\rho^*(z^*)$ curves. A typical gneiss station NEU is chosen, where long-period variations were also observed. ρ^* is a modified apparent resistivity considering the inductive effect of the top layers and defined by (Schmucker, 1979)

$$\rho^* = \rho_a \begin{cases} 2 \cos^2 \phi, & \phi \geq 45^\circ \\ 1/(2 \sin^2 \phi), & \phi \leq 45^\circ \end{cases} \quad (3)$$

It is assigned as a substitute resistivity to a depth $z^* = \sqrt{\rho_a / \omega \mu_0} \cdot \sin \phi$. Such representations allow first estimates of the conductivity-depth distribution, and also test the consistency of the impedance for the 1-D condition in which z^* must monotonically increase with period. Figure 7 contains $\rho^*(z^*)$ depth sections lying far apart for E - and B -polarisations, as to be expected. Only the $\rho^*(z^*)$ curves for the E -polarisation ($Z_{x'y'}$) should be considered as a representation of the conductivity-depth distribution. The z^* depth values concentrate at 20 km with apparent resistivities below $10 \Omega\text{m}$ for fast pulsations, reflecting the top of the conductor beneath the Schwarzwald crystalline com-

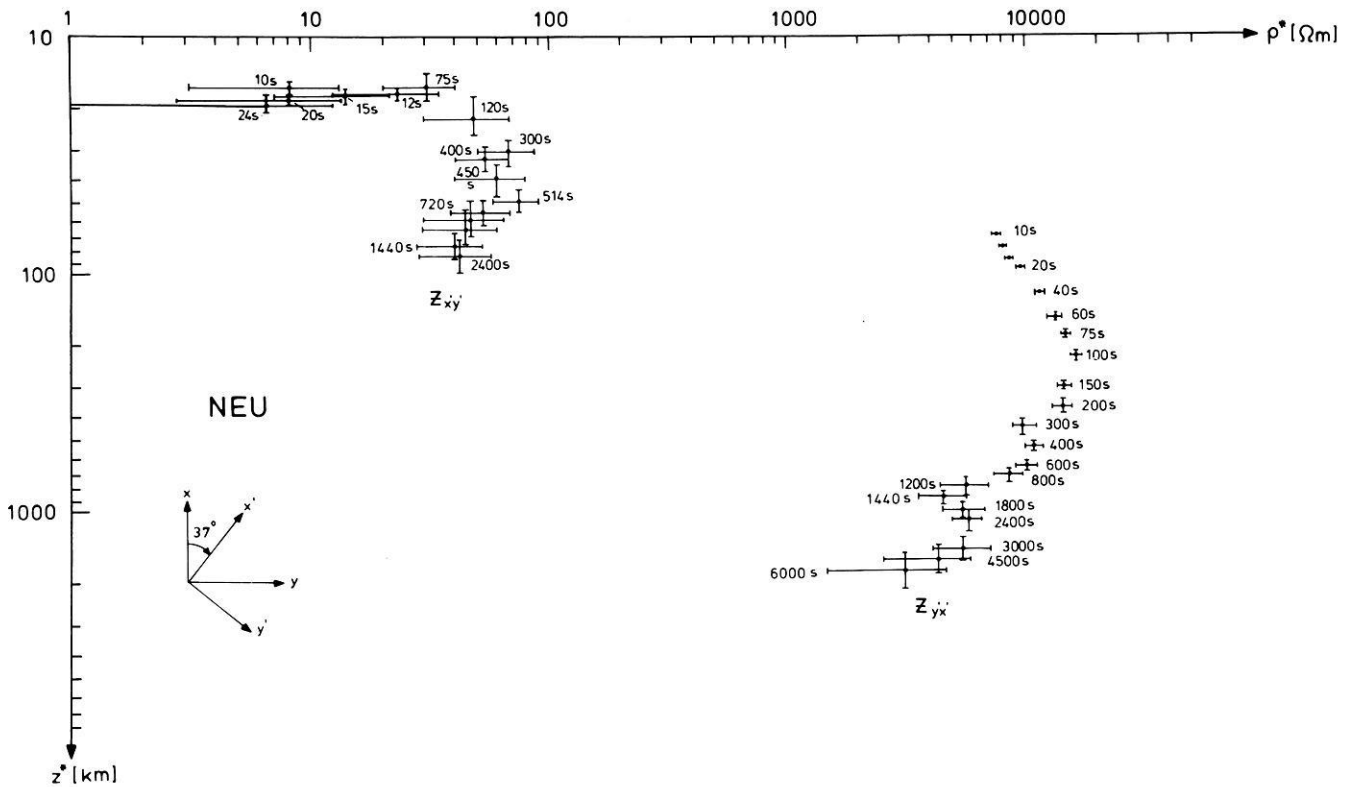


Fig. 7. $\rho^*(z^*)$ curves of E -($Z_{x'y'}$)- and B -($Z_{yx'}$)-polarisation for the Schwarzwald station NEU. Only the $\rho^*(z^*)$ curve for E -polarisation should be considered as a representation of the true conductivity distribution beneath the Schwarzwald. Note that z^* values concentrate at 20 km with apparent resistivities below 10 Ωm between 10 and 75 s, reflecting the top of the crustal conductor beneath crystalline. Observe the ascent in ρ^* below that depth, indicating a transition to a normal mantle resistivity of 50 Ωm

plex. A strong ascent of apparent resistivity begins at 75 s with peak values of 70 Ωm for 300–500 s and a depth z^* of 40 km. From 700 s onward, there is a descent of apparent resistivities to 40 Ωm , reflecting the resistivity of the deeper layer of the upper mantle beneath Schwarzwald. But note that the quoted values $\rho^*(z^*)$ are still subject to scaling factors.

Geomagnetic depth sounding

The interpretation of the magnetic transfer functions concerns the anomalies of the vertical magnetic field variations because no visible anomaly in the horizontal field exists in the Schwarzwald, as discussed before.

Figure 8 shows a map representation of the transfer functions (z_H , z_D) in the form of induction arrows. With the notation of Eq. (1), the induction arrows are defined by the real and imaginary part of \mathbf{u}

$$\mathbf{u} = z_H \cdot \hat{\mathbf{x}} + z_D \cdot \hat{\mathbf{y}}, \quad (4)$$

where $\hat{\mathbf{x}}$ and $\hat{\mathbf{y}}$ are unit vectors. Length and direction of these arrows are independent of the coordinate system and point away from the good conductor towards less-conducting zones. They are perpendicular to the strike of a 2-D anomaly. The closer a station is situated to a lateral contrast of conductivity, the larger is the anomalous Z and thus the length of \mathbf{u} .

As seen in Fig. 8, the induction arrows of all stations point away from the Rheingraben as a good conductor. The largest arrow lengths are found at the border stations

LAN and FRE, oriented perpendicular to the local eastern boundary of the Rheingraben. In all probability, the observed Z pulsations represent the graben effect and no substantial changes of conductivity are seen in the Schwarzwald crystalline complex itself, at least not in the analysed period interval. This applies especially to the good conductor beneath the Schwarzwald, which seems to have a regionally uniform depth and conductance.

A characteristic period dependence of the graben border anomaly is found. It can be inferred from the profile representations in Fig. 10, which also demonstrates the decrease of the graben anomaly with increasing distance from the Rheingraben of the four Schwarzwald stations LAN, FRE, SNH and TRI.

Interpretation of the transfer functions by models

Results of magnetotelluric and geomagnetic depth sounding contain different information about the conductivity distribution, as discussed earlier. Now, an attempt will be made to interpret them jointly with two-dimensional models.

However, the representation of impedance tensor elements in the form of telluric vectors shows that it will be difficult to find a model which is able to explain the large anisotropy as well as the locally very variable apparent resistivity. It can be assumed that surficial well-conducting veins in a poorly conducting environment do not change the magnetic variation field at sufficiently long periods. On the other hand, the amplitudes of the electric field can be severely affected, whereas their phases remain unchanged.

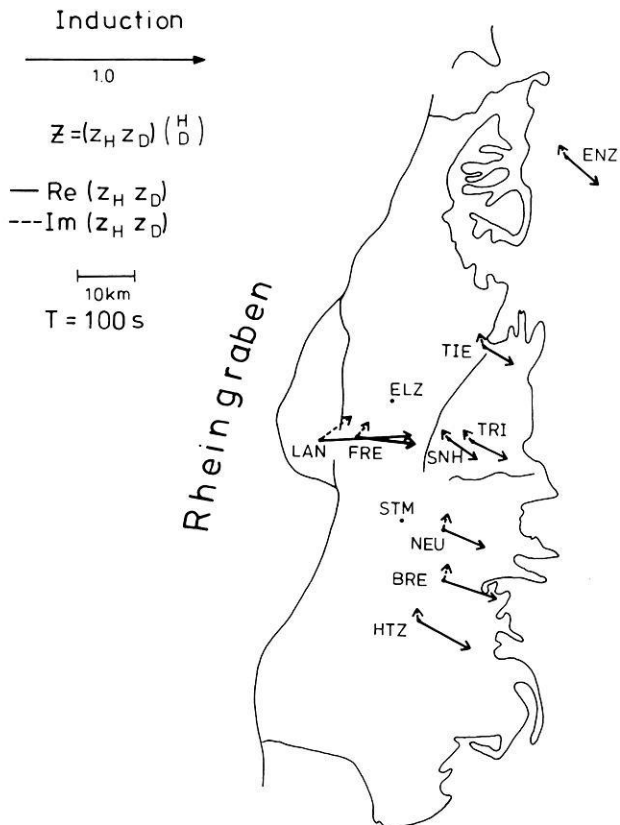


Fig. 8. Map representation of induction arrows for all Schwarzwald stations for a period of 100 s. Maximum Z values are observed at western border stations and all arrows point away from the Rheingraben as a good conductor. In all probability, the observed Z pulsations represent the graben effect and no substantial lateral changes of conductivity are seen in the Schwarzwald crystalline complex itself

For this reason, we try to calculate a 2-D model which explains the Rheingraben Z anomaly as well as the period dependence of the phase curves for the off-diagonal impedance elements $Z_{x'y'}$ and $Z_{y'x'}$. These are the data which can be reproduced by models.

First of all an unscaled 1-D model, which is not shown here, is derived from the telluric phases in E -polarisation. It is used as a starting model for the 2-D model calculations. The conductance of the Rheingraben sedimentary filling and the deeper conductivity distribution beneath it are adopted from Winter (1973) and Reitmayr (1974). Further north of the investigated area, Winter quoted 2000 S ($S = \text{Siemens}$) for a sedimentary thickness of 2 km. In the model,

a value of 1500 S is chosen because of the southwest decrease of the sedimentary thickness in the Rheingraben.

Before going into details, a fundamental difficulty must be mentioned. The calculated magnetic and electric transfer functions do not refer to the same coordinates: the Rheingraben in a N15E direction is chosen as the x'' strike direction of the 2-D model, with y'' as the direction of the model cross-section. The calculated magnetic Z anomaly for this cross section is compared directly with the observed transfer functions of Z . The model impedances $Z_{x''y''}$ and $Z_{y''x''}$, however, are compared with the observed impedances $Z_{x'y'}$ and $Z_{y'x'}$, referring to coordinates rotated by 43° from north, as determined by the Swift criterion. The discrepancy expresses the unavoidable deficiency of any interpretation by two-dimensional models. As discussed before, the (x', y') coordinates are optimal coordinates for the Schwarzwald impedances. This means that the coordinates for the Z anomaly and the impedances differ by 28° . The amplitudes of the electric field, i.e. the apparent resistivities derived by them, will remain unconsidered. Nevertheless, the model will explain those for E -polarisation, at least approximately.

The chosen 2-D model is shown in Fig. 9 with the coordinate system used for the magnetic and electric transfer functions. The observed border anomaly of Z and the phases of the off-diagonal elements of the impedance tensor are compared in Figs. 10 and 11 with model values obtained from the 2-D model in Fig. 9. $z_{D''}$ is the magnetic transfer function projected to the profile direction. The period dependence of the phase curves is critical for the modelling because of the regional uniformity of the phase for a fixed period.

The Rheingraben model above cannot explain the observed telluric graben anomaly alone; in particular, not in its phases. However, a well-fitting model can be obtained by adding a good crustal conductor beneath the Schwarzwald. Its depth and conductance can now be given by a joint interpretation of the graben anomaly in Z and the telluric phases.

The 2-D model cross-section in Fig. 9 for the Schwarzwald and Rheingraben successfully explains the local Z variations and the large offset between the phase curves of both polarisations. Ultimately, the sediments of the Rheingraben are the cause of the offset of the phase curves, but the conductivity structure beneath the Schwarzwald determines their course. The 2-D model now allows the scaling of the 1-D Schwarzwald model with the following results:

- 1) To a depth of 12 km, the Schwarzwald is poorly conducting ($> 200 \Omega\text{m}$) with no resolvable structure in the investigated period range.
- 2) Below that depth a thin conductor appears, underlain by a less-conducting deep crust ($1000 \Omega\text{m}$) over a well-conducting half-space at 40 km ($15 \Omega\text{m}$).

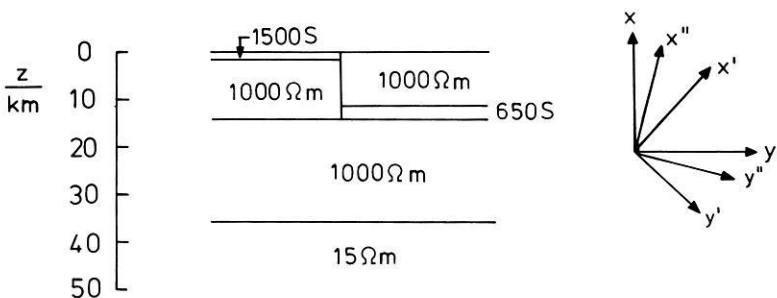


Fig. 9. 2-D model for the Rheingraben sediment to the left and the Schwarzwald crystalline complex to the right. The model is symmetric about the graben centre with a total graben width of 32 km. (x, y) , geographic coordinates; (x'', y'') , model coordinates used for a comparison with Z -transfer functions; (x', y') , optimal coordinates for the telluric field in the Schwarzwald, used for a comparison with the telluric transfer functions

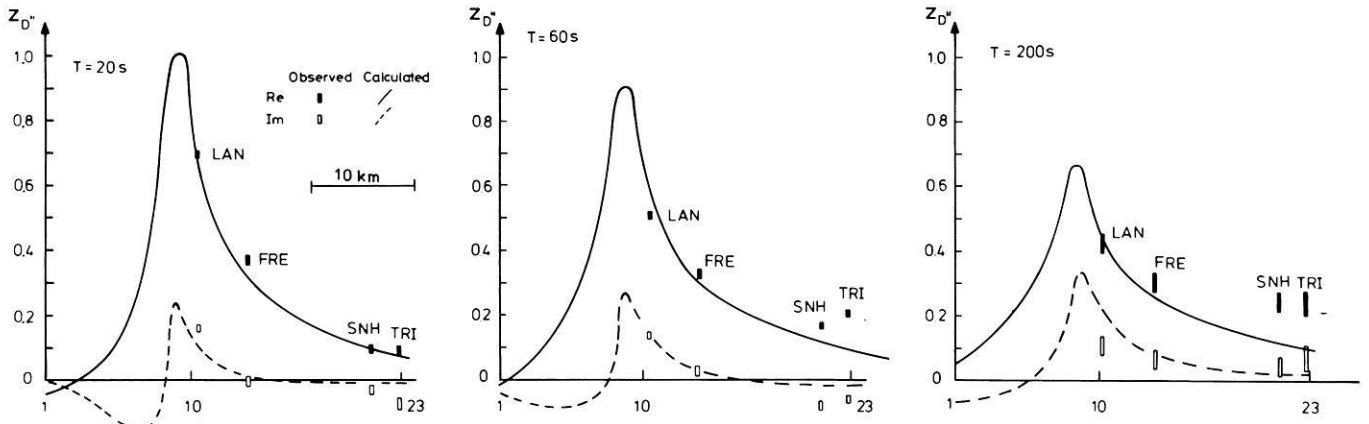


Fig. 10. In-phase and out-of-phase graben anomaly in Z , for the model in Fig. 9, as a function of distance from the graben centre. Observed and calculated transfer functions are compared for three periods. The indicated confidence limits refer to an error probability of 32%

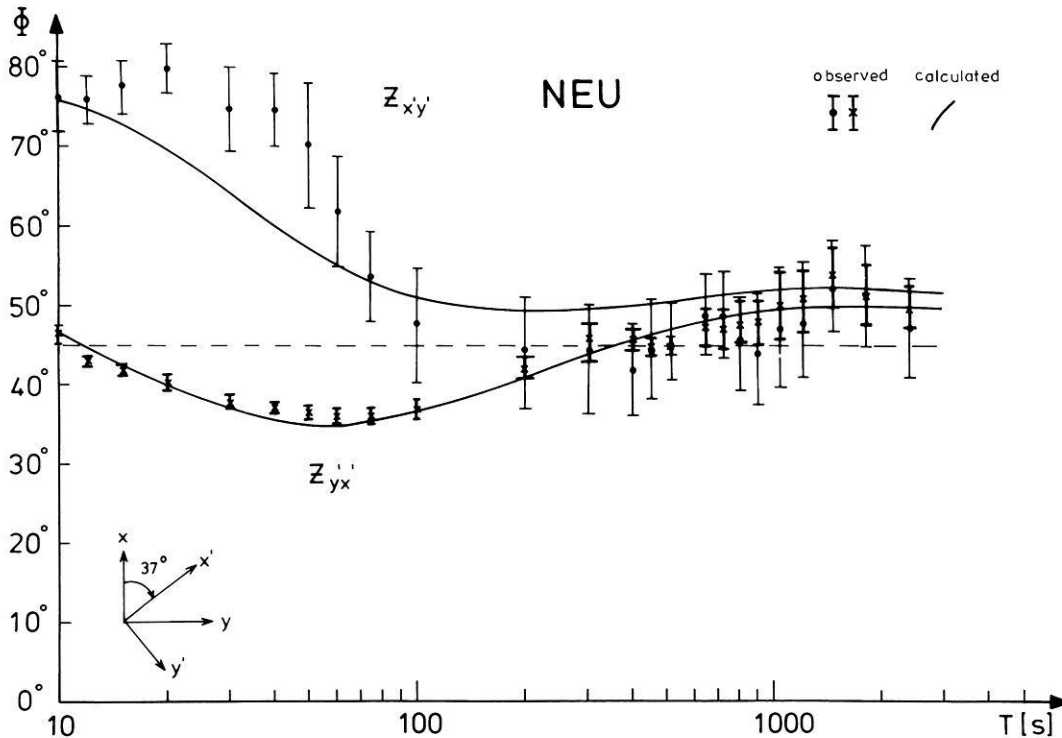


Fig. 11. Schwarzwald phase curves of the impedance, with their confidence limits referring to an error probability of 32%, for E - and B -polarisation for the model in Fig. 9 at 40 km distance from the graben centre. Calculated phases for periods from 10 to 3600 s are compared with empirical phases for gneiss station NEU at that distance. Note that on the Schwarzwald side, calculated and observed phases vary little with distance from the graben centre. Therefore, a comparable fit applies to all Schwarzwald stations

Numerical model studies show that some variations of the good conductor under the Schwarzwald are allowed, even though without this layer no satisfying fit can be obtained for Z variations as well as for the phases of the impedance. The best fit is obtained for a thin conductor at a depth of 12 km with a conductance of 650 S. The resistivity of this layer must be below $10 \Omega\text{m}$, corresponding to the ρ^* minimum in Fig. 7. A thorough investigation of acceptable models can be found in the discussion of observations in the northern Schwarzwald by Teufel (1986), who comes to similar conclusions.

Conclusion

The magnetic and electric transfer functions discussed can be considered as complete and conclusive. However, their interpretation with two-dimensional models is to be regarded as preliminary, in particular because calculated magnetic and electric transfer functions do not refer to the same coordinates when compared with observations.

Allowing for these principal difficulties, a two-dimensional conductivity distribution for the Schwarzwald was successfully derived:

A) The 2-D model of Fig. 9 explains the Z anomaly and the phases of the impedance in E - and B -polarisation.

B) The 2-D model calculations confirm the existence of a thin conductive layer under the Schwarzwald crystalline complex. The depth of this layer is at least 12 km and at most 18 km. The thickness of it cannot be resolved, but its conductance can be estimated to be 650 S.

C) The large anisotropy of the impedance and the variable apparent resistivities from station to station are not explained.

Acknowledgements: I wish to thank Prof. U. Schmucker for many stimulating discussions and for kindly reading the manuscript.

References

- Reitmayr, G.: Elektromagnetische Induktion im Erdinnern, studiert am Rheingraben. Diss. Fak. f. Geowissenschaften der Ludwig-Maximilians-Universität München, 1974
- Richards, M.L., Schmucker, U., Steveling, E., Watermann, J.: Erdmagnetische und magnetotellurische Sondierungen im Gebiet des mitteleuropäischen Riftsystem. Forschungsbericht T81-III, Bundesministerium für Forschung und Technologie, Bonn, 1981
- Schmucker, U.: Auswertungsverfahren Göttingen. Protokoll Kolloquium Elektromagnetische Tiefenforschung. Neustadt/Weinstraße, 163–188, 1978
- Schmucker, U.: Erdmagnetische Variationen und die elektrische Leitfähigkeit in tieferen Schichten der Erde. Sitzungsberichte und Mitteilungen der Braunschweigischen Wissenschaftlichen Gesellschaft. Sonderheft 4, Goltze Verlag, Göttingen, 45–102, 1979
- Schmucker, U., Weidelt, P.: Electromagnetic induction in the Earth. Lecture notes, Aarhus, 1975
- Schmucker, U., Tezkan, B.: Erdmagnetische und tellurische Untersuchungen im Schwarzwald. Bericht zum Unterantrag der Univ. Karlsruhe zum BMFT Förderungsvorhaben R683146, Inst. f. Geophysik, Univ. Göttingen, 1985
- Swift, C.M.: A magnetotelluric investigation of an electrical conductivity anomaly in South Western United States. Ph.D. Thesis, M.I.T., Cambridge, Mass., 1967
- Teufel, U.: Die Verteilung der elektrischen Leitfähigkeit in der Erdkruste unter dem Schwarzwald, ein Beispiel für Möglichkeiten und Grenzen der Interpretation von Audio-Magnetotellurik, Magnetotellurik, Erdmagnetischer Tiefensondierung. Diss. Fak. f. Geowissenschaften der Ludwig-Maximilians-Universität München, 1986
- Tezkan, B.: Einfluß von Graphitgängen auf EM-Sondierungen mit Pulsationen im südöstlichen Bayerischen Wald. Protokoll Kolloquium Elektromagnetische Tiefenforschung, Grafrath, 145–152, 1984
- Tezkan, B.: Erdmagnetische und magnetotellurische Untersuchungen auf den hochohmigen Kristallinstrukturen des Hochschwarzwaldes und des Bayerischen Waldes bei Passau. Diss. Math.-Nat. Fak., Univ. Göttingen, 1986
- Winter, R.: Der Oberrheingraben als Anomalie der elektrischen Leitfähigkeit, untersucht mit Methoden der erdmagnetischen Tiefensondierung. Diss. Math.-Nat.Fak., Univ. Göttingen, 1973

Received March 6, 1987; revised July 10, 1987

Accepted August 7, 1987

Interpretation of the magnetotelluric impedance tensor: regional induction and local telluric distortion

Karsten Bahr*

Ocean Research Division A-030, Scripps Institution of Oceanography, UCSD, La Jolla, Ca. 92093, U.S.A.

Abstract. A method for the interpretation of the magnetotelluric (MT) impedance tensor, the telluric-vector technique, is presented. The phase information of all impedance tensor elements is used to distinguish between local telluric distortion and regional induction. A model incorporating a superposition of the effects of local surface anomalies and a regional 1-D, 2-D or 3-D conductivity distribution is applied. In 2-D regional structures, a complete separation of the contributions of local and regional anomalies is possible if additional information from geomagnetic depth sounding (GDS) is used. A new skewness parameter derived from phases alone is introduced to measure the three-dimensionality of the regional structure independent of local distortions.

Key words: MT tensor — Static shift — Structural dimensionality — Separation into local and regional contributions

Introduction

Recently, two problems have often hindered an accurate interpretation of the magnetotelluric impedance tensor: (1) static shifts and (2) the so-called ‘three-dimensionality’ of the tensor. The first is caused either by local zones of anomalous conductivity, which are small compared to the penetration depth, or by folding of the stratum. These change the electric field in direction and magnitude. Thus, instead of an impedance, which correctly describes the resistivity of the subsoil, a ‘shifted’ impedance is obtained. The second problem paraphrases the fact that there is no coordinate system in which the diagonal elements of the impedance tensor disappear. Therefore, a model with a three-dimensional conductivity distribution must be used to explain the tensor impedance at a single site.

These two difficulties are of course somewhat related but have almost always been handled separately. Some authors remove a frequency-independent distortion matrix (Larsen, 1977; Kemmerle, 1977) and extract a scalar impedance from the remaining tensor. Others do not deal with the distortion matrix, but rather examine the inner properties of the impedance tensor. Both Swift’s (1967) diagonal minimization method for finding the strike in a 2-D structure as well as his use of the ‘skewness’ coefficient as a

measure of deviation from two-dimensionality have been widely applied. In the pure 2-D case the electromagnetic field is split into two separate modes, in each of which the electric and magnetic fields are perpendicular. Therefore, the diagonal elements of the impedance tensor should vanish as it is expressed by Swift’s condition. More recently, some authors forsook the demand for orthogonal electric and magnetic fields. Eggers’ (1982) eigenstate analysis of the impedance tensor allows for other angles between the two fields. He and some subsequent authors (La Torraca et al., 1986; Cevallos, 1986) suggest a more mathematical decomposition of the impedance tensor that retains all the information contained in the four complex impedances. However, these papers give no proof of the physical significance of the parameters extracted from the impedance tensor. Counil et al. (1986) also deal with non-orthogonal electric and magnetic bases. A detailed comparison of these decomposition methods is given by Yee and Paulson (1987).

In this paper the MT impedance tensor will be explained by a superposition of regional and local conductivity anomalies. ‘Regional’ means that the horizontal dimensions are comparable with the depth of penetration. ‘Local’ structures are much smaller than the penetration depth: they cause DC distortion. It will be shown that the conventional analysis, using orthogonal electric and magnetic bases, sufficiently describes a regional 2-D anomaly if the contribution of the local structure has been removed from the tensor. A new ‘skewness’ coefficient, that takes into account the three-dimensionality of the regional conductivity distribution only, will be introduced.

Regional 1-D resistivity distribution and local 3-D distortion

In magnetotellurics one assumes that in the frequency domain the horizontal electric field \mathbf{E} and the horizontal magnetic field \mathbf{B} are linked through the impedance tensor \mathbf{Z} :

$$\mathbf{E} = \mathbf{Z} \cdot \mathbf{B}.$$

For a resistivity distribution which is purely depth dependent except for a thin top layer of varying conductance, the general impedance tensor

$$\mathbf{Z} = \begin{pmatrix} a_{11} & a_{12} \\ a_{21} & a_{22} \end{pmatrix} \begin{pmatrix} 0 & Z_n \\ -Z_n & 0 \end{pmatrix} \quad (1)$$

will be obtained. The normal impedance Z_n contains all the depth sounding information. The distortion matrix ele-

* Present address: Institut für Geophysik der Universität Göttingen, Postfach 2341, D-3400 Göttingen, Federal Republic of Germany

ments a_{11} , a_{12} , a_{21} , a_{22} are independent of frequency and real in the frequency range in which the penetration depth is large compared to the extension of the top layer structures. All elements of a measured impedance tensor must have the same phase if they are to be described by Eq. (1). They yield four real values which are multiples of the elements of the distortion matrix and the phase factor of the normal impedance Z_n . A sixth degree of freedom is required to obtain the true magnitude of Z_n . So far, this distortion factor has been found by two methods:

1) Additional information about the top layer: Kemmerle (1977) pursued conductivity contrasts in the top layer with geoelectric methods in order to determine the elements of the distortion matrix.

2) Additional information about the mantle conductivity: Larsen (1977) calculated an undistorted impedance from the ratio of the vertical to the horizontal component of the Sq variation field. This 'Z:H method' was originally set up by Eckhardt (1963). Schmucker (1974) applied it to Sq variations. By expanding the frequency range of the MT method up to daily variations, the MT impedance can be linked to the undistorted impedance found with the Z:H method. The resulting distortion matrix can be applied to all shorter periods as long as only one phase appears in the impedance tensor. If this is the case, Eq. (1) is a valid model and the regional conductivity distribution can be considered 1-D.

Regional 2-D resistivity distribution and local 3-D distortion

The superposition of a large-scale regional 2-D conductivity anomaly and local resistivity changes in the top layer yields the general impedance tensor

$$\mathbf{Z} = \mathbf{A} \cdot \begin{pmatrix} 0 & Z'_{xy} \\ -Z'_{yx} & 0 \end{pmatrix}, \quad (2)$$

usually with different amplitudes and phases in Z'_{xy} and Z'_{yx} . Here, as well as in the subsequent sections, cartesian coordinates (x, y) refer to observations while coordinates (x', y') refer to a regional 2-D structure with x' normal to strike. The prime (') indicates tensor elements in coordinates (x', y') , i.e. Z'_{xy} means $Z_{x'y'}$ for shortness. \mathbf{A} is the distortion matrix. In using Eq. (2) we postulate that the appropriate coordinate system has already been found. This topic will be pursued in a later section. Additional information is necessary to obtain the correct amplitudes of the two impedances Z'_{xy} and Z'_{yx} . Apart from the impedance splitting according to Eq. (2), the large-scale regional anomaly causes a regional amplification of the vertical magnetic component B_z as well as spatial changes of the horizontal magnetic components B_x and B_y . With the 'geomagnetic depth sounding' method these changes can be deduced from simultaneous magnetic recordings at different sites. They can be used as an additional help for modelling the regional conductivity anomaly. The spatial differences between the magnetic fields at two sites (1, 2) are usually presented, following a suggestion by Schmucker (1970), by a perturbation matrix:

$$\begin{pmatrix} B_x(1) - B_x(2) \\ B_y(1) - B_y(2) \\ B_z(1) - B_z(2) \end{pmatrix} = \begin{pmatrix} h_H & h_D \\ d_H & d_D \\ z_H & z_D \end{pmatrix} \begin{pmatrix} B_x(2) \\ B_y(2) \end{pmatrix}. \quad (3)$$

The six complex dimensionless transfer functions h_H, \dots, z_D describe a linear relation between the components of the magnetic fields at two sites. If the conductivity varies only in one horizontal direction as described by Eq. (2), all elements except h_H and z_H in a suitable coordinate system will vanish. h_H and z_H belong to the E -polarization.

The 'conductivity reference' method

This section deals with situations where the strike of a regional structure, taken to be 2-D, is known from geology.

The combination of magnetotellurics and geomagnetic depth sounding (Bahr, 1983; Cerv et al., 1984) offers a powerful tool in overcoming the handicap that the impedances Z'_{xy} and Z'_{yx} in Eq. (2) are unknown. This is demonstrated with the interpretation of field data from station LAU (Laubach) in the Rhenish Massif, an uplifted and exposed section of the Variscian mountain belt in central Europe (see Fig. 1). The SW-NE-striking Hunsrück south edge, the so-called "Hunsrück-Südrandverwerfung" as a deep-reaching tectonic lineament between highly resistive Variscian sediments of the Rhenish Massif and unfolded past-Variscian sediments of higher conductivity, is described by a 2-D model. Three sets of field data are interpreted:

1) The tensor impedance, free from local distortions, of the 'reference station' SPO (Sponsheim) situated at the lower part of the Nahe river.

2) The tensor impedance at LAU in coordinates (x', y') rotated anti-clockwise by 40° . Z'_{yx} is the impedance of E -polarization and Z'_{xy} is the impedance of B -polarization.

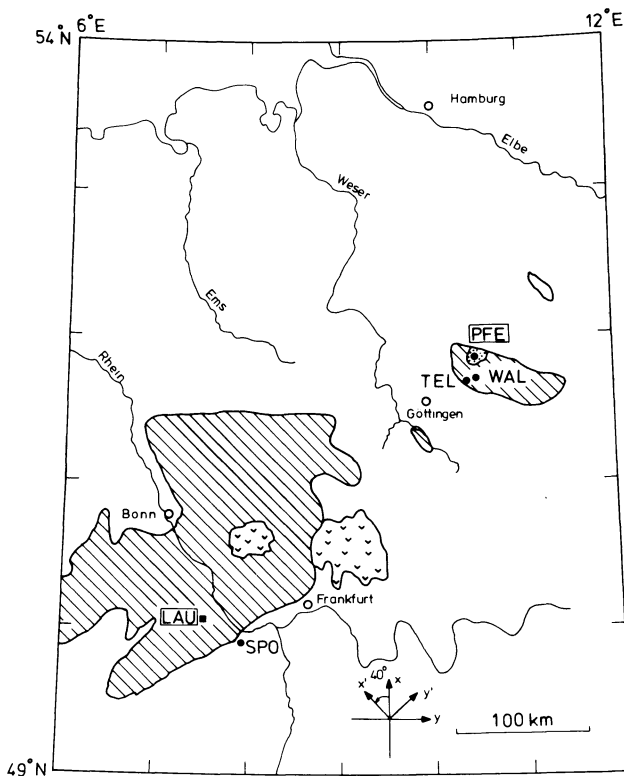


Fig. 1. MT sites within the Rhenish Massif and Harz Mountains (hatched areas) of the uplifted and exposed Variscian mountain belt in West Germany. (v) Tertiary volcanic areas of Vogelsberg and Westerwald, (...) gabbro massif of Bad Harzburg

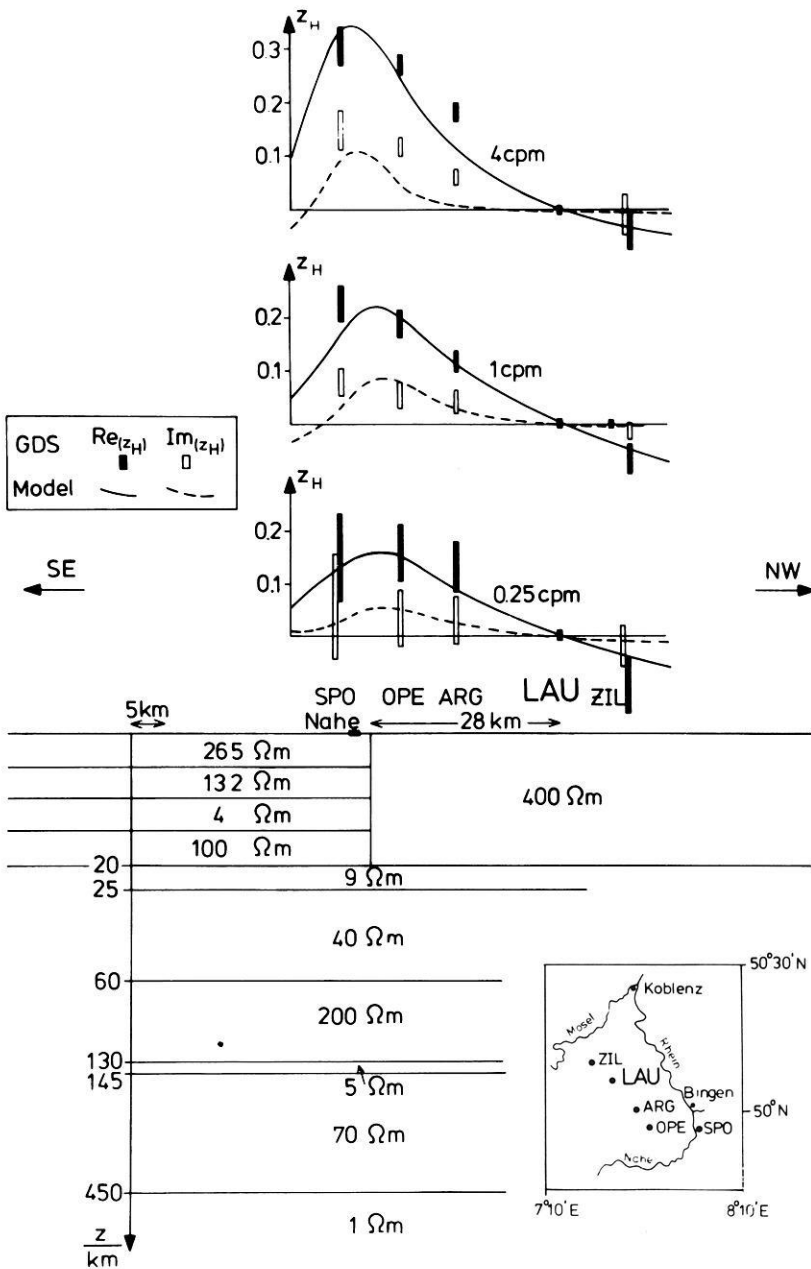


Fig. 2. Simplified 2D model of the resistivity distribution in a SE-NW-running vertical cut through the northern Rhinegraben and the Hunsrück. Site names SPO, OPE, etc. refer to z_H plots as well as to the conductivity cross-section. The *right block* and the laterally homogeneous layers from 20 km depth downwards show the vertical resistivity-depth profile of LAU as calculated from the impedance which is corrected for local distortions. The *left block* (up to 20 km depth) is derived from MT measurements at SPO. For further explanation, see text

3) Geomagnetic transfer functions z_H according to Eq. (3) on a depth sounding profile which connect both MT sites. z_H refers to the magnetic field in the x' direction.

Schmucker's (1971) 'inhomogeneous layer' algorithm is used for E - and B -polarization. The model is presented and explained in Fig. 2. Adapting the impedance of the model to that measured at SPO works well over the whole period range. Figure 2 shows the adaption of the model-generated anomalous magnetic field transfer function z_H to the measured one. Figure 3 shows the adaption of both impedances measured at LAU. In addition to the two phases, the frequency dependence of the anisotropy Z'_{xy}/Z'_{yx} is also shown. The anisotropy remaining after splitting off a frequency-independent distortion matrix must be explained solely by use of the regional conductivity model. However, the unmodified anisotropy is also influenced by local distortion. The model incorporates a conducting layer at 20 km depth underneath the Hunsrück. This layer explains why the phase

of the E -polarization Z'_{yx} at LAU is 70° at frequencies around 100 cycles per hour (Fig. 3). It was also found by Jödicke et al. (1983). Field and model data show, correspondingly: (1) At 600 cph the phases are almost equal and the anisotropy corrected for local effects is near unity, i.e. a '1D case'. (2) At longer periods the phase of the E -polarization Z'_{yx} exceeds that of the B -polarization z'_{xy} , and the anisotropy becomes larger than 1. The conducting layer underneath the Hunsrück acts as a continuation of the low-resistive subsoil of SPO and decreases the phase of the B -polarization below 45° even though site LAU is on the highly resistive Rhenish Massif.

The distortion factors of the impedance at LAU were found for very long periods by independently adapting each impedance Z'_{xy} , Z'_{yx} to the undistorted impedance obtained from the $Z:H$ method (Bahr, 1985). The result was $a_{22} = 0.70$, $a_{11} = 1.75$ and a_{12} and a_{21} about zero in coordinates (x', y') . Therefore, the correction factor of the anisotropy

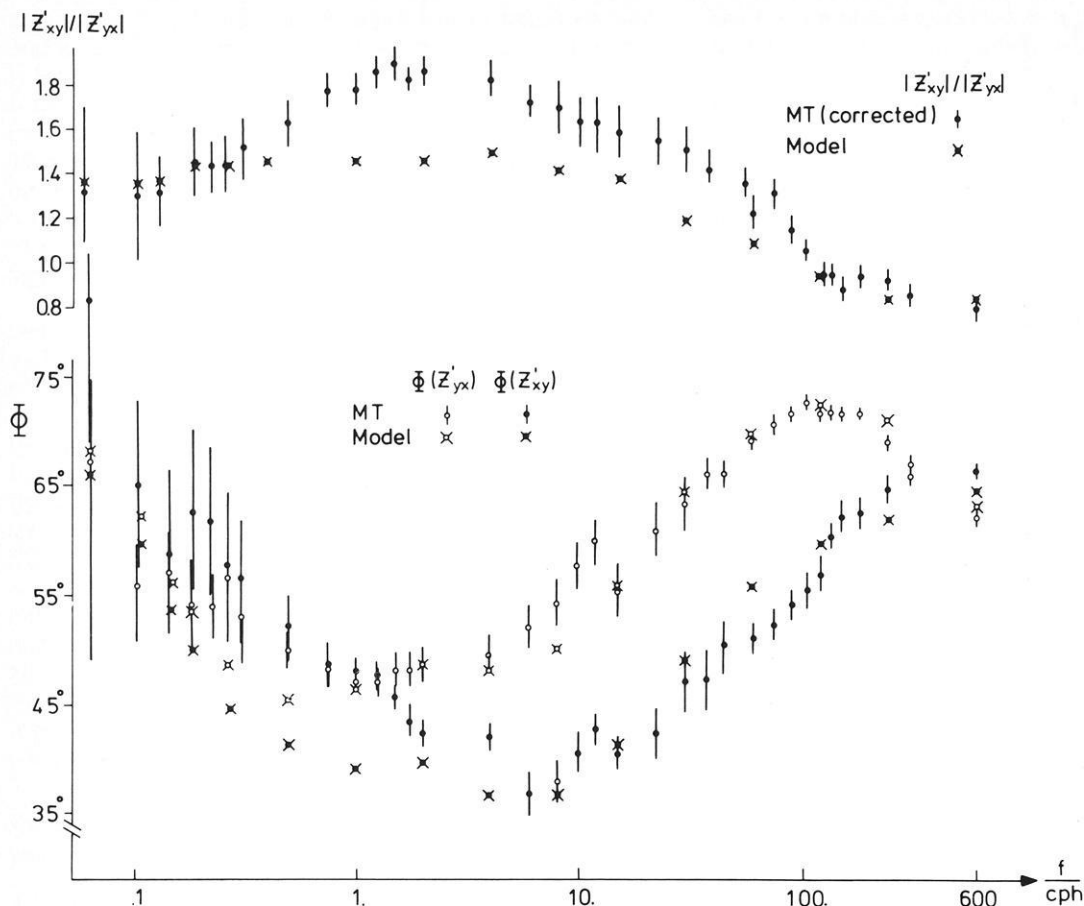


Fig. 3. Frequency dependence of the two phases and the impedance anisotropy of site LAU: measured values and those generated with the model described in Fig. 2. Z'_{yx} refers to E -polarization and Z'_{xy} refers to B -polarization

due to local distortion is $a_{11}/a_{22}=2.50$. This factor is determined again here for all periods by comparing the model anisotropy describing the regional anomaly with the measured one.

The differences between measured and synthetic impedances at periods over 1 h probably arise from modelling the Rhenish Massif as an infinitely extended 2-D structure, although the penetration depth at these periods corresponds to its true extent. The phase of the synthetic impedances at longer periods changes if, instead of a 2-D model calculation, a 3-D one is used (Wannamaker et al., 1984).

The regional amplification of the vertical magnetic field is caused by the spatial change of conductance (Schmucker, 1970). Therefore, single-frequency data of the z_H transfer function are insufficient to detect a hidden shift of the impedance at site LAU because such a shift would vary the 'conductance jump' from LAU to SPO only slightly. However, the resolution of this reference conductivity method is enhanced when considering a wide frequency range. The depth of the conductive layer under the Rhenish Shield, which would also be biased by a hidden shift, can be determined by adapting the model to geomagnetic transfer functions at suitable frequencies. By use of this technique, Tezkan (1986) determines the depth of a conductive layer under the Black Forest where local distortions shift the impedance, hindering an accurate determination of this depth from MT data only.

Decoupling of local and regional anomalies

This section deals with the frequently occurring situation that the strike of the regional anomaly is initially unknown. With Z_{\perp} and Z_{\parallel} as the undistorted impedances of B - and E -polarization and \mathbf{A} as the distortion matrix, the impedance tensor, in the coordinate system given by the strike of the regional anomaly, is:

$$\mathbf{Z} = \begin{pmatrix} a_{11} & a_{12} \\ a_{21} & a_{22} \end{pmatrix} \cdot \begin{pmatrix} 0 & Z_{\perp} \\ Z_{\parallel} & 0 \end{pmatrix} = \begin{pmatrix} a_{12} Z_{\parallel} & a_{11} Z_{\perp} \\ a_{22} Z_{\parallel} & a_{21} Z_{\perp} \end{pmatrix}. \quad (4)$$

Z_{\perp} and Z_{\parallel} are the impedances of the regional 2-D anomaly. Each of them appears in one column of the impedance tensor. We consider 'telluric vectors'

$$\mathbf{e}'_x = a_{12} Z_{\parallel} \hat{\mathbf{x}}' + a_{22} Z_{\parallel} \hat{\mathbf{y}}'$$

and

$$\mathbf{e}'_y = a_{11} Z_{\perp} \hat{\mathbf{x}}' + a_{21} Z_{\perp} \hat{\mathbf{y}}', \quad (5)$$

where $\hat{\mathbf{x}}'$ and $\hat{\mathbf{y}}'$ are unit vectors. \mathbf{e}'_x or \mathbf{e}'_y defines an in-phase and an out-of-phase telluric vector with regard to the north or the east components of the magnetic field, respectively. If local anomalies are absent or if they are quasi 2-D in the same coordinates, \mathbf{e}'_x points towards west and \mathbf{e}'_y towards north. In the particular coordinate system which is consid-

ered here, the in-phase and the out-of-phase vector are parallel, but they are rotated out of their normal position:

$$a_{11} \neq 1, \quad a_{21} \neq 0, \quad a_{22} \neq 1, \quad a_{12} \neq 0.$$

In the (x, y) coordinates all elements of the impedance tensor contain different linear superpositions of Z_{\perp} and Z_{\parallel} : the tensor is

$$\mathbf{Z} = \mathbf{T}^T \cdot \mathbf{A} \cdot \mathbf{Z}' \cdot \mathbf{T}, \quad (6)$$

where \mathbf{T} is a rotation tensor and $\mathbf{A} \cdot \mathbf{Z}'$ is the impedance tensor described by Eq. (4). While in Eq. (4) only two phases occur, now each element of the impedance tensor has a different phase (compare Fig. 4). The expressions

$$\begin{aligned} S_1 &= Z_{xx} + Z_{yy}, & S_2 &= Z_{xy} + Z_{yx}, \\ D_1 &= Z_{xx} - Z_{yy}, & D_2 &= Z_{xy} - Z_{yx} \end{aligned} \quad (7)$$

are considered in the following instead of the original impedances. Transformation of these modified impedances into a new coordinate system which is rotated clockwise by an angle α yields

$$\begin{aligned} D'_1 &= D_1 \cos(2\alpha) + S_2 \sin(2\alpha) \\ S'_2 &= S_2 \cos(2\alpha) - D_1 \sin(2\alpha), \end{aligned} \quad (8)$$

while S_1 and D_2 are rotationally invariant.

We wish to find the rotation angle α for which the transformed tensor takes the simple form of Eq. (4). The condition that the two elements Z_{xx} and Z_{yx} of the rotated impedance tensor which belong to the same telluric vector \mathbf{e}_x have the same phase is $\text{Im}(Z_{xx}/Z_{yx}) = 0$ or (Bahr, 1985)

$$\begin{aligned} \frac{\text{Re}(Z_{xx})}{\text{Re}(Z_{yx})} &= \frac{\text{Re}[S_1 + D_1 \cos(2\alpha) + S_2 \cdot \sin(2\alpha)]}{\text{Re}[-D_2 - D_1 \sin(2\alpha) + S_2 \cdot \cos(2\alpha)]} \\ &= \frac{\text{Im}[S_1 + D_1 \cos(2\alpha) + S_2 \cdot \sin(2\alpha)]}{\text{Im}[-D_2 - D_1 \sin(2\alpha) + S_2 \cdot \cos(2\alpha)]} \\ &= \frac{\text{Im}(Z_{xx})}{\text{Im}(Z_{yx})}. \end{aligned} \quad (9)$$

A similar condition exists which links the elements of the telluric vector \mathbf{e}_y .

The sine of the differences between the phases of each pair of impedances are now abbreviated by use of the 'commutators', e.g.

$$\begin{aligned} [S_1, S_2] &= \text{Re}(S_1) \text{Im}(S_2) - \text{Im}(S_1) \text{Re}(S_2) \\ &= \text{Im}(S_2 \cdot S_1^*) \end{aligned} \quad (10)$$

($[D_1, D_2]$, $[D_1, S_2]$ and $[S_1, D_2]$ correspondingly).

Equation (9) with (10) becomes

$$-A \sin(2\alpha) + B \cos(2\alpha) + C = 0,$$

where

$$\begin{aligned} A &= [S_1, D_1] + [S_2, D_2] \\ B &= [S_1, S_2] - [D_1, D_2] \\ C &= [D_1, S_2] - [S_1, D_2]. \end{aligned}$$

The solution is

$$\tan \alpha_{1,2} = \pm [(B+C)/(B-C) + (A/(B-C))^2]^{1/2} - A/(B-C). \quad (11)$$

The subscripts 1, 2, referring to the two different signs of the root in Eq. (11), describe two coordinate systems in which either the impedance tensor elements belonging to \mathbf{e}'_x or those belonging to \mathbf{e}'_y have the same phase.

If all elements of the impedance tensor have the same phase, it follows that $A=B=C=0$ and no strike angle is obtained. Then the regional conductivity distribution is only depth dependent and $Z_{\parallel} = Z_{\perp}$ and Eq. (4) corresponds to Larsen's formulation, Eq. (1).

If the impedance tensor is exactly described by Eq. (4) in the appropriate coordinate system, it should be the case that $\alpha_1 = \alpha_2 - 90^\circ$. Let

$$\mathbf{T}_{90} = \begin{pmatrix} 0 & 1 \\ -1 & 0 \end{pmatrix}$$

be the tensor of a 90° rotation. Thus,

$$\mathbf{T}_{90}^T \cdot \begin{pmatrix} a_{12} Z_{\parallel} & a_{11} Z_{\perp} \\ a_{22} Z_{\parallel} & a_{21} Z_{\perp} \end{pmatrix} \cdot \mathbf{T}_{90} = \begin{pmatrix} a_{21} Z_{\perp} & -a_{22} Z_{\parallel} \\ -a_{11} Z_{\perp} & a_{12} Z_{\parallel} \end{pmatrix}. \quad (12)$$

At a rotation of 90° , the phases of \mathbf{e}'_x and \mathbf{e}'_y are commutable. The condition that the two angles which are due to the two different signs of the root in Eq. (11) differ by 90° leads to

$$\cot(\alpha_1 - \alpha_2) = 0$$

and therefore

$$C = [D_1, S_2] - [S_1, D_2] = 0. \quad (13)$$

The term C is rotationally invariant because S_1 and D_2 are so and

$$[D'_1, S'_2] = [D_1, S_2]$$

as seen from Eqs. (8) and (10). C disappears, no matter which coordinate system is chosen, if the regional conductivity distribution is exactly two-dimensional. In a purely depth-dependent resistivity distribution, the condition

$$[D_1, S_2] = [S_1, D_2] = 0 \quad (14)$$

is fulfilled in addition.

A phase-sensitive skewness coefficient

The parameter C can be used to set up a new measure of the three-dimensionality of the regional conductivity distribution

$$\eta = \sqrt{|C|/|D_2|}. \quad (15)$$

It is related to the conventional skew

$$\kappa = |S_1|/|D_2| \quad (16)$$

by the ratio

$$\xi = \sqrt{|C|/|S_1|} = \eta/\kappa \quad (17)$$

of the phase-sensitive skew to the conventional skew. ξ^{-1} represents the relative contribution of local distortion to κ , e.g. for $\xi \ll 1$ it is totally determined by this distortion.

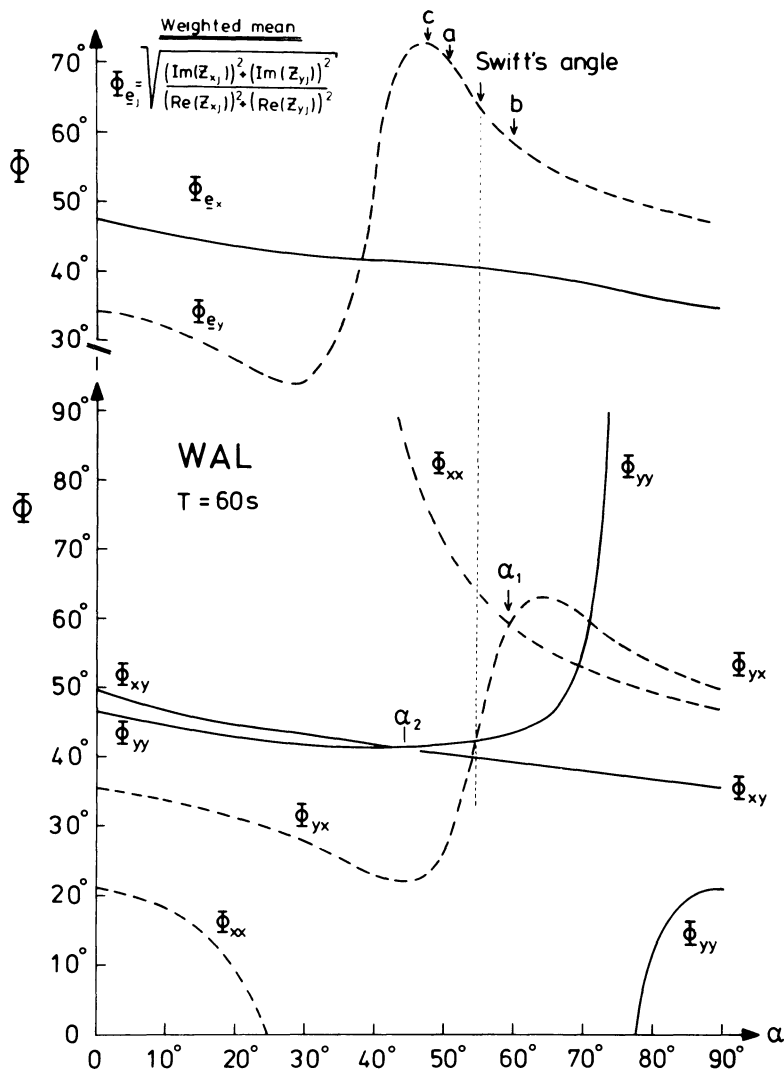


Fig. 4. Phases of the elements of the impedance tensor (*bottom*) and phases of the 'telluric vectors', according to Eq. (20), of site WAL, $T=1$ min, at a stepwise coordinate transformation. The impedances of the main diagonal elements are comparable with their confidence intervals for angles around 75° and 35° , and they have negative phases there. Then, it is not useful to calculate a phase according to Eq. (20) there. Elsewhere, $|\Delta Z/Z| < 0.1$ ($\beta = 68\%$) and $|\Delta \phi| < 5^\circ$; the errors of all phases are smaller than the referred differences between ϕ_{e_x} and ϕ_{e_y} . For further explanation, see text

The strike of a regional 2-D anomaly

Swift's (1967) method to determine the strike of a 2-D structure leads to the analytical solution

$$\tan(4\alpha) = 2 \operatorname{Re}(S_2 \cdot D_1) / (|D_1|^2 - |S_2|^2) \quad (18)$$

which depends on the moduli of the impedances, as does the skew [Eq. (16)]. Therefore, this formula may be inappropriate for finding the regional trend in the particular case where local telluric distortion determines those moduli.

A coordinate system in which one of the axes coincides with the strike of the regional anomaly and in which the impedance tensor takes the form of Eq. (4), can be found in various ways:

A) If $\eta < 0.1$, the regional anomaly is assumed to be exactly two-dimensional and C is set to zero:

$$\tan(2\alpha) = B/A. \quad (19)$$

To evaluate Eq. (11) or Eq. (19) the phases of all four elements of the impedance tensor have to be known. Random data errors can vary the value of η . If $\eta \neq 0$ due to data errors or deviations of the 2-D geometry, then $\alpha_1 - \alpha_2 \neq 90^\circ$. This is demonstrated by use of field data from site WAL, a site within the Harz Mountains, representing

another uplifted and exposed piece of the Variscian mountain belt (Fig. 1). The phases of the four impedance tensor elements and their dependence on the chosen coordinate system are illustrated in Fig. 4. At $\alpha_2 = 47^\circ$ the phases ϕ_{x_y} and ϕ_{y_y} which belong to e_y correspond, but the other two do not tally at all. At $\alpha_1 = 59^\circ$ the phases belonging to e_x are exactly identical, the other two are almost identical. This behaviour leads to the second method.

B) The coordinate system defined by α_1 , in which the phases of the 'rotation-sensitive' telluric vector e_x coincide, is used. That telluric vector is usually the one with the smaller moduli of impedance.

C) Changing from four to two phases can result in smoothing noisy data. Then, only the phases of the telluric vectors, defined by

$$\begin{aligned} \tan(\phi_{e_x}) &= \left[\frac{(\operatorname{Im} Z_{xx})^2 + (\operatorname{Im} Z_{yx})^2}{(\operatorname{Re} Z_{xx})^2 + (\operatorname{Re} Z_{yx})^2} \right]^{1/2} \\ \tan(\phi_{e_y}) &= \left[\frac{(\operatorname{Im} Z_{xy})^2 + (\operatorname{Im} Z_{yy})^2}{(\operatorname{Re} Z_{xy})^2 + (\operatorname{Re} Z_{yy})^2} \right]^{1/2} \end{aligned} \quad (20)$$

are analysed. ϕ_{e_x} means the phase of the entire electric field correlated with the north component of the magnetic field,

with respect to that north component. As in the second method, the telluric vector whose phase is changed more profoundly by rotation, for example e_x , is searched for.

In the particular case where $[S_1, D_2]=0$ and the skew κ is nevertheless non-zero, this skew can be explained by a maladjustment γ of the electrodes with respect to the magnetometer:

$$\frac{\text{Re}(S_1)}{\text{Re}(D_2)} = \frac{\text{Im}(S_1)}{\text{Im}(D_2)} = \tan(\gamma) \quad (21)$$

(Cox et al., 1980). This possibility cannot be distinguished from the case that in Eq. (4) one telluric vector dominates: $(a_{11}^2 + a_{21}^2)^{1/2} |Z_{\perp}| \gg (a_{12}^2 + a_{22}^2)^{1/2} |Z_{\parallel}|$. In that case, only Z_{\perp} determines the phase of S_1 and D_2 ; and $\tan(\gamma) = a_{11}/a_{21}$ is the rotation of this telluric vector caused by local distortion.

Application to field data in the Harz Mountains

Table 1 shows both the modulus-sensitive and the phase-sensitive skew of three stations in the Harz Mountains. The NW-SE-striking southwest edge of the Harz, which delimits the Variscian sediments from the younger sediments of the Harz' southern forelands, can be considered as a regional 2-D anomaly with respect to two sites WAL, TEL (see Fig. 5). But the folding of the Variscian sediments is rotated by 70° from this direction: 'The Harz Mountains have an inner structure which runs southwest-northeast and a Hercynian stretched contour which runs northwest-southeast' (Mohr, 1978). Although the conventional skew [Eq. (16)] is large for stations WAL and TEL, the regional conductivity distribution is two-dimensional as indicated by the small phase-sensitive skew from Eq. (15). The folding acts like a 'local' anomaly and causes a linear polarization of the electric field in one preferred direction. Because this direction does not coincide with one of the axes of the coordinate system given by the regional 2-D anomaly, the conductivity distribution looks three-dimensional: $\kappa > \eta$.

At site PFE, a site on the Harzburg's gabbro massif, the situation is reversed. Here the regional conductivity distribution appears to be 3-D, but is concealed by a nearly 2-D local distortion, in which a_{11} is much larger than a_{22} but with a_{12} and a_{21} nearly zero in proper coordinates. The pronounced anisotropy a_{11}/a_{22} causes D_2 to overwhelm S_1 . Therefore, the modulus-sensitive skew is small: $\kappa < \eta$.

The rotation angles for WAL, found with the help of Methods A), B), C), are marked in Fig. 4. Within the small angular interval $47^\circ < \alpha < 59^\circ$, one finds the phases $\phi_{e_y} = 40^\circ$ and $\phi_{e_x} = 60^\circ - 70^\circ$ according to Eq. (20). Swift's criterion Eq. (18) yields $\alpha = 55^\circ$. But if only the off-diagonal elements are analysed in this coordinate system, one finds $\phi_{x_y} \approx \phi_{y_x} \approx 40^\circ$. The phase bound to the telluric vector e_x is hidden by the distortion. The phases $\phi_{e_y} = 40^\circ$ and $\phi_{e_x} = 65^\circ$ at 1-min period correspond well to the two phases of site LAU (compare Fig. 3) and they can also be interpreted by a similar model of a high-resistive slab of a thickness limited to 20 km. Then, ϕ_{e_y} is the phase of the B -polarization with regard to the regional anomaly of the southwest edge of the Harz. But if both phases are taken to be about 40° according to Swift's criterion, there would be no clue to the lower boundary of the high-resistive domain.

Table 1. Skewness coefficients, according to Eqs. (15–17), of three sites at period $T=1$ min

Station	κ	ξ	η
PFE	0.15	2.28	0.35
WAL	0.61	0.26	0.16
TEL	1.09	0.07	0.08

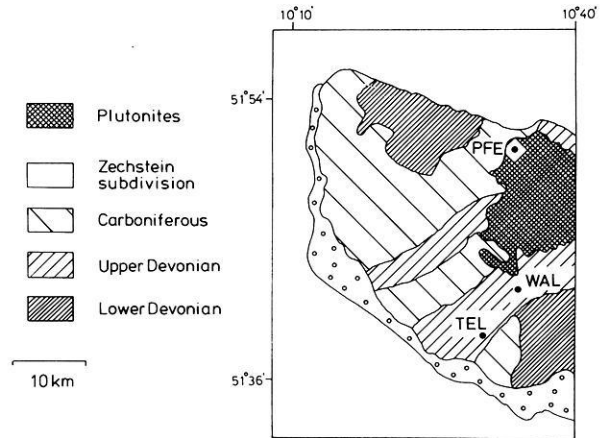


Fig. 5. MT stations in the Harz mountains

Comparison of methods

If only a regional 2-D structure but no top layer anomaly exists, the transformed impedances according to Eq. (7) reduce to

$$\begin{aligned} S'_1 &= 0 & S'_2 &= Z'_{xy} + Z'_{yx} \\ D'_1 &= 0 & D'_2 &= Z'_{xy} - Z'_{yx} \end{aligned}$$

in a coordinate system given by the strike of the regional structure. If the coordinate system is rotated by an angle α , the impedances

$$\begin{aligned} S_1 &= 0 & S_2 &= S'_2 \cos(2\alpha) \\ D_1 &= S'_2 \sin(2\alpha) & D_2 &= D'_2 \end{aligned}$$

are observed. The conventional method of strike determination, Eq. (18), of course recovers the original strike. The phase-sensitive method yields

$$\begin{aligned} A &= [S_2, D_2] = [S'_2, D'_2] \cos(2\alpha) \\ B &= -[D_1, D_2] = -[S'_2, D'_2] \sin(2\alpha) \\ C &= [D_1, S_2] = [S'_2, S'_2] \sin(2\alpha) \cos(2\alpha) = 0 \end{aligned}$$

and

$$\tan(2\alpha) = B/A$$

from Eq. (19). Thus this method, too, recovers the original strike and yields a skew $\eta=0$ according to Eq. (15).

In the opposite case, where only a surface anomaly exists, the conventional method [Eq. (18)] will still yield some strike direction. Gamble et al. (1982) suggest the determination of a regional strike from a generalization of Eq. (18). They replace the impedances D_1, S_2 by averages of those expressions obtained from several sites. This might result in an average of local strikes rather than a regional one.

Following Eggers (1982), those methods which try to give a complete representation of the impedance tensor are compared in the following, in terms of the number of degrees of freedom obtained:

1) The conventional coordinate transformation yields two principal impedances (4 degrees of freedom), the strike (1) and the skew (1). The ellipticity of the polarization ellipse S_1/D_2 provides additional information but not a full degree of freedom (Eggers, 1982). This method is 'incomplete' as it does not use all the information contained in the tensor.

2) Eggers' eigenstate formulation yields two complex eigenvalues (4), two non-orthogonal principal directions (2) and two ellipticities (2). This method gives a complete mathematical description of the MT tensor.

3) The method described in this paper deals with the impedances belonging to the two telluric vectors (4), the regional strike (1), the regional skew (1) and the distortion matrix (4). From the elements of the distortion matrix, the 'amplification' $(a_{12}^2 + a_{22}^2)^{1/2}$ and the angular deviation a_{12}/a_{22} of the telluric vector \mathbf{e}_x as well as the equivalent distortion terms of \mathbf{e}_y could be calculated. Ten independent parameters are necessary, while the impedance tensor provides only eight degrees of freedom. The additional two degrees of freedom are the static shifts of the impedances of the two telluric vectors: these amplifications, $(a_{12}^2 + a_{22}^2)^{1/2}$ and $(a_{11}^2 + a_{21}^2)^{1/2}$, remain unknown as long as no additional information besides the MT tensor is used.

The model of a regional 2-D conductivity structure and a superposed top layer anomaly has recently been treated by Zhang et al. (1987). They restrict their 'principal model' to a 2-D local structure. Therefore, the number of degrees of freedom due to local distortion is reduced by one; the four distortion matrix elements are replaced by a_{11} , a_{22} and the local strike. Assuming no regional skew, the principal model of Zhang et al. (1987) would have eight degrees of freedom, compared to ten degrees of freedom in the telluric-vector technique. Consequently, the authors offer a formula to calculate the two principal impedances without additional information besides the MT tensor. Any local structure should, however, have a limited extension. The model of a 2-D local structure, rather than a 3-D one, is a rough approximation which can be applied only in very few cases.

Haak (1972) suggested choosing a coordinate system for the electric field that minimizes the coherency between orthogonal electric components. The coordinate system of the magnetic field is rotated until the coherency between electric and magnetic fields reaches a maximum. An angular difference between the electric and magnetic coordinate systems indicates a 3-D conductivity distribution (Schwarz et al., 1984). This approach allows for non-orthogonal electric and magnetic fields, as does the telluric-vector technique. The latter, however, permits the two telluric vectors to have different deviations rather than associating one angular difference with the three-dimensionality of the strata.

Summary and conclusion

To choose an appropriate method of interpretation for a measured impedance tensor, one must ask whether all its elements have the same phase. If they do, it is sufficient to split the impedance tensor into a real distortion matrix and a scalar normal impedance. The distortion can be eliminated if either of these two quantities is known. They can both be determined by appropriate field measurements. If

the surface anomaly itself is of interest, the distortion matrix can be obtained from an examination of this surface anomaly by some DC method (Kemmerle, 1977). Where the conductivity of the mantle is to be investigated, the normal (undistorted) impedance can be calculated from magnetic long-period data with the $Z:H$ method (Larsen, 1977). The distortion matrix, which is obtained by comparing that normal impedance with the measured impedance tensor, can be applied to all shorter periods as long as only one phase appears in the tensor. Otherwise, the regional conductivity distribution is not purely depth dependent. By introducing a new, rotationally invariant skew, this paper suggests a test for the question of whether the regional structure is 2-D. It is the phases that are examined, not the amplitudes of the impedance tensor elements as in the conventional skewness analysis.

To explain the two phases of a seriously distorted impedance tensor of a site in the Rhenish Massif, a model calculation with a 2-D resistivity distribution which does not contain the local structures was carried out. Geomagnetic depth sounding data which are not influenced by the local structures were used as an additional check. As the model space includes a reference site with a known, undistorted impedance, there exists an initial value for the resistivity. By comparing the measured impedances with the modelled ones, real distortion coefficients were obtained. This 'reference conductivity' method offers another technique for removing DC distortion.

Acknowledgements. I would especially like to thank U. Schmucker for constant support and encouragement. Thanks are also due to J.H. Filloux and T. Koch for carefully reading the manuscript. My research was supported by the Deutsche Forschungsgemeinschaft under grant Ba 889/1.

References

- Bahr, K.: Joint interpretation of magnetotelluric and geomagnetic data and local telluric distortions. *J. Geomagn. Geoelectr.* **35**, 555–566, 1983
- Bahr, K.: Magnetotellurische Messung des elektrischen Widerstandes der Erdkruste und des oberen Mantels in Gebieten mit lokalen und regionalen Leitfähigkeitsanomalien. Diss. Math.-Nat. Fachb. Univ. Göttingen, 1985
- Cerv, V., Pek, J., Praus, O.: Models of geoelectrical anomalies in Czechoslovakia. *J. Geophys.* **55**, 161–168, 1984
- Cevallos, C.: Magnetotelluric interpretation – another approach. PhD thesis, Macquarie University, Sidney, 1986
- Counil, J.L., Le Mouél, J.L., Menvielle, M.: Associate and conjugate concepts in magnetotellurics. *Ann. Géophys.* **4**, B2, 115–130, 1986
- Cox, C.S., Filloux, J.H., Gough, D.I., Larsen, J.C., Poehls, K.A., Herzen, R.P. von, Winter, R.: Atlantic lithosphere sounding. *J. Geomagn. Geoelectr.* **32**, Suppl. I, SI 13–32, 1980
- Eckhardt, D.H.: Geomagnetic induction in a concentrically stratified earth. *J. Geophys. Res.* **68**, 6273–6278, 1983
- Eggers, D.W.: An eigenstate formulation of the magnetotelluric impedance tensor. *Geophysics* **47**, 1204–1214, 1982
- Gamble, T.D., Goubau, W.M., Miracky, R., Clarke, J.: Magnetotelluric regional strike. *Geophysics* **47**, 932–937, 1982
- Haak, V.: Bestimmung der Übertragungsfunktionen in Gebieten mit lateraler Änderung der elektrischen Leitfähigkeit. *Z. Geophys.* **38**, 85–102, 1972
- Jödicke, H., Untiedt, J., Olgemann, W., Schulte, L., Wagenitz, V.: Electrical conductivity structure of the crust and upper mantle beneath the Rhenish Massif. In: Plateau uplift, K. Fuchs, ed. Berlin, Heidelberg, New York, Tokyo: Springer 1983
- Kemmerle, K.: Magnetotellurik am Alpen-Nordrand mit Diskus-

- sion der lokalen Effekte und Darstellung einer Einzeleffekt-Auswertung. Diss. Fachb. Geowissenschaften, München, 1977
- Larsen, J.C.: Removal of local surface conductivity effects from low frequency mantle response curves. *Acta Geodaet., Geophys. et Montanist. Acad. Sci. Hung.* **12**, 183–186, 1977
- LaTorraca, G.A., Madden, T.R., Korrington, J.: An analysis of the magnetotelluric impedance tensor for three-dimensional structures. *Geophysics* **51**, 1819–1829, 1986
- Mohr, K.: *Geologie und Minerallagerstätten des Harzes*. Stuttgart: Schweizerbart 1978
- Schmucker, U.: Anomalies of geomagnetic variations in the southwestern United States. *Bull. Scripps. Inst. Ocean., Univ. Calif.*, **13**, 1970
- Schmucker, U.: Neue Rechenmethoden zur Tiefensondierung. In: *Protokoll Kolloquium Erdmagnetische Tiefensondierung, Rothenberge/Westfalen*, P. Weidelt, ed.: 1–31, Geophysical Institute, Univ. Göttingen, 1971
- Schmucker, U.: Erdmagnetische Tiefensondierung mit langperiodischen Variationen. In: *Protokoll Kolloquium Erdmagnetische Tiefensondierung, Grafrath/Bayern*, A. Berktold, ed.: 313–342, Geophysical Institute, Univ. München, 1974
- Schwarz, G., Haak, V., Martinez, E., Bannister, J.: The electrical conductivity of the Andean crust in northern Chile and southern Bolivia as inferred from magnetotelluric measurements. *J. Geophys.* **55**, 169–178, 1984
- Swift, C.M.: A magnetotelluric investigation of an electrical conductivity anomaly in the southwestern United States. Ph.D. thesis, M.I.T., Cambridge, Mass., 1967
- Tezkan, B.: *Erdmagnetische und magnetotellurische Untersuchungen auf den hochohmigen Kristallinstrukturen des Hochschwarzwaldes und des Bayerischen Waldes bei Passau*. Diss. Math.-Nat. Fachb. Univ. Göttingen, 1986
- Wannamaker, P.E., Hohmann, G.W., Ward, S.H.: Magnetotelluric responses of three-dimensional bodies in layered earths. *Geophysics* **49**, 1517–1533, 1984
- Yee, E., Paulson, K.V.: The canonical decomposition and its relationship to other forms of magnetotelluric impedance tensor analysis. *J. Geophys.* **61**, 173–189, 1987
- Zhang, P., Roberts, R.G., Pedersen, L.B.: Magnetotelluric strike rules. *Geophysics* **52**, 267–278, 1987

Received April 16, 1987; revised July 27, 1987

Accepted August 7, 1987

Investigation of non-linear tilt tides from the Charlevoix seismic zone in Quebec

J. Peters*¹ and H.-J. Kämpel²

¹ Oceanography Department, Dalhousie University Halifax, Nova Scotia, Canada, B3H 4J1

² Institute of Geophysics, Kiel University, D-2300 Kiel, Federal Republic of Germany

Abstract. Under certain conditions of crustal stress, non-linearities may be generated in the earth tide response. Non-linear constituents present in borehole tilt and tide gauge recordings from the Charlevoix seismic zone are studied in an attempt to discriminate between possible tectonically induced non-linear components and those resulting from non-linear interactions in the marine load tide. Mean tidal admittance estimates from harmonic analysis are compared with a loading model for constituents M_4 and M_6 , and time-variant analysis is used to determine the temporal behaviour of the tilt and tide gauge admittances. Agreement between the model and mean admittance results, confirmed by some similarities in the tilt and tide gauge admittance time variations, indicates that crustal non-linearities are absent or undetectable. If laboratory observations of non-linear behaviour of highly stressed rocks are representative of in situ processes, then the apparent absence of non-linear tidal anomalies implies that the special situation in which the rate of change of the tectonic stress is equal to the mean tidal stress rate does not apply in the Charlevoix region. The experiments at Charlevoix have also allowed us to evaluate the spatial stability of non-linearities in the tidal tilt. Simultaneous recordings from two boreholes only 80 m apart show considerable discrepancies among many of the tidal constituents. It is speculated that local inhomogeneities in the granite country rock at the site are responsible for the anomalies.

Key words: Tidal tilt – Loading tides – Non-linear tides

Introduction

Most earth tide studies have been concerned with the linear response of the earth to the combined astronomical forcing and secondary tidal loading. In this study of borehole tilt-meter data from the Charlevoix seismic zone, we examine signal components in tidal data arising from non-linear processes either from a marine source (through loading) or resulting from possible non-linearity in the transfer function of the local crust. Our aim is to determine to what extent the observed non-linear components may be explained by:

(a) crustal processes, (b) marine loading and (c) local inhomogeneities at the site.

The response of the earth to tidal forcing is generally described by infinitesimal linear elasticity theory. However, results from laboratory studies of brittle rock samples (Brace et al. 1966; Soga et al. 1978; Sobolev et al. 1978) have shown that at deviatoric stress greater than half the rock failure strength, volumetric strains arise due to the growth of microcracks (dilatancy). A number of models of non-linear elasticity have been proposed (Stuart, 1974; Mjachkin et al., 1975; Rice and Rudnicki, 1979) to explain both the laboratory results and field observations, in particular V_p/V_s precursors (Nersesov et al., 1969; Mjachkin et al., 1972; Whitcomb et al., 1973). As Beaumont (1978) points out, since the range of tidal stress (about 0.01 bar) is much smaller than the range of tectonic stress (about 5 kbar), the tidal response in this situation is essentially linear, though anisotropic, and governed by the state of the tectonic stress.

Scholz and Kranz (1974) showed in the laboratory that rocks subjected to cyclic loading at high deviatoric stress respond plastically and exhibit hysteresis; the energy loss is presumably due to the work against friction in opening and closing microcracks. Beaumont (1978) has described the possible effect on the tidal response where the tidal stress is superimposed on an accumulating tectonic stress field. In the case where the tectonic stress accumulation is either much less than or much greater than the mean tidal stress rate, the tidal response remains essentially linear. We should be able to distinguish between these two situations by examining the time dependence of the linear tidal response. If the response is constant then the tectonic stress, while possibly high, is only slowly varying or not varying at all. If the linear response is changing appreciably with time, this would imply that the tectonic stress rate is large and may be interpreted as being premonitory to rupture. Where the tectonic and mean tidal stress rates are approximately equal, the response is non-linear over the range of the tidal cycle. This would result in the generation of additional lines in the spectrum at sum and difference frequencies of the tidal constituents. These different styles of tidal response are therefore, in principle, diagnostic of the state of stress in the local crust. A study of time variations in the linear tidal response at Charlevoix (Peters and Beaumont, 1985) has not revealed an obvious tectonic signal, suggesting that the rate of tectonic stress accumulation is not large. It is among the aims of this study to determine

* Present address: Earth & Ocean Research Ltd., 22 Waddell Avenue, Dartmouth, Nova Scotia, Canada, B3B 1K3

Offprint requests to: H.-J. Kämpel

whether the tectonic stress rate is in the range of the tidal stress rate.

Agnew (1981) has studied the effect on the tidal response of intrinsic non-linearity in rocks based on evidence from seismic studies. He shows that for non-dissipative materials the strongest effect would occur at the second harmonic of the tidal constituents (for example M_4 , the second harmonic of M_2), whereas for dissipative materials the effects would be generated at the odd harmonics (for example M_6 , the third harmonic of M_2). The predicted non-linear strains (or tilts), however, are too small to be detected at the significance level of this study. It should be emphasized that this is a different problem from that described by Beaumont (1978). Whereas Agnew considers the intrinsic non-linearity of the rock, Beaumont is looking at non-linearity generated in response to applied stress close to the failure strength of the rock.

We must additionally consider the non-linear content of the tidal input. There have been numerous studies of non-linear harmonics in the marine tide (see, for example, Zetler and Cummings, 1967; Rossiter and Lennon, 1968; Gallagher and Munk, 1971). The prominent sources of these components are velocity and friction-dependent interactions in shallow water. Godin (1973) has made a detailed analysis of 8 years of tide gauge data from Québec City (150 km upstream from Charlevoix) showing the importance of the non-linear harmonics in the estuary. Since the observed tidal signal at Charlevoix is dominated by loading from the St. Lawrence estuary, there is abundant energy at the higher-order tidal harmonics (Peters and Beaumont, 1985), at least part of which must arise from shallow-water interactions. Another source of harmonics in the loading arises from rectification of the linear tide over drying areas (Zschau, 1979). This is not generally reflected in the tide gauge data since they are recorded in deep water.

Cavities, topography or geological inhomogeneities may produce strain-induced tilt anomalies that vary over short distances (Harrison, 1976). For example, Flach et al. (1975) reported an 8° phase difference in M_2 between two Askania borehole pendulums recording simultaneously in 15-m and 30-m boreholes located 10 m apart. Characteristics of the temporal variation of non-linear tides due to tectonic stress build-up or marine loading should not be masked by these local effects. They will merely result in constant phase shifts and/or constant amplitude differences between installations at various locations.

In this study we compare the mean amplitudes and Greenwich phase lags of M_4 and M_6 determined from the borehole tilt recordings taken at Charlevoix Observatory, with theoretical estimates based on a loading model of the St. Lawrence estuary. Time-variant analysis results of the tilt and nearby tide gauge data are compared to see to what extent the stability of the tidal tilt response is determined by the loading input. Finally, we consider local effects that distort the crustal tilt response in the vicinity of the site.

Data and analysis

The tilt data were recorded in two boreholes 80 m apart and 47 m deep, using Bodenseewerk (formerly Askania) borehole pendulums (Peters and Beaumont, 1985). The study was done in two parts: one using tide gauge data available from May 1, 1981 to December 31, 1982 and tilt-

Table 1. Data used in this study

Tilt	
Borehole 1	Nov. 27, 1981–Dec. 31, 1983
Borehole 2	Nov. 27, 1981–Dec. 31, 1983
Tide Gauge	
St. Joseph de la Rive	May 1, 1981–Dec. 31, 1983
Tadoussac	Jan. 1, 1983–Dec. 31, 1983

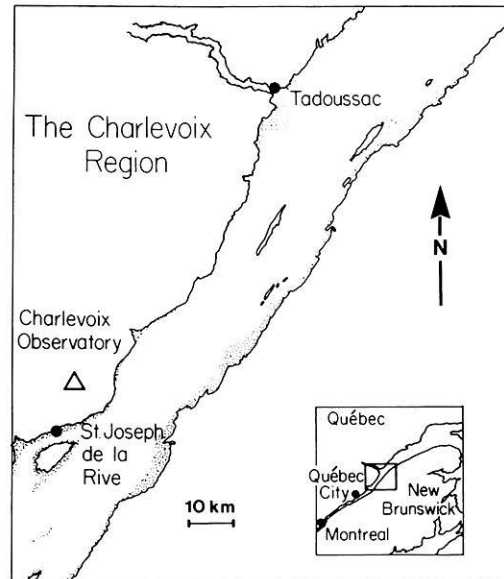


Fig. 1. Map of the St. Lawrence estuary near the Charlevoix observatory. The *stippled areas* are beaches. The location of the observatory is $47^\circ 32.9'N$, $70^\circ 19.3'W$

meter data from November 27, 1981 to July 24, 1983 for determining the spectral characteristics of the non-linear constituents; and the second using tilt and tide gauge data for all of 1983 for the mean admittance and time-variant analysis. The 1983 data set was used for the time-variant analysis because of the small number of gaps during that period, a factor which has considerable influence on the accuracy of the results. Table 1 lists details of the data analysed; Fig. 1 shows the relevant locations.

An adaptation of the Goertzel algorithm (Goertzel, 1958) was used to compute the amplitude spectra. Unlike the fast Fourier transform, the Goertzel method permits the rapid calculation of the direct Fourier transform for arbitrary frequencies for a time series of any length, without the need to process frequencies over the entire spectrum. The computation was done on a bandpass-filtered time series which had been multiplied by the Hanning window, so that the spectral resolution is $dw = 4\pi/(NdT)$, where dT ($=1$ h) is the sampling interval of the data and N the number of hourly data points. Distortions from data gaps were reduced by filling the gaps with harmonic constituents from a preliminary Fourier transform that was applied to data series with linearly interpolated gaps.

For the time-variant analysis, we have used the HYCON tidal harmonic analysis program of Schüller (1977). The data from 1983 were divided into overlapping 60-day subsets with the origin shifted for each set by 10 days. The output of the program is a sequence, for each tidal harmonic, of amplitude and phase estimates derived from ana-

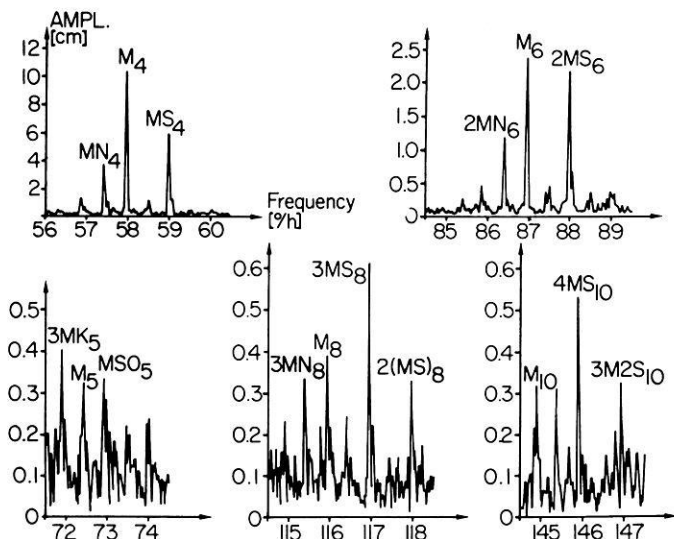


Fig. 2. High-resolution amplitude spectrum ($0.05^\circ/h$ bandwidth resolution) of St. Joseph de la Rive, showing the main non-linear tidal bands

lysis of the subsets, which together form a time-varying admittance function. A detailed description of the method is given in Peters and Beaumont (1985).

The marine tide

Spectrum of the marine tide

Figure 2 shows the amplitude spectrum for tidal frequencies greater than $56^\circ/h$ ($43 \mu\text{Hz}$) of the tide gauge at St. Joseph de la Rive for the period May 1, 1981 to December 31, 1982. Because of its close proximity to the site (Fig. 1), this tide gauge is representative of a major part of the loading at Charlevoix. The background noise level decreases from 0.3 cm within the quarter-diurnal band to 0.15 cm in the tenth-diurnal band.

Other tide gauge recordings in the estuary are shorter (in some cases less than 600 h), resulting in a lower spectral resolution. Adjacent frequencies then modulate one another, which for the shorter sets leads to biased estimates for the amplitudes and phases. Only M_4 and M_6 are free of significant interference within a bandwidth of $0.5^\circ/h$ ($0.386 \mu\text{Hz}$). It is for this reason that these frequencies were chosen for the comparison between the loading model and the observed mean amplitudes and phases; and for the time-variant analysis of 60-day ($0.5^\circ/h$ resolution) subsets of the 1983 data.

Tidal loading model

The load tilt calculations were made by the same method as Peters and Beaumont (1985) using the same triangular subdivision of the St. Lawrence estuary, but excluding the Saguenay River west of Tadoussac. The Green functions for the point load response of the Farrell Gutenberg Bullen Earth model (Farrell, 1972) were used and the integrated effect of the marine tide distribution found by convolving the Green functions with the in-phase and quadrature components of the discretized marine tide distribution. Calculations were made for the two extreme cases in which drying areas remain either wholly dry or wholly submerged. Realistic loading predictions will be affected by partial drying and should lie somewhere in between the extremes.

For the reasons mentioned above, empirical cotidal charts, based on observations from coastal tide gauges, were drawn for the non-linear constituents M_4 and M_6 only (Fig. 3a and b). Since the quarter- and sixth-diurnal tides are generally a localized shallow-water phenomenon, ocean areas beyond the mouth of the estuary were not included in the tidal distribution. Within the estuary, however, we have taken the liberty, in the absence of sufficient coastal gauges and the total lack of mid-stream stations, to freely interpolate co-amplitude and co-phase lines across the river. There is some justification for this. The across-stream depth profile is shallow on the south-eastern two-thirds (ranging from 0 to 5 m) throughout the middle part

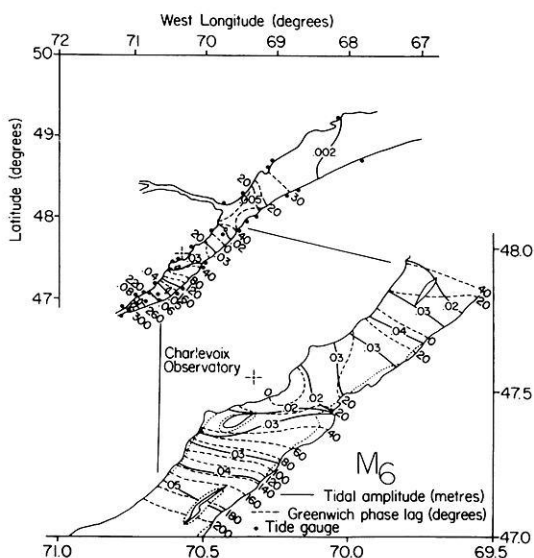
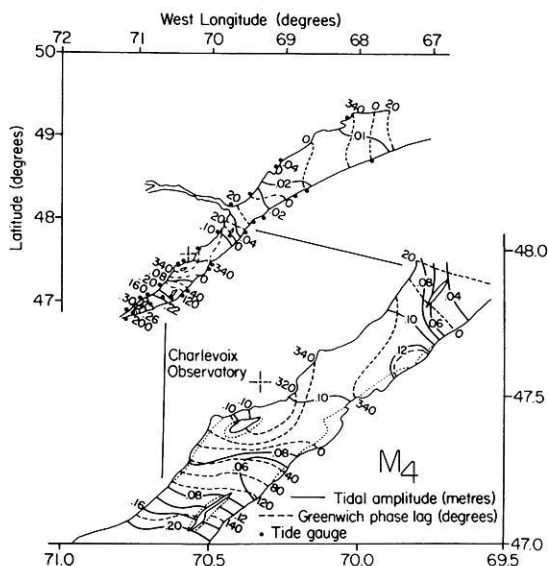


Fig. 3a and b. Empirical cotidal chart of **a** M_4 and **b** M_6 for the St. Lawrence estuary, with detail of the area adjacent to the Charlevoix site. Dots mark the location of tide gauge installations

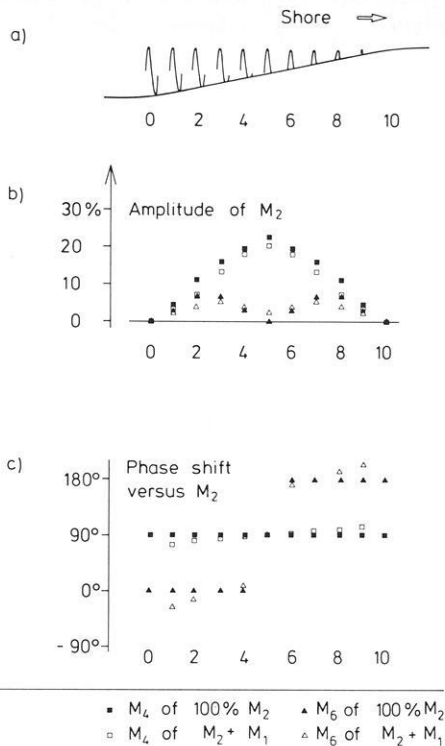


Fig. 4. **a** Schematic of a ramp-like beach showing the truncation of the linear tide as a function of position. **b** Relative amplitude of second- and third-order harmonics M_4 and M_6 of the simulated semi-diurnal M_2 tide plotted against position. **c** Phase shift of second- and third-order harmonics M_4 and M_6 of the simulated semi-diurnal M_2 tide plotted against position. Calculations were made for truncation of a single semi-diurnal wave of amplitude 1.0 (*full symbols*) and truncation of a combined 0.3-amplitude diurnal and 1.0-amplitude semi-diurnal wave series (*open symbols*), more closely resembling the real situation at Charlevoix

of the estuary, the deeper water being restricted to a channel along the north shore. We expect, therefore, non-linear interactions to occur throughout much of the shallow expanse. The least reliable part of the cotidal maps is in the area to the south of the Charlevoix site in which the steep gradient in amplitude and phase lag, for both constituents, is based on data from only two reliable tide gauges. This area clearly has the largest influence on the south tilt component, so that these results should be interpreted with caution.

Rectification of the linear tide

The non-linear tide loading model takes no account of rectification of the linear marine tide over drying areas. To estimate the effect on the loading, we simulated the truncation of the linear tide on a ramp-like beach (Fig. 4a). A set of 11 time series were synthesized to represent the tide at positions up the profile of the beach. Each series consisted of either a single sinusoid at semi-diurnal or two sinusoids at diurnal and semi-diurnal frequencies. Each series was then truncated using a gate function, the gate width determined according to position on the beach. The resulting series were Fourier transformed and amplitudes and phases of the second and third harmonics of the semi-diurnal tide (simulating M_4 and M_6) were plotted as a function of position on the beach (Fig. 4b and c). While the

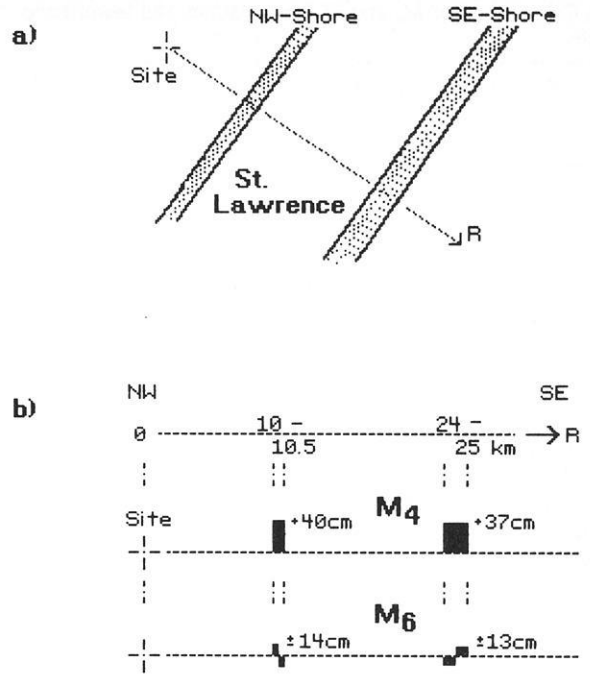


Fig. 5a and b. Geometry for loading calculations of rectified linear tide. **a** Strip-like beaches at 10.0–10.5 km and 24–25 km distance R from the site at the banks of the St. Lawrence River. **b** Maximum loading amplitudes over the whole beaches for the second-order harmonic M_4 and phase reversal midway up the beach for the third-order harmonic M_6

relative amplitudes of the harmonics, the second in particular, are quite high, there is a phase reversal of the third harmonics midway up the ramp, which results in a degree of cancellation. We will now use these results to arrive at a worst-case estimate of the effect of linear tide rectification on the non-linear loading at Charlevoix.

In the vicinity of the Charlevoix site, the width of the beaches, or drying areas, is small compared with their distance from the site. We calculated the loading tilt resulting from a 0.5-km-wide beach on the NW bank and a 1-km-wide beach on the SE bank of the St. Lawrence River (Fig. 5a). The amplitude of the marine M_2 amounts up to 2 m on the NW shore and up to 1.85 m on the SE shore (Peters and Beaumont, 1985). Taking 20% of this amplitude over the whole beach as a worst case for the second harmonic from Fig. 4b or 7% for the third harmonic, respectively, and considering partial cancellation due to phase reversal for the latter (Fig. 5b), we arrive at maximum effects of 30% of the loading model estimate of M_4 and 0.2% of the loading model estimate of M_6 (see next section). If, however, the whole drying areas were at heights represented by position 2 or 8 in Fig. 4a, no cancellation for the third-order harmonic would occur. The maximum effect could then be 40% of the loading model estimate of M_6 . Therefore, a significant input from the rectification of linear tides over tidal flats cannot be excluded.

The tilt tide

Comparison of mean tidal estimates

The mean tidal estimates from the HYCON analysis of the 1983 data from boreholes 1 and 2 are compared with

Table 2. Comparison of M_4 and M_6 observations and loading model results

	Borehole 1	Borehole 2	Loading model	
			100%	0%
South				
M_4	2.19 (340.2) ± 0.08 ± 3.9	3.08 (339.5) ± 0.11 ± 3.1	3.16 (341)	3.76 (340)
M_6	0.40 (98) ± 0.05 ± 7	0.44 (77) ± 0.06 ± 7	0.79 (68)	0.93 (64)
East				
M_4	6.80 (352.7) ± 0.17 ± 1.9	7.77 (352.9) ± 0.20 ± 2.1	6.53 (345)	6.84 (346)
M_6	1.58 (25.4) ± 0.08 ± 3.8	1.87 (22.8) ± 0.14 ± 5.0	1.68 (23)	1.78 (24)

Amplitude in nanoradians, Greenwich phase lag (brackets), 95% confidence limits

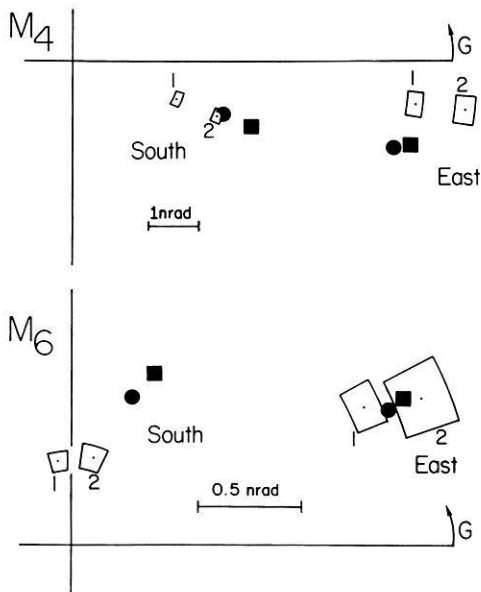


Fig. 6. Phasor plots of the M_4 and M_6 mean admittance estimates derived from the HYCON analysis of the south and east components of tilt measured in boreholes 1 and 2. The *solid dots* represent the loading model predictions for the two extreme cases in which there are no drying areas (*square dots*) and areas that do dry, doing so completely (*round dots*). Error sectors around each of the estimates are based on 95% confidence limits. *G* is Greenwich phase lag

the loading model predictions shown in Table 2. The results are displayed in the form of phasor diagrams in Fig. 6. Body tide amplitudes for M_4 are only 0.0059 nrad in EW and 0.0045 nrad in NS, using the development of Xi (1987), and even smaller for M_6 . They are far beyond the resolution of the tilt measurements.

Apart from M_6 from the south direction, the borehole 1 results are systematically smaller in amplitude than those of borehole 2, but are consistent in phase. The loading model results are in reasonable agreement with the observations, except in the case of M_6 south. For M_4 east the model favours borehole 1, although both observations lag the theory by about 7°. For the south direction the model

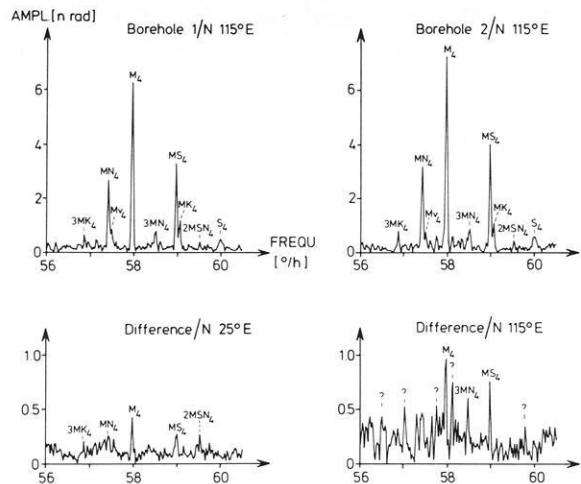


Fig. 7. High-resolution quarter-diurnal amplitude spectra (0.05°/h bandwidth resolution) of tilt in boreholes 1 and 2 and of the difference tilt signal at azimuth grossly parallel (N25°E) and perpendicular (N115°E) to the St. Lawrence River. N115°E is the azimuth at which most of the quarter-diurnal signal energy is observed

appears to overestimate the loading by as much as 100% for M_6 and by 70% and 20% for M_4 in boreholes 1 and 2, respectively, although we cannot rule out the possibility that local effects may be partly or wholly responsible for the disagreement.

Below, we examine more closely the coherency between the two borehole measurements to establish whether the differences are due to instrumental effects such as calibration or uncertainties in orientation.

Local tilt anomalies

Quarter-diurnal spectra of 20 months tilt recordings in boreholes 1 and 2 are plotted in Fig. 7. They essentially show the same tidal peaks as the tide gauge recordings in the St. Lawrence River (Fig. 2). A significant difference, however, can be seen between the tilt signals from the two boreholes. Spectra of the difference tilt signal contain non-linear tidal energy that seems to be polarized close to the azimuth of strongest marine loading.

Using the south and east admittances determined from both boreholes, we can derive the observed and difference tilt ellipses for each constituent (Tomaschek and Groten, 1963). The difference tilt for each constituent is formed from the difference between the admittance observed in boreholes 1 and 2. The ellipses are shown for the linear tides O_1 , K_1 , S_2 , M_2 and N_2 in Fig. 8a and for the non-linear constituents MS_4 , M_4 , MN_4 , $2MN_6$ and M_6 in Fig. 8b.

The observed ellipses for all constituents are strongly polarized towards the loading and in all cases, except the diurnals, the major axis for borehole 2 is larger. The most striking feature of these data is the polarization of the difference tilt ellipses (or tilt anomalies). The major axes of the linear tide anomalies lie in the range 60°–80° azimuth, whereas those of the non-linear anomalies are confined to azimuths in the range 110°–140° (see Fig. 9). Obviously, the linear tide anomalies (composed of body and loading components) are polarized 45°–60° anticlockwise with respect to the azimuth of the forcing, and the non-linear tidal anomalies are polarized 15°–40° clockwise with respect to the load only forcing. Calibration errors would result in

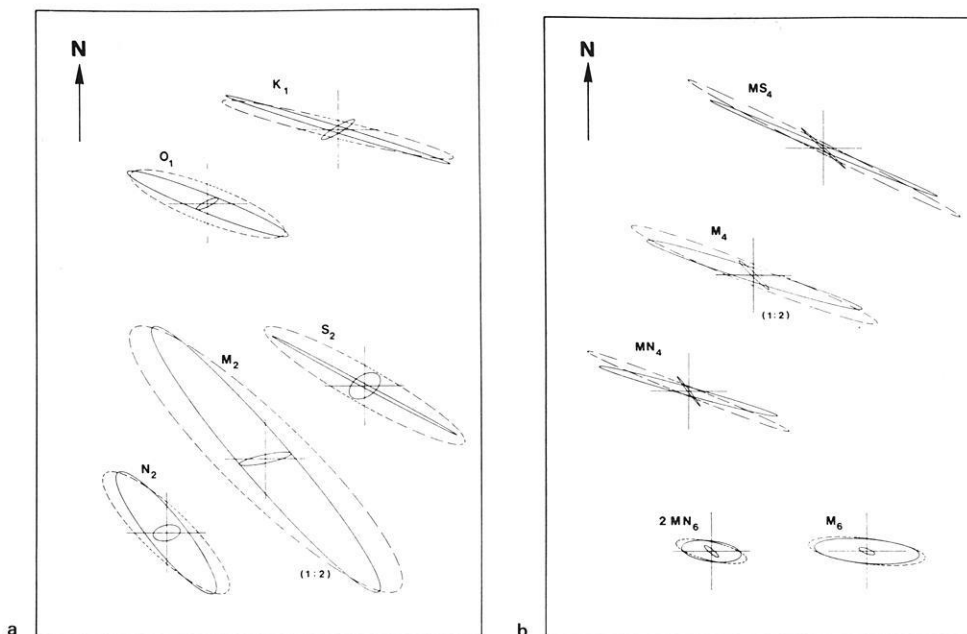


Fig. 8 a and b. Tilt ellipses of the observed tilt in borehole 1 (full line) and borehole 2 (dashed line) and the difference tilt shown for **a** linear tidal constituents, and **b** non-linear constituents. M_2 and M_4 are plotted on a double scale relative to the other constituents. The lengths of the lines in the centres of the ellipses are 24 nrad (48 nrad for M_2) in **a** and 2.4 nrad (4.8 nrad for M_4) in **b**

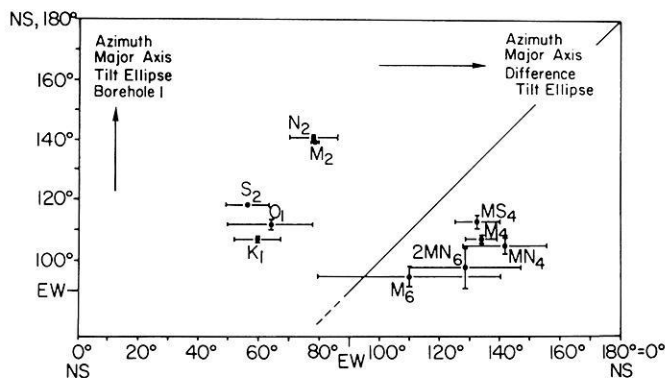


Fig. 9. Orientation of observed tilt ellipses for constituents measured in borehole 1 versus the orientation of the tilt ellipses for the same constituents of the difference between boreholes 1 and 2. Error bars reflect 95% confidence limits

anomalies aligned with the observed tilt ellipses (such anomalies would appear close to the oblique line running through the upper right corner in Fig. 9). Alignment errors of one or both tiltmeters would introduce anomalies characteristic of each tidal species, dependent on their frequency as well as their spatial distribution. Instead, we find a distinct grouping into linear and non-linear tidal components.

The alternative explanation for the observed anomalies involves the presence of a subsurface structural inhomogeneity (fault, fracture, geological contrast etc.) near one of the boreholes, through which strain-tilt coupling generates an anomaly governed by the nature and distribution of the forcing function. That the non-linear anomalies are polarized close to the azimuth of the loading is consistent with strain-tilt coupling arising from the non-linear load strain. In contrast, the linear tide, which has a body tide component, will produce an anomaly which is a function of both the body and the load strain. Furthermore, since the forcing distribution (load and body tide) for the diurnal and semi-diurnal constituents are different, strain-tilt coupling effects should also be different. Evidence for this is

seen in Fig. 9 in which N_2 and M_2 form a subgroup separate from O_1 and K_1 . That S_2 does not appear to fit into the scheme may reflect the influence of additional perturbing inputs, such as atmospheric tides, which are dominant within this frequency band.

The existence of subsurface inhomogeneities is known from a third borehole 80 m from the other two, in which a major water-bearing fracture was encountered at a depth of 130 m. Also, a subsurface discontinuity is inferred in the vicinity of boreholes 1 and 2 from a 90° shift in electric field polarization angle determined from magnetotelluric measurements at the site (R. Kurtz, personal communication).

Time variations in the M_4 and M_6 admittances

Because of the need for data continuity in time-variant analysis (Peters and Beaumont 1985), we have analysed tilt and tide gauge data recorded during 1983 in which relatively small data loss occurs (in the St. Joseph de la Rive data at a level of 13% and in borehole 1 at 2.7%). Figures 10 and 11 show the time-varying admittances in the form of trajectories in phasor space for M_4 and M_6 , estimated from the HYCON analysis of the south and east components of tilt and the tide gauges at St. Joseph de la Rive and Tadoussac.

For the east direction M_4 traces out an almost circular path, perhaps indicative of an annual component, with a range of 12% in amplitude and 11° in phase. While the south component admittance shows larger fractional changes (30%) than the east, the absolute range of the changes is approximately the same. Variations in each component are coherent between boreholes, suggesting that the tiltmeters are responding to a regional process. Also, from analysis 10 on, the south and east series behave in a similar way and, in terms of the phase lag with respect to the mean, are coherent with the variations at Tadoussac. There is no obvious correlation between the tide gauge at St. Joseph de la Rive and the other M_4 admittance trajectories.

The variations in M_6 are also coherent between bore-

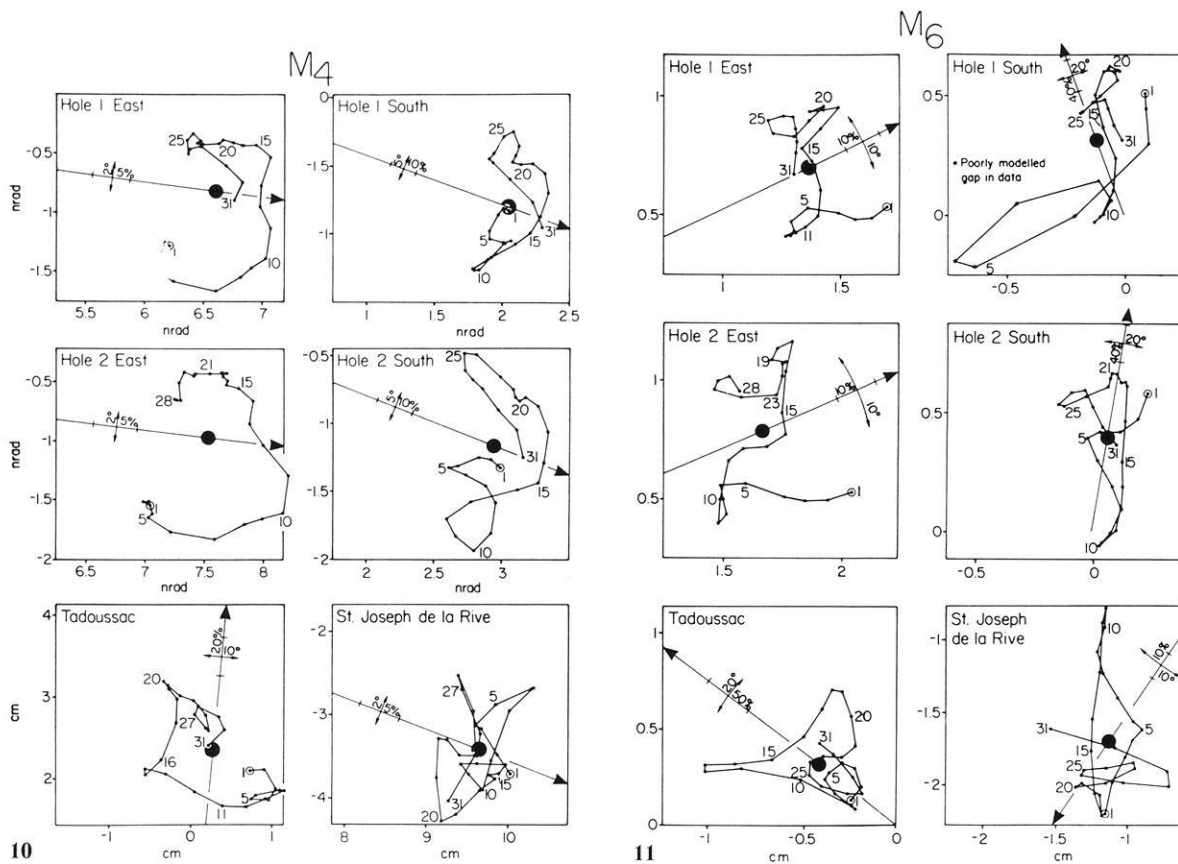


Fig. 10. Phasor trajectory plots of the M_4 admittance for tilt measured in boreholes 1 and 2 and tide gauges Tadoussac and St. Joseph de la Rive, estimated from HYCON sequential analysis. The mean admittance is indicated by the *round dot*. The *arrow* points in the direction of increasing amplitude. Fractional changes can be estimated from the amplitude and phase scales on the arrow which pertain to changes relative to the mean

Fig. 11. Phasor trajectory plots of M_6 . Details as for Fig. 10

holes for each component direction. For the east direction the amplitude changes are mainly confined to the start and the end of the year, with the phase lag varying during the middle period. For the south direction, apart from an anomalous excursion in the borehole 1 curve caused by a gap, the variations are predominantly in amplitude and cover a range of 200% because of the small signal. Nevertheless, the essential features of the larger-amplitude east component remain, with the absolute changes being approximately the same in both directions. There is no clear correlation between the tide gauge at Tadoussac and the tilt. However, the sustained amplitude cycle dominating the tilt variations during the first 8 months (analyses 1–20) is also clear in St. Joseph de la Rive results.

Discussion and conclusions

Without embarking on a rigorous and probably futile investigation of the inhomogeneous local strain field geometry at the Charlevoix site, we have established that the differences in the mean values of the non-linear tidal results for the redundant tilt observations are probably due to strain-tilt coupling and are not associated with instrumental effects.

Unlike most tidal studies which are concerned with explaining small perturbations in the tilt response, we are trying to find the source of the entire signal. The only non-

tectonic source of the non-linear M_4 and M_6 tidal signal is from tidal loading. Agreement between the observed mean admittance and the loading model results suggests that detectable tectonically induced non-linearities are not being generated in the Charlevoix area. The only major discrepancy occurs in the south component for M_6 in which the observed is about 50% smaller than predicted. It is likely that errors in the model due to the poorly constrained tide distribution south of the site are responsible for the disagreement.

In general, the level of agreement between the time-varying tide gauge admittances and the corresponding tilt results is only fair. This may be due to the small spatial scale of the shallow-water interactions, which makes a comparison between individual tide gauges and the tilt generally inappropriate. Also, in the case of St. Joseph de la Rive, the analysis results for data sets 21–27 were derived from data with gaps and were consequently heavily biased by the interpolation model. However, taken together, the mean admittance results and time-variant analysis results strongly indicate a marine origin for the non-linear harmonics in the tilt.

If the arguments of Beaumont (1978) are realistic, this result implies that the special condition in which the rate of change of the tectonic stress is equal to the mean tidal stress rate does not apply during the period covered by this study, or is not detectable within the prominent back-

ground of the non-linear loading. In their study of linear tidal admittance variations, Peters and Beaumont (1985) found no evidence for a high rate of stress accumulation in the region. Thus, from the combined evidence of both tidal response studies, the regional tectonic stress is stable or only slowly changing. These results are not unexpected considering the low level of earthquake activity during the period of the tiltmeter experiment. During 1983, the largest earthquake in the region was of magnitude 3.8, the epicentre of which was 38 km from the observatory.

Acknowledgements. This project was supported by the Air Force Geophysics Laboratory, Hanscom AFB under contracts F19628-80-C-0032 and F19628-83-K-0023, the Natural Sciences and Engineering Research Council through Operating and Equipment grants to C. Beaumont, and the Division of Geophysics, Geological Survey of Canada. The Marine Environment Data Service provided the tide gauge data. We would like to thank Chris Beaumont and Walter Zürn for helpful discussions and criticism, Tony Lambert and Don Bower for their interest and support throughout the program, and Jacques Lebreque for his invaluable assistance with operations at the Charlevoix Observatory. Benoit Dostaler and Dianne Lemieux maintained the array on a daily basis and John Fahey assisted with data reduction and analysis. H.-J. Kämpel acknowledges the support from a Killam fellowship during a 1-year stay at Dalhousie University, Halifax, Nova Scotia.

References

- Agnew, D.C.: Nonlinearity in rock: evidence from earth tides. *J. Geophys. Res.* **86**, 3969–3978, 1981
- Beaumont, C.: Linear and nonlinear interactions between the earth tide and a tectonically stressed earth. In: Applications of geodesy to geodynamics, I. Mueller, ed.: pp 313–318. Ohio State University Press 1978
- Brace, W.F., Paulding, B.W., Jr., Scholz, C.H.: Dilatancy in the fracture of crystalline rocks. *J. Geophys. Res.* **71**, 3939–3953, 1966
- Farrell, W.E.: Deformation of the Earth by surface loads. *Rev. Geophys. Space Phys.* **10**, 761–797, 1972
- Flach, D., Große-Brauckmann, W., Herbst, K., Jentzsch, G., Rosenbach, O.: Ergebnisse von Langzeitregistrierungen mit Askania-Bohrlochneigungsmessern – Vergleichende Analyse hinsichtlich der Gezeitenparameter und langperiodischer Anteile sowie instrumentelle Untersuchungen. *Deutsche Geodät. Komm.* **B211**, (M. Bonatz, ed.) 72–95, 1975
- Gallagher, B.S., Munk, W.H.: Tides in shallow water: spectroscopy. *Tellus* **XXIII**, 346–363, 1971
- Godin, G.: Eight years of observations on the water level at Quebec and Grondines 1962–1969. Manuscript Report Series **31**, Marine Sciences Directorate, Dept. Environment, Canada, 1973
- Goertzel, G.: An algorithm for the evaluation of finite trigonometric series. *Am. Math. Month.* **65**, 34, 1958
- Harrison, J.C.: Cavity and topographic effects in tilt and strain measurements. *J. Geophys. Res.* **81**, 319–328, 1976
- Mjachkin, V.I., Sobolev, G.A., Dolbilkina, N.A., Morosov, V.N., Preobrazensky, V.B.: The study of variations in geophysical fields near focal zones of Kamchatka. *Tectonophysics* **14**, 287–293, 1972
- Mjachkin, V.I., Brace, W.F., Sobolev, G.A., Dieterich, J.H.: Two models for earthquake forerunners. *Pageoph.* **113**, 169, 1975
- Neresov, I.L., Semenov, A.N., Simbireva, I.G.: Space-time distribution of the travel time ratios of transverse and longitudinal waves in the Garm area. In: The physical basis of foreshocks, Moscow: Nauka Publ. 1969
- Peters, J.A., Beaumont, C.: Borehole tilt measurements from Charlevoix, Quebec. *J. Geophys. Res.* **90**, 12791–12806, 1985
- Rice, J.R., Rudnicki, J.W.: Earthquake precursory effects due to pore fluid stabilization of a weakening fault zone. *J. Geophys. Res.* **84**, 2177–2193, 1979
- Rossiter, J.R., Lennon, G.W.: An intensive analysis of shallow water tides. *Geophys. J. R. Astron. Soc.* **16**, 275–293, 1968
- Scholz, C.H., Kranz, R.: Notes on dilatancy recovery. *J. Geophys. Res.* **79**, 2132–2135, 1974
- Schüller, K.: Tidal analysis by the hybrid least squares frequency domain convolution method. Proceedings of the Eighth International symposium on Earth Tides, M. Bonatz and P. Melchior eds., Institut für Theoretische Geodäsie der Univ. Bonn, FRG, 1977
- Sobolev, G., Spetzler, H., Salov, B.: Precursors to failure in rocks while undergoing anelastic deformations. *J. Geophys. Res.* **83**, 1775–1784, 1978
- Soga, N., Mizutani, H., Spetzler, H., Martin III, R.J.: The effect of dilatancy on velocity anisotropy in Westerly granite. *J. Geophys. Res.* **83**, 4451–4458, 1978
- Stuart, W.D.: Diffusionless dilatancy model for earthquake precursors. *Geophys. Res. Lett.* **1**, 261–264, 1974
- Tomaschek, R., Groten, E.: Die Residualbewegung in der horizontalen Gezeitenkomponente. *Geofisica Pura e Applicata* **56**, 1–15, 1963
- Whitcomb, J.H., Garmany, J.D., Anderson, D.L.: Earthquake prediction: variation of seismic velocities before the San Fernando earthquake. *Science* **180**, 632–635, 1973
- Xi, Qinwen: A new complete development of the tide-generating potential for the epoch J2000.0. *Bull. Inf. Marées Terrestres* **98**, 6744–6747, 1987
- Zetler, B.D., Cummings, R.A.: A harmonic method for predicting shallow water tides. *J. Marine Res.* **25**, 103–114, 1967
- Zschau, J.: Auflastgezeiten. Habilitation thesis, Kiel University, 1979

Received June 22, 1987; revised version September 10, 1987
Accepted September 10, 1987

Editors' note

Journal of Geophysics will cease to exist after Vol. 62; the present issue is the last one. So a long and good tradition comes to an end, and it certainly is adequate to comment briefly on this development from the part of the editors.

Journal of Geophysics was founded as *Zeitschrift für Geophysik* in 1924 by the Deutsche Geophysikalische Gesellschaft. It has formed since then, with a few years' interruption after the Second World War, the scientific forum of this society. Internationalisation of science in general and geophysics in particular in the 1960s turned the journal into an international journal, reflected best by the change in title to *Journal of Geophysics* in 1974. The new publisher, Springer-Verlag, contributed considerably to this positive development. Since then, on average, at least as many foreign authors contributed to the journal as German authors. Over the years since 1974 the manuscript situation was good, but never overwhelming; being international, the journal also experienced the competition between international journals. Therefore, one had to be open to new developments, in particular in the field of amalgamation of journals. In the summer of 1986 serious contact began between three societies in Europe – Deutsche Geophysikalische Gesellschaft, European Geophysical Society and Royal Astronomical Society – about merging their journals *Journal of Geophysics*, *Annales Geophysicae* (series B) and *Geophysical*

Journal of the Royal Astronomical Society. After fair and cooperative negotiations, the results of which were strongly supported by the societies, in particular by the members of Deutsche Geophysikalische Gesellschaft, an agreement was reached in July 1987 to publish the joint journal from January 1988 onwards under the title *Geophysical Journal*.

Probably, there are only a few members of Deutsche Geophysikalische Gesellschaft who will not view the end of *Journal of Geophysics* with some regret, because of its long tradition, continuity and high scientific level. However, we think that our society has made the right step at the right moment and that it gains more than it loses. Those members who subscribe to *Geophysical Journal* will obtain a considerably broadened spectrum of solid-earth geophysics (and note: at about the same price as before). Editorial influence on *Geophysical Journal* is guaranteed through adequate representation on the editorial board. Hopefully, many authors from our society will make use of the new possibilities that the wider circulation of *Geophysical Journal* offers.

**W. Dieminger
G. Müller
J. Untiedt
P. Weidelt**

The upper-mantle discontinuities underneath the GRF array from *P*-to-*S* converted phases

R. Kind¹ and L.P. Vinnik²

¹ Seismologisches Zentralobservatorium, Krankenhausstrasse 1, 8520 Erlangen, Federal Republic of Germany

² Institute of the Physics of the Earth, Academy of Sciences of the USSR, Moscow, USSR

Abstract. A data-processing method is applied which includes a rotation of the three components, normalization and delay-and-sum of broadband records of earthquakes from a large distance and azimuth distribution, recorded at a single station (or an array). Clear *P*-to-*S* converted phases at the mantle discontinuities are observed in the Gräfenberg records, after this data processing. Theoretical seismograms are computed for the PREM model and processed in the same way as the observed data. A comparison with the data shows that the depth interval between the two discontinuities in the mantle transition zone (those at 400 and 670 km depth in PREM) is around 240 km. The 670-km discontinuity is sharper than the 400-km discontinuity and is comparable in sharpness with the crust-mantle transition, as far as it is possible to judge from the broadband data used. There are indications of pronounced lateral heterogeneity of the 400-km transition, underneath GRF. We have also observed converted and multiply reflected shear waves in the crust, which set sensitive limits to the average crustal model underneath the array. These data suggest that the velocity jump at the Moho is smaller than indicated by refraction studies.

Key words: Upper-mantle transition zones – *P*-to-*S* conversions – Theoretical seismograms

Introduction

The bulk of the presently available seismic data on the structure of the upper-mantle discontinuities comes from observations of refracted and overcritically reflected body waves. The errors in the depth determinations of the mantle discontinuities from these data can reach a few tens of kilometres. Similarly, refracted waves are rather insensitive to the sharpness of a discontinuity. A poor lateral resolution is another deficiency of the method: refracted and overcritically reflected waves penetrating to a depth of 650 km return to the Earth's surface at a distance of about 3000 km from the epicentre, thus averaging the effects of lateral variations in the deep structure of the Earth. On the other hand, detailed and accurate seismic data on the properties of these discontinuities (depth, sharpness, lateral variations) are necessary for constraining models of mantle composi-

tion and dynamics (e.g. see Jeanloz and Thompson, 1983). Several attempts have been made to use converted phases to study the upper-mantle structure. For example, Paulssen (1985) has tried to detect converted shear waves in the *P* coda. Faber and Müller (1984) have observed long-period forerunners of *S*, converted at upper-mantle discontinuities.

To meet demands for higher resolution and accuracy, a technique of using teleseismic waves converted from *P* to *SV* at the upper-mantle discontinuities was developed (Vinnik, 1977). The converted phases are recorded in the *P*-wave coda with amplitudes of the order of a few percent of the *P*-wave amplitude. To detect such weak phases a special signal-processing procedure is required. This procedure is, in principle, a delay-and-sum method similar to the conventional velocity filtering; but instead of an array of seismic receivers, use is made of an array of sources. The technique has been applied so far to the records of a few seismograph stations (only one of them digital), and converted phases corresponding to the mantle discontinuities were consistently observed (Vinnik et al., 1983).

In this paper we present results of the application of a similar approach to the data of the Gräfenberg array. The main advantage of the Gräfenberg records lies in their broadband frequency content which makes them ideally suited for this purpose. The inversion of the observations for mantle structure has been carried out by generating synthetic records for a number of models, passing the synthetics through the same signal-processing procedure as the real seismograms and comparing the results of observation and modelling. The conclusions thus derived are summarized and discussed in the last section of the paper.

A method to detect converted phases

The method of detecting converted phases was described earlier (Vinnik 1977; Vinnik et al. 1983). We repeat these descriptions here with minor modifications. We consider the *P* wave of a distant earthquake converted to *SV* on the receiver side of the wave path and recorded by a three-component seismograph set (Fig. 1).

The *P* wave and noise with the same angle of incidence as the *P* wave are suppressed by projecting the record on the *H* axis which is perpendicular to the principal direction of the *P*-wave particle motion *L* and lies in the vertical plane (Fig. 1). In Fig. 1 the direction *L* is shown coinciding with that of the *P*-wave ray path, although in reality they are somewhat different. The angle *e* between *L* and the

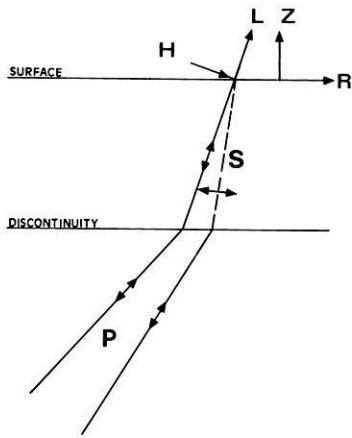


Fig. 1. Sketch of the coordinate systems used and of the ray path of a phase converted at an upper-mantle discontinuity

radial direction R can be found from the expression (Vinnik et al. 1983)

$$e = \tan^{-1} [\langle R(t) Z(t) \rangle / (\lambda - \langle Z^2(t) \rangle)].$$

$R(t)$ and $Z(t)$ are ground-motion components which correspond to the direction R and the vertical direction Z , respectively; t is time; $\langle \rangle$ denotes averaging over the time interval from the beginning to the end of the main P -wave train; λ is the biggest root of the equation

$$(\langle Z^2(t) \rangle - \lambda)(\langle R^2(t) \rangle - \lambda) - \langle R(t) Z(t) \rangle^2 = 0.$$

To detect the converted phases which are hidden in the P -wave coda, the H -component records of many seismic events should be stacked. To facilitate stacking, the differences between the records arising from differences in the magnitudes and source functions of various events are reduced by transforming the records into a standard form, which is the normalized crosscorrelation function of the H and L components. The standardized \hat{H} component can be expressed as

$$\hat{H}(t) = \frac{\int_{t_1}^{t_2} H(t + \tau) L(\tau) d\tau}{\int_{t_1}^{t_2} [L(\tau)]^2 d\tau}$$

where t is now the delay time between H and L , t_1 and t_2 correspond to the first-arrival time and the end of the main P -wave train, respectively. A similar matched filter procedure with the autocorrelation of the P -wave signal as normalizing function was used by Schlittenhardt (1986) to determine the PcP/P amplitude ratio.

Assuming that the form of the converted wave train is similar to that of the P -wave train, the maximum value of the function \hat{H} is equal to the amplitude ratio P_s/P ; the value of t which corresponds to this maximum is equal to the time interval between the P_s and P arrivals. This time interval is given by

$$t_{P_s} = \int_{r_c}^{r_0} (v_s^{-2} - p^2 r^{-2})^{1/2} dr - \int_{r_c}^{r_0} (v_p^{-2} - p^2 r^{-2})^{1/2} dr$$

where r is the radial distance, r_c is the location of the interface of conversion and r_0 is the earth's radius. $v_p(r)$ and $v_s(r)$ are the P and S velocities and p is the ray parameter

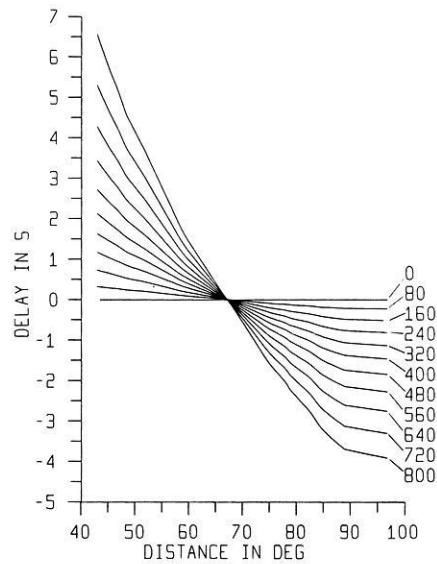


Fig. 2. Difference travel times of a converted phase and the P time as a function of distance and depth of an assumed discontinuity, normalized by the difference time at 67° . The numbers at the right are the depths of the discontinuity in km

of the P wave. This equation was derived on the assumption that the ray parameter values are the same for P and P_s , while in reality they are somewhat different. The exact values of t_{P_s} are somewhat lower than these estimates. For conversions in the upper mantle, the difference is of the order of a fraction of a second. Such accuracy is sufficient for estimating relative time delays for the phases corresponding to the same conversion depth and varying epicentral distances.

To enhance the waves converted at depth h and simultaneously reduce all other wave types, the \hat{H} components of many seismic events in a broad epicentral distance range are delayed and summed. The delay $\delta t_i(h)$ can be expressed as

$$\delta t_i = t_{P_s}^i(h) - t_{P_s}^0(h)$$

where $t_{P_s}^i(h)$ is calculated for the slowness p (or the corresponding distance) of the P wave of the i -th event, and $t_{P_s}^0(h)$ is calculated for a reference value of p which was taken equal to 6.4 s/degree (or 67° distance). The dependence of δt_i on p or epicentral distance is illustrated by Fig. 2. The summed records are normalized by dividing the amplitude by the number of events. The summation is performed for a number of trial conversion depths ("phasing depths"). The procedure is similar to the conventional array beam forming, but instead of an array of seismic receivers we use an array of sources; the apparent velocity and azimuth as unknown parameters are replaced by the phasing depth. In the case of the conventional beam forming, the best slowness and azimuth values of a seismic wave can be obtained from a comparison of beam amplitudes. Similarly, a rough estimate of the depth of conversion can be obtained from a comparison of amplitudes corresponding to the different phasing depths. The actual depth of conversion can be found much more accurately from the time delay of the converted phase. The proximity of both depth estimates implies that the phase is a true converted wave rather than an artefact of processing.

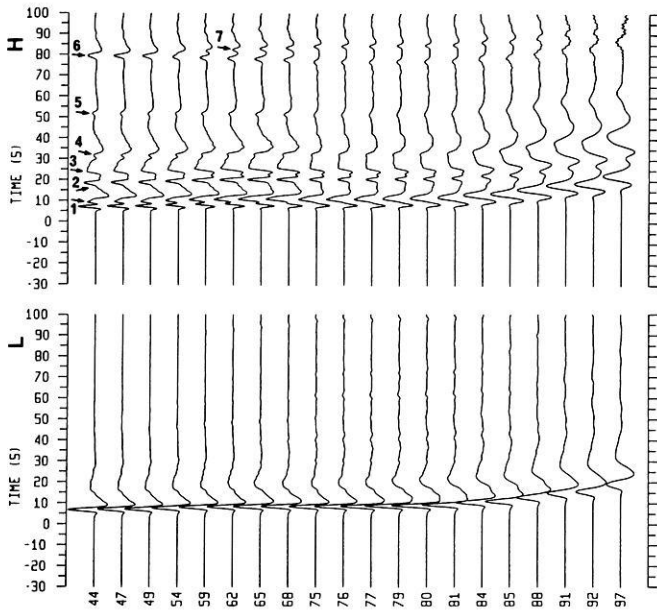


Fig. 3. Theoretical H and L components for the PREM model. All traces are normalized independently. Phase 1 is the conversion at the Moho, phase 2 is the PS multiple in the crust, phase 3 is the SS multiple in the crust, phase 4 is the conversion at 220 km, phase 5 is the conversion at 400 km, phase 6 is the conversion at 670 km and phase 7 is the PS multiple at the 200-km discontinuity. The rise time of the theoretical source function is 2.5 s

Computation of theoretical seismograms

The interpretation of the observed converted phases is carried out with the aid of theoretical seismograms. The version of the reflectivity method developed by Kind (1985) is used. This method provides complete body-wave seismograms for a buried source and different structures at source and receiver sides. We have used a dislocation point source buried at 750 km depth. This large source depth makes sure that there is no interference of the P -wave group with depth phases or a complicated near-source structure. Near-source effects in the observed data are reduced because of the summation of events from different regions and different source depths. We have avoided this complication in the theoretical seismograms by using a deep source and a smooth mantle at the source side. The complete response of the structure under the station, including effects of the free surface, are taken into account. A strike-slip source was used and a profile at 45° azimuth was computed. The same source orientation was used for all computed seismogram sections. The source-time function is a smooth ramp function in moment with the rise time as a parameter. The same broadband displacement filter which has been used to process the observed data has also been applied to the theoretical data. The distances have been chosen to cover the same range as the observed data; their spacing is also similar.

Figure 3 shows theoretical L and H components for the PREM mantle at the receiver side (Dziewonski and Anderson, 1981). The Jeffreys-Bullen model is used at the source side, because we wanted a smooth model near the source. The crustal layers of PREM have been replaced by a model more appropriate for Gräfenberg (Table 2, model B). A

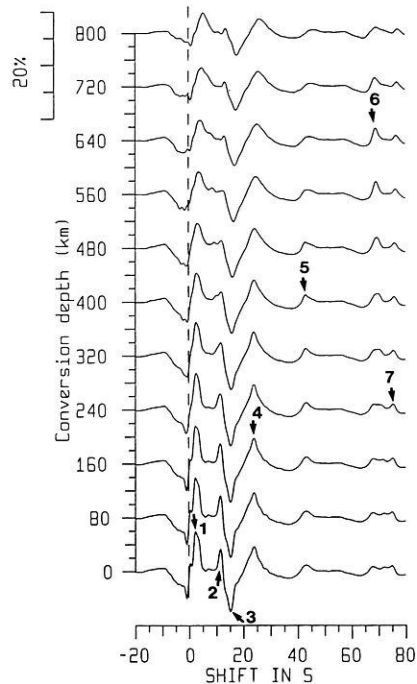


Fig. 4. Delayed and summed theoretical \hat{H} components from Fig. 3. The numbers refer to the same phases as in Fig. 3. It can clearly be seen that, for example, the signal improvement for the conversion at the 670-km discontinuity is best for a trial conversion depth close to 670 km. The amplitude scale is the ratio P_s/P in percent. The same scale is given in Figs. 7–10

fixed angle of 25° was used for the rotation of the coordinate system for all distances. We have, therefore, still some P energy on the H component. The theoretical seismograms in Fig. 3 are proportional to ground displacement. The rise time is 2.5 s. The H component is much more complicated than the L component. This is due to several converted or multiply reflected phases arriving as shear waves the station. The conversions at the Moho and at the 220-, 400- and 670-km discontinuities in PREM, and a few multiples, are marked in Fig. 3. All these phases have been identified by experiments with theoretical seismograms. The SV phases are very weak (a few percent of the P wave). It is understandable that such weak phases are difficult to detect directly in seismic records. Signal-generated noise in the real earth is easily larger than these weak conversions. The conversions have, however, a big advantage; they correlate, whereas the noise does not correlate over many records.

The theoretical seismograms in Fig. 3 have been processed exactly in the same way as the observed ones, for direct comparison with the observed data, using the method described in the previous section. The results of this processing procedure are shown in Fig. 4. The rise time of 2.5 s in Fig. 3 was used in order to reduce some high-frequency numerical noise. A rise time of 2.0 s in Fig. 4 is used because the high-frequency noise here is reduced by the summation. The conversions at the mantle discontinuities have their largest amplitudes at their appropriate conversion depths. The conversions or multiples in the crust have their largest amplitudes at zero or a small conversion depth (meaning zero or small delays for the summation). The conversion in PREM at 220 km interferes with the crustal multiples and is therefore difficult to see.

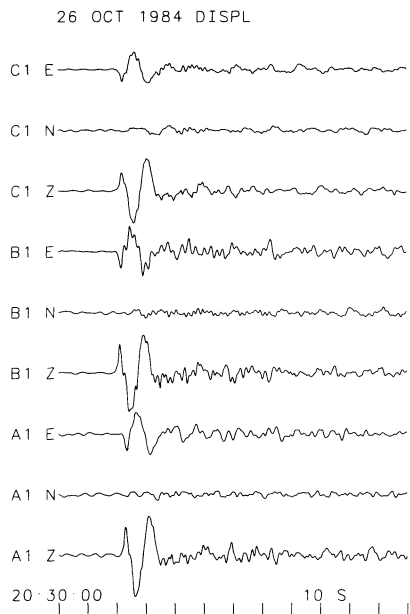


Fig. 5. Three-component displacement records of event 28, Table 1. The azimuth of this event is 80° . The *E* and *N* components are, therefore, practically the radial and transverse components, respectively

Observation of converted phases

The first step in processing the records of the GRF array was the summation of the vertical, radial and transverse components of its three 3-component stations. This has been done in order to improve the signal-to-noise ratio by suppressing microseisms and the incoherent signal-generated noise. The summed records were filtered with three different filters. The transfer function of the first filter is flat with respect to ground displacement in the frequency range between 0.05 and 5.00 Hz. The teleseismic *P* signals at the output of this filter usually contain frequencies between, approximately, 0.05 and 1.00 Hz. In order to analyse a possible frequency dependence in the observed wave field, two narrow band-pass filters were used. The cut-off frequencies were 0.065 and 0.130 Hz for the second filter and 0.125 and 0.250 Hz for the third one. The dominant periods at the outputs of the second and third filter were around 10 and 5 s, respectively. The subsequent processing was performed as described earlier.

The angles of incidence computed with the method described earlier are normal. Liu and Kind (1986) have observed unusually steep angles of incidence in particle-motion diagrams of short-period *P* waves at GRF. The reason for this is extremely low-velocity, but thin, sedimentary layers underneath the Jurassic layer (Frank Krüger, personal communication).

Figure 5 shows the displacement data of the three-component stations for event 28 (Table 1). The back azimuth of the event is 80° , so that the *E* component is practically the radial component and the *N* component corresponds to the transverse component. Figure 6 shows examples of the vertical component of some of the events used in the three frequency bands.

The list of processed events is given in Table 1. Criteria for event selection were: large amplitude of *P* relative to microseismic noise, relatively short duration of the main

P-wave train (usually not more than 40 s), absence of visible secondary phases like *pP* or *sP* in the critical part of coda. The length of the time windows of the *P* wave used varies between 30 and 50 s. Shallow or deep events are useful; intermediate-depth events are less suitable. Some events of Table 1 could satisfy the quality requirements only in one or two frequency bands. In the first (broad) and second (around 0.1 Hz) frequency bands, the number of usable records was fairly large (33 and 32, respectively). In the third frequency band (around 0.2 Hz), it was much lower (15). Many "good" events can be found in the distance range between 70° and 100° but, unfortunately, there are not enough events in the range between 35° and 60° . Representative samples of $\hat{H}(t)$ are shown in Fig. 7. The stacked records are presented in Fig. 8.

A visual inspection of stacked records in Fig. 8 leads to the following observations. In the first (broad) frequency range, the initial part of the stacked records is dominated by strong crustal converted and multiple reflected phases. The amplitude in the first 30 s decreases with growing conversion depth. In the time interval around 45 s at shallow conversion depths one can see a bay-like phase with a duration around 20 s. As the conversion depth comes closer to 400 km, the amplitude of this phase increases due to a contribution from higher frequencies. As the depth grows further, the amplitude decreases. The times around 45 s correspond to depths of conversion around 400 km; the amplitude distribution in the time interval around 45 s fits this depth perfectly. Thus, the phase with the time around 45 s is, most likely, formed by conversion at 400 km depth.

In the time interval around 68 s one can see a second clear mantle phase. As the depth of conversion comes to 640 km, this phase changes its shape from a bay-like feature to a nearly perfect triangle. This is caused by the improved correlation, especially at higher frequencies. This shape deteriorates as the depth exceeds 640 km. The times around 68 s correspond to depths of conversion around 640 km and thus, again, the amplitude versus depth distribution and the time are in good agreement with each other. We observe that the converted phase which is related to conversion at 640 km depth has higher frequencies than the first mantle phase.

The wave field in the second frequency band (0.1 Hz), like that in the broad band, is dominated by the crustal phases (first 30 s), the phase converted near 400 km depth and the phase converted near 640 km depth. The amplitude of the second mantle phase is notably larger. The value t_{ps} of a converted phase corresponds to the (positive) maximum of $\hat{H}(t)$. These values are 45.0 s and 68.2 s for the first and second mantle phase, respectively (they correspond to a reference slowness of 6.4 s/degree or 67° distance).

The third frequency band (0.2 Hz) is noisier than the other two. Nevertheless, both mantle phases are seen, especially the second one (at 68.2 s). Their t_{ps} values coincide with those found in the first and second frequency bands. The amplitude of the second phase in the 0.2-Hz frequency band is nearly 70% of that in the 0.1-Hz band.

To test the stability of the observed wave field and the accuracy of our estimates of the parameters, we have performed a series of numerical experiments. In these experiments, the available \hat{H} -component records were divided into groups and the records of each group were stacked separately. In the first experiment, the events were divided into two groups so that the epicentral distance range and

Table 1. List of events used in this study

No	Day	Month	Year	Origin time	Latitude	Longitude	Depth	Magnitude	Distance	Azimuth
01	09	03	1977	14 27 56.2	41.7N	131.1E	556	5.9	74.8	42
02	04	09	1977	15 40 55.0	51.1N	178.4E	20	5.6	79.0	8
03	16	08	1979	21 31 24.9	41.9N	130.9E	566	5.8	74.6	42
04	24	08	1979	04 26 54.5	9.0N	83.5W	43	5.2	86.3	279
05	24	08	1979	16 59 28.9	41.2N	108.1E	18	5.6	63.8	56
06	27	05	1980	14 51 00.3	37.5N	118.8W	22	5.7	82.6	322
07	05	07	1980	20 25 25.2	41.9N	77.4E	22	5.4	45.5	74
08	22	01	1981	19 34 43.0	38.3N	142.7E	35	6.1	82.6	37
09	04	09	1981	11 15 13.9	9.9N	124.0E	651	6.0	96.8	66
10	12	09	1981	07 15 53.8	35.7N	73.6E	30	6.2	46.6	83
11	25	10	1981	03 22 16.0	18.2N	102.0E	28	6.2	90.4	299
12	01	07	1982	07 41 53.7	51.4N	179.9W	51	6.3	78.8	7
13	04	07	1982	01 20 08.2	27.9N	137.0E	554	6.2	88.9	46
14	31	07	1982	06 29 13.2	51.8N	176.1E	18	6.2	78.1	10
15	24	01	1983	23 09 21.7	12.9N	93.6E	81	6.1	75.4	87
16	14	02	1983	08 10 04.3	55.0N	159.2W	37	6.0	75.4	354
17	01	05	1983	18 10 40.7	46.4N	153.4E	24	6.1	78.9	26
18	02	05	1983	23 42 37.7	36.2N	120.3W	7	6.2	84.3	323
19	02	06	1983	20 12 50.9	9.5S	71.2W	600	5.8	92.4	258
20	09	06	1983	12 49 02.7	40.3N	139.0E	22	6.3	79.4	38
21	09	06	1983	18 46 04.2	51.4N	174.1W	46	6.1	79.2	356
22	10	06	1983	02 13 23.2	75.5N	127.8E	10	5.5	48.5	18
23	21	06	1983	14 48 07.9	24.1N	122.4E	43	5.8	84.5	51
24	24	06	1983	07 18 22.3	21.8N	103.3E	18	6.0	75.2	74
25	24	06	1983	09 06 46.3	24.2N	122.4E	48	6.0	84.5	51
26	28	06	1983	03 25 16.7	60.2N	141.3W	14	5.9	68.2	346
27	07	07	1983	20 35 37.4	7.4S	27.9E	10	5.8	58.5	161
28	26	10	1984	20 22 21.8	39.2N	71.3E	33	6.0	43.1	80
29	01	05	1985	13 27 56.1	9.2S	71.2W	600	6.0	92.4	258
30	06	05	1985	03 04 22.7	30.9N	70.3E	37	5.6	47.5	90
31	14	05	1985	13 24 57.8	10.6S	41.4E	10	6.0	65.6	147
32	14	05	1985	18 11 08.9	10.5S	41.4E	10	6.4	65.6	147
33	16	05	1985	14 20 25.1	29.1S	77.7E	10	5.9	98.1	126
34	06	06	1985	02 40 12.9	0.9N	28.4W	10	6.3	59.2	227
35	26	04	1986	07 35 16.0	32.1N	76.3E	33	5.5	50.6	85
36	06	07	1986	19 24 26.3	34.4N	80.1E	33	5.8	51.6	80

the distribution of events within this range were nearly the same for each group. No attention was paid to the azimuths of events. The results for the first and second frequency band are presented in Fig. 9. A comparison shows that the times and amplitudes of the second phase (at 68.2 s) are nearly the same in the two groups. This result coincides with that obtained in a similar experiment with NORSAR data (Vinnik et al., 1983) and attests the estimates of the times and amplitudes of the converted phases as highly accurate. On the other hand, the appearance of the first phase (at 45.0 s) is rather different in the two groups. The difference is mainly in the frequency content, which is especially clear in the broad frequency band.

In another experiment, the events were divided into groups according to their azimuth. The first group assembled was of the events with an azimuth between 75° and 345°; the second group included all other events. Most of the available events are located to the east of the array. For this reason, the results for the first group correspond mainly to the east and south-east, while those for the second group are characteristic of the north and north-east. In the two groups, the amplitude of the second phase is nearly the same, while those of the first one are strongly different (Fig. 10). The difference is especially pronounced in the frequency band around 0.1 Hz, where the first phase is either

absent (Fig. 10d) or very strong and clear (Fig. 10c). This could indicate that the conversion at 400 km depth depends strongly on the azimuth.

Fitting the crustal data

The initial part of the summed \hat{H} -component records was used to infer the structure of the crust underneath the array. A similar method using unrotated and undelayed, but normalized and stacked records of teleseismic P waves was used by Owens et al. (1987) to derive the crustal structure underneath the RSTN stations in North America.

Figure 11 shows the comparison of undelayed summed \hat{H} components of observed and theoretical traces. These data are mainly sensitive to the structure of the crust, the crust-mantle boundary and the uppermost part of the mantle. Superimposed on each other are the observed displacement data from Figs. 8–10 for different subsets of events and for zero conversion depth. We have also added two more groups of events, where the data have been split by magnitude (larger or smaller than 6.0). The differences between the different data traces are indications of the reliability of the data. These differences are small compared to the amplitudes of the signal. This shows that we have stable information about the crust, which is independent of the

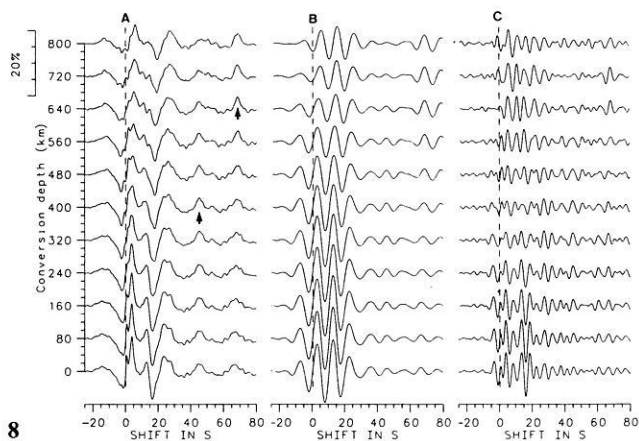
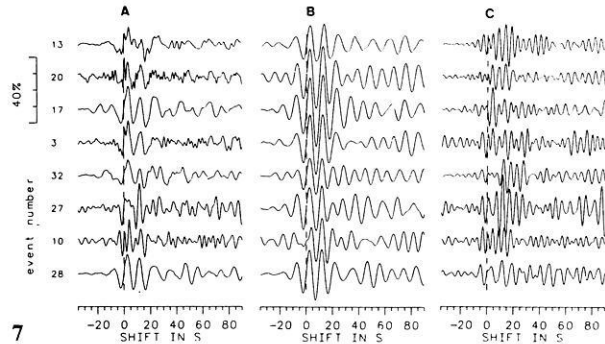
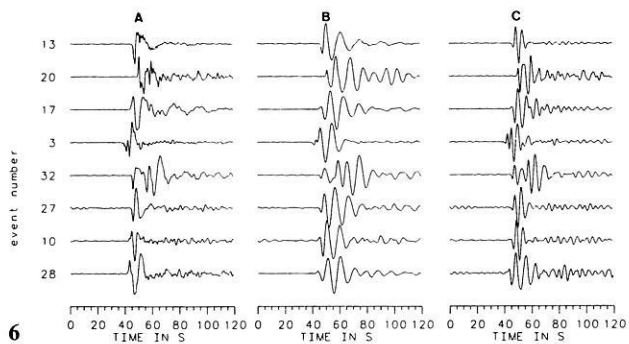


Fig. 6. Normalized vertical components of examples of records used in this study. The numbers on the left refer to the event numbers in Table 1. The seismograms labelled *A*, *B* and *C* are for displacement and bandpasses around 0.1 and 0.2 Hz, respectively

Fig. 7. \hat{H} components for the same earthquakes and filters as in Fig. 6

Fig. 8. Delayed and summed \hat{H} components for the same filters as in Figs. 6 and 7, and for all usable events. The delays from Fig. 2 are used for a number of trial conversion depths. At conversion depths near 400 and 640 km, the phases corresponding to the times around 45 and 68 s have their largest amplitudes (see *arrows*). These are the upper-mantle converted phases

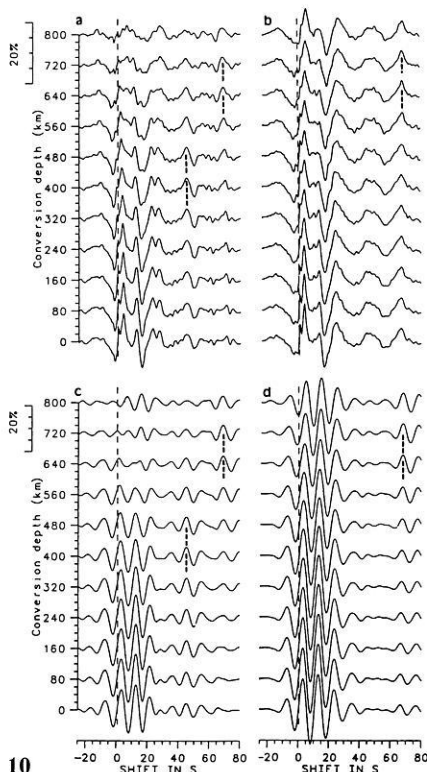
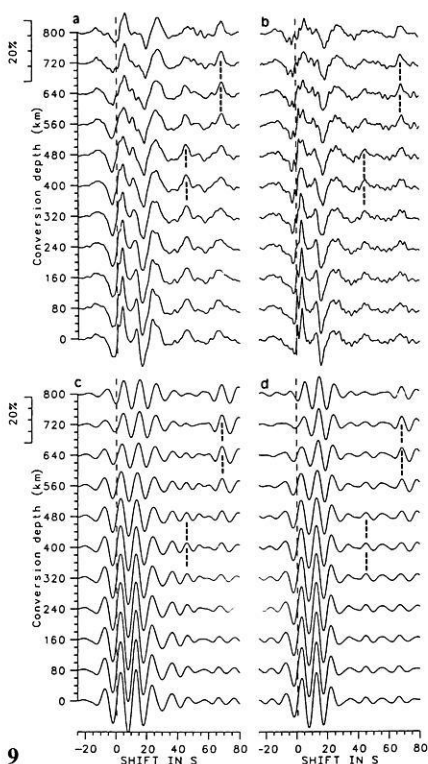


Fig. 9a–d. Delayed and summed \hat{H} components for two sub-groups of events [displacement (*a*, *b*), and 0.1-Hz bandpass filter (*c*, *d*)]. All distances are evenly distributed on both groups, the azimuth is disregarded. The marked converted phases do not vary significantly with the group

Fig. 10a–d. Delayed and summed \hat{H} components for two other sub-groups of events, same filters as in Fig. 9. The first group (*a* and *c*) contains all events between 75° and 345° azimuth. The second (*b* and *d*) contains the rest of the events. The conversion at the 400-km discontinuity (near 45 s) depends strongly on azimuth

subset of events. Since we have used summed records of the three-component stations of the GRF array, these data only provide information about the average structure of the area of the array. The same method applied to the individual stations of the array could possibly resolve differ-

ences in the crustal structure between the stations. Traces A–E in Fig. 11 are theoretical traces for different crustal models after the same data processing which was used for the observed data. All traces are on the same amplitude scale, so that the amplitudes can be compared directly. The

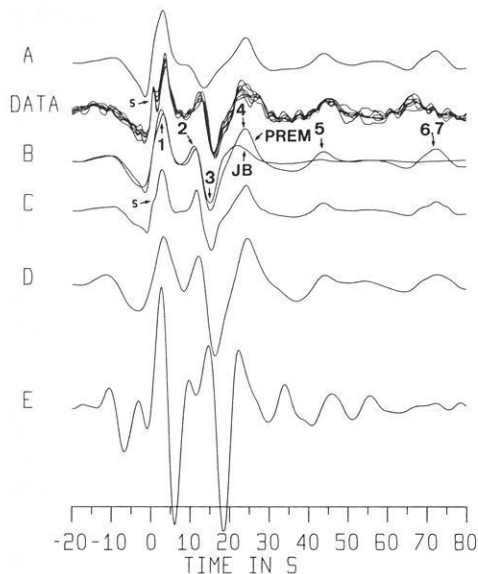


Fig. 11. Comparison of theoretical and observed \hat{H} functions. The displacement traces from Figs. 8–10 for zero delay are superimposed on each other in the DATA trace. The crustal models for the theoretical traces A, B, D and E are given in Table 2; the mantle model is PREM, except for the trace labelled JB. The rise time of the source function is 4.5 s, except for trace C, where it is 1.5 s; the crustal model for this trace is model B. The labelled phases are the same as in Figs. 3 and 4. Phase *s* is the conversion at the bottom of the sediments

Table 2. Crustal models used for the computation of theoretical seismograms in Fig. 11. Left column is depth in km, right column is *P* velocity in km/s. The *P*-to-*S* velocity ratio is 1.8 for models A and B, and 1.73 for models D and E

Model A		Model B		Model D		Model E	
0.0	5.00	0.0	5.00	0.00	2.00	0.0	3.00
0.2	5.00	0.2	5.00	0.83	5.60	4.0	3.00
0.2	2.50	0.2	2.50	2.50	5.80	4.0	6.00
0.8	2.50	0.8	2.50	4.58	5.95	30.0	6.00
0.8	5.80	0.8	5.80	4.58	5.70	30.0	8.11
30.0	8.11	30.0	7.90	12.50	5.70		
		30.0	8.11	15.00	6.30		
				20.00	6.40		
				24.20	6.90		
				30.00	7.20		
				30.00	8.11		

P velocities of the models used in Fig. 11 are given in Table 2. The assumed *P*-to-*S* velocity ratio is 1.8 for models A and B, and 1.73 for models D and E. The density derived from Birch's law was used. Note the thin low-velocity layers in models A and B underneath the high-velocity top layer, as mentioned before. The PREM upper-mantle model is used in most cases; only in traces B is the Jeffreys-Bullen model also used for comparison. The rise time used for all traces except C is 4.5 s. Trace C is computed for model B, but a rise time of 1.5 s is used. Trace C contains higher frequencies, which makes the conversion at the bottom of the sediments more easily visible. This theoretical conversion is still not strong enough compared with the observed one.

The data traces in Fig. 11 are in good agreement with each other up to about 20 s after zero time (which is the

P arrival time). After that, the scatter increases. The numbered phases 1–7 in trace B are the same phases as in Figs. 3 and 4. The phase labelled “*s*” is the conversion at the sediments. It seems astonishing that even this phase can be seen in the observed and theoretical (trace C), rather long-period data. It is clearly larger in the observed data than in the theoretical ones. But we are not trying to interpret this phase, since we are using summed data of three stations, and the sediments are different at each station. The signal forms and amplitudes of phases 1, 2 and 3 (the conversion at the Moho, the *PS* and *SS* multiples in the crust) in trace B are in very good agreement with the data. Models A and B are very similar. Their main difference is that the velocity jump at the Moho varies; and also the average gradient in the crust varies somewhat, but this is less important. Model A has no first-order discontinuity at the Moho at all, and model B has a *P*-velocity jump of 0.2 km/s there. The traces belonging to these models vary mainly in the amplitudes of phases 2 and 3. Although model A has no first-order discontinuity at the Moho, it is still able to produce relatively strong converted energy in the frequency range used.

Model D was obtained by Aichele (1976) from refraction studies near the GRF array. The general agreement of trace D with the data is fairly good, but multiples 2 and 3 are clearly too strong. The jump in *P* velocity of 0.9 km/s at the Moho is responsible for that.

A hypothetical model E, consisting of a homogeneous crust with a homogeneous sedimentary layer on top, is in complete disagreement with the data. Not only do the signal forms disagree but, also, the amplitudes of the converted crustal shear waves are much too large. Such types of models with strong discontinuities produce far too much converted and multiply reflected shear energy. The crustal reverberations of model E continue for a long time, which would make it impossible to observe conversions from upper-mantle discontinuities.

Phase 4 in the theoretical traces in Fig. 11 is the conversion at the 220-km discontinuity of the PREM model. For comparison, the Jeffreys-Bullen model has also been put underneath the crustal model of trace B. There is much energy in the data trace at this time, which is above the level predicted by the JB model. PREM is closer to the data than JB. We conclude from this that there possibly exists underneath the GRF array, at about 220 km depth, a discontinuity which, at a first approximation, is similar to that in PREM. A special effort is required in the future to add more details to the description of this discontinuity.

Phases 5 and 6 are the conversions at the 400- and 670-km discontinuities. Here and later we label the discontinuities as 400-km and 670-km discontinuities without implying that their real depths are 400 and 670 km. These phases are not very clear in Fig. 11 because the appropriate delays have not been used in this figure. This will be done next. The appropriate delays of the 200-km discontinuity have also not been used in Fig. 11, but this is less severe as Fig. 4 shows.

The upper-mantle discontinuities

Figure 12 shows the converted phases from both upper-mantle discontinuities. The 0.1-Hz filter is called LP in this figure, and the 0.2-Hz is called SP. The top traces are the displacement data. The SP data are computed for all usable

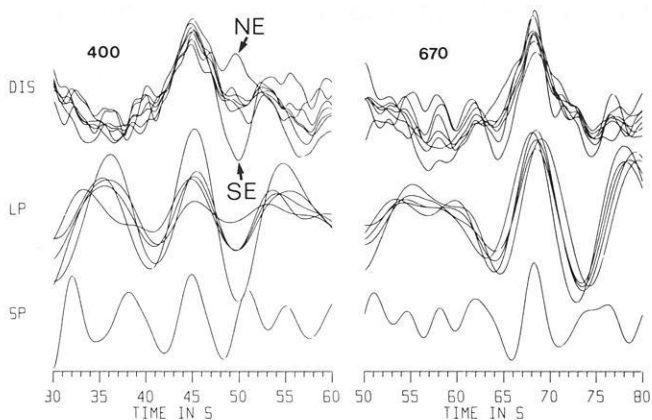


Fig. 12. Superposition of all mantle conversion data. Summation delays correspond to the 400- and 670-km conversion depths. *DIS*, *LP* and *SP* are displacement, 0.1- and 0.2-Hz filters. The records for different event azimuths (*NE*, *SE*) are strongly different at times around 49 s. All data are on the same amplitude scale

events, and the *LP* traces are computed for all events and the groups of events shown in Figs. 9 and 10. The displacement traces are shown for the same groups of events as the *LP* traces and, in addition, two groups are formed by dividing the events by magnitude (smaller and greater than 6.0). The largest difference between the traces is observed at about 49 s, when the data are divided according to the event azimuth. This could be due to a lateral heterogeneity of the 400-km transition in the vicinity of the array. The signal-to-noise ratio in the *SP* band is low for the 400-km conversion and fairly high for the 670-km phase.

In Fig. 13 we compare the signals from the Moho, the 400- and the 670-km discontinuities in the displacement records. The Moho data are plotted on a scale 3 times smaller than the upper-mantle data. Now we can compare directly the signal forms of the three different conversions. In Fig. 14, the converted phases from Fig. 13 are normalized to roughly the same maximum of the group containing all usable events. In addition, Fig. 14 shows the sum of the autocorrelation functions of the *P* wave of all events, normalized to the same maximum. Figures 13 and 14 demonstrate that the autocorrelation function of *P*, the conversion at the Moho and the 670-km conversion have a similar form (the conversion at the bottom of the sediments seen at the beginning of the Moho conversion must not be considered in this connection). The conversion at 400 km is about 1 s broader than the other signals. These observations imply that the sharpness of the 670-km discontinuity is comparable with that of the crust-mantle transition, while the 400-km discontinuity is less sharp than the other two. The reader should have in mind here that the crust-mantle transition includes not only the Moho boundary but the lower crust as well.

Since we want to compare theoretical and observed signal forms, the question of what rise times should be used for the computation of the theoretical seismograms is very important. For this purpose we matched theoretical and observed sums of autocorrelation functions of *P* waves. The theoretical data were summed up to 80° distance. If we use records from larger distances, then the broadening of the *P* signal at these distances contaminates the results. About two-thirds of our observed events are from distances shorter than 80°. As a test, we have summed only these

events and found good agreement with all other groups. The bottom traces in Fig. 15 shows the comparison of the autocorrelation functions of the theoretical and observed *P* signal. Good agreement is obtained with a rise time of 4.5 s. Now we can use this rise time for the theoretical seismograms and compare the theoretical conversions for the PREM model with the observed ones. We obtain from Fig. 15 the following clear results: the 400-km signal of PREM comes about 2 s earlier than the observed one at GRF; the 670-km signal of PREM is about 1 s later than the observed GRF signal. The amplitude of the 400-km signal of PREM is about 30% smaller than in the GRF data; the amplitude of the 670-km signal of PREM is in agreement with the GRF data. The PREM model clearly needs some adjustments to fit the GRF data.

In Fig. 16 we compare the observed upper-mantle signals with theoretical data for modifications of PREM. In the modification M of PREM, the 400-km discontinuity is moved to 417 km depth and the *P*- and *S*-velocity and density contrasts have been increased by 50%. The 670-km discontinuity is moved to 660 km depth, without any other change. The theoretical data for M agree reasonably well with our observations. In the modification MG of M, the first-order discontinuities of M are replaced by 20-km-thick gradient zones. As expected, the amplitudes of the conversions are reduced, but the signal is not broadened much. An increase in the contrast could again fit the amplitudes.

It should be noted that lateral velocity variations in the lithosphere-asthenosphere system are quite sufficient to account for the 2-s delay of the 400-km phase in the GRF data with respect to PREM. For this reason, the 417-km depth of this discontinuity in the M and MG models must be regarded as an arbitrary value. Similarly, velocity variations in the lithosphere and asthenosphere will affect the time of the 670-km phase. On the other hand, the lateral velocity variations in the 400–700 km depth range are less significant, which makes the value of the depth interval between the two discontinuities in M and MG (243 km) fairly reliable. This value is about 30 km less than in PREM.

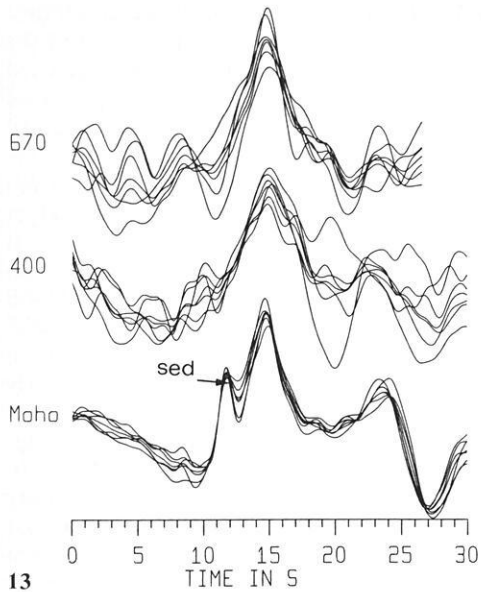
Conclusions

The data-processing method used has facilitated the detection of weak phases in noisy data. Relatively clear *P*-to-*S* converted phases with amplitudes less than 4% of the *P*-wave amplitude have been extracted from the coda of *P* phases. These observations throw new light on the fine *S*-velocity structure of the mantle discontinuities.

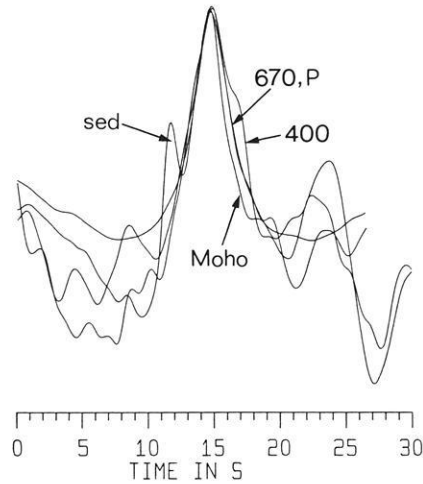
The same method has been applied by Vinnik et al. (1983) to the records of a few other stations. The observed times of the conversions from their paper and from the present study are (in seconds):

Station	$t_{Ps}(400)$	$t_{Ps}(670)$	$t_{Ps}(670)-t_{Ps}(400)$
TUC	47.5	70.1	22.6
GOL	46.3	69.8	23.5
NORSAR	44.5	68.0	23.5
Obninsk	43.2	66.7	23.5
GRF	45.0	68.2	23.2
PREM			26.0

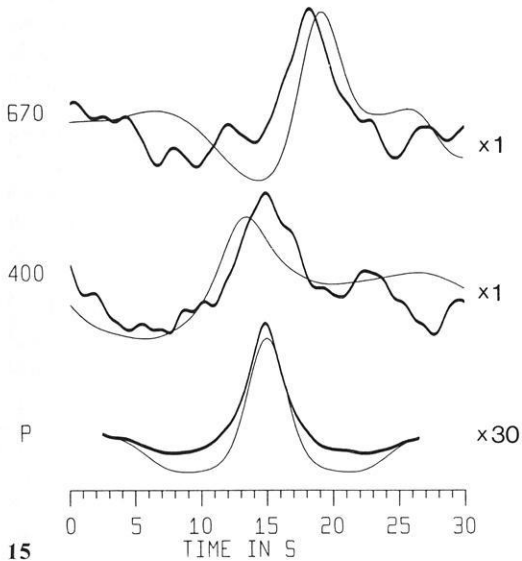
These values are valid for a reference slowness of 6.4 s/degree (or 67° distance). The difference between the times



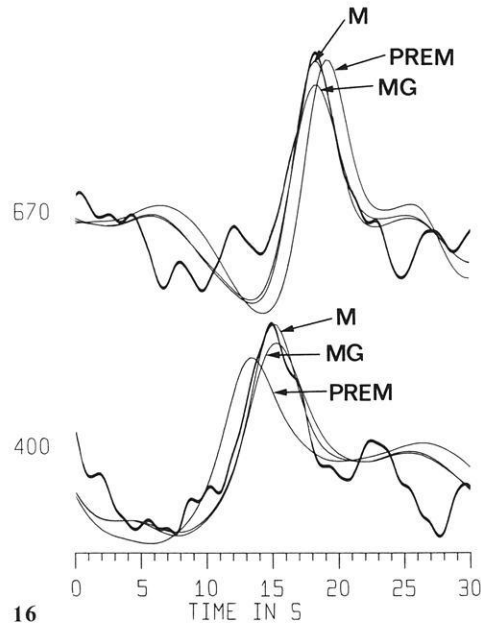
13



14



15



16

Fig. 13. Wave-form comparison of the conversions at the Moho and the upper-mantle discontinuities (displacement). The Moho conversion was reduced by a factor of 3. The conversion at the sediments is marked "sed"

Fig. 14. Wave-form comparison of the same conversions as in Fig. 13. Only the summation of all usable events is used. The amplitudes are normalized to the same maximum. The autocorrelation function of the *P* wave, summed over all events, is shown in addition. Figure 12 and this figure indicate that all wave forms are fairly similar, except the conversion at 400 km depth. This signal is about 1 s broader than the others

Fig. 15. Comparison of wave forms of the observed (*heavy lines*) and computed (*light lines*) upper-mantle conversions and the autocorrelation function of the *P* signal for the PREM model. A rise time of 4.5 s is used for the theoretical seismograms, which fits the observed autocorrelation of the *P* signal best. The amplitudes of the *P* traces have been reduced by a factor of 30

Fig. 16. Fit of observed and computed mantle conversions (displacement). Model *M* is a modification of PREM, where the 400-km discontinuity is moved to 417 km and its contrast is increased by 50%; the 670-km discontinuity is moved to 660 km. In model *MG*, the first-order discontinuities of *M* are replaced by 20-km-thick gradient zones. All traces are on the same amplitude scale

of the two recorded phases is remarkably stable: the average of the data for TUC, GOL, NORSAR and Obninsk is equal to the result for GRF. This difference is 2.8 s less than for PREM. It follows that the depth interval between the two discontinuities in PREM is biased by about 30 km. According to Vinnik et al. (1983) the error is, most likely, in the depth of the 670-km discontinuity.

Our data can also provide important constraints on the fine velocity structure of the 670-km transition. The amplitudes of the 670-km phase are different in different frequency bands (see Fig. 12). This would be impossible if the 670-km transition were a first-order discontinuity. Also, a complex structure is found near 400 km depth. The spectral content of the 400-km phase is clearly different in the

groups of events which are assembled according to their azimuth (Fig. 12). An accurate description of the corresponding fine structure of both discontinuities is difficult; therefore, we postpone attempts to do this until additional data have been accumulated. Processing of single-station records of the array seems to be especially promising in this respect.

In general, the method has proved to be very useful for detailed mapping of the fine structure of the upper mantle. High-quality data (especially broadband data) are necessary for its application. It is also extremely sensitive to crustal structure. Therefore, the method can be recommended for future applications in this broad field of research.

Finally we suggest that the method could also be applied to other weak phases, e.g. to *PcP* and to forerunners of *S* or *PP*.

Acknowledgements. This research has been made possible by the agreement between the Academy of Sciences of the USSR and the Deutsche Forschungsgemeinschaft. We wish to thank Winfried Hanka for help in the computations, and Gerhard Müller and Jörg Schlittenhardt for reading the manuscript.

References

Aichele, H.: Interpretation refraktionsseismischer Messungen im Gebiet des Fränkisch-Schwäbischen Jura. Dissertation, Universität Stuttgart, 1976

- Dziewonski, A.M., Anderson, D.L.: Preliminary reference Earth model. *Phys. Earth Planet. Inter.* **25**, 297–356, 1981
- Faber, S., Müller, G.: Converted phases from the mantle transition zone observed at European stations. *J. Geophys.* **54**, 183–194, 1984
- Jeanloz, R., Thompson, A.B.: Phase transitions and mantle discontinuities. *Rev. Geophys. Space Phys.* **21**, 51–74, 1983
- Kind, R.: The reflectivity method for different source and receiver structures and comparison with GRF data. *J. Geophys.* **58**, 146–152, 1985
- Liu Qiyuan, Kind, R.: Lateral variations of the structure of the crust-mantle boundary from conversions of teleseismic P waves. *J. Geophys.* **60**, 149–156, 1986
- Owens, T.J., Taylor, S.R., Zandt, G.: Crustal structure at regional seismic test network stations determined from inversion of broadband teleseismic P waveforms. *Bull. Seismol. Soc. Am.* **77**, 631–662, 1987
- Paulssen, H.: Upper mantle converted waves beneath the NARS array. *Geophys. Res. Lett.* **12**, 709–712, 1985
- Schlittenhardt, J.: Investigation of the velocity and Q structure of the lowermost mantle using PcP/P amplitude ratios at distances of 70°–84°. *J. Geophys.* **60**, 1–18, 1986
- Vinnik, L.P.: Detection of waves converted from P to SV in the mantle. *Phys. Earth Planet. Inter.* **15**, 39–45, 1977
- Vinnik, L.P., Avetisjan, R.A., Mikhailova, N.G.: Heterogeneities in the mantle transition zone from observations of P-to-SV converted waves. *Phys. Earth Planet. Inter.* **33**, 149–163, 1983

Received July 30, 1987; revised version October 2, 1987

Accepted October 2, 1987

The relation between Born inversion and standard migration schemes

F. Wenzel

Geophysikalisches Institut, Universität Karlsruhe, Hertzstrasse 16, D-7500 Karlsruhe 21, Federal Republic of Germany

Abstract. Born inversion represents a novel approach in reflection seismic data processing. Omission of multiple scattering effects and relying on a known reference velocity allows for true amplitude mapping of subsurface structures. Born inversion is closely related to classical migration concepts in terms of its provisions as well as its results. Consequent application of high-frequency approximations, generally accepted in reflection seismology, leads to simple relations between Born inversion, frequency-wavenumber migration and migration based on a Kirchhoff summation technique. The formulas are derived for the simple case of 3-D zero-offset geometry with a constant reference velocity. Modifications of Born inversion theory are presented if the particle velocity is measured instead of the pressure and if the influence of the free surface is incorporated.

Key words: Reflection seismology – Migration – Born inversion

Introduction

The seismic experiment aims at the extraction of information concerning a certain volume of space from measurements of physical quantities like pressure, particle displacement or velocity on parts of a boundary enclosing the volume. Refraction seismology derives velocity functions averaged over several wavelengths in space; the targets of reflection experiments are structural features of the subsurface. Actually, both notions, smoothed velocities and structural information, in general, refer to the same physical parameter – compressional velocity – but mean different spectral components. Velocity functions inverted from refraction data represent the low-wavenumber portion of the true velocity distribution, whereas reflection data allow for the inversion of the reflective properties of the structure caused by the high-wavenumber part of the true velocity function, see Claerbout (1985, pp. 46).

An intermediate result of reflection seismic data processing is the common-midpoint stacked section, that can be considered as an approximation of a zero-offset section defined by coincident source-receiver geometry. These sections represent seismic images of the earth, of the position and the strength of subsurface reflectors. It is, however, a distorted image. Dipping reflectors, for instance, appear at positions shifted away from the true ones. In addition, hyperbolically arranged diffraction onsets mark their end points.

The reconstruction of the true image of the subsurface structure is the ultimate goal of seismic migration. Originally the efforts concentrated on the reconstruction of geometric features, e.g. location and extend of reflectors, and thus required only geometric methods (Haagedorn, 1954). During the last 15 years migration was based on the acoustic wave equation and various approaches of its solution like ray theory, finite-difference methods, the Kirchhoff approach, and operations in the frequency-wavenumber domain. In general, a wave field recorded at the surface is downward continued and then subjected to an imaging condition. An overview on migration methods can be found in Robinson (1983) and Claerbout (1985).

Standard migration procedures model a zero-offset section with reflectors exploding simultaneously at a certain time, say $t=0$, and waves travelling upward in a medium with half the true velocity. The migration process downward continues the wave field and defines the (band-limited) reflectivity as its value at the imaging time $t=0$.

If one accepts the acoustic wave equation as appropriate for the description of reflection seismological phenomena, its exploitation in migration or inversion procedures could possibly lead to the reconstruction, not only of the proper position of reflectors but also to amplitudes that measure and express the reflection strength adequately and thus deliver an additional parameter for the interpretation. Any method aiming at this goal is called true amplitude migration. Born inversion, introduced, worked out and refined in recent years, belongs to this category. Its development is associated with the names of Bleistein, Cohen, Hagin and other workers, e.g. see Bleistein and Cohen (1982) or Cohen et al. (1986).

As Born inversion represents a rather new approach to the inverse problem of reflection seismology, one would like to know its similarities with and differences to standard migration procedures in terms of the basic physical and mathematical models used, and in terms of assumptions and approximations employed. This paper attempts to address this question and, besides the contribution of Bleistein and co-authors, uses the results of Cheng and Coen (1984) who also discuss the relationship between Born inversion and migration of common-midpoint stacked data.

In order to keep the analysis as simple as possible the following considerations are restricted to a constant reference velocity and to zero-offset geometry. An inversion aims at the true-amplitude recovery of the reflectivity of the earth. Therefore the basis of the inversion, the forward model,

e.g. the wave equation and Born's approximation, must be critically discussed in as far as it properly describes the physics of the seismic experiment. Another question refers to the measured quantity used for inversion, e.g. pressure or particle velocity, and the quantity desired as output, e.g. velocity perturbation or reflectivity. For an inversion it can be demonstrated that two essentially equivalent approaches, in spatial and in Fourier domain, are conceivable.

The basic equation

This section presents a detailed derivation of Born inversion for a case that reveals the main features of the theory but is simple enough to avoid cumbersome mathematics. The basic equation involved is the Helmholtz equation in three-dimensional (3-D) space.

$$\left[\nabla^2 + \frac{\omega^2}{v^2(\mathbf{x})} \right] p(\mathbf{x}, \mathbf{x}_s, \omega) = -\delta(\mathbf{x} - \mathbf{x}_s)$$

$$\mathbf{x}_s = (x_s, y_s, 0)^T, \quad \mathbf{x} = (x, y, z)^T. \quad (1)$$

It describes the behaviour of the pressure in a liquid medium with no or negligible density variations. In order to utilize Eq. (1) for reflection seismology the medium is assumed to consist of an upper halfspace with constant velocity continuously connected with a lower halfspace containing an arbitrary velocity distribution. The inhomogeneous part of the Helmholtz equation (1) represents a point source in the observational plane defined by $z=0$ with a spike-like, broadband source signal. The source radiates the pressure in all directions. Whereas no reflection can be expected from the upper halfspace, the variable velocity structure of the lower halfspace reflects a certain amount of energy that can be recorded in the observational plane.

The Helmholtz equation (1) and the concept of velocity structure do not ideally model the conditions of the reflection seismic experiment. Clearly the elastic equations should be employed instead of the acoustic equation. The upper halfspace should be simulated with a zero velocity, introducing free surface effects. The band limitation of the seismic source requests an additional frequency function in the inhomogeneous part of Eq. (1). Despite these shortcomings the Helmholtz equation (1) is generally considered as an appropriate mathematical tool in reflection seismology mainly because steep angle propagation and steep angle reflections prevent any relevant conversion of the source-generated compressional waves to shear waves; the medium behaves as if it were liquid. Consequently, the Helmholtz or the wave equation became the basis for most modern migration schemes. Nevertheless, the deficiencies of the equation as a model for reflection seismic experiments should be kept in mind, in particular whenever true amplitudes are concerned.

Delineation of 3-D structural features of the subsurface requires a 3-D seismic survey with sources and receivers distributed in the whole observational plane $z=0$. The seismograms used as input data for the Born inversion procedure discussed in this paper are zero-offset traces. In theory these seismograms could be recorded with coincident source-receiver geometry. In practice, such a measurement is of little use because shot-generated noise completely overrides the signals reflected from the subsurface. However, common-midpoint stacked data can be viewed as an approximation

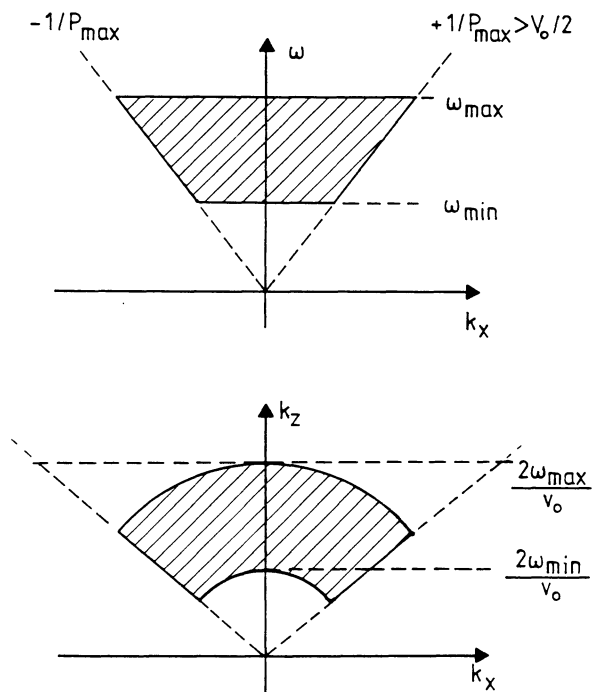


Fig. 1. Sketch of temporal and spatial band limitation for reflection data of a zero-offset section with reference velocity v_0 . The upper part shows that available information is restricted to a frequency band (ω_{\min} , ω_{\max}) and a ray parameter window ($\pm p_{\max}$). Lower part indicates the resulting map to the (k_x, k_z) plane utilizing the dispersion relation

of a zero-offset seismogram containing only the reflective response of the medium.

The ultimate goal of an inversion procedure based on Eq. (1) for seismic data is the derivation of the spatial velocity distribution. Born inversion does not fully accomplish this task. The velocity field is composed of a smooth, long-wavelength, low-wavenumber part and another one with short-wavelength oscillations. The low-wavenumber part, commonly referred to as the reference velocity, controls travel times and must be known as input for the inversion. Large-wavenumber constituents of the velocity field are responsible for the reflectivity of the medium. Only these components of the velocity field form the target of Born inversion. The following derivation assumes a constant reference velocity in order to keep the analysis as simple as possible. A treatment of arbitrary reference velocities can be found in Cohen et al. (1986).

The Helmholtz equation (1) is written for a source without any band limitation. In reality, however, field data as well as stacked sections are band-limited in frequency and wavenumber or ray-parameter content. Physical limitations of the source, the propagation properties of the medium and the receivers reduce the frequency content of seismic data to typically 10–100 Hz. In zero-offset sections the maximum ray parameter observable is $2/v_0$, twice the inverse of the reference velocity. Again the theoretical value often exceeds the true maximum encountered. One reason is the wavenumber (ray parameter) filtering property of arrays of sources and receivers commonly used as field techniques. In addition, zero-offset rays are often close to vertical.

The data consisting of a seismic trace for each receiver position (x_g, y_g) at the surface form a 3-D space in the obser-

vational variables (x_g, y_g, t) . The limited information attainable with reflection seismic measurements can be demonstrated in the corresponding Fourier space (k_x, k_y, ω) , where the data are confined to a slice of a cone defined by the frequency band and the maximum ray parameter. Figure 1 (upper panel) shows a cut through the cone in the $k_y=0$ plane. The data are used for the derivation of 3-D structural information, e.g. the velocity perturbation $a(x, y, z)$ or the reflectivity $c(x, y, z)$. The mapping function that defines the corresponding domain in Fourier space (k_x, k_y, k_z) that can be reconstructed from the data is the dispersion relation:

$$k_z^2 = \frac{4\omega^2}{v_0^2} - k_x^2 - k_y^2.$$

The lower panel of Fig. 1 shows this domain as a 2-D sketch. The 3-D situation is achieved by rotation around the k_z axis. Most calculations that follow in this paper are based on Eq. (1) and thus ignore the band-limited character of the data. This is acceptable because the relation between structural parameters and data is linear and the derivation would thus not be different. All one has to keep in mind is that the final integral operations are applied to band-limited functions.

Born approximation

An appropriate formulation of the forward problem serves as a starting point for the inversion. In the time domain in the acoustic wave equation governs the propagation of pressure fluctuations (p), excited by a broad-band source, located in the observational plane defined by $z=0$ at $(x_s, y_s, 0)$, in a liquid medium with constant density and arbitrary spatial velocity distribution. In the frequency domain the Helmholtz equation (1) replaces the acoustic wave equation; its unique solution is guaranteed by Sommerfeld's radiation conditions. The z -axis points downward, into the earth. A constant velocity characterizes the upper halfspace (negative z -axis). The velocity field in the lower halfspace is partitioned into a reference value \bar{v} and a dimensionless perturbation of v so that

$$\frac{1}{v^2(\mathbf{x})} = \frac{1}{\bar{v}^2(\mathbf{x})} [1 + a(\mathbf{x})]. \quad (2)$$

A corresponding decomposition of the pressure into

$$p = p_I + p_s$$

defines a pressure p_I whose propagation is controlled by \bar{v} :

$$\left[\nabla^2 + \frac{\omega^2}{\bar{v}^2(\mathbf{x})} \right] p_I(\mathbf{x}, \mathbf{x}_s, \omega) = -\delta(\mathbf{x} - \mathbf{x}_s). \quad (3)$$

The solution of this equation yields Green's function $g(\mathbf{x}, \mathbf{x}_s, \omega)$ for the reference velocity field.

If Eq. (2) and (3) are inserted into Eq. (1), an inhomogeneous Helmholtz equation results:

$$\begin{aligned} & \left[\nabla^2 + \frac{\omega^2}{\bar{v}^2(\mathbf{x})} \right] p_s(\mathbf{x}, \mathbf{x}_s, \omega) \\ &= -\frac{\omega^2}{\bar{v}^2(\mathbf{x})} a(\mathbf{x}) [p_I(\mathbf{x}, \mathbf{x}_s, \omega) + p_s(\mathbf{x}, \mathbf{x}_s, \omega)]. \end{aligned} \quad (4)$$

As the right-hand side acts as source term, Green's function allows for the integral representation of the solution as a spatial convolution of the inhomogeneous term and Green's function

$$\begin{aligned} & p_s(\mathbf{x}_g, \mathbf{x}_s, \omega) \\ &= \omega^2 \int \frac{a(\mathbf{x})}{\bar{v}^2(\mathbf{x})} [p_I(\mathbf{x}, \mathbf{x}_s, \omega) + p_s(\mathbf{x}, \mathbf{x}_s, \omega)] g(\mathbf{x}_g, \mathbf{x}, \omega) d^3 \mathbf{x} \end{aligned} \quad (5)$$

with the geophone location

$$\mathbf{x}_g = (x_g, y_g, z_g)^T.$$

Note that no approximations have been used so far.

Equations (3) and (5) represent just another view of the Helmholtz equation (1). The solution for the total pressure is approached by first finding Green's function for the reference velocity field, and then solving an integral equation that connects the residual pressure p_s with the previously evaluated Green's function and the scattering potential

$$\omega^2 \frac{a(\mathbf{x})}{\bar{v}^2(\mathbf{x})}.$$

As it stands the reformulation of the original Helmholtz equation is of little use because neither does it lend itself to exact solution techniques of the forward problem nor does it prove useful for an inversion. It serves, however, as the basis for the introduction of physical assumptions that allow for the Born approximation. Suppose that the reference velocity \bar{v} is known a priori, e.g. from refraction surveys or NMO analysis, then the scattering potential or the velocity perturbation remains the target of inversion. The solution of Eq. (3) is Green's function which incorporates all kinds of multiples, upward and downward travelling waves if \bar{v} varies in space. For Born's approximation, a solution containing only downward-propagating waves is sufficient. Such a solution results, for example, from splitting the wave equation into portions that yield separated upward- and downward-directed waves or from high-frequency approximations like asymptotic ray theory. Then p_I can be viewed as the wavefield generated by a source, travelling directly to the velocity perturbation, interacting with it and thus generating the scattered field p_s . Weak scattering can be defined by

$$|p_s| \ll |p_I|$$

which allows us to neglect p_s in the integrand of Eq. (5). This assumption is called Born's (first) approximation. Taking into account the particular geometry used in reflection seismology, and the circumstance that scattering comes exclusively from the lower halfspace, leads to

$$\begin{aligned} & p_s(\mathbf{x}_g, \mathbf{x}_s, \omega) \\ &= \omega^2 \int \frac{a(\mathbf{x})}{\bar{v}^2(\mathbf{x})} g(\mathbf{x}, \mathbf{x}_s, \omega) g(\mathbf{x}_g, \mathbf{x}, \omega) d^3 \mathbf{x} \end{aligned} \quad (6)$$

where, in addition, symbol p_I is replaced by Green's function, the solution of Eq. (3). Equation (6) relates the pressure measured in the observational plane $z=0$, through a linear Fredholm integral equation, to the unknown velocity perturbation $a(x, y, z)$. As the incident wavefield remains unaffected by the velocity perturbation, transmission losses or refractive effects caused by $a(x, y, z)$ are not considered.

Omitting the scattered wavefield in the integral in Eq. (5) implies that only the incident waves interact with the velocity perturbation, never the scattered waves. Consequently, multiple effects are not incorporated and again transmission and refraction phenomena of the upward-propagating scattered wave caused by $a(x, y, z)$ are neglected. The rather general Eq. (6) and its utilization for the inverse theory can be found in Cohen et al. (1986). In this paper the simple case of a constant reference velocity v_0 ,

$$\frac{1}{v^2(\mathbf{x})} = \begin{cases} \frac{1}{v_0^2} & z \leq 0 \\ \frac{1}{v_0^2} [1 + a(\mathbf{x})] & z > 0, \end{cases}$$

is considered. With Green's function for this particular case

$$g(\mathbf{x}, \boldsymbol{\xi}, \omega) = \frac{e^{j \frac{\omega}{v_0} |\mathbf{x} - \boldsymbol{\xi}|}}{4\pi |\mathbf{x} - \boldsymbol{\xi}|}$$

and coincident source and receiver coordinates, Eq. (6) becomes

$$p_s(\mathbf{x}_g, \omega) = \left(\frac{\omega}{4\pi v_0} \right)^2 \int a(\mathbf{x}) \frac{1}{r^2} e^{j \frac{2\omega}{v_0} r} d^3 \mathbf{x} \quad (7)$$

with

$$r = [(x - x_g)^2 + (y - y_g)^2 + z^2]^{\frac{1}{2}}.$$

With a guess of the reference velocity v_0 and broad-band observations in the plane $z=0$, one aims at the inversion of the linear integral equation (7) to derive the velocity perturbation. Two points should be mentioned before the inversion itself is tackled. Firstly, p standing for pressure in (7) specifies the measured quantity only in marine experiments and not in land-based reflection seismology where the vertical particle velocity replaces p . Secondly, the velocity perturbation does not represent an appropriate quantity measurable with and invertible from reflection data. These items will be discussed in detail later.

The inversion

An inversion of Eq. (7) can pursue two approaches. The first method utilizes spatial Fourier transforms and tries to find a simple, readily invertible relation between data and velocity perturbation in Fourier space. The second approach designs an approximate inverse operator without transforming the data.

Transform method

An attempt to Fourier transform Eq. (7) with respect to x_g any y_g encounters the problem that an analytic expression for the transform of

$$\frac{1}{r^2} e^{j \frac{2\omega}{v_0} r}$$

is not available. If Eq. (7) could be manipulated in a way that only the inverse of r instead of the inverse square of r appears, then Weyl's integral for the plane-wave decompo-

sition of a point source allows the evaluation of the correct Fourier transform:

$$\frac{e^{j \frac{2\omega}{v_0} r}}{4\pi r} = \frac{1}{8\pi^2} \int_{-\infty}^{+\infty} \frac{j}{v} e^{j[k_x(x-x_g) + k_y(y-y_g) + v|z|]} dk_x dk_y, \quad (8)$$

$$v = \begin{cases} \text{sgn}(\omega) \left(\frac{4\omega^2}{v_0^2} - k_x^2 - k_y^2 \right)^{\frac{1}{2}}, & \frac{4\omega^2}{v_0^2} \geq k_x^2 + k_y^2 \\ j \left(k_x^2 + k_y^2 - \frac{4\omega^2}{v_0^2} \right)^{\frac{1}{2}}, & \frac{4\omega^2}{v_0^2} < k_x^2 + k_y^2. \end{cases}$$

The introduction of modified data

$$q_s = -j \frac{\partial}{\partial \omega} \left(\frac{1}{\omega^2} p_s \right) \quad (9)$$

leads to the desired modification of Eq. (7)

$$q_s(\mathbf{x}_g, \omega) = \frac{1}{2\pi v_0^3} \int a(\mathbf{x}) \frac{e^{j \frac{2\omega}{v_0} r}}{4\pi r} d^3 \mathbf{x}. \quad (10)$$

The right-hand side of Eq. (10) represents an integral over the product of velocity perturbation and Green's function for a homogeneous space with velocity $v_0/2$. Therefore, the modified data must be a solution of

$$\left(\nabla^2 + \frac{4\omega^2}{v_0^2} \right) q_s(\mathbf{x}, \omega) = -\frac{a(\mathbf{x})}{2\pi v_0^3} \quad (11)$$

in a plane specified by $z=0$. This equation describes the propagation of a quantity q_s in a space with velocity $v_0/2$, whose sources explode at $t=0$. Its strength and spatial distribution is determined by $a(x, y, z)$. In other words, Eq. (11) represents the mathematical formulation of the exploding reflector model of Loewenthal et al. (1976), the well-known basis for migration of zero-offset sections. Born theory quantifies the exploding reflector model. It reveals the physical meaning of the source strength and the propagating and measured quantity. Whereas the standard view of the exploding reflector model assumes that the source strength is defined by the reflectivity and that the propagating quantity represents the pressure, Born theory tells us, rather, that this model relates velocity perturbation with modified data.

A Fourier transformation of both sides of Eq. (10), utilizing Eq. (8), results in

$$Q_s(k_x, k_y, \omega) = \frac{j}{4\pi v_0^3 v} A(k_x, k_y, -v) \quad (12)$$

where $Q_s(k_x, k_y, \omega)$ is the 2-D Fourier transform of $q_s(x_g, y_g, \omega)$ and

$$A(\mathbf{k}) = \int a(\mathbf{x}) e^{-j\mathbf{k}\cdot\mathbf{x}} d^3 \mathbf{x}, \quad \mathbf{k} = (k_x, k_y, k_z)^T. \quad (13)$$

The simple relation between Q_s and A in Fourier space can be considered as solution of the inverse problem

$$A(k_x, k_y, -v) = -4\pi j v_0^3 v \cdot Q_s(k_x, k_y, \omega). \quad (14)$$

In order to express the solution in spatial coordinates $a(x, y, z)$, an inverse Fourier transform must be performed. The inverse of Eq. (13) is

$$a(\mathbf{x}) = \frac{1}{(2\pi)^3} \int A(\mathbf{k}) e^{j\mathbf{k}\cdot\mathbf{x}} d^3\mathbf{k}. \quad (15)$$

As Eq. (14) expresses A in the variables $(k_x, k_y, -v)$ rather than (k_x, k_y, k_z) , the variables of integration in Eq. (15) must be changed according to

$$\begin{aligned} k_x &= k_x \\ k_y &= k_y \\ k_z &= -\text{sgn}(\omega) \left(\frac{4\omega^2}{v_0^2} - k_x^2 - k_y^2 \right)^{\frac{1}{2}}. \end{aligned} \quad (16)$$

The definition of the vertical component of the wave vector in Eq. (8) suggests that A can be determined for real and complex values. For the inversion, however, the real k_z values are sufficient. The mapping is one-to-one, the full 3-D space in (k_x, k_y, k_z) is projected into a double cone in (k_x, k_y, ω) . With the functional determinant

$$\frac{-4\omega}{v_0^2 v}$$

Eq. (15) can be written as

$$a(\mathbf{x}) = \frac{1}{2\pi^3 v_0^2} \iiint \frac{\omega}{v} A(k_x, k_y, -v) \cdot e^{-jvz} e^{j(k_x x + k_y y)} dk_x dk_y d\omega, \quad (17)$$

where the expression for A as a function of k_x, k_y and $-v$ can be replaced by Q_s using Eq. (14):

$$a(\mathbf{x}) = \frac{2v_0}{j\pi^2} \iiint \omega Q_s(k_x, k_y, \omega) \cdot e^{-jvz} e^{j(k_x x + k_y y)} dk_x dk_y d\omega. \quad (18)$$

This equation solves the inverse problem. It relates the velocity perturbation $a(x, y, z)$ to the modified data q_s with a formula strongly reminiscent of results from standard frequency-wavenumber migration, e.g. see Stolt (1978), Gazdag (1978) or Castle (1982). The physical view of migration is, however, quite different because there a wavefield propagating in a medium with velocity $v_0/2$ and recorded at $z=0$ is downward continued and then subjected to an imaging process.

Equation (18) solves the inverse problem correctly without assumptions beyond those inherent in Born's approximation. A simplification of Eq. (18) reintroducing the pressure is feasible if only high frequencies are involved. Again, two conceivable approaches can be pursued. The first one starts with Eq. (18) and relies on partial integration; the second one completely omits the modified data. It relinquishes a correct Fourier transform of Eq. (7) and uses a stationary-phase approximation instead.

Application of the rule of partial integration to the ω -integral in Eq. (18) results in

$$\begin{aligned} & \int_{-\omega_1}^{\omega_1} \omega Q_s e^{-jvz} d\omega \\ &= -j \left[\frac{P_s}{\omega} e^{-jvz} \right]_{-\omega_1}^{\omega_1} + j \int_{-\omega_1}^{\omega_1} \frac{P_s}{\omega^2} \left(1 - \frac{4jz\omega^2}{v_0^2 v} \right) e^{-jvz} d\omega. \end{aligned}$$

ω_1 indicates the maximum frequency for a particular wavenumber k . As the data will always be band-limited below

this value, the first term vanishes. In the expression appearing in the integral on the right-hand side the first term can be neglected if

$$\frac{z}{\lambda} \gg 1,$$

where λ is the maximum wavelength and in real data the dominant wavelength. Therefore, the inversion formula (18) can be written as

$$a(\mathbf{x}) = \frac{8z}{\pi^2 v_0} \iiint \frac{1}{jv} P_s(k_x, k_y, \omega) \cdot e^{-jvz} e^{j(k_x x + k_y y)} dk_x dk_y d\omega \quad (19)$$

an expression valid for depths exceeding a few wavelengths, e.g. a few hundred metres at most.

The same result arises if a high-frequency approximation is utilized in the Fourier transform of Eq. (7). As an exact transform is unknown, an approximate transform can be derived with the method of stationary phase. This method is commonly applied to integrals over one variable, e.g. see Bath (1968, p. 44) but can be extended to two (Papoulis, 1968, p. 241) or more dimensions (Bleistein, 1984, p. 283). Application of the technique in two variables results in

$$P_s(k_x, k_y, \omega) = \frac{j\omega}{16\pi v_0} \bar{A}(k_x, k_y, -v),$$

where \bar{A} is the 3-D Fourier transform of

$$\bar{a}(\mathbf{x}) = \frac{a(\mathbf{x})}{z}.$$

The reconstruction of $\bar{a}(x, y, z)$ from $\bar{A}(k_x, k_y, -v)$ follows the procedure outlined with Eq. (15)–(18) and leads directly to Eq. (19). The latter relation clarifies the connection between $f-k$ migration and Born inversion. The velocity perturbation can be recovered from the pressure by standard $f-k$ migration of the weighted pressure

$$\frac{1}{jv} P_s(k_x, k_y, \omega)$$

and subsequent multiplication of the result with z . It should be mentioned that a multiplication of the section with z after migration is not identical with a multiplication of the data with time before migration.

If one prefers a Kirchhoff summation technique as the numerical scheme for the inversion, the pressure in Eq. (19) must be written as the Fourier transform of x_g and y_g . If the order of integration is interchanged, Eq. (19) becomes

$$a(\mathbf{x}) = \frac{16z}{\pi v_0} \iint p_s(\mathbf{x}_g, \omega) \cdot \left\{ \frac{1}{2\pi} \iint \frac{e^{j[k_x(x-x_g) + k_y(y-y_g) - vz]}}{jv} dk_x dk_y \right\} d^2\mathbf{x}_g d\omega.$$

The expression in brackets gives exactly

$$\frac{1}{r} e^{-j\frac{2\omega}{v_0}r}$$

a result readily established if $-\omega$ is inserted in Eq. (8). Therefore,

$$a(\mathbf{x}) = \frac{16}{\pi v_0} \iint \frac{z}{r} p_s(\mathbf{x}_g, \omega) e^{-j \frac{2\omega}{v_0} r} d^2 \mathbf{x}_g d\omega \quad (20)$$

or, after a transform to the time domain,

$$a(\mathbf{x}) = \frac{16}{\pi v_0} \int \frac{z}{r} \tilde{p}_s\left(\mathbf{x}_g, t = \frac{2}{v_0} r\right) d^2 \mathbf{x}_g. \quad (21)$$

These Kirchhoff formulas state that the velocity perturbation $a(x, y, z)$ can be recovered by summing the weighted pressure along hyperboloids defined by

$$t = \frac{2}{v_0} [(x - x_g)^2 + (y - y_g)^2 + z^2]^{\frac{1}{2}}.$$

Inversion in space

This method tries to design a procedure for directly inverting Eq. (17) in the space domain. It was established by Beylkin (1985) and applied by Cohen et al. (1986) to 3-D Born inversion with arbitrary reference velocity. Equation (7) contains an integral over the velocity perturbation, an amplitude factor B and a phase factor $\omega \cdot \Phi$:

$$p_s(\mathbf{x}_g, \omega) = \left(\frac{\omega}{4\pi v_0}\right)^2 \int a(\mathbf{x}) B(\mathbf{x}, \mathbf{x}_g) e^{j\omega \Phi(\mathbf{x}, \mathbf{x}_g)} d^3 \mathbf{x}, \quad (22)$$

$$B(\mathbf{x}, \mathbf{x}_g) = \frac{1}{r^2}, \quad \Phi(\mathbf{x}, \mathbf{x}_g) = \frac{2}{v_0} r,$$

where $\omega \cdot \Phi$ varies rapidly compared to B if the frequency is high. Assume that the solution of the inverse problem can be written in the following form

$$a(\mathbf{x}) = \iint F(\omega) I(\mathbf{x}, \mathbf{x}_g) e^{-j\omega \Phi(\mathbf{x}, \mathbf{x}_g)} p_s(\mathbf{x}_g, \omega) d^2 \mathbf{x}_g d\omega. \quad (23)$$

This equation is the mathematical expression of the intuitive idea of migration. If the pressure is transformed to the time domain, Eq. (23) becomes

$$a(\mathbf{x}) = f(t) * \iint I(\mathbf{x}, \mathbf{x}_g) \tilde{p}_s(\mathbf{x}_g, t = \Phi(\mathbf{x}, \mathbf{x}_g)) d^2 \mathbf{x}_g dt,$$

where $f(t)$ and $\tilde{p}_s(\mathbf{x}_g, t)$ correspond to $F(\omega)$ and $p_s(\mathbf{x}_g, \omega)$, and $*$ symbolizes temporal convolution. The formula states that migration consists of a summation through the data field along the hyperboloids, defined by

$$t = \Phi(\mathbf{x}, \mathbf{x}_g).$$

$F(\omega)$ and $I(\mathbf{x}, \mathbf{x}_g)$ are still undefined at this stage, but will be determined later. Clearly Eq. (23) is not strictly correct because the exact Eq. (18) has a different form. Equation (20) which displays a form similar to Eq. (23) can be derived from Eq. (18) only if high-frequency approximations are used. The equals sign in Eq. (23) must be understood in this sense. Inserting Eq. (22) into Eq. (23) results in

$$\iint \left(\frac{\omega}{4\pi v_0}\right)^2 F(\omega) B(\xi, \mathbf{x}_g) I(\mathbf{x}, \mathbf{x}_g) \cdot e^{j\omega[\Phi(\xi, \mathbf{x}_g) - \Phi(\mathbf{x}, \mathbf{x}_g)]} d^2 \mathbf{x}_g d\omega = \delta(\xi - \mathbf{x}) \quad (24)$$

and thus determines the choice of the functions $F(\omega)$ and $I(\mathbf{x}, \mathbf{x}_g)$. If the phase fluctuates rapidly enough, the integral has only nonvanishing values if \mathbf{x} and ξ coincide or are

at least close together. Then one can expand the phase expression with the variables ξ around the variables \mathbf{x} , whereas the amplitude $B(\mathbf{x}, \mathbf{x}_g)$ is taken at \mathbf{x} . These qualitative considerations can be viewed as a high-frequency approximation because the condition of a rapidly oscillating phase is valid if the frequency is high enough. Beylkin (1985) established these facts more rigorously using results of the theory of generalized Radon transforms. With

$$\begin{aligned} \Phi(\xi, \mathbf{x}_g) &\approx \Phi(\mathbf{x}, \mathbf{x}_g) + \nabla \Phi \cdot (\xi - \mathbf{x}), \\ B(\xi, \mathbf{x}_g) &\approx B(\mathbf{x}, \mathbf{x}_g), \end{aligned} \quad (25)$$

Eq. (24) becomes

$$\iint \left(\frac{\omega}{4\pi v_0}\right)^2 F(\omega) B(\mathbf{x}, \mathbf{x}_g) I(\mathbf{x}, \mathbf{x}_g) \cdot e^{j\omega \cdot \nabla \Phi \cdot (\xi - \mathbf{x})} d^2 \mathbf{x}_g d\omega = \delta(\xi - \mathbf{x}) \quad (26)$$

with

$$\nabla \Phi \cdot (\xi - \mathbf{x}) = \frac{2\omega}{v_0} \cdot \frac{1}{r} (\mathbf{x} - \mathbf{x}_g) \cdot (\xi - \mathbf{x}).$$

A transform of variables according to

$$k_x = \frac{2\omega}{v_0 r} (x - x_g),$$

$$k_y = \frac{2\omega}{v_0 r} (y - y_g),$$

$$k_z = \frac{2\omega}{v_0 r} z,$$

then leads to

$$\frac{1}{(2\pi)^3} \int \frac{\pi v_0 r}{16z} F(\omega) I(\mathbf{x}, \mathbf{x}_g) e^{j\mathbf{k} \cdot (\xi - \mathbf{x})} d^3 \mathbf{k} = \delta(\xi - \mathbf{x}).$$

This identity is guaranteed if

$$F(\omega) = 1,$$

$$I(\mathbf{x}, \mathbf{x}_g) = \frac{16z}{\pi v_0 r}.$$

Thus the quantities $I(\mathbf{x}, \mathbf{x}_g)$ and $F(\omega)$, unknown when Eq. (23) was established, can be inserted there to obtain exactly Eq. (20), the formula for Kirchhoff summation.

The results derived in this section demonstrate the equivalence of different inversion procedures. An exact inversion with modified data and subsequent application of partial integration and a high-frequency approximation leads to the same $(f-k)$ migration formula for the pressure as if the high-frequency assumption is introduced in the evaluation of the Fourier transform of the equation describing the forward problem. In the case treated here, the formula for $(f-k)$ migration can be transformed exactly to a Kirchhoff migration scheme. The straight way to the Kirchhoff summation is the inversion in space without detour to the Fourier domain. The $(f-k)$ formulation of the inverse problem can be rewritten as a Kirchhoff summation even if different slowly varying weighting factors are associated with the pressure. The appropriate stationary-phase approximation is valid if the object of migration is a few wavelengths beneath the surface.

Input and output data

The previous section summarized principles of different inversion procedures with pressure as the input and velocity perturbation as the output quantity. However, only marine surveys record the pressure, whereas in land-based surveys the geophones are sensitive to the vertical component of the particle velocity. In addition, a theory as close as possible to the experimental situation should incorporate the free surface conditions instead of assuming a homogeneous space with some finite velocity above the reflectivity structure.

As indicated in the introduction of this paper, the velocity perturbation is not really the appropriate inversion quantity requested by reflection seismologists. They usually look for the short-wavelength part of the velocity field, e.g. the reflectivity. This requires additional modifications of the inversion results.

Marine versus continental reflection data

In marine reflection experiments, hydrophone streamers positioned several metres below the sea surface record the pressure of the seismic waves. Actually, not only are upcoming waves recorded but also the interaction between them and the reflection from the interface between water and atmosphere ideally associated with a reflection coefficient of -1 . In land-based experiments geophones usually record the vertical component w_s of the particle velocity which is related to the pressure in the frequency domain by

$$\frac{\partial p_s}{\partial z_g} = j\omega \rho_0 w_s. \quad (27)$$

ρ_0 represents the density at the geophone position. In order to carry out the calculations of the previous sections with w_s instead of p_s , a derivative with respect to z_g must be introduced in the Born approximation before z_g is set equal to zero. This derivative affects the amplitude and phase in Eq. (5) and thus leads to a near- and far-field term. For high frequencies or a depth of several wavelengths, the near-field contribution can be neglected and Eq. (7) that serves as the starting point of the Born inversion in the marine case must be replaced by

$$w_s(\mathbf{x}_g, \omega) = \frac{2}{\rho_0 v_0} \left(\frac{\omega}{4\pi v_0} \right)^2 \int a(\mathbf{x}) \frac{z}{r^3} e^{-j\frac{2\omega}{v_0}r} d^3\mathbf{x} \quad (28)$$

for continental environments. In Eq. (28) the sign of w_s is chosen in a way that a positive break is caused by a particle moving upwards in the negative z direction. Inversion provides, as the $(f-k)$ formula,

$$a(\mathbf{x}) = \frac{8\rho_0 z}{\pi v_0} \iiint \frac{\omega}{jv^2} w_s(k_x, k_y, \omega) \cdot e^{-jvz} e^{j(k_x x + k_y y)} dk_x dk_y d\omega \quad (29)$$

and, as the Kirchhoff summation,

$$a(\mathbf{x}) = \frac{8\rho_0}{\pi} \iint w_s(\mathbf{x}_g, \omega) e^{-j\frac{2\omega}{v_0}r} d^2\mathbf{x}_g d\omega. \quad (30)$$

Comparison to Eq. (20) shows that the weight factor z/r must be omitted in the inversion if the particle velocity is used as the input quantity instead of the pressure.

The influence of the free surface

The influence of the free surface can be introduced in Born's inversion scheme by an appropriate modification of Green's function. Remember that Eq. (6), which solves the forward problem in the frame of Born's approximation, combines a wave travelling downward from a source at $z=0$ with a wave travelling upwards towards the surface from any point inside the reflecting halfspace. This wave is represented by Green's function for a homogeneous space with a source point inside the lower halfspace. If a free surface exists at $z=0$, the wave reflected from the free surface must be added to form the new Green's function

$$g(\mathbf{x}_g, \mathbf{x}, \omega) = \frac{e^{j\frac{\omega}{v_0}r_1}}{4\pi r_1} - \frac{e^{j\frac{\omega}{v_0}r_2}}{4\pi r_2}, \quad (31)$$

where

$$r_{1,2} = [(x-x_g)^2 + (y-y_g)^2 + (z \mp z_g)^2]^{\frac{1}{2}}.$$

The first term represents the upward-travelling wave, the second one the reflected wave. Both are just connected by a subtraction because the free surface acoustic reflection coefficient is -1 , independent of the angle of incidence. Again the marine and continental case must be distinguished. For marine pressure data, expression (31) is exactly zero at $z=0$ because there both terms cancel each other. At a depth below the surface Green's function does not vanish and, if z_g is small compared to the dominant wavelength, can be approximately expressed as

$$g(\mathbf{x}_g, \mathbf{x}, \omega) = -\frac{4j\omega z_g}{v_0} \frac{z}{r} \frac{e^{j\frac{\omega}{v_0}r}}{4\pi r}.$$

For continental data the derivative of Eq. (31) with respect to z_g must be evaluated at $z_g=0$. The net effect of this step is the introduction of the scale factor 2 on the right-hand side of Eq. (6). Therefore, the free surface has no consequence if continental data are processed.

Marine data measured at z_g below the sea surface should be inverted or migrated according to

$$a(\mathbf{x}) = \frac{2z}{\pi v_0 z_g} \iiint \frac{1}{v^2} P_s(k_x, k_y, \omega) \cdot e^{-jvz} e^{j(k_x x + k_y y)} dk_x dk_y d\omega \quad (32)$$

if a $(f-k)$ program is preferred. The associated Kirchhoff formula is

$$a(\mathbf{x}) = \frac{2}{\pi z_g} \iint \frac{1}{-j\omega} p_s(\mathbf{x}_g, \omega) e^{-j\frac{2\omega}{v_0}r} d^2\mathbf{x}_g d\omega. \quad (33)$$

Comparison with Eq. (20) shows that the weight function z/r must be omitted and a frequency term should be introduced if the influence of the free surface is taken into account.

Reflectivity versus velocity perturbation

Despite the fact that the velocity always acts as a parameter describing the medium in the wave equation, it depends on the experimental configuration whether it might be the appropriate quantity for an inversion. Reflection seismology

ists know very well that they cannot get reasonable estimates of the velocity; rather, they map the spatial distribution of the reflective properties of the medium. These properties are dominated by the short-wavelength part of the spectrum of the velocity. Its long-wavelength part plays a role in stacking and migrating the data, but these processing steps are not too sensitive to the accuracy of the velocity estimates, and therefore rough spatial averages or estimates that can be determined by, for example, NMO analysis are sufficient.

The amplitude of a reflection is proportional to the reflection coefficient defined as

$$c(z) = \frac{1}{2v(z)} \frac{dv}{dz} \quad (34)$$

in the case of a 1-D velocity variation, constant density and vertical incidence. With the velocity perturbation, defined by Eq. (2) and $|a| \ll 1$, this expression becomes

$$c(z) = -\frac{1}{4} \frac{da}{dz}. \quad (35)$$

The reflectivity can, therefore, be viewed as mainly determined by the small-wavelength contribution to the Fourier spectrum of the velocity. It can be resolved within the bandwidth of the data, e.g. within an upper limitation but also within a lower limit defined by the smallest available frequency. In principle, the velocity perturbation as well as the reflectivity can be used as the inversion target. The velocity perturbation, however, inherently incorporates a large amount of small-wavenumber components, which cannot be resolved with reflection data, whereas the reflectivity emphasizes the high-wavenumber components according to

$$C(k_z) = -\frac{j}{4} k_z A(k_z). \quad (36)$$

Figure 2 illustrates this relationship for a thin layer. The reflectivity has a spectrum more equally distributed in the observational wavenumber range compared to the velocity perturbation. It appears, therefore, desirable to obtain the reflectivity as an inversion result. This concept requires a generalization of the definition of the reflectivity to an arbitrary medium with a 3-D velocity fluctuation. A straightforward extension of Eq. (34) is

$$c(\mathbf{x}) = \frac{1}{2v(\mathbf{x})} |\nabla v| \operatorname{sgn} \left(\frac{\partial v}{\partial z} \right). \quad (37)$$

The formula can be interpreted in the following way: given a spatial velocity distribution, the reflectivity at a point is determined by finding the direction of maximum variation of the velocity. The directional derivative scaled by the velocity defines the modulus of the reflectivity. If the velocity locally increases (decreases) with depth, a positive (negative) reflectivity results. In terms of the velocity perturbation, Eq. (37) becomes

$$c(\mathbf{x}) = -\frac{1}{4} |\nabla a| \operatorname{sgn} \left(\frac{\partial a}{\partial z} \right). \quad (38)$$

This last equation relates reflectivity and velocity perturbation in space if the parameters vary in three dimensions.

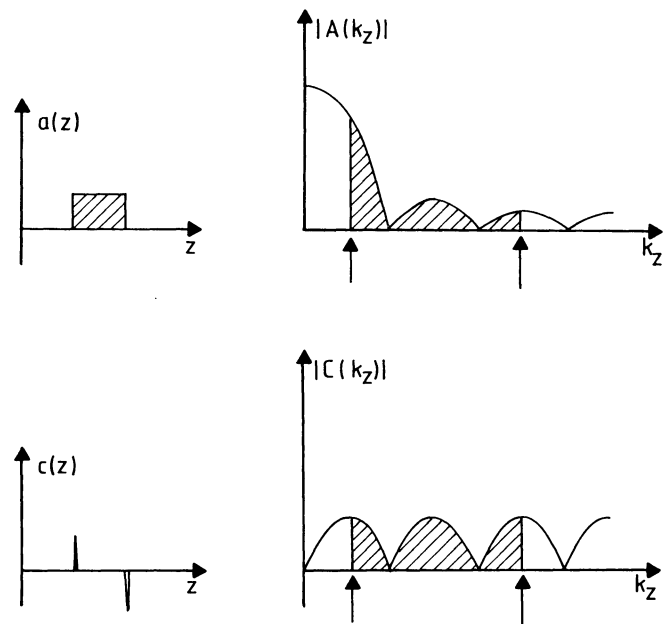


Fig. 2. Demonstration of the distribution of the wavenumber components in the Fourier transform of the velocity perturbation A (upper part) and the reflectivity C (lower part) for the case of a thin bed. Note that a substantial part of amplitudes for A are concentrated around $k_z = 0$ and thus not accessible for band-limited inversion, whereas for C amplitudes are more equally distributed along the k_z axis

For the inversion a relation in the Fourier domain is required, because once available one would simply insert the Fourier transform of the reflectivity for the transformed expression of the velocity perturbation in Eq. (12) and proceed with the inversion along the lines previously described. Whereas for a 1-D medium an exact relation between the transforms of $a(z)$ and $c(z)$ can be given, namely Eq. (36), only an approximate formula can be derived for the general case:

$$C(\mathbf{k}) = -\frac{j}{4} |\mathbf{k}| \operatorname{sgn}(k_z) \cdot A(\mathbf{k}). \quad (39)$$

This relation was proved by Bleistein (1984, p. 289) using stationary-phase approximations. If the medium is composed of domains of constant velocity, its spatial velocity distribution can be written as a sum of characteristic functions

$$v(\mathbf{x}) = \sum_i v_i F_i(\mathbf{x}),$$

where $F_i(\mathbf{x})$ represents a function with unit value inside and vanishing outside a given domain D_i . Inside D_i the velocity is v_i . The different domains are mutually disjoint.

$$F_i(\mathbf{x}) = \begin{cases} 1 & \mathbf{x} \in D_i \\ 0 & \mathbf{x} \notin D_i. \end{cases}$$

With

$$a_i = -\frac{2}{v_0} (v_i - v_0),$$

$|a_i| \ll 1$ and Eq. (2), the spatial distribution of the velocity perturbation becomes

$$a(\mathbf{x}) = \sum_i a_i I_i(\mathbf{x}). \quad (40)$$

The corresponding expression for the reflectivity is

$$c(\mathbf{x}) = \sum_i c_i \gamma_i(\mathbf{x}) \quad (41)$$

with the discrete reflection coefficient

$$c_i = \frac{1}{2v_0} (v_i - v_0)$$

and the singular function $\gamma_i(\mathbf{x})$ which has delta-function-like singularities at the surface where $I_i(x)$ jumps from zero to unity. Characteristic and singular functions can be viewed as generalisations of the 1-D Heaviside and delta functions. The Fourier transform integrals of $\gamma_i(\mathbf{x})$ and $I_i(\mathbf{x})$ can be evaluated approximately with the method of stationary phase. Then they are related by

$$\bar{\gamma}(\mathbf{k}) = -j|\mathbf{k}| \operatorname{sgn}(k_z) \bar{I}_i(\mathbf{k}). \quad (42)$$

Equation (39) results if Eqs. (40), (41) and (42) are properly combined. It holds if the medium is composed of areas of constant velocity. Reflectors are located at the interfaces between areas of different velocity. The stationary-phase approximation is reasonable wherever the product of R and k is much greater than unity, where R represents the radius of curvature. If k is associated with a wavelength, then the radius of curvature should exceed the dominant wavelength. Therefore, the approximation fits very well into the resolution capabilities of reflection seismology.

If the reflectivity is used instead of the velocity perturbation, the previously derived results are readily modified. In order to replace $a(x, y, z)$ by $c(x, y, z)$, for instance, in Eq. (14) one inserts

$$k_z = -v$$

into Eq. (39). v is defined in Eq. (8) where only real values are of interest. Then

$$C(k_x, k_y, -v) = \frac{j\omega}{2v_0} A(k_x, k_y, -v).$$

The further steps of the inversion procedure are simply applied to C instead of A . As a result, the data must be multiplied by the frequency factor

$$\frac{j\omega}{2v_0} \quad (43)$$

prior to migration. Then Eq. (18) becomes

$$c(\mathbf{x}) = \frac{1}{\pi^2} \iiint \omega^2 Q_s(k_x, k_y, \omega) \cdot e^{-jvz} e^{j(k_x x + k_y y)} dk_x dk_y d\omega \quad (44)$$

or Eq. (19) is modified to

$$c(\mathbf{x}) = \frac{4z}{\pi^2 v_0^2} \iiint \frac{\omega}{v} P_s(k_x, k_y, \omega) \cdot e^{-jvz} e^{j(k_x x + k_y y)} dk_x dk_y d\omega. \quad (45)$$

In the time domain the application of factor (43) corresponds to a differentiation of the seismic traces. If a stacked

section of continental data is to be inverted to an image of the spatial distribution of the velocity perturbation, the Kirchhoff formula (30) requires nothing but a straight summation along the diffraction hyperboloids through the section. If an image of the reflectivity is of interest, the data should be differentiated prior to the Kirchhoff summation.

Summary and conclusions

Born inversion represents a new look to the old problem of migration of reflection data. Its similarities with standard wave equation migration schemes originate in the fact that the wave equation is assumed to describe appropriately reflection seismic observations. It uses essentially the same simplifying assumptions about the earth's structure, its division in a slowly varying or even constant background or reference velocity that serves as input to the inversion, and unknown velocity perturbations representing the short-wavelength components of the velocity field causing the reflectivity of the medium. The omission of multiple scattering results in a linear integral equation between data and reflectivity that can be inverted analytically, at least in a stationary-phase sense. The stationary-phase approximations used are acceptable under the conditions generally faced in reflection seismology. The object of inversion is several wavelengths away from the receiver and a curvature is only properly mapped if its radius is larger than a wavelength.

Under these conditions it can be shown that Born inversion applied to a stacked section with constant reference velocity is essentially equivalent to frequency-wavenumber migration and to a Kirchhoff summation. There are, however, weighting factors involved which reflect different physical situations. For instance, if the reflectivity is requested as the inversion quantity instead of the velocity perturbation, then the integral operations must be applied on data multiplied by frequency or differentiated in the time domain. Using the pressure instead of the vertical component of the particle velocity requires a factor in the migration formula that weights the data close to the apex of a diffraction, compare Eq. (21) and (30). In the acoustic case treated here, the free surface plays a role only for marine data.

The circumstance that Born inversion in the applications discussed in this paper leads to results strongly reminiscent of classical migration should not be interpreted as a shortcoming. Those methods are often based on heuristic ideas, as, for example, the exploding reflector model, rather than on a straight inversion procedure. Therefore, Born approximation must be considered as a contribution to the theoretical justification and consolidation of classical migration. Born inversion can thus rely on well-tested numerical methods and simultaneously yield true amplitudes.

Acknowledgements. Financial support for this work was granted by the Federal Ministry of Research and Technology, project RG 8310/2. The manuscript was kindly typed by S. Stuhlert. I am indebted to H. Emmerich and G. Mueller, both Frankfurt, for many useful suggestions that helped to improve the paper. Geophysical institute contribution No. 340.

References

- Bath, M.: Mathematical aspects of seismology. Amsterdam: Elsevier Publishing Company 1968
- Beylkin, G.: Imaging of discontinuities in the inverse scattering problem by inversion of a causal generalized Random transform. *J. Math. Phys.* **26**, 99–108, 1985

- Bleistein, N.: *Mathematical methods for wave phenomena*. London: Academic Press Inc. 1984
- Bleistein, N., Cohen, J.K.: The velocity inversion problem – present status, new directions. *Geophysics* **47**, 1497–1511, 1982
- Castle, R.J.: Wave-equation migration in the presence of lateral velocity variations. *Geophysics* **47**, 1001–1011, 1982
- Cheng, G., Coen, S.: The relationship between Born inversion and migration for common-midpoint stacked data. *Geophysics* **49**, 2117–2131, 1984
- Claerbout, J.F.: *Imaging the earth's interior*. Oxford: Blackwell Scientific Publication 1985
- Cohen, J.K., Hagin, F.G., Bleistein, N.: Three-dimensional Born inversion with an arbitrary reference. *Geophysics* **51**, 1552–1558, 1986
- Gazdag, J.: Wave equation migration with the phase shift method. *Geophysics* **43**, 1342–1351, 1978
- Hagedoorn, J.G.: A process of seismic reflection interpretation. *Geophys. Prosp.* **2**, 85–127, 1954
- Loewenthal, D., Lu, L., Roberson, R., Sherwood, J.: The wave equation applied to migration. *Geophys. Prosp.* **24**, 380–399, 1976
- Papoulis, A.: *Systems and transforms with applications in optics*. New York: McGraw-Hill Book Company 1968
- Robinson, E.A.: *Migration of geophysical data*. Boston: International Human Resources Development Corporation 1983
- Stolt, R.H.: Migration by Fourier transform. *Geophysics* **43**, 23–48, 1978

Received September 10, 1987; revised version October 23, 1987

Accepted October 26, 1987

Restoration of broad-band seismograms (Part II): Signal moment determination

D. Seidl¹ and M. Hellweg²

¹ Seismologisches Zentralobservatorium Gräfenberg, Krankenhausstr. 1, D-8520 Erlangen, Federal Republic of Germany

² 57 Overhill Road, Orinda, CA 94563-3122, U.S.A.

Abstract. Two standard methods for the time-domain determination of the signal moment from displacement seismograms are studied theoretically and numerically using broad-band data. Investigation shows that the accuracy of the displacement integral method depends relatively little on the shape of the body-wave displacement pulse, but strongly on the ratio of the pulse duration d to the seismometer period T_0 . For a single-sided wavelet of duration d , the signal moment can be determined with a relative error $\langle e$ if the seismometer period $T_0 \gg 2\pi d/e$. The displacement impulse method for wavelets with corner frequencies greater than the cut-off frequency of the seismograph is discussed for the broad-band channel of the Gräfenberg array. The theoretical results are illustrated using broad-band recordings of the Gräfenberg array.

Key words: Source moment – Displacement integral – Displacement impulse – Broad-band seismograms – Restoration

Introduction

The inversion of displacement waveforms is the basis for the determination of source parameters such as focal depth, fault-plane parameters and moment. The wider the bandwidth of the recording, the more accurate the seismic interpretation can be. The Wielandt-Streckeisen broad-band seismometer (Wielandt and Streckeisen, 1982), which records ground motion as velocity or displacement from 0.2 s to 20 s, and the improved Wielandt-Steim very broad-band version (Wielandt and Steim, 1986), with an upper corner period of 360 s, produce such wide-band recordings. The characteristic properties of digital broad-band seismographs – low seismometer noise, an exact transfer function, high linearity, large bandwidth and high dynamic range – allow the upper corner period to be increased still further numerically. In addition, velocity seismograms can easily be converted to displacement seismograms.

With the advent of broad-band digital seismographs, the accuracy and resolution of signal parameters used in source studies can be improved using wide-band restoration. Restoration of broad-band seismograms Part I (Seidl and Stammer, 1984) discussed the seismograph characteristics of the Gräfenberg array in the time and frequency domains, various methods for the computation of synthetic seismograms and the instrumental correction for the measurement of arrival times and first-motion signs. Part II ad-

dresses the problem of wide-band restoration and the determination of signal moment.

Signal moment determination

The source moment M_0 can be calculated from the P - or S -wave signal moment

$$m_u = \int_0^{\infty} u(t) dt = \bar{U}(0), \quad (1)$$

using the expression

$$M_0 = G \cdot m_u. \quad (2)$$

$u(t)$ is the displacement wavelet [$u(t)=0$ for $t<0$] of the P or S wave and $\bar{U}(0)$ is its spectral value at frequency zero. G corrects for the radiation pattern of the source, the geometrical amplitude spreading and the attenuation factor of the propagation path.

If $u(t)$ is recorded by a seismograph with the frequency characteristics $\bar{H}(j\omega)$, the spectrum $\bar{S}(j\omega)$ of the seismogram $\bar{s}(t)$ has the form

$$\bar{S}(j\omega) = \int_0^{\infty} \bar{s}(t) \exp(-j\omega t) dt = \bar{U}(j\omega) \cdot \bar{H}(j\omega). \quad (3)$$

The seismogram moment m_s , obtained from Eq. (3) for $\omega=0$, is

$$m_s = \int_0^{\infty} \bar{s}(t) dt = \bar{U}(0) \cdot \bar{H}(0) = 0 \quad (4)$$

since $\bar{H}(0)=0$ for seismometers with mechanical pendulum sensors.

The approximate signal moment m_u is usually estimated in the frequency domain by the sequence of operations: Selection of a seismogram window \rightarrow Fourier transform $\bar{S}(j\omega) \rightarrow$ instrument correction $\bar{U}(j\omega) = \bar{S}(j\omega)/\bar{H}(j\omega) \rightarrow$ extrapolation of the “low-frequency plateau range” of $|\bar{U}(j\omega)|$ to frequency zero.

In the time domain, the moment can be approximated using the displacement integral with a finite upper limit t_0 . This finite integral corresponds to the extrapolation of the displacement spectrum into the frequency interval $\{0, 1/t_0\}$. The displacement time function for the integration must be determined by restoration from a recorded velocity or displacement seismogram. In this case, restoration means increasing the seismometer period using numerical methods

until the seismogram becomes unstable due to the long-period noise.

For a small signal-to-noise ratio, a sufficient base-line correction cannot be performed by linear trend removal and high-pass filtering. In this case, analysis in the time domain has an advantage over the frequency domain because the instantaneous low-frequency trend of the seismogram can be used as the time axis for the computation of the displacement integral. Such a correction for the low-frequency noise is not possible in the frequency domain.

The displacement integral method

To a certain extent, the effects of signal shape, seismometer frequency and integration interval on the accuracy of the signal moment determination can be investigated theoretically. The far-field displacement P or S waveform for a unilateral rupture with finite fault length and finite slip function rise time is a single-sided wavelet with a spectrum proportional to ω^{-2} for high frequencies. The time function

$$u(t) = m_u \cdot a^2 \cdot t \cdot \exp(-a \cdot t) \cdot \bar{h}(t), \quad (5)$$

where $\bar{h}(t)$ is the unit step response, can be used as an analytically simple signal model for such a displacement pulse with the moment m_u . A practical definition of the signal duration d is the time within which the signal decays to about 0.7% to the maximum amplitude:

$$d = \frac{8}{a}. \quad (6)$$

The wavelet in Eq. (5) has the Laplace transform

$$U(s) = \frac{m_u \cdot a^2}{(s+a)^2} \quad (7)$$

and the Fourier transform $\bar{U}(j\omega) = U(s)|_{s=j\omega}$. The wavelet spectrum $|\bar{U}(j\omega)|$ is a negative monotonic function with the upper corner frequency

$$f_c = \frac{\sqrt{\sqrt{2}-1}}{2 \cdot \pi} \cdot a \approx 0.1024 \cdot a \quad (8)$$

and a spectral fall-off $\sim \omega^{-2}$ for high frequencies.

For a displacement seismometer with critical damping, angular eigenfrequency ω_0 and the transfer function

$$H(s) = \frac{s^2}{(s+\omega_0)^2}, \quad (9)$$

the response $\bar{s}(t)$ to the input wavelet in Eq. (5) is obtained by evaluating the inverse Laplace transform of the rational function $U(s)H(s)$:

$$\begin{aligned} \bar{s}(t) = m_u \cdot a^2 \left\{ \left[\frac{\omega_0^2 \cdot t}{(a-\omega_0)^2} - \frac{2 \cdot a \cdot \omega_0}{(a-\omega_0)^3} \right] \exp(-\omega_0 \cdot t) \right. \\ \left. + \left[\frac{a^2 \cdot t}{(a-\omega_0)^2} - \frac{2 \cdot a \cdot \omega_0}{(a-\omega_0)^3} \right] \exp(-a \cdot t) \right\}. \quad (10) \end{aligned}$$

In the special case $a = \omega_0$, Eq. (10) becomes indeterminate. However, $\bar{s}(t)$ can still be described analytically using L'Hospital's rule:

$$\bar{s}(t) = m_u \left(t - \omega_0 t^2 + \frac{\omega_0^2}{6} t^3 \right) \exp(-\omega_0 t). \quad (11)$$

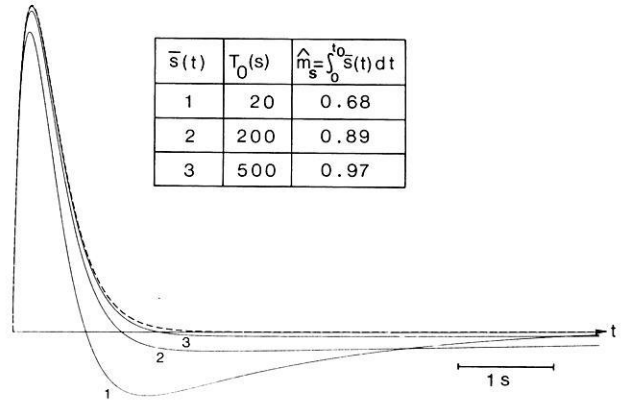


Fig. 1. Theoretical seismograms for two broad-band (solid lines 1 and 2) and one very broad-band (solid line 3) displacement seismographs (period T_0) for the displacement wavelet $u(t) = m_u \cdot a^2 \cdot t \cdot \exp(-a \cdot t)$ (dashed line) with moment $m_u = 1$. a has the value 4.88 s^{-1} corresponding to an upper corner frequency of $f_c = 0.5 \text{ Hz}$. The apparent seismogram moment $\hat{m}_s = \int_0^{t_0} \bar{s}(t) dt$ (t_0 time of zero crossing) tends to the input moment $m_u = 1$ for $T_0 \rightarrow \infty$

Equation (10) shows that the seismogram $\bar{s}(t)$ approaches the input wavelet $u(t)$ if the seismometer frequency ω_0 tends to zero:

$$\lim_{\omega_0 \rightarrow 0} \bar{s}(t) = m_u \cdot a^2 \cdot t \cdot \exp(-a \cdot t). \quad (12)$$

In Fig. 1 the theoretical seismograms calculated using Eq. (10) approach the input wavelet when the seismometer period T_0 is increased. Since $\int_0^{\infty} \bar{s}(t) dt = 0$ [Eq. (4)], the seismogram $\bar{s}(t)$ crosses zero at least once at t_0 and overshoots for any finite seismometer period. The finite displacement integral $\int_0^{t_0} \bar{s}(t) dt$ will be called the apparent seismogram moment \hat{m}_s . Hence, the moment m_u of the input wavelet can be written as follows:

$$m_u = \int_0^{t_0} \bar{s}(t) dt + e(f_c, T_0). \quad (13)$$

Equation (13) is illustrated in Fig. 1. For a wavelet with a time function described by Eq. (5) and upper corner frequency as in Eq. (8), and given an error $e > 0$, there exists a seismometer period T'_0 such that $|m_u - \hat{m}_s| < e$ for $T_0 > T'_0$.

How does the error term in Eq. (13) depend on the shape of the input wavelet? The response of the seismometer in Eq. (9) to a rectangular wavelet of duration d and moment m_u

$$u(t) = \frac{m_u}{d} [\bar{h}(t) - \bar{h}(t-d)] \quad (14)$$

is given by

$$\begin{aligned} \bar{s}(t) = \frac{m_u}{d} \{ (1 - \omega_0 t) \exp(-\omega_0 t) \bar{h}(t) - [(1 - \omega_0(t-d)) \\ \cdot \exp(-\omega_0(t-d))] \bar{h}(t-d) \}. \end{aligned}$$

As in Eq. (12), the seismogram tends to the input wavelet in Eq. (14) for the limit $\omega_0 \rightarrow 0$.

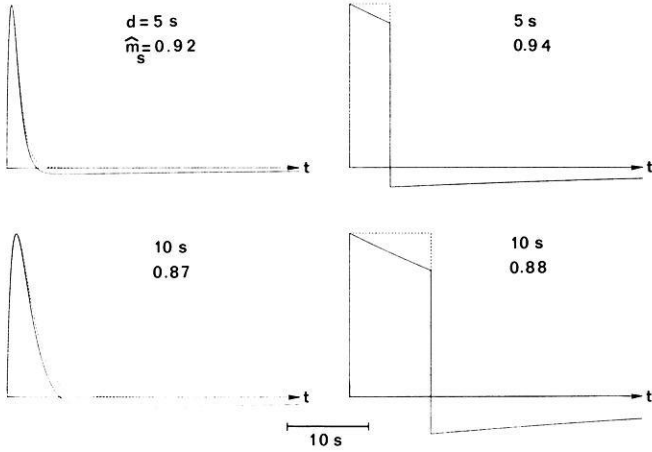


Fig. 2. Apparent moment and wavelet shape: theoretical seismograms (solid lines) and apparent moments \hat{m}_s for a very broad-band seismograph ($T_0 = 500$ s) for the exponential [Eq. (5), left] and rectangular [Eq. (14), right] input wavelet (duration d). \hat{m}_s has nearly the same value for both wavelets

Linearizing Eq. (15) for $\omega_0 \cdot t \ll 1$ and integrating over the interval d gives an approximation for the apparent moment

$$\hat{m}_s = m_u \cdot (1 - \omega_0 \cdot d). \quad (16)$$

The relative error is then $e = (\hat{m}_s - m_u)/m_u = -\omega_0 \cdot d$.

Figure 2 shows that \hat{m}_s has nearly the same value for the exponential wavelet in Eq. (5) and for the rectangular wavelet in Eq. (14). A similar result is obtained for a half-cycle sinusoidal pulse. Since the spectra of single-sided time functions are all negatively monotonic and flat near frequency zero, \hat{m}_s depends only weakly on the shape of the input wavelet.

Figure 3 shows a diagram of the apparent moment \hat{m}_s versus the duration d for an exponential and a rectangular wavelet and for displacement seismometers with different periods. The straight lines defined by Eq. (16) satisfactorily approximate both curves for $\omega_0 \cdot d \ll 1$. As a rule of thumb, the relative error is less than about 10% if the seismometer period $T_0 > 20\pi d$ [Eq. (16)]. For a very broad-band seismometer ($T_0 = 360$ s) the relative error is therefore less than 10% for pulse durations up to about 6 s.

The displacement impulse method

If the upper corner frequency of the displacement wavelet is greater than the cut-off frequency of the seismograph, the seismogram $\bar{s}(t)$ has approximately the form $\bar{s}(t) \approx m_u \cdot h(t)$, where $h(t)$ is the displacement impulse response of the seismograph and m_u is the moment of the input wavelet. This approximation follows from the series representation of the seismogram in terms of the derivatives $h^{(k)}(t)$ and the moments

$$m_{uk} = \int_0^\infty t^k u(t) dt \quad k=0, 1, 2, \dots \quad (17)$$

of the input wavelet (see, for example, Papoulis, 1977):

$$\bar{s}(t) = \sum_{k=0}^\infty (-1)^k \cdot m_{uk} \cdot h^{(k)}(t) = m_u \cdot h(t) + m_{u1} \cdot h'(t) + \dots \quad (18)$$

with $m_{u0} = m_u$.

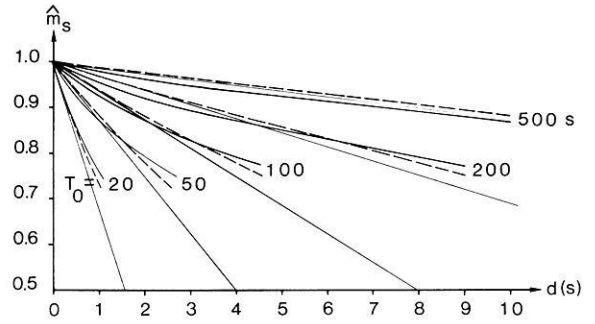


Fig. 3. Apparent seismogram moment \hat{m}_s versus duration d for two input wavelets with moment $m_u = 1$ (solid curves – exponential wavelet; dashed curves – rectangular wavelet) for displacement seismographs with periods T_0 . The straight lines $\hat{m}_s = m_u \cdot (1 - \omega_0 \cdot d)$ of Eq. (16) approximate both curves for $\omega_0 \cdot d \ll 1$, where $\omega_0 = 2\pi/T_0$ is the angular eigenfrequency of the seismometer

Inserting the exponential wavelet in Eq. (5) into Eq. (17), it follows

$$m_{uk} = m_u \cdot a^2 \cdot \int_0^\infty t^{k+1} \cdot \exp(-a \cdot t) dt = m_u \cdot \frac{(k+1)!}{a^k}. \quad (19)$$

Expressing a in terms of the wavelet duration in Eq. (6), Eq. (19) can be written as

$$m_{uk} = m_u \frac{(k+1)!}{8^k} d^k. \quad (20)$$

Substituting Eq. (20) into Eq. (18) gives

$$\begin{aligned} \bar{s}(t) &= m_u \sum_{k=0}^\infty \frac{(-1)^k \cdot (k+1)!}{8^k} \cdot h^{(k)}(t) \cdot d^k \\ &= m_u \left[h(t) - \frac{1}{4} h'(t) \cdot d + \frac{3}{32} h''(t) \cdot d^2 + \dots \right]. \end{aligned} \quad (21)$$

Hence, for small duration d of the input wavelet, the seismogram is approximately given by the first term in the expansion $m_u \cdot h(t)$. For the broad-band velocity channel of the Gräfenberg array, the range of pulse durations for which this approximation is valid is shown in Fig. 4. The theoretical seismograms are calculated using the impulse invariant transformation (Seidl and Stammer, 1984). For upper corner frequencies of the exponential wavelet $f_c \geq 5$ Hz, the seismograms can be described by the function $b(f_c) \cdot m_u \cdot \tilde{h}(t)$, where $b(f_c)$ is the maximum amplitude of the synthetic response in terms of the corner frequency f_c . $b(f_c)$ decreases very slowly from $b = 1.0$ for high frequencies to $b = 0.86$ for $f_c = 5$ Hz (cut-off frequency of the Gräfenberg seismograph) and $\tilde{h}(t)$ has nearly the same shape as the impulse response $h(t)$. For $f_c < 5$ Hz, $b(f_c)$ decreases very rapidly (for example, $b = 0.2$ for $f_c = 2$ Hz) and the seismogram shows increasing deviation from the impulse response. This sharp transition is caused by the steep slope of 36 dB per octave of the amplitude response of the Gräfenberg velocity channel. Thus, the influence of a change in moment on the observed pulse amplitude can be separated from the effects of a change in the corner frequency. The usually steep fall-off generated by the anti-aliasing filter of a digital seismograph is therefore very useful for the application of the displacement impulse method.

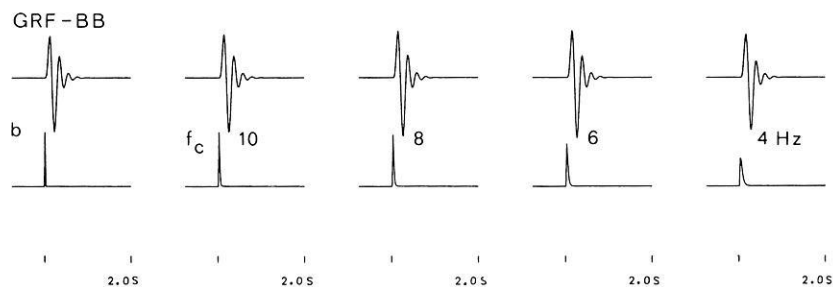
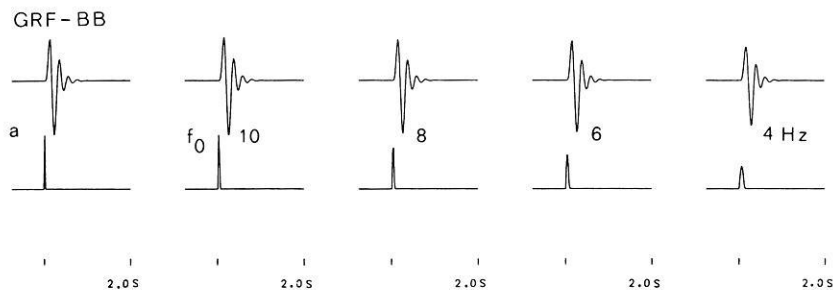


Fig. 4a and b. Synthetic seismograms for the broad-band velocity channel of the Gräfenberg array for **a** a half-cycle sinusoidal wavelet with frequency f_0 and **b** the exponential wavelet from Eq. (5) with corner frequency f_c . In both cases the first seismogram is the displacement impulse response. The input wavelets are normalized to the moment $m_u = 1$

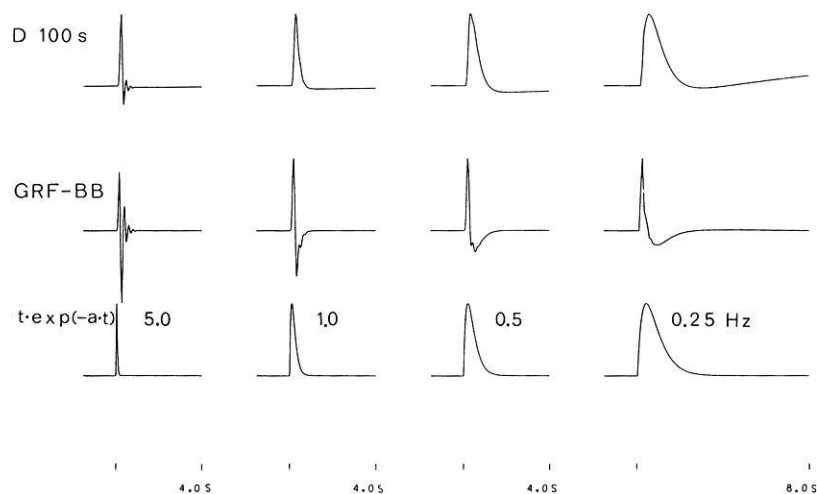


Fig. 5. Restoration of synthetic seismograms. *Bottom*: exponential displacement wavelets with various corner frequencies normalized to the maximum amplitude. *Middle*: the corresponding synthetic seismograms for the Gräfenberg velocity channel (GRF-BB). *Top*: restoration of the GRF-BB synthetic seismograms for a displacement seismograph ($T_0 = 100$ s) including the Gräfenberg anti-aliasing filter

In contrast, the transition in $b(f_c)$ and $h(t)$ for the standard narrow-band seismographs with a flatter high-frequency fall-off is more gradual. The separation of moment and corner frequency effects at intermediate frequencies is therefore not as easy. For example, Randall (1972) has described the method using WWSSN-LP seismograms.

The most important application of the displacement impulse method is the moment estimation for local events, especially the determination of relative moments for shock sequences.

Restoration of broad-band seismograms

Restoration is the approximate reconstruction of the true ground motion from the seismogram. One possible procedure is performed for a displacement seismograph by shifting the seismometer period to higher values. The long-period boundary is limited mainly by the low-frequency noise. For a velocity seismograph, an additional integration is necessary. For small signal-to-noise ratio, a base-line correction should be performed by linear trend removal and high-pass filtering. Of the many well-known procedures, a practical time-domain method is increasing the seismometer period

stepwise and integration for velocity seismograms until the seismogram form remains nearly unchanged or the seismogram becomes unstable due to amplified low-frequency noise.

Figure 5 uses synthetic seismograms to demonstrate restoration. The high-quality result is due to the lack of noise in the original seismograms. The deviations are caused by the anti-aliasing filter and the overshoot effect described in Eq. (4). The synthetic and restored signals are calculated using the impulse invariant transformation (Seidl and Stammler, 1984).

Practical examples

Figure 6 shows the time-domain restoration for the Gräfenberg velocity recording of a teleseismic P wave. The restoration was performed using a recursive simulation filter for a seismometer-galvanometer system with amplitude characteristics proportional to displacement in the period band from 0.2 s to the indicated upper period (Seidl, 1980). Overshooting in the displacement seismograms decreases with increasing upper period, in good agreement with Eq. (10), indicating a single-sided P wavelet. For upper periods

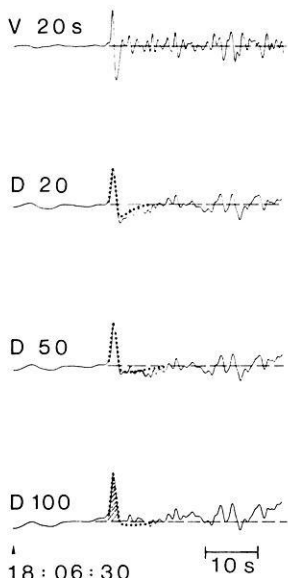


Fig. 6. Gräfenberg broad-band velocity recording (V) of a teleseismic P wavegroup and the restored displacement seismograms (D) for increasing seismograph period. Notice the decrease in overshoot with increasing period. The *dots* indicate the synthetic seismograms of Eq. (10).

Station GRF-A1Z, epicentral distance 84° , Honshu 09/24/1980, $mb=6.0$, depth = 73 km. Apparent seismogram moment of the P pulse (shaded area) $\hat{m}_s = 0.32 \times 10^{-5} \text{ m} \cdot \text{s}$

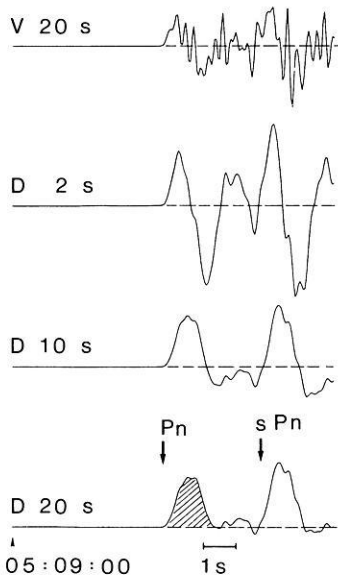


Fig. 7. Gräfenberg broad-band velocity recording (V) of a short-period local $Pn-sPn$ wavegroup and the restored displacement seismograms (D) for increasing seismograph period.

Station GRF-A1Z, epicentral distance 220 km, Swabian Jura 09/03/1978, $MS=5.5$, depth = 6.5 km. Apparent seismogram moment of the Pn pulse (shaded area) $\hat{m}_s = 6.2 \times 10^{-6} \text{ m} \cdot \text{s}$. Source moment $M_0 = 0.34 \times 10^{17} \text{ Nm}$ (Haessler et al., 1980)

greater than 100.0 s, the overshooting is less than the noise level. The signal duration is about 2.5 s and the relative error of the apparent moment is about 15%.

Figure 7 shows the restoration of a $Pn-sPn$ wavegroup, using the procedure described for Fig. 6. For an upper period $T_0=20.0$ s, a nearly single-sided pulse of about 1.5 s duration is obtained. The overshooting is less than

for the synthetic seismogram 1 in Fig. 1, calculated for a seismometer period $T_0=20.0$ s and a pulse duration $d=1.6$ s. This indicates that the P pulse is a composite and/or non-single-sided wavelet. The apparent moment should therefore be used with caution for the determination of the source moment by applying standard geometric P -wave spreading factors. In this case, waveform inversion using theoretical seismograms should be preferred to estimate the source moment.

Conclusions

The moment of a single-sided wavelet can be determined from a broad-band displacement seismogram using a finite displacement integral. Velocity recordings must first be converted to displacement seismograms by a wide-band restoration procedure. The relative error of the seismogram moment depends mainly on the ratio of the seismogram wavelet duration to the upper period of the seismograph. An advantage of this time-domain method is the ability to correct for long-period noise in the wideband displacement seismograms.

If the upper corner frequency of a wavelet is greater than the cut-off frequency of the seismograph, the seismogram is nearly the impulse response of the seismograph. In this case, the moment can be estimated from the maximum seismogram amplitude. The frequency range for the valid application of this method can be determined using synthetic seismograms.

Correctly applied, these methods may improve the accuracy of signal moment determination. Although the corrections are small compared to the uncertainties due to path and radiation effects, they may reduce scatter in moment vs. energy or moment vs. magnitude curves studied in shock sequences.

Acknowledgements. This paper was part of a joint project of the Institute for Meteorology and Geophysics of the University of Frankfurt and the Central Seismological Observatory Gräfenberg, supported by the German Research Council. We would like to thank E. Wielandt for many detailed comments, especially for discovering Eq. (16). The Gräfenberg array is part of the Bundesanstalt für Geowissenschaften und Rohstoffe (Federal Institute for Geosciences and Natural Resources) and is supported by the Deutsche Forschungsgemeinschaft (German Research Council).

References

- Haessler, H., Hoang-Trong, P., Schick, R., Schneider, G., Strohbach, K.: The September 3, 1978, Swabian Jura earthquake. *Tectonophysics* **68**, 1–14, 1980
- Papoulis, A.: *Signal analysis*, pp. 102–104. McGraw-Hill 1977
- Randall, M.J.: Multipolar analysis of the mechanisms of deep-focus earthquakes. In: *Methods in computational physics*, Vol. 12, pp. 280–283. New York and London: Academic Press 1972
- Seidl, D.: The simulation problem for broad-band seismograms. *J. Geophys.* **48**, 84–93, 1980
- Seidl, D., Stammer, W.: Restoration of broad-band seismograms (Part I). *J. Geophys.* **54**, 114–122, 1984
- Wielandt, E., Steim, J.M.: A digital very-broad-band seismograph. *Ann. Géophys.* **4**, 227–232, 1986
- Wielandt, E., Streckeis, G.: The leaf-spring seismometer. Design and performance. *Bull. Seismol. Soc. Am.* **72**, 2349–2367, 1982

Received September 2, 1987; revised version October 26, 1987

Accepted October 27, 1987

A study of diffraction-like events on DEKORP 2-S by Kirchhoff theory

W. Kampfmann

Institute of Meteorology and Geophysics, Feldbergstr. 47, D-6000 Frankfurt 1, Federal Republic of Germany

Abstract. A method is described for calculating the seismic response of an arbitrarily shaped interface below a homogeneous medium by the Kirchhoff integral in the time domain. It is shown, by comparison with other numerical techniques, that this method yields accurate results for reflections. The errors in calculating diffractions are tolerable if the distance of the receiver from the shadow boundary of reflection is not too large; this is usually the case in horizontal seismic profiling. The method has been applied to model qualitatively some typical features in record sections of the deep seismic reflection profile DEKORP 2-S. This profile is characterized by numerous strongly curved events that are concentrated mainly in two areas of the profile. These signals can be addressed as diffractions from an interpretation of the travel times. Dynamic calculations, however, show that the surprisingly high amplitudes cannot be explained by diffracting elements like fault edges or small-scale inhomogeneities; instead, one has to assume cylindrically or spherically curved reflectors with a radius of at least 4 km. Some possible geological explanations for these structures, like diapiric intrusions or antiformal stacks, are discussed in view of the tectonic evolution of the Central European Variscides.

Key words: Kirchhoff theory – Diffractions – DEKORP 2-S

Introduction

Forward modelling of seismic data has become an important tool in interpretation for both seismology and exploration geophysics. From the numerous methods that exist for the calculation of synthetic seismograms, the Kirchhoff-Helmholtz theory has been used in this paper because it is one of the few treatments – besides approaches that are based on the direct numerical solution of the elastodynamic equations – that incorporates the generation of diffractions in laterally strongly heterogeneous media.

Kirchhoff theory has found wide-spread application in reflection seismology since the work of Hilterman (1970). Early formulations of the Kirchhoff theory were based on the assumption of a constant-velocity medium and a constant reflection coefficient (e.g. Trorey, 1970, 1977; Berryhill, 1977). The method has been extended to media with variable velocities and arbitrary reflectivities by Carter and Frazer (1983), Deregowski and Brown (1983) and Frazer and Sen (1985). The accuracy of the high-frequency approxi-

mation that is inherent to all these implementations when modelling diffraction amplitudes has recently been discussed by Hutton (1987). Kirchhoff theory has also been used for the migration of seismic data (Schneider, 1978) and for the inversion of common-offset sections (Sullivan and Cohen, 1987).

This paper uses a time-domain formulation of the Kirchhoff integral for two dimensions to calculate the seismic response of an arbitrarily shaped reflector by a superposition of the elementary scattered waves that are radiated from each point of the reflector. The medium above this interface is assumed to have constant velocity or a linear increase in velocity with depth.

The algorithm is tested by comparison with the finite-difference method and the reflectivity method and then applied to model some conspicuous arched events in seismogram sections, on a near-vertical deep seismic reflection profile in southern Germany, that have been explained as diffractions in an earlier interpretation (DEKORP Research Group, 1985).

Formulation of the Kirchhoff method

Theory

The derivation of Kirchhoff theory can be found, for example, in Trorey (1970), Hilterman (1970) or Frazer and Sen (1985). Therefore, only a brief outline of the time-domain formulation of the Kirchhoff integral for computing synthetic seismograms will be given in the following.

We start with the Helmholtz equation for two dimensions

$$\nabla^2 U + k^2 U = 0, \quad (1)$$

where $k = \omega/c$ is the wavenumber, ω the frequency, c the velocity and $\nabla^2 = \partial^2/\partial x^2 + \partial^2/\partial z^2$. Here, U is the Fourier transform of any quantity that solves the acoustic wave equation in a homogeneous medium. This may be the pressure, the x or z component of P or SV displacement, the horizontal displacement in the case of SH waves, or the displacement potential for P or S waves.

Assume two functions F and G , where F satisfies Eq. (1) within a cross-section A , and G is the Green's function of Eq. (1): $\nabla^2 G(r, r_0) + k^2 G(r, r_0) = -4i \cdot \delta(r - r_0)$. Then the Kirchhoff integral states that the value of F , at a point P inside A , is fixed if F and G and their normal derivatives

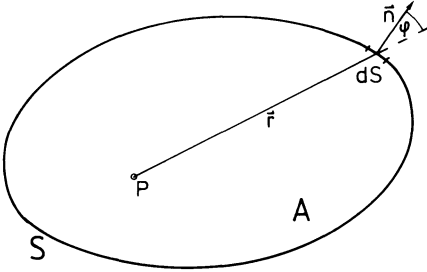


Fig. 1. The area A and its boundary S . \mathbf{n} is the outward unit normal to S . \mathbf{r} is the vector from the receiver at P to the boundary and φ is the angle between \mathbf{r} and \mathbf{n} . The wavefield at P can be calculated by integration over S

$\partial F/\partial n$ and $\partial G/\partial n$ are known on the boundary S of A (see Fig. 1):

$$F_P = \frac{i}{4} \cdot \int_S \left(F \frac{\partial G}{\partial n} - G \frac{\partial F}{\partial n} \right) ds \quad (2)$$

($ds = ds \cdot \mathbf{n}$; \mathbf{n} is the outward-pointing normal unit vector).

Now we identify F with the unknown function U and take G as the Hankel function of the second kind and order zero,

$$G = H_0^{(2)}(kr). \quad (3)$$

In the far field, G takes the asymptotic form

$$G = (2/\pi kr)^{1/2} \exp[-i(kr - \pi/4)]. \quad (3a)$$

Inserting Eq. (3) into Eq. (2) leads to

$$U_P = -\frac{i}{4} \cdot \int_S \left[U \cdot H_1^{(2)}(kr) k \cos \varphi + H_0^{(2)}(kr) \frac{\partial U}{\partial n} \right] ds \quad (4)$$

(see Fig. 1 for the meaning of r and $\cos \varphi$).

After transformation of Eq. (4) into the time domain, the Kirchhoff formula reads:

$$u_P(t) = \frac{1}{2\pi} \cdot \int_S \left[\frac{\partial u}{\partial t} * \frac{t \cdot H(t-r/c)}{r(t^2-r^2/c^2)^{1/2}} \cos \varphi + \frac{\partial u}{\partial n} * \frac{H(t-r/c)}{(t^2-r^2/c^2)^{1/2}} \right] ds \quad (5)$$

(* denotes convolution, $H(t)$ is the Heaviside step function).

To evaluate the wavefield u_P at the point of observation P , we have to know both the time derivative $\partial u/\partial t$ and the normal derivative $\partial u/\partial n$ on the boundary S . These derivatives are retarded by the travel time $T=r/c$ from the boundary to P and low-pass filtered.

In the far-field approximation corresponding to Eq. (3a) we replace the terms t and $t+r/c$ by r/c and $2r/c$, respectively, but keep the differences $t-r/c$. This yields

$$u_P(t) = \frac{1}{2\pi} \cdot \int_S \left[(2rc)^{-1/2} \left(\frac{\partial u}{\partial t} \cos \varphi + \frac{\partial u}{\partial n} \cdot c \right) * \frac{H(t-r/c)}{(t-r/c)^{1/2}} \right] ds. \quad (6)$$

To calculate reflections at some point P above a reflector by means of Eq. (6), we identify the closed boundary S with the reflector and complete it with a half circle with radius R to enclose P . The contribution from the half circle cannot be set to zero as $R \rightarrow \infty$ because the term in square brackets of Eq. (6) decays no stronger than $1/R$ and $ds \sim R$. It can be neglected by the argument that this contribution arrives at infinite time.

If the radius of curvature of the reflector is large compared to the dominant wavelength, it is reasonable to approximate the reflected wavefield by use of the reflection coefficient R for plane waves and plane interfaces and the Green's function, Eq. (3a),

$$u = R(\varphi') \cdot \frac{1}{2\pi} \cdot \sqrt{\frac{c}{2r'}} \cdot p(t) * [H(t-r'/c)/\sqrt{t-r'/c}] = R(\varphi') \cdot (r^*)^{-1/2} \cdot f(t-r^*/c), \quad (7)$$

where $p(t)$ is the input wavelet, r' is the distance from the source Q to ds , and r^* the distance from the image source Q^* to ds (Fig. 2). To model a desired output wavelet, it is convenient to define $f(t)$ instead of $p(t)$ in the coding.

Now we can replace $\partial u/\partial n$ and $\partial u/\partial t$ in Eq. (6) by the time derivative \dot{f} and get (neglecting terms of the order $(r^*)^{-3/2}$ in the far field)

$$\frac{\partial u}{\partial n} \approx R(\varphi') \cdot (r^*)^{-1/2} \cdot \dot{f}(t-r^*/c) \cdot (-1/c) \cdot \frac{\partial r^*}{\partial n} = R(\varphi') \cdot (r')^{-1/2} \cdot \dot{f}(t-r'/c) \cdot \cos \varphi'/c, \quad (8a)$$

$$\frac{\partial u}{\partial t} = R(\varphi') \cdot (r^*)^{-1/2} \cdot \dot{f}(t-r^*/c) = R(\varphi') (r')^{-1/2} \cdot \dot{f}(t-r'/c). \quad (8b)$$

We define

$$g(t) = \dot{f}(t) * H(t)/\sqrt{t} \quad (9a)$$

and obtain

$$\dot{f}\left(t - \frac{r'}{c}\right) * \frac{H(t-r/c)}{(t-r/c)^{1/2}} = g\left(t - \frac{r'+r}{c}\right) = g(t) * \delta\left(t - \frac{r'+r}{c}\right). \quad (9b)$$

If we insert Eqs. (8) and (9) into Eq. (6), we come finally to an expression that is appropriate for the numerical calculation of synthetic seismograms

$$u_P(t) = g(t)/[2\pi \cdot (2c)^{1/2}] * J(t), \quad (10)$$

with the impulse seismogram

$$J(t) = \int_S \delta\left(t - \frac{r'+r}{c}\right) \cdot R(\varphi') \cdot (r' \cdot r)^{-1/2} \cdot (\cos \varphi + \cos \varphi') ds.$$

Equation (10) can be interpreted as a mathematical formulation of Huygens' principle: Each segment ds of the reflector contributes one impulse to the impulse seismogram at the receiver. This impulse is delayed by the proper travel time from the source via ds to P and weighted by the reflection

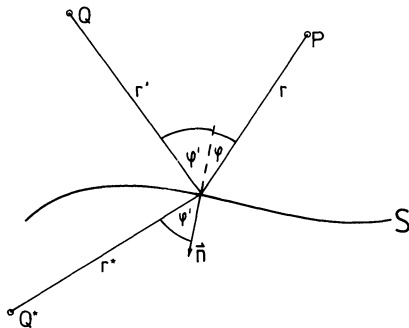


Fig. 2. Source and receiver rays r' and r , and image source ray r^* for a reflector S in a homogeneous medium. Q and P are the positions of source and receiver, Q^* is the image source. \mathbf{n} is the downward-pointing unit normal vector to S

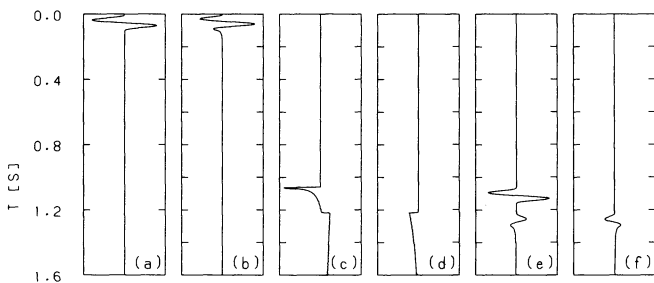


Fig. 3a-f. Example for the different steps in calculating reflections and diffractions from a half-plane by means of Eq. (10). **a** input wavelet $f(t)$; **b** $g(t)$; **c** and **d** impulse seismograms $J(t)$ in the illuminated zone (**c**) and in the shadow zone (**d**); **e** and **f** seismograms obtained by convolving **c** and **d** with **b**

coefficient R , the 2-D spreading term and the so-called Kirchhoff directivity factor ($\cos \varphi + \cos \varphi'$). The impulse seismogram $J(t)$ is the convolved with the function $g(t)$.

This approach includes the contributions from all parts of the reflector, and the seismogram is built up by constructive or destructive interference of the elementary waves. Hence, the Kirchhoff approach is different from ray theory where only the point of specular reflection generates a response.

It should be noted here that Eq. (10) violates the law of reciprocity in cases where one expects it to hold, e.g. in the case where $u_p(t)$ is the vertical displacement due to a vertical single force. The reason is that exchanging the shotpoint and receiver locations will not keep the reflection coefficient the same in Eq. (10). Some attempts to overcome this defect will be discussed later.

For computational purposes, the interface is approximated by straight reflector elements. The sampling has to be fine enough to avoid diffractions from the endpoints. These elements are further subdivided into integration intervals ds which have to be small compared to the wavelength of the incident wave.

Figure 3 illustrates the different steps of the computation for a reflecting/diffracting half-plane from $x = -\infty$ to $x = 0$ km. The source is at $x = 0.0$ km and two receivers are placed at $x = -4.2$ km (illuminated zone) and at $x = 4.2$ km (shadow zone). The velocity is 5.5 km/s. Figure 3a is the input wavelet $f(t)$ and Fig. 3b follows from 3a by Eq. (9a). Figure 3c and d shows the impulse seismograms $J(t)$ if the

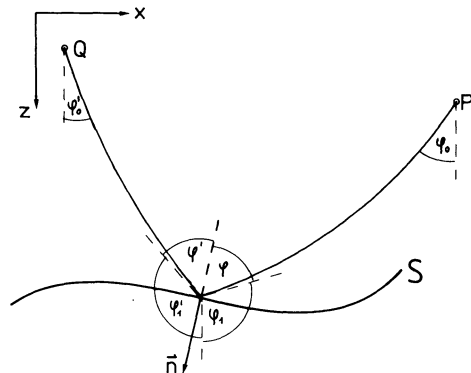


Fig. 4. Ray paths from the source Q to the receiver at P and definition of angles for a reflector below a medium with linear increasing velocity $c = c_0 + az$

receiver lies within the zone of reflection (Fig. 3c) or in the shadow region (Fig. 3d). The reflection arrives at 1.06 s in Fig. 3c and the diffraction arrives in both cases at 1.20 s. Figure 3e and f shows the resulting seismograms obtained by convolving Fig. 3b with Fig. 3c or d. It is evident from Fig. 3c and d that a diffraction changes its sign when the receiver crosses the shadow boundary; this is well known from analytical Kirchhoff diffraction theory (e.g. Hilterman, 1970; Trorey, 1970).

In the case of supercritical reflection ($\varphi' > \varphi_{cr}$), $R(\varphi')$ is complex: $R(\varphi') = R_R(\varphi') + iR_I(\varphi') \cdot \text{sgn } \omega$. In this case the reflection (7) has to be replaced by a linear combination of the input wavelet $f(t)$ and its Hilbert transform $f_H(t)$:

$$u = (r^*)^{-1/2} [R_R(\varphi') \cdot f(t - r^*/c) + R_I(\varphi') \cdot f_H(t - r^*/c)]. \quad (11)$$

The resulting synthetic seismogram is obtained from Eq. (10) by inserting $R_R(\varphi')$ instead of $R(\varphi')$, and adding a similar term that contains $R_I(\varphi')$, and the Hilbert transform $g_H(t)$ instead of $g(t)$. This formulation accounts for the change in the pulse shape with increasing reflection angle $\varphi' > \varphi_{cr}$. It does not include the head wave that will also occur in this case.

The calculation of synthetic seismograms for inhomogeneous media with an equation similar to Eq. (10) requires a large amount of two-point ray tracing to calculate the angles φ and φ' and the travel times T and T' as an equivalent to r/c and r'/c . This has to be done for every integration intervals ds (see Fig. 4 for notation). For this reason, only a special case where the velocity depends linearly on depth, $c = c_0 + az$, has been considered here. In this case the ray paths are circular arcs and can be calculated analytically. The far-field approximation of the Green's function takes the following form in analogy to Eq. (3a):

$$G(S, P) = A(S, P) \cdot \left[\frac{2c(P)}{\pi\omega} \right]^{1/2} \exp \left[-i \left(\omega T - \frac{\pi}{4} \right) \right] \quad (12)$$

where $A(S, P)$ is the amplitude at S of a wave that starts from P , and T is the travel time from P to S :

$$A(S, P) = A_0 \cdot \left[\frac{\rho(P) \cdot c(P)}{\rho(S) \cdot c(S)} \right]^{1/2} \cdot \left[\frac{l_0^2 \cdot \sin \varphi_0}{x \cdot \cos \varphi_1 \cdot |\partial x / \partial \varphi_0|} \right]^{1/2} \quad (13)$$

(Müller, 1977), where A_0 is the amplitude at some reference distance l_0 , ρ is the density and x is the horizontal distance from P to S . For $c=c_0+az$:

$$x = \frac{c_0}{a} \left\{ \cot \varphi_0 \mp \left[\frac{1}{\sin^2 \varphi_0} - \left(\frac{\zeta \cdot a}{c_0} + 1 \right)^2 \right]^{1/2} \right\} \quad (14)$$

where ζ is the vertical distance from P to S ,

$$\frac{\partial x}{\partial \varphi_0} = \frac{c_0}{a \cdot \sin^2 \varphi_0} \cdot \left\{ \pm \cot \varphi_0 \left[\frac{1}{\sin^2 \varphi_0} - \left(\frac{\zeta \cdot a}{c_0} + 1 \right)^2 \right]^{1/2} - 1 \right\}. \quad (14a)$$

Thus plus sign in Eq. (14) and the minus sign in Eq. (14a) have to be taken if the ray has passed its turning point.

The travel time T is

$$T = \frac{1}{a} \left[\ln \left(\tan \frac{\varphi_1}{2} \right) - \ln \left(\tan \left(\frac{\varphi_0}{2} \right) \right) \right]. \quad (15)$$

Inserting Eq. (12) into Eq. (2) and transforming into the time domain gives finally, in analogy to Eq. (10),

$$u_P(t) = \frac{1}{2\pi \cdot \sqrt{2 \cdot c(P)}} \cdot g(t) * J(t)$$

$$J(t) = \int_S \left[\delta(t - (T + T')) \cdot \frac{c(P)}{c(S)} \cdot R(\varphi') \cdot A(S, Q) \cdot A(S, P) \cdot (\cos \varphi + \cos \varphi') \right] ds. \quad (16)$$

T' and $A(S, Q)$ correspond to the ray from Q to S (Fig. 4) and are calculated from expressions analogous to Eqs. (15) and (13), respectively.

Numerical tests

As mentioned before, the approximation of the reflected wavefield above the interface with the aid of the reflection coefficient for plane waves and plane interfaces is valid only if the radius of curvature of the reflector is large compared with the wavelength of the incident wave. The applicability of this approximation to strongly curved reflectors and to diffracting structures has to be tested by comparison with exact numerical methods.

The first example is the SH reflection from a syncline (Fig. 5a). To avoid supercritical reflection in this case, the S velocities were $v_1 = 1.5$ km/s and $v_2 = 1.0$ km/s, and the densities were $\rho_1 = 2$ g/cm³ and $\rho_2 = 1$ g/cm³. The calculations have been performed for a symmetrical split-spread configuration with the shotpoint above the focus of the syncline. Figure 5c shows the result of a FD calculation (Temme, 1984), and Fig. 5b is the same profile calculated by the Kirchhoff method. The results for the reflections and diffractions from the syncline were practically identical, except for small differences in the amplitudes on the near-focus traces.

This model provided a hard test, because two approximations made in the derivation of Eq. (10) are not strictly fulfilled. Firstly, the average depth to the reflector is about 3 times the dominant wavelength and this is not a typical

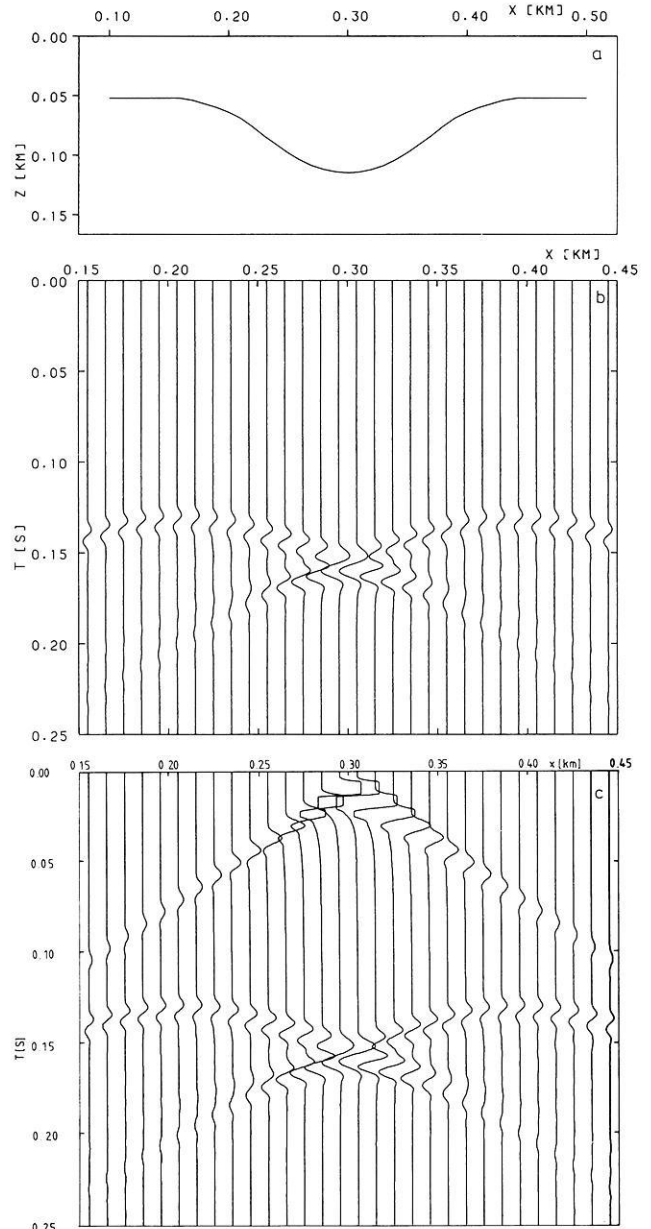


Fig. 5. **a** Syncline model from Temme (1984), the source is at $x=0.3$ km; **b** Single-shot record, calculated by Kirchhoff theory; **c** Single-shot record, calculated by the finite-difference method (from Temme, 1984)

far-field situation. Secondly, the radius of curvature of the syncline is about 80 m, which is less than 3 times the dominant wavelength and so the assumption of Eq. (7) may not be fully justified for this case. The surprisingly good results indicate that the range of applicability is broader than one might initially expect.

The model of the second example is a reflecting and diffracting edge (Fig. 6a). Figure 6b and c shows the SH seismograms for a single shot, calculated by the Kirchhoff (Fig. 6b) and FD methods (Fig. 6c), respectively. The reflection seen between 1.0 and 1.2 s in the left half of the seismogram sections merges with the diffraction at the shadow boundary at $x=1.5$ km. The signal arriving later than 1.7 s in Fig. 6b is a diffraction from the critical point. This phenomenon will be discussed later. The decay of the normal-

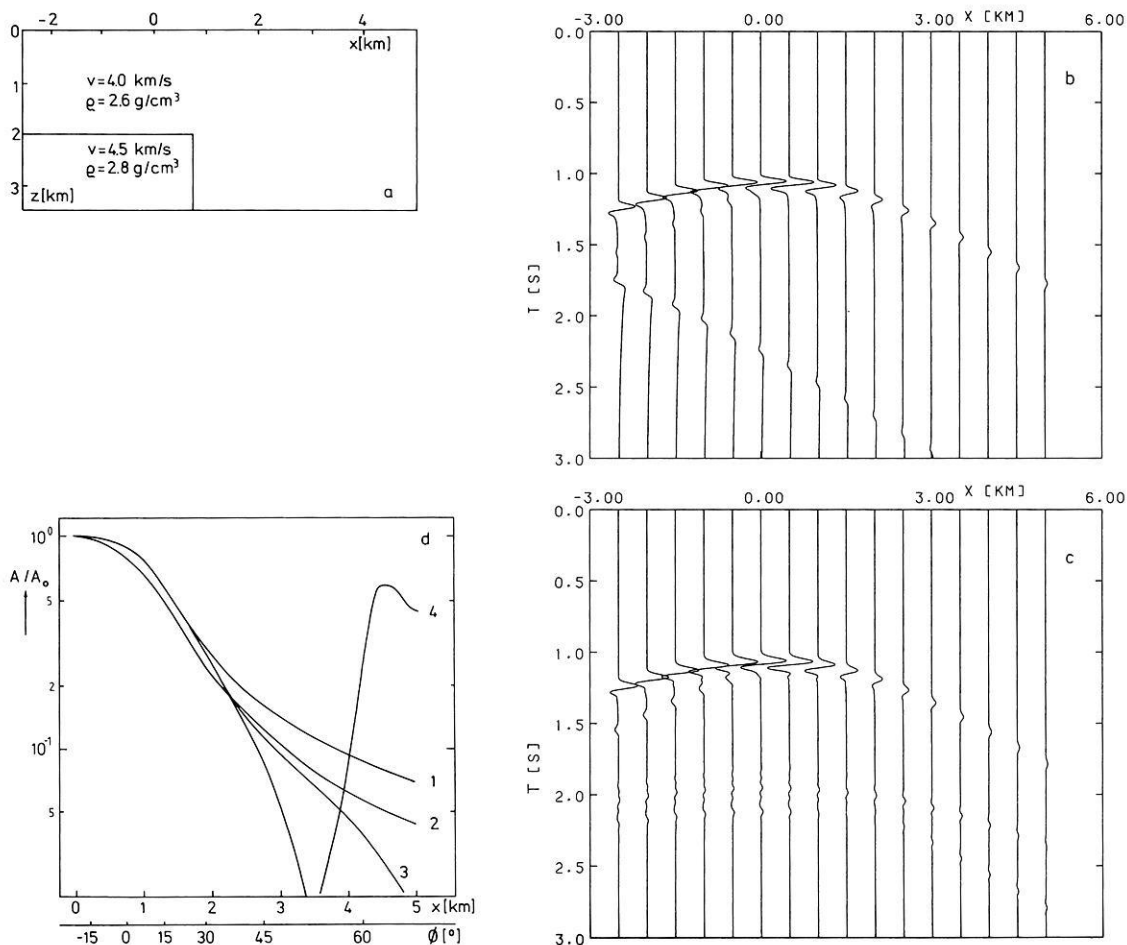


Fig. 6. **a** Reflecting/diffracting edge in a homogeneous medium, the source is at $x=0$ km; **b** Single-shot record, calculated by Kirchhoff theory; **c** Single-shot record, calculated by the finite-difference method. The events at $T > 2$ s are multiple reflections and diffractions, and reflections from the bottom of the model. **d** Normalized reflection/diffraction amplitudes as a function of distance. 1 – Kirchhoff method without reciprocity, $R=R(\varphi')$; 2 – finite-difference method; 3 – Kirchhoff method with reciprocity, $R=R[(\varphi+\varphi')/2]$; 4 – Kirchhoff method with reciprocity, $R=[R(\varphi)+R(\varphi')]/2$. ϕ is the radiation angle from the edge

ized peak-to-peak amplitudes as a function of distance from the diffracting edge is shown in Fig. 6d, lines 1 and 2. For this configuration of source and receivers lying on the same side of the reflecting-diffracting half-plane, Kirchhoff theory gives diffraction amplitudes which are too high compared to the FD method. The errors are tolerable if the radiation angle ϕ at the diffracting edge is not too large, but they reach 50% at $\phi=60^\circ$. They are at least partially caused by the fact that in Kirchhoff theory only the reflected field at the upper side of the reflector is continued upwards, whereas the transmitted field is not considered. The contribution by forward scattering is small at the shadow boundary for reflection, but it increases with increasing distance from the boundary (Fertig and Müller, 1979).

It has been stated above that Eq. (10) violates the law of reciprocity by choosing the reflection coefficient at the angle of incidence φ' . This is of no importance for reflections where $\varphi=\varphi'$, but it may influence diffraction amplitudes. One can enforce reciprocity either by averaging the angles φ and φ' (Deregowski and Brown, 1983) or by averaging the reflection coefficients at φ and φ' (Fertig and Müller, 1979).

Both methods have been tested with the model (Fig. 6d, curves 3 and 4). Calculating the reflection coefficient at

$(\varphi+\varphi')/2$ gives better results for small angles, but for larger angles the magnitude of the errors are comparable to those of the unmodified formula (10). Averaging the reflected wavefields yields large errors in the diffraction amplitudes when ϕ approaches the Brewster angle (here 47.6°) or the critical angle (here 62.7°).

The third example demonstrates the validity of the modification of Eq. (10) by use of Eq. (11). The model consists of a 30-km-thick layer over a halfspace. Again *SH* waves are considered. The *S* velocities are 3.5 km/s in the layer and 4.3 km/s in the halfspace, the densities are 2.8 and 3.3 g/cm³. The Brewster angle, where $R(\varphi)=0$, is reached at a distance $x=61$ km from the shotpoint, and the critical distance is at $x=84$ km. Figure 7a and b shows the seismograms for $x=60$ –160 km, as calculated with the Kirchhoff and reflectivity methods.

Both methods yield practically identical results beyond the critical angle, both in absolute amplitude and in pulse shape. The Kirchhoff method produces significant errors in the amplitude near the critical distance (traces 3 and 4 in Fig. 7a). Due to the very rapid variation of the reflection coefficient near the critical angle, the critical point on the interface acts like a diffractor; note arrivals at 10.8 and 10.2 s on traces 1 and 2 of Fig. 7a and the diffraction hyper-

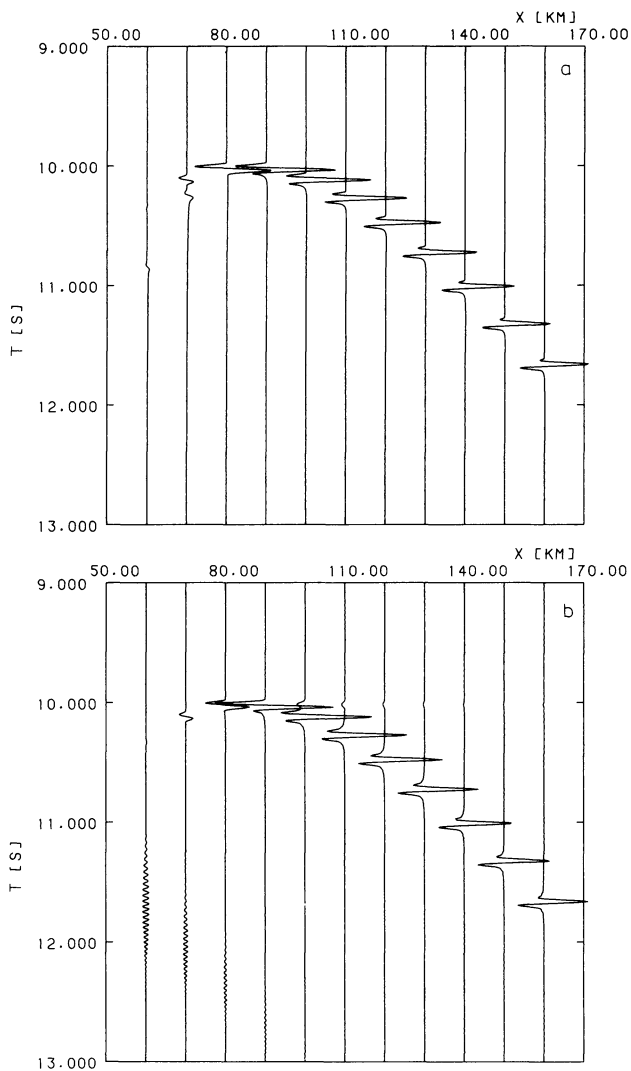


Fig. 7a and b. Single-shot sections for a layer over a halfspace at $z = 30$ km. Time scale is reduced by $v_{red} = 4.3$ km/s. **a** Calculation by Kirchhoff theory; **b** Calculation by the reflectivity method

bola in the left half of Fig. 6b for $t > 1.7$ s. This effect has also been reported by Sen and Frazer (1985). Furthermore, it can be seen in this example that the head wave (weak arrivals at 10 s in Fig. 7b) is not produced by the Kirchhoff method.

These tests show that Kirchhoff theory, in the form presented here, is a reliable method for computing synthetic seismograms for a medium that is bounded at the bottom by an arbitrarily shaped first-order discontinuity. The shortcomings at diffractors and near critical incidence that showed up in the examples must not be taken too seriously, but they should be kept in mind in quantitative interpretations. The computing time depends mainly on the length of the reflector, on the integration interval along this reflector and on the number of receivers per shotpoint. With the model of Fig. 6, the Kirchhoff method was 10 times faster than the FD method. It is an efficient method for simulating recording techniques used in seismic prospecting, such as common-midpoint gathers and zero-offset sections, or even for constructing stacked sections; in these cases, the use of FD methods would often be highly uneconomical. For special problems, the Kirchhoff theory is superior to

ray-theoretical methods because diffractions are calculated kinematically and – to a certain degree – are dynamically correct.

The Kirchhoff theory presented here is used for the case of only one reflector. The extension to a multilayered model requires, in general, the evaluation of manifold integrals along each interface in both reflection and transmission. This would make the method highly time consuming. By introducing a generalized interaction coefficient instead of the plane-wave reflection coefficient, Frazer and Sen (1985) could reduce this case to a single-fold path integral.

Application to seismic data

Diffractions on profile DEKORP2-S?

The deep seismic reflection profile DEKORP2-S (Fig. 8) was observed in 1984. An overview of the measurements, the data processing and a preliminary interpretation are given in DEKORP Research Group (1985). The 250-km-long profile extends from SE to NW in southern Germany and crosses the boundaries between the Variscan units Moldanubian, Saxothuringian and Rhenohercynian. Figure 9 shows a line-drawing of the stacked section, corresponding to the southern part of the time profile north of the Ries crater. [See DEKORP Research Group (1985), Figs. 20–25, for a complete representation of the data.]

As in other deep seismic sounding profiles from the European Variscides (e.g. see Matthews and Cheadle, 1986), the upper crust is nearly void of reflections down to about 5 s TWT. By contrast, the lower crust contains many short and sub-horizontal reflections that terminate at the Moho at about 10 s. The upper mantle is again transparent. This part of the profile is dominated by numerous strongly curved events that can be correlated up to 20 km. They are concentrated around km 40 to km 60 and seem to be arranged more or less vertically between 5 and 10 s. A similar cluster of such curved events is also observed in the northern part of the profile below the Spessart mountains (km 150 to 170). These signals were regarded as diffractions in the first interpretation (DEKORP Research Group, 1985).

Diffractions are well known, in reflection seismics, to occur at faults or pinchouts. However, a critical inspection of these arcuate events on the stacked section indicates that they are different from diffractions in mainly two ways. Firstly, they cannot be interpreted as edge diffractions from a reflector that is ending or offset because the accompanying reflection that has to be expected in this case at the apex of the diffraction, is missing here. Secondly, the amplitude of a diffraction reaches a maximum of half the reflection amplitude at the shadow boundary of reflection and decreases very rapidly as the distance from this point increases (see Fig. 6). By contrast, the curved events on the DEKORP2-S profile are the dominating signals of the section and can be correlated over much longer distances than the sub-horizontal reflections from the lower crust.

For a more detailed investigation, common-shot gathers with diffractions have been studied. Figure 10 shows a shot record from the same region that is represented in Fig. 9. No manipulation like AGC, a time-dependent gain function, or trace equalization has been applied. Some prominent reflection events have been marked by *R*, and diffractions by *D*. The interpretation of these latter events as dif-

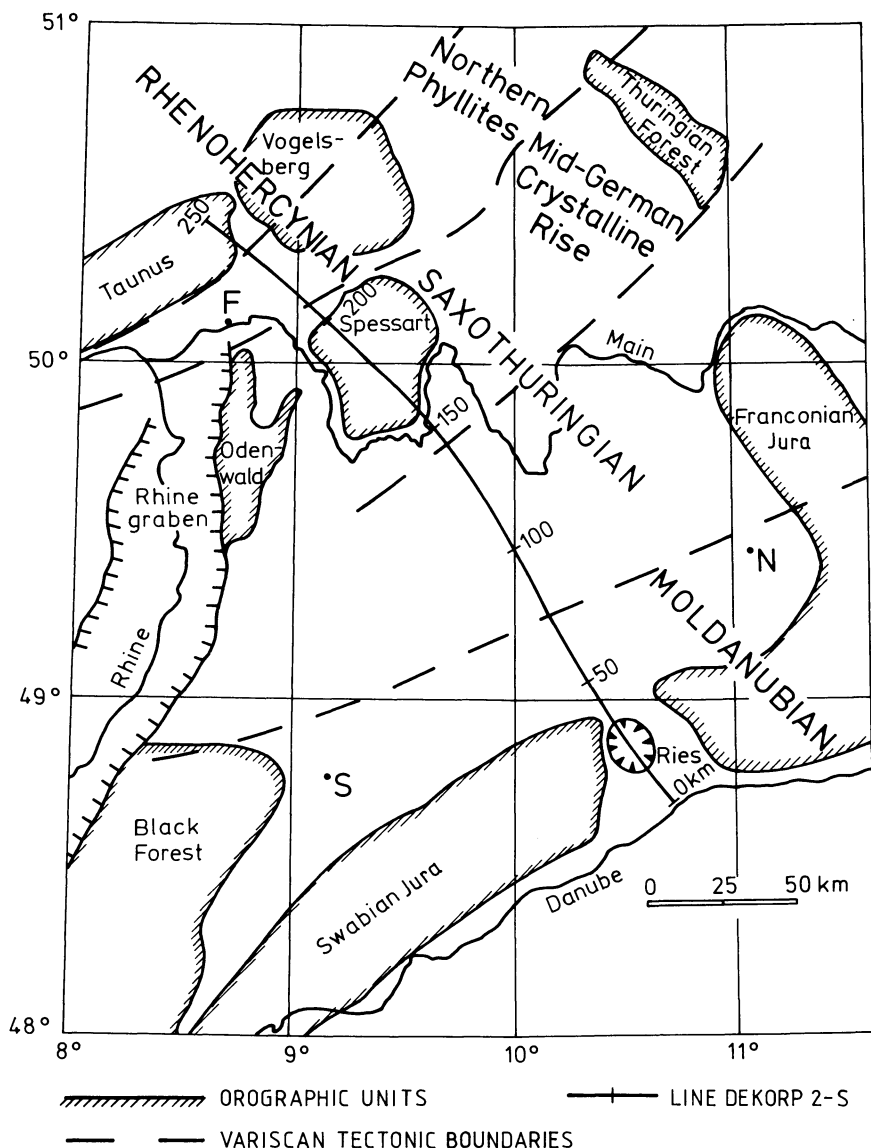


Fig. 8. Location map of the DEKORP2-S profile. F – Frankfurt; S – Stuttgart; N – Nürnberg

fractions follows from a kinematic analysis as demonstrated by Fig. 11. The same event was picked on three different shot records and an attempt was made – after static correction – to fit a diffraction travel-time curve to the three groups of data points. One single point diffractor located at km 55 and at a depth of about 16 km can explain the data very well, even at large offsets. Thus, from travel times alone the diffraction interpretation is well founded. However, it is evident from Fig. 10 that the amplitudes of the so-called diffractions are at least comparable to those of the reflections and that they show no significant decrease in amplitudes along the spread. This is in disagreement with diffraction theory.

Therefore, the diffraction interpretation should be questioned and one should look for alternative subsurface structures. A hint as to where to look comes from the observation that the kinematic analysis yields a rms velocity of 6.4 km/s at 5.5 s TWT, which exceeds the optimum stacking velocity derived from the reflections by almost 20%. Schilt et al. (1981) have reported a similar discrepancy between velocities derived from a diffraction analysis on stacked sections and refraction data in Hardeman County, Texas. They ex-

plain these differences by assuming dome models with a radius of several kilometres instead of point diffractors and have used the velocity differences to estimate their radii. Spherical inhomogeneities lead to over-estimates of the velocity when interpreted as point diffractors on a stacked section, but not on single-shot records, as will be seen later.

Model calculations

Forward modelling of amplitudes can possibly give clearer hints about the nature of the structures responsible for the arcuate events than a purely kinematic analysis.

The amplitudes of a line diffractor and different cylindrically curved reflectors (Fig. 12) have been calculated for a single-shot configuration similar to that of Fig. 10 and have been compared with those of a horizontal reflector with the same impedance contrast. The seismograms have been calculated for the vertical component of the *PP* reflection; the velocity and density contrasts are indicated on Fig. 12. The dominant wavelength of the direct wave is 500 m. Figure 13 shows two examples for these calculations: Fig. 13a is the seismogram section for a line diffractor at $x=0$ km

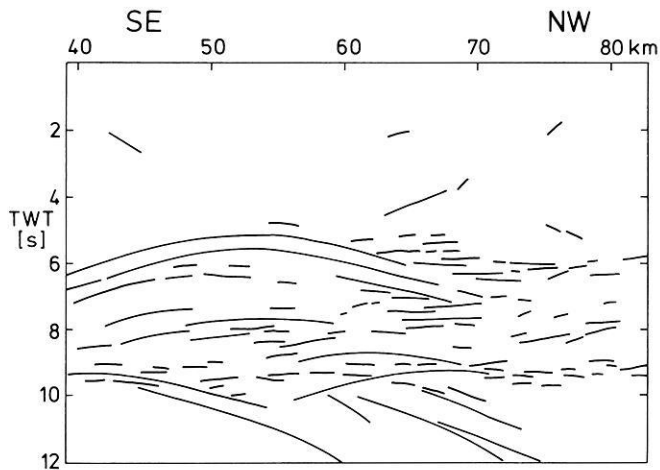


Fig. 9. DEKORP2-S, Dinkelsbühl area; line-drawing, not migrated

and $z=14$ km; Fig. 13b is that of a curved reflector with a radius of curvature of 2 km, i.e. 4 times the dominant wavelength. The centre of curvature is also located at $x=0$ km and $z=14$ km. The source is positioned at the leftmost trace in both cases. The sections have been normalized for plotting purposes, but the amplitudes of the curved reflector exceed those of the diffractor by a factor of 3. It should be noted that the line diffractor in this example is modelled by a strip of half a wavelength width, and not

by an edge as in Fig. 6. Consequently, no phase reversal can be observed in this case.

Figure 13c shows the relative amplitudes along the spread for a horizontal reflector, an edge diffractor, a line diffractor and several curved reflectors with different radii of curvature (given in units of the dominant wavelength). They have been normalized to the vertically incident reflection and, hence, they do not depend significantly on the special velocity and density model. The amplitudes of the strip diffractor (which is, of course, a geologically unreasonable model) are only about 10% of the reflection amplitudes along the whole spread. The amplitudes of the edge diffractor decay very rapidly; they fall to about 50% of the reflection amplitude at the shadow boundary ($x=3$ km), as one expects, and coincide with the curve for the line diffractor at larger offsets. The amplitudes of the curved reflectors fall between the curves of the diffractor and the horizontal reflector, and they also show only a weak dependence on offset. The maximum amplitudes of the diffraction-like events D_1 – D_3 in Fig. 10 are comparable to those of the reflections. They decrease by a factor of about 3 along the spread and not by a factor of 10 or more as the diffraction in Fig. 13c. It follows, therefore, that structures with a radius of at least 6–10 times the dominant wavelength are required to explain these comparatively big amplitudes of the curved events in the data.

The response of curved reflectors of this size can certainly not be called a diffraction because their dimensions are significantly greater than the Fresnel zone, which has a radi-

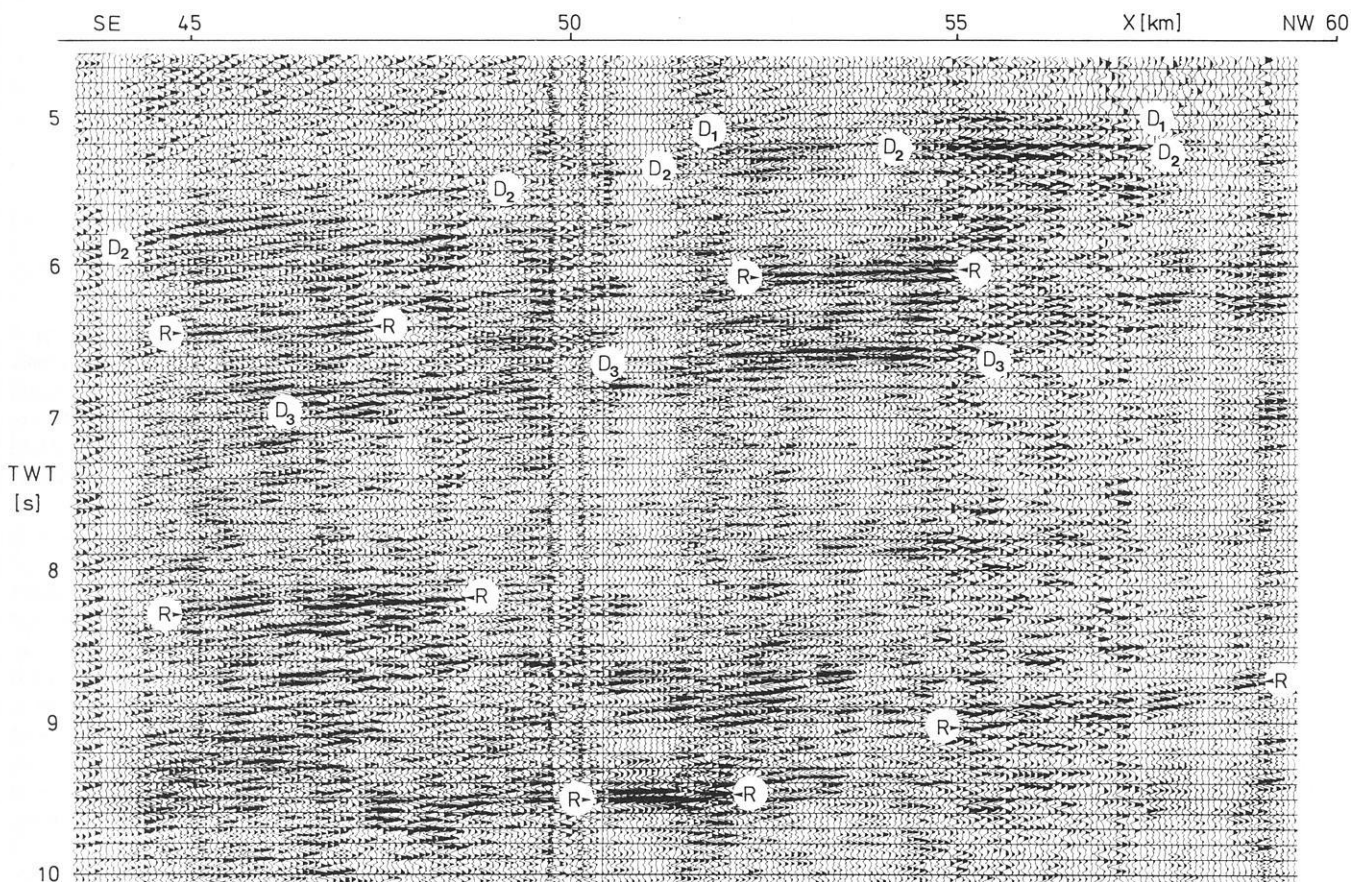


Fig. 10. DEKORP2-S, Dinkelsbühl area; single-shot record (SP 844). R – reflections; D_1 – D_3 – diffraction-like events. The shotpoint is at the NW end of the section

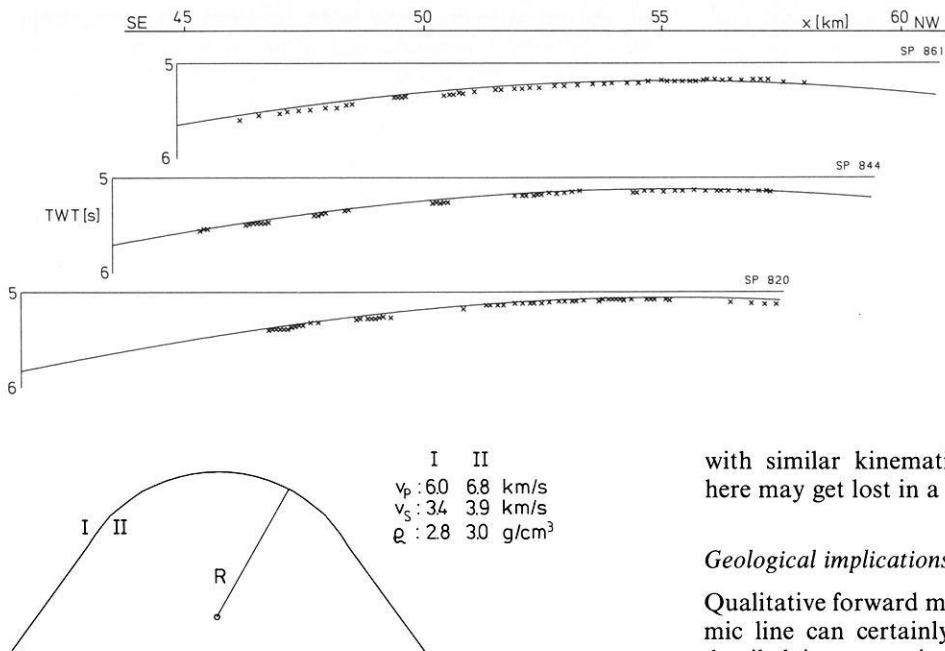


Fig. 12. Diapir-shaped model used for the amplitude calculations of Fig. 13. Depth of centre is $z = 14$ km

us of 1.8 km and, hence, 3–4 wavelengths at this depth [$r_F = (\lambda z/2)^{1/2}$]. Yet, by a purely kinematical analysis these events would be interpreted as diffractions, as can be seen from Fig. 13d. The travel-time curves of the bow-shaped reflectors (solid lines) are practically identical to those of diffractors positioned just at the top of the structures in a medium with the correct velocity, 6.0 km/s. The discrepancies reach a maximum of half a period for $R = 10\lambda$ and large offsets (Fig. 13d, dashed line) and they could easily be explained in real data by residual statics or slight lateral velocity variations.

By contrast to the single-shot records, a travel-time analysis on a zero-offset section would lead to velocities which are systematically too high as already shown by Schilt et al. (1981). For example, a zero-offset section over the reflector with $R = 4\lambda$ (when interpreted with the line diffractor model) gives an erroneous velocity of about 6.3 km/s. The high velocities obtained by a diffraction analysis on single shots from the DEKORP profile (see Fig. 11) cannot yet be explained satisfactorily.

These considerations indicate that the conspicuous curved events, which dominate large parts of profile DEKORP2-S between 5 and 10 s TWT, are not simply diffractions in the usual sense. They can be better explained by strongly curved interfaces in the middle or lower crust. Assuming a velocity of about 6 km/s and a dominant signal frequency of 15–20 Hz for the measurements (DEKORP Research Group, 1985), their radii of curvature can be estimated with the amplitude arguments (see Fig. 13c) to be at least 3–4 km.

One might think that the discrimination between “diffraction” and “reflection” is purely academic in this context. However, once a curved event has been considered as a diffraction, it is often used to obtain velocity information from it. Consequently, a migration process is judged on how good it contracts these events and, hence, structures

Fig. 11. Crosses: arrival times of a diffraction-like event on three shot records. The shot is at the NW end of the spread; the sections are plotted according to their relative position on the profile. Solid lines: travel-time curves for a point diffractor model at $x = 55.1$ km, $z = 16.1$ km and $v_{rms} = 6.4$ km/s

with similar kinematic characteristics to those proposed here may get lost in a subsequent interpretation.

Geological implications

Qualitative forward modelling of certain aspects of one seismic line can certainly not supply a sufficient basis for a detailed interpretation, but it may allow a discussion of the possible origins of this unusual seismic character.

As mentioned previously, the so-called diffraction clusters are concentrated mainly in two regions along profile DEKORP2-S: one south of the boundary between the Saxothuringian and the Moldanubian, and the other in the Mid-German Crystalline Rise (profile km 160 to 180). They are rather uniformly distributed in a limited time interval. Both observations imply that the geological structures responsible for these events are either aligned vertically, or – if one takes three-dimensional effects into account – that they are arranged along a band that strikes approximately normal to the seismic line, i.e. parallel to the Variscan tectonic boundaries.

This seismic pattern can be generated by different geological structures (see also Schilt et al., 1981), for example:

- Igneous intrusions in tectonically active regions
- Antiformal stacks or duplex structures in regions of compressional thrust tectonics
- Undulated or strongly folded interfaces
- Combinations or intermediate stages of these examples

Diffractions generated at faults are caused by an abrupt change in impedance contrast at the end of a reflector. Consequently, they should occur at the termination of a reflection signal. Moreover, their amplitudes decay very rapidly with increasing distance from the edge. There is no evidence for these effects in the data.

Synthetic zero-offset seismograms for a three-dimensional undulated interface have been calculated by Blundell and Raynaud (1986). Their section is qualitatively similar to the stacked DEKORP2-S data in showing many criss-crossing curved events over a certain span of time. But the concentrated appearance of these signals along the profile would require such undulated surfaces to occur only in rather narrow zones with no continuation outside.

The first two examples seem to be more likely candidates for an explanation of the so-called diffractions if one regards the tectonic evolution of the European Variscides. An overview of the Variscan orogenesis in Central Europe is given, for example, by Behr et al. (1984) and Weber (1984), and will therefore only be briefly summarized here.

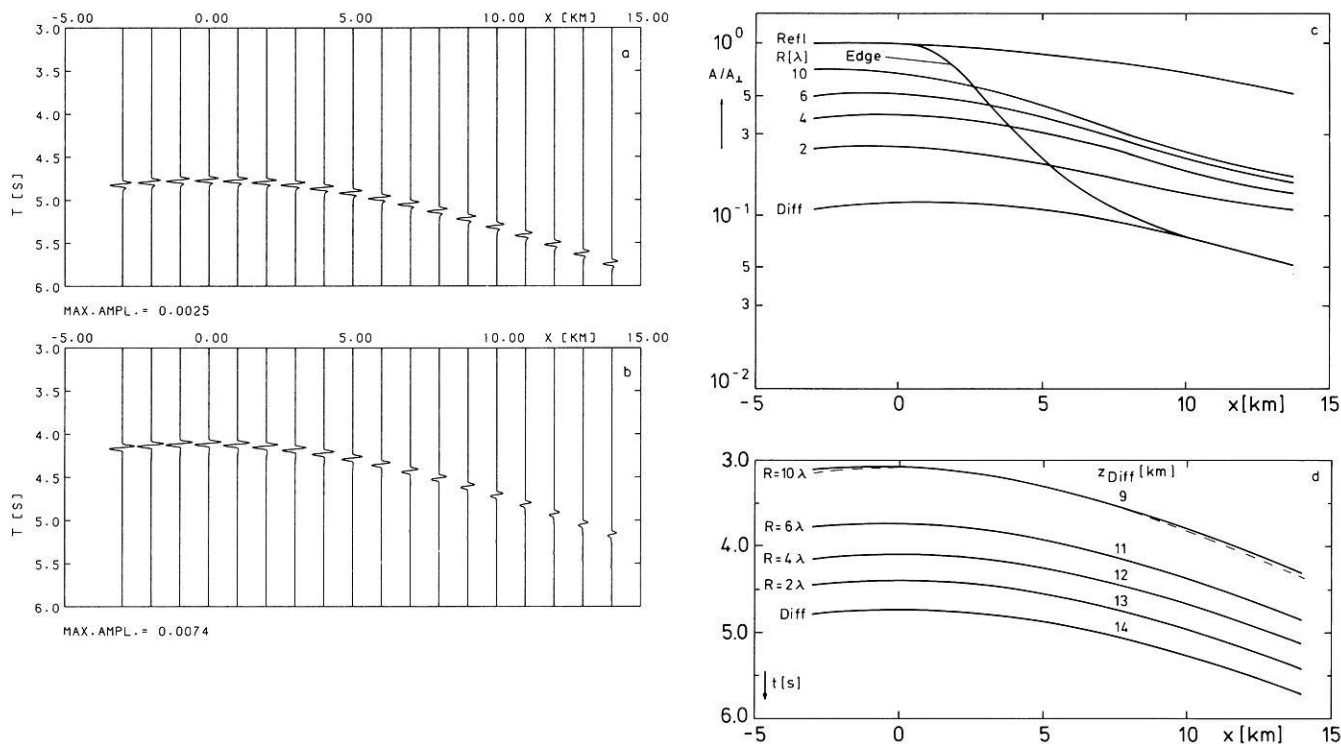


Fig. 13. **a** Response of a line diffractor at $x=0$ km and $z=14$ km. Model parameters as in Fig. 12; **b** Response of a curved reflector with $R=4\lambda=2$ km. Centre of structure at $x=0$ km, $z=14$ km. The source is at $x=-3$ km in both cases; **c** Normalized amplitudes of different models as a function of distance. *Refl* – horizontal reflector; *Edge* – horizontal half-plane; *Diffd* – line diffractor. The figures indicate the radius R of different curved reflector models in units of the wavelength ($\lambda=500$ m); **d** Solid lines: travel-time curves of a diffractor and of several curved reflectors as picked from seismogram sections like *a* and *b*. Numbers labelled z_{Diff} indicate the depth of a point diffractor with approximately the same travel-time curve. Maximum discrepancy between both models is given by the dashed line for $R=10\lambda$.

A rifting phase in the early Paleozoic led to the intrusion of granitic melts into the crust and to the formation of sedimentary basins. This extensional process was followed by compression and crustal shortening in a SE-NW direction from the Lower Devonian to the Upper Carboniferous. A period of folding and medium-pressure high-temperature metamorphism of the early Paleozoic rocks and a subsequent uplift and cooling changed with continuing compression into a more brittle deformation regime. This is indicated by the formation of nappes with a NE transport direction, like the Münchberg Massif in the Saxothuringian of Eastern Bavaria, and by the occurrence of mylonite zones at the northern margin of the Mid-German Crystalline Rise and along the boundary between the Saxothuringian and the Moldanubian in the northern Black Forest and at the Erbdorf line at the western margin of the Bohemian Massif. These zones are probably the surficial indications of deep-reaching SE-dipping fault zones. According to the concept of horizontal thrust and nappe tectonics, the Mid-German Crystalline Rise is thrust northward upon the Northern Phyllites and the Moldanubian has been pushed into the Saxothuringian.

Syn- and late-orogenic granites that are now exposed in the Black Forest, the Odenwald, the Fichtelgebirge and south of the Erbdorf line suggest the intercalation of extensional phases. The Variscan orogenesis ended in the Lower Permian with eruptions of rhyolites and melaphyres, which again indicate the transition to a dilatational stress regime.

This geotectonic environment offers several possibilities for the nature of the structures responsible for the diffraction-like pattern of the seismic observations. Both event clusters lie in or near one of the major SE-dipping fault zones. The SE-dipping reflections between 60 and 80 km and between 2 and 4 s in Fig. 9 can probably be seen in connection with the boundary between the Saxothuringian and the Moldanubian.

Deformation processes at the ramps of these thrust systems may have created horses, antiformal stacks or imbricate zones which should strike approximately parallel to the tectonic boundaries. Such highly inhomogeneous zones can give rise to the complicated seismic pattern if their internal structure provides sufficient impedance contrast.

Diapir-like intrusions, also, can not be excluded. Following the strike of the tectonic boundaries, syn- and late-orogenic granites and/or post-orogenic rhyolites are found to the NE as well as to the SW of both event clusters, e.g. in the Saxothuringian in the Odenwald and the Thuringian Forest, and at the boundary to the Moldanubian in the Black Forest, the Fichtelgebirge and the Oberpfalz.

Igneous intrusions have, in general, no internal structure that could be detected by seismic methods. The approximately vertical alignment of overlapping curved events in the time sections would, in this case, be better explained by a linear arrangement of such bodies with a strike more or less normal to the seismic line. The gravity map of southern Germany (see DEKORP Research Group, 1985, Fig. 5) shows two NE-striking chains of Bouguer minima with am-

plitudes of about 10–20 mGal that cross the profile just at the event clusters. Setto and Meissner (1986) have modelled a 2-D gravity profile along the seismic line by introducing there low-density bodies in the lower crust. This interpretation seems to support the assumption of igneous intrusions. However, the gravity map of southern Germany (DEKORP Research Group, 1985, Fig. 5) suggests that a three-dimensional interpretation is necessary. It is questionable whether the accuracy of the gravity data that are available at present could resolve such small anomalies. For example, a spherical body with a radius of 4 km buried at a depth of 15–20 km and with a density contrast of 0.25 g/cm³ would result in a gravity anomaly of only 1–2 mGal and a half-width of 25–30 km. The gravity pattern may simply reflect the coarse structure of the basement (Edel, 1982) or the NE-striking Permo-Carboniferous troughs in southern Germany.

By using the shotpoints of profile DEKORP2-S and a stationary group of 108 receivers perpendicular to the seismic line at $x=40$ km, a profile P1 could be constructed that runs parallel to the main line at 5 km distance to the east from $x=20$ km to $x=72$ km (DEKORP Research Group, 1985). This profile shows similar clusters of curved events, as in the main profile. When the traces of P1 are plotted at the common midpoints, these clusters seem to be offset to the SE by several kilometres relative to the main profile, but some prominent groups of curved events can still be correlated (DEKORP Research Group, 1985, Fig. 31). However, the close distance between the two profiles does not allow discrimination between the two models proposed here; namely, linear structures like antiformal stacks or diapiric intrusions with a diameter of several kilometres.

Conclusions and discussions

It has been shown that Kirchhoff theory is a valuable and efficient tool in calculating the response of an arbitrarily shaped reflector. It is faster than the finite-difference method and it is, for the purpose of this study, superior to ray-theoretical algorithms because it also includes the generation of diffractions.

This method has been applied to examine some strong diffraction-like events on a deep seismic reflection profile in southern Germany. In order to model the amplitudes of these signals, at least qualitatively, it was necessary to investigate single-shot records because the amplitudes of a stacked section are too strongly distorted by the processing steps involved in stacking. Synthetic seismograms for several dome-shaped models demonstrated that a simple diffractor hypothesis is not able to explain the surprisingly big amplitudes of these arched signals. Instead, one has to assume larger structures in the middle or lower crust with a radius of curvature of at least 3–4 km. Due to the similar travel-time curves of such strongly curved reflectors and diffractors, this result could not have been obtained by a purely kinematic analysis alone.

Whether these structures have approximately spherical upper surfaces, like diapirs, or a mostly two-dimensional geometry, like antiformal stacks, cannot be decided on the basis of the data available.

Two-dimensional theory has been applied to data from a 3-D real world in this study. The difference in the spread-

ing terms ($1/\sqrt{r}$ vs. $1/r$) is not critical and, moreover, it mainly cancels by comparing signals with approximately equal travel times. One should expect, in 3-D theory, slightly different amplitude ratios between the response of a horizontal reflector, diapir-shaped models and point diffractors. In this case the models may have a finite radius of curvature in both x and y directions, and, hence, their defocussing effect will be greater. But this would not affect the main arguments outlined above.

Acknowledgements. This study was financed by the German Ministry of Research and Technology under contract number RG 8702. I am greatly indebted to G. Müller for his help and for many discussions on the subject of this paper. The single-shot data have been provided by the DEKORP Processing Centre, Clausthal, and plotted by Preussag AG, Hannover. I also thank I. Hörnchen for her efficient typing of the manuscript.

References

- Behr, H.-J., Engel, W., Franke, W., Giese, P., Weber, K.: The Variscan Belt in Central Europe: main structures, geodynamic implications, open questions. *Tectonophysics* **109**, 15–49, 1984
- Berryhill, J.R.: Diffraction response for nonzero separation of source and receiver. *Geophysics* **42**(6), 1158–1176, 1977
- Blundell, D.J., Raynaud, B.: Modeling lower crust reflections observed on BIRPS profiles. In: Reflection seismology: a global perspective, Barazangi, M., Brown, L., eds.: pp. 287–295. AGU Geodynamics Series, Vol. 13, Washington D.C., 1986
- Carter, J.A., Frazer, L.N.: A method for modeling reflection data from media with lateral velocity changes. *J. Geophys. Res.* **88**, 6469–6476, 1983
- DEKORP Research Group: First results and preliminary interpretation of deep-reflection seismic recordings along profile DEKORP2-South. *J. Geophys.* **57**, 137–163, 1985
- Deregowski, S.M., Brown, S.M.: A theory of acoustic diffractors applied to 2-D models. *Geophys. Prosp.* **31**, 293–333, 1983
- Edel, J.B.: Le socle varisque de l'Europe moyenne apports du magnétisme et de la gravimétrie. *Sci. Géol. Bull.* **35**, 207–224, 1982
- Fertig, J., Müller, G.: Approximate diffraction theory for transparent half-planes with application to seismic-wave diffraction at coal seams. *J. Geophys.* **46**, 349–367, 1979
- Frazer, L.N., Sen, M.K.: Kirchhoff-Helmholtz reflection seismograms in a laterally inhomogeneous multi-layered elastic medium – I. Theory. *Geophys. J.R. Astron. Soc.* **80**, 121–147, 1985
- Hilterman, F.J.: Three-dimensional seismic modeling. *Geophysics* **35**(6), 1020–1037, 1970
- Hutton, G.D.: The perfectly reflecting wedge used as a control model in seismic diffraction modelling. *Geophys. Prosp.* **35**, 681–699, 1987
- Matthews, D.H., Cheadle, M.J.: Deep reflections from the Caledonides and Variscides west of Britain and comparison with the Himalayas. In: Reflection seismology: a global perspective. Barazangi, M., Brown, L., eds.: pp. 5–19. AGU Geodynamics series, Vol. 13, Washington D.C., 1986
- Müller, G.: Earth-flattening approximation for body waves derived from geometric ray theory – improvements, corrections and range of applicability. *J. Geophys.* **42**, 429–436, 1977
- Schilt, F.W., Kaufman, S., Long, G.H.: A three-dimensional study of seismic diffraction patterns from deep basement sources. *Geophysics* **46**(12), 1673–1683, 1981
- Schneider, W.A.: Integral formulation for migration in two and three dimensions. *Geophysics* **43**, 49–76, 1978
- Sen, K.S., Frazer, L.N.: Kirchhoff-Helmholtz reflection seismograms in a laterally inhomogeneous multi-layered elastic medium – II. Computations. *Geoph. J.R. Astron. Soc.* **82**, 415–437, 1985
- Setto, I., Meissner, R.: Support of gravity modelling for seismic interpretation. *Terra Cognita* **6**, 346, 1986

- Sullivan, M.F., Cohen, J.K.: Prestack Kirchhoff inversion of common-offset data. *Geophysics* **52**(6), 745–754, 1987
- Temme, P.: A comparison of common-midpoint, single-shot, and plane wave depth migration. *Geophysics* **49**, 1896–1907, 1984
- Trorey, A.W.: A simple theory for seismic diffractions. *Geophysics* **35**(5), 762–784, 1970
- Trorey, A.W.: Diffractions for arbitrary source-receiver locations. *Geophysics* **42**(6), 1177–1182, 1977
- Weber, K.: Variscan events: early Palaeozoic continental rift metamorphism and late Palaeozoic crustal shortening. In: *Variscan tectonics of the North Atlantic region*. Hutton, D.H.W., Sanderson, D.J., eds.: pp. 3–22. Special publication of the Geological Society. Oxford: Blackwell, 1984

Received September 8, 1987;
revised version November 2, 1987
Accepted November 4, 1987

Numerical methods for K -scaling from digital data, applied to records from Wingst Observatory

Jürgen Wendt

Institut für Geophysik der Universität Göttingen, Herzberger Landstraße 180, Postfach 2341, D-3400 Göttingen, Federal Republic of Germany

Abstract. Digital recordings obtained by Wingst Observatory for the year 1981 are investigated by methods which are essentially based on the application of numerical filters, in order to derive the non- K -variations and to estimate the K -values of terrestrial magnetism. The best result of the methods presented in this paper is an 81.8% agreement between the K -values estimated from digital recordings and the K -values estimated by an observer using analog recordings of the same time interval. At the same time the derivation of the non- K -variations by this method is attempted in a reasonable way.

Key words: K -values – K -scaling – Handscaled K -values – Digital K -values – K -variations – Non- K -variations

Introduction

The K -index was introduced by Bartels (1938). It should measure the intensity of solar particle (P) radiation effects (called K -variations) at any station for each of the intervals 00–03, 03–06, ..., 21–24 h UT (Bartels, 1957).

Originally the solar particle radiation was not considered to be responsible for a regular variation of the magnetic field. However, after the discovery of the continuous solar wind a regular variation caused by solar particle radiation was found (e.g. Mead, 1964). Therefore, K -variations are defined as the irregular disturbances due to solar particle radiation (Siebert, 1971).

Each station has a K -scale of 10 grades, $K=0-9$, chosen once and for all from a limited number of standard scales. This choice is governed, in general, by the geomagnetic latitude of the station (Bartels, 1957).

In practice, a major difficulty of K -scaling is the elimination of the solar wave (W) radiation effects (called non- K -variations). The non- K -variations can be directly observed in the magnetograms, solely on quiet days. Furthermore, they not only vary with season and sunspot cycle (as well as with the lunar phase), but they may also vary irregularly from day to day, in which case irregular and systematic variations can be of the same order of magnitude (Siebert, 1971). For the derivation of the non- K -variations, an observer is required to make a subjective judgement based on special knowledge of their local shape. Riddick and Stuart (1984) showed that trained observers only reached

an 85% agreement, measuring independently over a 6-month period, using the same records.

A practical procedure for estimating the K -index is “to plot on the magnetogram, for a particular field component and for the 3-h interval considered, two parallel smooth curves representing the non- K -variation, the one touching the actual trace from below, the other one touching it from above: the vertical distance of these two smooth curves, multiplied by the scale-value, gives the range for that field component” (Bartels, 1957). The larger of the two ranges found for the components H and D (or X and Y) is used nowadays to decide on the index K -by means of a quasi-logarithmical scale which is well defined for each observatory. In recent years digital data acquisition has come more and more into use and is now supplementing or replacing the old standard photographic systems at most of the observatories. In connection with that change, certain questions arise. How precisely can the K -values of terrestrial magnetism be estimated when digital data acquisition is used? Can these estimations, which are based on numerical algorithms, be made by computers?

At some digital observatories K -indices are handscaled from digital data (Loomer et al., 1984). Computer methods for obtaining digital K -are described by several authors (Allredge, 1960; Allredge and Saldukas, 1964; Rangarajan and Murty, 1980). Some methods were tested at UK observatories (Riddick and Stuart, 1984). In the following sections, results of K -scaling and deriving non- K -variations for Wingst Observatory are presented and discussed. They have been reached by the max-min method, by numerical filters or by methods which chose the most appropriate filter considering the activity, the season and the eight intervals of the day.

Data sampling

At Wingst magnetic observatory, the components H , D and Z are recorded in analog form and, simultaneously, X , Y and Z are recorded digitally. The digital data have a sampling rate of 1 min; variations with a range of 1000 nT can be recorded with a remaining uncertainty of ± 1 nT (Schulz, 1983). The methods represented were applied to digital records obtained from 349 days of the year 1981. Before applying a method, the digital X and Y values were converted into H and D values. For 14 days no K -values were estimated, as on those days 180 or more minute values were not

recorded. The K -scaling for the first and the last day of 1981, which is possible to a certain degree, has been omitted.

Criteria for the quality of a method

The K -indices which have been estimated by a method are compared to the K -values an observer has found using respective analog records (usual estimation). The agreement reached by a method $U(K)$ for a certain K -value (e.g. $K=3$) is the ratio of the number $A_D(K)$ of correctly estimated values ($K=3$) based on digital records and the number $A_N(K)$ of values ($K=3$) estimated in the usual way:

$$U(K) = \frac{A_D(K)}{A_N(K)}$$

The total agreement reached by a method for all K -values is defined by

$$\sum U(K) = \frac{\sum_{K=0}^9 A_D(K)}{\sum_{K=0}^9 A_N(K)}$$

$U(K)$ and $\sum U(K)$ can both be taken as a measure of agreement. Which one is meant can easily be seen from the context.

A scale for the quality $\sum U(K)$ of a method is the 85% agreement which Riddick and Stuart (1984) discovered analysing values estimated in the usual way by two observers. As a result of the underestimation of the peaks by digital records, the frequency distribution of the digital K -indices should be shifted to smaller values in comparison with the frequency distribution of analog K -values. Besides, the trace of the non- K -variations found numerically should not differ too much from the trace found in the visual way.

Application of the maximum-minimum method

The max-min method has already been applied to UK observatory records (Riddick and Stuart, 1984). Using the max-min method, the maxima and minima of the records are determined for every 3-h interval. The K -values are then estimated from the differences between the maxima and minima of the most disturbed component (Fig. 1). When the max-min method is applied the non- K -variations are not eliminated, so that the K -values estimated this way are higher than handscaled values. Figure 2 shows that K -values higher than 3 can be well estimated by the max-min method. Actually, in the case of very strong magnetic disturbances, the observatories refrain from deriving non- K -variations, which corresponds to an application of the max-min method.

In 1981 a 55.4% agreement was reached for Wingst with the max-min method. Table 1 shows that in the 3-h intervals E3 and E4, when the S_q trace is particularly strong, the agreement is bad; whereas in the intervals E1 and E8, an agreement of more than 80% is reached.

Application of numerical filters

In this paper low-pass trapezoidal filters are used to determine the non- K -variations. The ideal frequency response

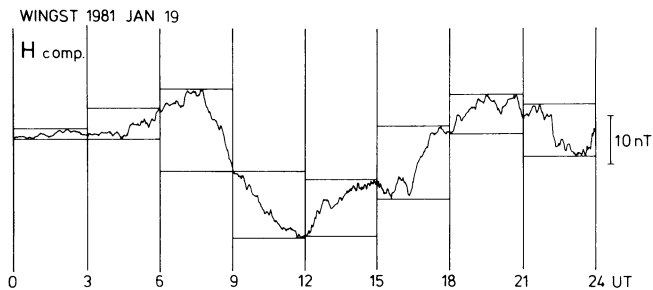


Fig. 1. Application of the max-min method to a recording of the H component

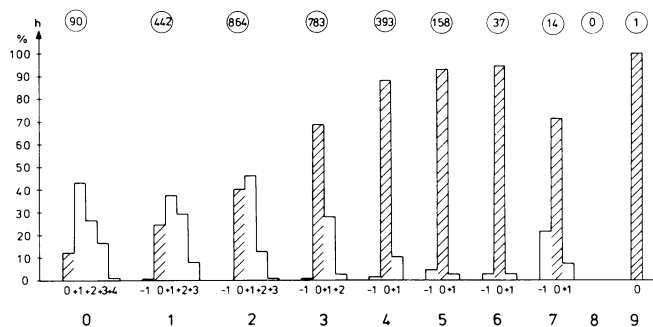


Fig. 2. Comparison between indices found by the max-min method and handscaled K -indices for 2782 3-h intervals in 1981. The numbers in circles are the absolute frequencies of the handscaled values. h shows the relative frequencies with which the numerically scaled values are estimated correctly (0), too small ($-1, -2, \dots$) or too large ($+1, +2, \dots$)

function of a low-pass trapezoidal filter with a cut-off frequency $f_0 = (f_1 + f_2)/2$ is

$$\tilde{w}(f) = \begin{cases} 1 & |f| \leq f_1 \\ (f_2 - f)/(f_2 - f_1) & f_1 \leq |f| \leq f_2 \\ 0 & |f| \geq f_2 \end{cases} \quad (1)$$

The filtering procedure is undertaken in the time domain, the length of the filter being $\tau = 2N \cdot \Delta t$, where Δt is the sampling rate and $N + 1$ is the number of filter coefficients. As the filter length is finite, the frequency response function will generally deviate from the ideal shape described by Eq. (1), especially $\tilde{w}(0) \neq 1$.

Using the additional condition $\tilde{w}(0) = 1$, Schmucker (1978) calculates special filter coefficients which produce trapezoidal filters of almost ideal shape. These filters have a length $\tau = q/f_0$, where q is a positive integer. The quality of the filters is improved with increasing q which, on the other hand, affords a large number of filter coefficients.

The choice of filter parameters f_0 and q depends on the estimated influence of the first four solar and lunar harmonics on the analysis. The amplitudes of these harmonics have already been found by Gupta and Chapman (1968).

Trapezoidal filters of quality $q = 5$ and with cut-off periods of 3–7 h yielded agreements between 70.3% and 80.9% during the seasons JFND, MASO, MJJA and for 1981 (Fig. 3). In all four cases, the best results are obtained with a filter with a cut-off period of $T_0 = 5$ h. However, agreements reached by a filter method differ from season to season, influenced by seasonal changes of activity.

Whereas small values are well estimated by a filter with cut-off period $T_0 = 3$ h, the filter with $T_0 = 5$ h is better for finding large values (Fig. 4). One can generally say that K -

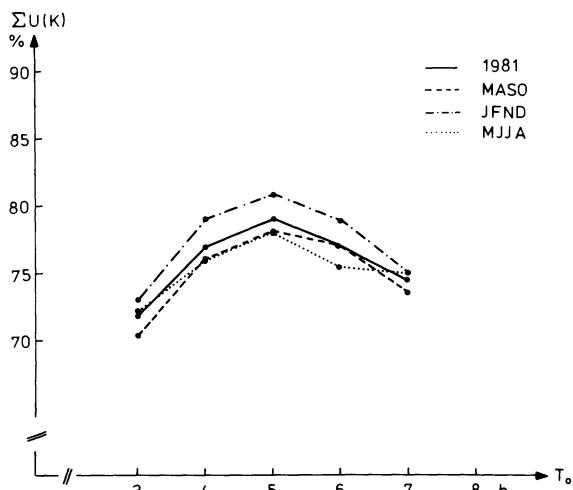


Fig. 3. Agreement between K -values estimated by filters with cut-off periods of 3–7 h and handscaled values for JFND, MASO, MJJA and 1981

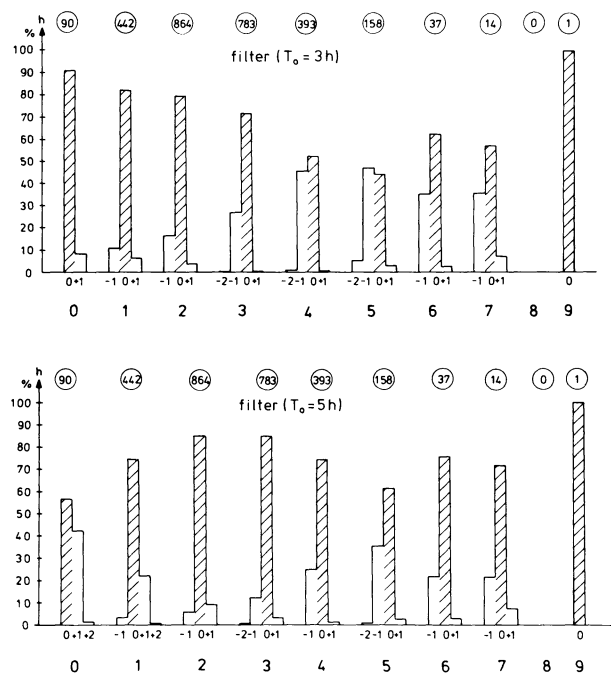


Fig. 4. Results of comparisons between digitally derived indices using a filter with cut-off period $T_0 = 3$ h, and a filter with cut-off period $T_0 = 5$ h, and the handscaled indices for 2782 3-h intervals in 1981

values < 2 , found in the usual way with filters with cut-off periods from $T_0 = 3$ h to $T_0 = 7$ h, are estimated correctly more often if a lower cut-off period is chosen. For K -values > 2 , this is true for larger cut-off periods. The usually scaled values $K = 2$ are found most correctly with a filter with cut-off period $T_0 = 5$ h. Table 1 shows the agreements in the different 3-h intervals which were reached using different filters. The max-min method is understood as a filter with a cut-off period $T_0 \geq 12$ h.

When the activity is low, the filter with cut-off period $T_0 = 3$ h is the best for deriving the non- K -variations (Fig. 5a). For higher activity this is no longer the case (Fig. 5b). The disturbances in the intervals E6, E7 and E8 (there is a loss of data in E5 and at the beginning of E6) are much too closely approached by the trace of the non- K -variations which have been found by the filter. In the process of filtering, both disturbed and undisturbed values are used and, due to the low-pass filter, a smoothing of the record takes place. As long as the parts of the K -variations above and below the trace to be eliminated are approximately the same, a filtering process offers reasonable results. When disturbances occur, e.g. as in interval E8 or especially with bay disturbances, one finds the above-mentioned disagreements between the digitally derived trace and the actual trace of non- K -variations. So the digital method leads to values which are smaller than the real ones.

With longer cut-off periods, the undesired approach is considerably less pronounced (Fig. 6); now one finds a vertical shift between the whole derived trace and the actual trace of the non- K -variations. The shape of the two traces, however, is approximately the same, which is solely decisive for the scaling of K -values.

This means that for the actual derivation: although the phenomenon of the undesired approach cannot be avoided, its effect can be diminished by choosing an appropriate filter. Therefore, the effect of the systematic scaling errors, which is connected with the filtering procedure, depends on the choice of cut-off period. For every activity there can be found an appropriate cut-off period. Therefore, filter methods can be used for K -scaling.

Combination of different filters depending on the time of day or the activity

As filters with different cut-off periods yield variable results for different times of day and with altering activity, one can try to improve the result of the filtering ($\sum U(K) = 79\%$ for 1981, $T_0 = 5$ h) by a skilful combination of several filters. If one uses for each 3-h interval the filter which is empirically found to have the most suitable cut-off period for that time (Table 1), one reaches an 80.4% agreement for 1981. If in

Table 1. Agreements $\sum U(K)$ in the day's eight 3-h intervals reached by several methods in the year 1981 (in %)

Method	T_0 [h]	E ₁	E ₂	E ₃	E ₄	E ₅	E ₆	E ₇	E ₈
Filter	3	68.2	73.9	76.5	72.5	71.1	66.8	69.3	76.2
Filter	4	75.6	78.2	76.8	75.9	77.9	73.4	75.6	82.5
Filter	5	77.1	79.1	77.1	79.4	77.7	77.9	79.4	84.5
Filter	6	75.9	75.1	70.2	76.2	79.4	80.5	75.6	84.8
Filter	7	75.4	71.3	63.6	74.5	73.9	75.1	78.8	84.2
Max-min	≥ 12	82.8	52.7	26.6	17.8	45.8	57.0	75.6	85.1

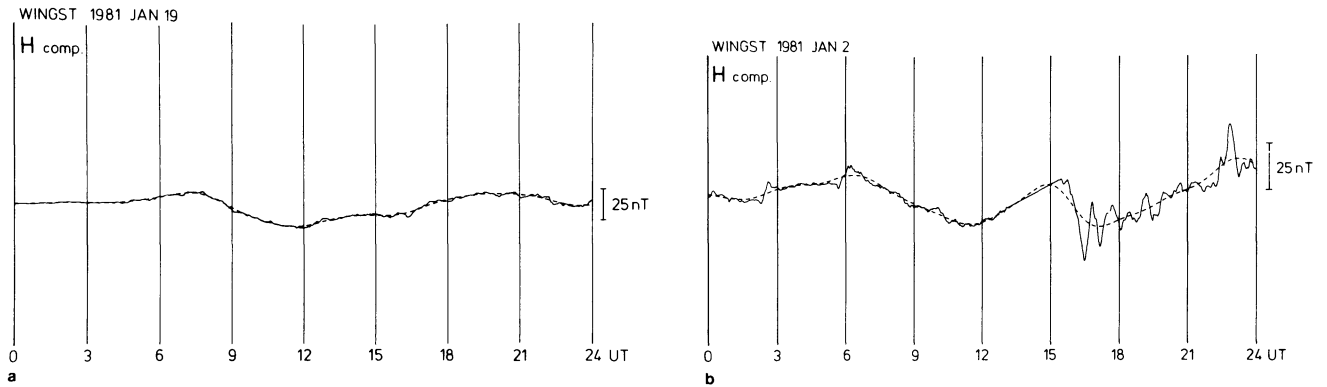


Fig. 5a and b. Application of a filter ($T_0=3$ h) to recordings of the H component. The *dashed lines* show the traces of the non- K -variations which have been found by the filter. **a** The non- K variations are well derived when the activity is low. **b** For higher activity, this is no longer the case

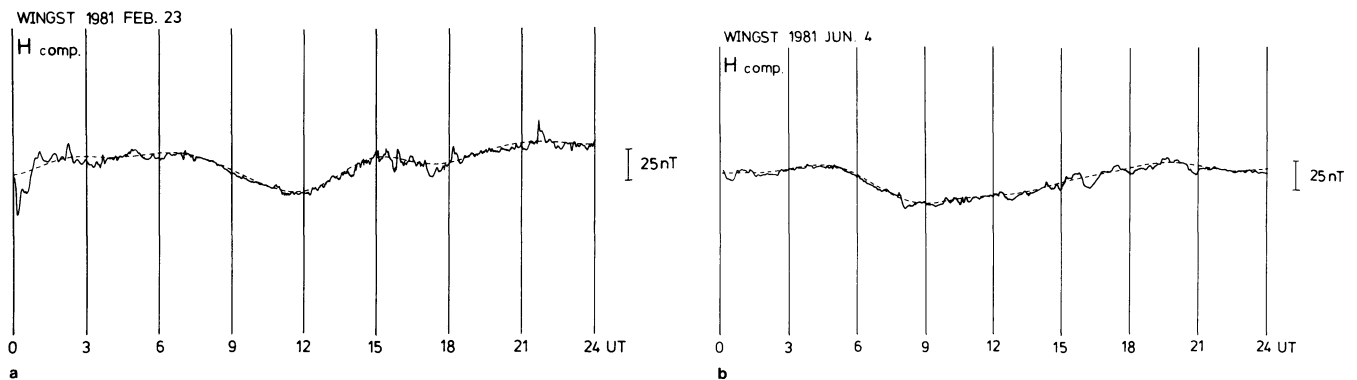


Fig. 6a and b. Application of a filter ($T_0=5$ h) to recordings of the H component. There exists a very good correlation between the derived and actual traces of the non- K -variations, except for a shift of the basis

addition to that one takes the season into account, deciding upon the most appropriate cut-off period, one reaches agreements of 80.5% for JFND, 83.5% for MASO, 79.8% for MJJA, and thus an 81.8% agreement for the year 1981.

The activity is a further criterion for the selection of the method to use. The best results for 1981 in the range $K \leq 1$ were reached by a filter with cut-off period $T_0=4$ h, in the range $3 \leq K \leq 4$ by a filter with $T_0=6$ h and in the range $K \geq 6$ by the max-min method. The first method is used for estimating the values $K=0$ and $K=1$, the second one for the values $K=3$ and $K=4$ and the third method for values $K > 5$. This way, however, there remain some intervals of no particular K -value. They get either the index $K=2$ or $K=5$; K shall equal 2 if the second method has estimated a value $K < 3$ for that interval, and K shall equal 5 if the second method has estimated a value $K > 4$. If there are several indices for one interval, that index is chosen which has been estimated by the second method.

With this combination one reaches an agreement of $\sum U(K)=80.1\%$ for 1981. The computing time of this combination is approximately 3 times longer than that of a filter with cut-off period $T_0=5$ h.

A second procedure takes the activity into account and chooses the method according to the terrestrial magnetic activity in that interval for which the K -value shall be estimated and also in its surrounding intervals. First of all, the filter with $T_0=5$ h is applied. For each interval a sum of five K -values (SK) is formed, consisting of the interval's K -value and the K -values of the two preceding and the

two following intervals. Then, depending on SK , the method of index determination for intervals is chosen. By applying a filter with cut-off period $T_0=4$ h for $SK \leq 11$ and $T_0=6$ h for $11 < SK < 22$ and the max-min method for $SK \geq 22$, an agreement of 80.3% for 1981 has been reached. The computing time of this combination is twice as much as that of a filter with cut-off period $T_0=5$ h.

Discussion and conclusions

The max-min method and numerical filters were applied to digital registrations of Wingst Observatory in order to derive the index K . The use of a filter with a cut-off period of $T_0=5$ h provided the best result; namely a 79% agreement with the usual handscaled values for 1981.

It has been shown that for higher activity the non- K -variations and thus the indices can be derived in a better way by filters with longer cut-off periods because K -variations and non- K -variations cannot be distinguished well when using filters with lower cut-off periods. In the case of lower activity, the non- K -variations and the indices can be found in a better way with filters with lower cut-off periods. This is probably due to the influence of higher solar harmonics which are not suppressed by filters with longer cut-off periods; their existence, however, may – in spite of the low amplitudes – lead to incorrectly estimated values in the case of lower activity. The different results which were reached when methods were used for different times of the day and for changing activity implied the use of criter-

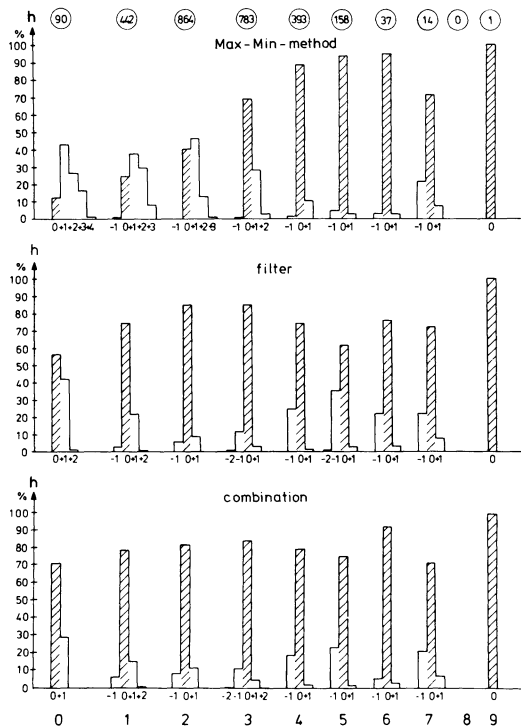


Fig. 7. Results of comparisons between digitally derived indices using the max-min method, the best filter ($T_0 = 5$ h) and one combination (activity) and the handscaled indices for 2782 3-h intervals in 1981

ia considering these influences to choose the most appropriate scaling method. A filter combination which takes the time of day into account had the best result of 81.8% agreement, and a combination which considers the activity reached an 80.3% agreement. Figure 7 shows a comparison between the result of the max-min method, the best result of the filtering procedures and the best result of a filter combination which takes activity into account. Values which are estimated by the max-min method and which are too large compared with handscaled values usually occur in the case of low activity, as there is no elimination of non- K -variations. The incorrectly estimated values of the filter with cut-off period $T_0 = 5$ h, however, are too small (exceptions are, naturally, those values estimated for intervals where a handscaled value yields $K = 0$) and are distributed among all ranges of activity, which is a basic requirement for an acceptable method. Compared to that filter, the combination of methods leads to an improvement in scaling, especially in the case of low ($K < 2$) and high ($K > 4$) activity. Besides, the combination can provide a satisfactory estimation of the non- K -variations.

The mere performance of a filtering procedure needs a lot of computing time. The combinations, which take activity into account, need 2 or 3 times as much computing time as a filtering procedure with a cut-off period $T_0 = 5$ h. Therefore, the practical application of those methods might

exceed the capacity of small computers. However, as the described filters use every minute value for the derivation of the non- K -variations, a lot of computing time could be saved using every tenth minute value.

The methods introduced in this paper yield reasonable results, except the max-min method. It cannot be said which of them is the best. Firstly, the investigated time series was too short; secondly, the results derived for Wingst Observatory might not be reached when applying the methods to other stations. Therefore, for each station it is recommended to test the methods before using one of them for K -scaling.

Similar results can probably be expected by applying the scaling methods to observatories at middle latitudes which have similar amplitudes of solar and lunar harmonics as Wingst. Because of the increase of activity from the equator to the auroral zones, which is considered by a suitable value classification, respectable results can also be expected when filter methods are used at higher latitudes. In the case of larger amplitudes of the solar harmonics, the results for observatories at lower latitudes, however, will certainly be of poorer quality because of the narrow classification.

References

- Allredge, L.R.: A proposed automatic standard magnetic observatory. *J. Geophys. Res.* **65**, 3777–3786, 1960
- Allredge, L.R., Saldukas, I.: An automatic standard magnetic observatory. *J. Geophys. Res.* **69**, 1963–1970, 1964
- Bartels, J.: Potsdamer erdmagnetische Kennziffern, 1. Mitteilung. *Z. Geophys.* **14**, 68–78, 1938
- Bartels, J.: The technique of scaling indices K and Q of geomagnetic activity. *Annals of the IGY* **4**, 215–226, 1957
- Gupta, J.C., Chapman, S.: Manual of the coefficients of the first four harmonics of the solar and lunar daily geomagnetic variations computed from IGY/C and certain other data. **98**, National Center Atmospheric Research, Boulder, Colorado, 1968
- Loomer, E.I., Jansen Van Beek, G., Niblett, E.R.: Derivation of K -indices using magnetograms constructed from digital data. *IAGA News* **22**, 87–90, 1984
- Mead, G.D.: Deformation of the geomagnetic field by the solar wind. *J. Geophys. Res.* **69**, 1181–1195, 1964
- Rangarajan, G.K., Murty, A.V.S.: Scaling K without subjectivity. *IAGA News* **19**, 112–118, 1980
- Riddick, J.C., Stuart, W.F.: The generation of K -indices from digitally recorded magnetic data. In: *Geomagnetic observatory and survey practice*, W.F. Stuart, ed.: pp. 439–456. Dordrecht, Boston 1984
- Schmucker, U.: Auswerteverfahren Göttingen. Protokoll Kolloquium “Elektromagnetische Tiefenforschung”, Neustadt/Weinstraße, 163–188, 1978
- Schulz, G.: Experience with a digitally recording magnetometer system at Wingst Geomagnetic Observatory. *Dt. Hydrogr. Z.* **36**, 173–190, 1983
- Siebert, M.: Maßzahlen der erdmagnetischen Aktivität. In *Handb. der Phys.*, Bd. 49/3, S. Flügge, ed. Berlin-Heidelberg-New York: Springer-Verlag 1971

Received July 9, 1987; revised October 22, 1987
Accepted October 22, 1987

Variation of magnetic properties and oxidation state of titanomagnetites within selected alkali-basalt lava flows of the Eifel-Area, Germany

M. Herzog¹, H. Böhnel¹, H. Kohnen¹, and J.F.W. Negendank²

¹ Institut für Geophysik, Universität Münster, Corrensstr. 24, D-4400 Münster, Federal Republic of Germany

² Abteilung Geologie, Universität Trier, Postfach 3825, D-5500 Trier, Federal Republic of Germany

Abstract. In three lava flows from the Quaternary Eifel volcanic field, magnetic and petrologic properties were studied in four vertical and one horizontal profiles to obtain information concerning magnetic stability and possible effects for the paleomagnetic record in volcanic rocks. Only two of the profiles exhibited marked and correlating trends of high-temperature (HT) oxidation state, natural remanent magnetization (NRM) intensity, magnetic susceptibility and magnetic stability parameters. The variations may be interpreted to depend on the HT oxidation state of the titanomagnetites present in the lavas. In two other profiles, more complex variations of most petrological and magnetic parameters were found, probably due to combined effects of HT oxidation, maghemitization and variations of titanomagnetite volume content and grain size. Although the magnetic stability and dispersion of paleodirections show some relation to HT oxidation state, no evidence was found within a unit for systematic deviations of paleomagnetic directions from the paleofield. An apparent relation between directional trends and petrological and magnetic parameters in one of the lavas is interpreted to be due to viscous deformation or differential movement of parts of this flow as a result of interactions between almost solid and remaining liquid material overflowing it.

Key words: Paleomagnetism – Rockmagnetism – Lava flows – Volcanics – Oxidation state – Magnetic stability – Quaternary – Eifel (Germany)

Introduction

Since the 1950s paleomagnetism has become a tool widely used in geosciences, first in plate tectonics and later in a variety of applications, e.g. concerning the evolution of microplates and orogenic belts. Many results are from volcanic rocks which are thought to be the most reliable recorders of the geomagnetic field, due to the origin and stability of the remanence-carrying oxide minerals.

Present addresses: M. Herzog: Wintershall AG, Friedrich-Ebert-Strasse 160, D-3500 Kassel, Federal Republic of Germany
H. Böhnel: Laboratorio de Paleomagnetismo, Instituto de Geofísica, UNAM, Del. Coyoacan. 04510 México D.F.
H. Kohnen: Alfred Wegener Polarinstitut, Bürgermeister-Schmidt Strasse 20, D-2850 Bremerhaven

Offprint requests to: H. Böhnel

Iron-titanium oxides have been intensely studied to understand remanence origin and stability and the effects of mineral alterations. Most of such studies used laboratory-grown minerals to obtain grains of controlled composition, size and form (e.g. Akimoto et al., 1958; O'Reilly and Banerjee, 1967; Hauptmann, 1974; Levi and Merrill, 1978; Tucker and O'Reilly, 1980; Keefer and Shive, 1981; Özdemir and O'Reilly, 1981, 1982; Nishitani and Kono, 1983; Özdemir, 1987). In other cases minerals were separated from natural rocks and subsequently conveniently prepared (e.g. Dankers, 1978; Harstra, 1982), but only few investigations used the same samples commonly used for paleomagnetic purposes (e.g. Watkins and Haggerty, 1965; Ade-Hall et al., 1968, 1971; Wilson et al., 1968; Grommé et al., 1969; Hargraves and Petersen, 1971; Lawley and Ade-Hall, 1971; Petersen, 1976; Kono, 1987). As reviewed by Moskowitz (1987), studies on synthetic materials show serious and systematic differences concerning even basic properties such as Curie temperature, cell size etc., which may be due to non-ideal starting material used in the experiments as well as to differing methods for evaluation of the experiments. Vincenz (1987) has pointed out that results from natural material diverge even more as its composition and structure apparently disagrees largely from laboratory-grown minerals.

Nevertheless, from the studies cited above, it follows that the magnetic properties of igneous rocks depend on factors such as magma composition, cooling history, reheating, etc. In particular, the high-temperature (deuteric) oxidation of titanomagnetites during the late cooling phase and low-temperature oxidation, which may occur any time later, may influence magnetic properties such as remanence intensity, magnetic susceptibility, Curie temperature, coercivity, and therefore may affect the paleomagnetic record.

High-temperature (HT) oxidation is characterized by a multiphase intergrowth of titanomagnetite (TM) with hemimilmenite or other phases. The development of such microstructures may be responsible for a reduction of the effective grain size, which in turn has effects on intensity of magnetization, coercivity, susceptibility, etc. (e.g. Graham, 1953; Watkins and Haggerty, 1965; Ade-Hall et al., 1968, 1971; Strangway et al., 1968; Larson et al., 1969; Evans and Wayman, 1974; Davis and Evans, 1976; Haggerty, 1976; Price, 1980). Tucker and O'Reilly (1980), on the other hand, ascribe changes of magnetic properties in the course of oxidation to the origin of interlamellar spinel phases, differing in composition from the initial TM and

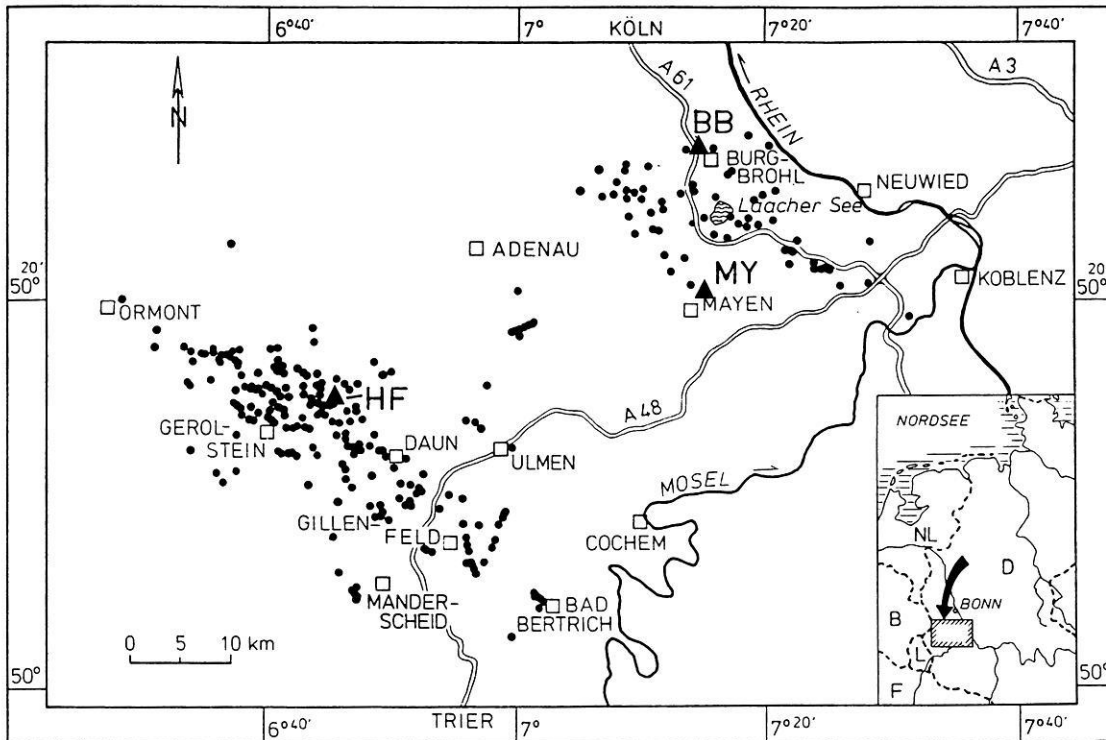


Fig. 1. Eruption centres in the quaternary Eifel area (dots) and the location of the lava flows studied (triangles): BB=Bausenberg, MY=Mayen, HF=Hohenfels/Mühlenberg. Modified from Büchel and Mertes (1982)

in the progressed oxidation states to the development of very fine-grain magnetite in hemoilmenite matrix.

Low-temperature (LT) oxidation (=maghemitization) normally occurs in igneous rocks at temperatures below the Curie temperature of the minerals present, and may proceed by addition of oxygen or by Fe migration out of the grains (e.g. O'Reilly, 1984). In any case, the structure and chemistry of the minerals changes, affecting most magnetic properties and, under certain conditions, the direction of remanent magnetization (e.g. Johnson and Merrill, 1972, 1974; Merrill, 1975; Petersen et al., 1979; Heider and Dunlop, 1987; Smith, 1987).

In an attempt to obtain data from material as used for standard paleomagnetic work, selected igneous rock lava suites from the Quaternary Eifel area (Fig. 1) were studied for their paleomagnetic, rock magnetic and opaque petrological properties.

Field and laboratory procedures

Samples were taken with a gasoline-powered corer at spacings of approximately 0.5 m on the vertical profiles and about 2.0 m on the horizontal profile and later cut into 25-mm-long specimens. A Digico magnetometer (Molynex, 1971) served to determine intensity and direction of magnetization, a low-field susceptibility bridge (Bison 3101A) to measure initial magnetic susceptibility. Specimens were stepwise alternating-field (*af*) demagnetized using a two-axis tumbler. Magnetic stability was investigated by applying different stability criteria: median destructive field (MDF); S_{200} (Wilson et al., 1968), considering directional stability as well as intensity variations; PSI (Symons

and Stupavsky, 1974), giving information only about directional changes. Additionally, difference vector variations (Hoffman and Day, 1978) were analysed to look for stable directional endpoints.

The magnetic minerals, and their oxidation states, were identified by reflected light microscopy. Oxidation number M_{ox} was determined as described by Negendank (1972), using the classification scheme of Wilson and Haggerty (1966) and Ade-Hall et al. (1968); mean overall grain size was obtained using the counting method proposed by Wilson et al. (1968).

Specimens from the Hohenfels lava showed trends of remanent magnetization directions and rock-magnetic parameters along the vertical profile and were subjected to additional experiments to explain this observation: thermomagnetic curves were obtained with a horizontal magnetic balance (e.g. see Collinson, 1983) in fields of ca. 180 kA/m (≈ 240 mT); to reduce chemical alteration during the experiment, the sample region was continuously flooded by Ar gas; heating and cooling rate was 40° C/min, with maximum temperature errors during the whole cycle of about 10° C. Anisotropy of magnetic susceptibility was determined with a KLY-2 bridge, and high- and low-temperature variation of a strong artificial isothermal remanent magnetization (IRM) with a modified Digico magnetometer. The ore petrology was completed by scanning electron microscopy (SEM) using the backscattered electron method, which also allows semi-quantitative analyses of oxides and silicates, and, for selected specimens, by microprobe analysis of the titanomagnetites. Facilities for most of these measurements were available only after 1982, resulting in a delay of this study which had started in 1977.

The lava flows

The Eifel region comprises a Tertiary and a Quaternary lava suite. Figure 1 shows the distribution of Quaternary eruption centres and the location of the three lava flows studied for this paper, which are all of Upper Brunhes age.

From the Bausenberg (BB) volcano a basanitic lava flow extends about 4 km eastwards, comfortably exposed along a road cut, transecting almost perpendicular to the flow direction. At this exposure the flow thickness varies between 10 and 12 m, but the base was not accessible for sampling. Samples were taken near the flow base along a 200-m-wide horizontal profile on the eastern part of the exposure, at 9–10 m below the top of the flow. Two vertical profiles (total lateral spacing 2 m) were sampled at 0.2–9.9 m and 0.2–8.6 m below the top, respectively, separated about 50 m by the highway.

The Mayen lava flow (MY) is a leucite-nephelinite tephrite and has a thickness of about 15–25 m. The flow extends from the Ettringer Bellerberg about 3 km southward with lateral dimensions between 1.0 and 1.5 km. Samples were taken in two vertical sections with a lateral offset of about 8.0 m, covering a total vertical distance of 12.5 m.

The Hohenfels lava (HF) is one of the largest basalt lava occurrences in the Eifel (Fig. 2) with a thickness of around 10 m. Three quarries permit observations of lateral and vertical variations. In the northern part the melilite-nephelinite lava formed at the base a 1-m-thick layer of a dense rock with horizontal laminae, upwards followed by a 4- to 5-m-thick porous lava of 5- to 10-cm-thick laminae, inclined up to 30°. In this layer lava pillars with diameters up to 3 m are found, in contrast to the uppermost part with smaller vertically oriented pillars and no lamination.

In the southern part the lava flow shows a subdivision into a lower porous lava with partly inclined laminae, similar to the situation in the north, and an upper layer without stratification. The subdivision of the lava is pronounced by the orientation and diameter of the pillars being smaller in the lower part. Around the sampling location (Fig. 2) the orientation of the lava pillars beneath the transition zone is not vertical but protruding, suggesting a lava flow in a highly viscous state at the end of the lava cooling process. Possibly this can be explained by a late lava supply, not at the top but in the centre or lower part of the flow. In the southeast a contact between two lavas can be observed, leading to the idea that lava at first flowed to the southeast, forming a barrier for a subsequent erupting lava therefore extending more to the north. An alternative explanation would be the flow of viscous lava over irregular topography.

In conclusion from the field observations, probably the first lava outflow was in a southeastern direction until it formed a barrier. Subsequently delivered material resulted in an irregular flow and led to the deformation of the underlying and largely quenched but still viscous lava. Even a differential tilting of already solid parts may have occurred. Such deformations surely would have depended on factors such as lava thickness, temperature, degassing state, ground subsidence, etc. and, therefore, widely on the morphology of the flow basement. This could explain the varying lamination of the lower lava layer.

For the present study, samples were obtained from an inclined profile situated in the southern part of the complex

Geological map of Hohenfels region

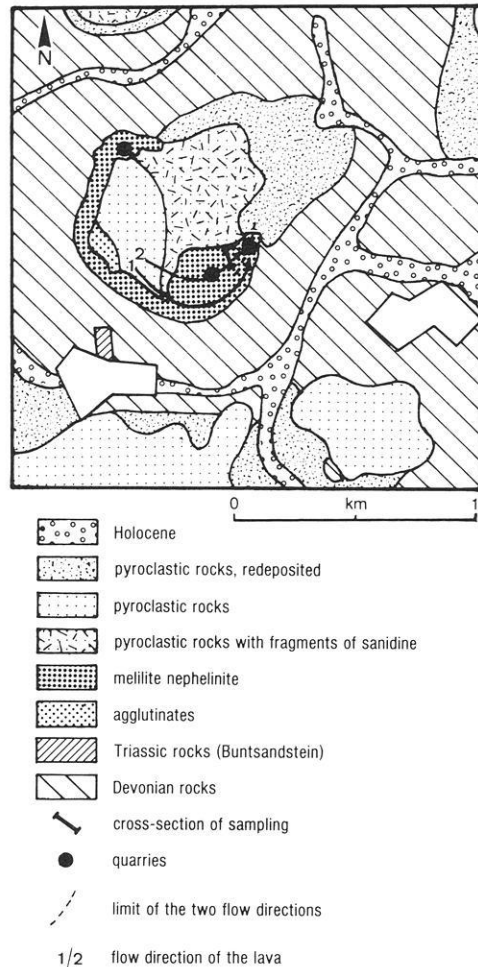


Fig. 2. Geology of Hohenfels lava flow according to Rahm (1956)

(Fig. 2), intersecting both layers over a vertical distance of about 9.7 m, and a horizontal distance of about 20.0 m. During the first field campaign in 1977 the extension of the quarries was neither big enough to give insight into the situation explained above, nor was sufficient attention paid to the uncommon lava pillar formation. A second sampling was performed in 1982, including more detailed field work in the meanwhile extended quarries, to explain the data obtained previously. Unfortunately, the quarried area had meanwhile been much extended and the lower section of the first profile had partly disappeared. The additional samples therefore are from a profile up to 10 m from the original one.

Results

Common to all lava flows studied is the dominance of titanomagnetites and their oxidation products. Besides HT oxidation, maghemitization mainly of low to intermediate degree was observed in 17% (BB-east) to 80% (HF) of the samples. Granulation was restricted to the BB-west and BB-horizontal profiles and occurred in about half of the samples. According to the age of the rocks and in contrast to the evidence cited by Ade-Hall et al. (1968, 1971), granulation here must have originated in a relatively short time

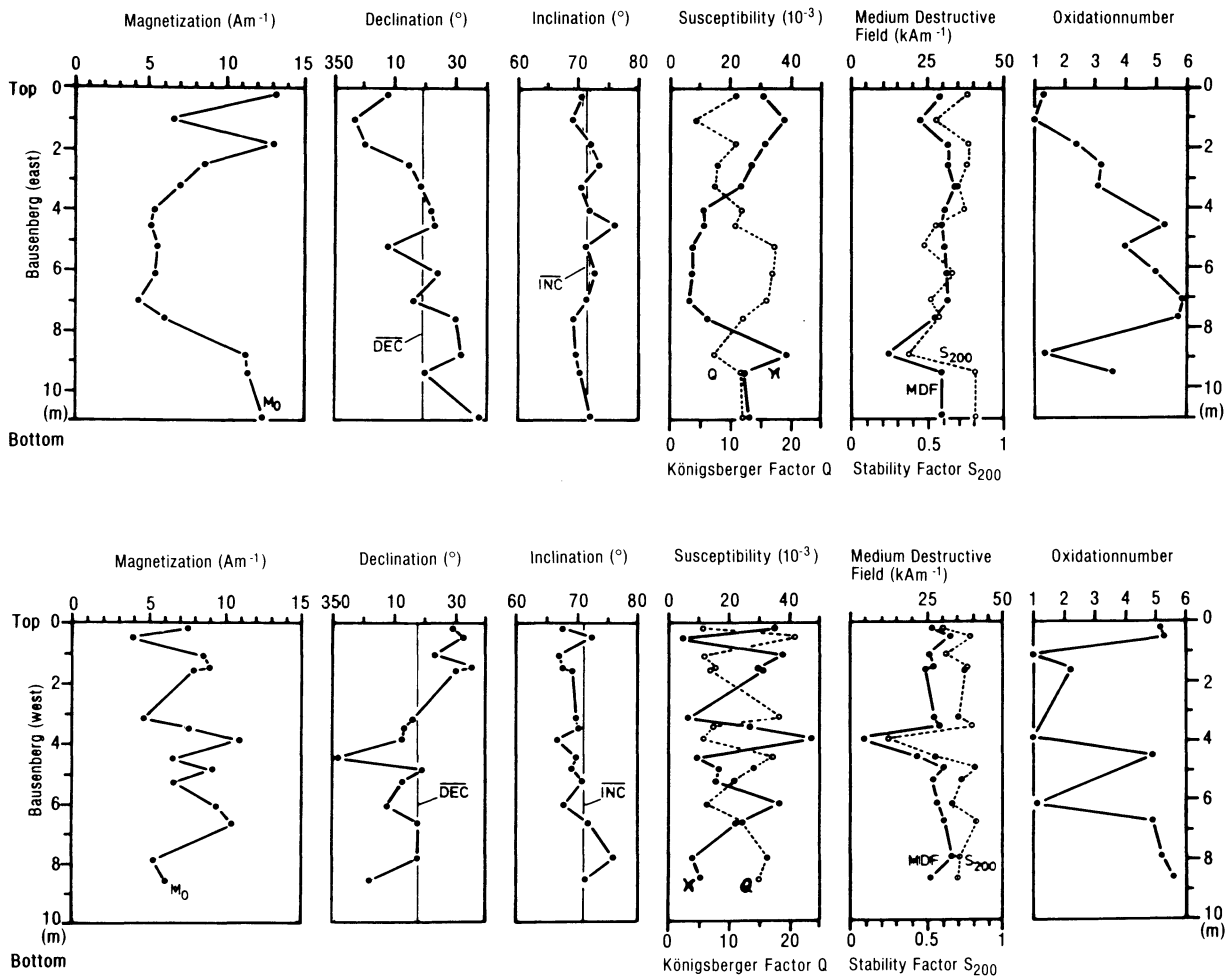


Fig. 3. Variation of magnetic and petrological parameters in vertical profiles of Bausenberg lava flow. See text for further explanations

span and without burial or substantial reheating of the flows.

Most TM had idiomorphic to hypidiomorphic habits. The volume content was rather similar for samples from BB-east, BB-horizontal, MY and HF, with means of $3.5\% \pm 0.4\%$ ($n=12$), $3.8\% \pm 1.2\%$ ($n=3$), $3.4\% \pm 0.6\%$ ($n=5$) and $4.1\% \pm 0.9\%$ ($n=3$), respectively. For most of these samples, mean overall grain size was determined, yielding values of $1.9 \pm 0.3 \mu\text{m}$ to $4.7 \pm 0.8 \mu\text{m}$, which indicates single-domain (SD) and pseudo-SD particles as remanence carriers. No obvious trend of volume content and grain size was observed in any of the profiles studied.

Bausenberg and Mayen lava flows, vertical profiles

Figures 3 and 4 show the variation of paleomagnetic, petrological and rock magnetic parameters with the vertical position of the samples in the BB and MY lava flows.

The Bausenberg East profile exhibits similar trends for natural remanent magnetization (NRM) intensity and susceptibility, changing from high values near the top to lower values in the middle part and again high values approaching the base of the flow. In the Mayen lava a similar trend is visible but no increase of NRM intensity and susceptibility is seen towards the bottom of this profile, probably be-

cause the flow base is still several metres downwards. Intensity and susceptibility variations in these flows correspond to results, e.g., of Petersen (1976). In contrast, NRM intensity and susceptibility in the Bausenberg West profile exhibit irregular, though correlating, variations with depth.

Compared with NRM intensity and susceptibility, the HT oxidation number shows a reversed trend in BB-east and MY, with low values at the top and bottom of the profile and high values in the middle part. Watkins and Haggerty (1965) and Wilson et al. (1968) observed similar variations but, in contrast to our data, a strong correlation of NRM intensity and oxidation state. BB-west lava shows a contrary oxidation trend with high values at the upper and lower margin and low values in the central part of the flow; such variations are in accordance with data obtained by Hargraves and Petersen (1971) and Lawley and Ade-Hall (1971). Vertical variations of the stability parameters Q, MDF and S_{200} (Figs. 3 and 4) show similar trends but no obvious relation with other parameters.

Directions exhibited small variations along the profiles, resulting in parameters k and α_{95} of 111–397 and 1.4° – 2.5° , respectively (considering all samples of a flow, even outliers). Minor apparent trends of declination with depth are not really important in view of inclinations $> 70^\circ$. Inclinations showed only small and statistical variations along the profiles.

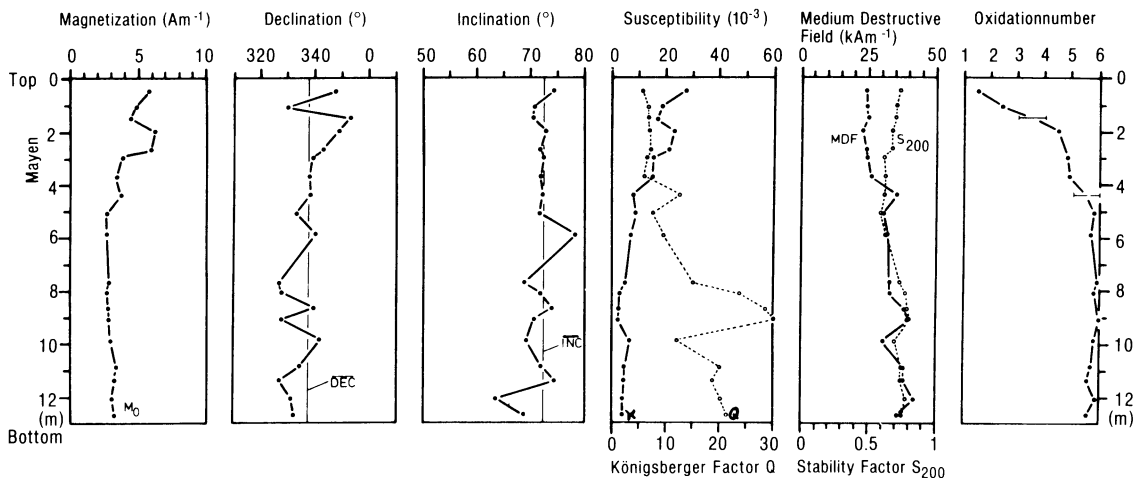


Fig. 4. Variation of magnetic and petrological parameters in a vertical profile of Mayen lava flow. See text for further explanations

Bausenberg, horizontal profile

Along the 225-m profile oxidation state varies largely, showing low values beneath the northern margin and several maxima and minima southwards (Fig. 5). No evident relation is observed with NRM intensity; however, susceptibility exhibits a negative correlation and the stability parameters Q , MDF and S_{200} a positive correlation with oxidation number.

Preliminarily, we may conclude that the four profiles show considerable and partly contrasting variations of most parameters. In some cases a correlation is probable between petrological and magnetic parameters. In particular, this may hold for the profiles BB-east and MY which exhibit similar and marked vertical variations of oxidation degree, NRM intensity M_0 , susceptibility χ , with smaller variations of stability parameters. The correlation between oxidation state and M_0 and χ may be due to the increasing replacement of initial TM by less-magnetic and non-magnetic phases with increasing oxidation (e.g. Tucker and O'Reilly, 1980). Alternatively, the correlation may be accidental and the variations of M_0 and χ reflect variations of the volume content of TM. Besides the parallel trend of M_0 and χ , this interpretation is supported by the rather constant coercivity, given by MDF and S_{200} , which is thought to change during HT oxidation (e.g. Strangway et al., 1968; Lawley and Ade-Hall, 1971; Tucker and O'Reilly, 1980). As we have no TM volume content determinations from BB-east, the situation remains unclear. From the MY profile five evenly spaced determinations pointed to nearly constant TM volume content, 3.4 ± 0.6 vol%, favouring the hypothesis of an oxidation related variation of NRM intensity and susceptibility.

Profiles BB-west and BB-horizontal showed much more complex variations of most parameters. This may be due to combined changes of HT oxidation, TM grain size, TM volume content and LT oxidation, which were not determined in sufficient detail.

Hohenfels, vertical profile

The results from the Hohenfels profile exhibit a drastic change of most rock magnetic parameters at about 6 m below the top of the lava (Fig. 6). This level coincides with

the transition from the "normal" upper part to the lower layer of porous lava with inclined laminae, and with a marked change of the HT oxidation state of the TM. Highly oxidized phases ($M_{ox} = 5-6$) were found in the upper part of the flow, coinciding with low values of NRM intensity and susceptibility, but high values of the Königsberger factor, MDF, and S_{200} . On the other hand, the bottom part showed low HT oxidation state ($M_{ox} = 1$), obviously causing reversed behaviour of the magnetic properties. The most interesting fact is that here, in contrast to the other lava flows, the paleodirections exhibited a strong trend which cannot be explained only in terms of scatter (Fig. 6). One might argue that these abnormal directions could be due to uncleaned secondary components present in the corresponding specimens. From Fig. 7 it can be demonstrated that this is not the case. Although we admit that the specimens exhibited low coercivities (MDF had values of 3-7 kA/m), the directional behaviour during the demagnetization procedure was univectorial or nearly so, leading to reasonably well-defined characteristic remanence directions.

In the lower part of the flow, most of the non-oxidized titanomagnetites are altered to maghemite at a moderate to high degree which may reduce magnetic stability (e.g. Akimoto and Kushiro, 1969; Merrill, 1975; Manson et al., 1979; Smith, 1987). Ellwood (1981), however, did not find any variability of intensity and directions in magnetically cleaned maghemitized samples compared with unaltered material. Prévot et al. (1981) found a strong dependence of magnetic properties on the grain size in maghemitized rocks, affecting susceptibility, Q factor and coercivity. According to these and other authors (e.g. Johnson and Merrill, 1972, 1974; Merrill, 1975; Heider and Dunlop, 1987), multi-domain TM may acquire a chemical remanent magnetization (CRM) during maghemitization. Since the bottom part contained a fraction of multi-domain grains, theoretically a CRM could have developed here, accounting for the large directional change. Considering the gradual directional change in the profile, this explanation could only be valid if the maghemitization protruded from the transitional zone downwards to produce a CRM recording a period of largely increased secular variation of the geomagnetic field. We regard this possibility as highly improbable.

Further magnetic properties were studied to look for

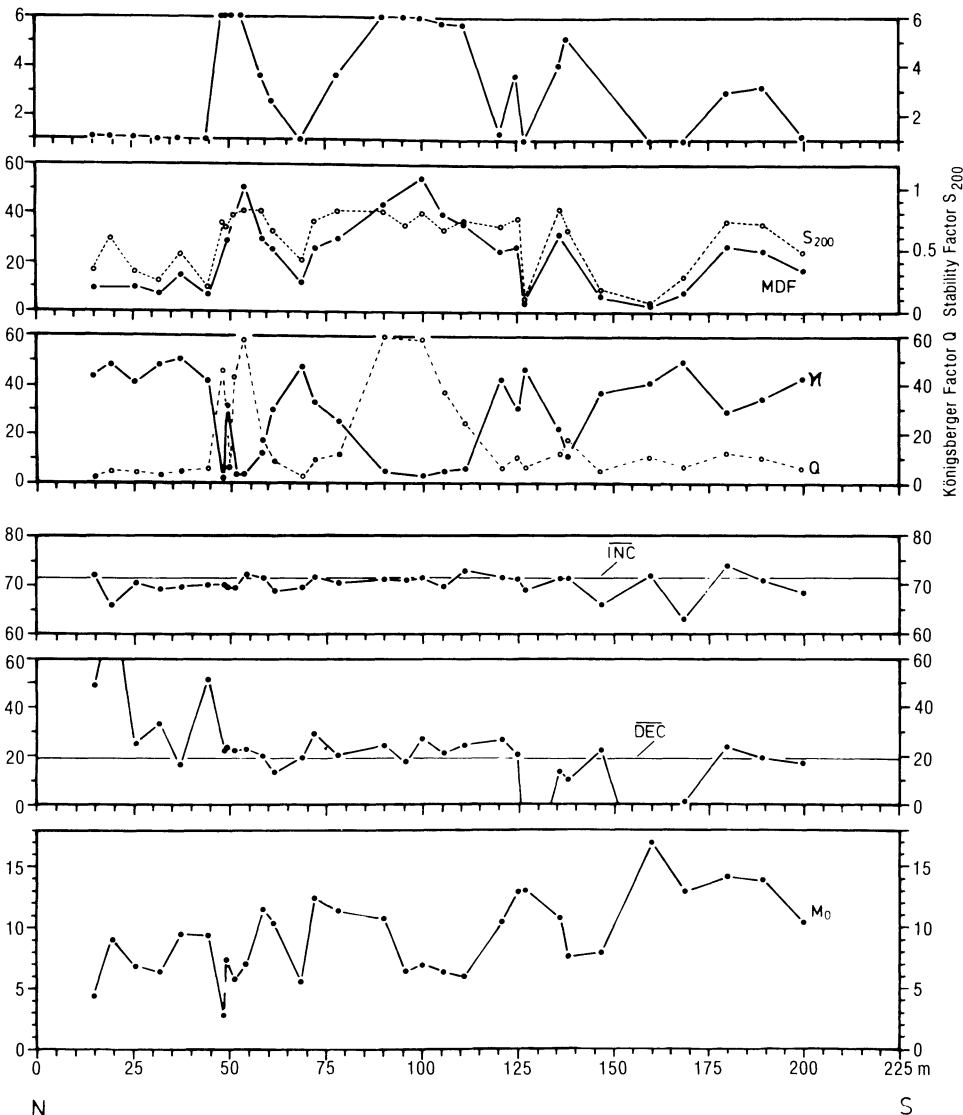


Fig. 5. Variation of magnetic and petrological parameters in a horizontal profile of Bausenberg lava flow, from N to S. See text for further explanations

possible correlations with the directional variations. All specimens were subjected to thermomagnetic analysis. Two distinct types of thermomagnetic curves were obtained, again corresponding to the vertical position (Fig. 8). The upper part exhibited thermomagnetic curves pointing to the presence of two magnetic phases with Curie temperatures T_c around 350°C and 560°C (Fig. 6, points and triangles, respectively). The lower Curie point corresponds to unoxidized TM which were observed in low concentration in the samples. These TM presumably were not maghemitized because of their small grain size (Petersen and Vali, 1987). The higher Curie temperature might be due to the exsolved magnetite of highly HT oxidized TM. Alternatively, it could point to the inversion of maghemitized TM of larger grain size than mentioned above. According to, e.g., Özdemir (1987), titanomaghemite inverts above about $250^\circ\text{--}300^\circ\text{C}$ to nearly stoichiometric TM and hematite or other non-magnetic oxides. Overall maghemitization degree should be low in our specimens ($z \leq 0.2$, see Özdemir, 1987) as no pronounced peak of saturation magnetization was observed

at temperatures above inversion. The final inversion product had a lower Curie temperature than the first inversion product, and its saturation magnetization at room temperature was slightly stronger than that of the starting material, in agreement with results of Özdemir (1987).

Thermomagnetic curves for the lower part of the profile point to the presence of only one magnetic component with high Curie temperature, which in accordance with ore petrology is TM with low Ti content. As the curves were almost reversible with no indications of an inversion peak or increase of saturation magnetization (Fig. 8), the contribution of maghemite to the specimens magnetic properties must be rather low.

Microprobe studies on unaltered TM grains from specimens of both parts of the flow resulted in almost invariable Ti/Fe ratios of 0.13–0.16 (standard deviation 0.04), pointing to TM compositions of ca. $x = 0.35\text{--}0.40$ and Curie temperatures of about $320^\circ\text{--}360^\circ\text{C}$. This agrees only with the lower Curie temperature in the upper flow part, as the lower layer specimens exhibited Curie temperatures typical for

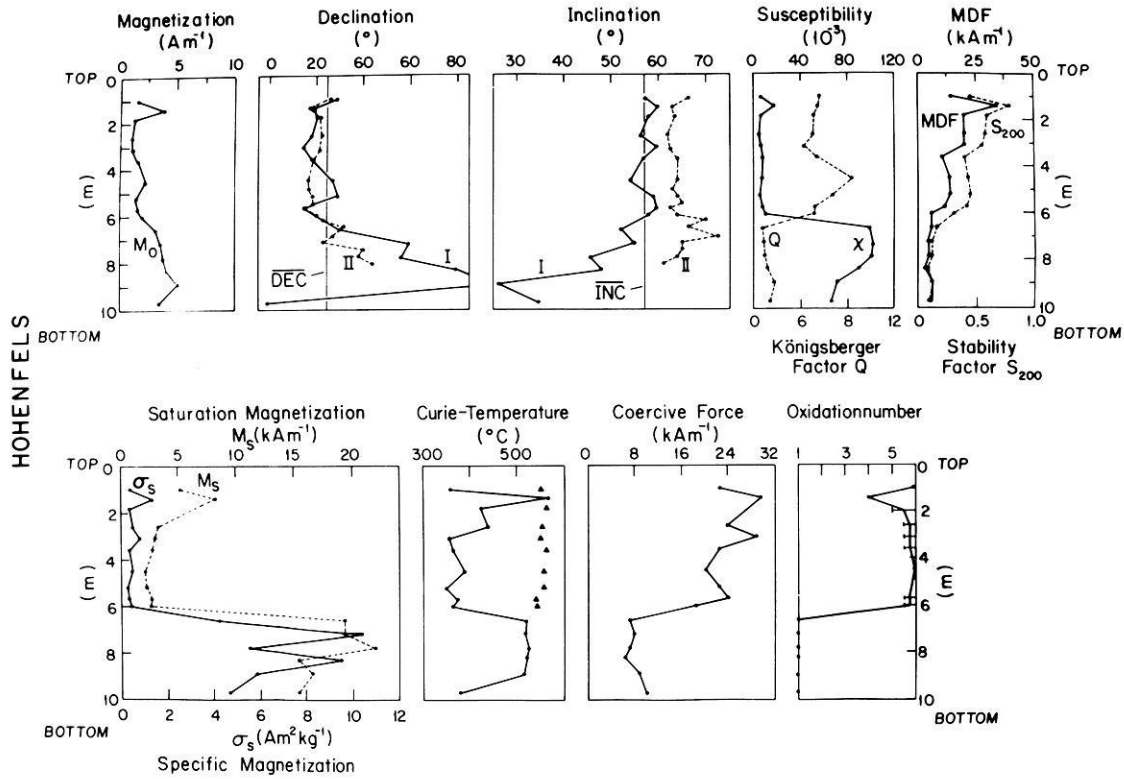


Fig. 6. Variation of magnetic and petrological parameters in a vertical profile of Hohenfels lava flow. Declination and inclination curves marked with *I* and *II*, respectively, correspond to partly differing profiles sampled during field campaigns I and II. Triangles in the Curie temperature diagram indicate high-temperature Curie points. See text for further explanations

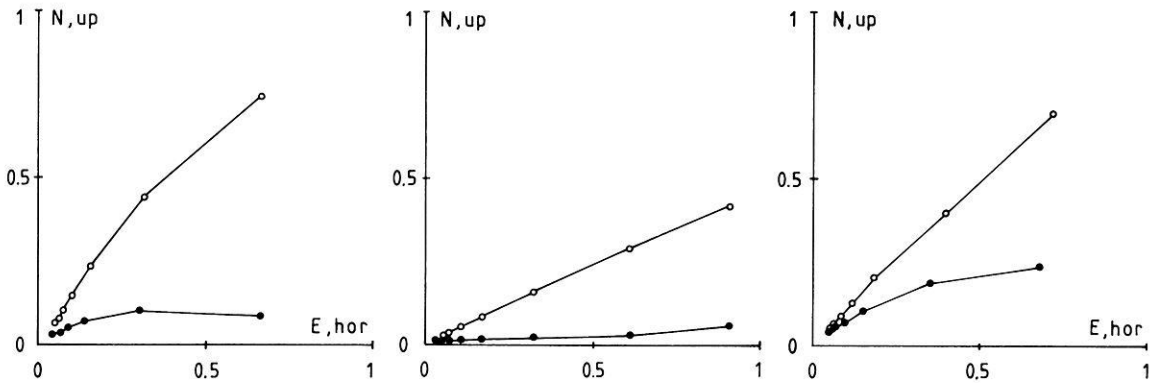


Fig. 7. Orthogonal vector diagrams (Zijderveld, 1967) for samples from the lower part of the Hohenfels profile. Full (open) circles represent the horizontal (vertical) component of remanent magnetization

Ti-poor TM ($x \approx 0$). The only explanation for this contradiction could be that the unaltered TM from the lower part does not represent the bulk magnetic properties.

The specific magnetizations determined with the magnetic balance correlated well with the NRM intensities. All magnetic components present in the specimens contributed to the observed magnetization which, therefore, corresponds to the original thermoremanent magnetization. Saturation magnetization and specific magnetization follow each other quite well in the upper part of the profile; in the lower part they show similar trends but some scatter. This may be explained by the much higher porosity of the lower layer and consequently varying density of the paleomagnetic specimens used for saturation magnetization mea-

surements. Specific magnetization was determined on weighted material.

The changes of specific and saturation magnetization are related to the degree of HT oxidation. This is in accordance with results obtained by Grommé et al. (1969), Lawley and Ade-Hall (1971) and Tucker and O'Reilly (1980), indicating that these properties decrease during HT oxidation by a factor of 5 or more, due to a decrease of bulk TM and a corresponding increase of hemoilmenite.

Coercive force was high in the upper part and reduced by a factor of about 3 towards the base, obviously related to the degree of oxidation. Similar trends were observed by Tucker and O'Reilly (1980).

In order to look for possible inhomogeneities in the

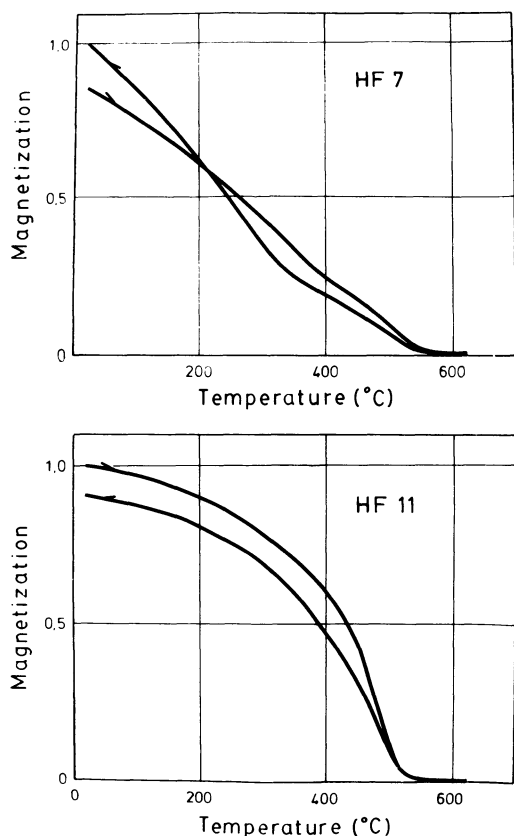


Fig. 8. Typical thermomagnetic curves for specimens from the Hohenfels lava flow

oxide grains, e.g. of the Fe distribution as a result of the migration of Fe ions during the maghemitization process (Petersen et al., 1979; Petersen and Vali, 1987), polished sections were SEM studied. The phase contrast photo (backscattered electrons) for a typical specimen from the lower part of the lava indicates a moderate maghemitization of the titanomagnetite reflected by the contraction cracks traversing the grain (Fig. 9a). The Fe- and Ti-distribution patterns (Fig. 9b and c, respectively) are very regular and exclude the origin of a CRM acquired later because of maghemitization progressing temporally and spatially. Apart from this aspect, the SEM results are very similar to those from the reflected light microscopy. However, the SEM could resolve unoxidized titanomagnetites of very small grain sizes besides highly oxidized titanomagnetites in the upper part of the lava. Maghemitization of the lower part was observed in the SEM, indicated as well by X-ray diffractometry.

Low-temperature variation of saturation isothermal remanence (SIRM) supported some of the above results. During cooling, specimens from the upper part of the flow (Fig. 10 HF 1) showed only a small variation of IRM but a significant decrease during rewarming which is characteristic of exsolved and maghemitized titanomagnetites (Dankers, 1978; Harstra, 1982). Specimens of the lower part (Fig. 9, HF 92), on the other hand, exhibited a strong decrease of SIRM cooling down to -196°C , and the pronounced gradient around -155°C points to the dominance of magnetite. On rewarming remanence recovered only moderately, which indicates an important contribution of

multi-domain particles (Levi and Merrill, 1978). This interpretation agrees much better with the observed Curie temperatures than with the microprobe data.

Anisotropy of magnetic susceptibility (AMS) was measured to examine a possible relation with the directional variations. For interpretation we use the maximum, intermediate and minimum susceptibility magnitudes χ_1 , χ_2 and χ_3 , respectively, and their directions. The susceptibility magnitudes define the lination factor $L = \chi_1/\chi_2$, foliation factor $F = \chi_2/\chi_3$ and anisotropy degree χ_1/χ_3 (e.g. see Hrouda and Janak, 1971); the latter with values between 1.002 and 1.022. Because of the relation of foliation and lination, evident from Fig. 11, most specimens are characterized by the presence of more oblate than prolate magnetic particles. The axes of the anisotropy ellipsoids are plotted in Fig. 12 for the two parts of the lava flow. In the upper layer, the directions of the maximum susceptibility axes are well grouped and obviously define a local flow direction to the south. The lower part, in contrast, showed no well-defined anisotropy directions, although the maximum susceptibility directions appear to be mainly deflected to westerly directions. We interpret this phenomenon as the result of a (viscous?) deformation or differential tilting of these parts of the lava after acquisition of remanence, which would also explain the inclined laminae in this layer. The deflection to the west corresponds to a clockwise rotation, which is in accordance with the observed directional trend (Fig. 6). An alternative explanation would be that strain or stress, restricted locally within the lava, has produced the observed deflection of AMS and magnetization directions. Such phenomena are known from folded rocks rather than unfolded young lavas (see review of MacDonald and Ellwood, 1987), therefore we reject this possibility as unlikely.

The idea of a mechanical, rather than rock magnetic or petrographic, origin of the directional change is further supported by the paleomagnetic results obtained from the samples collected during a second field campaign. In the upper part sampling was possible more or less along the original profile, but below a depth of 6 m results come from samples which are displaced 5 m or more horizontally. Declinations and inclinations in this displaced sub-profile showed a similar but much less distinct change with depth. The viscous deformation or differential tilting obviously differed locally, which may correlate with the observed change of laminae orientation. Finally, reference samples taken separated from the profile near the flow base showed remanence directions which are in good agreement with the 'normal' upper layer specimens.

The extreme change of rock magnetic and petrographic parameters between the two parts of the lava flow in this interpretation is due to the complicated origin of the Hohenfels lava. The first outflow produced a low oxidized and slowly cooling layer. In contrast to, e.g., Grommé et al. (1969), high Curie temperatures and high specific/saturation magnetizations here are related to low and not to high degrees of oxidation. Consequently, the TM in this layer have a near-magnetite composition. In the upper part of the flow the TM were much Ti richer, resulting in ilmenite - titanomagnetite (Ti poor) exsolution by means of HT oxidation. This difference in composition may be due to some kind of temporal/spatial magma evolution which did not considerably change the whole rock chemistry but increased the amount of Ti in the later outflow.

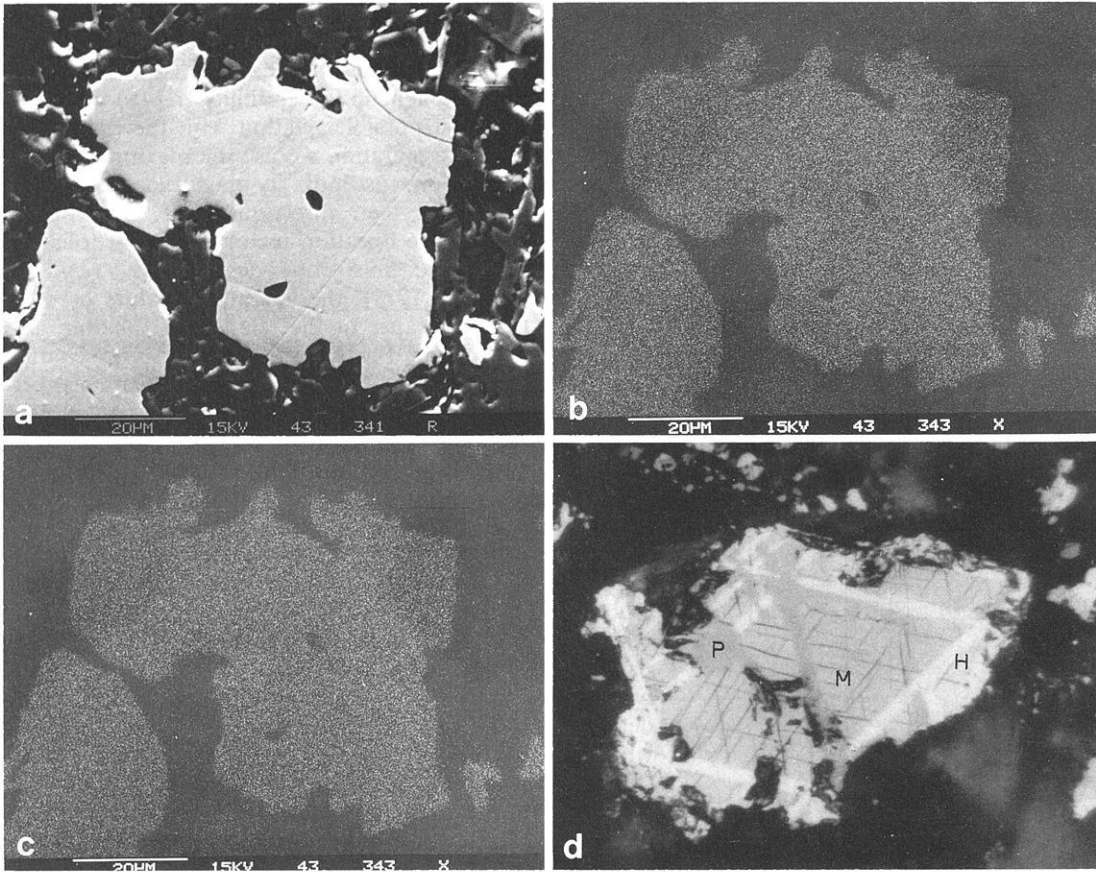


Fig. 9 a–d. SEM micrograph (backscattered electron method) of **a** titanomagnetites in a sample from Hohenfels lava flow, and the distribution of **b** Fe- and **c** Ti-cations; **d**: large phenocryst ($d \approx 1$ mm), totally oxidized in the marginal zones to hematite (H) and pseudobrookite (P), with weakly altered titanomagnetite (M) in the centre of the grain

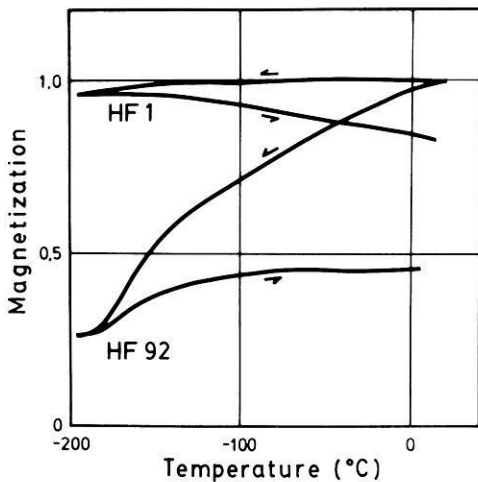


Fig. 10. Variation of strong artificial isothermal remanence (normalized) at temperatures between 20°C and -196°C for typical specimens from the upper (HF 1) and lower (HF 92) part of the Hohenfels lava flow

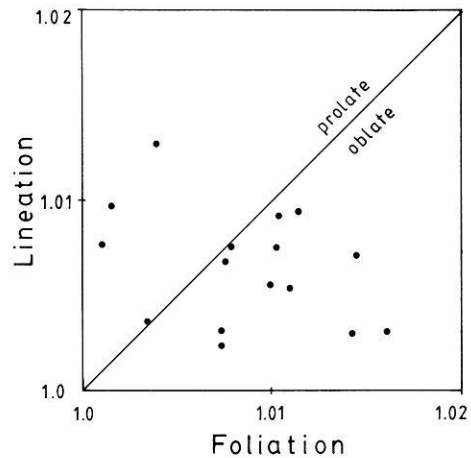


Fig. 11. The relationship between lineation and foliation for specimens from the Hohenfels vertical profile

Discussion

As shown above, the variation of petrological and magnetic parameters differs largely in the lava flows studied, and even varies between profiles of one flow (Bausenberg). Any correlation of magnetic and/or petrological properties de-

rived from only one profile could represent local effects rather than give information about general relationships. We therefore compiled the results from all flows to look for correlations of HT oxidation, stability parameters and dispersion of magnetization directions with other parameters.

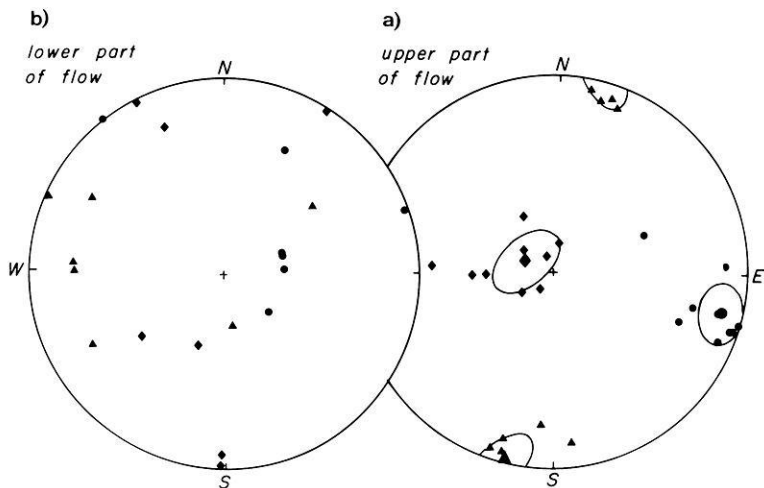


Fig. 12 a and b. Equal area plot of magnetic anisotropy axes χ_1 (triangles), χ_2 (full circles) and χ_3 (rhombs) for specimens from **a** the upper and **b** lower part of the Hohenfels lava flow. Mean directions are shown by bigger symbols, with their confidence limits

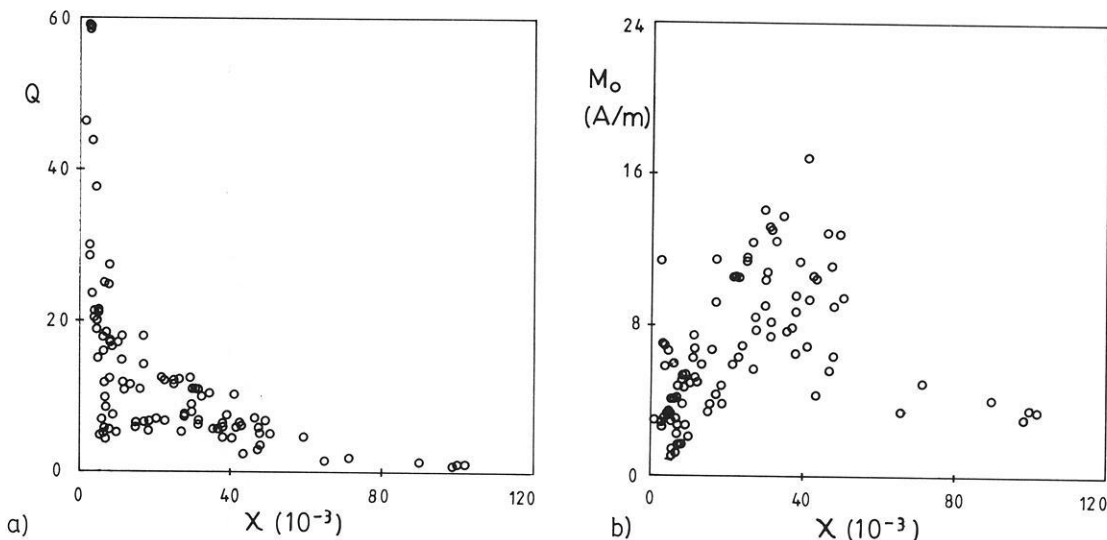


Fig. 13 a and b. Relationship between susceptibility and **a** Königsberger factor Q and **b** NRM intensity M_o

Besides other properties (e.g. composition, oxidation degree), remanence intensity and susceptibility both depend on the volume content of TM. Assuming constant grain size and composition, remanence intensity and susceptibility should increase in parallel with volume content. Figure 13b shows such a correlation for low values. Revision of Figs. 3–6 indicates that low values are always associated with high oxidation numbers. Therefore, we believe that low NRM intensities and susceptibilities are due to an increase of weak or non-magnetic phases at the expense of initial TM during HT oxidation. The observed trend from low NRM intensities at high susceptibilities to high intensities at intermediate susceptibilities may be explained in terms of a reduction of the effective grain size during oxidation, resulting in higher coercivity and higher remanence because of exsolution of Ti-poor TM (e.g. Larson et al., 1969; Tucker and O'Reilly, 1980; Kono, 1987).

The Königsberger factor Q exhibits a large initial decrease with increasing susceptibility (Fig. 13a) and supports the above interpretation of reducing grain sizes. For a variation only of the volume content, Q would remain constant. We may conclude that NRM intensity and susceptibility variations are primarily related to other factors than TM

content which, also according to microscopic observations, was rather constant.

In Fig. 14b the oxidation number M_{ox} is plotted versus susceptibility. With increasing oxidation, susceptibility first drops sharply and then decreases moderately but continuously. A similar variation was found, e.g., by Wilson et al. (1968) and Lawley and Ade-Hall (1971). The strong initial decrease may be due to stress developing within the grains, and/or incipient exsolution of ilmenite lamellae.

NRM intensity shows rather strong scatter, but an increase is recognizable up to intermediate oxidation numbers, followed by a decrease towards higher oxidation states (Fig. 14a). Similar variations were also found by Tucker and O'Reilly (1980), although our results show rather high NRM intensities for some highly oxidized samples ($M_{ox} \approx 6$). This may be due to the presence of unaltered TM within a highly oxidized ($M_{ox} = 6$) surrounding (Fig. 9d), producing a much stronger than expected remanence. Alternatively, very small ($\leq 1 \mu\text{m}$) non-oxidized magnetites, occasionally observed within mafic phases of the groundmass (which are difficult to determine exactly by ore petrological methods), are responsible for such strong magnetizations.

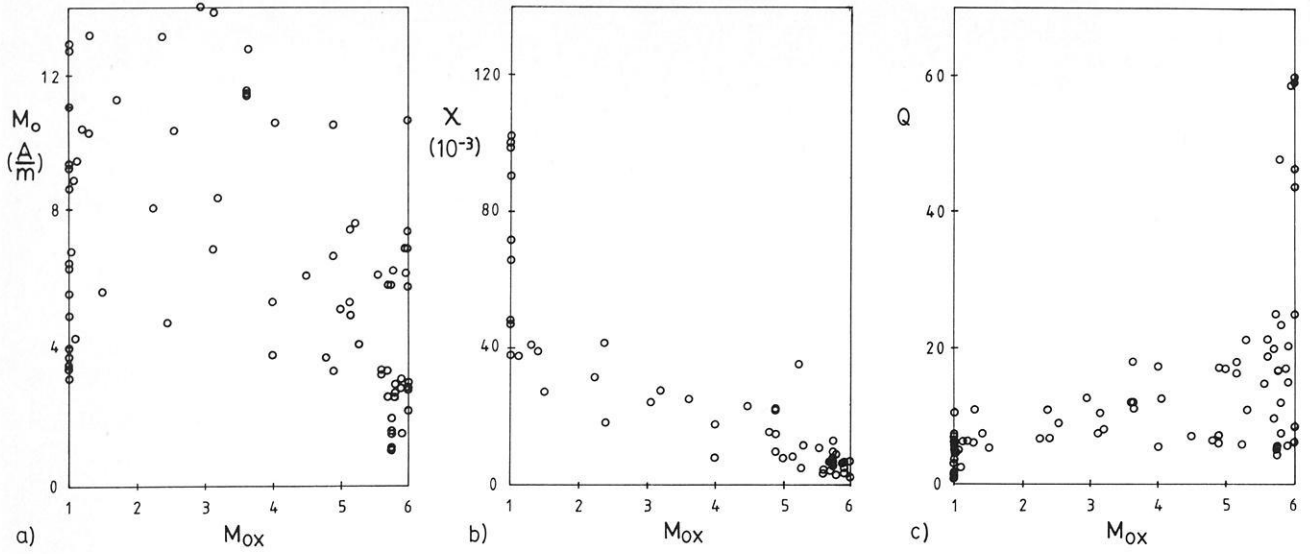


Fig. 14a-c. Relationship between oxidation number M_{ox} and **a** NRM intensity M_o , **b** susceptibility and **c** Königsberger factor Q

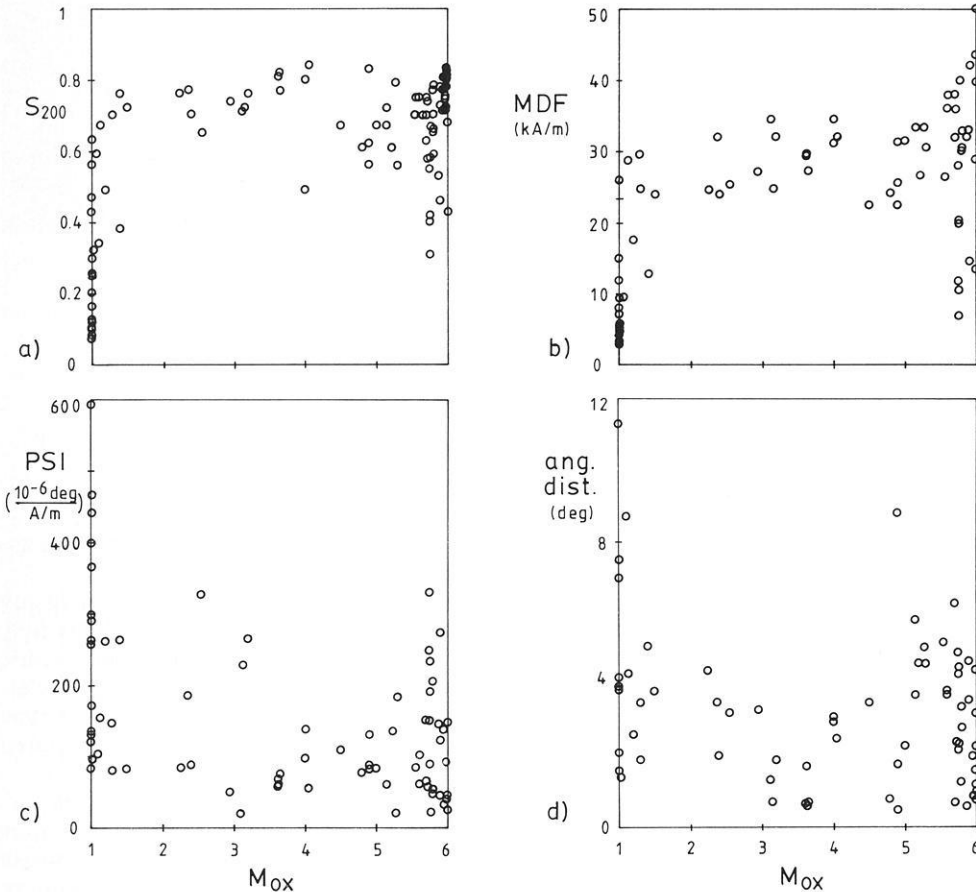


Fig. 15a-d. Relationship between oxidation number M_{ox} and **a** S_{200} , **b** MDF, **c** PSI, and **d** specimen's angular distance from profile mean direction (see text for further explanation)

It should be mentioned here that similar variations of NRM intensity were also observed as a result of LT oxidation (e.g. Petersen et al., 1979; Smith, 1987). Indeed, we have arguments against an important contribution of titanomaghemite to the bulk magnetic properties: according to Smith (1987), the Königsberger factor Q should sharply decrease with LT oxidation. In contrast to that, we observed an increase of Q with oxidation degree (Fig. 14c). This increase may be due to a reduction of the effective

grain size (e.g. Price, 1980) and/or to the origin of very small-sized magnetite particles (Tucker and O'Reilly, 1980) with progressing HT oxidation.

Stability parameters S_{200} and MDF exhibit similar variations with oxidation degree (Fig. 15a and b). Stability is low at $M_{ox} \leq 1.5$ with rather high dispersion of S_{200} and MDF values. With increasing oxidation, up to $M_{ox} \approx 5$, stability is high and nearly uniform. For $5 < M_{ox} \leq 6$, MDF and S_{200} remain at this level but dispersion is again high.

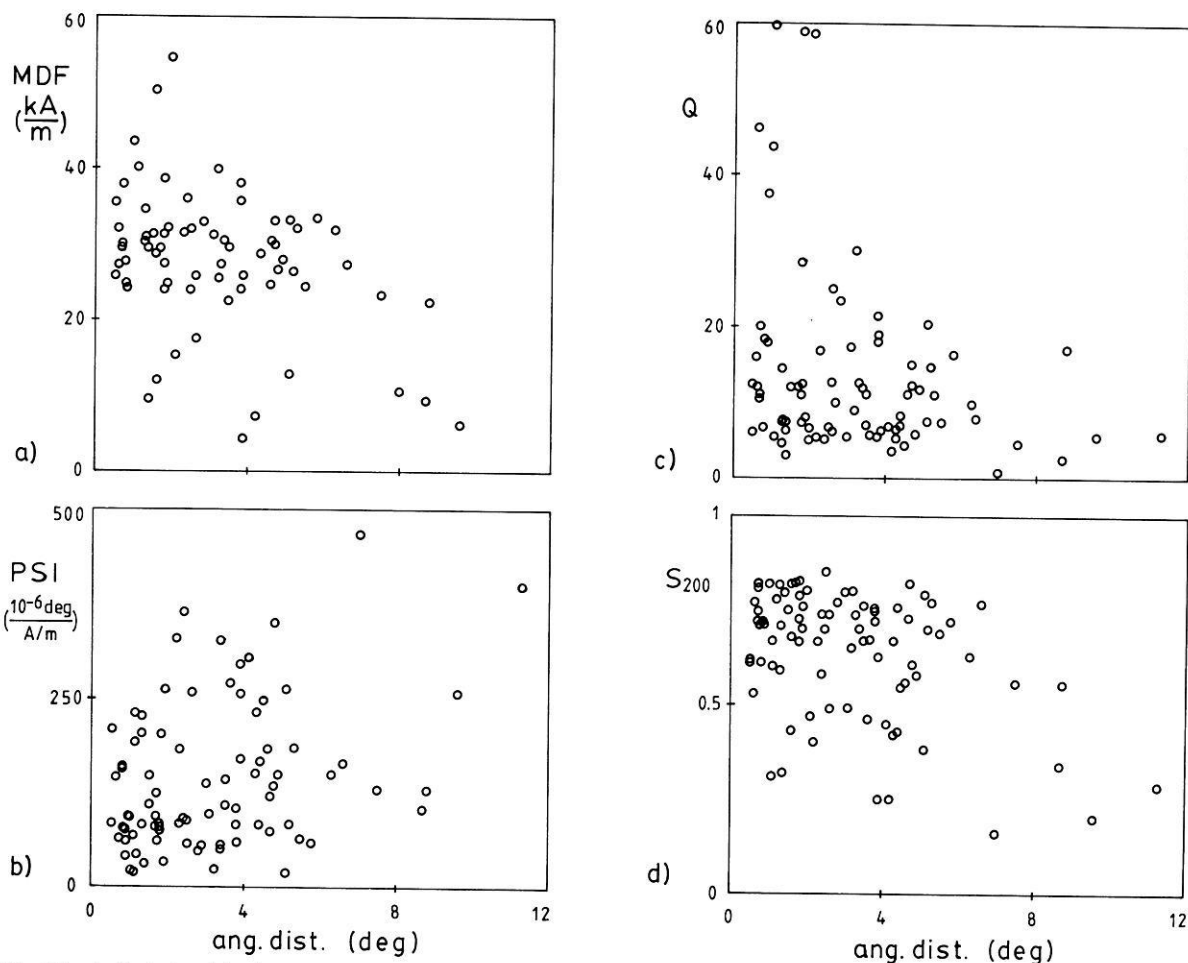


Fig. 16a–d. Relationship between specimen's angular distance from the corresponding profile mean direction and **a** MDF, **b** PSI, **c** Königsberger factor Q and **d** S_{200}

A few highly oxidized samples ($M_{ox} \approx 6$), all from the HF profile, showed nearly as low stability as non-oxidized samples. PSI exhibits a similar but, according to its definition, reversed trend with oxidation as S_{200} and MDF (Fig. 15c). The same highly oxidized samples characterized by low magnetic stability also exhibited low directional stability.

The angular distance of characteristic magnetization to the profile mean is plotted versus M_{ox} in Fig. 15d. Directional dispersion tends to diminish towards intermediate oxidation degrees ($M_{ox} \approx 3.5$) and to increase with further oxidation, probably related to changes in magnetic stability. Figure 16 shows that angular dispersion decreases with increasing MDF, Q , S_{200} and increases with decreasing PSI. Obviously, the directions of magnetically less stable samples deviate most from the profile mean direction. We believe that high-coercivity rocks acquire less secondary magnetizations whose coercivity spectrum may, additionally, be more separated from the thermoremanent magnetization (TRM) spectrum than in unstable rocks. These are favourable conditions for magnetic cleaning of NRM by *af* demagnetization to obtain the TRM direction.

We may conclude that the variation of magnetic properties, stability parameters and dispersion of paleodirections are related to the HT oxidation state of titanomagnetites. The observed relations are sometimes not marked, which may be due to interference of the measured properties with

parameters and properties which are not known for part or even all of the samples or which were not determined quantitatively, such as degree of maghemitization, volume content and grain size of titanomagnetite, and saturation magnetization.

Acknowledgements. The authors thank the anonymous reviewers for their helpful comments on earlier versions of the manuscript. This work was supported by the Deutsche Forschungsgemeinschaft.

References

- Ade-Hall, J.M., Khan, M.A., Dagley, P., Wilson, R.L.: A detailed opaque petrological and magnetic investigation of a single tertiary lava flow from Skye, Scotland, I, II. *Geophys. J.R. Astron. Soc.* **16**, 375–399, 1968
- Ade-Hall, J.M., Palmer, H.C., Hubbard, T.P.: The magnetic and opaque petrological response of basalts to regional hydrothermal alteration. *Geophys. J. R. Astron. Soc.* **24**, 137–174, 1971
- Akimoto, S., Kushiro, I.: Natural occurrence of titanomaghemite and its relevance to the unstable magnetization of rocks. *J. Geomagn. Geoelectr.* **11**, 94–110, 1969
- Akimoto, S., Katsura, T., Yoshida, M.: Magnetic properties of $TiFe_2O_4 - Fe_3O_4$ system and their change with oxidation. *J. Geomagn. Geoelectr.* **9**, 137–174, 1958
- Büchel, G., Mertes, H.: Die Eruptionszentren des Westfälischer Vulkanfeldes. *Z. Dt. geol. Ges.* **133**, 409–429, 1982

- Collinson, D.W.: Methods in rock magnetism and palaeomagnetism. London-New York: Chapman and Hall 1983
- Dankers, P.H.M.: Magnetic properties of dispersed natural ironoxides of known grain-size. PhD thesis, Utrecht 1978
- Davis, P.M., Evans, M.E.: Interacting single-domain properties of magnetite intergrowths. *J. Geophys. Res.* **81**, 989–994, 1976
- Ellwood, B.B.: Weathering effects on the magnetic properties of the Milledgeville granite, Georgia. *Earth Planet. Sci. Lett.* **55**, 311–316, 1981
- Evans, M.E., Wayman, M.L.: An investigation of the role of ultrafine titanomagnetite intergrowths in paleomagnetism. *Geophys. J.R. Astron. Soc.* **36**, 1–10, 1974
- Graham, J.W.: Changes in ferromagnetic minerals and their bearing on magnetic properties of rocks. *J. Geophys. Res.* **58**, 243–260, 1953
- Grommé, C.S., Wright, T.L., Peck, D.L.: Magnetic properties and oxidation of iron-titanium oxide minerals in Alae and Makapuhi lava lakes, Hawaii. *J. Geophys. Res.* **74**, 5277–5293, 1969
- Haggerty, S.E.: Oxidation of opaque mineral oxides in basalts. In: Oxide minerals. Mineral. Soc. Am., Short Course Notes, No. 3, D. Rumble ed: 1976
- Hargraves, R.B., Petersen, N.: Notes on the correlation between petrology and magnetic properties of basaltic rocks. *J. Geophys.* **37**, 367–382, 1971
- Harstra, R.L.: Some magnetic parameters for natural iron-titanium oxides. PhD thesis, Utrecht 1982
- Hauptmann, Z.: High temperature oxidation, range of non-stoichiometry and Curie point variation of cation deficient titanomagnetite $Fe_{2.4}Ti_{0.6}O_4 + \gamma$. *Geophys. J. R. Astron. Soc.* **38**, 29–47, 1974
- Heider, F., Dunlop, D.J.: Two types of chemical remanent magnetization during the oxidation of magnetite. *Phys. Earth Planet. Inter.* **46**, 24–45, 1987
- Hoffman, K.A., Day, R.: Separation of multi-component NRM: A general method. *Earth Planet. Sci. Lett.* **40**, 433–438, 1978
- Hrouda, F., Janak, F.: A study of hematite fabric of some red sandstones on the basis of their magnetic susceptibility anisotropy. *Sediment. Geol.* **6**, 187–199, 1971
- Johnson, H.P., Merrill, R.T.: Magnetic and mineralogical changes associated with low temperature oxidation of magnetite. *J. Geophys. Res.* **77**, 334–341, 1972
- Johnson, H.P., Merrill, R.T.: Low temperature oxidation of single domain magnetite. *J. Geophys. Res.* **79**, 5533–5534, 1974
- Keefer, C.M., Shive, P.N.: Curie temperature and lattice constant reference contours for synthetic titanomaghemites. *J. Geophys. Res.* **86**, 987–998, 1981
- Kono, M.: Changes in TRM and ARM in a basalt due to laboratory heating. *Phys. Earth Planet. Inter.* **46**, 1–8, 1987
- Larson, E.E., Ozima, M., Nagata, T., Strangway, D.W.: Stability of remanent magnetization of igneous rocks. *Geophys. J. R. Astron. Soc.* **17**, 263–292, 1969
- Lawley, E.A., Ade-Hall, J.M.: A detailed magnetic and opaque petrological study of a thick paleogene tholeiitic lava flow from northern Ireland. *Earth Planet. Sci. Lett.* **11**, 113–120, 1971
- Levi, S., Merrill, R.T.: Properties of single-domain, pseudo single-domain, and multidomain magnetite. *J. Geophys. Res.* **83**, 309–323, 1978
- MacDonald, W.D., Ellwood, B.B.: Anisotropy of magnetic susceptibility: sedimentological, igneous, and structural-tectonic applications. *Rev. Geophys.* **25**, 905–909, 1987
- Manson, A.J., O'Donovan, J.B., O'Reilly, W.: Magnetic rotational hysteresis loss in titanomagnetites and titanomaghemites – application to non-destructive mineral identification in basalts. *J. Geophys.* **46**, 185–199, 1979
- Merrill, R.T.: Magnetic effects associated with chemical changes in igneous rocks. *Geophys. Surv.* **2**, 277–311, 1975
- Molyneux, L.: A complete result magnetometer for measuring the remanent magnetization of rocks. *Geophys. J.* **24**, 429–433, 1971
- Moskowitz, B.M.: Towards resolving the inconsistencies in characteristic physical properties of synthetic titanomaghemites. *Phys. Earth Planet. Inter.* **46**, 173–183, 1987
- Negendank, J.F.W.: Volcanics of the Valley of Mexico, part II: the opaque mineralogy. *N. Jb. Miner.* **117**, 183–195, 1972
- Nishitani, T., Kono, M.: Curie temperature and lattice constant of oxidized titanomagnetite. *Geophys. J.R. Astron. Soc.* **74**, 585–600, 1983
- O'Reilly, W.: Rock and mineral magnetism. Glasgow: Blackie 1984
- O'Reilly, W., Banerjee, S.K.: The mechanism of oxidation in titanomagnetites: a magnetic study. *Mineral. Mag.* **36**, 29–37, 1967
- Özdemir, Ö.: Inversion of titanomaghemites. *Phys. Earth Planet. Inter.* **46**, 184–196, 1987
- Özdemir, Ö., O'Reilly, W.: Laboratory synthesis of aluminium-substituted titanomaghemites and their characteristic properties. *J. Geophys.* **49**, 93–100, 1981
- Özdemir, Ö., O'Reilly, W.: Magnetic hysteresis properties of synthetic monodomain titanomaghemites. *Earth Planet. Sci. Lett.* **57**, 437–447, 1982
- Petersen, N.: Notes on the variation of magnetization within basalt lava flows and dikes. *Pageophys.* **114**, 175–193, 1976
- Petersen, N., Vali, H.: Observation of shrinkage cracks in ocean floor titanomagnetites. *Phys. Earth Planet. Inter.* **46**, 197–205, 1987
- Petersen, N., Eisenach, P., Bleil, U.: Low temperature alteration of the magnetic minerals in ocean floor basalts. *AGU, Maurice Ewing Series* **2**, 169–209, 1979
- Prévot, M., Lecaille, A., Mankinen, E.A.: Magnetic effects of maghemitization of oceanic crust. *J. Geophys. Res.* **86**, 4009–4020, 1981
- Price, G.D.: Exsolution microstructures in titanomagnetites and their magnetic significance. *Phys. Earth Planet. Inter.* **23**, 2–12, 1980
- Rahm, G.: Der quartäre Vulkanismus im zentralen Teil der Westeifel. *Decheniana* **109**, 11–51, 1956
- Smith, B.M.: Consequences of maghemitization on the magnetic properties of submarine basalts: synthesis of previous works and results concerning rocks from mainly D.S.D.P. Legs 51 and 52. *Phys. Earth Planet. Inter.* **46**, 206–226, 1987
- Strangway, D.W., Larson, E.E., Goldstein, M.: A possible cause of high magnetic stability in volcanic rocks. *J. Geophys. Res.* **73**, 3787–3795, 1968
- Symons, D.T.A., Stupavsky, M.: A rational paleomagnetic stability index. *J. Geophys. Res.* **79**, 1718–1720, 1974
- Tucker, P., O'Reilly, W.: The laboratory simulation of deuteric oxidation of titanomagnetites: effects on magnetic properties and stability of thermoremanence. *Phys. Earth Planet. Inter.* **23**, 112–133, 1980
- Vincenz, S.A.: Discrepancies between experimental observations in natural and synthetic samples. *Phys. Earth Planet. Inter.* **46**, 164–172, 1987
- Watkins, N.D., Haggerty, S.E.: Some magnetic properties and the possible petrogenetic significance of oxidized zones in an Icelandic olivine basalt. *Nature* **206**, 797–800, 1965
- Wilson, R.L., Haggerty, S.E.: Reversals of the earth's magnetic field. *Endeavor* **95**, 104–109, 1966
- Wilson, R.L., Haggerty, S.E., Watkins, N.D.: Variation of palaeomagnetic stability and other parameters in a vertical traverse of a single Icelandic lava. *Geophys. J. R. Astron. Soc.* **16**, 79–96, 1968
- Zijderveld, J.D.A.: A.c. demagnetization of rocks: analysis of results. In: Methods in palaeomagnetism. D.W. Collinson, K.M. Creer and S.K. Runcorn, eds: Amsterdam: Elsevier 1967

Received July 7, 1987; revised November 5, 1987

Accepted November 26, 1987

Analytical presentation of statistically estimated magnetotelluric transfer functions by a set of polynomials

Andreas Junge

Institut für Geophysik, Postfach 2341, D-3400 Göttingen, Federal Republic of Germany

Abstract. In magnetotelluric studies time variations of the horizontal telluric and magnetic field components at the earth's surface are compared to get detailed information of the electrical conductivity structure of the earth's interior. The development of conductivity models from the data demands the thorough estimation of the transfer functions in the frequency domain between the Fourier transforms of the recorded time series. The analytical presentation of the estimated transfer functions allows an individual selection of a number of frequencies for further investigation. Larsen's presentation (Larsen, 1975, 1980) of the transfer functions by single polynomials demands a complicated calculation of confidence limits. Therefore, the transfer functions are presented here by the sum of polynomials which fulfil an orthogonality criterion. The orthogonality criterion allows a rather simple estimation of the frequency-dependent confidence limits of the transfer functions. The polynomial method is applied to a 100-day record of the magnetic and telluric field variations near Göttingen. As the telluric field is usually partially disturbed during such a long time interval, the polynomial method is extended to treat telluric time series with missing data. The comparison of the smooth polynomial transfer functions with band-averaged estimates yields a good correlation between the estimates as well as between their confidence intervals.

Key words: Confidence limits – disturbed telluric time series – Smooth polynomial MT transfer functions

Introduction

In magnetotelluric investigations time variations of the horizontal components of the telluric field, E_x and E_y , and of the three components of the magnetic field, B_x , B_y and B_z , are simultaneously recorded at the earth's surface. The comparison of E_x , E_y or B_z with B_x and B_y in the frequency domain may yield sophisticated models of the electric conductivity structures of the earth's interior beneath the site of interest. Thus, complex frequency-dependent transfer functions between the different Fourier-transformed field quantities have to be estimated as precisely as possible.

This paper concentrates on the estimation of transfer functions between the telluric and magnetic field variations. It first deals with Larsen's method (Larsen, 1975, 1980) which represents the transfer function by a 1-D transfer function times a power series in square-root frequency using N terms. The 1-D transfer function approximates the actual

transfer functions so that the power series is approximately frequency independent and is non-dimensional. This helps in dealing with data gaps and outliers and avoids the problem that transfer functions can probably not, in general, be represented by polynomials. However, as the polynomial coefficients are statistically dependent, the full covariance matrix of their errors must be used to construct confidence limits for the resulting transfer function.

Therefore, in this paper each transfer function is presented by a sum of special polynomials which fulfil an orthogonality condition and thus offer a simpler way of calculating confidence limits.

A numerical example compares the transfer functions from the new method with band-averaged estimates. Furthermore, the influence of data gaps in the electric time series on the estimation of transfer functions is discussed.

Theory

It is assumed that there exist complete sets of N discrete and equally spaced data of the simultaneously recorded telluric and magnetic field components. Then a harmonic analysis will yield $M = N/2$ complex harmonic coefficients, e.g. $E_x(f_i)$, $i = 1, \dots, M$, where $f_i = i/T$ denotes the frequency and T is the length of the time series. A linear bivariate approach is chosen to estimate the transfer functions between the harmonic coefficients of the telluric and magnetic field

$$E(f_i) = X(f_i) B_x(f_i) + Y(f_i) B_y(f_i) + \delta E(f_i) \quad (1)$$

where $X(f_i)$ and $Y(f_i)$ are the transfer functions which have to be estimated and $\delta E(f_i)$ is the uncorrelated residuum. $E(f_i)$ stands for either $E_x(f_i)$ or $E_y(f_i)$ as the calculations for both components are done separately but follow the same scheme. Furthermore, it is assumed that $B_x(f_i)$ and $B_y(f_i)$ are "noise-free" compared to $E(f_i)$. In the following, the argument f_i will be omitted for clarity.

Estimates of X and Y are calculated by minimizing the weighted residual power $\langle W|\delta E|^2 \rangle$ by the method of least squares assuming that in the investigated period range δE is normally distributed. $W(f_i)$ is a non-negative weight function and is set to zero if there is evidence for a periodic signal at a certain frequency in the spectrum. Furthermore, W can be used to whiten the residuum δE .

There are different ways to represent the frequency dependence of X and Y :

a) In the band-average method estimates of X and Y are calculated for separate frequency bands from the normal equations yielding, e.g. for X ,

$$\hat{X} = \frac{\langle EB_x^* \rangle \langle |B_y|^2 \rangle - \langle EB_y^* \rangle \langle B_y B_x^* \rangle}{\langle |B_x|^2 \rangle \langle |B_y|^2 \rangle - |\langle B_x B_y \rangle|^2} \quad (2)$$

where $\langle \rangle$ denotes the sum of the auto- or cross-spectra of each frequency band. However, if X is not a constant or a linear function of frequency this method might yield severely biased estimates \hat{X} for wide frequency bands. On the other hand, a reduced width of the frequency bands may result in large confidence intervals.

b) Larsen (1975, 1980) describes another approach. He uses a preliminary model and then approximates the real model by the multiplication of the preliminary transfer function with an estimated power series in \sqrt{f} . Choosing a uniform half-space as the start model, the preliminary transfer function is proportional to \sqrt{f} and thus $X(f)$ and $Y(f)$ can be expanded as follows:

$$X(f) = \sum_{n=0}^{N_x-1} a_n(f) \frac{n+1}{2}, \quad Y(f) = \sum_{n=0}^{N_y-1} b_n(f) \frac{n+1}{2} \quad (3)$$

The least-squares method then serves to estimate the complex coefficients a_n and b_n . Inserting Eq. (3) into Eq. (1) will lead to the normal equations

$$\begin{aligned} & \sum_{n=0}^{N_x-1} a_n \left\langle W |B_x|^2 f^{\frac{n+m+2}{2}} \right\rangle + \sum_{n=0}^{N_y-1} b_n \left\langle W B_x^* B_y f^{\frac{n+m+2}{2}} \right\rangle \\ & = \left\langle W E B_x^* f^{\frac{m+1}{2}} \right\rangle \\ & \sum_{n=0}^{N_y-1} b_n \left\langle W |B_y|^2 f^{\frac{n+m'+2}{2}} \right\rangle + \sum_{n=0}^{N_x-1} a_n \left\langle W B_y^* B_x f^{\frac{n+m'+2}{2}} \right\rangle \\ & = \left\langle W E B_y^* f^{\frac{m'+1}{2}} \right\rangle \end{aligned} \quad (4)$$

where $\langle \rangle$ indicates the summation over the whole investigated frequency range and $m=0, \dots, N_x-1$, $m'=0, \dots, N_y-1$. Then a_n and b_n are calculated by matrix inversion. Thus, $X(f)$ and $Y(f)$ will be smooth functions of frequency and can easily be used to determine X and Y for any frequency in the analysed interval.

However, the full covariance matrix of the errors of the coefficients a_n and b_n , respectively, has to be known to calculate confidence limits for the transfer functions $X(f)$ and $Y(f)$.

c) Extending Larsen's approach, an orthogonality condition is introduced by forming the expressions

$$\begin{aligned} X(f) B_x(f) &= \sum_{n=0}^{N_x-1} c_n B_{x,n}(f), \\ Y(f) B_y(f) &= \sum_{n=0}^{N_y-1} d_n B_{y,n}(f) \end{aligned} \quad (5)$$

with

$$B_{x,n}(f) = \sqrt{f} B_x(f) P_n(f), \quad B_{y,n}(f) = \sqrt{f} B_y(f) Q_n(f)$$

with P_n, Q_n being real polynomials in f_i of the order n

$$P_n(f_i) = \sum_{l=0}^n p_{n,l}(f_i)^l, \quad Q_n(f_i) = \sum_{l=0}^n q_{n,l}(f_i)^l \quad (6)$$

such that

$$\begin{aligned} \langle B_{x,n} B_{x,k}^* W \rangle &= \delta_{n,k} \langle |B_{x,n}|^2 W \rangle, \\ \langle B_{y,n} B_{y,k}^* W \rangle &= \delta_{n,k} \langle |B_{y,n}|^2 W \rangle \end{aligned} \quad (7)$$

with $\delta_{n,k} = 1$ for $n=k$ and $\delta_{n,k} = 0$ for $n \neq k$.

An algorithm to calculate the polynomial coefficients $p_{n,l}$ and $q_{n,l}$ was developed by Forsythe (1957) and is described in Appendix A.

The transfer functions X and Y are now represented by the sum of the polynomials P_n and Q_n

$$X(f) = \sqrt{f} \sum_{n=0}^{N_x-1} c_n P_n(f), \quad Y(f) = \sqrt{f} \sum_{n=0}^{N_y-1} d_n Q_n(f) \quad (8)$$

Similarly to Eq. (4), the normal equations are

$$\begin{aligned} & \sum_{n=0}^{N_x-1} c_n \langle W |B_x|^2 P_n P_m f \rangle + \sum_{n=0}^{N_y-1} d_n \langle W B_x^* B_y Q_n P_m f \rangle \\ & = \langle W B_x^* E P_m \sqrt{f} \rangle \\ & \sum_{n=0}^{N_y-1} d_n \langle W |B_y|^2 Q_n Q_m f \rangle + \sum_{n=0}^{N_x-1} c_n \langle W B_y^* B_x P_n Q_m f \rangle \\ & = \langle W B_y^* E Q_m \sqrt{f} \rangle \end{aligned} \quad (9)$$

$$m=0, \dots, N_x-1, \quad m'=0, \dots, N_y-1$$

and the coefficients c_n and d_n are determined by matrix inversion.

The multiple squared coherency r^2 is the ratio of the predicted and the measured telluric field

$$r^2 = [\langle |E|^2 W \rangle]^{-1} \left\langle \left| \sum_{n=0}^{N_x-1} c_n B_{x,n} + \sum_{n=0}^{N_y-1} d_n B_{y,n} \right|^2 W \right\rangle \quad (10)$$

It is assumed that B_x and B_y are not correlated except for some periodicities at f_j where $W(f_j)$ is set to zero. Then the right terms on the left side of Eq.(9) can be neglected and, using the orthogonality condition in Eq.(7), a quadratic equation for the errors Δc_n and Δd_n can be written (Jenkins and Watts, 1968):

$$\begin{aligned} & \sum_{n=0}^{N_x-1} \langle |B_{x,n}|^2 W \rangle |\Delta c_n|^2 + \sum_{n=0}^{N_y-1} \langle |B_{y,n}|^2 W \rangle |\Delta d_n|^2 \\ & \leq \frac{v_1}{v_2} (1-r^2) \langle |E|^2 W \rangle F_{v_1, v_2}(\beta) \end{aligned} \quad (11)$$

with $v_1 = 2(N_x + N_y)$, $v_2 = 2(M - N_x - N_y)$; M is the number of spectral lines averaged in $\langle \rangle$; r^2 is the multiple squared coherency according to Eq.(10) and β is the error probability with which the value F_{v_1, v_2} of the Fisher-probability function is exceeded. Equation (11) describes a quadratic form with Δc_n and Δd_n as parameters which allows estimation of the maximum error of c_n and d_n for a given error probability β :

$$|\Delta c_n|^2 = \frac{v_1}{v_2} \frac{\langle |E|^2 W \rangle}{\langle |B_{x,n}|^2 W \rangle} (1-r^2) F_{v_1, v_2}(\beta)$$

$$|\Delta d_n|^2 = \frac{v_1}{v_2} \frac{\langle |E|^2 W \rangle}{\langle |B_{n,y}|^2 W \rangle} (1-r^2) F_{v_1, v_2}(\beta) \quad (12)$$

Equation (12) can be extended for related magnetic field components B_x and B_y by considering terms with $\Delta c_n \Delta d_n$ in Eq.(11).

Finally, the frequency-dependent error limits $\Delta X(f)$ and $\Delta Y(f)$ of the transfer functions $X(f)$ and $Y(f)$ are calculated from Eqs. (8) and (12)

$$\begin{aligned} |\Delta X(f_i)|^2 &= f_i \sum_{n=0}^{N_x-1} |\Delta c_n|^2 |P_n(f_i)|^2, \\ |\Delta Y(f_i)|^2 &= f_i \sum_{n=0}^{N_y-1} |\Delta d_n|^2 |Q_n(f_i)|^2 \end{aligned} \quad (13)$$

To get an idea about the optimal numbers N_x and N_y , the squared coherency r^2 from Eq.(10) is split up into the contributions $(r_{x,n})^2$ and $(r_{y,n})^2$ of each polynomial P_n and Q_n using the orthogonality condition of Eq.(7) and the assumption that B_x and B_y are uncorrelated:

$$\begin{aligned} r^2 &= \sum_{n=0}^{N_x-1} \left(\frac{\langle |B_{x,n}|^2 W \rangle |c_n|^2}{\langle |E|^2 W \rangle} \right) + \sum_{n=0}^{N_y-1} \left(\frac{\langle |B_{y,n}|^2 W \rangle |d_n|^2}{\langle |E|^2 W \rangle} \right) \\ &= \sum_{n=0}^{N_x-1} (r_{x,n})^2 + \sum_{n=0}^{N_y-1} (r_{y,n})^2 \end{aligned} \quad (14)$$

Following an estimation of Goodman (1957), only those polynomials P_n and Q_n are used which give a significant contribution $(r_{x,n})^2$ or $(r_{y,n})^2$, e.g.

$$\left. \begin{aligned} (r_{x,n})^2 \\ (r_{y,n})^2 \end{aligned} \right\} \geq \frac{10}{v_2} \quad (15)$$

with v_2 being the number of degrees of freedom. Additional polynomials will not yield a remarkably better estimation of the transfer functions X and Y .

Numerical example

The above method is applied to a set of simultaneously recorded time series of the horizontal magnetic and telluric field variations at Göttingen. Each time series exists of hourly mean values of a continuous 100-day registration. As there are long-periodic trends in the electric field it is high-pass filtered with a cut-off period of 2 days; therefore, the analysis covers the frequency range from 0.5 cpd(=cycles per day) to the Nyquist frequency of 12 cpd with frequency spacing of 0.01 cpd.

As the harmonic coefficients of B_x and B_y are very large and highly correlated in a small frequency band of 0.03cpd width at the frequencies of the solar daily variation 1, 2, 3, 4 cpd and thus would cause the bivariate approach to fail, the weight function W is set to zero for these frequencies and to unity otherwise. It is also set to zero in a 0.03-cpd-wide frequency band centred at 1.93 cpd, the lunar tidal period M_2 , where a sharp peak in the residual electric field is found. With allowance for the missing frequencies, the number of analysed harmonic coefficients is $M=1151-5 \cdot 3=1136$.

The squared coherency $(r_{xy})^2$ between B_x and B_y is very small for the analysed frequency interval: $(r_{xy})^2=0.0003$.

Table 1. Parts $(r_{x,n})^2$ and $(r_{y,n})^2$ of the estimated squared coherency r^2 according to Eq. (14). The boldface numbers exceed the significant boundary value of 0.0044 according to Eq. (15)

n	0	1	2	3	4
$(r_{x,n})^2$	0.1405	0.0065	0.0001	0.0035	0.0008
$(r_{y,n})^2$	0.2731	0.0372	0.0162	0.0018	0.0019

Table 1 lists the different contributions $(r_{x,n})^2$ and $(r_{y,n})^2$ to the estimated multiple squared coherency r^2 .

The coherency condition according to Eq.(15) is 0.0044. It follows that $X(f)$ is sufficiently presented by the first two polynomials and $Y(f)$ by the first three polynomials.

Figure 1 shows the resulting real and imaginary parts of X and Y for $N_x, N_y=1, \dots, 5$ in comparison with the band-averaged estimates. The solid curves represent the transfer functions which are chosen by the coherency condition. Especially for higher frequencies do the band-averaged estimates of X scatter strongly. Consequently, additional polynomials of higher order do not alter the pattern of the transfer function. There is a significant difference just between the curves of the imaginary part of X corresponding to $N_x=1$ and $N_x=2$. This difference is responsible for the improved squared coherency in Table 1 and the acceptance of $N_x=2$ as the optimal number.

There is less scattering for the estimates of Y . For the real and imaginary parts, polynomials of higher order than $N_y=2$ do not significantly change the shape of the transfer functions. The comparison of the smooth polynomial presentation with the band-averaged transfer function shows good agreement and thus confirms the validity of the coherency condition. The following section will demonstrate that the calculation of the confidence limits is also consistent for both methods.

Treatment of disturbed electric field records

Generally, long records of electric field variations are partially interrupted because of artificial noise, problems with the electronic devices, etc., while the records of the magnetic field variations usually are less disturbed. In the case of an undisturbed record of the magnetic field, an iteration procedure is applied to estimate the transfer function on the basis of all the available electric field data.

The disturbed intervals in the electric field record are linearly interpolated and preliminary transfer functions are estimated from the *complete* time interval. The preliminary transfer functions serve to estimate the electric field variations during the gap interval. Then the calculation of the transfer functions is repeated using the new electric field record. If the ratio q of the sum of the gaps to the length of the time series is not too large, e.g. $q \leq 0.2$, and the quality of the data is not too bad, the new estimated transfer function will yield an improved squared coherency r^2 . The iteration procedure will be repeated until r^2 does not change by more than 5%.

As the iteration procedure will pretend a higher confidence of the estimation, three corrections have to be considered for the calculation of the confidence intervals. In the following and in Appendix B, the prime marks the uncorrected quantities.

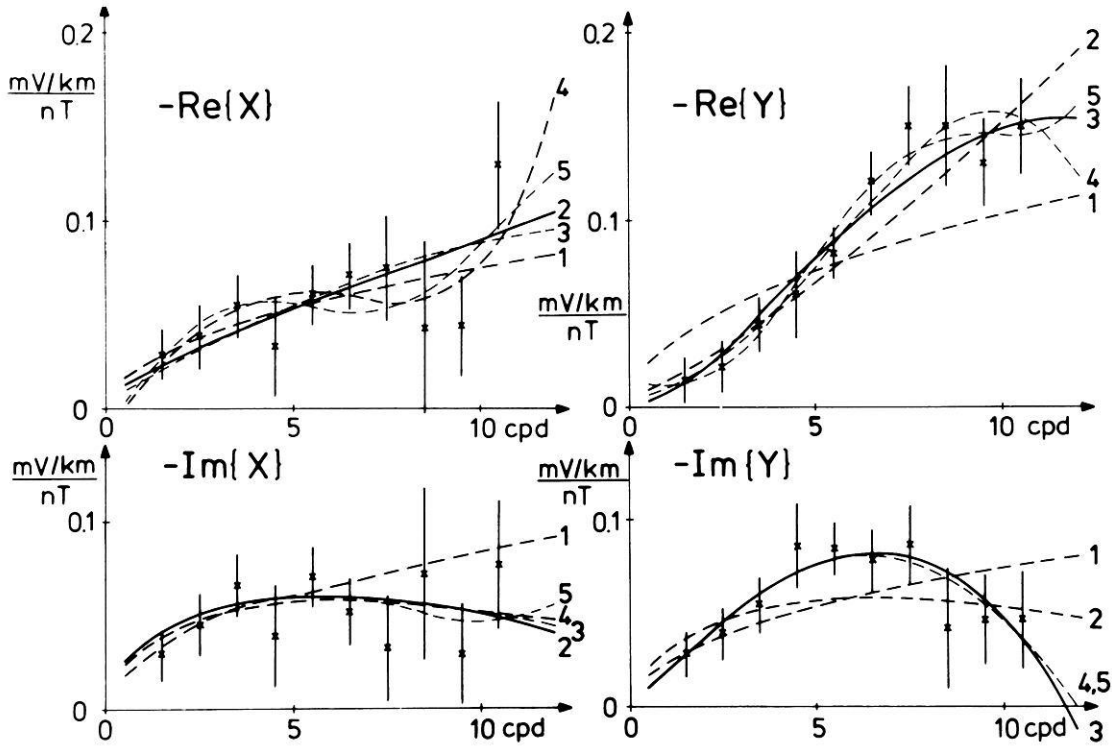


Fig. 1. Transfer functions $X(f)$ and $Y(f)$ between the telluric east component and the magnetic north and east components near Göttingen calculated from a 100-day record. *Dashed and solid curves* represent the polynomial representation for $N_x, N_y = 1, \dots, 5$. *Crosses* mark the estimates which result from the band-average method (Parzen windows of equivalent bandwidth 1.0 cpd, centred at 1.5, 2.5, ..., 10.5 cpd) with 68% error bars. Confidence limits for the polynomials were omitted for clarity; they are shown in Fig. 2

a) $v' = 2(M - N_x - N_y)$ is the number of degrees of freedom from the whole time series as if there were no gaps. It follows directly that

$$v = v'(1 - q) \quad (16)$$

b) As the power of the residual electric field $\langle |\delta E|^2 \rangle$ results from the undisturbed part of the time series it has to be enlarged by the factor $1/(1 - q)$

$$\langle |\delta E|^2 \rangle = \frac{\langle |\delta E'|^2 \rangle}{1 - q} \quad (17)$$

c) The multiple squared coherency r^2 will change (see Appendix B) according to

$$r^2 = \frac{(1 - q)(r')^2}{1 - q(r')^2} \quad (18)$$

Figure 2 demonstrates the influence of data gaps on the estimation of the complex transfer function Y treated in the last section and its confidence intervals. For this purpose, four intervals (46, 65, 40 and 87 h) of the 100-day time series were arbitrarily chosen as gaps, thus yielding a total amount of 10% "disturbed" data. Analogously, doubled lengths of the gaps produced 20% loss of data. The transfer functions are again compared to the band-averaged estimates (see Fig. 1). The relative error of the polynomial presentation decreases towards higher frequencies, until above 10 cpd the polynomials of higher order obviously create the increase of the relative error. By the influence of data gaps, the imaginary part of Y is apparently underestimated in the frequency range around 6 cpd. In this

frequency range the relative error also increases significantly. However, the polynomial approach seems to be rather stable with allowance to the confidence region.

Additionally, the size of the confidence regions calculated by the polynomial approach reflects very well the pattern of the band-averaged estimates and the size of their error bars. This fact confirms the consistency among the estimated confidence regions!

Appendix A

Calculation of the coefficients of weighted orthogonal polynomials

In Eq. (6), polynomials $P_n(f_i)$ and $Q_n(f_i)$ are introduced which fulfil the orthogonality condition in Eq. (7). The algorithm to calculate the polynomial coefficients $p_{n,i}$ and $q_{n,i}$ is described by Forsythe (1957) and shall be summarized for $P_n(f_i)$ only, as the calculation follows the same scheme for $Q_n(f_i)$.

Equation (6) is rewritten as

$$P_{ni} = P_n(f_i) = \sum_{i=0}^n p_{n,i}(f_i)^i \quad (19)$$

$$n = 0, \dots, N_x, \quad i = 1, \dots, M$$

Equation (7) yields

$$\sum_{i=1}^M P_{ni} P_{n'i} w_i = \begin{cases} \sum_{i=1}^M (P_{ni})^2 w_i & \text{for } n = n' \\ 0 & \text{for } n \neq n' \end{cases} \quad (20)$$

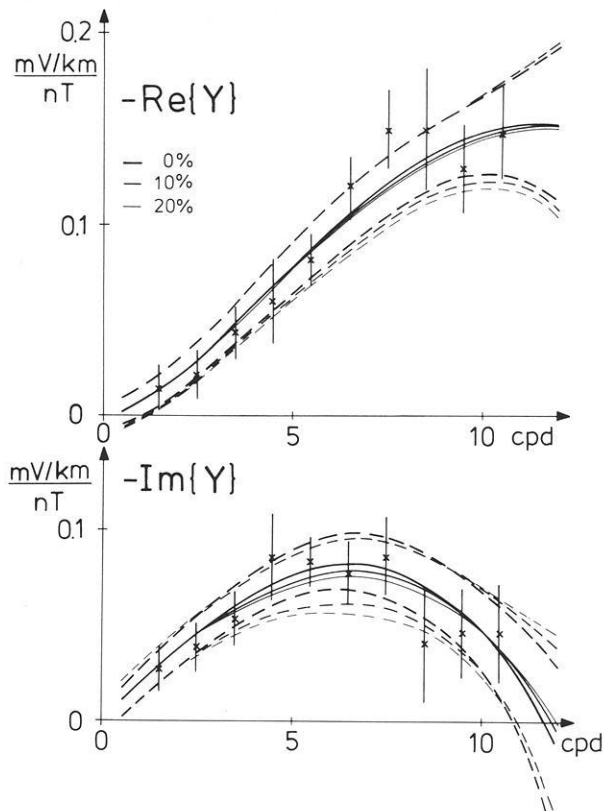


Fig. 2. Influence of disturbed data on the estimation of the transfer function Y at Göttingen. The *solid curves* refer to the polynomial approach with three polynomials including their 68% confidence limits (*dashed lines*). The decreasing thicknesses of the lines mark the estimates of the analysis with 0%, 10% and 20% disturbed data. They are compared to the band-averaged estimates (*crosses with vertical bars*) taken from the undisturbed time series as in Fig. 1

with $w_i = f_i |B_x(f_i)|^2 W(f_i)$ being a non-negative weight function.

The polynomials P_n are presented by a recursive formula with an additionally defined polynomial P_{-1}

$$\begin{aligned} P_{(-1)i} &= 0 \\ P_{0i} &= 1 \\ P_{(n+1)i} &= (f_i - \alpha_{n+1}) P_{ni} - \beta_n P_{(n-1)i}, \quad n=0, \dots, N_x-1; \end{aligned} \quad (21)$$

α_n and β_n can be determined using the orthogonality condition (20). Multiplying the third equation of Eq. (21) with P_{ni} and $P_{(n-1)i}$, respectively, and summing over i with allowance for w_i yields

$$\alpha_{n+1} = \frac{\sum_{i=1}^M f_i (P_{ni})^2 w_i}{\sum_{i=1}^M (P_{ni})^2 w_i} \quad \beta_n = \frac{\sum_{i=1}^M f_i P_{ni} P_{(n-1)i} w_i}{\sum_{i=1}^M (P_{(n-1)i})^2 w_i} \quad (22)$$

The polynomial coefficients $p_{n,i}$ can be calculated using Eqs. (19) and (21). The numerical evaluation of $p_{n,i}$, however, is of minor interest, as the values of $P_n(f_i)$ are numerically determined by the recursion formula (21).

Appendix B

Squared coherency in the case of an analysis with data gaps in the telluric field

According to Eq. (1), each harmonic coefficient of the telluric field $E(f_i)$ is the sum of the predicted telluric field $E_p(f_i)$ and the uncorrelated residuum $\delta E(f_i)$

$$E(f_i) = E_p(f_i) + \delta E(f_i) \quad (23)$$

As $\langle \delta E' E_p^* \rangle = 0$ because of the normal equations (9), the squared coherency $(r')^2$ from Eq. (10) can be rewritten as

$$r^2 = \frac{\langle |E_p|^2 \rangle}{\langle |E|^2 \rangle} = \frac{1}{1 + \langle |\delta E|^2 \rangle / \langle |E_p|^2 \rangle} \quad (24)$$

Let q be the ratio of the sum of the intervals with missing data to the length of the time series. Then the calculated residuum $\langle |\delta E|^2 \rangle$ is, according to Eq. (17),

$$\langle |\delta E|^2 \rangle = (1-q) \langle |E|^2 \rangle \quad (25)$$

Therefore, the calculated coherency $(r')^2$ is biased and has to be corrected by inserting Eq. (25) into Eq. (24)

$$r^2 = \frac{1}{1 + \langle |\delta E|^2 \rangle / \langle |E_p|^2 \rangle} = \frac{(1-q)(r')^2}{1 - q(r')^2} \quad (26)$$

Acknowledgements. I thank Prof. Dr. U. Schmucker for many helpful discussions and two anonymous reviewers for their critical and helpful remarks.

References

- Forsythe, G.E.: Generation and use of orthogonal polynomials for data-fitting with a digital computer. *J. Soc. Indust. Appl. Math.* **5**, No. 2, 74-88, 1957
- Goodman, N.R.: On the joint estimation of the spectra, co-spectrum and quadrature spectrum of a two-dimensional stationary Gaussian process. Scientific paper **10**, Engineering Statistics Lab., New York University 1957
- Jenkins, G., Watts, P.: *Spectral analysis and its applications*. San Francisco: Holden Day 1968
- Larsen, J.C.: Low frequency (0.1-6.0 cpd) electromagnetic study of deep mantle electric conductivity beneath the Hawaiian Islands. *Geophys. J. R. Astron. Soc.* **43**, 17-46, 1975
- Larsen, J.C.: Electromagnetic response functions from interrupted and noisy data. *J. Geomagn. Geoelectr.* **32**, 17-46, 1980

Received October 13, 1987; revised version December 14, 1987
Accepted December 16, 1987